

PART I:
PETROLOGY AND PETROGENESIS OF THE TRINITY PERIDOTITE,
NORTHERN CALIFORNIA

PART II:
PETROGENESIS OF LUNAR BRECCIA 12013

Thesis by
James Edward Quick

In Partial Fulfillment of the Requirements
for the Degree of
Doctor of Philosophy

California Institute of Technology
Pasadena, California

1981
(Submitted July 18, 1980)

ACKNOWLEDGMENTS

I am indebted to numerous persons for scientific, technical, logistical and financial support during my graduate work at the California Institute of Technology.

Arden L. Albee suggested the problem that constitutes Part II of this thesis, and has continued to provide valuable scientific course corrections for both my lunar and terrestrial studies. Odette B. James contributed many significant observations and interpretations to Part II, as well as excellent short courses in petrography, journalism and petrology of lunar breccias. Discussions with fellow graduate student Robert Gregory, and with Robert Coleman and Françoise Boudier greatly enhanced my understanding of the Trinity peridotite. My father, George L. Quick, was the instrument man during the plane table mapping of Vicki and Lou Ann Bluffs.

The electron microprobe laboratory at the California Institute of Technology was used extensively in my thesis work, and Arden L. Albee and Arthur A. Chodos are gratefully acknowledged for creating and maintaining that excellent facility. Arthur A. Chodos also provided many hours of assistance in creating new programs for the automated microprobe and for data reduction.

Lou Ann Cordell suffered through many retypings of the lunar work and typed most of the tables in this thesis.

Vicki, my wife, provided all of the logistical support, both in the field and at home, put up with a lot, and kept the squirrels at bay.

This research was generously funded by Arden L. Albee through NSF grants EAR-75-03416-A03 and EAR-7919786 and NASA grant NGL-05-002-338, and by Geological Society of America grants 2139-76, 2244-77 and 2386-78.

ABSTRACT

Part I presents the results of a petrologic investigation of the Trinity peridotite, an enormous ultramafic massif in northern California. The Trinity is an easterly dipping sheet several km thick and composed of a diverse assemblage of ultramafic rocks including dunite, harzburgite, lherzolite, plagioclase lherzolite and clinopyroxene-rich dikes. Because of this diversity and the limited serpentinization, it is an excellent natural laboratory for studying the petrogenesis of ultramafic rocks. The structural history of the peridotite was outlined by detailed field mapping at scales of 1:31,250 and 1:240 at the northeast margin of the massif in the vicinity of Mount Eddy and China Mountain during the summers of 1977-1978. A combined petrographic and electron microprobe investigation was made on selected samples to determine their petrology, mineral chemistry and major element whole rock compositions.

The Trinity peridotite is inferred to have originated in the upper mantle at a depth of not less than ~30 km and perhaps as deep as 100 km based on textural evidence for a transition from the spinel lherzolite (>10 kb) stability field to the plagioclase lherzolite (<10 kb) stability field, and on high equilibration temperatures (>1150° C.) preserved in cores of large pyroxene grains. During ascent through the mantle, the rocks deformed plastically, partially melted and reacted with transient melts derived from greater depth. Plastic deformation produced two generations of folds and a penetrative foliation. Pervasive partial melting of the plagioclase lherzolite produced feldspathic segregations, plagioclase-rich veins and resorption textures in pyroxenes and spinel; the composition of the veins suggests that this melt was essentially basaltic. Another melt, not in equilibrium with the peridotite, but also of basaltic

affinity, passed through the peridotite, reacted with the ultramafic wall rocks to produce large tabular dunite bodies surrounded by zones of harzburgite and lherzolite, and crystallized clinopyroxene-rich dikes. The end of the ascent of the Trinity through the mantle is marked by intrusion of gabbro, hornblende diorite, diabase and albite granite, and the onset of brittle deformation circa 450-480 m.y. based on zircon ages of the granites (Mattinson and Hopson, 1972). The Trinity was subsequently thrust into the crust at about 380 m.y. based on Rb-Sr dates on rocks of the underlying Central Metamorphic Belt. It is suggested that the passage of the Trinity through the mantle may have occurred beneath an actively spreading back-arc basin.

Part II of this thesis is a petrologic investigation of Lunar Rock 12013, one of the most significant lunar samples because of its extreme enrichments in incompatible elements (K, REE, U, etc.) and abundant "granitic" material.

Rock 12013 is best interpreted as a complex mixture of two polymict, impact generated breccias--one black, the other gray. The black breccia is a fragment-laden melt-rock formed by mixing cold, impact-derived mineral and lithic clasts with superheated impact melt of basaltic composition. The melt is now crystallized to an aphanite of minute grain size. The gray breccia was also formed as a mixture of melt and impact-derived clasts, but the melt was granitic and crystallized to a fine grained felsite. The clasts in the breccias were derived from lithologies common in Highlands breccias, with the gray breccia dominated by feldspathic gabbro and basalt clasts and the black breccia dominated by quartzofeldspathic and norite clasts. A combined neutron activation, petrographic and electron microprobe analysis demonstrates that the incompatible elements in 12013 are concen-

trated in the melt-derived lithologies. The origin and relationships of the melts is problematic. Textural relations suggest that the two melts coexisted but did not mix, and some aspects of their major element abundances are compatible with a genetic relationship involving silicate liquid immiscibility (SLI). However, details of their trace element abundances are incompatible with SLI.

It is suggested that 12013 is exotic to the Apollo 12 site and was formed by an impact(s) into a terrane of norite and quartzofeldspathic plutonic rocks, gabbro and basalt hypabyssal or extrusive rocks, and a thin regolith cover. The two breccia were derived from different parts of this terrane and mixed violently in the ejecta cloud. Most of the radiometric clocks were reset by this event, and Rb-Sr, U-Th-Pb and ^{40}Ar - ^{39}Ar yield ages of ~ 4.0 AE. Rb-Sr data, however, may be interpreted to suggest an age for the felsite protolith of ~ 4.5 AE. An alternative explanation, consistent with the petrography of the rock, is that the Rb-Sr data reflect mixing and partial equilibration at 4.0 AE of materials no older than 4.2 AE.

TABLE OF CONTENTS

PART I: PETROLOGY AND PETROGENESIS OF THE TRINITY PERIDOTITE,
NORTHERN CALIFORNIA

INTRODUCTION	2
REGIONAL SETTING	7
PREVIOUS INVESTIGATIONS	16
INVESTIGATION METHODS	21
Field Work	22
Laboratory Methods	22
ROCK TYPES OF THE STUDY AREA	29
Introduction	30
Peridotite	30
Introduction	30
Plagioclase Lherzolite	34
Lherzolite	38
Harzburgite	39
Dunite	40
Clinopyroxene-Rich Rocks	44
Associations and Spatial Relationships	48
Serpentinization	56
Plagioclase-Rich Veins	61
Gabbro and Related Accumulate Rocks	62
Introduction	62
Interlayered Wehrlite and Dunite	63
Interlayered Pyroxenite and Olivine-Pyroxenite	67
Feldspathic Clinopyroxenite	67
Gabbro	67
Accumulate Origin	70
Pegmatitic Gabbro Dikes	70
Microgabbro Dikes	71
Alteration	74
Nature of the Peridotite-Gabbro Contact	74
Albite Granite	75
Hornblende Diorite	76
Diabase	77
Paleozoic(?) Sedimentary and Volcanic Rocks	77
Quaternary Deposits	78
STRUCTURAL HISTORY	80
Introduction	81
The Vicinity of Mount Eddy and China Mountain	82
Relative Ages of Events	82
Absolute Ages of Events	92
Summary	94

Trinity Alps	96
Synthesis	100
PETROGRAPHY	102
Introduction	103
Primary Mineralogy and Textures	104
Plagioclase Lherzolite	104
Lherzolite	121
Harzburgite	121
Dunite	122
Clinopyroxene-Rich Dikes	126
Alteration	131
Conclusions	132
MINERAL CHEMISTRY	136
Introduction	137
Olivine	138
Orthopyroxene	148
Clinopyroxene	161
Spinel	165
Plagioclase	175
Progressive Changes in Mineral Composition	179
Summary and Conclusions	190
BULK COMPOSITIONS	198
EQUILIBRATION TEMPERATURES AND PRESSURES	203
DISCUSSION	211
Introduction	212
Mantle Origin of the Trinity Peridotite	213
Regional Partial Melting of the Plagioclase Lherzolite	215
Evidence	215
Composition of the Melt	220
Petrogenesis of Large Dunite Bodies	230
Websterite Dikes and Depleted Zones	235
Reaction Between Melt and Wall Rocks	240
Summary and Conclusions	248
Origin of the Gabbroic Rocks	250
P-T Trajectory	252
Speculations on the Tectonic Setting	258
Conclusions	271
REFERENCES	276
APPENDIX TO PART I	287
PLATES	
I Geologic Map of the Trinity Peridotite in the Vicinity of Mount Eddy and China Mountain, Northern California	in pocket
II Geology of Vicki Bluff, Trinity Peridotite, Northern California	in pocket

PLATES (cont.)

III Geology of Lou Ann Bluff, Trinity Peridotite,
Northern California

in pocket

FIGURES

1	Distribution of ultramafic, gabbroic and granitic rocks in northern California	10
2	Generalized geologic map of the Trinity peridotite	15
3	Electron microprobe analyses of the Boyd forsterite	24
4	IUGS classification of peridotite	33
5	Plagioclase lherzolite, harzburgite and dunite in outcrop	36
6	Clinopyroxene pods and grains, wehrlite layers, and hand specimen appearance of ariegite	43
7	Relationships between websterite dikes and wall rocks	51
8	Websterite dikes	55
9	Plagioclase-rich veins	60
10	Cumulate structures, Toad Lake gabbro	65
11	Gabbro and diabase in outcrop	69
12	Microgabbro dikes in outcrop	73
13	Structures in the Trinity peridotite	84
14	Orientations of Structures at Vicki and Lou Ann Bluffs	87
15	Deformation effects in the Trinity Alps	99
16	Representative textures of peridotite	106
17	Textures of orthopyroxene porphyroclasts	109
18	Deformation features in olivine and orthopyroxene	112
19	Textures of interstitial clinopyroxene	115
20	Textures of interstitial plagioclase and pyroxene	117
21	Plagioclase-spinel relationships	120
22	Textures of clinopyroxene-rich rocks	129
23	Fo-content of olivine	140
24	Fo-content of olivine as function of distance from spinel	142
25	CaO and NiO concentrations in olivine	144
26	Pyroxene quadrilateral (quantitative analyses)	147
27	Pyroxene composition in peridotite (point count data)	150
28	Pyroxene compositions in clinopyroxene-rich rocks and gabbro (point count data)	152
29	Pyroxene composition in plagioclase lherzolite 8W67	155
30	Al and Cr traverses across orthopyroxene	157
31	Point count study of a single pyroxene	159
32	Al, Cr, Ti, and Na traverses across clinopyroxene	163
33	Compositions of spinels in the Trinity peridotite	167
34	Variations in spinel composition across a depleted zone and a transition to dunite from plag. lherz.	169
35	Microprobe traverse across a spinel grain	172
36	Plagioclase compositions	174
37	Variation in olivine composition across a transition from plag. lherz. to dunite	178
38	Variation in spinel composition across a transition from plag. lherz. to dunite	181
39	Point Count traverses across lithologic boundaries	183
40	Variation in olivine composition across a depleted zone	186

FIGURES (cont.)

41	Variation in spinel composition across a depleted zone	188
42	Equilibration temperatures and pressures of pyroxenes in 8W67 and 9W20	210
43	Composition of plagioclase-rich vein projected onto the plane: Di-Ol-Si	223
44	Oxide-MgO diagrams depicting compositions of major peridotite lithologies	226
45	Compositions of websterite dikes and associated depleted zones normalized to host plag. lherz composition	238
46	Peridotite composition projected on Di-Ol-Si plane	244
47	Postulated P-T trajectory of the Trinity peridotite	254
48	Structural section of the Trinity "ophiolite", Samail ophiolite, and mean oceanic crust	261
49	Possible tectonic setting for the Trinity peridotite	267
50	Topographic map of the study area showing place names referenced in text	288

TABLES

1	Structural history of the Trinity peridotite	95
2	Petrography, mineralogy, and mineral chemistry of the Trinity peridotite	123
3	Petrography, mineralogy, and mineral chemistry of dikes, bands and veins.	124
4	Modal abundances of minerals in the Trinity peridotite	125
5	Petrography, mineralogy, and mineral chemistry of gabbro and related accumulate rocks	134
6	Petrography, mineralogy, and mineral chemistry of hornblende diorite, albite granite and diabase	135
7	Representative analyses of olivine	192
8	Representative analyses of orthopyroxene	193
9	Representative analyses of clinopyroxene	194
10	Representative analyses of spinel	195
11	Representative analyses of plagioclase	196
12	Representative analyses of amphibole	197
13	Major element abundances in the Trinity peridotite	200
14	Major element abundances in feldspathic or spinel lherzolites and model compositions for the mantle	201
15	Calculated equilibration temperatures for coexisting minerals in the Trinity peridotite	206
16	Estimated depth and sequence of events in the mantle history of the Trinity peridotite	255

PART II: PETROGENESIS OF LUNAR BRECCIA 12013

INTRODUCTION	290
GEOLOGY OF THE LANDING SITE	293
EXPERIMENTAL TECHNIQUES	295
HAND SPECIMEN DESCRIPTION	298
PETROGRAPHY	305
Petrographic overview	306
Introduction	306
Gray Breccia	306
Black Breccia	308
Major Distinction Between the Black and the Gray Breccias	309
Detailed Petrology of the Gray Breccia	310
Introduction	310
Lithic Clasts > 140 μm	310
Gabbro and Basalt	311
Granulated Norite	312
Tonalite	315
ANT-Suite Melt-Rock	315
Mineral Clasts > 140 μm	315
Deformation Textures in Clasts	316
Matrix (Clasts < 140 μm and Interstitial Felsite)	319
Felsite	326
Texture	326
Mineral Chemistry	331
Detailed Petrology of the Black Breccia	336
Introduction	336
Lithic Clasts > 140 μm	337
Quartzofeldspathic Rocks	343
Granulated Norite	344
Basalt	347
ANT-Suite Melt-Rock	347
ANT-Suite Hornfels	348
Plagioclase Porphyry	348
Pyroxene Lathwork	348
Mineral Fragments > 10 μm	349
Deformation Textures	350
Groundmass	351
Post-Consolidation Recrystallization and Reaction Features	361
CHEMICAL COMPOSITIONS OF THE FELSITE AND THE BLACK BRECCIA GROUNDMASS	381
Introduction	382
Sample Processing and Analytic Technique	382
Results	391
Distribution of Elements Between Phases	400

AGE CONSTRAINTS	405
Rb-Sr Systematics	406
Other Isotopic Data	409
Summary	411
DISCUSSION	413
Introduction	414
Breccia Genesis	414
Black Breccia	415
Gray Breccia	421
Relationships Between the Breccias	424
Temperature History	425
Black Breccia	425
Gray Breccia	428
Single vs. Multiple Impact Events	429
Melt Components	431
Introduction	431
Criteria for Silicate Liquid Immiscibility	433
Felsite as a Product of SLI	434
Black Breccia Groundmass as a Product of SLI	435
Felsite-Black Breccia Groundmass Relationship	436
Rb-Sr Systematics	445
Black Breccia	446
Gray Breccia	450
Evolved Rocks at 4.5 AE?	451
Source Terrane	460
Synthesis	466
REFERENCES	472
FIGURES	
1 Sawed surface of slab 12013,10	301
2 Composite of thin sections 12013,10,#13, #14 and #15	303
3 Textures of lithic clasts in the gray breccia	314
4 Textures of matrix and interstitial felsite in the gray breccia	318
5 Gross textures of felsite patches in the gray breccia	322
6 Textures of felsite in the gray breccia	324
7 Plagioclase compositions in the gray breccia	325
8 Pyroxene compositions in the gray breccia	327
9 Olivine compositions in the gray breccia	328
10 Ilmenite compositions in the gray breccia	329
11 Spinel compositions in the gray breccia	330
12 Compositions of felsite feldspars in the gray breccia	332
13 Compositions of felsite pyroxenes in both breccias	333
14 Bulk compositions of lithic clasts, felsite and black breccia groundmass	334
15 Normative compositions of lithic clasts, felsite and black breccia groundmass	335
16 Compositions of plagioclase in the black breccia	338
17 Compositions of pyroxene in the black breccia	339
18 Compositions of olivine in the black breccia	340
19 Compositions of ilmenite in the black breccia	341

FIGURES (cont.)

20	Compositions of spinel in the black breccia	342
21	Textures of lithic clasts in the black breccia	345
22	Texture of the black breccia	353
23	Gross textures of felsite in the black breccia	356
24	Texture and morphology of felsite in the black breccia	358
25	Compositions of feldspars in felsite in the black breccia	360
26	Recrystallization and reaction textures	362
27	Photomicrographs of black breccia sample 12013,10,16B	385
28	Maps of black breccia sample 12013,10,16B	387
29	Photomicrograph and map of part of gray breccia sample 12013,10,16B	388
30	Elemental abundances in breccia samples	394
31	Elemental abundances in felsite and black breccia groundmass	396
32	Rb-Sr evolution diagram for 12013	407
33	Photomicrographs and X-ray scans of felsite-black breccia groundmass contact	439
34	Photomicrographs and X-ray scans of immiscible silicate melts in 14310,6	441
35	Model for the Rb-Sr evolution of the gray breccia	458

TABLES

1	Relative abundances of clasts in gray breccia	367
2	Petrography, mineralogy, and mineral chemistry of gray breccia lithic clasts	368
3	Compositions of gray breccia lithic clasts	369
4	Textures and compositions of gray breccia mineral clasts	370
5	Representative feldspar analyses	371
6	Representative pyroxene compositions	372
7	Representative olivine compositions	373
8	Representative ilmenite compositions	374
9	Representative spinel compositions	375
10	Representative compositions of accessory phases	376
11	Relative abundances of clasts in black breccia	377
12	Petrography, mineralogy, and mineral chemistry of black breccia lithic clasts	378
13	Compositions of black breccia lithic clasts	379
14	Textures and compositions of black breccia mineral clasts	380
15	Compositions of the felsite and black breccia groundmass	392
16	Major, minor and trace element compositions of samples of the gray and black breccias	392
17	Calculated trace element composition of the felsite and black breccia groundmass	397
18	Least-squares compositional analysis of the black breccia	398

TABLES (cont.)

19	Least squares compositional analysis of the gray breccia	398
20	Sample descriptions for Figure 32	408

PART I:

PETROLOGY AND PETROGENESIS OF THE TRINITY PERIDOTITE,
NORTHERN CALIFORNIA

INTRODUCTION

This thesis presents the results of a detailed field, petrographic and electron microprobe study of a large ultramafic body situated in northern California — the Trinity peridotite. Evidence that is presented suggests that the Trinity peridotite originated in the upper mantle, and that many of its structures, and petrographic and chemical characteristics are records of processes that occurred while the peridotite was still resident there. The description and interpretation of these features constitute the focus of this report.

The nature of mantle processes is of fundamental importance to petrology and tectonics. The origins of the most voluminous extrusive rock in the earth's crust, basalt, are ultimately traced to partial melting of a peridotite mantle (Bowen, 1928; O'Hara, 1965; Ringwood, 1975, Yoder, 1976), and the great tectonic features of the world — orogenic belts, midocean ridges, transform faults and subduction zones — are generally regarded to be the crustal expression of events that are deeply rooted in the mantle. It is, therefore, natural that much attention has been devoted to understanding mantle processes and the literature is replete with references to and conjectures on their nature. Models such as partial melting (equilibrium and disequilibrium), zone refining, metasomatism, plastic deformation, convection and diapirism are frequently invoked. These concepts have been based on studies of peridotite xenoliths in basalts and kimberlites, on geochemical investigations of basalts, on geophysical investigations, and on field studies of fragments of mantle that have been emplaced in the crust. The advantage of the field investigations is that they provide geometric constraints at scales that are not resolvable by the other approaches.

Ultramafic rocks in orogenic belts have been termed alpine type ultramafic rocks (Benson, 1926; Hess, 1938), and appear to be natural field laboratories for mantle studies. These bodies of peridotite or serpentinitized peridotite are commonly deformed and metamorphosed, range in size from square centimeters to massifs of many thousand square kilometers, and are found in mountain belts throughout the world. The origin of these rocks has been a subject of debate from the 1920's to the 1970's. Crystallization from an ultramafic magma was championed by Hess (1938, 1955). Other investigators supported an igneous origin but preferred to form the peridotites as cumulates from basaltic magmas (Thayer, 1960, Challis, 1965; McTaggart, 1971). Recent theories hold that these rocks are fragments derived directly from the mantle although geologists differ on the mechanism by which they are emplaced into the crust. Emplacement has been postulated to be by diapirism (Loomis, 1972, 1975; Green 1964; Avé Lallemant, 1976) thrust emplacement of oceanic crust and underlying mantle onto the margins of continents (Coleman, 1971; Dewey and Bird, 1971) or by intracontinental thrusting that taps the mantle (Boudier, 1978). The significant point is that there has been an increasing consensus of opinion within the last 20 years that many ultramafic rocks in orogenic belts are fragments of the mantle. This hypothesis appears to be on solid ground in light of: (1) similarities in texture and mineralogy between these rocks and xenoliths of known mantle origin (Mercier and Nicolas, 1975); (2) density and seismic velocity constraints for the upper mantle (e.g. Woollard, 1970; Wang, 1970); and (3) the similarity between ophiolites and the seismic models for the oceanic crust and upper mantle (Christensen and Salisbury, 1975). Therefore,

these ultramafic rocks may contain important keys to the understanding of the processes that occur in the mantle.

Most ultramafic bodies are highly serpentized and contain only harzburgite and/or dunite, and, therefore, display an extremely limited primary mineralogy consisting of olivine \pm orthopyroxene \pm spinel. Investigations of mantle-derived xenoliths in basalts and kimberlites (e.g. Mercier and Nicolas, 1975; White, 1966; Boyd and Nixon, 1975) indicate that more mineralogically-diverse lithologies are present in the mantle. Furthermore, dunite and harzburgite are too strongly depleted in many elements (e.g. Al, Na, K, Ti, Ca and incompatible trace elements such as REE) to be appropriate source regions for mid-ocean ridge basalts (Ringwood, 1975). The enormous volume of these basalts indicates, therefore, that much of the mantle must be composed of other lithologies, and harzburgite and dunite are interpreted by many investigators (Dick, 1977; Coleman, 1977) to be the refractory residue left over after extensive removal of basaltic melt from a more "fertile" peridotite such as plagioclase, spinel or garnet lherzolite (Al-phase + opx + cpx + ol). Much of the evidence of the processes involved have, presumably, left the rocks with the basaltic component. It follows that the optimum place to study the physical relationships and processes that occur in the mantle is a peridotite body with a diverse assemblage of rocks that includes "fertile" peridotite as well as dunite and harzburgite.

The Trinity peridotite is an excellent natural laboratory for studying the conditions and processes that occur in the mantle. Located in the eastern Klamath Mountains of northern California, it is the largest outcrop of ultramafic rocks in North America. This mas-

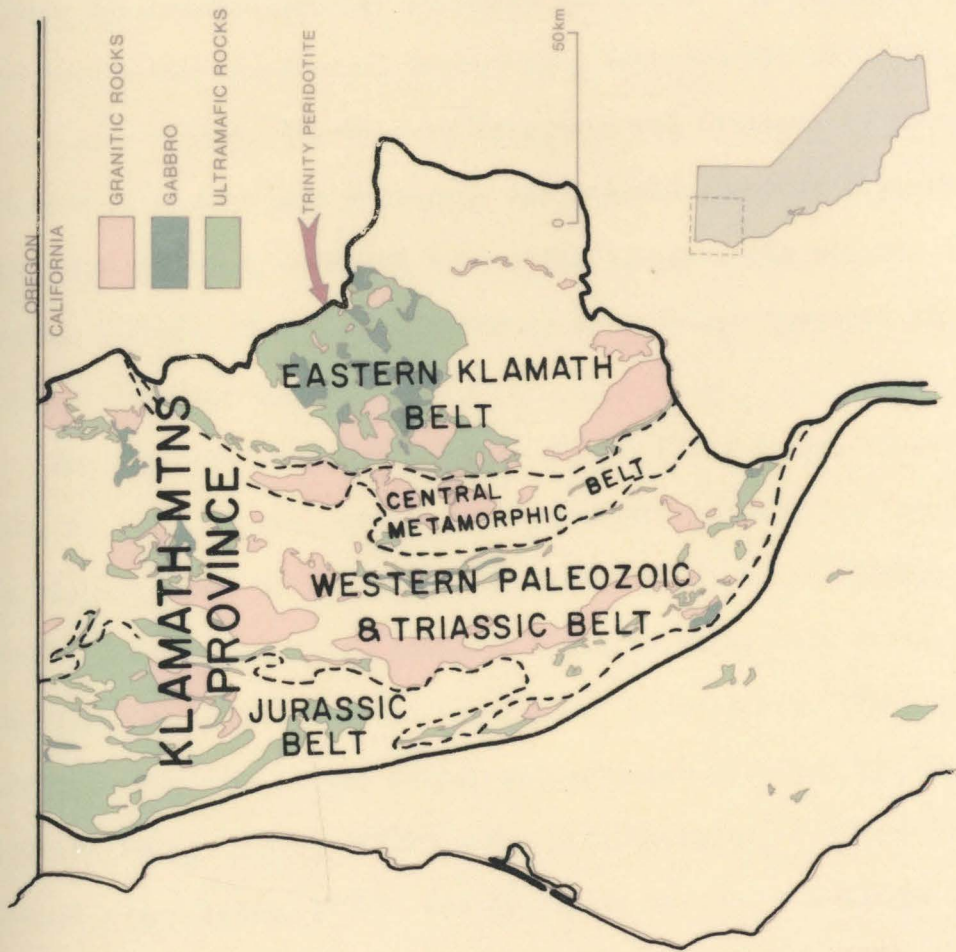
sif is made up of a diverse assemblage of ultramafic rocks including dunite, harzburgite, plagioclase lherzolite, and clinopyroxene-rich lithologies. Although much of the peridotite is highly serpentized, its structural history and the relationships between these lithologies are well displayed in large glaciated outcrops of relatively un-serpentized peridotite. Both petrographic and mineral composition data support a high pressure and high temperature origin for the Trinity peridotite (Quick and Albee, 1979a). The rocks at the northeastern margin of the massif preserve a record of metamorphic and deformational events that occurred during the ascent of the peridotite through the upper mantle from an initial depth of at least 30 km (Quick and Albee, 1979a, 1979b; Quick et al., 1980), and the rocks at the southwestern margin preserve a record of the crustal emplacement of the peridotite and subsequent metamorphism and deformation during intrusion of Mesozoic granitic plutons (Lipman, 1964). This thesis reports on the mantle history of the Trinity peridotite as it is inferred from field mapping at the northeast margin of the massif and detailed petrographic and electron microprobe investigations of selected samples.

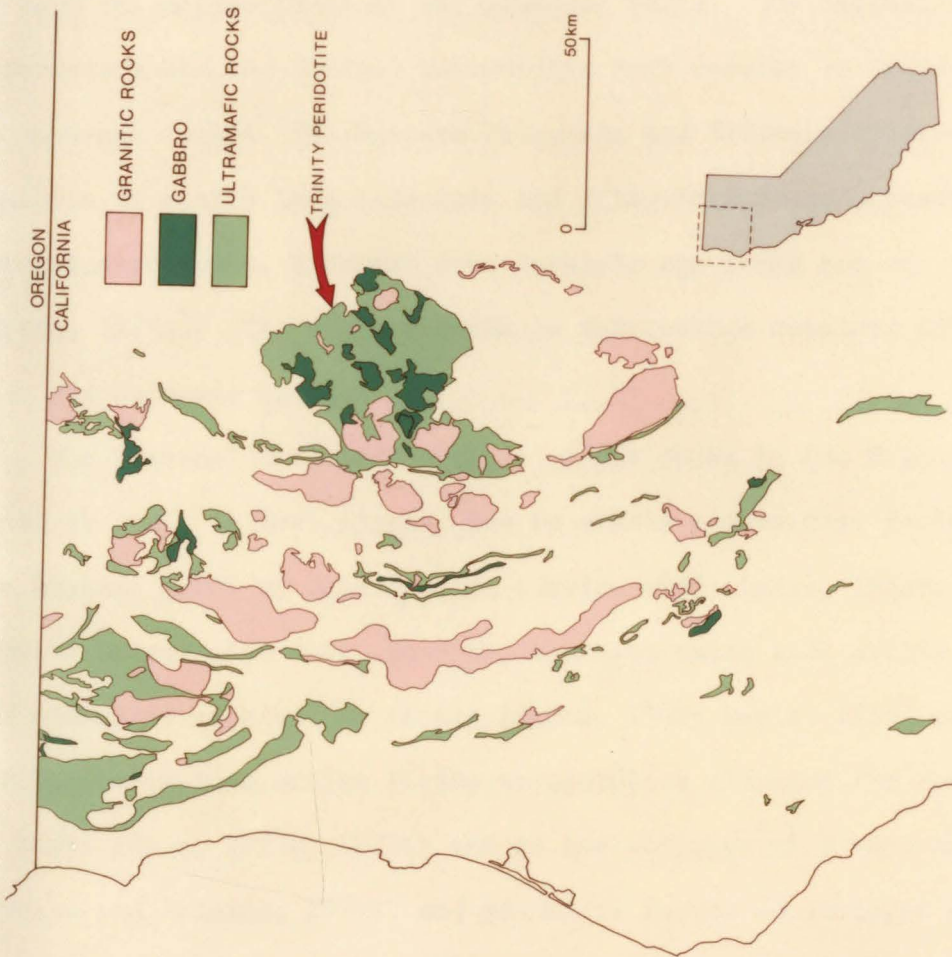
REGIONAL SETTING

The Trinity peridotite underlies an extensive area in northern California between the latitudes of 40°50' and 41°30' north and the longitudes of 123° to 122°15' west. The peridotite truly constitutes a massif in every sense of the term. Contiguous outcrops of ultramafic rocks occur over an area that is about 50 km wide and 75 km long, covering an area of about 2100 km², and rising topographically up to 1000 m above the surrounding volcanic and sedimentary rocks to form the crest of the eastern Klamath Mountains. This massif is situated in the eastern Klamath Mountains, and is centered about 40 km west of Mount Shasta and about 60 km south of the Oregon-California border.

Figure 1 is a map of northern California depicting the location of the Trinity peridotite relative to the larger gabbro and granitic bodies and the other occurrences of ultramafic rocks. The Trinity peridotite is located within the eastern part of the Klamath Mountains province and is overlain by the younger Cenozoic rocks of the Cascade province to the northeast. The Klamath province is underlain mostly by Paleozoic and Mesozoic metasedimentary and metavolcanic rocks, but also contains significant amounts of peridotite and gabbroic and granitic rocks. Regional mapping (Irwin 1960, 1966, 1972, 1977a; Davis et al., 1965; Ando et al., 1977) demonstrated that these rocks are divisible into separate terranes that differ significantly in age, and/or structural and metamorphic history, and which are, in fact, easterly dipping, thrust-bounded sheets that are allocthonous and stacked upon one another. The rocks within each of these terranes constitute coherent stratigraphic sequences of rocks with similar age and/or similar metamorphic and structural histories. For the

Figure 1: Distribution of ultramafic, gabbroic and granitic rocks in northern California. Clear plastic overlay shows the boundaries of the subprovinces of the Klamath Mountains province.





most part, these terranes are currently interpreted as fragments of ophiolites and/or island arc complexes (Davis et. al., 1978; Hamilton, 1969, 1978; Snoke et al., 1977; Ando et al., 1977).

Irwin (1960, 1966, 1972) divided the Klamath Mountains into four subprovinces based on the recognition of these thrust faults and intervening terranes. From east to west these are the Eastern Klamath subprovince, the Central Metamorphic Belt, the Western Paleozoic and Triassic subprovince, and the Western Jurassic subprovince. A general tendency for these rocks to young to the west is reflected in the ages of both the metasedimentary and plutonic rocks. The Eastern Klamath subprovince and the Central Metamorphic Belt consist of Ordovician to Jurassic rocks. The Western Paleozoic and Triassic subprovince consists of mostly Late Paleozoic and Triassic metasedimentary and metavolcanic rocks, although some Jurassic age rocks are now identified (Irwin, 1977a). The Western Jurassic subprovince consists of rocks that are Jurassic in age.

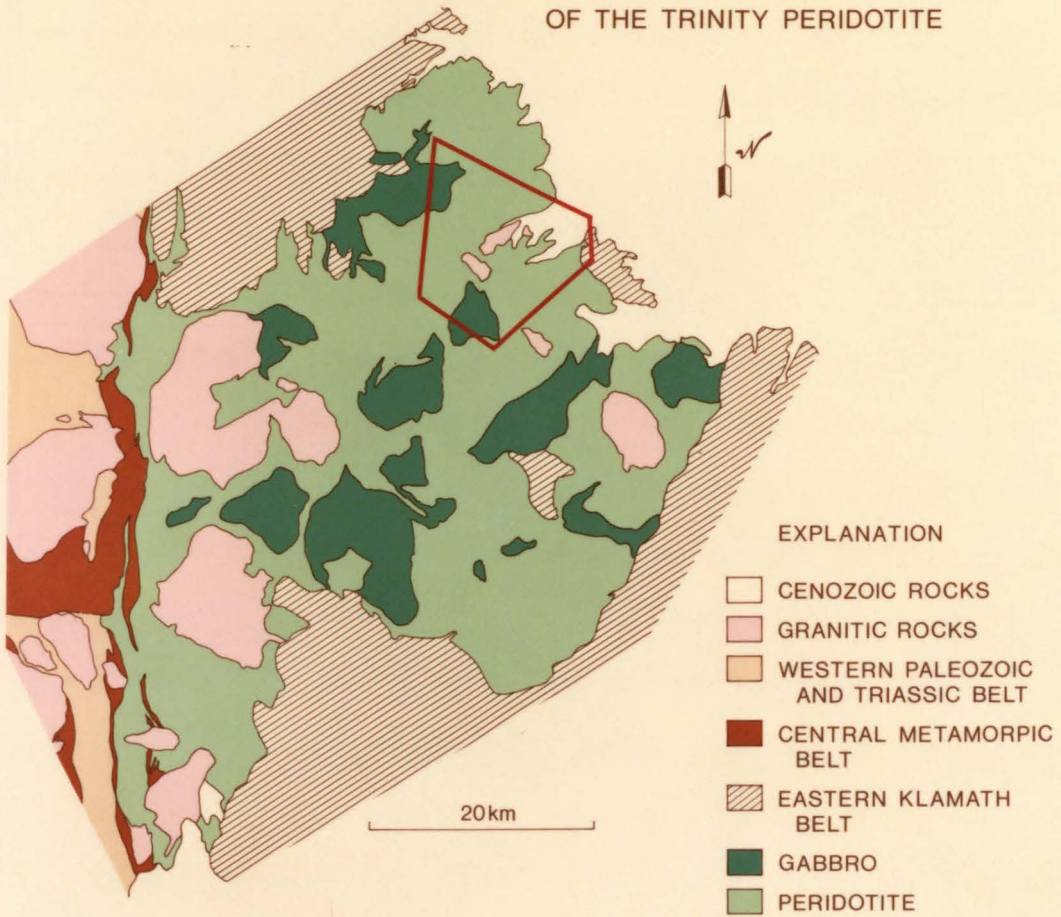
The regional metamorphic grade of the rocks in the Klamath Mountains is low. In most places, low to middle greenschist facies is the highest grade of metamorphism (Irwin, 1966; Davis, 1966). The Central Metamorphic Belt, however, contains rocks that attain epidote and almandine amphibolite facies (Irwin, 1966; Davis, 1966) and further north blue schist facies metamorphism affected the rocks west of Yreka (Hotz, 1973a, 1973b) and in the vicinity of Condry Mountain (Donato and Coleman, 1979), and granulite facies assemblages are developed in the vicinity of Seiad Mountain (Medaris, 1975).

The relationships between the Trinity peridotite and the surrounding rocks are displayed in the generalized geologic map in

Figure 2. Regional mapping (Irwin, 1966; Irwin and Lipman, 1962; Lipman, 1964) suggests that the peridotite forms an easterly dipping sheet that is sandwiched between the overlying Eastern Klamath Subprovince and the underlying Central Metamorphic Belt. This hypothesis is supported by gravity and magnetic modeling by Griscom (1977) who also concluded that the Trinity peridotite extends to the northeast under the cover of Cenozoic volcanic rocks of the Cascade Province.

The Trinity peridotite is important within the context of the regional geology of the Klamath Mountains for several reasons. First, isotopic age determinations of up to 480 m.y. on gabbroic plutons that intrude the peridotite (Lanphere et al., 1968; Mattinson and Hopson, 1972) are the oldest dates determined in the Klamath Mountains and provide a minimum age for the Trinity peridotite. This indicates that any discussion of the evolution and regional geology of the Klamath Mountains must begin with the Trinity peridotite. Second, the fact that the Trinity peridotite overlies the Central Metamorphic Belt suggests that the Trinity peridotite may be in some way related to the higher grade metamorphism of those rocks. Third, the Trinity peridotite may be in some way genetically related to the overlying rocks of the Eastern Klamath Belt. Lindsley-Griffin (1977) suggested that, in fact, the Trinity peridotite is the basal ultramafic section of a lower Paleozoic ophiolite and that the mafic portion of that ophiolite comprises the base of the Eastern Klamath Belt to the north of the Trinity massif.

Figure 2: Generalized geologic map of the Trinity peridotite. The area mapped for this thesis is indicated by the polygon.

GENERALIZED GEOLOGIC MAP
OF THE TRINITY PERIDOTITE

PREVIOUS INVESTIGATIONS

Only two detailed studies (Lipman, 1964; Goullaud, 1977) have been made on portions of the Trinity peridotite despite its large size and regional significance. Most of the geologic investigations that were conducted in the vicinity of the peridotite were physically and/or topically peripheral to it. These include: (1) regional mapping in the vicinity of the Trinity peridotite (Hinds, 1935; Irwin and Lipman, 1962; Ando et al., 1977); (2) exploration for mineral resources within the peridotite (Southern Pacific Co.); (3) structural and stratigraphic studies of subjacent and superjacent rocks (Lindsley-Griffin, 1977; Rohr and Bucot, 1971; Rohr and Potter, 1973; Davis et al., 1965) (4) investigations of younger granitic intrusive rocks (Lipman, 1963; Vennum, 1980); (5) isotopic age determinations on younger intrusive and metamorphic rocks (Lanphere et al., 1968; Mattinson and Hopson, 1972); and (6) regional geophysical studies (Irwin and Bath, 1962; LaFehr, 1966; Griscom, 1977). As a result, some constraints may be placed on the gross structure of the Trinity peridotite, and on the sequence and, in some cases, the actual ages of events that have affected it. However, neither a good picture of the internal structure of the entire body, nor a complete synthesis of the petrogenetic and structural events and conditions attending those events exists. In view of the immense size of the Trinity massif and its old age, these data are clearly critical to tectonic reconstructions of the eastern Klamath Mountains.

The early studies that considered the Trinity peridotite were regional in scope. Hinds (1935) first recognized the body as a large outcrop of ultramafic rocks during mapping of the Weaverville 30 minute quadrangle at the southern margin of the peridotite and named

it the Trinity Alps Batholith. Much of what is known about the internal distribution of gabbroic and granitic rocks within the peridotite was determined by unpublished reconnaissance mapping by the Southern Pacific Company during a regional survey for economic deposits. Irwin and Lipman (1962) determined on the basis of regional mapping that the Trinity and other peridotite bodies, although not connected at the surface, tend to be located at the boundary between the Central Metamorphic Belt and the Eastern Klamath subprovince. From this relationship, they concluded that the Trinity peridotite is the largest exposed fragment of an easterly dipping sheet of ultramafic rocks that was once a regionally extensive sheet.

Subsequent detailed studies of the ultramafic rocks were limited to small areas ($<75 \text{ km}^2$) in the vicinities of Gibson and Granite Peaks (Lipman, 1964), Coffee Creek (Goullaud, 1977) and Boulder Peak (Goullaud, 1977). Lipman (1964) performed detailed mapping at the southwestern margin of the Trinity peridotite, and produced significant information on the emplacement history of the peridotite. Lipman (1964) concluded that the peridotite was emplaced as a hot slab of completely or nearly completely crystalline material. Lipman (1963) also published a detailed description of the petrology, chemistry and emplacement history of a granitic pluton that intruded the Trinity peridotite. Goullaud (1977) performed detailed studies of the gabbro-peridotite contacts and concluded that the gabbros are intrusive into the Trinity peridotite rather than deposited upon it as might be inferred from current models for ophiolites. In addition, Goullaud (1977) worked out the detailed structural evolution of the Trinity peridotite in the vicinities of Coffee Creek and Boulder Peak.

The remaining field studies have not been directly concerned with the Trinity peridotite. The stratigraphy, structure and metamorphic history of the Central Metamorphic Belt immediately adjacent to the western margin of the Trinity peridotite were treated in Ph.D. theses by Davis (1961), Holdaway (1962), Romey (1962) and Lipman (1962). This work is summarized in a single publication by Davis et al. (1965). The most important contribution of this paper, insofar as the Trinity peridotite is concerned, is the recognition that structural complexity and metamorphic grade increase upward toward the overlying Trinity peridotite. More recently, Lindsley-Griffin (1977) studied the lower Paleozoic rocks that intrude and overlie the Trinity peridotite in the vicinity of Kangaroo Lake and China Mountain. Based on field mapping, Lindsley-Griffin (1977) concluded that the peridotite was intruded and overlain by a complex of mafic rocks that includes gabbro, diabase and pillow basalt, and that all of these rocks taken together have the necessary requisites to identify them as components of an ophiolite. Stratigraphic studies by Rohr and Potter (1973) in the Callahan-Gazelle area identified diabase and diorite cobbles in late Ordovician conglomerates. Based on this discovery, Rohr and Potter (1973) concluded that the mafic complex was exposed in late Ordovician time.

Regional geophysical studies provide some additional constraints on the thickness and buried extent of the Trinity peridotite. LaFehr (1966) identified a large gravity high that extends northward from the vicinity of Mount Eddy as far as Yreka. LaFehr (1966) interpreted this feature to indicate that relatively unserpentinized ultramafic rocks were present at depth below the peridotite, and the lower Paleo-

zoic and Cenozoic cover to the north. LaFehr (1966) estimated a thickness of about 2 km and a near horizontal dip for the peridotite sheet in the vicinity of China Mountain based on the gravity data and assumed and measured densities. Irwin and Bath (1962) published aeromagnetic traverses across the Trinity peridotite. Griscom (1977) interpreted available gravity and magnetic data and corroborated the conclusions of LaFehr (1966) and the hypothesis (Irwin and Lipman, 1962) that the Trinity peridotite is an easterly dipping sheet.

There are no published isotopic data on the peridotite, but isotopic age measurements that were determined on other rocks in the area are significant to the history of the Trinity peridotite. Lanphere et al. (1968) determined K-Ar ages of 439 ± 18 and 418 ± 18 m.y. on hornblende from a gabbro body that intrudes the Trinity peridotite to the east of Scott Mountain. More recent age determinations (oral communication, M. L. Lanphere, 1979) yielded ages over 450 m.y.. Mattinson and Hopson (1972) determined zircon ages of 430 and 480 m.y. on plagiogranite dikes that cut gabbros that intrude the Trinity peridotite. Lanphere et al. (1968) also obtained a Rb-Sr age of about 380 m.y. on muscovite separates and whole rocks from the metamorphic rocks of the Central Metamorphic Belt in the vicinity of Coffee Creek.

INVESTIGATION METHODS

FIELD WORK

Field investigations were conducted on the Trinity peridotite at a range of scales during the summers of 1976 through 1979. A preliminary regional study of the peridotite was made during six weeks in the summer of 1976 to locate the optimum area for detailed mapping. As a result of this work, an area of approximately 190 km² was mapped at a scale of 1:31,250 (Figure 2) during the summers of 1977 and 1978 in the vicinity of Mount Eddy and China Mountain near the northeast margin of the peridotite. The topographic base map was made up of enlarged portions of the Weed and China Mountain 15 minute quadrangles. The compiled geologic map is presented in Plate 1. Figure 50 shows the approximate boundaries of the study area on the 15 minute quadrangles; place names used in the text may be located with reference to this map. Additional mapping was performed during two weeks of the summer of 1979 on two selected outcrops--Vicki Bluff (Plate 2) and Lou Ann Bluff (Plate 3)--in High Camp Creek Basin. These maps were made at a scale of 1:240 and were designed to delineate features that are too small to map at a scale of 1:31,250. Mapping was performed with a telescopic alidade equipped with a Beaman arc and Seibinger drum and a plane table using the techniques described by Lahee (1961).

Representative samples were taken during all four field seasons for petrographic and electron microprobe investigations.

LABORATORY METHODS

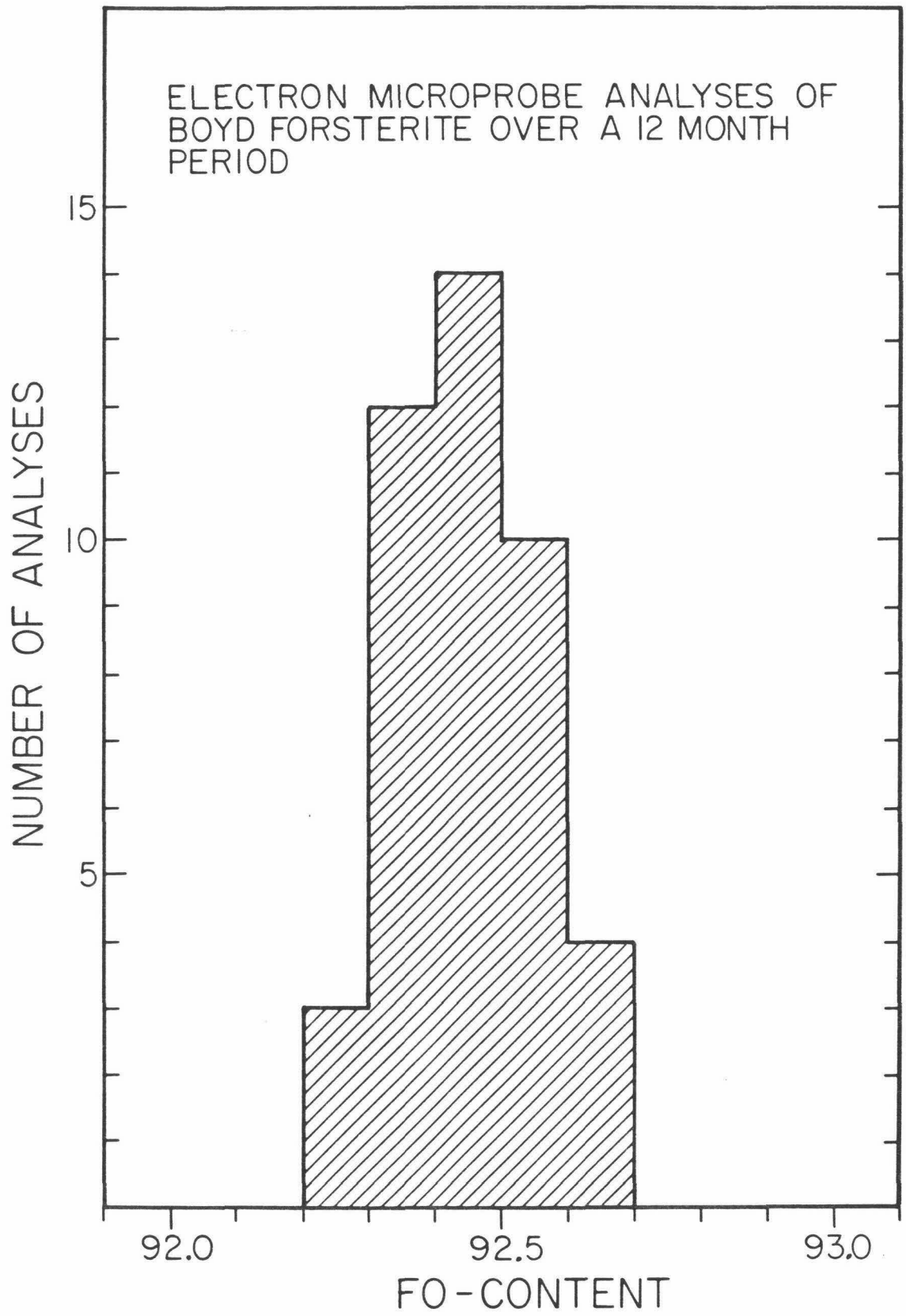
Petrographic examinations were made on approximately 150 thin sections to characterize the petrography of the Trinity peridotite and associated intrusive rocks in the study area, and to select samples

for detailed electron microprobe analysis. The subsequent electron microprobe investigation was limited to those samples that showed the least evidence of alteration (i.e., serpentine, brucite, epidote, etc.)

Quantitative electron microprobe analyses were performed on representative minerals in the selected samples using an automated MAC-5-SA3 electron microprobe equipped with three crystal spectrometers and an ORTEC Si(Li) solid state detector interfaced with a NS 880 multichannel analyzer. Quantitative analyses of primary minerals were performed for 9 to 15 elements for each phase using the crystal spectrometers. Operating conditions were 15 kV accelerating voltage and 0.05 μ A sample current (on brass). A PDP-8/L computer was programmed for spectrometer control and on-line data processing using the methods described by Chodos et al. (1973).

Determination of small compositional variations in minerals was one of the goals of this study. Champion et al. (1975) found that the reproducibility of the above system on two samples of known composition over a 13 month period was 1.5 percent (for elements with abundances >1 percent) to 3 percent for elements with abundances of 0.1-1.0 percent). However, much smaller variations were found when considering only the analyses produced by any single user during this time. Analyses on a forsterite standard of known composition (Boyd forsterite) were performed in this study to further assess the reproducibility of our system. Figure 3 illustrates that the Fo-content of this standard was reproducible within ± 0.5 mole percent over a 12 month period. Furthermore, replicate analyses performed during the same microprobe run were reproducible with less than ± 0.1 mole percent Fo-content.

Figure 3



Quantitative analyses of hydrous alteration products, such as serpentine and brucite, were performed utilizing the solid state detector; operating conditions were 15 kV accelerating voltage and 0.005 μ A sample current (on brass). Energy dispersive analysis was employed for the specific purpose of reducing beam damage of these hydrous phases. The analytical precision of energy dispersive analysis has been demonstrated by our laboratory to be approximately a factor of two less than obtained by analysis using the crystal spectrometers (Albee et al., in press).

Twenty-five samples were selected for automated electron microprobe point counting to determine the accurate modal mineralogy and the average composition of each phase in each thin section. From this information, it is also possible to infer the prealteration modal mineralogy and to calculate the bulk composition of the thin sections. This analytical technique is described by Chodos et al. (1977) and Albee et al. (in press), and the underlying philosophy is as follows. The composition of any mineral may be represented by either the abundance of each oxide or by the abundance of theoretical end-member compositions. The former may be thought of as representing the composition in oxide abundance space, and the latter as representing it in phase space. These equivalent representations are related by simple linear transformations. In practice, it is fastest and most convenient in the point count to substitute K-values (background subtracted counts in unknown/ background subtracted counts in standard), which approximate oxide weight percent abundances. This may be thought of as representing the composition of the mineral in K-value space. Basically, a computer is programmed to examine the energy

spectrum that is produced by excitation by the electron beam at a single discrete point. Background subtracted K-values are calculated and the identity of the phase is determined by simple matrix transformation from K-value space to phase space. The stage is moved so that a polished thin section is sampled by the beam during five second counts at discrete grid points. These data are stored sequentially along with the location of the grid point. Approximately 2500 grid points spaced at distances equal to the average grain size were found to be statistically adequate for characterizing most thin sections (Albee et al., 1977).

An underlying assumption of the automated point count technique is that the phases in the sample are all in chemical equilibrium. This is equivalent to stating that there are no compositional degeneracies among the phases. This is necessary because the matrix transformation requires an inversion of a composition matrix for a series of reference minerals, and compositional degeneracies among the reference minerals prohibits this inversion calculation. Furthermore, considering the problem independently of this inversion calculation, if the compositions of the three phases, A, B, and C are related by:

$$A + B = C,$$

then simple inspection of the X-ray energy spectrum cannot distinguish between excitation of phase C and excitation of the grain boundary between phases A and B.

This problem is a major hurdle that must be crossed in order to perform an automated point count on samples of the Trinity peridotite. If the rocks had pristine primary assemblages, they would be composed of only olivine + spinel + orthopyroxene + clinopyroxene + plagioclase

+ amphibole, and there would be no compositional degeneracies. Unfortunately, all the samples are slightly to highly altered to hydrous assemblages that contain serpentine + magnetite + brucite + talc + chlorite + clinozoisite + secondary amphibole + pyrope(?). H₂O and Na₂O are not detected by the energy dispersive detector in the point count mode, and, therefore, the energy spectra produced by certain combinations of these minerals are indistinguishable from those produced by combinations of the primary phases. Therefore, in the absence of additional data, there is no unique interpretation of many energy spectra encountered while point counting these rocks.

Fortunately, petrographic relationships make the automated point count tractable for the Trinity peridotite. Two simple, but significant observations were employed in this study. First, the complexity of the alteration assemblages increases drastically with increasing degree of alteration, and, therefore, the task of the automated point count is greatly simplified by selecting samples with minimal alteration of primary minerals for study. Furthermore, in samples that show only minor alteration (<10 percent), essentially all serpentine, brucite and magnetite are replacement products of olivine, and all clinozoisite is replacing plagioclase. The other primary minerals are essentially pristine, and, therefore, reconstruction of the primary modal mineralogy is easier and based on fewer assumptions. Second, veins of serpentine, magnetite and brucite occur along almost all grain boundaries, and therefore, beam excitation of an olivine-orthopyroxene grain boundary is extremely unlikely. It follows that points that appear to be mixtures of olivine and pyroxene are, in fact, mostly serpentine. This allows serpentine grains to be identi-

fied early in the point count process by a simple compositional filter.

Determination of the range and distribution of mineral compositions in a given rock is one of the most important conclusions from the automated point count process. Some difficulty was encountered in determining these parameters for samples of the Trinity peridotite because of the compositional spread introduced at each individual point by the poor counting statistics inherent in a five second counting time. For example, during a five second count at a grid point on an olivine grain, approximately 100 counts would be expected to accumulate under the Fe peak. The first standard deviation based on the counting statistics would be ± 10 counts or ± 10 percent of the total counts. This would translate to a first standard deviation in the Fo-content of the olivine grain of 10 mole percent, and would swamp the very small variations (about 1-3 mole percent) that are actually present in the olivine of the Trinity peridotite. This problem was circumvented by averaging the analyses of each phase ten at a time before plotting any of the point count data. The result is to reduce the total apparent number of data points in each diagram for each point count by a factor of 10 and to increase the effective counting time for each of the plotted data points to 50 seconds. This greatly reduced the spread in data, bringing it into line with the results of the quantitative analyses. This calculation has the drawback of obscuring ranges in mineral composition such as fractionation trends. However, extensive and detailed quantitative analysis of minerals in the Trinity peridotite demonstrated that the ranges in mineral composition for the pyroxenes and olivines are extremely restricted and much smaller than the spread produced by statistical variations during the point counts.

ROCK TYPES OF THE STUDY AREA

INTRODUCTION

This section describes the field appearances of the rock types that were identified in the field and presents field observations that are significant to the structural and petrologic evolution of the Trinity massif. Although this study focuses on the peridotite, field descriptions of the other lithologies are included for completeness and because they have bearing on the petrogenesis of the ultramafic rocks.

Most of the 70 square miles that were mapped in the vicinity of Mount Eddy and China Mountain are underlain by the Trinity peridotite. However, other lithologic units crop out over significant portions of the map area (Map 1). The peridotite is intruded by younger stocks and plugs of gabbro and hornblende diorite, and dikes of microgabbro, pegmatitic gabbro, hornblende diorite, diabase and albite granite. At the eastern margin of the study area, sedimentary and volcanic rocks are faulted against the Trinity peridotite. Glacial and stream deposits cover most of the valley floors throughout the study area.

PERIDOTITE

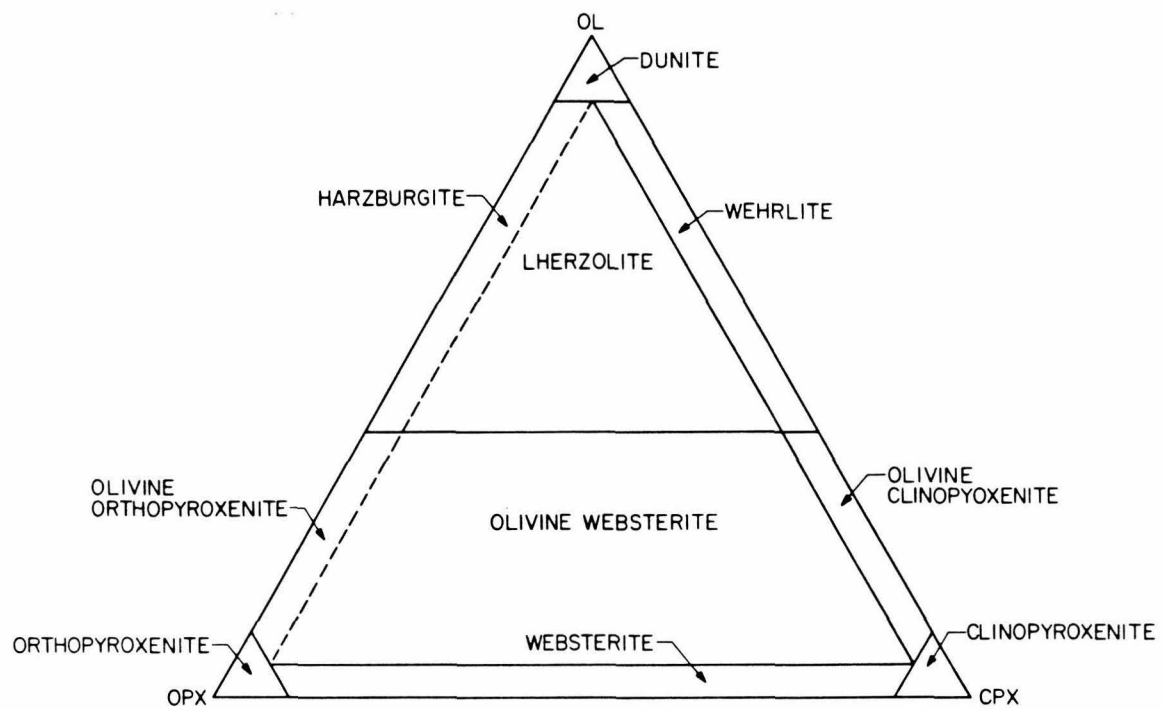
INTRODUCTION

Peridotite is used in this study to include all rocks that are composed of olivine and pyroxene with only minor (<10 percent) amounts of other minerals. Phases that are larger than about 1 mm in diameter are readily identifiable in the field if the rocks are less than about 50 percent serpentized. This is the upper limit to serpentization throughout most of the study area, so that field identification

of lithologies was practical.

The lithologies that were identified in the field were named, with one significant exception, according to the recommendations of the IUGS Subcommittee on the Systematics of Igneous Rocks (1973). This terminology is represented graphically in Figure 4. With reference to this figure, the types of peridotite that were identified in the field were plagioclase lherzolite and harzburgite, lherzolite, harzburgite, dunite, websterite and olivine websterite, wehrlite, olivine clinopyroxenite, and clinopyroxenite. In the IUGS classification, the distinctions between plagioclase lherzolite and plagioclase harzburgite and between lherzolite and harzburgite are based solely on clinopyroxene abundance; plagioclase lherzolite and lherzolite contain more than 5 modal percent clinopyroxene and plagioclase harzburgite and harzburgite contain less than 5 modal percent clinopyroxene. Examination of the sample modes presented in Table 2 reveals that both harzburgitic and lherzolititic rocks are present in the Trinity massif. However, this distinction is extremely difficult to utilize in the field because the clinopyroxene abundances of these rocks tend to fall very close to the arbitrary dividing line of 5 percent. Therefore, a more practical set of definitions was employed in the field and will be used throughout the remainder of this paper. The rocks were termed lherzolite or plagioclase lherzolite, as appropriate, if visible clinopyroxene was present in handspecimen, but were termed plagioclase harzburgite or harzburgite if there was no clinopyroxene visible in handspecimen. Using this terminology, plagioclase lherzolite is by far the most abundant feldspathic ultramafic lithology and plagioclase harzburgite is extremely rare.

Figure 4: Classification of peridotite according to recommendations by the IUGS Subcommittee on the Systematic of Igneous Rocks (1973). In this study, the distinction between harzburgite and lherzolite is based on whether or not clinopyroxene porphyroblasts are visible in outcrop; the boundary between harzburgite and lherzolite is dashed to emphasize this.



Plagioclase lherzolite and harzburgite, lherzolite, harzburgite and dunite comprise the main mass of the Trinity peridotite into which the websterite, olivine websterite, wehrlite, olivine clinopyroxenite and clinopyroxenite were emplaced as dikes or as cumulates at the base of intrusive gabbroic bodies. The cumulate peridotite will be described in a separate section dealing with the gabbroic rocks. The following discussion is intended to emphasize macroscopic differences between the remaining types of peridotite in terms of mineralogy and outcrop appearance, and the relationships between these rock types will be treated in another section.

There are several progressive changes in these macroscopic characteristics in the series plagioclase lherzolite, lherzolite, harzburgite and dunite. The mineralogy becomes less diverse, there is decreased resistance to weathering, outcrop surfaces tend to be smoother, and weathering colors tend to be lighter shades. These characteristics are mentioned now to alert readers before they are lost in the following detailed discussion.

PLAGIOCLASE LHERZOLITE

Plagioclase lherzolite forms blocky, yellow-brown to red-brown weathering outcrops with extremely rough weathering surfaces (Figure 5), and somewhat variable mineralogy. These rocks are composed of about 70-80 percent yellow-brown weathering olivine, 15-20 percent green to brown orthopyroxene, 2-10 percent emerald-green clinopyroxene, 1-2 percent black spinel, 2-10 percent plagioclase, and minor amounts of black amphibole. Olivine forms the groundmass throughout which the other minerals are dispersed; it is highly fractured, so that grain

Figure 5: Appearance of plagioclase lherzolite, lherzolite, harzburgite and dunite in outcrop.

- (A) Contact between lherzolite (upper left) and plagioclase lherzolite (lower right) north of Toad Lake. Note foliation in the plagioclase lherzolite defined by resistant feldspathic lenses and the smoother appearance of the lherzolite.
- (B) Contact between harzburgite (left) and dunite (right) at Vicki Bluff (Plate 2). Note nubby surface of the harzburgite produced by resistant orthopyroxene grains and the smooth surface of the dunite.
- (C) Banding in harzburgite defined by variations in orthopyroxene abundance (Granite Creek, Trinity Alps). Resistant bands are more orthopyroxene-rich.
- (D) Banding in plagioclase lherzolite on the ridge south of Bull Creek. Resistant bands are more plagioclase- and pyroxene-rich and are referred to as ariegite.



size is difficult to determine in outcrop. Orthopyroxene forms equant to slightly flattened grains that range in size from <0.3 to 0.7 cm across. Clinopyroxene forms small, equant grains up to 0.3 cm in diameter. Spinel grains, in general are 0.1-0.3 cm in size but grains occur locally up to 0.6 cm across. Plagioclase grains are generally ≤ 0.2 cm across, and are, in most places, pseudomorphed by chalky-white clinozoisite; where plagioclase is preserved, the grains are clear and glassy.

The rough appearance of the outcrops is due to a penetrative foliation (Figure 5) that is best defined by flattened orthopyroxene grains and flattened lenses of mostly plagioclase, pyroxene and spinel. The lenses range in size from 1-5 cm long and 0.3-0.6 cm wide. These lenses are resistant to weathering and stand out as tiny ridges above the less resistant, intervening olivine matrix. Locally, the feldspathic lenses are shaped like flattened pencils, the long axis of which defines a lineation within the plane of the foliation.

Banding is developed locally in the plagioclase peridotite (Figure 5). It is defined by sharp variations in the modal mineralogy; resistant bands of plagioclase-rich (about 10 percent) and pyroxene-rich (about 30-40 percent) rock alternate with layers of plagioclase-poor (<5 percent) and pyroxene-poor (<5 percent) rock. The characteristics of the pyroxene- and plagioclase-rich bands are discussed in the section on clinopyroxene-rich rocks. These bands range in thickness from 0.25 to 15 cm and are continuous in some outcrops for distances up to 20 m, although discontinuous bands occur that terminate abruptly and bluntly. In most of its occurrences, this banding

is cut by the foliation at relatively high (>20 degrees) angles, but in some outcrops, banding is essentially parallel to the foliation.

Plagioclase lherzolite constitutes about 15 percent of the peridotite within the study. As can be seen from Plate 1, it is most abundant in large, tabular zones that are up to about 150 m thick and as long as 3000 m, and occur on the south and southeast flanks of Mount Eddy and in the western part of the study area south of China Mountain. It also occurs as isolated blocks contained within other peridotite lithologies (e.g. Plate 2); these occurrences will be detailed in a separate section on peridotite relationships.

Other occurrences of plagioclase lherzolite in the Trinity peridotite have been described by other investigators. Goullaud (1977) noted the presence of this lithology in the Boulder Peak vicinity to the south and Lindsley-Griffin (1977) described it as underlying Corey Peak to the west. In addition, I have located large areas of plagioclase lherzolite on and near Scott Mountain to the west.

LHERZOLITE

Lherzolite is quite distinct from the plagioclase lherzolite in outcrop; it has a smoother outcrop surface without an obvious foliation (Figure 5) and is devoid of plagioclase. Like the plagioclase lherzolite, it has blocky, yellow-brown to red-brown weathering surfaces.

An estimated typical composition in outcrop is 70-80 percent yellow-brown olivine, 15-20 percent olive-green to brown orthopyroxene, 5-10 percent emerald green clinopyroxene, and 1-2 percent black spinel. The pyroxenes and spinel occur as evenly disseminated grains throughout a matrix of olivine; these minerals weather out with positive relief,

giving the rock a nubby appearance. The outcrop surface is nevertheless much smoother than that of the plagioclase lherzolite due to the absence of the high-relief plagioclase-rich segregations. As a result, macroscopic measurement of the foliation in this rock is difficult.

Banding that is similar to that in the plagioclase lherzolite in terms of thickness and continuity is also present in the lherzolite. It is defined by abundance of pyroxene; pyroxene-rich (40-70 percent) layers alternate with pyroxene-poor (<20 percent) layers. As in the plagioclase lherzolite, the layers range in thickness from .2 to 25 cm.

HARZBURGITE

Harzburgite forms orange to yellow-brown, blocky outcrops with nubby surfaces (Figure 5). The typical mineralogy as seen in outcrop is approximately 75-85 percent yellow-brown olivine, about 5 percent olivine-brown orthopyroxene and 1-2 percent black spinel. By definition, clinopyroxene is not visible in handspecimen. The grain sizes of these minerals are essentially identical to the respective minerals in the plagioclase lherzolite and lherzolite. Like the lherzolite, the rock is relatively smooth in appearance, due to the absence of feldspathic segregations.

The harzburgite is generally cut by an obscure foliation, which may be determined only by close inspection of elongated single spinel grains and spinel trails.

Banding is developed locally in the harzburgite and is defined by the abundance of orthopyroxene relative to olivine. These bands are illustrated in Figure 5. Resistant bands from .25 to 25 cm thick

of pyroxene-rich peridotite alternate with bands of less resistant, pyroxene-poor peridotite. The pyroxene-rich bands contain up to about 40-50 percent orthopyroxene while the pyroxene-poor bands may be almost devoid of orthopyroxene. The contacts between these bands are generally gradational over several centimeters. The bands are similar in thickness to those in the lherzolite and plagioclase lherzolite. Outcrops to the north of Mount Eddy and to the south of China Mountain contain banding in harzburgite that is continuous for up to 50-60 m. Further south, in the Trinity Alps, spectacular banding in harzburgite that is continuous for up to 125 m has been described by Lipman (1964).

Harzburgite is the most abundant lithology in the study area, comprising approximately 60-70 percent of the peridotite by volume. My reconnaissance suggests that harzburgite is the most abundant lithology throughout the entire Trinity complex. Within the study area, it tends to be somewhat more abundant north of the high ridge joining Mount Eddy and China Mountain and less abundant relative to plagioclase lherzolite to the south.

DUNITE

Dunite forms outcrops that are much lighter shades of yellow-brown to orange than the harzburgite, and forms extremely-smooth weathering surfaces that contrast sharply with the other peridotite lithologies (Figure 5). The mineralogy, as estimated in outcrop, is extremely uniform, consisting of about 95-99 percent yellow-brown weathering olivine, 1-2 percent black spinel and 0-2 percent pyroxene. The olivine grains are highly fractured so that grain sizes are difficult to measure. However, single crystals up to 5 cm across have been

identified in outcrop by their uniformly reflecting surfaces. Spinel grains are generally ≤ 0.2 cm and are equant to flattened in shape. In some rocks, large concentrations of spinel form chromitite pods up to 1 m across. Spinel may comprise nearly 100 percent of these pods or may be less abundant and fill interstices between equant olivine grains. Where present, orthopyroxene generally occurs as local concentrations that are essentially small patches of harzburgite. Locally, however, there are disseminations of equant orthopyroxene grains, 0.1-0.2 cm across, that comprise less than 10 percent of the rock, so that it is actually an orthopyroxene-bearing dunite. Clinopyroxene occurs locally as isolated poikilitic grains that range in size from 1 to 30 cm, and as large poikilitic pods up to 1 m across (Figure 6).

Banding is extremely rare in the dunite bodies in the study area. Locally, however, banding is defined by the relative abundances of spinel and olivine. Spinel-rich (>10 percent) bands alternate with spinel-poor (1-2 percent) bands. Bands up to 2-3 cm thick are developed, but nowhere are they as continuous as the banding in the harzburgite, lherzolite and plagioclase lherzolite, and rarely do they exceed a few meters in length.

Most of the dunite bodies are cut by a penetrative foliation that is defined by the shapes and arrangements of spinel grains. Flattened spinel grains and spinel trails define a penetrative planar fabric. In some places, close inspection of the spinel orientations reveals the presence of nearly isoclinal mesoscopic folds with the limbs defined by slightly convergent spinel trails and the hinges defined by flattened spinel grains that are bent. Thus, it would

- Figure 6: Appearance of clinopyroxene pods and grains, and wehrlite layers in dunite, and hand specimen appearance of ariegite.
- (A) Poikilitic clinopyroxene grains in a small dunite body within harzburgite (Bluff Lake Basin).
 - (B) Large, poikilitic clinopyroxene grain within a large dunite body (Bluff Lake Basin).
 - (C) Wehrlite interlayered with dunite above Dobkins lake. Note backpack at base of outcrop for scale.
 - (D) Hand specimen of an ariegite dike. Spinel grains (black) are about 1 cm long and are rimmed by white plagioclase. Large gray minerals are clinopyroxene grains; groundmass is clinopyroxene, orthopyroxene, olivine and plagioclase. Sample location: Bull Creek.



appear that the spinel trails that define the foliation in the dunite are actually limbs of tightly folded but discontinuous spinel bands. These structures are probably present in the harzburgite, lherzolite and plagioclase lherzolite but camouflaged by the abundant pyroxene grains.

The large poikilitic clinopyroxene grains, where present, are commonly smeared out with length to width ratios of up to 6:1. These grains also define a foliation that is always consistent with the foliation defined by the spinel grains and trails.

Dunite has several modes of occurrence in the study area, forming small bodies centimeters to meters in size within the harzburgite (Plate 2) as well as large bodies up to 100 m thick and 3-4 km long (Plate 1). The large, tabular bodies are developed throughout the study area (Plate 1) and trend east-west in the vicinity of Mount Eddy and east of north near China Mountain. Collectively, these dunite bodies are estimated to comprise 15-20 percent of the peridotite in the study area. Similar occurrences of dunite were found throughout the Trinity peridotite during my reconnaissance work.

CLINOPYROXENE-RICH ROCKS

Clinopyroxene-rich rocks comprise no more than 1 percent of the Trinity peridotite by volume. Three fundamental types of clinopyroxene-rich rocks are recognized: (1) dikes and bands with spinel as the primary aluminous phase; and (2) dikes with plagioclase as the primary aluminous phase; and (3) concordant clinopyroxene-rich layers in large dunite bodies. The first type will be referred to as ariegite, the second type as websterite, and the third as wehrlite to emphasize

the mineralogical differences.

The term, ariegite, refers to aluminous peridotite in which spinel is the aluminous phase. The ariegite in the Trinity peridotite is composed of approximately 10-20 percent olivine, 5-10 percent orthopyroxene, 60-70 percent clinopyroxene, 5-10 percent pargasitic hornblende, 2-5 percent spinel, and 5-10 percent plagioclase (Figure 6). Olivine weathers yellow-brown, orthopyroxene olive-brown, clinopyroxene emerald green, spinel and amphibole black, and plagioclase white. Pyroxene grains range in size from 0.1 to 0.3 cm and form clusters up to 0.5 m across. Spinel forms large ragged and flattened grains that range in size from 0.1 to 1 cm. Olivine, plagioclase and amphibole are interstitial to the pyroxenes, and range from <0.1 to 0.2 cm in size. Plagioclase forms prominent white envelopes around spinel grains and appear to have formed as a secondary aluminous phase that partially replaced spinel (Figure 6). Therefore, the term ariegite was selected to identify this lithology to emphasize its apparent primary mineralogy.

Ariegite forms swarms of parallel, tabular bodies that are referred to as bands, and isolated, more randomly oriented tabular bodies that are referred to as dikes. Both occurrences are restricted to lherzolite and plagioclase lherzolite hosts. The geometry of the ariegite bands is discussed in the section of plagioclase lherzolite; the dikes are about 10-20 cm thick and continuous across exposures up to 30 m wide. Both the dikes and bands are most common in the southwestern part of the study area, between Mount Eddy and Bull Creek.

There is considerable field evidence of deformation in the ariegite. The plagioclase envelopes and the enclosed spinel grains tend to be smeared out and to define a prominent penetrative foliation

(Figure 6). Some isoclinal folds have been identified in the ariegite bands on the ridge south of Bull Creek. The axes of these fold are parallel to the penetrative foliation.

Websterite dikes have an extremely variable mineralogy. Most commonly they are composed of 50-70 percent emerald green clinopyroxene, 10-30 percent olivine, 10-20 percent orthopyroxene, and minor amounts of plagioclase and amphibole. Locally, olivine comprises up to 50 percent of the dikes. Clinopyroxene is typically equant and ranges from 0.5 to 2 cm in diameter. Olivine and plagioclase, if present, fill interstices between the larger clinopyroxene grains. Observed thickness range from about 0.2 cm to 0.5 m, and with increasing thickness, the dikes tend to be more clinopyroxene-rich. Some of the thicker dikes are essentially clinopyroxenites composed of greater than 90 percent clinopyroxene. These dikes contain up to 10-20 percent black amphibole as rims on clinopyroxene and minor amounts of sphene.

Unlike the ariegite bands and dikes, most of the websterite dikes are devoid of internal foliation. No isoclinal folds were observed in these dikes, although small, open mesoscopic folds are common. However, some of the dikes do tend have a preferred orientation of clinopyroxene crystals, which are elongate normal to the dike wall and protrude inward into the dike. The cores of these dikes tend to be more plagioclase-rich than the rims.

The distribution and morphology of these dikes are also in contrast to the ariegite bands and dikes. Websterite dikes are found throughout the study area, and are not restricted to the plagioclase lherzolite in occurrence. Instead, they intrude plagioclase lherzolite, lherzolite, harzburgite and dunite, although they are most common in the first two

lithologic units. The websterite dikes range in thickness from about 0.5 to 1 m. Unlike the ariegite bands and dikes, they branch and, locally, are discontinuous along strike. No attempt was made to determine their orientation throughout the study area. However, to the south of China Mountain, they occur in swarms of steeply dipping dikes with a consistent southwesterly orientation.

Black-weathering wehrlite layers that are 1-3 m wide and inter-layered with dunite are contained within a large dunite body above Dobkins lake on the north side of Mount Eddy (Figure 6). Thin layers tend to be discontinuous and appear boudined, while thick layers (2-3 m) are continuous across outcrops about 100 m long. In hand specimen, the rock appears to be composed of about 98 percent black pyroxene and about 2 percent red-weathering olivine. The pyroxene imparts a distinctive black color to the rock on both fresh and weathered surfaces, making it readily distinguishable from the other types of peridotite. These pyroxenes form distinct, highly fractured grains that range in size from about 0.1 to 1.0 cm in size. These grains are elongate, with length to width ratios of up to 3:1, and have a weak preferred orientation that defines a foliation. This foliation is concordant with the layers and discordant with the regional foliation. Olivine is completely interstitial to the pyroxene. These layers are distinct from the other clinopyroxene-rich rocks by virtue of their color and finer grain size. They are significant because they appear to parallel the trend of the host dunite body, rather than crosscut it. This and the interlayering with dunite suggest that they may be genetically related in some way to the large dunite bodies.

ASSOCIATIONS AND SPATIAL RELATIONSHIPS

The distribution of the principal ultramafic lithologies and the spatial relationships that exist between them are important keys to their petrogenesis. These relationships are as follows: (1) plagioclase lherzolite and lherzolite are always contained within a harzburgite host; (2) at least three types of dunite may be discriminated on the basis of field relationships; (3) a distinctive lithologic sequence always occurs between plagioclase lherzolite and dunite; (4) many websterite dikes that cut plagioclase lherzolite are bounded by zones of plagioclase-free peridotite, or "depleted zones"; and (5) these websterite dikes and associated depleted zones appear to be small scale analogues of the large dunite bodies. These observations are presented in detail below.

Harzburgite is the dominant rock type in the Trinity peridotite and may be thought of as the matrix in which irregular to tabular bodies of lherzolite and plagioclase lherzolite occur. Plagioclase lherzolite and lherzolite tend to occur as isolated, irregular shaped bodies within harzburgite (Plate 2). These bodies range in size from a few centimeters across to hundreds of meters across and are irregular in shape. In some places, such as the south of Mount Eddy and China Mountain (Plate 1), the plagioclase lherzolite bodies increase in size and abundance until they are the dominant lithology. Where plagioclase lherzolite bodies are in close proximity but isolated, such as at Vicki Bluff (Plate 2), the banding and foliation are parallel from one body to another. Furthermore, the foliations in these bodies are parallel to the foliation in the host harzburgite and/or dunite, and banding can be traced in some outcrops from the plagioclase

lherzolite, through the adjacent lherzolite and into the host harzburgite. However, the banding is typically truncated by the dunite bodies.

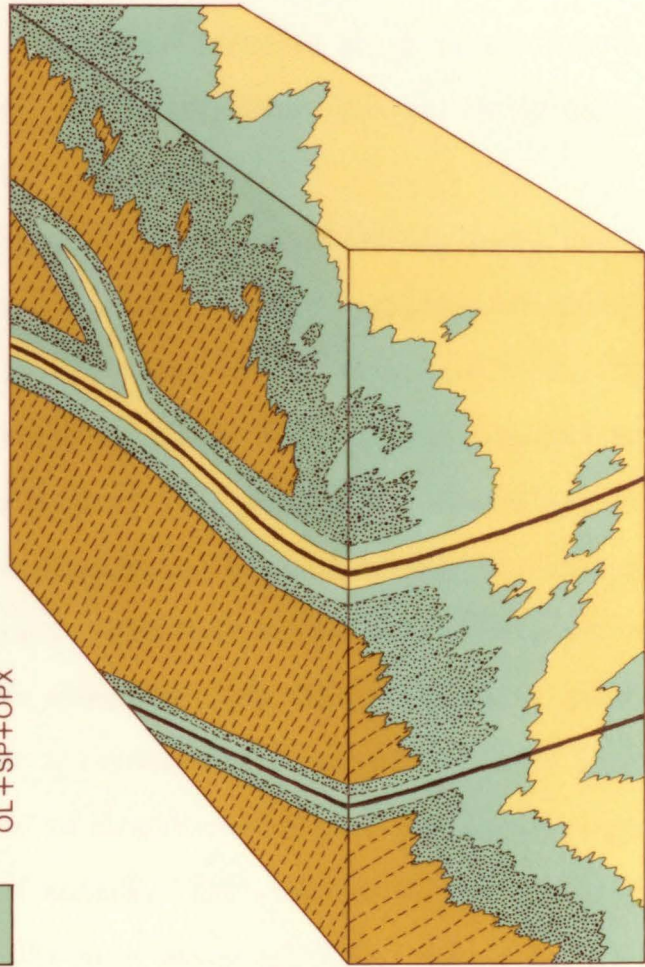
There are multiple modes of dunite occurrence in the Trinity complex. Dunite forms: (1) large tabular bodies with thicknesses up to 100 m and continuous for distances of up to several kilometers (Plate 1); (2) smaller, irregular-shaped patches of dunite that are contained within a harzburgite host (Plate 2); and (3) small tabular bodies or "dikes" that flank or appear to replace some websterite dikes (Figure 7). The first two types of dunite are by far the most abundant, and all three are in most places discordant with the foliation.

The larger dunite bodies were mapped as separate units on the small scale map of the study area (Plate 1). This map illustrates that these bodies have an outcrop pattern that suggests they are roughly tabular in three dimensions, and that they are generally discordant to the foliation. Although the boundaries of the dunite bodies appear to be sharp and regular at a scale of 1:31,250, they are, in detail, ragged and extremely complex. Irregular patches of dunite that are contained in the harzburgite become more abundant toward the large tabular dunite bodies until dunite is the dominant lithology. Harzburgite persists as irregular blocks contained within the dunite and ranging in size from centimeters to tens of meters. In general, the size of these blocks decreases with distance into the large dunite bodies. "Arms" or projections of dunite extend into the harzburgite from the large dunite bodies. These observations suggest that the large dunite bodies and the smaller patches are closely related.

Contacts between the plagioclase lherzolite and lherzolite,

Figure 7: Schematic diagram illustrating relationships between the websterite dikes (cpx-rich dikes in diagram) and the plagioclase lherzolite, lherzolite, harzburgite, and dunite. Dikes range in thickness from 0.2 cm to 0.5 m; depleted zones range from about 1 cm to 0.5 m wide. Foliation is shown schematically by dashed lines.

GENERALIZED CPX-RICH DIKES



lherzolite and harzburgite, and harzburgite and dunite tend to be ragged and deeply embayed where they are at high angles to the foliation, but are much sharper and straighter where they are nearly parallel to the foliation (Plate 2). The trends of the embayments are parallel to the strike of the foliation; this can be observed in the map of Vicki Bluff (Plate 2), and is represented by equal area projections in Figure 14. These observations are discussed in the chapter on the structural history of the peridotite. The preferred interpretation is that the lithologic contacts formed prior to the foliation and that the embayments are, at least partly, the result of folding during the formation of the foliation.

An extremely significant systematic relationship links the peridotite lithologies throughout the study area -- plagioclase lherzolite is never in contact with dunite except where juxtaposed by faults. Instead, at every scale, there is always a transition sequence between plagioclase lherzolite and dunite: (1) plagioclase lherzolite grades into lherzolite with the disappearance of plagioclase; (2) this lherzolite grades into harzburgite with both decreasing overall pyroxene abundance and clinopyroxene abundance; (3) this harzburgite grades into dunite with the abrupt disappearance of pyroxene. This gradation from plagioclase lherzolite to dunite occurs over distances ranging from about 15 cm to tens of meters. The plagioclase-out and pyroxene-out transitions are typically very sharp and occur over a few millimeters, whereas the transition from lherzolite to harzburgite is gradational and is marked by the gradual reduction in the abundance of clinopyroxene porphyroclasts that are visible in the outcrop.

The above relationships are interpreted as evidence that much,

if not all of the dunite, harzburgite and lherzolite were produced from a plagioclase lherzolite protolith by subtraction of plagioclase, clinopyroxene and orthopyroxene. Furthermore, this appears to have happened before plastic deformation of the rocks, as recorded by the foliation, ceased.

The detailed relationships between some of the websterite dikes and the peridotite wall rocks into which they are emplaced are also significant. Many of the websterite dikes that cut the plagioclase lherzolite are bordered by tabular zones of plagioclase-free peridotite (Figures 7 and 8). These borders will be referred to as depleted zones throughout the remainder of the paper to emphasize that they have been depleted in plagioclase and pyroxene relative to the plagioclase lherzolite. These depleted zones display characteristic lithologic zonations that are summarized in Figure 7. In the most extreme cases, the websterite is surrounded by dunite, which is surrounded in turn by harzburgite, lherzolite and, finally, the plagioclase lherzolite host. An excellent example of this relationship is exposed near the center of Vicki Bluff (Plate 2, Figure 8). More commonly, however, no zone of dunite is present and the websterite is immediately bordered by zones of harzburgite and/or lherzolite. Examples of this relationship are abundant at Lou Ann Bluff (Plate 3, Figure 8), but are found wherever there are exposures of plagioclase lherzolite. Some websterite dikes that have depleted zones can be traced from the plagioclase lherzolite through lherzolite and harzburgite, and into large dunite bodies. Examples are found at both Vicki and Lou Ann bluffs. The dikes clearly crosscut the dunite bodies but become discontinuous and disappear with increasing distance into the dunite.

Figure 8: Websterite dikes cutting plagioclase lherzolite.

- (A) Websterite dike bordered by dunite (smooth surface), harzburgite and dunite (nubby surface), and the host plagioclase lherzolite (foliated surface). The pencil is oriented parallel to the foliation in the plagioclase lherzolite and along the axial plane of a small open fold in the dike. (Vicki Bluff, Plate 2)
- (B) Undeformed websterite bordered by a plagioclase-free zone of lherzolite (nubby surface) and by the host plagioclase lherzolite (foliated). The pencil is oriented parallel to the foliation. (Ridge south of Bluff Lake.)



The significant point that must be made about the depleted zones is that the sequence of lithologies in them is identical to the sequence that is developed between the large dunite bodies and the plagioclase lherzolite (Figure 7). This suggests that the depleted zones may have formed in a manner analogous to the formation of the larger dunite bodies. If this is the case, then the wehrlite layers and clumps of poikilitic clinopyroxene that occur within the large dunite bodies may be analogs of the websterite dikes. This hypothesis and its implications are treated in detail in the discussion section of this thesis.

SERPENTINIZATION

All of the peridotite within the study area has been altered, at least incipiently, to serpentine and associated minerals such as magnetite, brucite, talc and clinozoisite. Although the details of the alteration products are not generally discernible in outcrop, the degree of serpentinization may be estimated on the basis of certain megascopic characteristics that change with increasing serpentinization. Peridotite that is less than 10 percent serpentinized tends to be yellow-green and glassy on freshly broken surfaces and weathers to form a thin (<0.5 cm thick) yellow-brown crust. Plagioclase, if present, is vitreous even on weathered surfaces, and clinopyroxene is a bright emerald green that contrasts sharply with the olive green of orthopyroxene. The outcrop tends to be blocky with joint blocks maintaining sharp edges. With increasing serpentinization, in outcrops that are more than 10 percent serpentinized: (1) the fresh surfaces become an increasingly darker green and have a sugary texture; (2) weathered surfaces take on an increasingly reddish hue and

have thicker alteration crusts; (3) plagioclase loses its vitreous luster, having completely altered to clinozoisite in rocks that are more than 10 percent serpentinized; and (4) clinopyroxene loses its distinctive emerald green color and appears more olive green and increasingly difficult to distinguish from orthopyroxene after serpentinization exceeds about 50 percent. In outcrops that are essentially 100 percent serpentinized, the rocks weather white rather than reddish-brown, and are noticeably less dense than essentially unserpentinized peridotite. Meeker and Albee (1979) demonstrated that the alteration crusts are produced by an advancing front along which magnetite from an earlier pervasive serpentinization is oxidized; the process does not involve alteration of the silicate minerals. Therefore, increased amounts of serpentinization will enhance the formation of thicker crusts. Detectible crusts were observed to form within one year on surfaces that were broken during sampling in the previous year.

The outcrop form of the peridotite also reflects the degree of serpentinization. With progressive serpentinization, the outcrops have a more subdued topographic expression: corners of blocks become more rounded and outcrops less prominent. Saddles in ridges tend to correspond to zones of intense serpentinization.

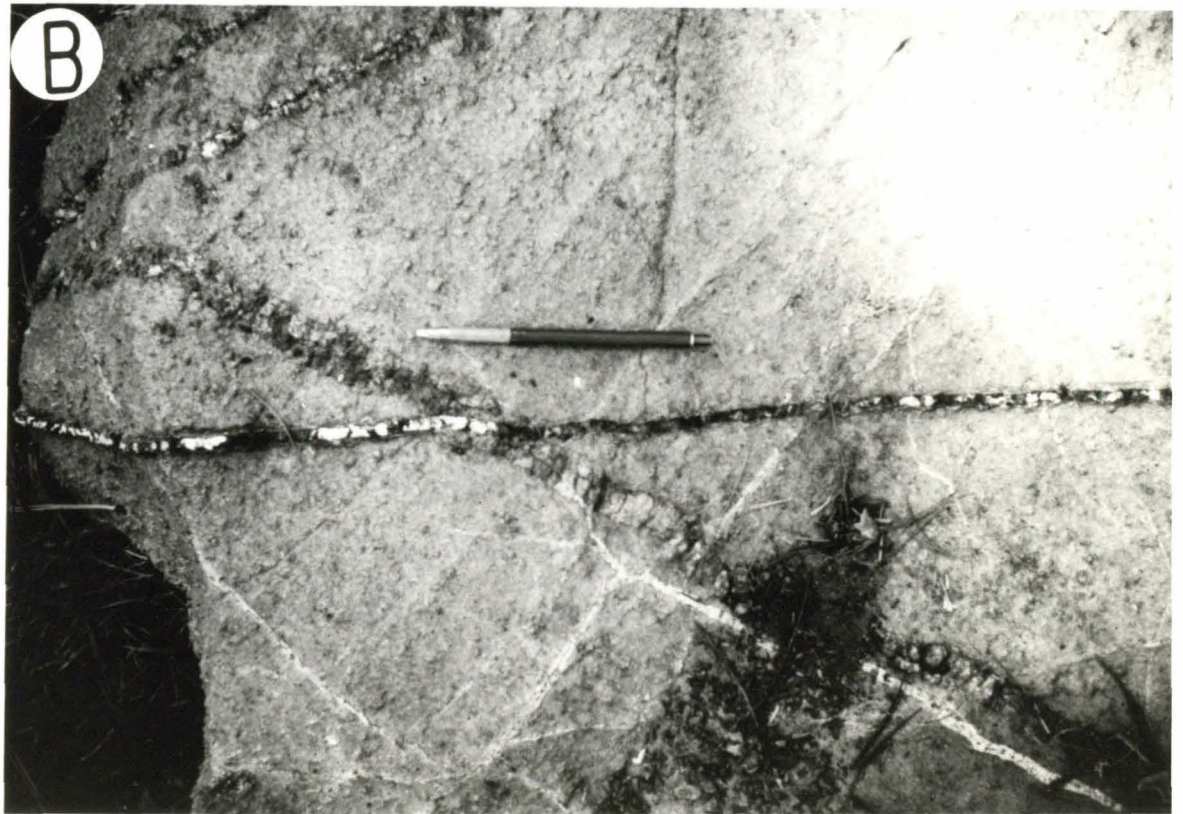
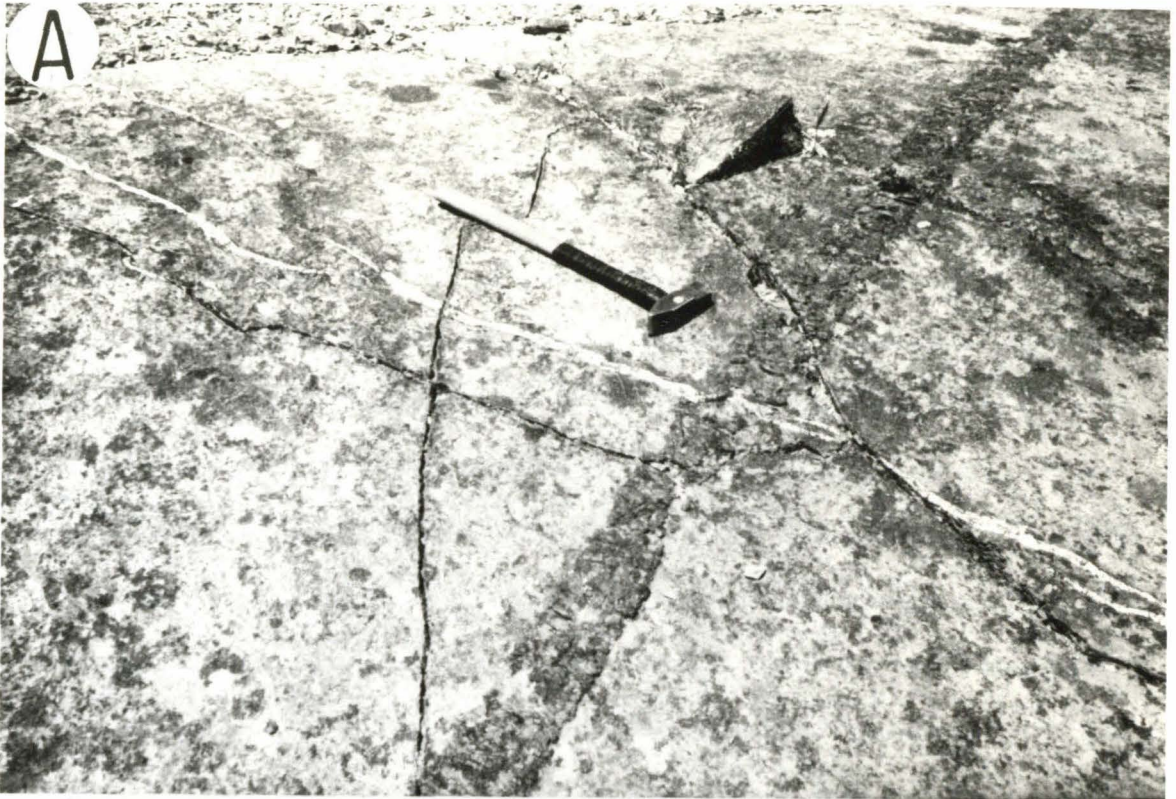
Most of the peridotite in the study area is about 20-50 percent serpentinized. Zones of most intense serpentinization tend to fall into one of two categories: (1) fault zones, and (2) contacts with intrusive bodies. Fault zones, which were identified by truncations of peridotite structures and/or gabbro and diorite bodies, typically are flanked by zones of intensely serpentinized peridotite that range in width from about 1 to 25 m. These serpentinized zones generally

have a foliation that is subparallel to the attitude of the fault. Locally, however, they consist of tectonic breccias composed of angular serpentine blocks with a seriate size distribution up to 0.5 m across. Where the faults are intruded by dikes of diabase or hornblende diorite such as along south face of Mount Eddy, the serpentinization zones are up to 50 m. Serpentinization aureoles up to 50 m wide are developed around the large hornblende diorite intrusions that are west of Mount Eddy. Tremolite occurs locally within about 10 m of some of these contacts. Serpentinization also increases with proximity to the gabbro peridotite contacts. To some extent, this serpentinization may be related to faulting, which is common along these contacts. However, a serpentinization zone, approximately 10 m thick is developed along the western contact of the gabbro body south of Mount Eddy, and appears unrelated to faulting.

Peridotite that is less than 10 percent serpentinized occurs in two somewhat discontinuous, narrow belts. One belt trends approximately north-south and is located about 2 km west of the Trinity River. This belt extends from south of Bull Creek, to north of Bluff lake and is up to ~0.3 km wide. The second belt trends northwesterly and extends from Crater Lake to Parks Creek about 3.5 km south of Stewart Springs. These belts are not continuous because serpentinization may be locally very great near faults and/or intrusive bodies. Although other pockets of relatively un-serpentinized peridotite were located, these belts are distinctive because of their linear extent and low degree of serpentinization. Samples of dunite, harzburgite, lherzolite, plagioclase lherzolite, and clinopyroxene-rich dikes that are less than 5 percent serpentinized have been collected from these

Figure 9: Plagioclase-rich veins.

- (A) Vein of predominantly plagioclase (type C) with minor amphibole (white) cutting a large websterite dike north of Mount Eddy.
- (B) Vein of plagioclase and black amphibole (parallel to pencil) cutting a websterite dike on the ridge south of Toad Lake.



belts.

PLAGIOCLASE-RICH VEINS

Rare plagioclase-rich veins (Figure 9) are scattered throughout the study area and have no particular spatial association with larger intrusive bodies. These features are referred to as veins rather than dikes because they are typically narrow and discontinuous. They are distinct from the clinopyroxene-rich dikes, layers and bands in that plagioclase constitutes >50 percent of the modal mineralogy. Three types have been recognized: (A) plagioclase (~ 50 percent) and clinopyroxene (~ 50 percent) veins; (B) plagioclase (about 50 percent) and amphibole (about 50 percent) veins; and (C) veins of predominantly plagioclase (>90 percent) and minor pyroxene and amphibole (<10 percent). Types (A) and (B) tend to be thin (less than 0.3 cm wide) branching veinlets that are not traceable in outcrop for more than a few meters. Furthermore, they appear to be restricted to the plagioclase lherzolite. Clinopyroxene and amphibole both weather black and form anhedral grains that are essentially the width of the vein; white weathering plagioclase fills the gaps between these grains. Type (C) forms thicker (≤ 4 cm) branching and anastomosing veins that are traceable over outcrops for 10-20 m. In these veins, black weathering pyroxene is concentrated in narrow zones of uniform thickness along the vein walls and white weathering plagioclase fills the interior of the veins. As can be seen in Figure 8, types (B) and (C) crosscut the websterite dikes and are, therefore younger.

Local derivation of these veins is suggested by: (1) their thinness and discontinuity; (2) the lack of obvious association with larger

intrusive bodies; and (3) the apparent restriction of types (A) and (B) to plagioclase lherzolite hosts. If vein types (A) and (B) had formed by injection of foreign melts into the peridotite, then one would expect them to also intrude dunite and harzburgite. Therefore vein types (A) and (B) may have been internally derived from the host plagioclase lherzolite by partial melting and concentration of the melt (see discussion).

GABBRO AND RELATED ACCUMULATE ROCKS

INTRODUCTION

The Trinity peridotite is intruded by sequences of coarse-grained gabbro and related ultramafic cumulate rocks. The two major occurrences of this rock association are exposed on China Mountain and on the peaks to the west and southwest of Toad Lake. These will be referred to as the China Mountain and Toad Lake bodies, respectively. These gabbro bodies are composed of basal sections of clinopyroxene rich cumulates that grade upward into a massive gabbro. The most complete lithologic sequence is exposed in the Toad Lake body near Bear Creek where the section from bottom to top is: (1) interlayered wehrlite and clinopyroxene-bearing dunite; (2) interlayered olivine pyroxenite and foliated pyroxenite; (3) feldspathic pyroxenite; and (4) massive clinopyroxene, hornblende gabbro. This section is described in detail below.

The China Mountain body is similar to the Toad Lake body except that the layered sequence is not well exposed. On the north side of China Mountain, massive clinopyroxenite rests directly on harzburgite and dunite and grade upward into gabbro. On the east and south sides of China Mountain and South China Mountain, the contacts are faulted

and only minor amounts of layered clinopyroxene-rich cumulates are preserved in fault slices.

INTERLAYERED WEHRLITE AND DUNITE

The interlayered wehrlite and clinopyroxene-bearing dunite are composed of layers of wehrlite and clinopyroxenite that range in thickness from 0.3 to 5 cm and are mainly defined by variations in the relative abundance of olivine and clinopyroxene. Figure 10 illustrates the typical appearance of this unit 0.5 km north of Bear Creek.

The dunite, in most places contains less than 10 percent green clinopyroxene in a matrix of olivine and trace amounts of spinel. Locally, however, pyroxene reaches about 20 percent in abundance. The pyroxene weathers gray and ranges from 0.05 cm to 10 cm in size; the larger grains are commonly poikilitic and form elongate clumps and stringers up to about 2 cm thick and 10-15 cm long that tend to parallel the layering (Figure 10). The smaller grains tend to be equant and evenly disseminated.

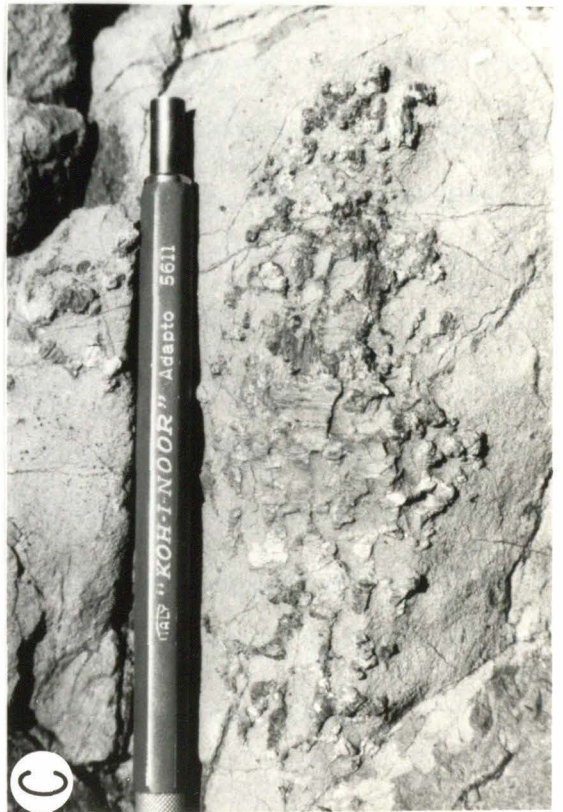
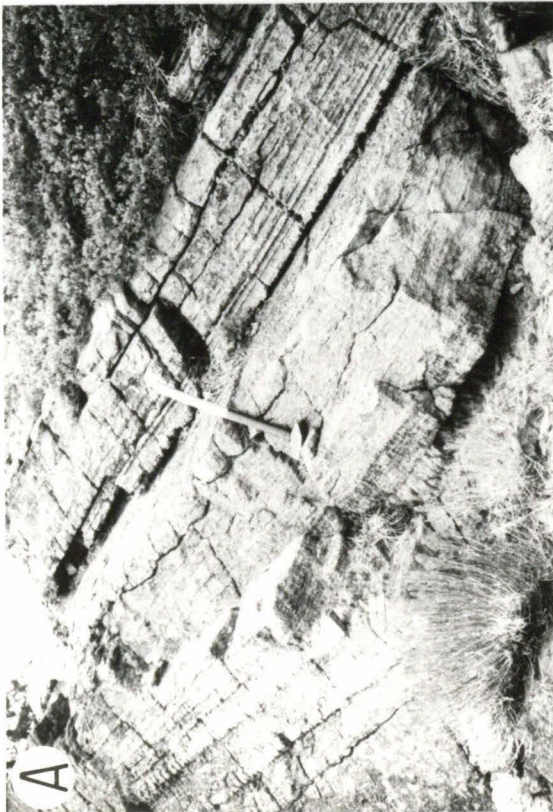
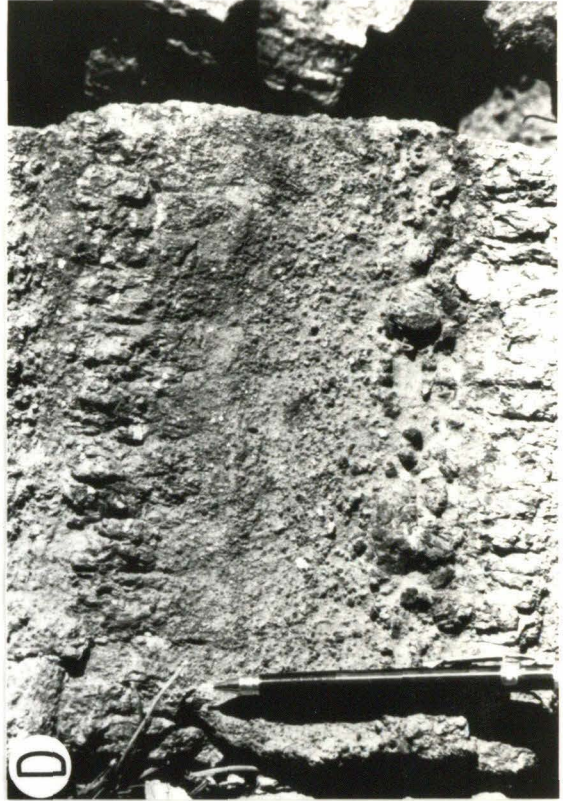
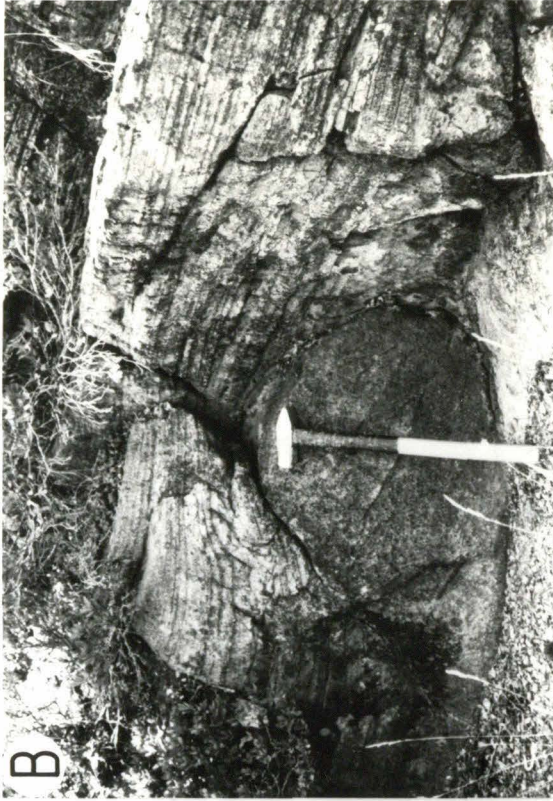
Most of the boundaries between the dunite and wehrlite are marked by a sharp change in modal mineralogy and pyroxene grain size. In contrast to the dunite, the wehrlite layers are typically composed of about 0-30 percent olivine and 70-100 percent clinopyroxene, and have pyroxene grains 0.1-0.5 cm in size. Some of the contacts, however, are gradational and are marked by a gradual change in pyroxene abundance and grain size.

There are several structures in these rocks in addition to the layering. In some places, bedding is graded with respect to both grain sized and pyroxene abundance (Figure 10). Near the base of the layered sequence, drape folds are developed in layers that overlie

Figure 10: Structures and textures in the lower cumulate ultramafic rocks of the Toad Lake Gabbro. All photographs are from Bear Creek.

- (A) Interlayered dunite and wehrlite (resistant).
- (B) Drap^e folds in interlayered dunite and wehrlite.
- (C) Poikilitic clinopyroxene grain in cumulate dunite.
- (D) Size-graded bedding in interlayered wehrlite and dunite.

Resistant grains that define grading are clinopyroxene.



1-2 m sized dunite "blocks" (Figure 10). Isoclinal folds in the layering are developed locally, and only involve small packages of layers no more than about a meter thick. Layering above and below these folds is essentially undisturbed so that the appearance of these structures is reminiscent of soft-sediment folds in sedimentary rocks. The layering is cut by wehrlite dikes that range in thickness from about 1 to 3 m and are composed of 80-100 percent coarse-grained (2-20 cm), green clinopyroxene and 0-20 percent interstitial, red-weathering olivine. These dikes are distinct from websterite dikes that cut the country rock peridotite by virtue of their greater thickness, coarser grain size, and mineralogy.

The base of the layered sequence is exposed in an outcrop about 0.5 km north of Bear Creek beside a major logging haul road. Here, the layered dunite and wehrlite rest on a basement of dunite and harzburgite. The transition from the basement rocks to the cumulates occurs over a distance of about 100 m and the contact between the cumulate and older peridotite is difficult to locate. As the cumulate rocks are approached from the basement rocks, dunite becomes more abundant relative to harzburgite until, at the base of the well defined layers, dunite is the principal lithology. Within the dunite, poikilitic pyroxene becomes more abundant as the layering is approached. This relationship is similar to the peridotite to cumulate transitions described in Cyprus (George, 1978) and in Oman (Hopson et al., 1979). The gradational nature of this contact is in contrast to the clear intrusive nature of the contacts at the top of the gabbro.

INTERLAYERED PYROXENITE AND OLIVINE-PYROXENITE

The layered dunite-wehrlite rocks grade upward into olivine pyroxenite and pyroxenite with increasing pyroxene abundance relative to olivine. The rocks are composed of 80-100 percent euhedral green pyroxene and 0-20 percent olivine (Figure 11). Pyroxene grains range in size from 0.25 to 2 cm and tend to be slightly elongated with the long axis oriented in a plane. This preferred orientation defines a planar fabric that is parallel to the layering in the rocks and is, therefore, interpreted to be a primary magmatic feature.

FELDSPATHIC CLINOPYROXENITE

The pyroxenite and olivine-pyroxenite rocks grade upward into pyroxenites that contain minor amounts of plagioclase (Figure 11). The feldspathic pyroxenites have highly variable modes. In most places, they are composed of 70-80 percent euhedral, green clinopyroxene and 10-20 percent interstitial, white plagioclase, and 10-20 percent olivine. These rocks are essentially massive; although near the base of this unit, pyroxene euhedra define a weak foliation that is approximately parallel to the layering in the underlying rocks.

GABBRO

The feldspathic pyroxenite grades upward into gabbro over a distance of about 10-30 m with an increase in the abundance of plagioclase. The gabbro is extremely variable in modal mineralogy and grain size. In most places, it is a coarse grained intergrowth of 40-50 percent green clinopyroxene and 50-60 percent white plagioclase. The clinopyroxene forms equant to slightly elongate, euhedral crystals that range in size from about 0.25 to 2.5 cm and weathers red-brown

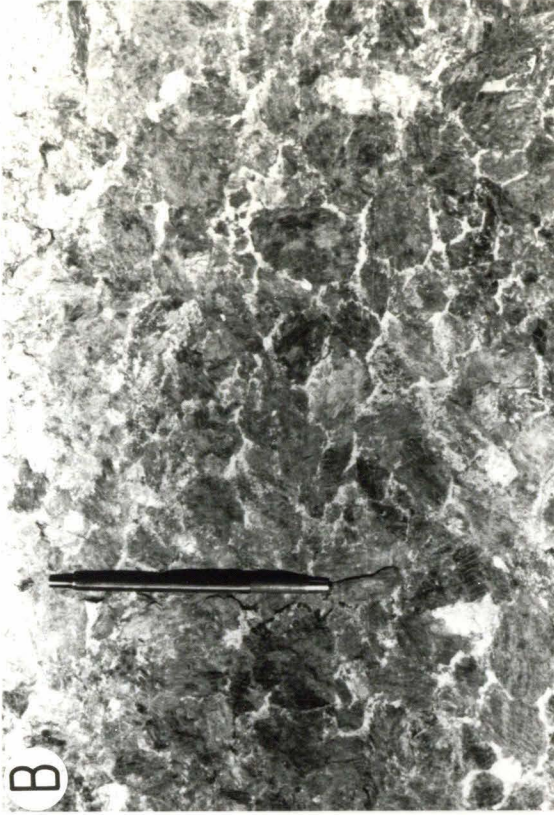
Figure 11: Outcrop appearance of gabbroic rocks and diabase dike.

(A) Texture of pyroxenite exposed south of Bear Creek.

(B) Texture of feldspathic pyroxenite exposed south of Bear Creek. Plagioclase (white) fills interstices between ortho- and clinopyroxene.

(C) Coarse grained facies of the Toad Lake Gabbro exposed south of Bear Creek.

(D) Diabase dike cutting hornblende diorite in creek below Dobkins lake. Darker color of the interior of the dike is due to coarser grain size.



The plagioclase is interstitial to the clinopyroxene and forms chalky, white weathering, anhedral to tabular grains from 0.1 to 0.5 cm in size. Toward the upper portions of the gabbro, black amphibole forms rims around the pyroxene and forms as much as 10 percent of the rocks. Locally, clinopyroxene segregations that are >90 percent clinopyroxene and <10 percent plagioclase form bodies that range in size from 2m to tens of meters across. These bodies tend to be very coarse grained and have euhedral pyroxene crystals up to 1 m long (Figure 11).

Both the gabbro and clinopyroxene segregations are massive and essentially without structures. Layering, defined by variations in the modal abundance of pyroxene, was observed in some float blocks in the glacial till, but these are not abundant and the layering has not been observed in place.

ACCUMULATE ORIGIN

The accumulate origin of the basal layered sequence and the pyroxenites is suggested by: (1) the poikilitic texture of many of the pyroxene grains in the dunite; (2) the well developed layering; (3) rare size-graded bedding; (4) possible "soft-sediment" folds in the layering; (5) drape folds of thinly layered dunite and wehrlite over large dunite blocks; (6) the preferred orientation of the pyroxene grains in the pyroxenites; and (7) the gross texture of the wehrlites and clinopyroxenites, which is consistent with intercumulus growth of olivine and/or plagioclase between euhedral cumulate clinopyroxene grains.

PEGMATITIC GABBRO DIKES

Pegmatitic gabbro dikes occur in swarms within the peridotite near the China Mountain and Toad Lake gabbro bodies. These dikes

have extremely variable modal mineralogy, and are composed of about 30-40 percent green clinopyroxene, 60-70 white plagioclase, and 0-40 percent black amphibole. The dikes tend to be intruded into conjugate joints and shear planes. At Vicki Bluff (Plate 2), offsets in the contacts between the peridotite lithologies are common across these dikes. The dikes contrast to the microgabbro dikes in that they are coarser grained, contain only one pyroxene, sometimes have abundant amphibole, and show no evidence of folding or foliation.

These dikes range in thickness from 0.5 cm to 2 m. With increasing thickness, the grain size of the pyroxene and/or amphibole increase from about 0.5 cm across up to about 0.5 m, and the modal abundance of amphibole increases at the expense of pyroxene.

MICROGABBRO DIKES

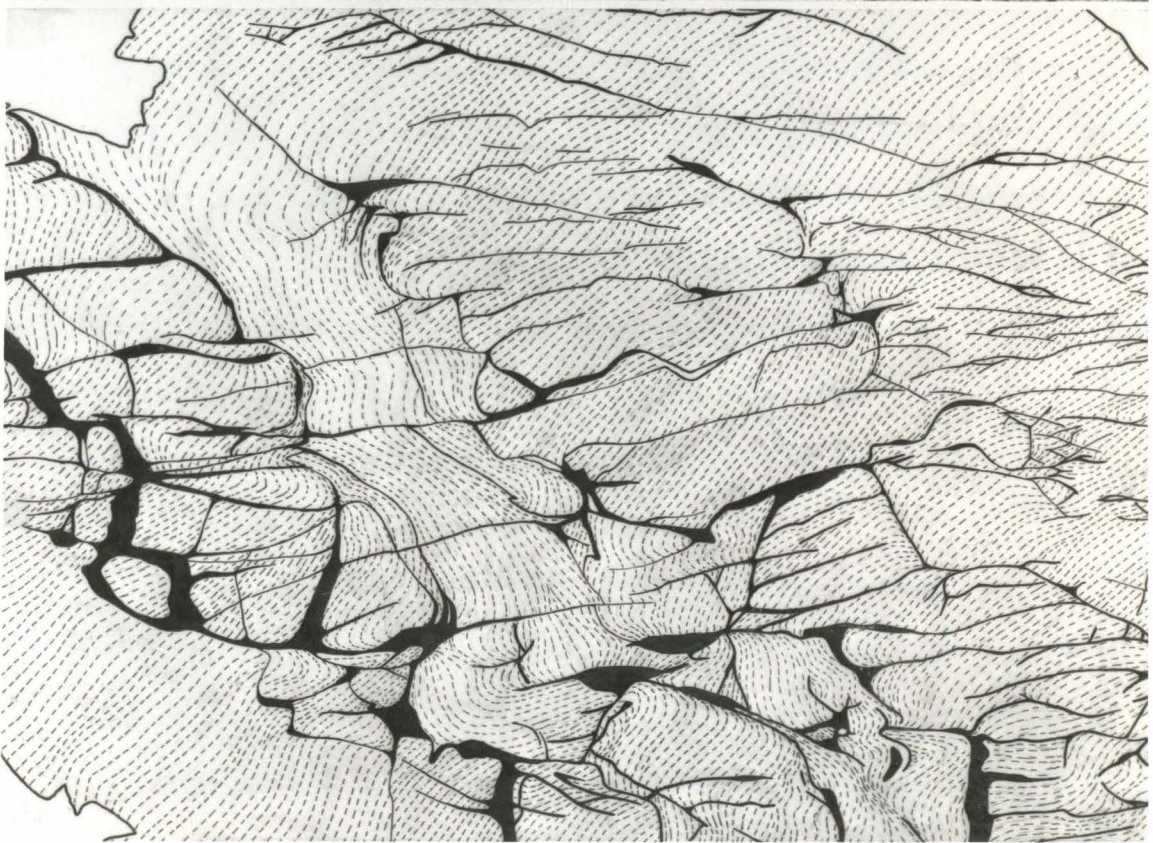
Microgabbro dikes intrude the Trinity peridotite on the west-facing cirque wall above Dead Fall Lakes, on the crest of the north-south trending ridge south of the Toad Lake gabbro body, and on the ridge crest northwest of Bull Lake. These swarms of dikes and veins range from 0.5 cm to 1 m in width and are oriented along two sets of conjugate planes. A photograph and map of one of these dikes are shown in Figure 12. The foliation in the host peridotite is highly deformed in the vicinity of these dikes and locally is folded into tight folds. Figure 12 suggests that the dominant set of dikes is also folded and that the lesser conjugate set was injected into the peridotite from the crests of these folds.

There is considerable variation in modal mineralogy; the small dikes tend to be close to 100 percent plagioclase while the thicker dikes have plagioclase and two pyroxenes. Typically, the rock consists

Figure 12: Microgabbro dikes cutting plagioclase lherzolite in upper Dead Fall Lakes Basin.

Top: Photograph of outcrop surface.

Bottom: Map of above outcrop showing distribution of the dikes (solid black) and the orientation of the foliation (dashed lines) in the peridotite.



of a fine-grained (0.05-0.1 cm) intergrowth of about 35 percent white plagioclase, about 35 percent olive-green pyroxene, and about 30 percent black pyroxene. The larger dikes have a gneissic texture defined by lighter-colored, plagioclase-rich zones about 0.1-0.3 cm wide and 3-6 cm long. This banding tends to parallel the walls of the dikes, suggesting that it is flow banding produced during emplacement.

ALTERATION

All of the gabbroic and associated accumulative ultramafic rocks are pervasively altered. Plagioclase is almost completely saussuritized and relict grains are extremely rare. Clinopyroxene is replaced by amphibole and orthopyroxene by talc. Olivine is altered to serpentine and magnetite.

NATURE OF THE GABBRO-PERIDOTITE CONTACT

Goullaud (1977) studied in detail the nature of the contacts between gabbroic bodies and the Trinity peridotite in the vicinity of Coffee Creek and in the vicinity of Boulder Peak. His results indicate that these contacts are more complex than the classic gabbro-peridotite relationship in ophiolites as described by Coleman (1977). My investigation of the gabbro-peridotite contacts of the Toad Lake and China Mountain bodies appears to corroborate those of Goullaud (1977).

The base of the gabbro bodies appears to be resting on a peridotite platform. As discussed above, an example of this contact is visible near Bear Creek. Mapping in this vicinity and to the north of China Mountain (Plate 1) demonstrates that the floor of the gabbro on the north sides of both the Toad Lake and China Mountain bodies dips

about 25-45 degrees to the south. Although the contacts are not well exposed, attitudes on the north side of China Mountain indicate that the base of the gabbro truncates the foliation in the peridotite at a high angle.

However, these gabbro bodies are not simply deposited on a peridotite basement. The upper gabbro of the Toad Lake body intrudes the overlying peridotite country rock to the southwest of Toad Lake. The intrusive nature of this contact is indicated by: (1) truncation of the foliation in the peridotite by the contact; (2) increased serpentinization of the peridotite with proximity to the gabbro; (3) inclusions of peridotite within fine grained gabbro near this contact; (4) chilling of the gabbro to a fine grained border facies within about 30-50 m of the contact; and (5) the presence of pegmatitic gabbroic dikes that cut the peridotite near the larger gabbro body. This contact of the Toad Lake body dips to the east, away from the gabbro body, and therefore, appears to be near the roof of the gabbro body. This suggests that the gabbro bodies may be emplaced into the peridotite as isolated intrusions that approach laccoliths in shape rather than deposited as a gabbro sheet of enormous lateral extent on top of a peridotite basement.

ALBITE GRANITE

Albite granite dikes intrude the peridotite near the summit of Mount Eddy and at the southeast corner of the study area. The dikes are up to 6 m in thickness and have serpentinized aureoles about 30 m wide. Typically they consist of a 0.1-0.5 cm intergrowth of about 10-20 percent quartz and 60-70 percent gray plagioclase with 10-20

percent green to black amphibole and/or epidote(?). The plagioclase forms discrete tabular crystals; the interstices are filled by finer grained anhedral quartz, plagioclase and amphibole. The overall texture is granular with a seriate grain size, and appears strongly cataclastic. Angular xenoliths of white weathering serpentized peridotite up to 2 m across are included in the dike. There is no field evidence for a genetic relationship linking the albite granite to any other lithology in the study area.

HORNBLLENDE DIORITE

Hornblende diorite occurs as stocks, plugs and some dikes that are intruded into the peridotite along faults. These bodies are most abundant to the immediate north and west of Mount Eddy (Plate 1). In hand specimen, the rock is seen to consist of about 20-30 percent black amphibole phenocrysts, and 0-30 percent equant, euhedral to rounded, white plagioclase phenocrysts. These minerals are set in a fine-grained, white to gray groundmass of feldspar and amphibole. The amphibole phenocrysts are elongate to acicular and range in length and width from about 0.25 and 0.1 cm to about 0.25 and 0.02 cm. Plagioclase phenocrysts, where present, reach 0.2-0.5 cm in size. In the finer grained rocks, acicular amphibole is common and plagioclase phenocrysts are rare; in the coarser grained rocks, plagioclase phenocrysts are abundant.

The hornblende diorite clearly intrudes the peridotite. Evidence for this relationship is: (1) the diorite contacts crosscut the foliation in the peridotite; (2) the presence of peridotite inclusions in the diorite; (3) local metamorphism of the peridotite within 50 m

of the contact to serpentine and tremolite bearing assemblages; and (4) intrusion of the diorite along fault zones that offset the units of the peridotite. Furthermore, the hornblende diorite contains inclusions of the layered wehrlite and dunite from the gabbro sequence and truncates layering of the Toad Lake body to the north of Bear Creek. This indicates that the hornblende diorite was intruded after the gabbro and related rocks.

DIABASE

Diabase dikes intrude the peridotite along fault zones that displace the other units in the peridotite, and also directly intrude both the hornblende diorite north of Dobkins Lake (Figure 11) and the Toad Lake gabbro body. The dikes are generally 1-5 m wide and crop out sporadically along some fault zones for distances of 4-5 km. In hand specimen, the diabase is a dark gray to black, dense aphanitic rock. These dikes are surrounded by wide zones of serpentinized peridotite where they intrude the ultramafic rocks, and may be partially to completely rodingitized. These dikes are readily distinguished from the fine grained hornblende diorite dikes by their darker color, higher density and absence of acicular hornblende, and from the micro-gabbro dikes by the presence of a wide aureole of serpentinization.

PALEOZOIC(?) SEDIMENTARY AND VOLCANIC ROCKS

The Trinity peridotite is faulted against sedimentary and volcanic rocks near the eastern margin of the study area. Within the study area, these rocks are about 20-30 percent black, well-laminated shale

and about 70-80 percent volcanic rocks. The volcanic rocks consist mostly of red-weathering, gray-green plagioclase porphyry. Phenocrysts of plagioclase are blocky, are about 0.1-0.5 cm in size, and show discontinuous zoning in hand specimen with white rims surrounding gray cores. The volcanic rocks also include some agglomerate that is composed of angular, purple, aphanitic clasts up to 30 cm across set in an aphanitic gray matrix.

These rocks were not studied in detail and no attempt was made to subdivide them into separate mappable units. Previous mapping by the Regional Geologic Mapping Program of the Southern Pacific Company Land Department is published in the California State geologic map of the Weed Sheet (Strand, 1964). This map identifies these units as Devonian(?) or older metavolcanic rocks and Mississippian marine rocks. Parts of the Kennett and Bragdon formations described by Kinkel et al. (1956), Albers and Robertson (1961) and Albers (1964) are similar to the shales and volcanic rocks that are exposed on the east flank of Mount Eddy. The shale is similar to rocks cropping out approximately 15 km to the south on the Castella road near Boulder Peak; these rocks are also faulted over the Trinity peridotite (personal communication, Lee Goullaud, 1977).

QUATERNARY DEPOSITS

A significant amount of the study area is covered by Quaternary deposits (Plate 1). For the most part, these deposits are concentrated on the floors of the wide glaciated valleys. However, some deposits are also perched on the valley walls.

Two ages of glacial till as well as more recent stream deposits,

colluvium and tillus are identified. The younger glacial till is composed of unconsolidated and unsorted sediments ranging in grain size from boulders to silt. This till fills the valley floor, and along with stream deposits, colluvium and tillus is lumped on the maps as deposits of Quaternary age. These sediments are all locally derived and sample only the parts of the basin immediately upstream. The source areas of samples that were collected from the glacial till in the lower valleys have been located in the cirque walls of the upstream valleys. The older glacial deposits are mapped as older deposits of Quaternary age. They crop out as well-indurated, unsorted conglomerate perched high on valley walls. No detailed study of any of these rocks was attempted. Sharp (1960) described glacial deposits of Wisconsin age and an older deposit of possible pre-Wisconsin age in the Trinity Alps to the southeast.

STRUCTURAL HISTORY

INTRODUCTION

This chapter reports the sequence of events in the structural history of the Trinity peridotite. Although these observations will be used to place constraints on the petrogenesis of the peridotite, this chapter will minimize petrogenetic interpretations.

The structural history of the Trinity peridotite as discussed in this work is based primarily on field observations. Goullaud (1977) has presented some petrofabric data on samples from the vicinities of Coffee Creek and Boulder Peak. This study showed that, although the minerals in the peridotite displayed only a weak shape fabric, olivine and orthopyroxene have strong preferred orientations that are asymmetric to the principal foliation and each other. Goullaud (1977) inferred that these features were produced during high temperature flow of the peridotite involving plastic deformation and recrystallization.

The peridotite preserves a complex structural record of multiple deformation and petrogenetic events. The following events, in order of their occurrence, are recognized: (1) formation of banding in the peridotite; (2) isoclinal folding of this banding; (3) intrusion of ariegite dikes; (4) formation of large bodies of dunite and harzburgite; (5) formation of a pervasive foliation with attendant minor folding; (6) formation of websterite dikes and wehrlite layers; (7) local, open folding of the websterite dikes; (8) faulting followed by intrusion of gabbro; (9) intrusion of hornblende diorite and albite granite followed by additional faulting; and (10) intrusion of diabase dikes.

THE VICINITY OF MOUNT EDDY AND CHINA MOUNTAIN

RELATIVE AGES OF EVENTS

The oldest mesoscopic structure in the Trinity peridotite is the banding that is defined by variations in modal mineralogy (Figure 5). This banding is well developed on the ridge south of Bull Creek, at Vicki Bluff, and in the basin north of Mount Eddy. Locally, these bands are continuous across lithologic boundaries from plagioclase lherzolite through lherzolite and into harzburgite. Thicknesses remain essentially unchanged from one lithology to another, but the minerals that define the layering change; plagioclase is not involved in the lherzolite and clinopyroxene is not involved in the harzburgite.

Some northeast-trending, easterly-dipping, open to isoclinal mesoscopic folds were identified in the banding (Figure 13). These folds are taken as evidence that the peridotite experienced folding early in its history although such folds have not been widely recognized in the study area. The axial planes of these folds are not related to the observed penetrative foliation in the peridotite. The best displayed and most accessible example is at Vicki Bluff (Plate 2) and is shown in Figure 13. The isoclinal shape of these folds is probably the reason that they were not identified throughout the study area; in the absence of a well exposed fold hinge they are undetectable.

The emplacement of the ariegite dikes is postulated to postdate the isoclinal folding event although there are actually insufficient data to make a definitive statement on the relative ages of these events. Most of the ariegite dikes are relatively undeformed. Some of the dikes are tightly folded, but the axial planes of the folds are paral-

Figure 13: Structures in the Trinity peridotite.

- (A) Small mesoscopic fold in the banding of the peridotite (east flank of Mount Eddy).
- (B) Large, isoclinal fold in banding at Vicki Bluff. Hammer is on and parallel to fold axis. Note that fold axis is also folded.
- (C) Large, tabular dunite body cutting banding at Vicki Bluff. Dunite is the smooth rock at the top of the photograph.
- (D) Dunite body cutting ariegite dike at Vicki Bluff.



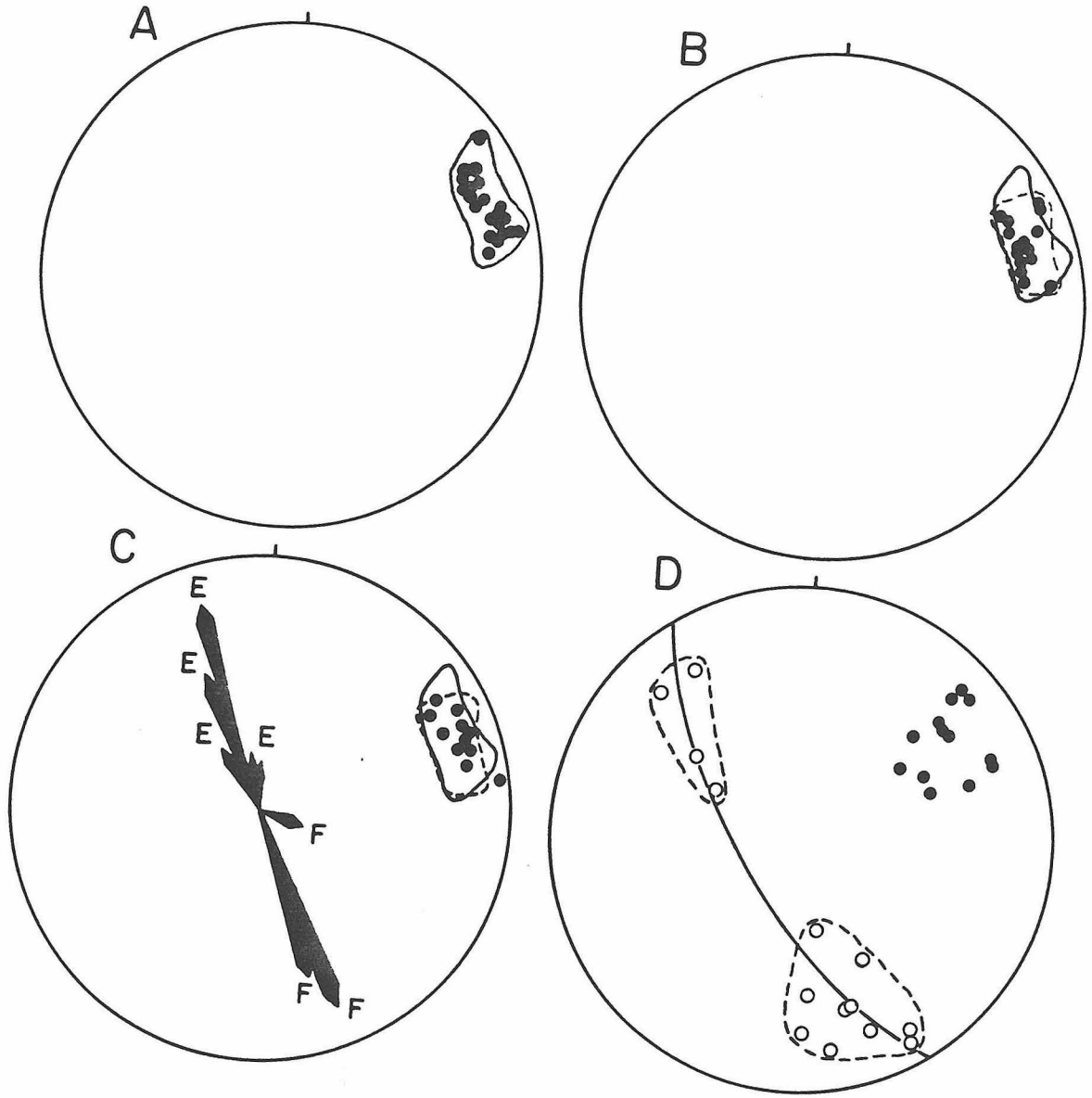
lel to the foliation in host peridotite and the dike. Therefore, the folding of these dikes appears to coincide with the formation of the foliation rather than with the earlier isoclinal folding event.

Crosscutting relationships suggest that the formation of large dunite and harzburgite bodies postdated the emplacement of the ariegite dikes and the isoclinal folding event. Large dunite bodies truncate the aforementioned layering and ariegite dikes, and at Vicki Bluff (Figure 13), crosscut the axis of a large isoclinal fold. The consistently repeated lithologic zoning from plagioclase lherzolite to lherzolite to harzburgite to dunite suggests that the dunite, lherzolite and harzburgite formed as in situ replacements of a preexisting plagioclase lherzolite. This interpretation is consistent with: (1) the occurrence of irregular shaped blocks of plagioclase lherzolite in harzburgite; (2) the occurrence of irregular shaped blocks of harzburgite in dunite; (3) the parallel attitudes of layering and isoclinal folds in these isolated blocks; and (4) the observation that layering is locally traceable across lithologic contacts.

The next event appears to have been the formation of a penetrative foliation. Parallel foliations are present in plagioclase lherzolite, lherzolite, harzburgite, dunite, and ariegite. This observation is illustrated by the maps of Vicki Bluff and of Lou Ann Bluff and in the equal area projections of foliation attitudes in Figure 14. The coincidence between the foliation planes in plagioclase lherzolite, harzburgite and dunite in Figure 14 suggests that these lithologies are cut by the same foliation. Of course, it is possible that the foliation predated the petrogenetic event that formed the dunite, harzburgite and lherzolite, and that the parallelism of this

Figure 14: Lower hemisphere, equal area projections and rose diagrams showing orientations of structures in Vicki Bluff (A-C) and Lou Ann Bluff (D).

- (A) Poles to foliation in dunite (24 points). Foliation defined by flattened spinel grains and trails of spinel grains. Envelope (solid) drawn to enclose all points and reproduced in Figures 14B and 14C for reference.
- (B) Poles to foliation in harzburgite, lherzolite, and plagioclase lherzolite (15 points). Foliation defined by flattened spinel grains and trails of spinel grains in harzburgite and lherzolite; foliation in plagioclase lherzolite defined by plagioclase lenses. Envelope (dashed) drawn to enclose all points and reproduced in Figure 14C for reference.
- (C) Poles to axial planes of embayments in harzburgite-dunite contacts (11 points) and rose diagram showing trend of embayments in harzburgite-dunite contacts (32 measurements; marked as "E") and trend of axial planes to folds in websterite dikes (12 measurements; marked as "F"). Dashed and solid envelopes from (A) and (B).
- (D) Poles (solid) to foliation and orientation of lineation (open) in plagioclase lherzolite. Solid great circle is approximate average foliation.



structure throughout these lithologies is due to its preservation through the petrogenetic event. The contacts between these lithologies, however, appear to predate the formation of the foliation. These contacts are carefully depicted in the map of Vicki Bluff (Plate 2), and are highly crenulated and embayed. The map indicates that these structures are parallel to the local foliation. This observation is reinforced by Figure 14C, which shows a rose diagram of trends of contact crenulations and embayments, poles to the axes of some of these structures, and the locus of poles to the foliation. The poles to the foliation coincide with the poles on the crenulations and embayments and fall in the plane that is normal to the rose diagram plot for the crenulations and embayments. These observations are consistent with formation of the embayments and crenulations as folds for which the foliation is an axial plane foliation. Therefore, the formation of the foliation appears to postdate or, at least, continued to form after the formation of the dunite, harzburgite and lherzolite at Vicki Bluff. Similar observations throughout the study area suggest that this is the order of events almost everywhere.

Some dunite bodies, however, do not appear to be affected by the foliation event. Local occurrences of poikilitic clinopyroxene and undeformed spinel pods (Figure 6) do not display preferred orientations related to the regional foliation. The dunite above Dobkins Lake is interlayered with wehrlite that has a foliation discordant to the regional foliation. These features, therefore, are interpreted to have formed subsequent to the cessation of foliation formation, and may suggest a later, post-foliation episode of dunite and, by analogy, formation of harzburgite and lherzolite.

Most of the websterite dikes appear to crosscut all of the above structures, and none is foliated. However, there is clearly more than one generation of websterite dike emplacement. This is indicated by crosscutting relationships at Vicki Bluff (Plate 2) and elsewhere. In general, there is a tendency for thicker dikes to cut thinner ones and for the feldspathic dikes to cut the nonfeldspathic dikes. Furthermore, there is a suggestion that some of the websterite dikes may have formed just prior to the cessation of foliation formation. These dikes are folded into open folds with their fold axes parallel to the foliation. This is illustrated in Figure 8, which is a folded websterite dike at Vicki Bluff, and in Figure 14C, which is a rose diagram of fold axis trends combined with a stereographic projection of poles to measurements on the foliation at Vicki Bluff. Figure 14C demonstrates that the poles to the foliation lie in a plane that is normal to the trend of fold axes, which is consistent with the fold axes and foliation being coaxial and cogenetic.

Depleted zones of dunite and harzburgite are developed on some websterite dikes that crosscut plagioclase lherzolite. At Lou Ann Bluff and Vicki Bluff, some of these dikes can be traced into and across large dunite bodies (Plates 2 and 3). This relationship suggests that the formation of these depleted zones represents another episode of dunite formation that is independent of the formation of the large dunite bodies.

Locally, for example at Lou Ann Bluff, the websterite dikes occur in swarms (Plate 3). This suggests that their emplacement may have been, to some extent, controlled by preexisting joints or faults. However, conjugate sets of websterite dikes have not been recognized

in the field, as would be expected of joint-controlled emplacement, nor have offsets of peridotite lithologies across these dikes been observed, as would be expected of fault-controlled emplacement. Furthermore, many of the dikes are curved and branching or anastomosing, which is somewhat inconsistent with emplacement along faults or joints.

Faulting, followed by the intrusion of pegmatitic gabbro dikes and large gabbro bodies, are the next events that affected the Trinity peridotite. Gabbro dikes and the gabbro plutons are not crosscut by the penetrative foliation that cuts the peridotite, and gabbro dikes are straight and unfolded. Gabbro dikes that crosscut the websterite dikes at Lou Ann and Vicki Bluffs (Plates 2 and 3) and the websterite dikes in the vicinity of Toad Lake are affected by the intense serpentinization that is developed in the peridotite wall rocks near the Toad Lake gabbro. The occurrence of pre-gabbro faulting is well documented at Lou Ann and Vicki Bluffs (Plates 2 and 3) where gabbro dikes are emplaced along faults that offset the contacts between the different peridotite lithologies. This observation is consistent with mapping by Lindsley-Griffin to the immediate west of the study area. Lindsley-Griffin (1977) describes faults that cut the peridotite with major offsets to the west of China Mountain that are in turn crosscut by the China Mountain gabbro.

Hornblende diorite stocks, plugs and dikes were intruded into the peridotite after the emplacement of the gabbro. All of these diorite intrusions are surrounded by aureoles of serpentinized peridotite and locally, west of Dead Fall Lake, tremolite bearing assemblages are developed in the peridotite near the diorite contact. These diorite bodies also clearly crosscut the foliation that pervades the

peridotite. The absence of internal structures in the diorite bodies suggests that they postdate all significant penetrative deformation events. The hornblende diorite stocks and plugs clearly post-date the gabbro intrusions because the diorite body that is south of Dead Fall Lake both cuts the layering in the lower cumulate sequence of the Toad Lake gabbro and contains xenoliths that are derived from that sequence of rocks.

Hornblende diorite dikes are clearly intruded along fault zones that cut the peridotite and some of the gabbro intrusion. Examples are exposed on the ridge east of Dead Fall Lake basin where, a diorite dike intrudes a fault that crosscuts the peridotite, and along the east flank of China Mountain where diabase dikes intrude a fault that juxtaposes the China Mountain gabbro and the Trinity peridotite. However faulting continued after the emplacement of the hornblende diorite; a fault that offsets the diorite is exposed on the northern wall of Dead Fall Lakes basin.

The intrusion of the diabase dikes postdates the emplacement of the hornblende diorite. Diabase dikes are intruded into faults that crosscut the peridotite, and north of Dobkins Lake a diabase dike with chilled margins crosscuts a hornblende diorite stock (Figure 11).

The intrusion of the albite granite dikes is not well constrained in the context of the above sequence of events by field relationships. These dikes intrude the peridotite near the top of Mount Eddy, but all occurrences of plagiogranite are isolated from other intrusive lithologies. The plagiogranite dikes on Mount Eddy are crosscut by a fault that also cuts the hornblende diorite. These dikes are

straight, occur in a parallel set, and do not pinch and swell. These features are consistent with but do not require intrusion of the dikes along joint sets.

The timing of the emplacement of the microgabbro dikes is also uncertain. These dikes are isolated from other intrusive lithologies so that cross-cutting relationships cannot be determined. Their mode of occurrence as conjugate sets (Figure 12) suggests that they were emplaced after the peridotite was capable of brittle fracture, but the folding of the foliation in the peridotite suggests that the peridotite was still capable of plastic flow.

The different environments of serpentinization suggests that several episodes of serpentinization may have occurred. The earliest episode is serpentinization associated with the emplacement of the gabbroic bodies, followed by serpentinization during the emplacement of hornblende diorite intrusions, and then by serpentinization during the emplacement of diabase dikes. Serpentinization is also associated with faults that post-date the gabbro intrusions.

ABSOLUTE AGES OF EVENTS

Some constraints can be placed on the absolute ages of events based on isotopic and stratigraphic investigations that were conducted, for the most part, outside the limits of the study area. The available data are: (1) K-Ar age dates on amphibole from the China Mountain and Scott Mountain Gabbro bodies (Lanphere *et al.*, 1968); (2) zircon age dates for plagiogranites that cut gabbro bodies to the immediate west of China Mountain (Mattinson and Hopson, 1972); and (3) mapping of faults that cut Cenozoic rocks to the south of and to the east of

the Trinity peridotite.

The isotopic data yield a range of ages for the gabbroic rocks which, in turn, suggests a lower limit for the age of the Trinity peridotite. Lanphere et al. (1968) obtained ages of 400 to 450 m.y. for the Scott Mountain and China Mountain gabbros, respectively. Recently, K-Ar ages of more than 450 m.y. were obtained on samples from the same gabbro bodies (Marvin Lanphere, oral communication, 1980). These should be interpreted as minimum ages for these rocks because the range in age may reflect Ar-loss more than an actual difference of 50 m.y.. This interpretation is supported by a K-Ar age determination of another gabbro body that is located in the Coffee Creek drainage (Lanphere et al., 1968). This gabbro body is in close proximity to several Mesozoic intrusions. The K-Ar age of this body is only 330 m.y., which is consistent with Ar-loss during emplacement of the Mesozoic intrusions. The zircon data of Mattinson and Hopson (1972) yield ages of 450 and 480 m.y., which are consistent with the K-Ar age dates if argon loss is assumed. From the above data, the Toad Lake and China Mountain gabbro bodies and the gabbro dikes are inferred to have been intruded into the Trinity peridotite at about 450-480, and the Trinity peridotite is inferred to be older than this age.

The major faults that cut the Trinity peridotite appear to be either northeasterly trending or westerly to northwesterly trending. Faults with northeasterly orientations offset Cenozoic rocks near the southern margin of the Trinity peridotite (Irwin, 1963), and the northerly trending faults in the vicinity of Stephans Pass are active and have been the loci of earthquakes as recently as 1977 (Bennett et al.,

1978). The relationships between these fault systems is difficult to determine in the field. The westerly trending system appears to be truncating faults of the northerly trending system near the headwaters of the Trinity River, but the exposures are insufficient to document this properly. The westerly trending faults have a much more pronounced topographic expression suggesting that they may, indeed, be younger. Therefore, it appears that the Trinity peridotite may have been affected by faulting since or prior to the intrusion of the gabbro at 450-480 m.y. until the late Cenozoic.

SUMMARY

The structural history of the northeastern portion of the Trinity peridotite is summarized in Table 1. It is possible to divide this history into two major periods based on the previous discussion. The earliest period involved formation of banding, isoclinal folding, emplacement of ariegite and websterite dikes, multiple episodes of dunite, harzburgite and lherzolite petrogenesis, and formation of penetrative foliation. The significant features of this period are that the peridotite deformed by plastic flow as evidenced by the isoclinal folds and penetrative foliation, and that there is no evidence of brittle deformation. The second period includes emplacement of the gabbro plutons and dikes, emplacement of the hornblende diorite intrusions, and emplacement of the diabase dikes. This period is characterized by brittle deformation of the peridotite as evidenced by extensive faulting and jointing, and does not include evidence for continued plastic deformation. The albite granite dikes are assigned to the second period on the inference that they may have been emplaced along joints in the peridotite, and that albite granite intrudes the

Table 1: Structural History of the Trinity Peridotite
in the Vicinity of China Mountain and Mount Eddy

<u>Structure or Rock Type</u>	<u>Significant Relationships</u>
Banding	Isoclinally folded
Isoclinal Folds	Axial planes are folded into open folds; cut by foliation; cut by websterite dikes.
Ariegite Dikes	No apparent isoclinal folds; primary Al-phase is spinel, which is partially replaced by plagioclase; cut by foliation; cut by websterite dikes.
Large Dunite Bodies, Harzburgite and Lherzolite	Contacts between these units crosscut banding, isoclinal folds and ariegite dikes; these contacts are folded with axial planes parallel to foliation; foliation penetrative in most of these rocks.
Foliation	Cuts all of the above features except the interiors of the some of large dunite.
Websterite Dikes and Associated Depleted Zones	Crosscut most of above features; depleted zones are cut by regional foliation but most are not; some dikes have open folds with axes parallel to foliation; dikes occur in swarms, branch and anastomose; plagioclase is primary Al-phase in dikes.
Faulting	Offset all of the above features.
Gabbro	Pegmatitic gabbro intrudes faults and joints; gabbro plutons crosscut all of above features, serpentinize peridotite, and contain peridotite xenoliths.
Faulting and Hb Diorite Intrusion	Faults crosscut gabbro but are intruded by Hb diorite; Hb diorite crosscuts structures in peridotite and gabbro, and contains xenoliths of gabbro.
Albite Granite	Intruded along joints.
Faulting, Diabase Intrusion and Serpentinization	Diabase intrudes faults that cut all of the above features. Serpentinization associated with all faults and diabase.

gabbroic rocks to the west of the study area (Lindsley-Griffin, 1977). The microgabbro dikes appear to represent an event that bridges the two periods. The apparent intrusion of these dikes and veins along conjugate planes suggests that the peridotite was capable of brittle deformation, but the deformation of the foliation in the vicinity of these intrusions demonstrates that the peridotite was still capable of plastic flow.

The transition between the two periods is dated by the emplacement of gabbro intrusions into the peridotite circa 450-480 m.y.. Brittle deformation appears to have affected the peridotite from that time to present.

TRINITY ALPS

There is evidence for an additional, intense deformation event in the vicinity of the Trinity Alps to the southwest of the study area. Lipman (1964) studied the peridotite and underlying rocks of the Central Metamorphic Belt in the the Trinity Alps and made the following observations. First, the rocks of the Central Metamorphic Belt increase in metamorphic grade and intensity of deformation as the Trinity peridotite is approached. Within a few hundred meters of the contact, the sequence of subjacent rocks with increasing proximity to the peridotite is: (1) the Stuart Fork formation (greenschist) (2) the Salmon hornblende schist (epidote amphibolite); and (3), closest to the peridotite, the Grouse Ridge formation (epidote to almandine amphibolite). Second, the primary mineralogy of the peridotite is replaced by intergrowths of antigorite, chrysotile, talc, magnetite,

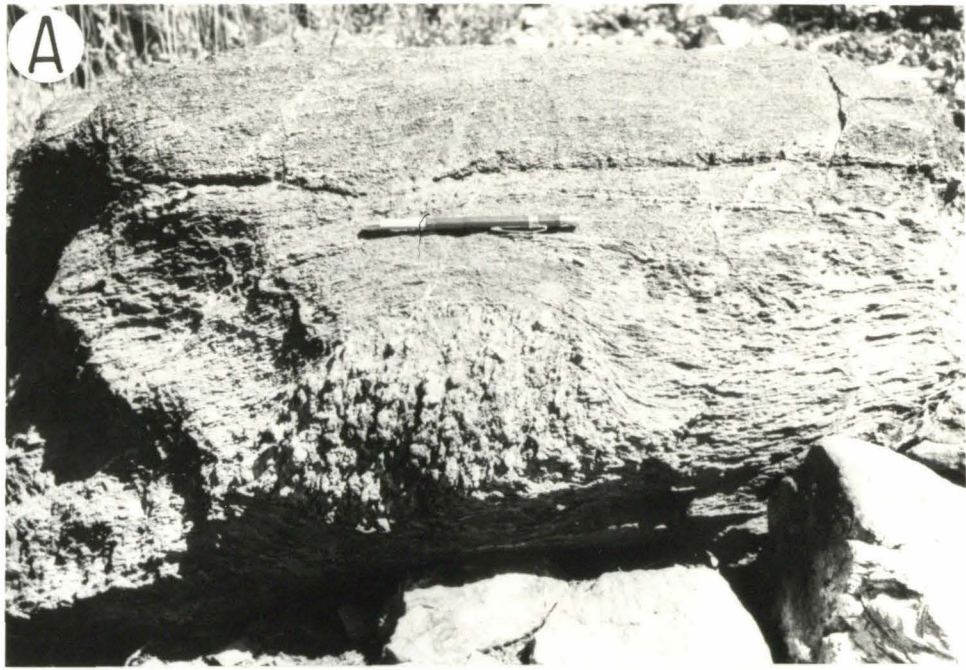
tremolite, and chlorite. Third, this alteration of the ultramafic rocks increases dramatically near the base of the peridotite. Fourth, the peridotite is cut by a foliation defined by smears of serpentine, chlorite and magnetite. Fifth, this foliation parallels the base of the peridotite. Lipman (1964) interpreted these observations to indicate that this foliation, the hydrous assemblage in the peridotite, and the deformation and metamorphism of the underlying rocks of the Central Metamorphic Belt were produced during the emplacement of the peridotite as an "essentially crystalline mass" over the Central Metamorphic Belt.

The deformation and recrystallization in the Trinity Alps described by Lipman (1964) appears to postdate the plastic deformation events that affected the rocks in the Mount Eddy-China Mountain area. Rotated boudins of peridotite (Figure 15) are exposed below Summit Lake, about 300-500 m above the base of the ultramafic rocks. These boudins contain a foliation defined by flattened pyroxene grains that is similar to the pervasive foliation in the vicinity of Mount Eddy and China Mountain. Surrounding these boudins is recrystallized and hydrated peridotite with a foliation defined by clots of serpentine and chlorite and magnetite. As can be seen from Figure 15, the two foliations are discordant, with the foliation defined by serpentine, chlorite and magnetite cutting the foliation defined by pyroxene. Furthermore, tabular dunite bodies or "dikes" that are essentially undeformed in the vicinity of Mount Eddy and China Mountain are strongly deformed in the Trinity Alps (Figure 15). Some of these "dikes" appear to postdate the foliation in the Mount Eddy-China Mountain area, suggesting that a younger plastic deformation event has occurred in the

Figure 15: Deformation effects in the Trinity Alps.

(A) Rotated peridotite boudin. See text for description.

(B) Stretched dunite "dike". See text for description.



Trinity Alps. Therefore, it appears that the structures, textures and mineralogy that are preserved in the peridotite in the Mount Eddy-China Mountain area were obscured by a second event of plastic deformation in the Trinity Alps.

Significantly, these two areas correspond to the top and the base of the ultramafic sheet that is the Trinity peridotite. The structures, textures and hydrous mineral assemblages described by Lipman (1964) in the Trinity Alps may have been produced in a zone of intense plastic deformation at the base of this sheet of ultramafic rocks when it was thrust over the underlying Central Metamorphic Belt. The older structures, textures and mineral assemblages may be preserved in the Mount Eddy-China Mountain area because these rocks were well removed from the zone of intense deformation at the base of the thrust sheet.

An estimate may be made for the age of this later deformation event. Lanphere et al. (1968) measured an Rb/Sr whole rock and muscovite separate isochron age of 380 m.y. on samples of amphibolite from the Central Metamorphic Belt from the vicinity of Coffee Creek. This age may date the emplacement of the peridotite if the metamorphism of the the amphibolite did coincide with thrusting.

SYNTHESIS

A brief summary and some speculations are offered at this point to tie together the structural history of the Trinity peridotite and to provide a framework for the following chapters.

In the Mount Eddy-China Mountain area, the Trinity peridotite was affected by an episode of plastic deformation followed by an epi-

sode of brittle deformation. The transition between these two episodes is marked by the intrusion of gabbro dikes and plutons at about 450-480 m.y.. It is inferred that the plastic deformation occurred while the peridotite was resident in the upper mantle. The following features formed during this period: banding, ariegite dikes, websterite dikes, large dunite bodies, isoclinal folds, penetrative foliation and a second set of folds. The subsequent brittle deformation may have occurred when the the peridotite was at or very near the base of the crust to be consistent with the emplacement of gabbro, hornblende diorite, albite granite and diabase, which are rocks of clear crustal affinity. A younger deformation is recorded in the Trinity Alps area, or, equivalently, at the base of the Trinity peridotite. This deformation may have postdated the others by as much as 100 m.y. and may record the emplacement on the Trinity peridotite into the crust.

PETROGRAPHY

INTRODUCTION

This section focusses on the petrography of the primary mineralogy of the peridotite. The primary mineralogy is defined as those minerals that predate the serpentinization or contact metamorphism of the rocks. Minerals and textures that were produced during serpentinization will be referred to as alteration products and will be discussed only briefly.

A summary of the petrography of the ultramafic lithologies is presented in Tables 2 and 3, and photomicrographs illustrating textural relationships are presented in Figures 16-22. Modal mineralogies determined by both automated point counts and petrographic point counts are listed in Table 4. The mineral chemistry for each peridotite lithology will be detailed in a separate section. The petrography of the alteration products is discussed collectively for all peridotite lithologies. The petrography of the other map units of the study area will not be detailed in this section, but brief summaries of the gabbro, microgabbro, hornblende diorite, diabase, and albite granite are presented in Tables 5 and 6 for comparison.

The peridotite displays several systematic mineralogic and textural variations in the series, plagioclase lherzolite, lherzolite, harzburgite and dunite. First, the decreasing mineralogic diversity along this series that is apparent in outcrop is confirmed by thin section examination of these rocks. The modal abundance of all minerals other than olivine and spinel decreases. Lherzolite is distinct from plagioclase lherzolite by a complete absence of plagioclase, and dunite from the other lithologies by a virtual absence of all other phases other than olivine and spinel. However, orthopyroxene and

clinopyroxene do persist in both harzburgite and dunite as rare interstitial phases that are not detectable macroscopically. Second, spinels become less ragged and more equant and euhedral. Third, spinels become less translucent, changing from translucent red-brown in the feldspathic lherzolite and lherzolite to opaque in the dunite.

The petrography of the peridotite is described with these progressive changes in mind. The plagioclase lherzolite, which is mineralogically and texturally the most complex, is described first. The other lithologies are described in order of decreasing complexity.

PRIMARY MINERALOGY AND TEXTURES

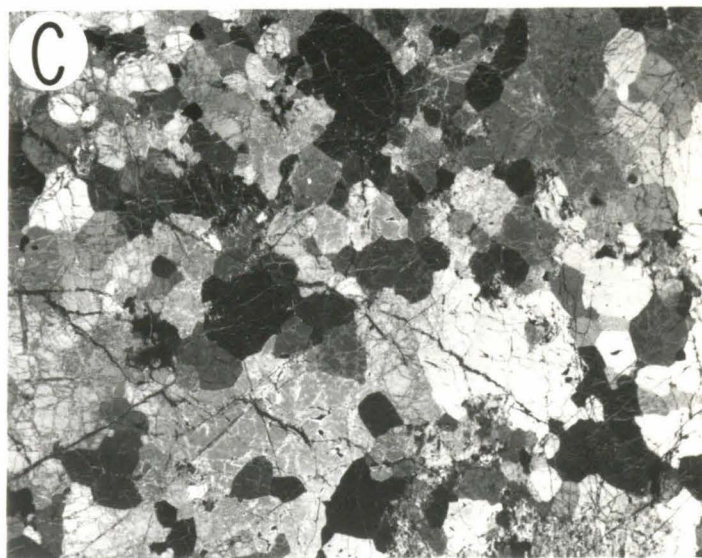
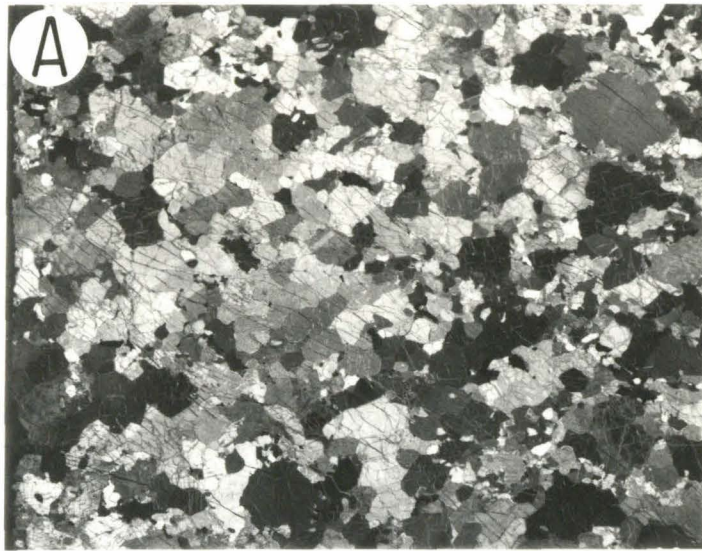
Plagioclase Lherzolite

Table 4 demonstrates that the modal mineralogy of the plagioclase lherzolite is variable. Typically, it is composed of 70-80 percent olivine, 15-20 percent orthopyroxene, 2-6 percent clinopyroxene, <1 percent spinel, 3-8 percent plagioclase, and <1 percent amphibole. Locally, the abundance of clinopyroxene is sufficiently low (<5 percent) that the rocks are technically plagioclase harzburgite rather than plagioclase lherzolite.

There is a range in textures present in the plagioclase lherzolite. The most common texture contains evidence of extreme deformation. These rocks contain large grains of olivine and pyroxene, which are termed porphyroclasts, set in a distinctly finer-grained, mosaic-textured matrix of olivine, pyroxene, spinel, plagioclase, and amphibole (Figure 16). Both the porphyroclasts and matrix grains show some degree of flattening and a preferred orientation that defines the penetrative

Figure 16: Representative textures of peridotite.

- (A) Equigranular texture in sample 9W20: a relatively equigranular intergrowth of large grains of olivine, orthopyroxene, and clinopyroxene and smaller interstitial grains of pyroxene, spinel and plagioclase. Crossed nicols. Horizontal field about 18 mm.
- (B) Porphyroclastic texture in sample CM 2: large, flattened pyroxene and olivine grains are set in a matrix of finer-grained, more equant olivine, pyroxene, spinel and plagioclase. Crossed nicols. Horizontal field about 18 mm.
- (C) Equigranular texture in dunite sample 7W228: a mosaic of polygonal olivine grains. Crossed nicols. Horizontal field about 18 mm.

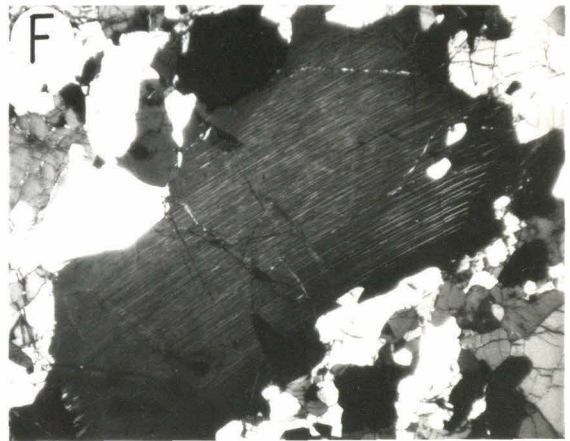
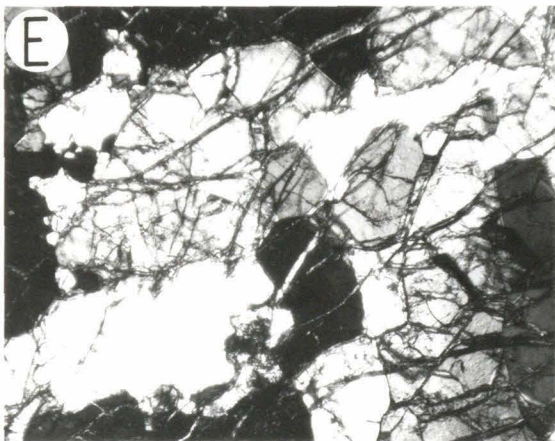
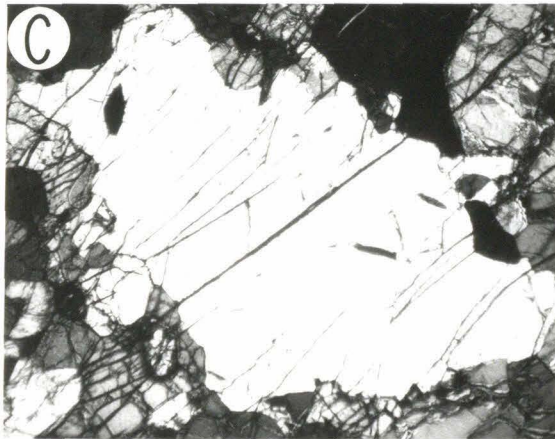
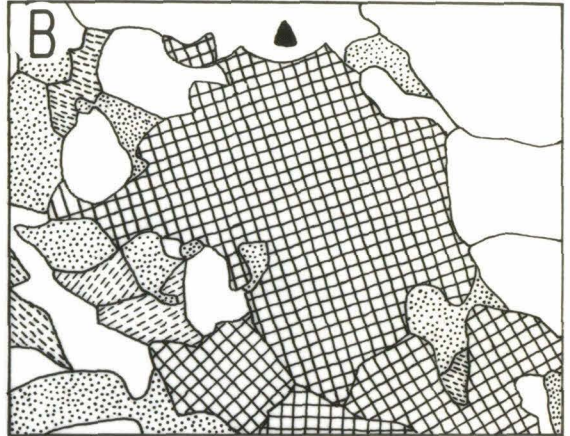


foliation of the rocks. This texture has been termed porphyroclastic by Mercier and Nicolas (1975) who recognized it in ultramafic xenoliths and in alpine-type ultramafic massifs. Some rocks are more equigranular (Figure 16). Olivine tends to form larger grains than the pyroxene, and grain boundaries tend to be more interlocking to cusped, and less mosaic-textured. Most importantly, the grains do not define a prominent foliation. This texture was also described in ultramafic xenoliths and alpine-type ultramafic massifs by Mercier and Nicolas (1977) who termed it equigranular. Within the plagioclase lherzolite of the Trinity massif, there is a complete gradation between these two textural end members. The transition between the two may be very abrupt, and both may be represented in different parts of the same thin section. The porphyroclastic texture is described first.

In the porphyroclastic rocks, large porphyroclasts of orthopyroxene (1-3 mm) and clinopyroxene (0.4-1 mm) and olivine (1-8 mm) are set in a finer grained (<1 mm) matrix of predominately olivine and lesser amounts of orthopyroxene, clinopyroxene, spinel, and plagioclase (Figure 16). Locally, plagioclase and spinel form discrete flattened segregations up to 0.6 mm long and 0.1 mm wide. Pyroxene porphyroclasts tend to form mosaic textured clusters about 2 mm across.

The orthopyroxene porphyroclasts in all samples of plagioclase lherzolite display evidence of recrystallization and replacement by other phases. The interiors of these grains contain abundant lamellae of high-Ca pyroxene that are oriented parallel to (100) and range in width from <1 to 2 microns (Figure 17). In some grains, these lamellae widen into elliptical grains up to 0.02 mm across. Few of the exsolution

- Figure 17: Textures of pyroxene porphyroclasts in the Trinity peridotite.
- (A) Clinopyroxene porphyroclast in in 9W20. Partially crossed nicols. Horizontal scale about 2.4 mm.
- (B) Map of figure 17A detailing textural relations. Grid, clinopyroxene; dashed lines, orthopyroxene; dotted, plagioclase; open, olivine. Note embayments on clinopyroxene porphyroclast filled by olivine and plagioclase.
- (C) Orthopyroxene porphyroclast with slight to moderate development of embayments in sample 8W67C. Orthopyroxene porphyroclast is the illuminated grain in the center of the field. Surrounding matrix is finer grained olivine, pyroxene, plagioclase and spinel. Partially crossed nicols. Horizontal field about 3 mm.
- (D) Orthopyroxene porphyroclast with deep, olivine-filled embayments in sample 9W20B. Orthopyroxene porphyroclast is the illuminated grain in the center of the field. Surrounding matrix is mostly olivine. Note cusped, concave shape of embayments. Partially crossed nicols. Horizontal field about 3 mm.
- (E) Deeply corroded orthopyroxene porphyroclast in 9W20A. The two illuminated, elongate grains that trend from lower left to upper right are in optical continuity and presumably are relicts of a larger, preexisting porphyroclast. Partially crossed nicols. Horizontal field about 3 mm.
- (F) Orthopyroxene porphyroclast (extinct) in 8W67B showing moderate embayments and exsolution lamellae (illuminated). Crossed nicols. Horizontal field about 3 mm.



lamellae extend to the edges of the porphyroclasts and the outer 0.05 mm of these grains are generally free of exsolution lamellae. The rims of the porphyroclasts are pockmarked with deep cusped embayments that are filled with fine grained (0.05-0.1 mm) olivine (Figure 17). Many of these olivine grains are in optical continuity although isolated from one another. There is a textural progression (Figure 17) from large embayed porphyroclasts to extremely ragged and embayed porphyroclasts, to ragged and embayed relicts of porphyroclasts that are in optical continuity but physically separated. The embayed rims and this textural progression suggest replacement of orthopyroxene by olivine. Dick (1977) described similar textures in the Josephine Peridotite and suggested that the embayments were produced by pressure dissolution of the orthopyroxene during anatexis.

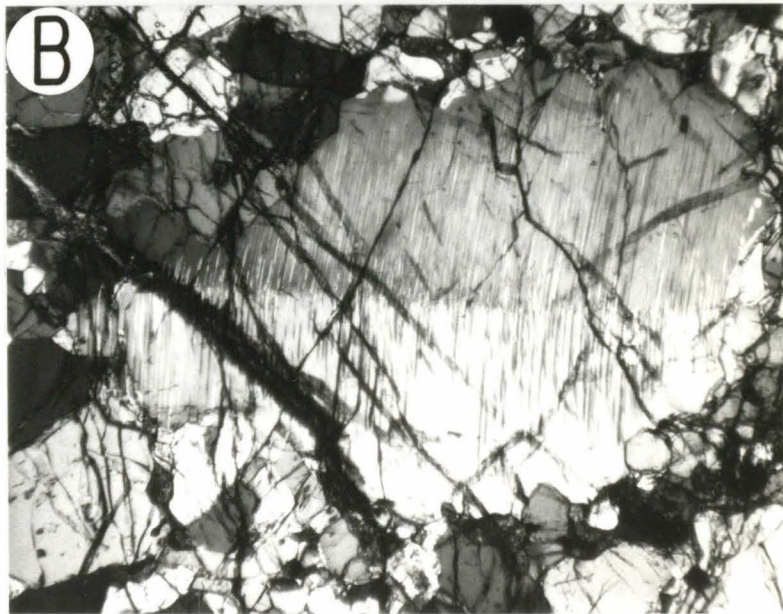
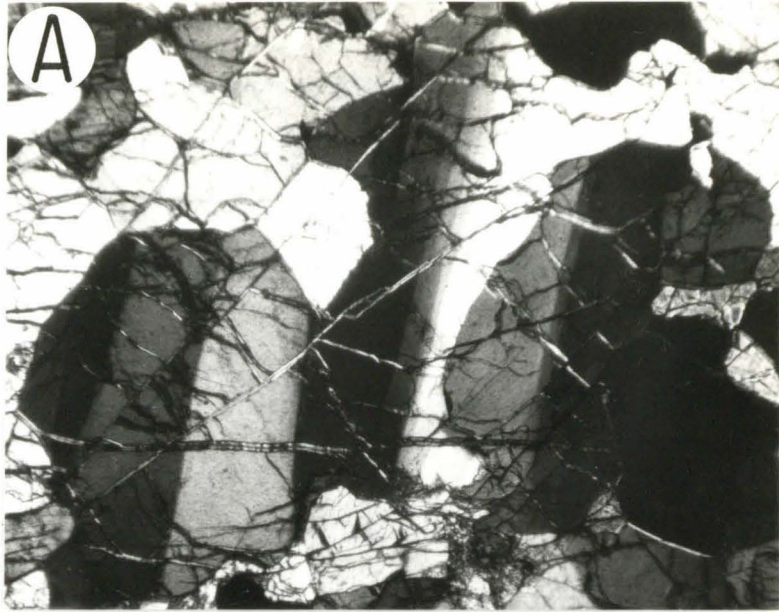
The clinopyroxene porphyroclasts (Figure 17) are similar in appearance to the orthopyroxene porphyroclasts except that they are green in transmitted light and tend to be smaller and devoid of exsolution lamellae. Deep, cusped embayments in the rims are abundant and similar to the embayments in the orthopyroxene porphyroclasts in that they are filled by fine grained olivine.

Olivine forms the largest porphyroclasts, ranging in size from 1-8 mm in thin section. The larger grains are deeply embayed and have length to width ratios of 2:1 to 3:1, whereas the smaller grains tend to be equant and devoid of embayments. The porphyroclasts show only minor evidence of intracrystalline deformation (Figure 18). Some grains have kink bands, or are fractured, or have undulatory extinction. Evidence of extreme deformation, such as bent exsolution lamellae and extreme aspect ratios are generally absent. These fea-

Figure 18: Deformation features in olivine and orthopyroxene in the Trinity peridotite.

(A) Kink bands in olivine. Crossed nicols. Horizontal scale about 3mm.

(B) Kink band in deformed orthopyroxene porphyroclast. Note discontinuity in exsolution lamellae. Partially crossed nicols. Horizontal field about 3 mm.



tures are developed in other parts of the Trinity peridotite such as in the vicinity of Scott Mountain to the west. Pyroxene porphyroclasts from from this area are commonly smeared out with length to width ratios of 4:1 to 5:1 and display S-shaped bending of exsolution lamellae.

Olivine is the dominant phase in the matrix. It forms a mosaic of equant to irregular shaped grains that come together with abundant triple-grain boundaries 120 degrees apart (Figures 19, 20 and 21). The olivine grains display undulatory extinction but are, otherwise, optically uniform.

Orthopyroxene and clinopyroxene also occur in the matrix as small anhedral grains about 0.05-0.1 mm in size (Figures 19 and 20). These pyroxene grains are generally interstitial to olivine and are particularly common at junctions between olivine grains, and extend along olivine-olivine grain boundaries from these triple junctions as narrow septa about 0.01-0.05 mm wide. Isolated matrix pyroxene grains in close proximity are commonly in optical continuity suggesting that they are continuous out of the plane of the thin section.

Red-brown spinel forms both small (0.05-0.5 mm) equant grains (Figure 19) that are interstitial to or included in olivine and larger ragged, "holly-leaf" shaped grains that occur along grain boundaries of the silicate minerals (Figure 21). Some of the larger grains have deep embayments filled by plagioclase or its alteration product clinzoicite (Figure 21).

Anhedral plagioclase occurs as isolated grains, as clusters of grains that are interstitial to olivine and pyroxene and as collections of grains that mantle spinel. These occurrences are illustrated in Figures 20 and 21. Typical grain sizes range from about 0.1 to 0.6 mm. Isolated

Figure 19: Textures of interstitial clinopyroxene in the Trinity peridotite.

- (A) Interstitial clinopyroxene in sample 9W20A. Partially crossed nicols. Horizontal field 1.2 mm.
- (B) Map of grains in Figure 19A. Grid, clinopyroxene; black, spinel; dashed lines, orthopyroxene; dotted, plagioclase; open, olivine. Note "arms" of clinopyroxene extending along grain boundaries between olivine and association of clinopyroxene, orthopyroxene and plagioclase.
- (C) Interstitial clinopyroxene grain in sample 9W20B. Partially crossed nicols. Horizontal field 1.2 mm.
- (D) Map of grains in Figure 19C. Same symbols as in 19B with addition of amphibole (crosses).

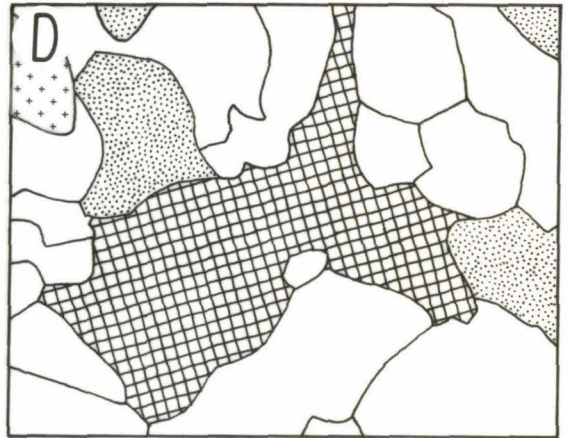
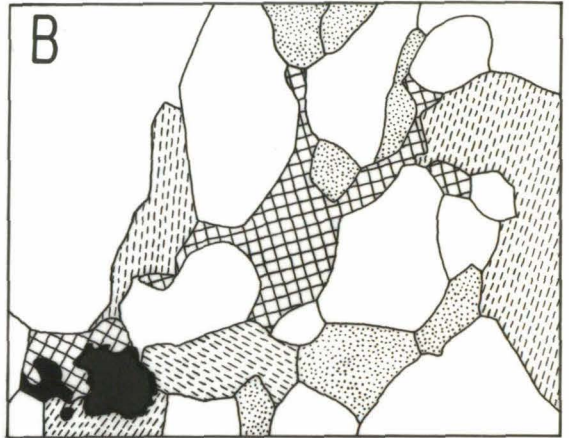
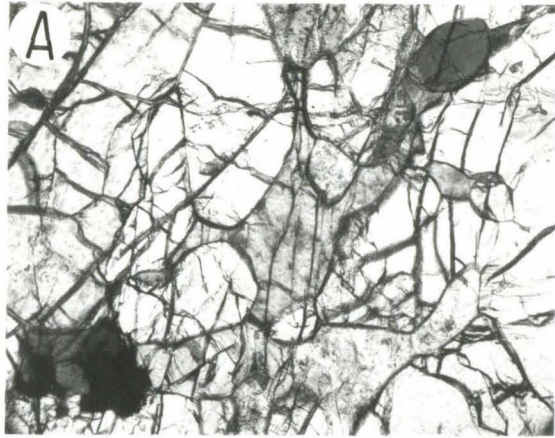
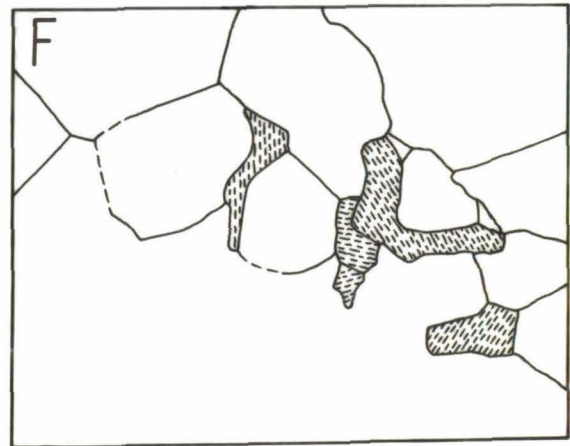
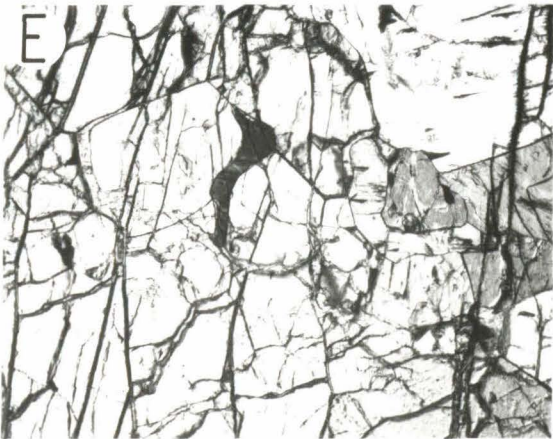
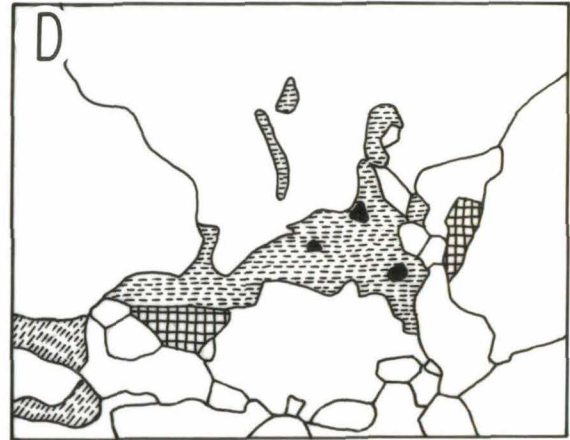
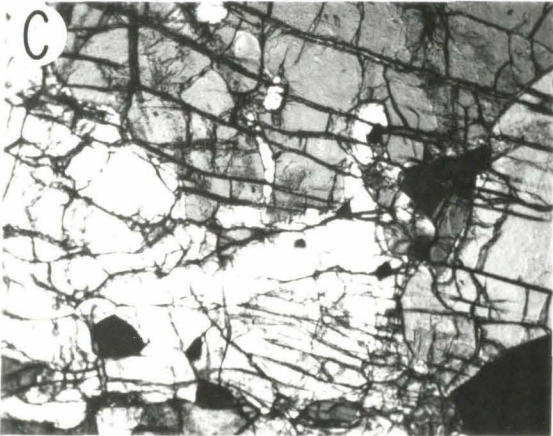
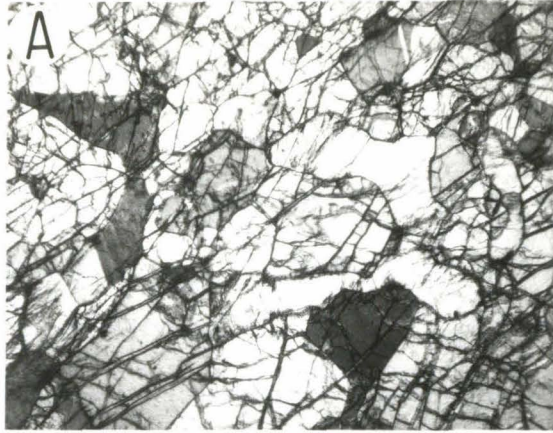


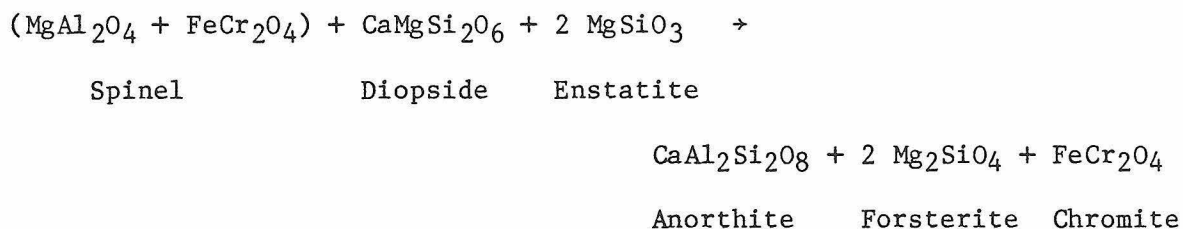
Figure 20: Textures of interstitial plagioclase and orthopyroxene in the Trinity peridotite.

- (A) Plagioclase in sample 9W20A. Partially crossed nicols. Horizontal field about 3 mm.
- (B) Map of grains in Figure 20A. Dotted, plagioclase; dashed lines, orthopyroxene; open, olivine. Note interstitial occurrence of plagioclase and isolation of many these grains from pyroxene and spinel.
- (C) Interstitial orthopyroxene in sample 9W20A. Partially crossed nicols. Horizontal field about 2.4 mm.
- (D) Map of grains in Figure 20C. Dashed lines, orthopyroxene; grid, clinopyroxene; black, spinel; open, olivine. Orthopyroxene grains with parallel dashed lines are in optical continuity.
- (E) Interstitial orthopyroxene in sample 9W20A. Partially crossed nicols. Horizontal fields about 2.4 mm.
- (F) Map of grains in Figure 20C. Dashed lines, orthopyroxene; open, olivine. Note distribution of orthopyroxene along grain boundaries of larger olivine grains.



plagioclase grains and clusters are similar in morphology to the groundmass pyroxenes. They tend to be concentrated at triple grain junctions, have curved contacts with olivine that are convex toward the plagioclase grains, and extend as narrow septa along olivine-olivine grain boundaries.

The deep embayments on the spinel grains suggest replacement of spinel by plagioclase. Similar textures involving spinel and plagioclase were noted by Green (1964) in the Lizard peridotite where embayed red-brown spinel was mantled by plagioclase. Locally, the cores of the spinel grains were high-Al, green spinel. Green (1964) interpreted these textures as evidence of plagioclase replacing spinel according to the reaction:

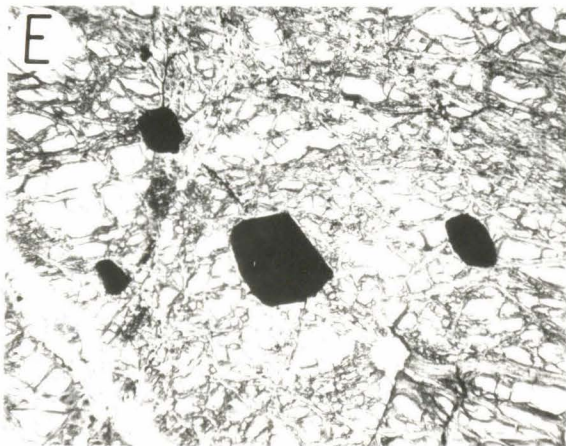
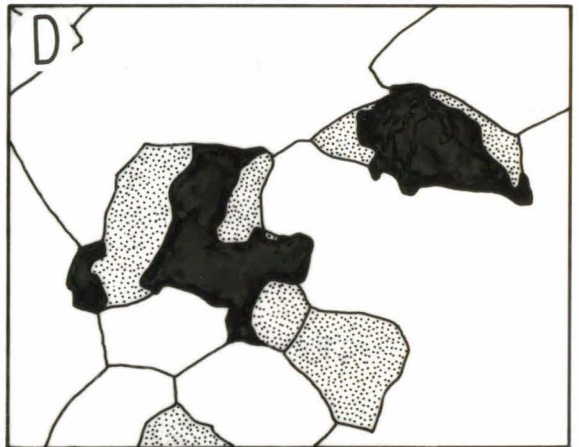
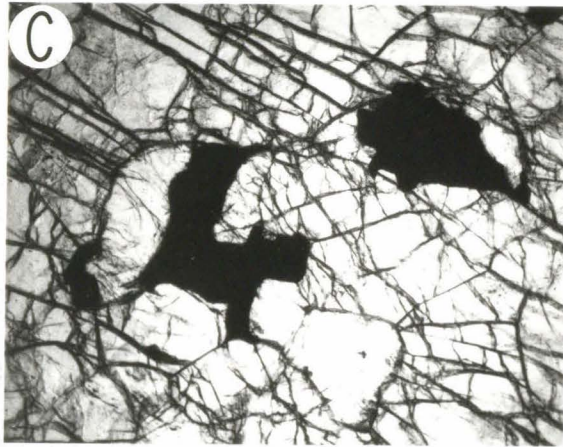
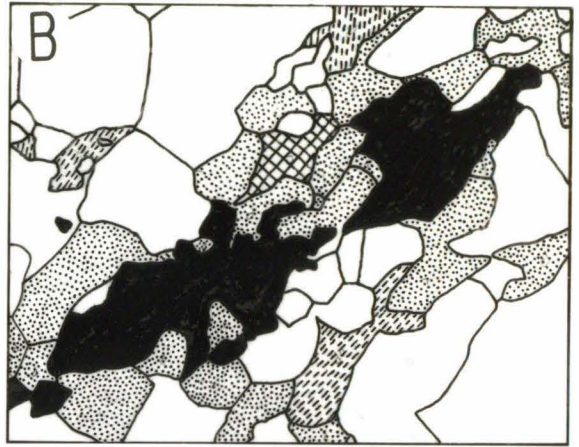
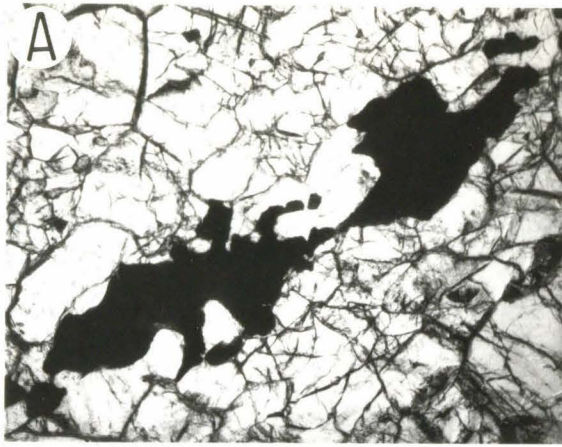


Amphibole also tends to occur as small (0.1 to 0.3 mm) isolated grains that are intersitial to olivine and pyroxene. In some rocks, it forms thin mantles on rounded clinopyroxene grains. In most samples, it is colorless, but in some a pink pleochroism is present.

The equigranular texture (Figure 16) differs from the porphyroclastic texture in that the minerals are more equigranular, larger, and show effects of annealing. Kink bands in olivine and pyroxene are set farther apart and are sharper, suggesting annealing. The range in grain sizes between the two textures overlap, but there are more grains larger than 1 mm in the protogranular rocks. Fine grained

Figure 21: Plagioclase-Spinel relationships in the Trinity peridotite.

- (A) Plagioclase surrounding a ragged spinel grain in sample 8W67B. Spinel is typical of the "hollyleaf-textured" spinel grains in the plagioclase lherzolite. Unpolarized light. Horizontal field about 2.4 mm.
- (B) Map of grains in Figure 21A. Dotted, plagioclase; solid, spinel; grid, clinopyroxene; dashed lines, orthopyroxene; open, olivine.
- (C) Associated plagioclase and spinel in sample 9W20B. Unpolarized light. Horizontal field about 2.4 mm.
- (D) Map of grains in Figure 21C. Dotted, plagioclase; solid, spinel; open, olivine. Note absence of pyroxene.
- (E) Equant, subhedral spinel grains in dunite. Compare to morphology of spinel in Figures 21A and C. Unpolarized light. Horizontal field about 3 mm.
- (F) Spinel rimmed by plagioclase in ariegite sample 8W500. Plagioclase now altered to clinozoisite. Matrix of rock is made up of olivine, clino- and orthopyroxene, plagioclase amphibole and spinel. Partially crossed nicols. Horizontal field about 18 mm.



(<0.5 mm) plagioclase, orthopyroxene, clinopyroxene, olivine and spinel do fill interstices between the larger grains of olivine and pyroxene, but the size distribution is less bimodal, and large grains are not floating in a groundmass of small grains. The recrystallization textures that were described in the porphyroclastic rocks are also present in the protogranular rocks. Elongate plagioclase-rich segregations define a weak foliation.

Lherzolite

Lherzolite is mineralogically and texturally similar to plagioclase lherzolite except that plagioclase is totally absent; no equigranular textured rocks were found. These rocks are composed of about 80-85 percent olivine, 10-15 percent orthopyroxene, 2-6 percent clinopyroxene, 0.5-1 percent spinel and trace amounts of primary amphibole. The texture of these rocks is dominantly porphyroclastic and the details of the textural relationships are identical to those in the plagioclase lherzolite except for the absence of plagioclase.

Harzburgite

Harzburgite is mineralogically distinct from lherzolite and plagioclase lherzolite in that plagioclase and primary amphibole are totally absent and clinopyroxene porphyroclasts are extremely rare. The typical range in modal mineralogy is 75-85 percent olivine, 15-25 percent orthopyroxene, 0.5-1 percent spinel, and <2 percent clinopyroxene.

The dominant texture is a porphyroclastic intergrowth with large orthopyroxene (1-6 mm) and olivine (1-9 mm) porphyroclasts set in a mosaic textured matrix of mostly olivine and minor amounts of ortho-

pyroxene and spinel. Clinopyroxene occurs in some rocks as small (<0.3 mm), anhedral grains that are interstitial to orthopyroxene and olivine, and as extremely rare, larger (1-1.5 mm) grains that are pock marked with deep, olivine-filled, cusped embayments. Orthopyroxene porphyroclasts may be somewhat more deeply embayed than in the plagioclase lherzolite or lherzolite, but this observation is difficult to quantify. Spinel forms grains that are more equant and euhedral, and are generally less translucent than in the plagioclase lherzolite or lherzolite.

Dunite

Typically, the dunite is seen in thin section to consist of an essentially biminerally intergrowth of about 98-100 percent olivine and 0-2 percent spinel. However, large patches of poikilitic clinopyroxene + plagioclase and patches of spinel occur locally.

Olivine forms a mosaic of equant to amoeboid and irregular grains that range in size from 0.15 to 8 mm; the irregular grains come together in complex interlocking grain boundaries illustrated in Figure 16C. As in the other peridotite lithologies, triple grain junctions of 120 degrees are common, and extreme aspect ratios are rare. Spinel occurs as small subhedral to euhedral grains that tend to be concentrated near olivine grain boundaries. Rare orthopyroxene and clinopyroxene occur as interstitial grains with curved contacts that are convex toward the pyroxene grains. As in the other lithologies, these interstitial pyroxenes tend to occur at triple grain junctions and as septa extending between olivine grains from these junctions. The shapes of these grains are compatible with their formation as

TABLE 2: PETROGRAPHY, MINERALOGY AND MINERAL CHEMISTRY OF THE TRINITY PERIDOTITE

Lithology	Texture	Mode and Grain Size	Mineral Compositions
Plagioclase Iherzolite	Porphyroclastic to protogranular: A bimodal grain size distribution in which large elongate orthopyroxene, clinopyroxene and olivine porphyroclasts are isolated within a finer grained, granoblastic matrix of olivine, orthopyroxene, clinopyroxene, spinel, plagioclase and amphibole. Porphyroclasts are slightly flattened but length/width ratios rarely exceed 2/1. Pyroxene porphyroclasts contain exsolution lamellae and are pockmarked with cusped embayments filled with olivine. Orthopyroxene porphyroclasts have discontinuous rims of fine grained (50-100 microns) olivine and pyroxene. Exsolution lamellae are not present in the outermost 50 microns of orthopyroxene porphyroclasts. Clinopyroxene porphyroclasts form isolated clusters. Matrix pyroxene, spinel, plagioclase and amphibole are interstitial to porphyroclasts and matrix olivine; they commonly occur at intersections between three or more olivine grains, and extend along binary grain boundaries. Many spinels are "holly-leaf" textured with embayments filled by plagioclase. Plagioclase also occurs as isolated interstitial grains and as mosaic textured segregations. Amphibole forms isolated interstitial grains with cusped contacts. Foliation defined by flattened porphyroclasts, matrix olivine, "holly-leaf" textured spinels and plagioclase segregations. Deformation is recorded by kink bands in olivine and pyroxene porphyroclasts and by bent or broken twin lamellae in pyroxene porphyroclasts. Recrystallization has widened and sharpened kink bands and polygonalized olivine, plagioclase and pyroxene. Interpretation: textures reflect recrystallization, plastic deformation and anatexis.	Porphyroclasts: olivine 1-8 mm orthopyroxene 1-3 mm clinopyroxene .4-1 mm Matrix olivine .05-1 mm orthopyroxene .05-1 mm clinopyroxene .05-.5 mm plagioclase .1-.6 mm spinel .05-1.5 mm amphibole .05-.3 mm	Fog9, 5-92.6 Cores: En66-89Wo6-2Fs9-9 Al ₂ O ₃ ~ 2.5-3 wt. % Rims: ~ En89, 5Wo1.5Fs9 Al ₂ O ₃ ~ 1.5-2 wt. % Cores: En54-49Wo42-47Fs4 Al ₂ O ₃ ~ 3.5-5 wt. % Rims: En51-49Wo44-48Fs5-3 Fog9, 5-92.6 En91-89Wo1-2Fs8-9 Al ₂ O ₃ < 2 wt. % En50-47Wo46-48Fs4-5 Al ₂ O ₃ < 3 wt. % An81-91; mostly An>85 Fe ⁺⁺ /Mg+Fe ⁺⁺ = .35-.45 Cr/Cr+Al = .43-59
Iherzolite and Harzburgite	Porphyroclastic to protogranular: large, elongate orthopyroxene and olivine porphyroclasts and more equant clinopyroxene porphyroclasts are set in a matrix of olivine, orthopyroxene and spinel. Length/width ratios of olivine, orthopyroxene and olivine porphyroclasts are 2/1 to 4/1. Clinopyroxene porphyroclasts are extremely embayed and rare. Orthopyroxene porphyroclasts have exsolution lamellae and are surrounded by olivine grains that are finer grained than the typical matrix. Some orthopyroxene porphyroclasts have "outliers" of isolated interstitial orthopyroxene that are physically separated but in optical continuity. The matrix is mostly mosaic textured olivine with interstices filled by orthopyroxene and, more rarely, by clinopyroxene. In Iherzolites, the matrix also contains interstitial amphibole. Matrix pyroxenes tend to occur at junctions of three or more olivine grains and extend along binary grain boundaries. Most spinels form equant subhedral to rounded grains located at olivine triple junctions; some occur as inclusions in olivine and orthopyroxene porphyroclasts. "Holly-leaf" textured spinels are rare. Interpretation: textures reflect recrystallization, deformation and anatexis.	Porphyroclasts: olivine 1-9 mm orthopyroxene 1-6 mm clinopyroxene 1-1.5 mm Matrix olivine .3-1 mm clinopyroxene 1-.5 mm spinel .05-1.5 mm amphibole .05-.3 mm	Fog9, 8-92.2 En86-89Wo6-2Fs8-9 En54-Wo42-47Fs3-5 Fog9, 8-92.2 En52-49Wo43-48Fs5-3 Fe ⁺⁺ /Mg+Fe ⁺⁺ = .3-.45 in Iherzolite = .4-.48 in harzburgite Cr/Cr+Al = .36-.5 in Iherzolite = .54-.60 in harzburgite
Dunite	Porphyroclastic to granoblastic: Olivine forms an equi- to inequigranular mosaic. Large grains tend to be elongate and flattened with length/width ratios of 4/1 to 5/1. These grains define the foliation in the rock. Some of them exhibit "necking" with large area in optical continuity connected by a narrow join. Complex, interlocking contacts are common. Small grains are more equigranular and polygonal. Rare orthopyroxene or clinopyroxene form small interstitial grains. Locally, large poikilitic clinopyroxene grains are developed and may or may not be flattened in the plane of the foliation. Spinel forms very equant grains interstitial to or included within olivine. Interpretation: textures reflect recrystallization and deformation; poikilitic pyroxenes and spinels may have crystallized from melt. "Necking" of olivine may reflect anatexis.	olivine 98-99 % orthopyroxene 0-.4 % clinopyroxene 0-0.7 % spinel .3-1 %	Fog8, 2-92.2 En88, 4Wo1, 7Fs9, 9 ~ En47-48Wo48-49Fs4 Fe ⁺⁺ /Mg+Fe ⁺⁺ = .36-.48 Cr/Cr+Al = .46-.63; most are >.60

TABLE 3: PETROGRAPHY, MINERALOGY AND MINERAL CHEMISTRY OF DIKES, BANDS AND VEINS IN THE TRINITY PERidotITE

Lithology	Texture	Mode and Grain Size	Mineral Compositions
Wehrlite Bands	Xenomorphic to hypidiomorphic granular; most of the rock is made up of large anhedral grains of orthopyroxene and clinopyroxene that are grown together with polygonal and interlocking contacts. Smaller, anhedral orthopyroxene, clinopyroxene, olivine and plagioclase occur at grain boundaries. Amphibole rims pyroxene and forms euhedral thombs in optical continuity within pyroxene. Spinel forms equant subhedral grains that are scattered throughout interstitial pyroxene and as rare inclusions in rims of large clinopyroxene grains. Interpretation: texture is igneous in origin with anhydrous minerals forming as cumulate or intercumulate phases. Crystallization sequence is inferred to be: (1) cpx; (2) cpx + ol + opx + sp; (3) cpx + ol + opx + sp + plag. Amphibole is inferred to be a product of deuteric alteration.	olivine orthopyroxene clinopyroxene plagioclase spinel	Fog7 En ₆₇₋₈₆ Wo _{1-1.5} Fs _{12-12.5} En ₄₈₋₄₉ Wo ₄₇₋₄₆ Fs ₅
Ariegite	Xenomorphic to hypidiomorphic granular; large anhedral to subhedral clinopyroxene and orthopyroxene grains form a network with interlocking to cusped contacts. Clinopyroxene grains contain exsolution lamellae 1-2 microns wide in cores; lamellae are absent within 100 microns of rims. Orthopyroxene grains are free of exsolution lamellae. Interstices between large pyroxene grains are filled by an anhedral intergrowth of colorless amphibole, plagioclase, olivine, and red-brown spinel. Interpretation: The texture is igneous in origin but overprinted by recrystallization. Initial crystallization sequence is inferred to be: (1) cpx + opx; (2) cpx + opx + ol + sp; (3) cpx + opx + ol + plag + amph + sp.	olivine orthopyroxene clinopyroxene plagioclase amphibole spinel	~ Fog1 En ₈₉₋₉₀ Wo ₁₋₂ Fs ₉ clusters around: En ₅₀ Wo ₄₆ Fs ₄ Ab ₈₄₋₉₂
Websterite Dikes	Xenomorphic to hypidiomorphic granular; inequigranular intergrowth of clinopyroxene, orthopyroxene, olivine, plagioclase, amphibole and spinel. Large, anhedral to subhedral clinopyroxene grains come together with simple polygonal to complex interlocking contacts; some pairs of grains form "graphic" intergrowths with one another. Exsolution lamellae, 1-5 microns wide, and spaced 10-20 microns apart are ubiquitous in these grains. Interlocking contacts parallel these lamellae for short distances. Rare, large orthopyroxene grains with few exsolution lamellae have rounded grain boundaries. Small, anhedral grains of olivine, clinopyroxene, plagioclase, orthopyroxene, amphibole and spinel are interstitial to the large pyroxenes. Plagioclase and olivine form local mosaic-textured segregations up to 5 mm across. Rounded olivine grains are also included in large clinopyroxene and orthopyroxene grains. Spinel also occurs as inclusions near the margins of large clinopyroxene grains. Interpretation: The texture is igneous in origin with the minerals crystallizing as cumulate or intercumulate phases. Inferred crystallization sequence: (1) ol + ol + cpx; (2) ol + cpx + opx + sp; (3) ol + cpx + opx + sp + plag + amph.	olivine orthopyroxene clinopyroxene plagioclase amphibole spinel	Fog ₉ , 6-90.4 ~ En ₈₈ Wo _{1.5} Fs _{10.5} En ₅₃₋₄₈ Wo ₄₃₋₄₇ Fs ₄₋₅ Ab _{>90}
Plagioclase- Pyroxene Veins	Xenomorphic to hypidiomorphic granular; clinopyroxene and orthopyroxene form large anhedral to subhedral grains that tend to occur in mosaic textured clusters up to 1 cm across. Contacts tend to be polygonal rather than interlocking. Clinopyroxene contains exsolution lamellae that extend to the edges of the grains. Orthopyroxene is free of exsolution features. Small, equant, anhedral grains of plagioclase, orthopyroxene and clinopyroxene form a mosaic-textured intergrowth that is interstitial to the large pyroxenes. Plagioclase forms segregations up to 1 cm across. Olivine forms rounded inclusions in orthopyroxene and rare grains that are interstitial to plagioclase, orthopyroxene and clinopyroxene. Interpretation: textures formed by crystallization from a melt. Inferred crystallization sequence: (1) ol; (2) ol + cpx + opx; (3) ol + cpx + opx + plag.	olivine clinopyroxene orthopyroxene plagioclase	Fog ₀₋₉₁ En ₄₉ Wo ₄₆ Fs ₅ En ₈₈ Wo ₂₋₃ Fs ₉ Ab ₈₉₋₉₁
Amphibole- Plagioclase Veins	Discontinuous linear array of interstitial grains; linear arrays of anhedral, pleochroic pink pargasite define veins. Pargasite forms isolated grains that are interstitial to the olivine and pyroxene of the host rock rather than crosscutting. Pargasite tends to have smooth, cusped contacts and occurs in embayments in pyroxene and at triple junctions between olivine and pyroxene. Plagioclase is also interstitial to olivine and pyroxene and has curved contacts with pargasite. Interpretation: crystallization from an interstitial melt. Curved contacts between pargasite and plagioclase suggest coprecipitation.	amphibole plagioclase	50 % 50 %

Table 4: Modal Abundances of Primary Minerals in the Trinity Peridotite

<u>Rock Type and Sample</u>	<u>Ol</u>	<u>Opx</u>	<u>Cpx</u>	<u>Plag</u>	<u>Amph</u>	<u>Sp</u>
Plagioclase Lherzolite						
8W40D	76.1	14.3	4.0	4.6	0.2	0.8
8W67	71.7	16.7	6.4	4.1	0.2	0.9
8W82A	71.8	18.7	2.9	5.2	0.4	1.0
9W2	76.0	18.8	1.0	3.3	0.3	0.5
9W20	70.6	19.0	2.2	7.7	0.2	0.3
7W10*	82.5	10.1	1.9	3.6	1.2	0.6
Lherzolite						
8W40F	80.4	14.2	4.7		0.04	0.6
8W40H	83.1	10.4	6.0			0.5
8W82B	81.8	14.9	2.4	0.04	0.1	0.7
8W82C	79.2	16.7	2.9		0.3	0.9
9W3	83.1	13.4	2.5		0.04	1.1
Harzburgite						
9W4	74.1	23.8	1.7		0.03	0.4
7W41*	78.9	18.4	1.7			1.0
7W8*	84.0	14.3	1.3			0.5
Dunite						
9W5	98.9	0.1	0.2			0.8
9W6	98.8	0.4				0.8
7W11*	99.5	0.2				0.3
7W43*	98.9		0.7			0.5
Wehrlite Dikes						
8W82D	13.6	19.3	63.0	3.1	0.5	0.5
8W40I	32.8	14.5	52.2		0.5	
8W40I4	23.4	13.3	62.9		0.4	
Ariegite Band						
8W69	14.0	21.0	48.6	11.1	4.5	0.8
Plag-Pyx Vein						
9W21	3.5	26.9	23.1	46.4	0.1	

*Optical point count; all others are automated electron microprobe point counts.

relicts of porphyroclasts that have been largely replaced by olivine. Alternatively, the local occurrence of large poikilitic clinopyroxene grains suggests that some of these interstitial pyroxenes may actually have nucleated at sites centered at triple junctions between olivine grains.

Clinopyroxene-rich Dikes

A typical ariegite dike was investigated using the automated point count technique. The primary modal (Table 4) mineralogy is about 49 percent clinopyroxene, 14 percent olivine, 21 percent orthopyroxene, 5 percent amphibole, 1 percent spinel, and 11 percent plagioclase.

The ariegite dikes are texturally complex. Equant clinopyroxene and orthopyroxene form large (0.3-1.5 mm) grains that come together to form a xenomorphic granular intergrowth. Contacts are irregular and locally interlocking. The cores of the clinopyroxene grains contain low-Ca pyroxene, but these lamellae do not extend to within 0.1 mm of the rims. Orthopyroxene is devoid of exsolution features. Olivine, orthopyroxene and clinopyroxene form an equigranular mosaic of 0.1-0.3 mm sized grains that are interstitial to the diopside porphyroclasts. Spinel, amphibole and plagioclase form irregular shaped intergrowths that tend to be concentrated at triple grain junctions between olivine and/or pyroxene. Spinel tends to occur as rounded to irregular shaped and embayed inclusions within the plagioclase and amphibole grains (Figures 6D and 21F). The interstitial silicate-silicate contacts tend to be smoothly curved and cusped, with these grains coming together to form abundant triple grain junctions with 120 degree angles.

The overall texture suggests that the rock formed initially as an accumulate with intercumulous olivine, spinel and pyroxene deposited between larger clinopyroxene phenocrysts. Subsequent recrystallization produced the distinctive foliation, the deep embayments in the clinopyroxene porphyroblasts, the cusped contacts between grains, and the plagioclase and amphibole mantles on the spinel grains.

Three samples from websterite dikes were studied using the automated point count technique (Table 4). The ranges in modal mineralogy were 13-33 percent olivine, 50-63 percent clinopyroxene, 13-20 percent orthopyroxene, about 0.5 percent amphibole, 0-0.5 percent spinel and 0-3 percent plagioclase. The variations in modal mineralogy that are visible in outcrop, however, are much greater than these, and extend from essentially clinopyroxenite to websterite to olivine websterite.

The websterite dikes, like the ariegite dikes, are texturally complex. However, they do not appear to have been as extensively recrystallized. The overall texture is dominated by a xenomorphic to hypidiomorphic granular intergrowth of large (0.5-4 mm) clinopyroxene grains (Figure 22). The contacts between these grains are irregular and interfingering, with extensions of adjacent grains extending up to 1 mm into one another. Locally these intergrowths are texturally similar to myrmekitic or graphic intergrowths of quartz and feldspar (Figure 22). These grains contain ubiquitous exsolution lamellae of low-Ca pyroxene that extend to the rims of the grains. Small anhedral grains (<0.5 mm) of clinopyroxene, orthopyroxene, olivine, plagioclase, amphibole, and spinel are interstitial to the large clinopyroxene grains; locally these interstitial grains form mosaic-textured clusters. Olivine also occurs as inclusions in large clinopyroxene grains.

Figure 22: Textures of clinopyroxene-rich rocks in the Trinity peridotite.

(A) Texture of wehrlite layers in dunite. Sample 7W89.

Sample is an intergrowth of mostly clinopyroxene, subordinate olivine and minor orthopyroxene. Crossed nicols. Horizontal field about 18 mm. Compare to 22B.

(B) Texture of websterite dike. Sample 8W40I4. Sample is

an intergrowth of mostly clinopyroxene with subordinate amounts of olivine and orthopyroxene, and trace amounts of plagioclase. Note interlocking pyroxene contacts. Partially crossed nicols. Horizontal field about 18 mm.

(C) Texture of websterite dike in Figure 8W40I4. Intersti-

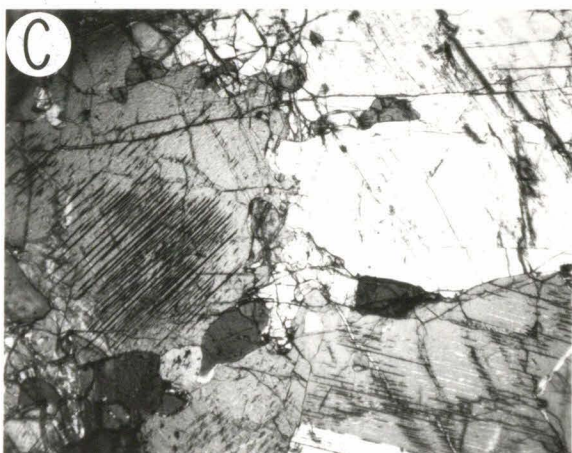
ces between large clinopyroxene grains are filled with clino- and orthopyroxene, olivine and trace amounts of plagioclase. Partially crossed nicols. Horizontal field about 3 mm.

(D) Contact between interlocking clinopyroxene grains in

websterite dike 8W82D. Note how contacts locally parallel exsolution lamellae. Partially crossed nicols. Horizontal field about 3 mm.

(E) Three intergrown clinopyroxene grains in websterite dike

8W82D. Two smaller grains (extinct and illuminated) are intergrown and contained within a third of different optical orientation. Partially crossed nicols. Horizontal field about 3 mm.



The textures of these dikes are interpreted to result from crystallization from a melt followed by, at most, only minor amounts of recrystallization to form the mosaic textures of the interstitial grains and the exsolution lamellae in clinopyroxene. The crystallization sequence is difficult to determine but appears to be: olivine, olivine + clinopyroxene, olivine + clinopyroxene + orthopyroxene + plagioclase.

One thin section of a black wehrlite layer from above Dobkins Lake was analyzed with the automated microprobe technique (Table 3). This sample was composed of about 93 percent clinopyroxene, 6 percent orthopyroxene, about 1 percent olivine, and trace amounts of amphibole and spinel. The overall texture of the rock is hypidiomorphic to xenomorphic granular, with clinopyroxene forming an intergrowth of 1-8 mm sized anhedral to subhedral grains (Figure 22). These grains exhibit length to width ratios of up to 4:1 and have a strong preferred orientation that defines a planar fabric. Smaller (0.1-0.6 mm) grains of clinopyroxene, orthopyroxene, olivine, amphibole and spinel occur interstitially to the large clinopyroxene grains. Low-Ca exsolution lamellae are ubiquitous throughout the clinopyroxene grains. Spinel forms equant euhedral grains that are scattered throughout the interstices and as inclusions in the rims of the large clinopyroxene grains; these disseminations are responsible for the characteristic black color of the rock. All phases are free of strain features.

The texture of the rock also appears to be essentially igneous in origin, with the orthopyroxene, olivine, amphibole, and spinel forming as intercumulous phases between cumulate clinopyroxene grains. The planar fabric is inferred to have formed by cumulate processes

because of the absence of evidence for strain and the overall texture of the rock.

ALTERATION

All of the samples of the Trinity peridotite were at least incipiently altered to hydrous assemblages of serpentine, magnetite, brucite, talc, chlorite, clinozoisite, tremolite, hydrogarnet(?), clacite and Fe-Ni sulfide. The serpentine polymorphs form cross fiber veins or mesh texture (Maltman, 1978), and were identified tentatively on the basis of their morphology as chrysotile and lizardite, respectively. The bladed mat texture that is characteristic of antigorite (Maltman, 1978) was not observed in samples from the study area, although it is present in the metamorphosed peridotite in the Trinity Alps. All of the other alteration products, except hydrogarnet, were identified optically and on the basis of their composition as determined by the electron microprobe. Hydrogarnet was inferred to be present on the basis of the composition of some discrete grid points in some highly serpentinized samples that were point counted with the electron microprobe. This identification has not been substantiated optically.

The alteration assemblages are functions of the bulk compositions of the rocks, and only serpentine and magnetite are ubiquitous. Clinozoisite is only developed in plagioclase peridotite. Brucite is most common in altered dunites where talc is absent. In pyroxene bearing rocks, talc is present rather than brucite. Tremolite is an important mineral in highly altered clinopyroxene-rich dikes and in the clinopyroxene-rich cumulate rocks.

The alteration assemblages are also functions of the intensity of alteration. In extremely "fresh" samples, alteration is limited to the development of serpentine veins along grain boundaries and in cracks in olivine grains. These veins are generally less than 20 microns wide and are filled with fibrous serpentine oriented normal to the vein and disseminated 1-2 micron-sized magnetite grains. Pyroxenes, amphibole, and plagioclase are essentially unaltered. With increasing alteration (20-30 percent), plagioclase alters completely to an extremely fine-grained, dark intergrowth of clinozoisite, serpentine and chlorite. Serpentine generally forms complete rims around these intergrowths. Locally, radiating bundles of tabular clinozoisite crystals (up to 25 by 300 microns) are developed. Orthopyroxene undergoes minor alteration to talc, and spinels are mantled by discontinuous rims of magnetite. In rocks that are 50 percent or more altered, orthopyroxene is more completely replaced by talc, and hydrogarnet(?) is associated with the intergrowths of clinozoisite, chlorite and serpentine.

CONCLUSIONS

The primary mineralogy of the Trinity peridotite has three significant features. First, and most important, the Trinity peridotite is unique among North American peridotite massifs in that it contains plagioclase lherzolite. The occurrence of plagioclase in peridotite massifs is extremely rare and, thus far, reports of such occurrences in the literature have been limited to a few peridotite massifs in Europe, north Africa and South America (Green , 1963, 1964; Kornprobst, 1969; Boudier, 1978; Dickey, 1970; Menzies and Allen, 1974). Second, the mineralogical diversity of the Trinity peridotite is remarkable, with a wide spectrum

of rock types present and encompassing dunite, harzburgite, lherzolite, plagioclase lherzolite, wehrlite and websterite. Therefore, it is possible to study the field relationships between many different peridotite lithologies to place constraints on their petrogenesis. For example, it has become widely theorized that harzburgite and dunite are the highly depleted residues left by partial melting and extraction of a basaltic component from a less refractory protolith (Dick, 1977). This hypothesis is untestable in most peridotite bodies because only harzburgite and/or dunite are present. Therefore, the mineralogy of the Trinity peridotite presents an unusual opportunity to test theory. Third, because of this diversity, the rocks record some evidence of reactions involving replacement of spinel by plagioclase and of orthopyroxene and clinopyroxene by olivine.

The relatively low degree to which the primary minerals are altered is also significant. In most peridotite massifs, the rocks are typically 60-70 percent altered to greenschist facies, hydrous assemblages of serpentine, magnetite, brucite, talc, clinozoisite, and chlorite (Evans, 1979). Indeed, throughout much of the Trinity peridotite alteration has consumed more than 60-70 percent of the primary minerals. However, the Mount Eddy-China Mountain area has been only slightly affected by this alteration, and, in many places, the rocks show less than 10 percent alteration. As a result, these rocks are excellent samples for studying the primary mineral chemistry of a peridotite massif.

TABLE 5: PETROGRAPHY, MINERALOGY AND MINERAL CHEMISTRY OF GABBRO AND RELATED ACCUMULATE ROCKS

Lithology	Texture	Mode and Grain Size	Mineral Composition
Interlayered Dunite and Wehrlite	Hypidiomorphic Granular to Poikilitic: clinopyroxene grains with serial size distribution form clumps of grains with complex interlocking contacts; all grains contain exsolution lamellae that are 1-2 microns wide and extend to grain boundaries. Some grains show poly-synthetic twinning. Large grains poikilitically enclose olivine, and some small grains are interstitial to olivine. Olivine forms mosaic-textured concentrations that are interstitial to the larger clinopyroxene grains and have curved cusped contacts with them. Blocky equant spinel is interstitial to olivine although some is included in clinopyroxene. Dumite and wehrlite are distinguished on the basis of clinopyroxene abundance with clinopyroxene comprising less than 10 percent of dumite. Interpretation: textures reflect crystal accumulation from a melt. Inferred crystallization sequence: sp, ol + sp, ol + cpx + sp.	Clinopyroxene 5-50 % .1-3 mm Olivine 50-95 % .1-1.5 mm Spinel trace .05-.3 mm	~ En ₄₈ Wo ₄₈ Fs ₄ ; ~1.5 % Al ₂ O ₃ Fo ₈₈ .5; NiO < 0.22 %; CaO < 0.02 % Cr/Cr+Al ~ 0.67 Fe ⁺⁺ /Mg+Fe ⁺⁺ ~ 0.53
Olivine Pyroxenite	Hypidiomorphic Granular: intergrowth of anhedral to subhedral intergrowth of orthopyroxene, clinopyroxene, olivine and spinel. Contacts tend to be curved. In some rocks, smaller clinopyroxene, olivine and rare plagioclase are interstitial to and have concave contacts against orthopyroxene. In other rocks, the phases are more equigranular, and none are distinctly interstitial. Interpretation: textures reflect crystal accumulation from a melt with essentially simultaneous crystallization of olivine, orthopyroxene, and clinopyroxene recorded in most rocks.	Clinopyroxene 20-40 % .1-1 mm Orthopyroxene 40-60 % .1-1.5 mm Olivine ~20 % .1-3 mm Spinel <5 % .03-.15 mm Plagioclase tr .1-1.3 mm	En ₄₈ -50Wo ₄₈ Fs ₃₋₄ ; ≤ 1 % Al ₂ O ₃ ~ En ₈₈ .5Wo _{1.5} Fs ₁₀ ; ~1 % Al ₂ O ₃ Fo ₈₆₋₈₉ ; CaO < 0.02; NiO = 0.2-0.3 Cr/Cr+Al ~ 0.65; Fe ⁺⁺ /Mg+Fe ⁺⁺ ~ 0.49
Feldspathic Pyroxenite	Hypidiomorphic Granular: anhedral plagioclase and olivine fill the interfaces between subhedral clinopyroxene and orthopyroxene. Both pyroxenes have euhedral faces against plagioclase, but come together with one another with anhedral contacts that are irregular and slightly interlocking. Clinopyroxene contains abundant exsolution lamellae; orthopyroxene is essentially devoid of exsolution features. Amphibole (magmatic ?) forms rims on clinopyroxene and is intimately intergrown with some clinopyroxene grains forming a "graphic" texture. Interpretation: textures reflect crystal accumulation from a melt with olivine and plagioclase forming as intercumulous phases between cumulous ortho- and clinopyroxene.	Clinopyroxene 75-85 % .5-2 mm Orthopyroxene 1-5 % .5-1.5 mm Olivine tr <.1 mm Plagioclase <20 % .1-1.5 mm Amphibole minor .5-2 mm Spinel tr <0.1 mm	~ En ₄₉ Wo ₄₆ Fs ₅ An ₉₃₋₉₇ Cr/Cr+Al ~ 0.50 Fe ⁺⁺ /Mg+Fe ⁺⁺ ~ 0.52
Gabbro	Hypidiomorphic Granular: plagioclase fills interstices between elongate (length/width = 1/1 to 4/1) clinopyroxene grains. Clinopyroxene contains ubiquitous exsolution lamellae, and is rimmed and intergrown with magmatic(?) amphibole. Quartz forms interstitial patches between plagioclase and pyroxene. Pyroxenes are intensely unutilized and plagioclase is intensely saussuritized. Interpretation: textures reflect crystallization from a melt. Inferred crystallization sequence: clinopyroxene followed by plagioclase, quartz and amphibole.	Clinopyroxene 10-30 % 0.3-3 mm Plagioclase 40-60 % 0.3-3 mm Amphibole <30 % 0.3-3 mm Quartz 1-2 % <0.3 mm	~ En ₄₄ Wo ₄₆ Fs ₁₀ ; 2.6-3.0 % Al ₂ O ₃ ~ En ₇₆ Wo ₂ Fs ₂₂ ; ~1.7 % Al ₂ O ₃ An ₉₀₋₉₅
Microgabbro	Hypidiomorphic Granular to Granoblastic: plagioclase clinopyroxene and orthopyroxene form an equigranular intergrowth with curved, cusped contacts. Orthopyroxene is pleochroic pink, and both pyroxenes are devoid of exsolution lamellae. Locally, plagioclase forms polygonal intergrowths of grains with straight sides that include small, rounded pyroxene grains and appears more granoblastic than hypidiomorphic. Near the host peridotite, plagioclase is completely saussuritized. Interpretation: textures reflect rapid crystallization from a melt followed by local recrystallization.	Clinopyroxene 35-50 % .1-1 mm Orthopyroxene 20-25 % .1-1 mm Plagioclase 30-40 % .1-1 mm	~ En ₄₄ Wo ₄₆ Fs ₁₀ ; 2.6-3.0 % Al ₂ O ₃ ~ En ₇₆ Wo ₂ Fs ₂₂ ; ~1.7 % Al ₂ O ₃ An ₉₀₋₉₅

TABLE 6: PETROGRAPHY, MINERALOGY AND MINERAL CHEMISTRY OF HORNBLENDE DIORITE, PLAGIOGRANITE AND DIABASE

Lithology	Texture	Mode and Grain Size	Mineral Compositions
Hornblende Diorite	<p><u>Porphyritic</u>: large elongate amphibole grains and large, blocky plagioclase grains are set in a groundmass of anhedral plagioclase, quartz and opaque minerals. Amphibole is pleochroic blue-green and shows oscillatory zoning. The groundmass contains rounded clinopyroxene grains that are altered to magnetite, biotite and amphibole.</p> <p><u>Hydiomorphic Granular</u>: plagioclase forms a network of interlocking laths. Amphibole is euhedral to skeletal, blue green pleochroic and shows continuous optical zoning. Clinopyroxene occurs as rounded, corroded inclusions in amphibole. Opaques are rounded to blocky inclusion in amphibole.</p>	<p>Phenocrysts Amphibole .5-.5 mm Plagioclase .5-10 mm Matrix Plagioclase .02-.2 mm Amphibole .01-.05 mm Quartz .1-.2 mm Diopside trace Opaques trace</p> <p>Amphibole 25 % Plagioclase 65 % Quartz 10 % Clinopyroxene 1 % Opaques 5 %</p>	
Plagiogranite	<p><u>Protomylonitic</u>: Large crushed grains of plagioclase, microcline and quartz are separated by narrow zones of extremely fine-grained, mosaic-textured quartz and feldpat. These zones tend to be best developed along a single plane, giving the rock a weak foliation. All the large grains have bent or broken twin lamellae and/or undulatory extinction. Fractures in plagioclase are filled by mosaic-textured quartz.</p>	<p>Quartz 50-60 % .01-1 mm Plagioclase 40-50 % .5-2 mm Opaque trace .01-.5 mm</p>	An<10
Diabase	<p><u>Intergranular</u>: spaces between randomly oriented plagioclase laths are filled by tabular clinopyroxene grains, anhedral plagioclase, equant subhedral opaque grains, and anhedral quartz. Plagioclase is normally zoned. Amphibole pseudomorphs clinopyroxene and is, in turn, replaced by chlorite. Plagioclase is highly saussuritized.</p>	<p>Plagioclase 60-70 % .3-.6 mm Clinopyroxene 30-35 % .05-.4 mm Opaques 2-3 % .01-.1 mm Quartz 2-3 % <.1 mm</p>	An5-11 about En26Wo28Fs46

MINERAL CHEMISTRY

INTRODUCTION

This section reports on range in composition of the primary minerals in the peridotite and establishes a data set that may be used to place additional constraints on the petrogenesis and P-T history of the Trinity peridotite. The term, "primary mineral", is used as in the petrography section to refer to phases in the peridotite that predate the serpentinization of the rocks.

Quantitative analyses of olivine, orthopyroxene, clinopyroxene, spinel, plagioclase, and amphibole were performed as described in the section on analytical techniques. The nature and extent of chemical zoning within individual grains was determined as well as elemental partitioning between coexisting minerals since these data are useful for constraining the P-T history of the Trinity peridotite. An effort was also made to detect progressive changes in mineral chemistry associated with progressive changes in mineral abundance from one lithology to another. This was approached by quantitative analysis of mineral compositions in samples that were collected across transition zones from plagioclase lherzolite to dunite and across depleted zones around clinopyroxene-rich dikes that cut plagioclase lherzolite. These data were augmented with results of automated microprobe point counts performed on the very same samples.

The data are organized as follows. Representative analyses of olivine are presented in Table 7, orthopyroxene in Table 8, clinopyroxene in Table 9, spinel in Table 10, plagioclase in Table 11, and amphibole in Table 12. Presentations of the data on these minerals are made graphically in Figures 23 through 41.

The following discussion will deal first with the ranges in

mineral compositions for each phase that are measurable within single thin sections and will then present progressive changes that occur over the scale of an outcrop.

OLIVINE

All the Fo-contents in olivine that were determined from samples of the Trinity peridotite are presented in Figure 23. The olivines are all Mg-rich, ranging from Fo₈₈ to Fo₉₃. The analyses are subdivided in in Figure 23 in terms of lithology. From this diagram it is clear that the Fo-contents of olivines from plagioclase lherzolite, lherzolite, harzburgite and dunite all show considerable overlap and that these lithologies cannot be distinguished solely on the basis of Fo-content alone.

The olivine grains were essentially unzoned throughout all samples with one major exception. Olivine analyses performed near (<100 um) spinel grains were found to be significantly more Mg-rich than analyses performed on olivine grains that were farther than 100 um from spinel grains. Figure 24 illustrates the range in Fo-content of olivine as a function of distance from a spinel grain in lherzolite sample 8W40H. The Fo-content decreases sharply from Fo_{92.3} within 5 microns of the the spinel to Fo_{90.5} at distances farther than about 75 microns from the spinel. This distribution in Fo-content is suggestive of local reequilibration between olivine and spinel on a scale of approximately 75 microns. No analogous variations in olivine composition were found near any other phases; olivine is homogeneous within the detection limits of the microprobe regardless of proximity to orthopyroxene, clinopyroxene, plagioclase or amphibole grains.

Figure 23: Forsterite content of olivine in samples of the Trinity peridotite and cumulate ultramafic rocks. Fo-content is defined as $100 \times \text{Mg}/\text{Mg}+\text{Fe}^{++}$ where Mg and Fe^{++} are cation percents and all Fe is assumed to be Fe^{++} .

Mg / Mg + Fe IN OLIVINE

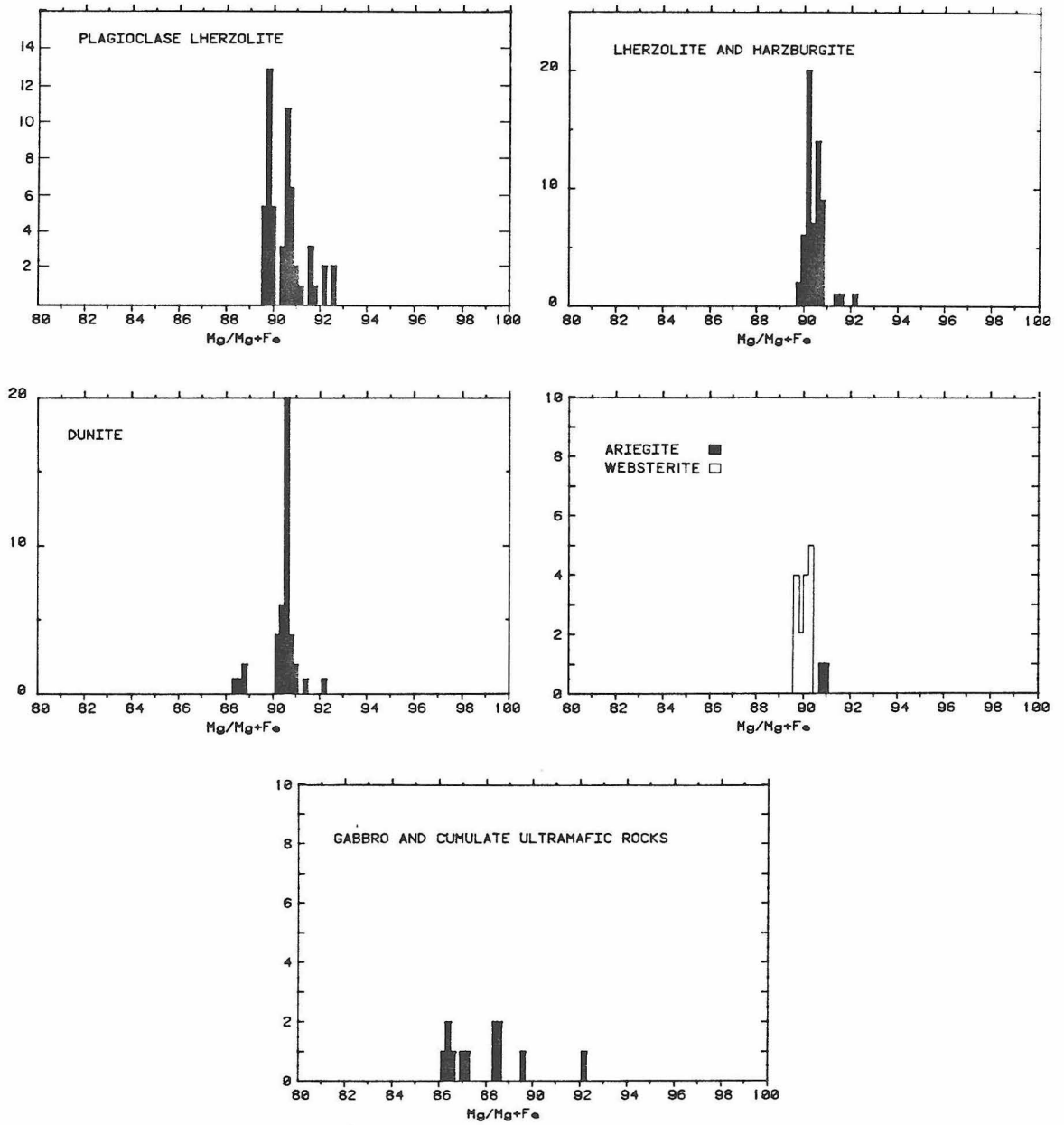


Figure 24: Forsterite of olivine in sample 8W40 as a function of distance from a large spinel grain. Reproducibility is estimated to be ± 0.1 mole percent Fo-content based on replicate analyses of an olivine standard of known composition.

FO-CONTENT OF OLIVINE

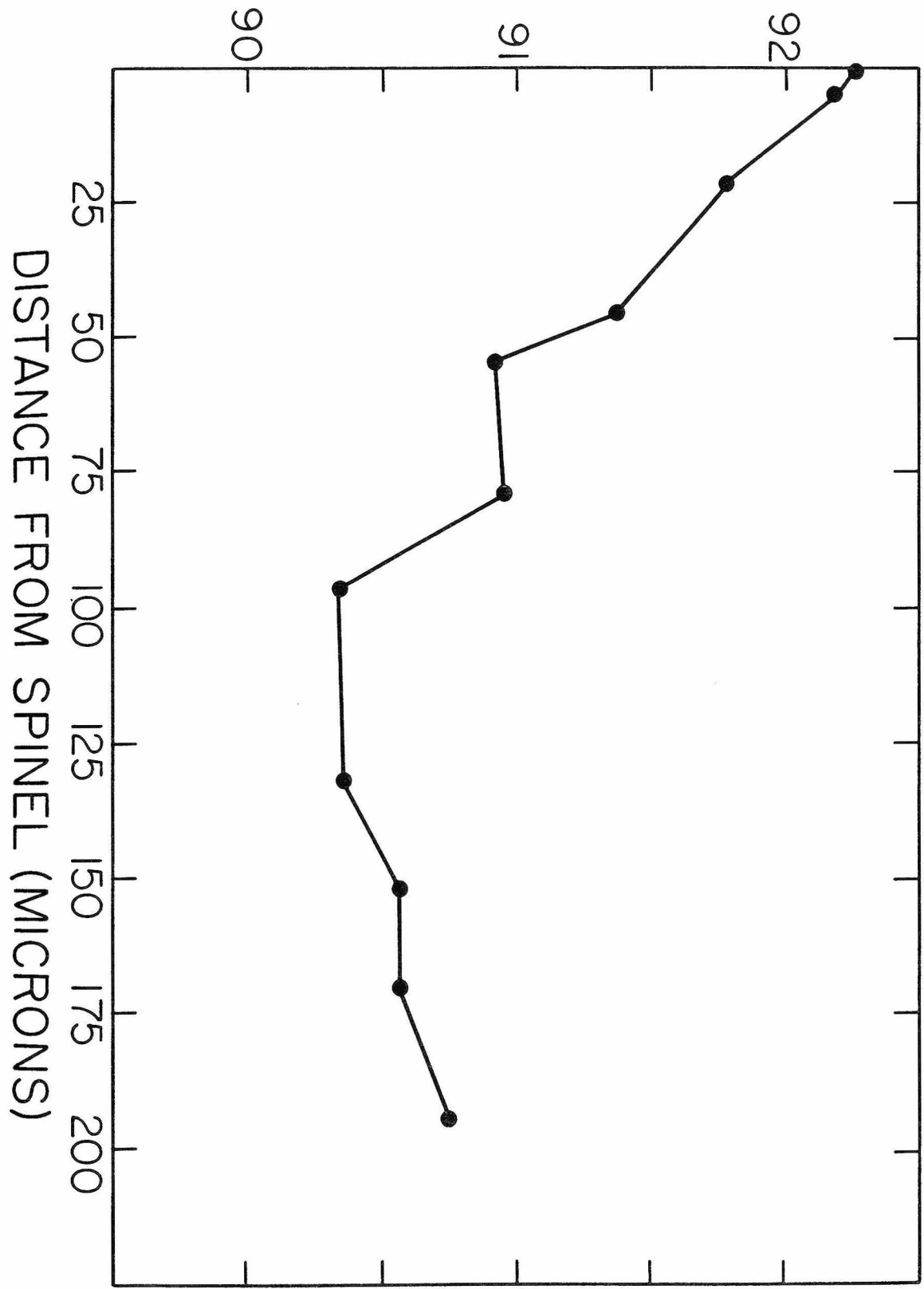


Figure 25: CaO and NiO concentrations in olivines from the different rock types of the Trinity peridotite and the cumulate ultramafic rocks. Approximate error bars ($\pm 1 \sigma$) calculated from counting statistics are illustrated in each figure.

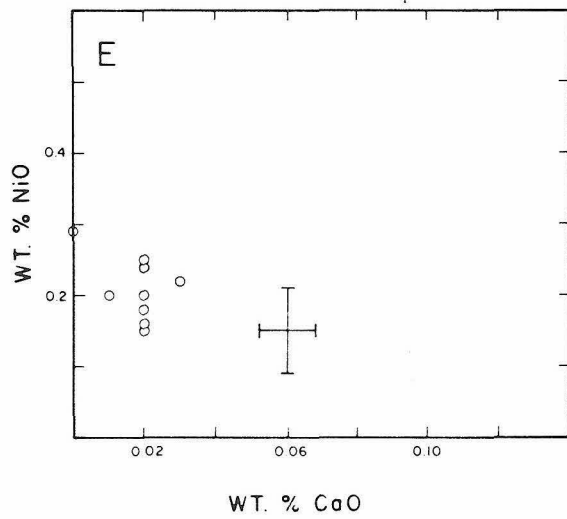
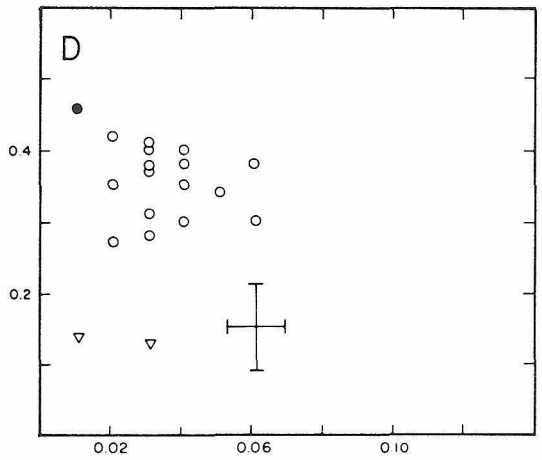
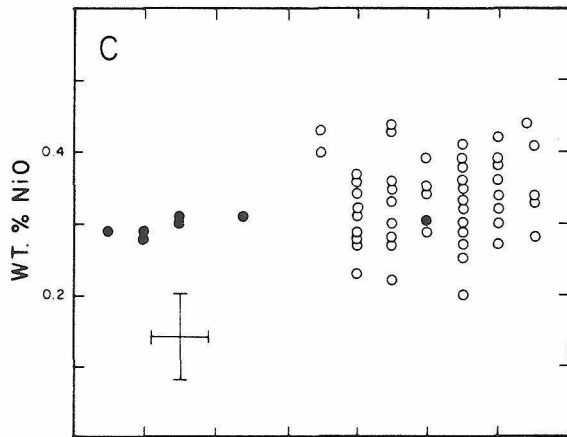
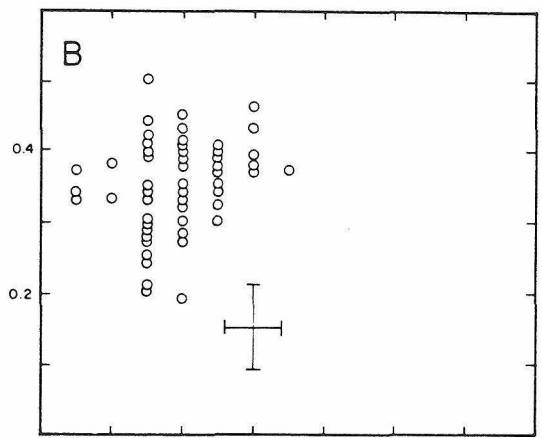
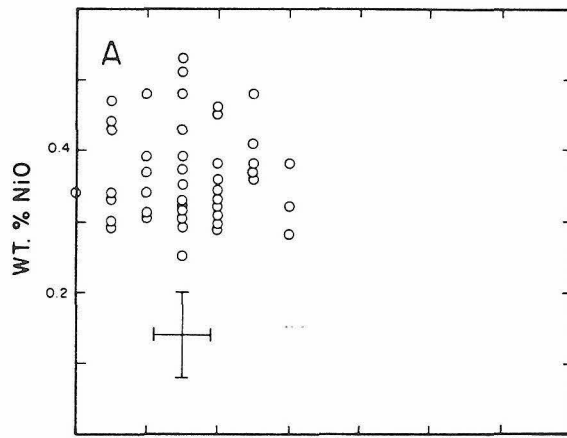


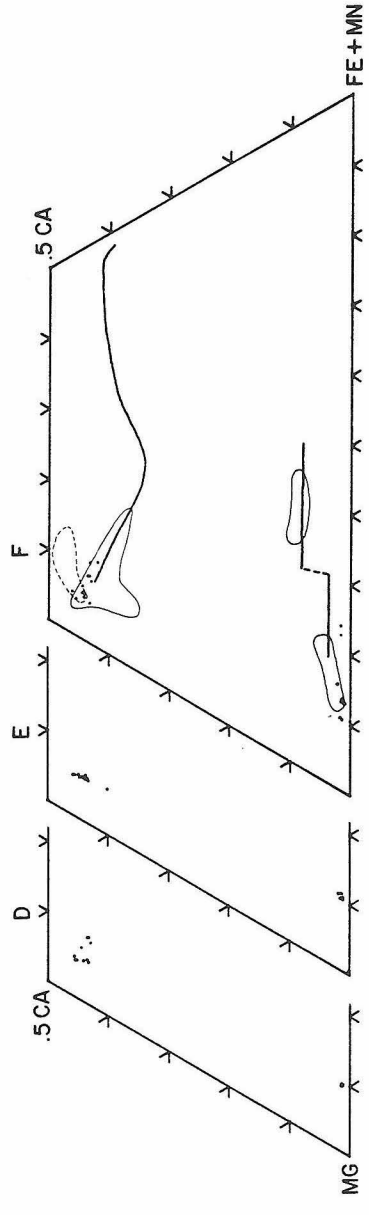
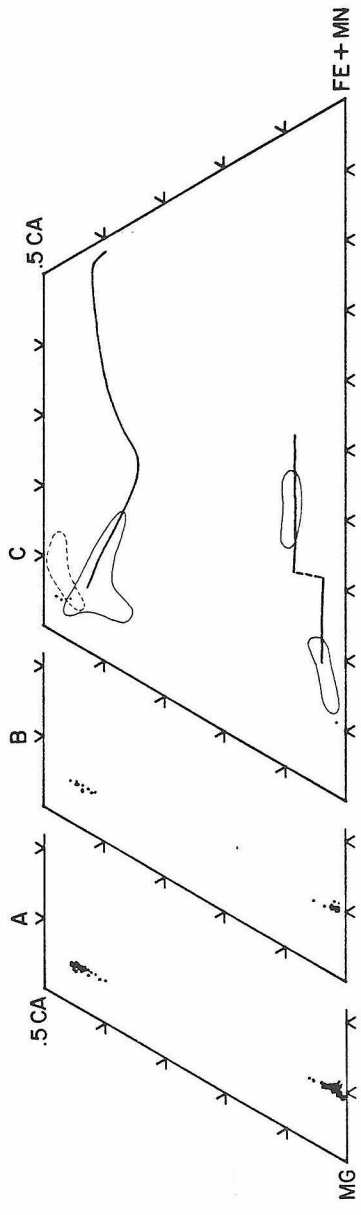
Figure 25 illustrates the range in CaO and NiO concentrations in the olivines from the different rock types of the Trinity peridotite. Taking all the analyses together, CaO concentrations range from <0.01 to about 0.13 weight percent and NiO concentrations range from about 0.2 to about 0.5 weight percent. Neither CaO-content nor NiO-content show enough variation to discriminate between the plagioclase lherzolite, lherzolite and harzburgite. However, olivine in dunite samples from the margins of the large tabular dunite bodies tends to be more Ca-rich (≥ 0.08 wt. %) than the other rock types (mostly ≤ 0.06 wt. %). Olivine compositions were also determined in the interior of large dunite bodies and near clinopyroxene-rich pods and wehrlite layers. The CaO contents of these olivines were generally less than 0.08 weight percent, and more similar to the olivine from the plagioclase lherzolite, lherzolite and harzburgite than to the "high-Ca" olivine from the margins of the large dunite bodies. Olivines in the ariegite bands and websterite dikes are also indistinguishable from the plagioclase lherzolite, lherzolite and harzburgite in terms of CaO and NiO. The olivines in the wehrlite bands, however, are low in NiO (< 0.15 wt. %) and low in CaO (≤ 0.03 wt. %); these concentrations are more similar to those in the olivines in the cumulate ultramafic rocks than to those of the other rock types of the Trinity peridotite.

The ranges in Fo-content, and NiO and CaO concentrations in the Trinity peridotite are similar to those reported for alpine-type peridotites (Dick, 1977; Green, 1964; Himmelburg and Coleman, 1968; Loney *et al.*, 1971), for ultramafic sections of ophiolites (Coleman, 1977; Coleman *et al.*, in press), and for high-temperature peridotites (Green, 1964; Boudier, 1978). These olivine analyses are distinguished from

Figure 26: Compositions of pyroxenes in the Trinity peridotite and gabbroic and related cumulate ultramafic rocks. All points represent a quantitative analysis for 9 elements. Also shown in Figures C and F are the ranges of composition of Skaergaard pyroxenes (heavy solid lines; Wager and Brown, 1967), Muskox pyroxenes (light, solid envelopes; Irvine and Findlay, 1972), and Alkaline intrusions (dashed envelope, Irvine and Findlay, 1972)

(A) Plagioclase lherzolite (236 points).
(B) Lherzolite and harzburgite (49 points).
(C) Dunite (4 points).
(D) Ariegite bands and dikes (39 points).
(E) Websterite dikes (78 points).
(F) Gabbro and related cumulate ultramafic rocks (45 points).

PYROXENE COMPOSITIONS



analyses of olivine from stratiform intrusions such as the Stillwater, Skaergaard and the Bushveld (Wager and Brown, 1967; Jackson, 1969) by being more Mg-rich; the olivine of the stratiform intrusions tending to be less than Fo₈₈.

ORTHOPYROXENE

Quantitative orthopyroxene analyses for the Trinity peridotite are presented by rock type in pyroxene quadrilaterals in Figure 26. Like the olivine, the orthopyroxene in the Trinity peridotite is extremely Mg-rich. The analyses taken together show very little spread, with a total range from En_{91.0}Wo_{.8}Fs_{8.2} to En₈₇Wo₄Fs₉, and show considerable compositional overlap between the various lithologies. The pyroxenes in the plagioclase lherzolite, lherzolite, harzburgite and dunite have essentially the same range in composition, although, as will be discussed, there are differences across transitions from plagioclase lherzolite to dunite and across depleted zones around websterite dikes. The clinopyroxene-rich rocks (i.e. websterite, ariegite and wehrlite) also contain pyroxenes with essentially the same compositions as the host peridotites. Figure 26F shows the compositions of the orthopyroxenes in the gabbro and cumulate ultramafic rocks that intrude the Trinity peridotite. The pyroxenes in the Trinity peridotite are similar in Ca, Mg and Fe ratios to the most magnesian pyroxenes in the gabbroic rocks.

Figures 27 and 28 present the results of automated electron microprobe point counts on samples of the Trinity peridotite and of the gabbroic rocks. These data represent a more complete sampling of more indi-

Figure 27: Pyroxene compositions in plagioclase lherzolite, lherzolite and harzburgite determined by automated electron microprobe point count analysis. Each point represents the average of 10 analyses (5 seconds each) of ortho- or clinopyroxene. Envelopes and pyroxene trends in Figures E and K are for reference and are the same as in Figure 26.

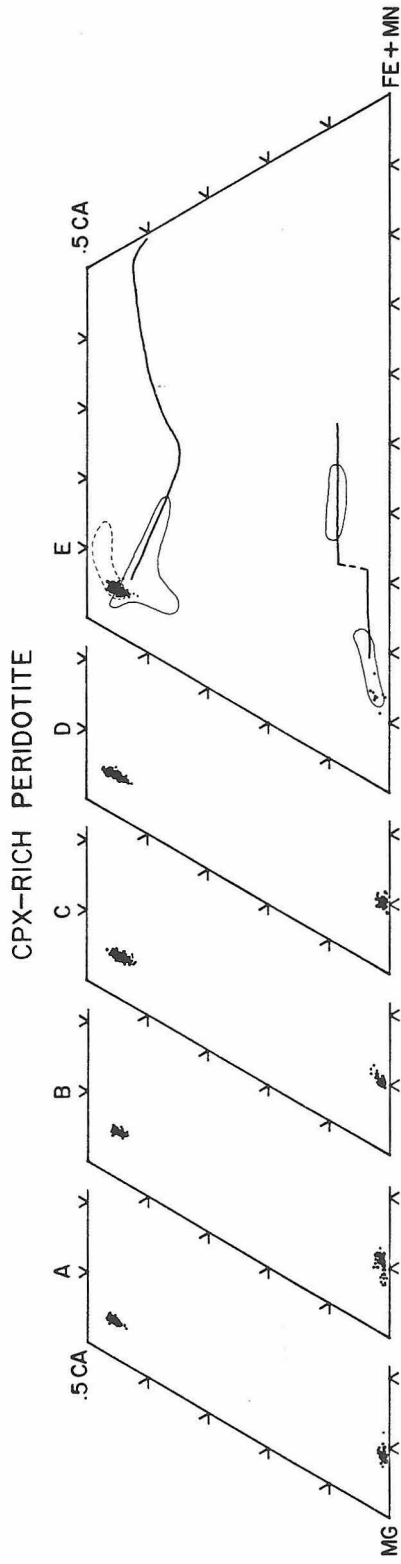
Plagioclase lherzolite:

- (A) Sample 8W67 (57 points).
- (B) Sample 9W20 (54 points).
- (C) Sample 8W82A (66 points).
- (D) Sample 8W40D (26 points).
- (E) Sample 9W2 (46 points).

Lherzolite and harzburgite:

- (F) 8W82B (50 points).
- (G) 8W82C (40 points).
- (H) 8W40H (33 points).
- (I) 8W40F (49 points).
- (J) 9W3 (37 points).
- (K) 9W4 (75 points).

PYROXENE COMPOSITIONS (POINT COUNT ANALYSIS)



GABBRO AND RELATED CUMULATES

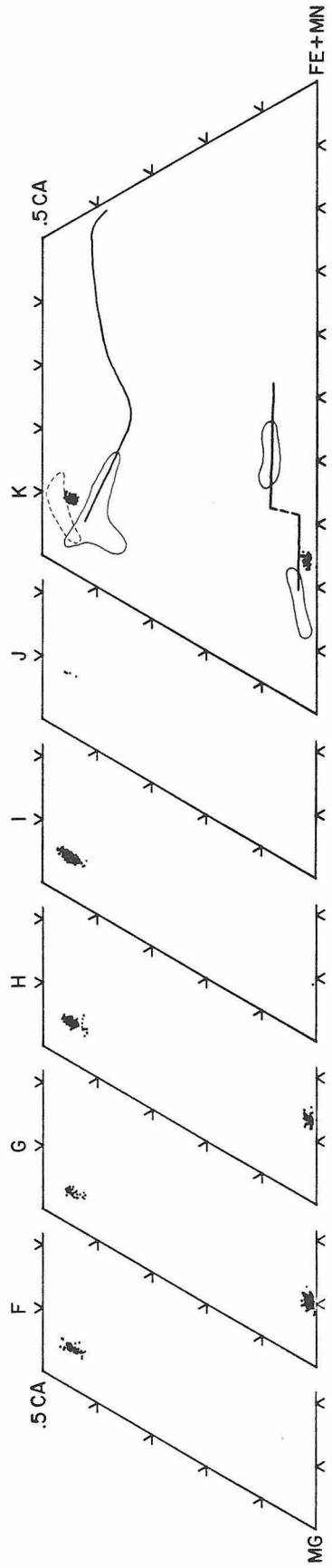


Figure 28: Pyroxene compositions in clinopyroxene-rich rocks from the Trinity peridotite (ariegite bands and dikes, websterite dikes and wehrlite layers) and in gabbroic and related cumulate ultramafic rocks. Each point represents the average of 10 analyses (5 seconds each) of ortho- or clinopyroxene. Envelopes and pyroxene trends in Figures E and K are for reference and are the same as in Figure 26.

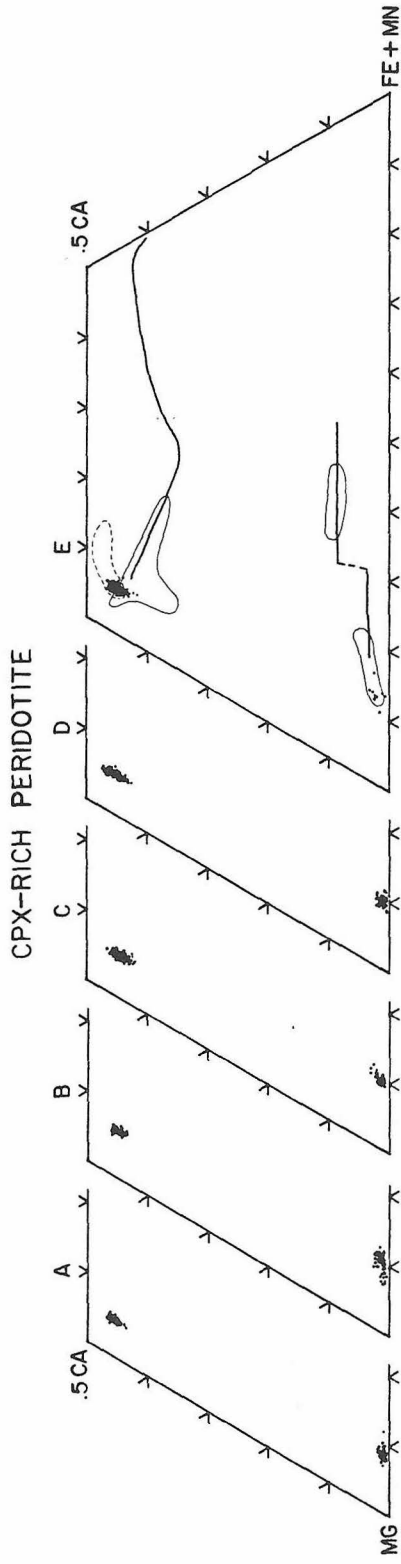
Clinopyroxene-rich peridotite:

- (A) Ariegite band, sample 8W69 (183 points).
- (B) Ariegite dike, sample 8W500 (152 points).
- (C) Websterite dike, sample 8W40I (259 points).
- (D) Websterite dike, sample 8W82D (253 points).
- (E) Wehrlite layer above Dobkins Lake, sample 7W89 (225 points).

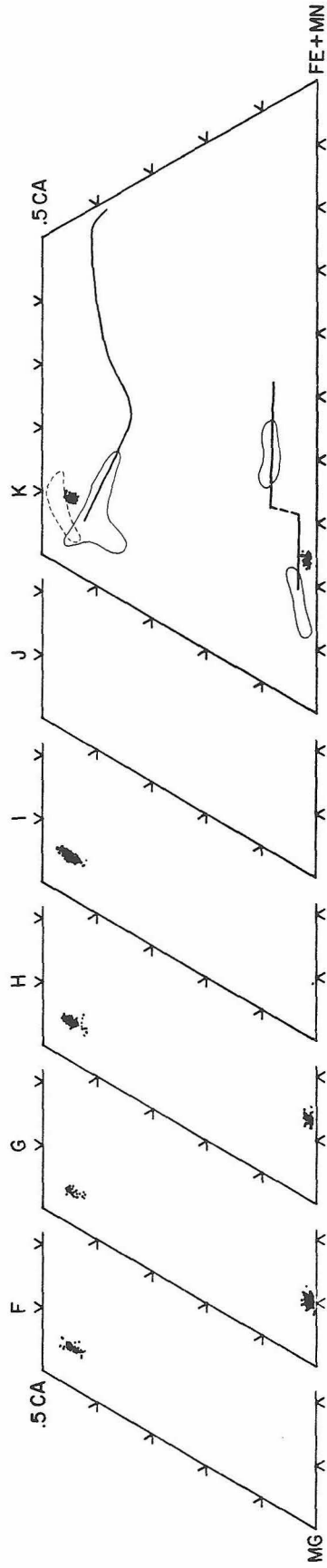
Gabbro and related cumulate ultramafic rocks:

- (F) Cumulate wehrlite, sample 7W121 (48 points).
- (G) Cumulate olivine pyroxenite, sample 7W134 (179 points).
- (H) Cumulate olivine pyroxenite, sample 7W140 (190 points).
- (I) Feldspathic pyroxenite, samples 7W108 & 109 (134 points).
- (J) Microgabbro, sample 8W100 (131 points).

PYROXENE COMPOSITIONS (POINT COUNT ANALYSIS)



GABBRO AND RELATED CUMULATES



vidual rocks than the data in Figure 26. However, the conclusions are essentially the same. The orthopyroxene compositions in the Trinity peridotite are limited to extremely Mg-rich ortho- and clinopyroxene, and distinctions between the orthopyroxenes in plagioclase lherzolite, lherzolite, harzburgite and dunite are difficult to make. The clinopyroxene-rich rocks have orthopyroxenes with essentially the same composition as the host peridotites. The gabbroic and related cumulate rocks taken together have orthopyroxenes that cover a small range in composition, showing a small Fe-enrichment and overlapping slightly with the compositions of the pyroxenes in the Trinity peridotite.

As described in the petrography section, orthopyroxene has an essentially bimodal distribution in most of the peridotite lithologies, occurring both as large porphyroclasts and as small interstitial grains. Also, the large porphyroclasts appear to have distinct cores and rims defined by the presence or absence of high-Ca pyroxene exsolution lamellae, respectively. These petrographically distinct types of orthopyroxene were investigated for differences in composition.

A measurable range in orthopyroxene composition occurs within single thin sections. Analyses from porphyroclast cores and rims and from interstitial orthopyroxene grains from plagioclase lherzolite sample 8W67 are presented graphically in Figure 29. The cores of orthopyroxene grains are generally more Ca-rich than the rims, and the interstitial orthopyroxene grains and the porphyroblast rims are similar in composition in terms of Mg, Ca and Fe. All three types of orthopyroxene are low in Ti and similar in Al/Al+Cr although both Al and Cr are lower in the rims than in the cores. The ranges in composition across three grains from core to rim is illustrated in Figure 30 for

Figure 29: Compositions of ortho- and clinopyroxene in sample 8W67. Each point represents a quantitative analysis for 9 elements. Solid circles, matrix pyroxene grains; open triangles, rims of porphyroclasts; solid triangles, cores of porphyroclasts. Lines are drawn to connect core and rim compositions from the same grain.

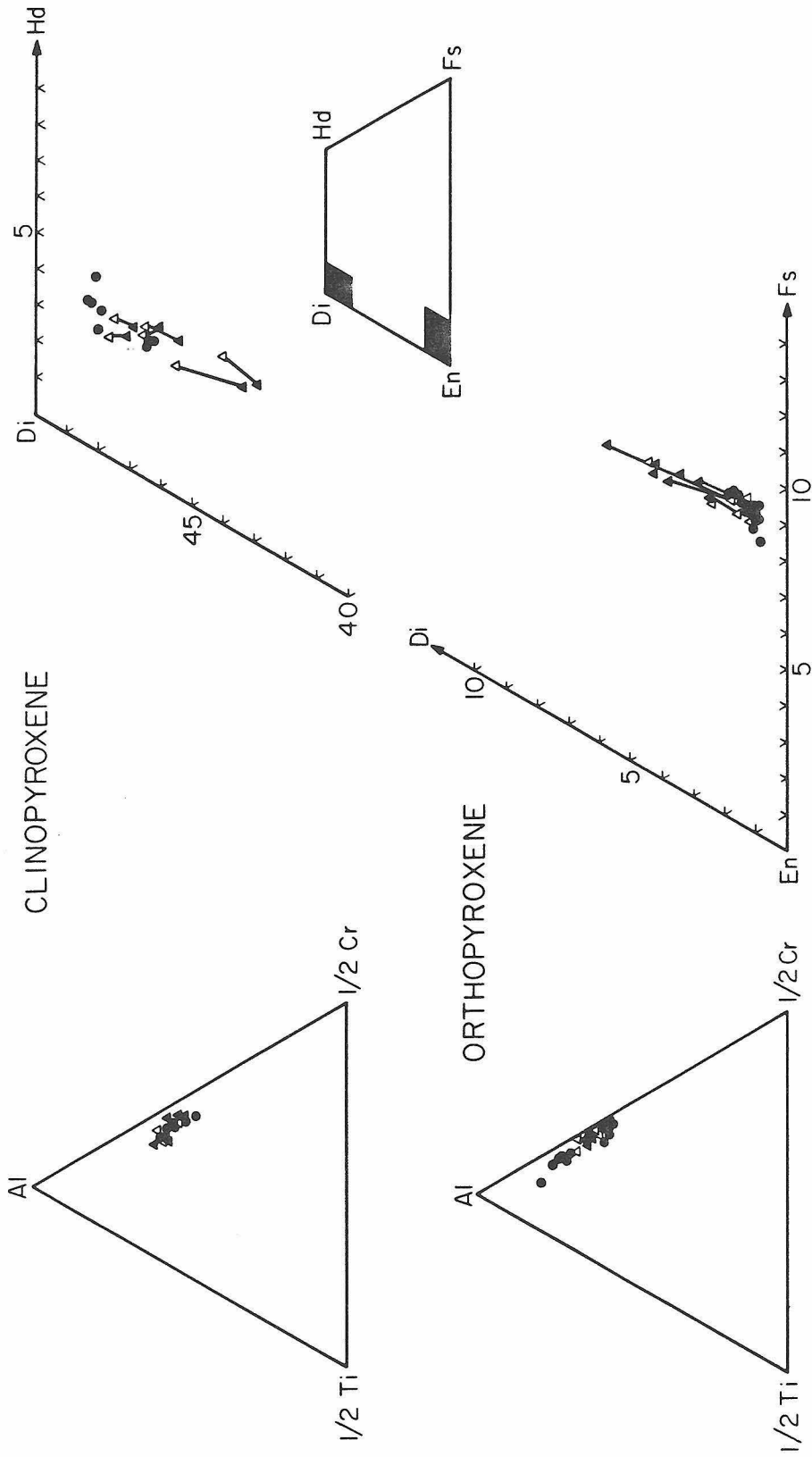


Figure 30: Al_2O_3 and Cr_2O_3 traverses from rim to core across three orthopyroxene grains. Each point represents a complete quantitative analysis for 9 elements. Errors (1σ) based on counting statistics are ± 0.03 weight percent for Al_2O_3 and ± 0.06 weight percent for Cr_2O_3 .

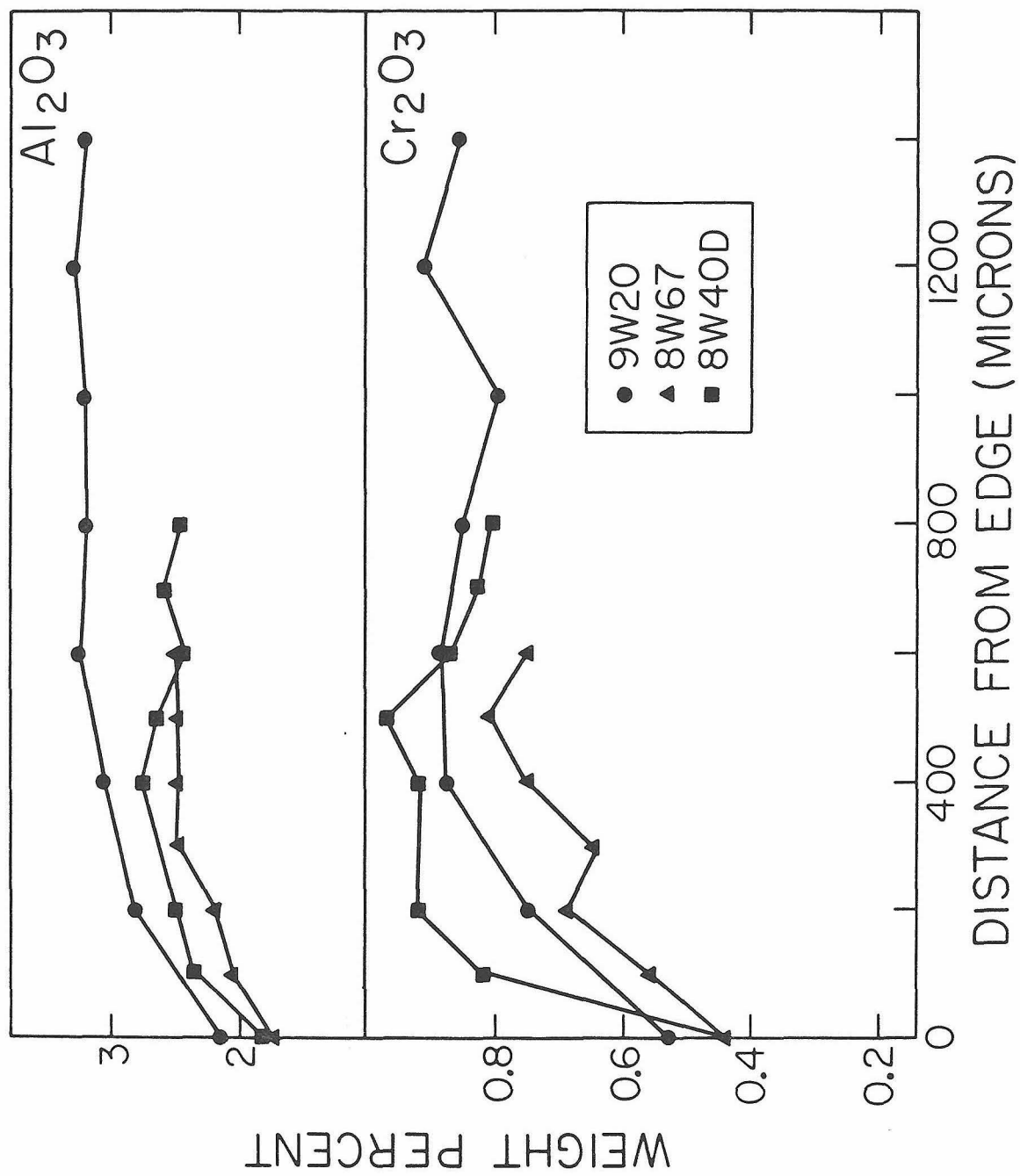
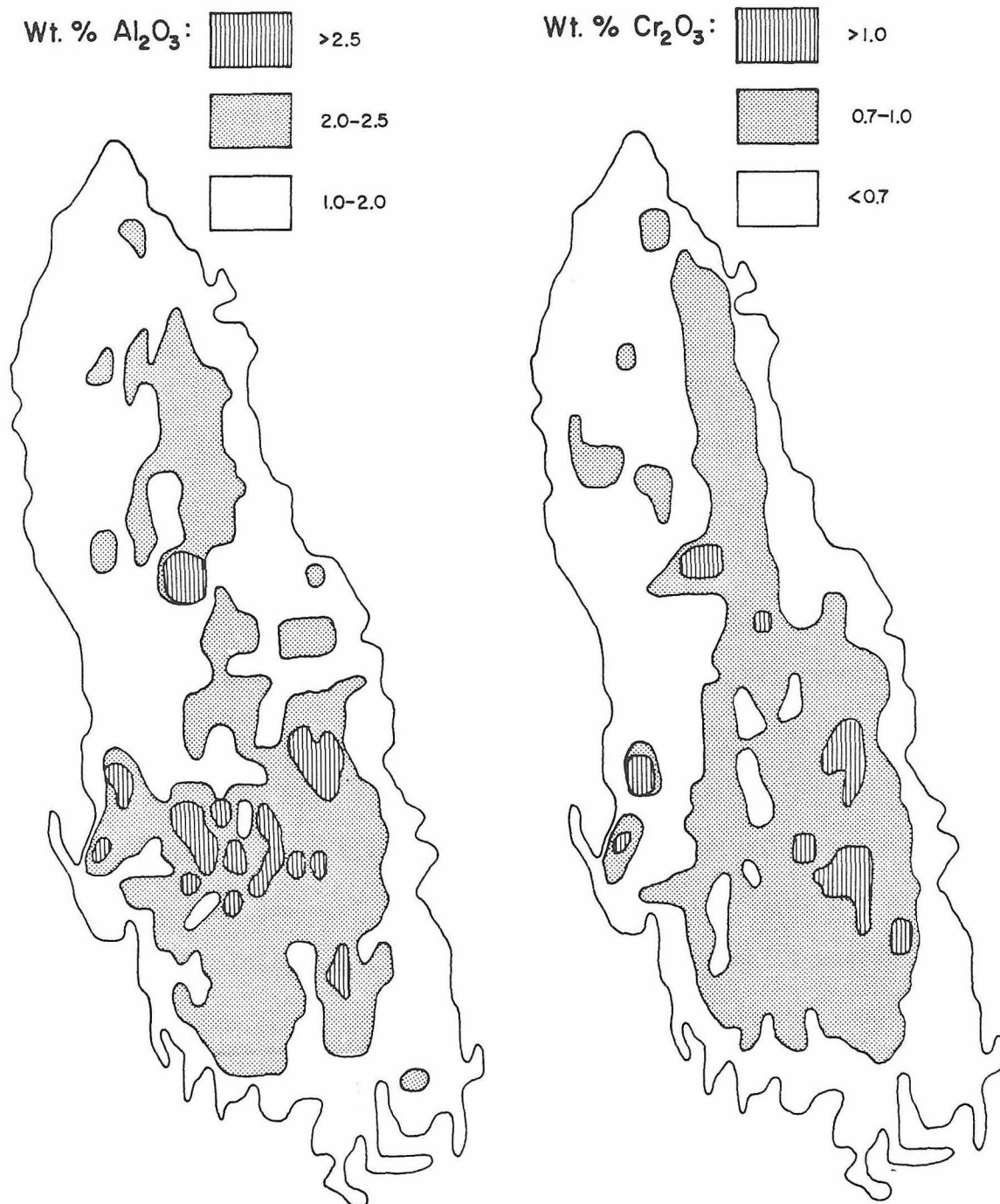


Figure 31: Point count results for a single orthopyroxene grain contoured by weight percent Al_2O_3 and Cr_2O_3 . Approximately 2000 points were measured utilizing the automated electron microprobe point count. At each grid point, intensities were collected for 5 seconds for Al and Cr using crystal spectrometers. The edge of the grain is the outermost contour; the grain is surrounded by olivine.

8W40: Al_2O_3 AND Cr_2O_3 DISTRIBUTION IN OPX

Al_2O_3 and Cr_2O_3 concentrations. From rim to core, Al_2O_3 ranges from about 2 to over 3 weight percent, and Cr_2O_3 from about 0.5 to over 0.8 weight percent. Figure 31 shows the results of a point count of a single orthopyroxene grain in harzburgite sample 8W40H contoured with respect to Al_2O_3 and Cr_2O_3 concentrations. These results reinforce the observations illustrated in Figure 30, and demonstrate that the Al_2O_3 and Cr_2O_3 zoning in orthopyroxene porphyroblasts are more or less concentric and parallel to the edges of the grains. The traverse data (Figure 30) suggest diffusion controlled concentration gradients for Al and Cr, and, therefore, that the rims formed by reequilibration of preexisting pyroxene. If the rims formed as simple overgrowths of lower-Ca, -Cr, and -Al orthopyroxene over preexisting orthopyroxene, the profiles in Figure 30 might show a distinct discontinuity at the boundary of old and new pyroxene. The tendency for porphyroblast rims and interstitial orthopyroxene grains to be less calcic than the cores of the porphyroblasts is also consistent with limited reequilibration of the rims at lower temperatures where the pyroxene solvus is wider.

The Ca, Mg, Fe, Al and Cr concentrations in the orthopyroxene in the Trinity peridotite, like that of the olivine, are similar to those reported for alpine-type peridotites (Dick, 1978; Himmelberg and Coleman, 1968; Loney *et al.*, 1970), for ultramafic sections of ophiolites (Coleman, 1977). The orthopyroxene analyses from the high-temperature peridotites (Green, 1964; Boudier, 1978; Obata, 1976), however, are somewhat higher in Al-content than those from the Trinity peridotite, and in terms of this parameter, the Trinity peridotite orthopyroxene is more similar to the alpine-type and ophiolite orthopyroxene. As with the olivine, the orthopyroxene from the

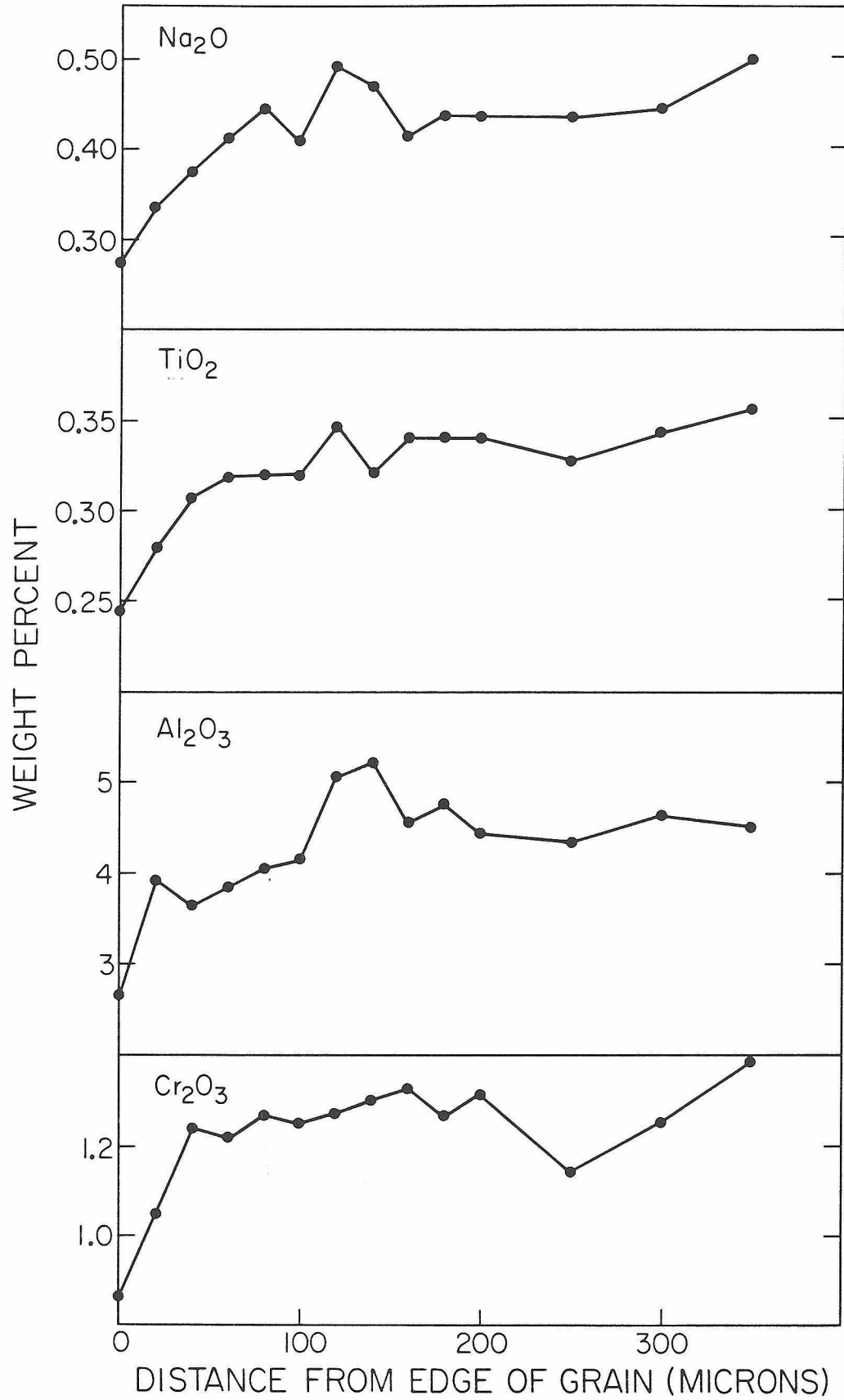
Trinity peridotite is distinct from those from stratiform intrusions such as the Skaergaard, the Bushveld, and the Stillwater (Wager and Brown, 1967; Jackson, 1969) by being substantially more Mg-rich. The orthopyroxene in these intrusions is generally less magnesian than En_{90} .

CLINOPYROXENE

All of the quantitative analyses of clinopyroxene are plotted in pyroxene quadrilaterals in Figure 26. The analysed clinopyroxene displays a limited range in composition, ranging from $En_{54}Wo_{41}Fs_5$ to $En_{49}Wo_{48}Fs_3$. As for the orthopyroxene analyses, there is considerable compositional overlap between the clinopyroxene analyses from the different rock types of the Trinity peridotite. The clinopyroxene in the plagioclase lherzolite, lherzolite, harzburgite, dunite and clinopyroxene-rich lithologies are essentially indistinguishable in these diagrams. As in the case of orthopyroxene, some very small compositional differences can be determined between these lithologies by careful sampling and analysis. These differences are discussed in the section on progressive changes in mineral composition. The clinopyroxenes in the gabbro and related cumulate rocks show a small range in composition, defining a small Fe-enrichment trend and overlapping slightly with the compositions of the clinopyroxenes in the Trinity peridotite.

Clinopyroxene compositions determined by automated electron microprobe analysis are also shown in Figures 27 and 28. As for the orthopyroxenes, the point count results are essentially in agreement with the results of the quantitative analyses. However, the clinopyroxene

Figure 32: Traverse from rim to core across a clinopyroxene porphyroclast in sample 9W20. Each point represents a complete quantitative analysis for 9 elements. Errors (1σ) based on counting statistics are ± 0.01 weight percent for Na_2O , ± 0.01 weight percent for TiO_2 , ± 0.04 weight percent for Al_2O_3 and ± 0.04 weight percent for Cr_2O_3 .



compositions in the microgabbro determined by point count analysis are slightly more Ca-rich than the results of the quantitative analyses (most Fe-rich clinopyroxenes in Figure 26F). This is interpreted to be an artifact of the data reduction procedure used in plotting the point count results rather than a real difference in sampling of this rock.

Clinopyroxene grains within single thin sections show a range in composition that is analogous to that of the orthopyroxene. Figure 29 illustrates that cores of clinopyroxene porphyroclasts in sample 8W67 tend to be more Mg-rich than the rims of the same grains. Also the rims of the porphyroclasts are similar in composition to the interstitial clinopyroxene grains. Figure 31 displays the results of a microprobe traverse from core to rim across a single clinopyroxene grain from plagioclase lherzolite sample 9W20. Al_2O_3 and Cr_2O_3 are highest in the interior of the grain, reaching 5 and 1.2 weight percent, respectively. These values decrease toward the rims where Al_2O_3 and Cr_2O_3 are about 2.7 and 0.9 weight percent, respectively. Similarly Na_2O and TiO_2 decrease in concentration from about 0.45 and 0.33 weight percent at the core, respectively, to about 0.30 and 0.25 weight percent at the rim. The profiles for Al_2O_3 and Cr_2O_3 concentrations are similar to those for the orthopyroxene porphyroclast that were illustrated in Figure 30, and suggests that, as in the case of the orthopyroxene, the rims were altered in composition by reequilibration of Al, Cr, Ti and Na in the rims of preexisting pyroxene grains. However, the irregularities in this particular profile are much larger than the errors due to counting statistics. The local highs in Na_2O and Al_2O_3 profiles at about 120 microns from the edge may be local relicts of pyroxene that were not reequilibrated. The lower concentration of $(\text{Mg,Fe})\text{SiO}_3$ in

the rims (Figure 29) suggests that the final reequilibration of the rims occurred at lower temperatures (or pressures) than at which the cores were formed, where the pyroxene solvus is wider.

The compositions of the clinopyroxene in the Trinity peridotite is similar to that in high-temperature peridotites (Green, 1964; Boudier, 1978) except that the Trinity clinopyroxenes are somewhat lower in Al-content. A comparison with most alpine-type ultramafic bodies and basal ultramafic sections of ophiolites is not possible since these rocks are generally devoid of clinopyroxene. The clinopyroxene in the Trinity peridotite are distinct from those in stratiform intrusions such as the Skaergaard, the Bushveld and the Stillwater (Wager and Brown, 1967; Jackson, 1969) by being both more Mg-rich and Ca-rich.

SPINEL

Spinel shows greater range in composition than any other phase in the Trinity peridotite. This is in part due to the extensive solid solution that exists in the spinel group minerals. The general spinel formula is AB_2O_4 . In compositions of interest to this investigation, "A" represents the divalent cations Mg, Fe^{++} , and Mn, and "B" represents the trivalent cations Fe^{+++} , Al and Cr. Substitution of a titanium end-member, A_2TiO_4 , is also possible. Irvine (1967) presented a systematic review of the chemical characteristics of the spinel group minerals and concluded that plots of $Cr/Cr+Al$ and $Fe^{+++}/Cr+Al+Fe^{+++}$ versus $Fe^{++}/Mg+Fe^{++}$ are adequate to describe the chemical variations in most natural spinels. Table 10 demonstrates that although there is very little variation in the TiO_2 and Fe_2O_3 concentrations in the spinels of the Trinity peridotite, there is a large range in Al_2O_3 and Cr_2O_3 concentrations.

Figure 33: Cr/Cr+Al and $\text{Fe}^{++}/\text{Mg}+\text{Fe}^{++}$ in spinels in the Trinity peridotite. Each point represents a complete analysis for 10 elements. Fe^{++} is calculated assuming stoichiometry. Dots, plagioclase lherzolite; triangles, lherzolite and harzburgite; squares, dunite. Fields for spinels from stratiform intrusions and alpine-type ultramafic bodies from Irvine and Findlay (1972).

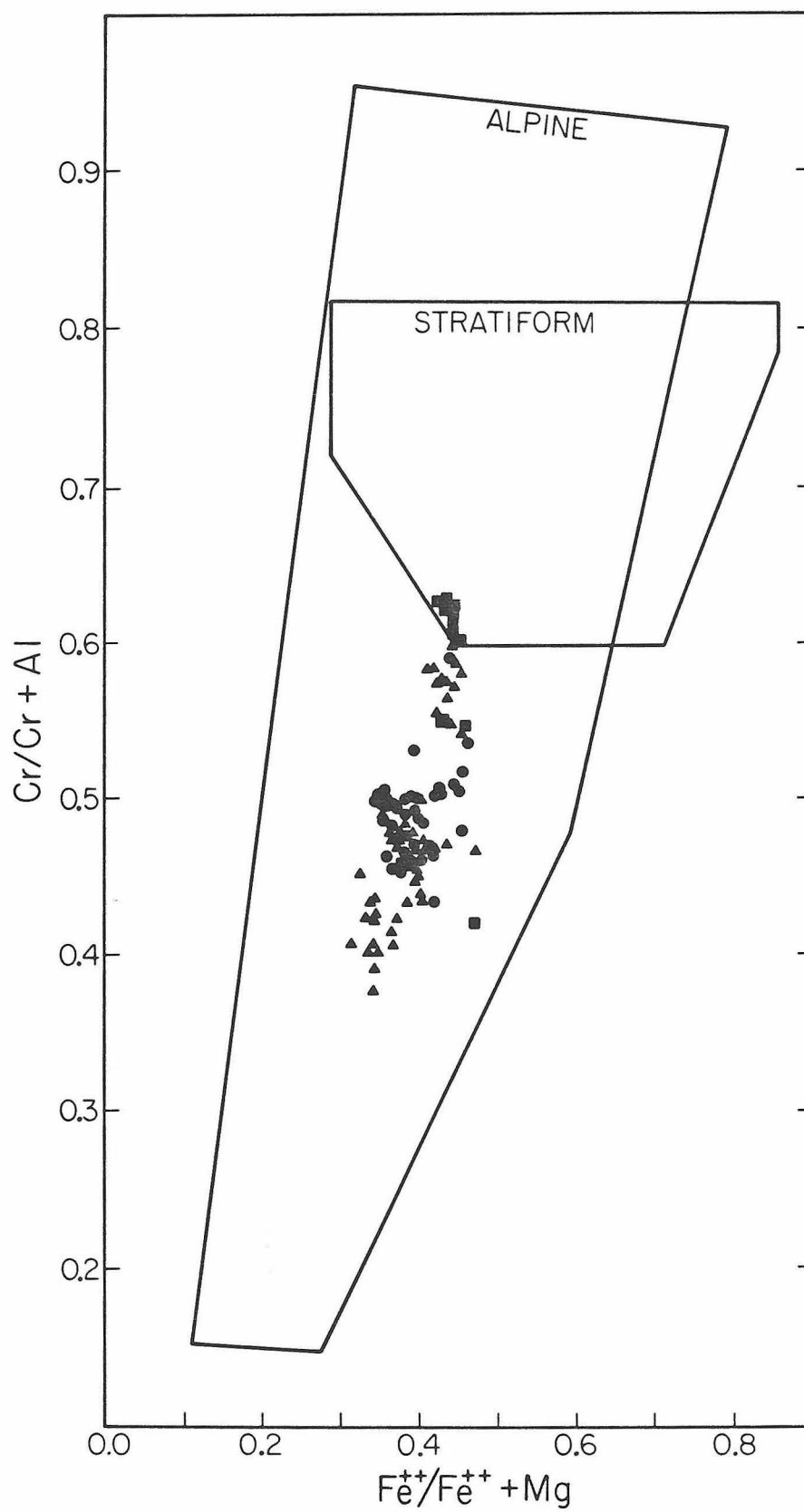


Figure 34: Variations in spinel composition across a transition from plagioclase herzolite to dunite and across a depleted zone around a websterite dike. Each point represents a complete analysis for 10 elements. Fe^{++} is calculated assuming spinel stoichiometry.

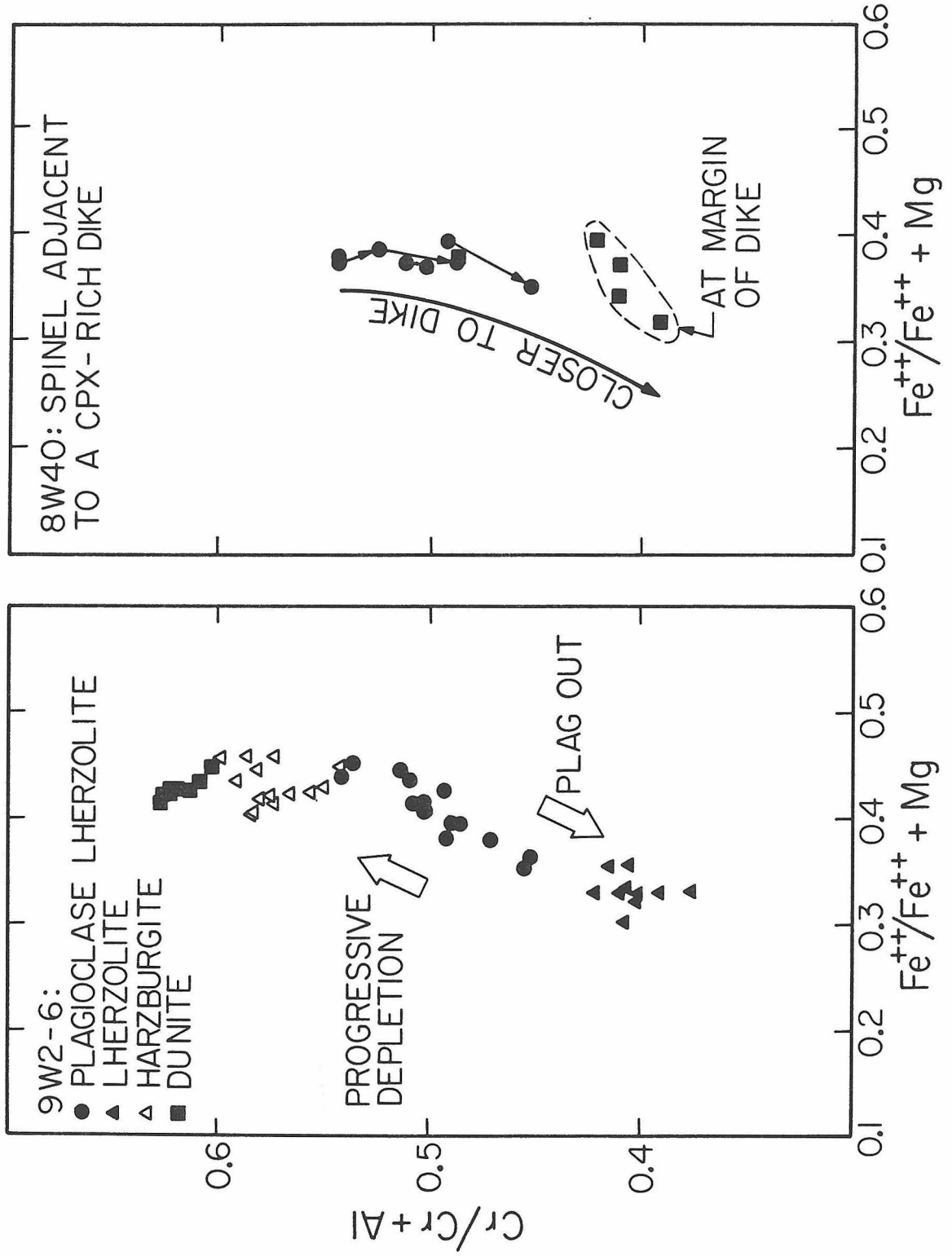


Figure 33 summarizes Cr/Cr+Al, and Fe⁺⁺⁺/Mg+Fe⁺⁺ variation for analyzed spinels from the Trinity peridotite. Fe⁺⁺⁺ and Fe⁺⁺ were calculated from microprobe analyses for total Fe by assuming the spinels to be stoichiometric. The ranges in compositions are about .35 to .63 for Cr/Cr+Al and about .55 to .70 for Mg/Mg+Fe⁺⁺. Figure 34 illustrates that spinels are most Cr-rich in the dunite samples, followed in order of decreasing Cr/Cr+Al by harzburgite, plagioclase lherzolite and lherzolite. This observation will be discussed in more detail in the description of progressive changes in mineral composition. It is significant, however, because it is the most consistent difference in mineral composition between the different lithologies.

The spinels in some rocks show chemical variation from one grain to another. These variations are most pronounced in the plagioclase lherzolite and lherzolite and are reflected in the large spread of compositions in Figures 33 and 34 for these lithologies; variations of up to 10 percent occur in Cr/Cr+Al in different grains of a single thin section. In general, spinels that are included within pyroxene or, to a lesser extent, within olivine tend to be more Cr-rich while interstitial spinel grains tend to be more Al-rich. Variations in Fe⁺⁺/Fe⁺⁺⁺+Mg are generally antipathetic to variations in Cr/Cr+Al.

Spinel in dunite samples, in contrast, tend to have an extremely limited range of composition that is reflected by tight clusters in Figures 33 and 34.

Spinel grains also display some chemical variation within individual grains. Figure 35 illustrates that, in general, rims of spinel grains are more Fe⁺⁺ rich than the cores. This feature is present in all samples of the Trinity peridotite and is opposite in sense to

Figure 35: Electron microprobe traverse across a spinel grain. Each point represents a complete analysis for 10 elements. Fe⁺⁺ and Mg in catatom percents. Fe⁺⁺ calculated assuming spinel stoichiometry.

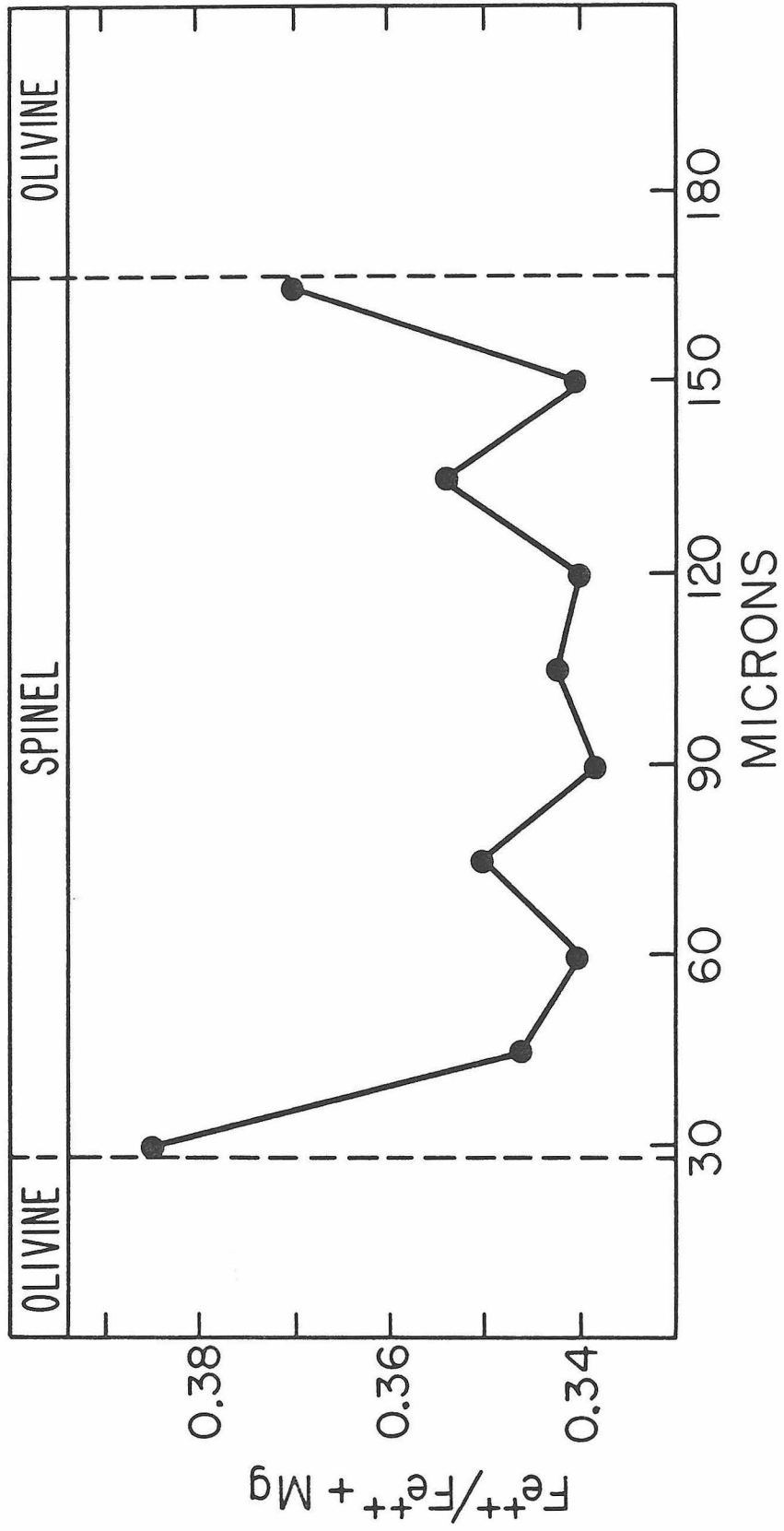
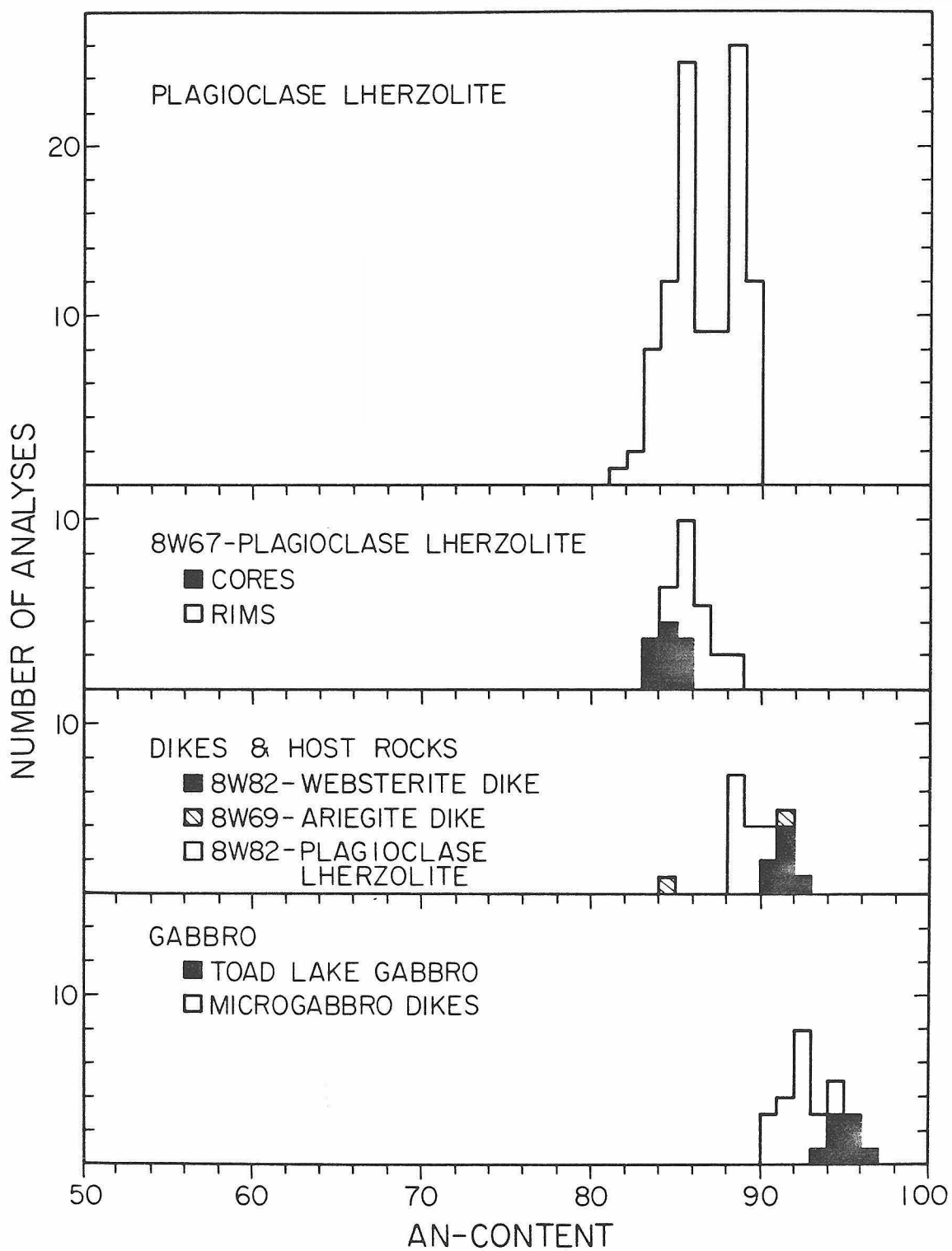


Figure 36: An-content of plagioclase in samples of the Trinity peridotite and gabbroic rocks. An-content is calculated for this diagram to be $\text{Ca}/(\text{Ca}+\text{Na}+\text{K})$ where Ca, Na and K are in cation percent. The upper diagram summarizes all analyses in plagioclase lherzolite.



the $\text{Fe}^{++}/\text{Mg}+\text{Fe}^{++}$ zoning in the surrounding olivine (Figure 24). This suggests that the zoning in the spinel and surrounding olivine was produced by exchange of Fe^{++} and Mg during local reequilibration.

The spinels in the Trinity peridotite are most similar to those in the ultramafic portions of ophiolites and in alpine-type ultramafic rocks. Figure 31 illustrates that in terms of $\text{Mg}/\text{Mg}+\text{Fe}^{++}$ and $\text{Cr}/\text{Cr}+\text{Al}$ the compositions of the spinels from the Trinity peridotite fall in the field of alpine-type peridotites but are, for the most part, outside the field of spinels from stratiform intrusion (Irvine and Findlay, 1972). The $\text{Cr}/\text{Cr}+\text{Al}$, $\text{Fe}^{++}/\text{Mg}+\text{Fe}^{++}$ and Fe^{+++} -contents of spinels in the harzburgite and dunite (Table 10) are similar to the compositions of spinels from the ultramafic sections of ophiolites (Coleman, 1977), and the same parameters for the spinels in the the plagioclase lherzolite and lherzolite (Table 10) are similar to those reported by Green (1964) and Boudier (1978) for high-temperature peridotites except that the range in compositions never reach Al-enrichments as high. All of the spinels in the Trinity peridotite differ from the spinels of Alaskan-type ultramafic bodies by being less Fe^{+++} -rich and from spinels of the stratiform-type intrusions by being lower in $\text{Cr}/\text{Cr}+\text{Al}$ and higher in $\text{Mg}/\text{Mg}+\text{Fe}^{++}$.

PLAGIOCLASE

The An-contents of plagioclase from the Trinity are shown in Figure 36. Most of the compositions in the plagioclase lherzolite fall in the narrow range, An_{83} to An_{90} , although some of the plagioclase grains are as sodic as An_{81-82} . Plagioclase from clinopyroxene-rich dikes and from plagioclase-rich veins are significantly more calcic

than those in the plagioclase lherzolite, and tend to have An-contents of $An_{>90}$. The plagioclase from all the lithologies is low in K_2O (<0.1 weight percent) and FeO (<0.2 weight percent).

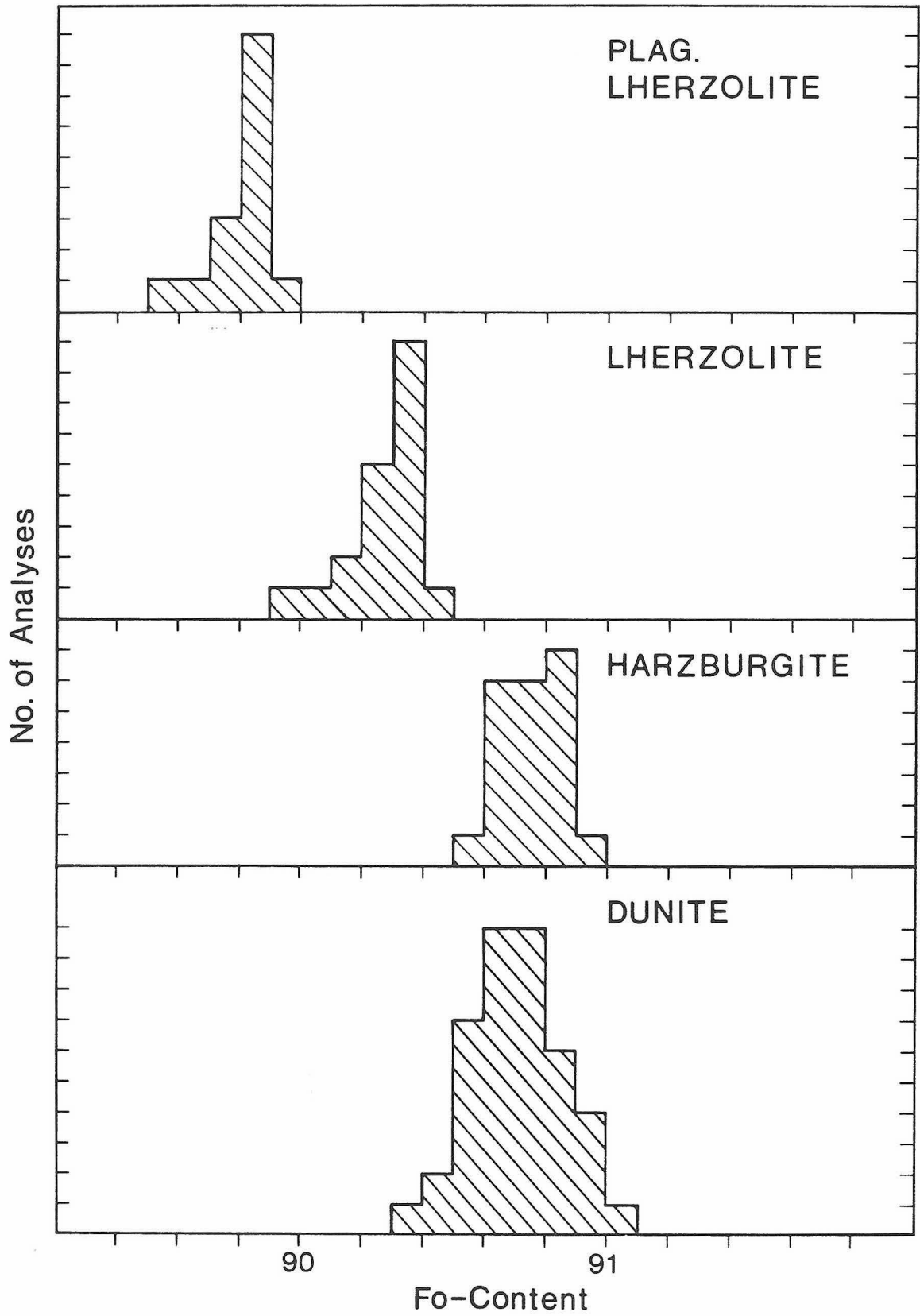
There is a slight suggestion of compositional zoning in the plagioclase of some peridotites. This is best illustrated by the histogram of plagioclase An-content for sample 8W67 (Figure 36). Cores of plagioclase grains tend to be slightly more sodic than rims (outer 20 microns). Unfortunately, this observation was difficult to test with electron microprobe traverses across single grains because of the extensive alteration of plagioclase in the rocks.

Figure 36 also illustrates that plagioclase tends to be slightly less calcic in the plagioclase lherzolite ($An_{<90}$) than in the websterite dikes (An_{90-93}), and significantly less calcic than the plagioclase in the gabbroic rocks (An_{90-97}).

There is very little data on the compositions of plagioclase from other peridotite bodies because the occurrence of plagioclase is exceedingly rare in ultramafic rocks, and because where it was present, it is generally altered to clinozoisite or some other mineral produced during serpentinization. The plagioclase in the Trinity peridotite is more calcic than the plagioclase in Lanzo peridotite (An_{74-85} ; Boudier, 1978), but similar to the plagioclase in the Othris peridotite (An_{87} ; Menzies, 1974). The extremely calcic nature of the plagioclase in the Trinity is similar to plagioclase xenocrysts that have been described in some oceanic tholeiites (Duncan and Green, 1980), and sets them apart from plagioclase (generally $An_{<85}$) in stratiform intrusions such as the Skaergaard, the Bushveld and the Stillwater (Wager and Brown, 1967; Jackson, 1969).

Figure 37: Fo-content ($\text{Mg}/\text{Mg}+\text{Fe}$) of olivine across a transition from plagioclase lherzolite to dunite (samples 9W2-6). Each analysis is a complete quantitative analysis for 9 elements. Reproducibility of each analysis is estimated to be ± 0.1 mole percent Fo-content based on repeated analyses of an olivine standard of known composition. Locations of each sample relative to the plagioclase-out boundary are shown graphically in Figure 39.

OLIVINE COMPOSITIONS



PROGRESSIVE CHANGES IN MINERAL COMPOSITION

It is not possible, as discussed above, to distinguish most of the peridotite lithologies solely on the basis of mineral compositions because of the large overlap that occurs between the mineral compositions in the different lithologies. (Notable exceptions are, of course, plagioclase and spinel.) However, small but significant progressive changes in mineral composition are detectable across transitions from plagioclase lherzolite to large dunite bodies and across depleted zones from plagioclase lherzolite to websterite dikes.

Quantitative analyses were performed on spinel and olivine grains in samples of plagioclase lherzolite, lherzolite, harzburgite and dunite from a plagioclase lherzolite to dunite transition exposed at Vicki Bluff. Figure 37 is a histogram of Fo-content that illustrates the progressive changes in olivine composition across this transition. Samples were taken across a transition from plagioclase lherzolite to dunite that is about 1 m wide; the distribution of the samples relative to the plagioclase-out boundary is illustrated graphically in Figure 39A. Olivine analyses were performed on grains that were isolated from and, therefore, not affected by local exchange of Mg and Fe with the spinel. The analyses were performed during one electron microprobe run to minimize systematic errors introduced by restandardization from day to day. Figure 37 illustrates that there is a progressive increase in Fo-content from plagioclase lherzolite (Fo_{99.8}) to the harzburgite and dunite (Fo_{90.8}). Meaningful variations in CaO and NiO concentrations were not detected between the plagioclase lherzolite, lherzolite and harzburgite, but olivines in the dunite were more Ca-rich by a

Figure 38: Cr/Cr+Al in spinel across a transition from plagioclase herzolite to dunite. Each analysis is a complete quantitative analysis for 10 elements. Samples (9W2-6) are the same as in Figure 37 and locations relative to the plagioclase-out boundary are shown graphically in Figure 39.

SPINEL COMPOSITIONS

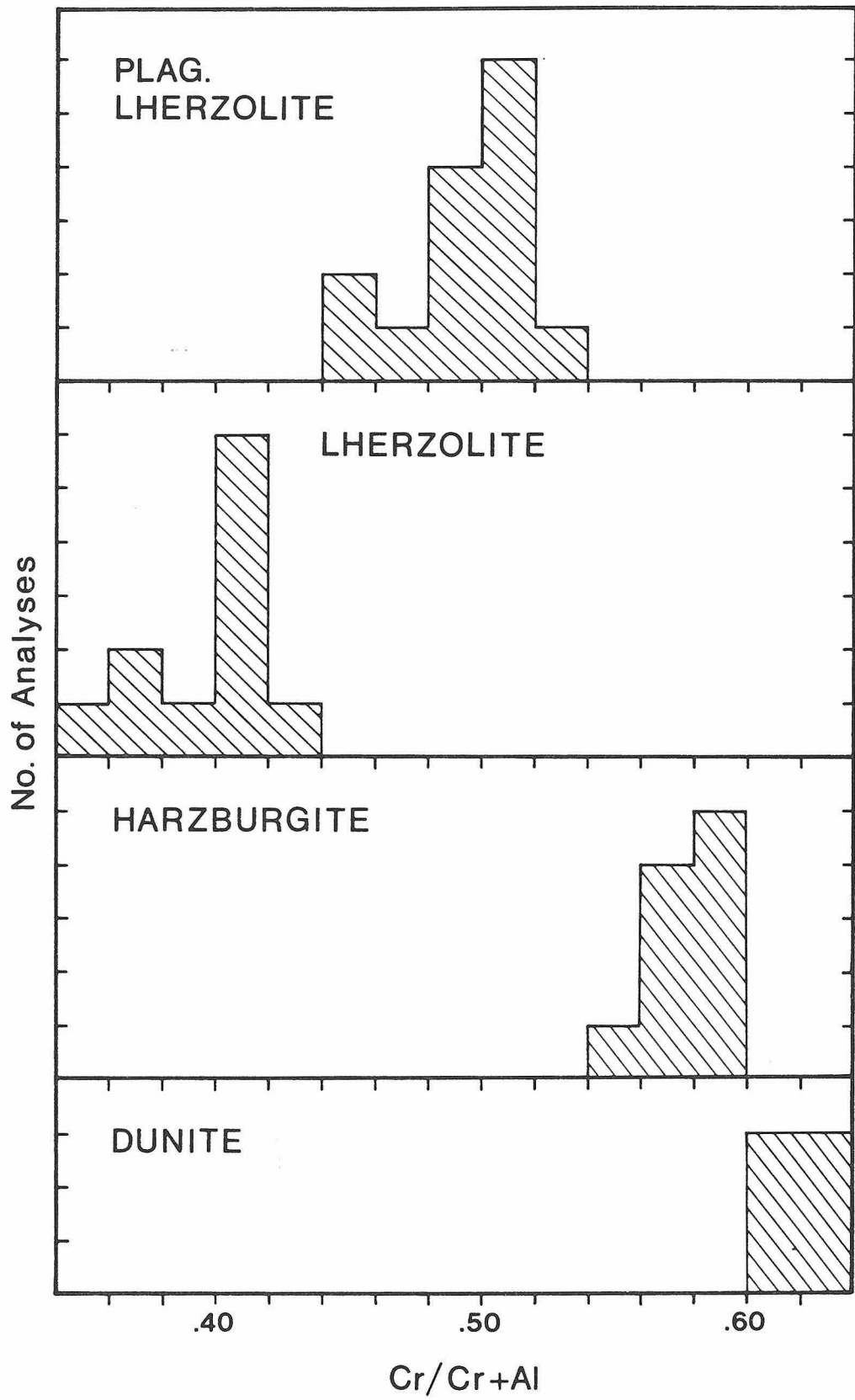
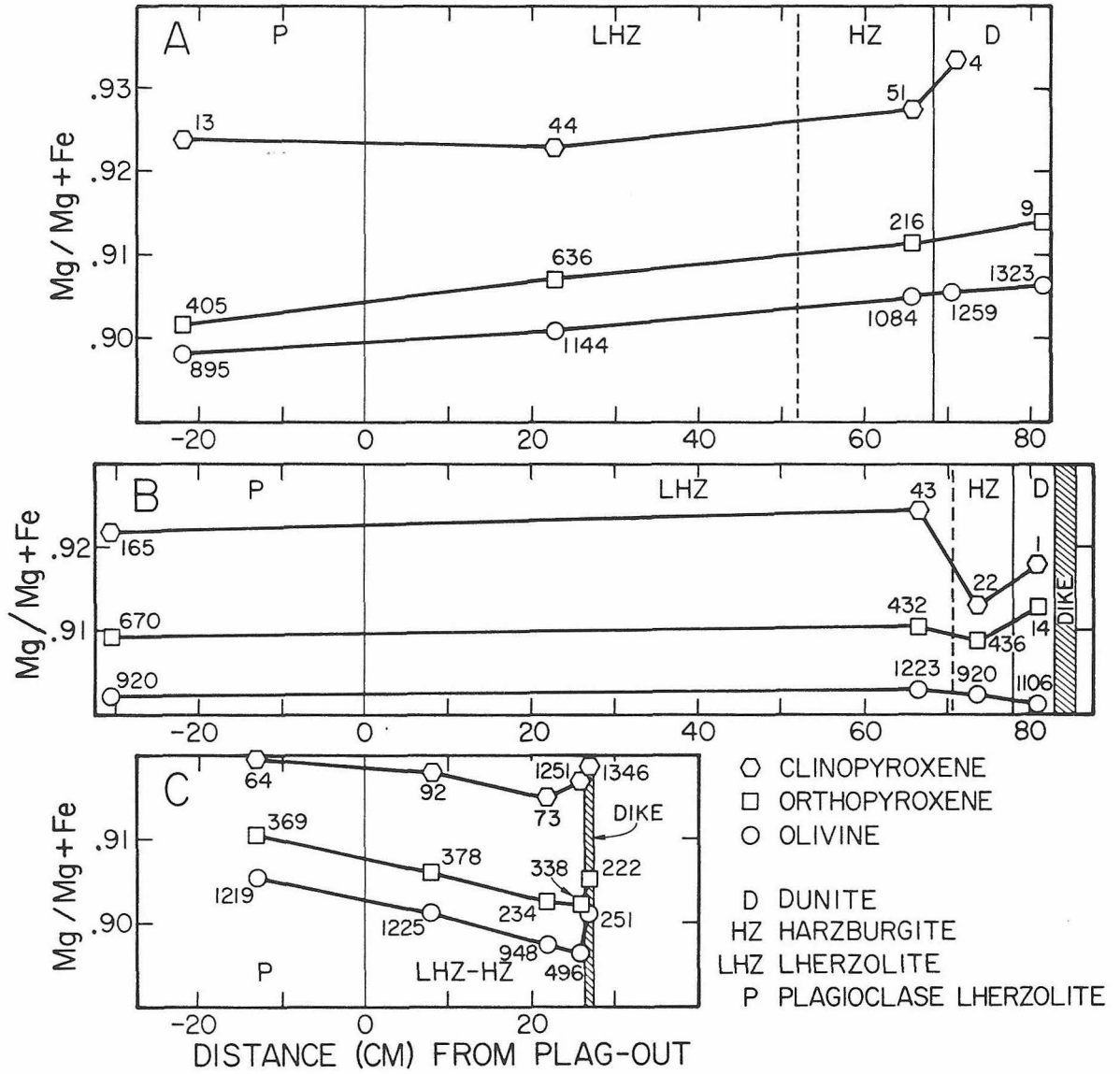


Figure 39: Average $Mg/Mg+Fe^{++}$ in olivine, orthopyroxene and clinopyroxene as a function of distance from the plagioclase-out boundary across some lithologic transitions. Each datum is an average of all analyses for the phase performed by an automated electron microprobe point count of the sample. Numbers beside data points are total number of analyses that contributed to the average.

- (A) Traverse across a transition from plagioclase lherzolite to dunite (9W2-6).
- (B) Traverse across a depleted zone adjacent to a websterite dike at Vicki Bluff (9W7-9).
- (C) Traverse across a depleted zone adjacent to a websterite dike south of Bull Creek (8W40).



factor of two (Figure 25; see discussion of olivine analyses). Figure 38 is a histogram of Cr/Cr+Al values for spinel grains across this transition. From plagioclase lherzolite to lherzolite there is a distinct Al-enrichment in the spinels manifested by a lowered Cr/Cr+Al in the spinels of the lherzolite. From the lherzolite to the dunite, the trend is reversed and the spinels become increasingly richer in Cr relative to Al.

Variations in the compositions of orthopyroxene and clinopyroxene are more difficult to assess because of the zoning in the porphyroclasts and because of the bimodal occurrence of these phases as porphyroclasts and as matrix grains. Automated electron microprobe point counts were performed across the transition zone to determine changes in the average compositions of these minerals across the transition zone, and to test the results of the quantitative analyses on olivine and spinel.

Figure 39 illustrates the changes in average $Mg/Mg+Fe^{++}$ in orthopyroxene, clinopyroxene, and olivine compositions as a function of distance from the plagioclase lherzolite-lherzolite contact. As demonstrated by the quantitative analyses, the average olivine composition becomes more Mg-rich. Furthermore, the average orthopyroxene and clinopyroxene compositions also become more Mg-rich. Therefore, the results of the point counts are compatible with the quantitative analyses of olivine and indicate that both orthopyroxene and clinopyroxene, as well as olivine, become more Mg-rich across the transition from plagioclase lherzolite to dunite. This latter point is significant because it excludes Fe-Mg partitioning between different ratios of olivine and pyroxene in these lithologies as a mechanism for producing the Mg-enrichment in the olivine.

Figure 40: Fo-content of olivine across a depleted zone around a websterite dike in sample 8W40. Each analysis is a complete analysis for 9 elements, and reproducibility is estimated to be ± 0.1 mole percent Fo-content based on repeated analyses of an olivine standard of known composition. Locations of samples are shown graphically in Figure 39C.

- (A) Plagioclase lherzolite sample 8W40D.
- (B) Lherzolite sample 8W40F.
- (C) Lherzolite sample 8W40H.
- (D) Lherzolite sample immediately adjacent to the websterite dike (8W40I).

8W40: OLIVINE

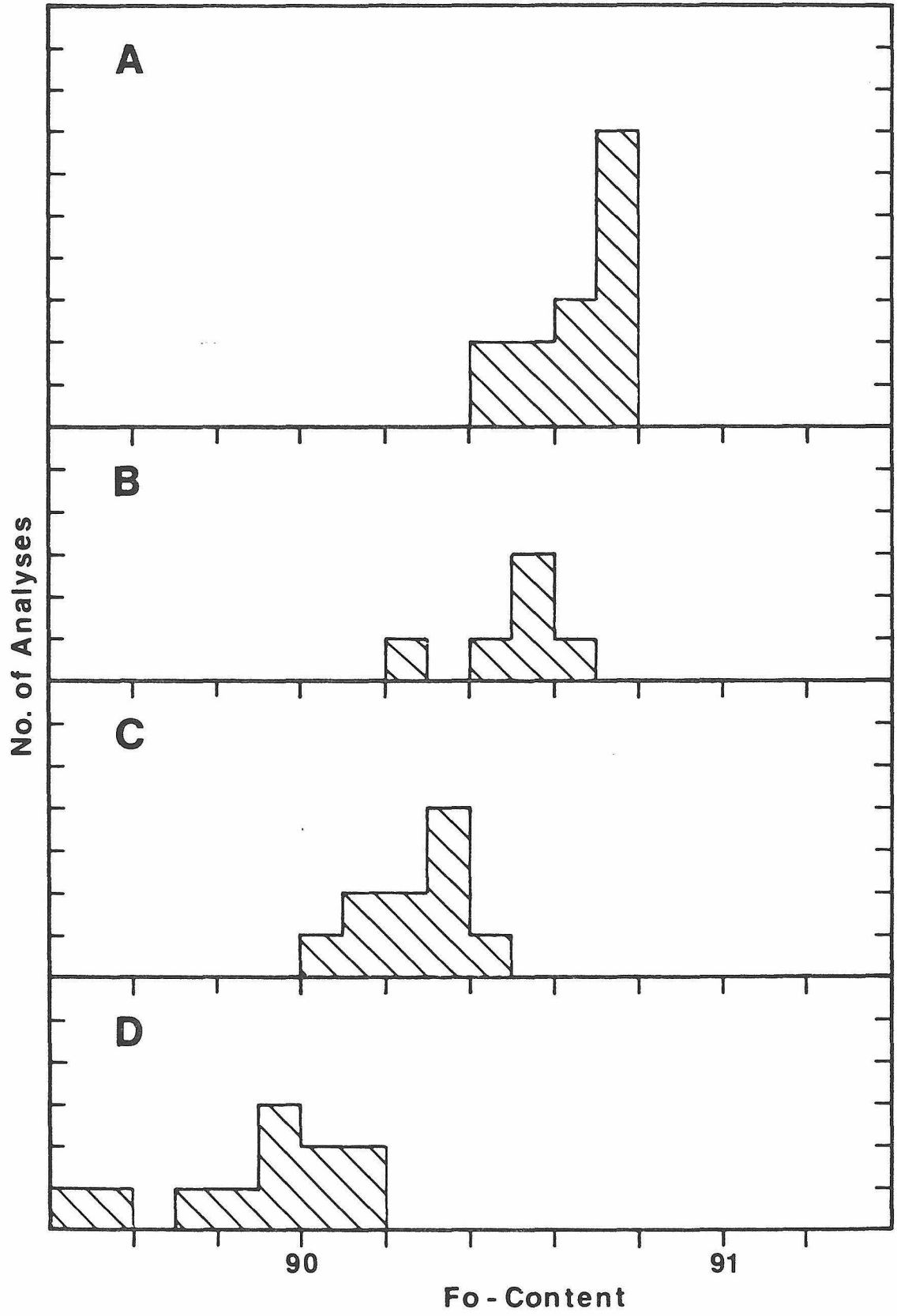
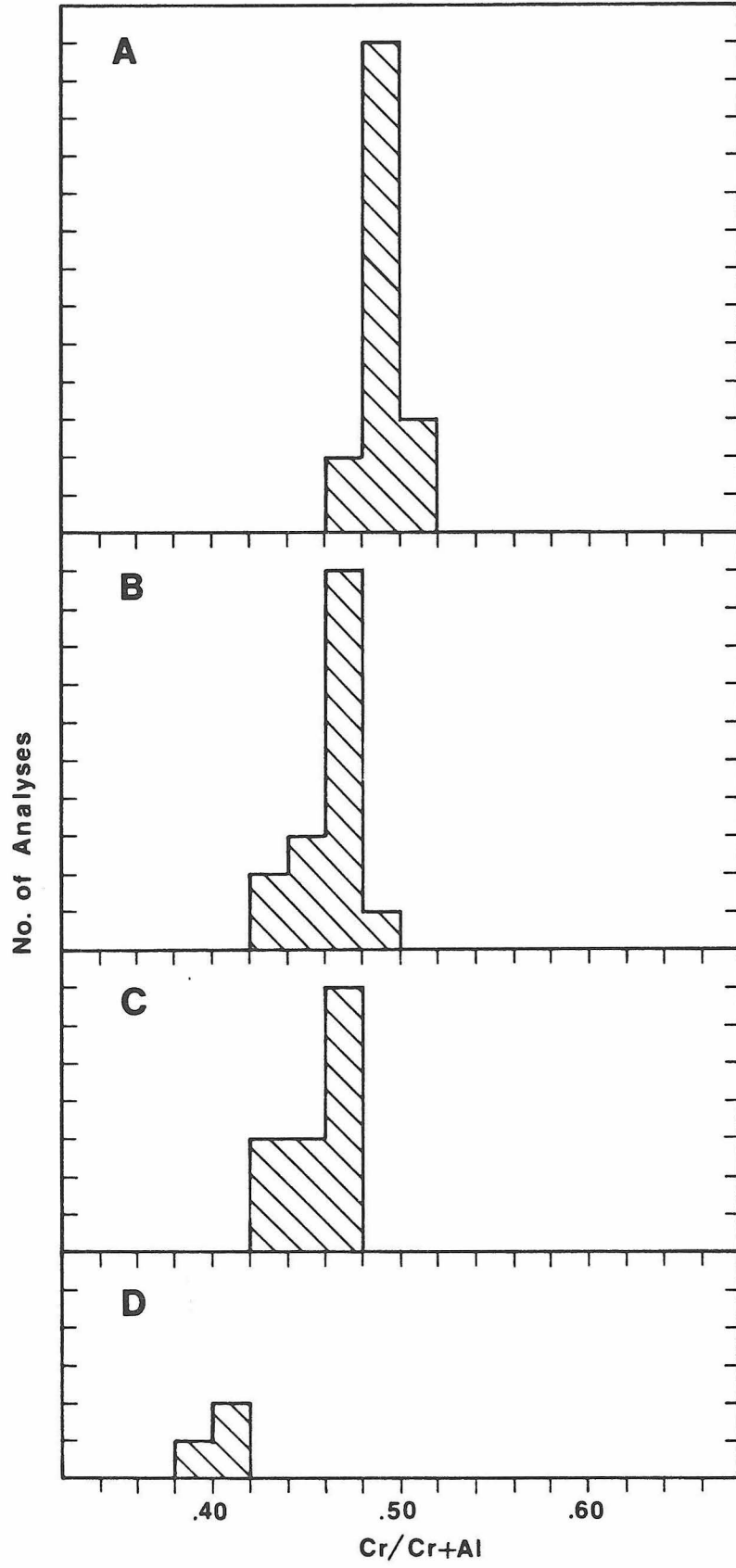


Figure 41: Cr/Cr+Al in spinel across a depleted zone around a websterite dike in sample 8W40. Each analysis is a complete analysis for 10 elements. Samples are the same as in Figure 40 and locations are shown graphically in Figure 39C.

- (A) Plagioclase lherzolite sample 8W40D.
- (B) Lherzolite sample 8W40F.
- (C) Lherzolite sample 8W40H.
- (D) Lherzolite sample immediately adjacent to the websterite dike (8W40I).

8W40: SPINEL



Traverses across two different depleted zones adjacent to websterite dikes were performed in order to test for progressive changes in mineral composition and to compare these changes with those that occur across the transition from plagioclase lherzolite to large dunite bodies described above. One depleted zone, sample 8W40, consisted of harzburgite-lherzolite zone developed adjacent to a websterite dike that intrudes plagioclase lherzolite. This was sampled collecting a boulder large enough to contain the host, the dike and the depleted zone. The boulder was then dissected in the laboratory for preparation of polished thin sections cut parallel to and at carefully measured distances from the websterite dike. The second depleted zone consisted of consecutive zones of dunite, harzburgite, and lherzolite around a websterite dike that intrudes plagioclase lherzolite (samples 9W7, 8 and 9). A photograph of the dike, depleted zone and host rock is presented in Figure 8. Samples of each of these lithologies were collected in and distances to the websterite dike were measured in the field.

Figures 40 and 41 illustrate the changes in olivine and spinel compositions in sample 8W40 that were determined by quantitative analyses of carefully selected points, and Figure 39C illustrates the changes in average composition of olivine, orthopyroxene, clinopyroxene and spinel that were determined by automated electron microprobe analysis. From these two figures it is clear that progressive changes in composition across depleted zones can be determined, and that in sample 8W40, at least, the changes are different from those that occur across the plagioclase lherzolite-dunite transition. The average compositions of olivine, orthopyroxene and clinopyroxene are more Fe-rich in the depleted zone than in the host plagioclase lherzolite, and these phases

appear to display progressive Fe-enrichment with increasing proximity to the dike. The spinel compositions show progressive decrease in Cr/Cr+Al as the dike is approached. An additional observation is that the plagioclase in the dikes are consistently more anorthitic than the plagioclase in the plagioclase lherzolite host (Figure 36).

The samples across the second depleted zone (9W7, 8 and 9) were studied with the automated microprobe point count. The results are presented in Figure 39B in terms of average Mg/Mg+Fe of olivine, orthopyroxene and clinopyroxene as a function of distance from the plagioclase-out boundary. Olivine, orthopyroxene and clinopyroxene have essentially constant Mg/Mg+Fe values from plagioclase lherzolite, to lherzolite, to harzburgite and to dunite as the websterite dike is approached. The excursions in Mg/Mg+Fe for clinopyroxene are rather large but probably reflect errors due to poor counting statistics since clinopyroxene is relatively scarce (<50 points) in samples other than the plagioclase lherzolite. This suite of samples, therefore, shows very little compositional change in the silicate minerals and represents a situation that might be considered intermediate to the compositional trends across the plagioclase lherzolite-dunite transition (Figure 39A) and across the depleted zone in sample 8W40 (Figure 39C).

SUMMARY AND CONCLUSIONS

The magnesian silicate minerals and plagioclase in the Trinity peridotite show very restricted ranges in composition that may be described as extremely refractory. The refractory nature and very limited compositional range of similar minerals in other peridotite bodies has

been cited as evidence that those peridotites formed as residua of partial melting of a less refractory protolith (Dick, 1977; Coleman, 1977; Boudier and Coleman, in press). Indeed, the compositions of these phases and of the spinels in the Trinity peridotite are most like those of similar phases in alpine-type ultramafic bodies and the ultramafic portion of ophiolites.

There is detectible compositional zonation in the pyroxenes, olivine, spinel and possibly in plagioclase reflecting local reequilibration. The effects of this reequilibration are recorded by: (1) loss of Al and Cr from rims of orthopyroxene porphyroclasts; (2) loss of Al, Cr, Na and Ti from rims of clinopyroxene porphyroclasts; (3) widening of the pyroxene solvus; (4) local exchange of Fe^{++} and Mg between olivine and spinel; and (5) possible increase in An-content toward the rims of plagioclase.

Progressive variations in phase composition can be detected across transitions from plagioclase lherzolite to large dunite bodies and across depleted zones around websterite dikes. In the first instance, the phases become more refractory with proximity to the dunite body. This could be consistent with formation of the lherzolite, harzburgite and the margin the dunite body as in situ residua of melt extraction from a plagioclase lherzolite protolith but might involve some other process as will be discussed in a later section. In contrast, the same phases become less refractory across depleted zones as websterite dikes are approached.

Table 7: Representative Analyses of Olivine from the Trinity Peridotite and Associated Gabbroic Rocks.

	1	2	3	4	5	6	7	8	9
SiO ₂	40.24	40.76	40.88	41.09	40.59	40.77	40.79	40.88	40.74
TiO ₂	0.01	0.00	0.00	0.00	0.00	0.02	0.00	0.00	0.00
Al ₂ O ₃	0.00	0.00	0.00	0.00	0.00	0.00	0.00	0.00	0.00
Cr ₂ O ₃	0.05	0.04	0.09	0.10	0.00	0.00	0.00	0.00	0.00
MgO	48.90	49.37	49.37	49.78	49.52	49.65	49.49	49.25	50.57
CaO	0.04	0.05	0.03	0.11	0.04	0.04	0.06	0.04	0.01
MnO	0.14	0.15	0.12	0.16	0.08	0.17	0.17	0.21	0.13
FeO	9.71	9.32	8.93	8.91	8.92	9.17	9.29	9.54	8.85
NiO	0.33	0.35	0.41	0.39	0.38	0.19	0.37	0.38	0.46
Sum	99.42	100.04	100.13	100.54	99.53	100.01	100.17	100.30	100.76
Catatoms Normalized to 3.0									
Si	0.992	0.997	0.998	0.999	0.996	0.996	0.996	0.999	0.985
Ti	0.000	0.000	0.000	0.000	0.000	0.000	0.000	0.000	0.000
Al	0.000	0.000	0.000	0.000	0.000	0.000	0.000	0.000	0.000
Cr	0.001	0.001	0.002	0.002	0.000	0.000	0.000	0.000	0.000
Mg	1.797	1.800	1.807	1.804	1.811	1.808	1.802	1.794	1.824
Ca	0.001	0.001	0.001	0.003	0.001	0.001	0.002	0.001	0.000
Mn	0.001	0.001	0.001	0.003	0.002	0.004	0.004	0.004	0.003
Fe	0.200	0.191	0.182	0.181	0.183	0.187	0.190	0.195	0.179
Ni	0.007	0.007	0.008	0.008	0.008	0.004	0.007	0.007	0.009
Mg/Mg+Fe+Mn	89.8	90.3	90.7	90.7	90.7	90.5	90.3	90.0	90.9
	10	11	12	13	14	15	16		
SiO ₂	41.23	41.12	39.96	41.02	40.78	40.83	40.26		
TiO ₂	0.01	0.02	0.01	0.00	0.01	0.00	0.00		
Al ₂ O ₃	0.00	0.00	0.00	0.00	0.00	0.00	0.00		
Cr ₂ O ₃	0.09	0.04	0.05	0.01	0.04	0.00	0.00		
MgO	49.32	49.69	47.68	48.98	48.99	50.09	46.97		
CaO	0.08	0.10	0.03	0.02	0.02	0.02	0.02		
MnO	0.09	0.03	0.17	0.15	0.19	0.10	0.17		
FeO	9.27	8.11	12.33	11.18	10.95	10.03	13.14		
NiO	0.28	0.30	0.12	0.25	0.20	0.17	0.18		
Sum	100.37	99.39	100.35	101.61	101.17	101.24	100.75		
Catatoms Normalized to 3.0									
Si	1.006	1.008	0.985	0.994	0.992	0.987	0.993		
Ti	0.000	0.000	0.000	0.000	0.000	0.000	0.000		
Al	0.000	0.000	0.000	0.000	0.000	0.000	0.000		
Cr	0.002	0.001	0.001	0.000	0.001	0.000	0.000		
Mg	1.794	1.816	1.753	1.770	1.777	1.805	1.728		
Ca	0.002	0.003	0.001	0.001	0.000	0.000	0.001		
Mn	0.002	0.001	0.004	0.003	0.004	0.002	0.004		
Fe	0.189	0.166	0.254	0.227	0.223	0.203	0.271		
Ni	0.005	0.006	0.002	0.005	0.004	0.003	0.004		
Mg/Mg+Fe+Mn	90.4	91.6	87.2	88.5	88.7	89.8	86.3		

Traverse across a plag. lherzolite to dunite transition:

1. Plag. lherzolite, 9020-601
2. Lherzolite, 9030-1201
3. Harzburgite, 9040-2301
4. Dunite, 9050-1001

Traverse across depleted zone, dike and wall rock:

5. Plag. lherzolite, 4020-801
6. Depl. zone, 8 cm from plag. lherz., 4090-101
7. Depl. zone, 23 cm from plag. lherz., 4030-801
8. Websterite dike, 4010-902

9. Ariegite band, 211-501

10. Large dunite body, 90-401
11. large dunite body, 7910-101
12. Websterite layer, 7900-802
13. Cumulate dunite, Toad Lake gabbro, 140-401
14. Cumulate wehrlite, Toad Lake gabbro, 1210-601
15. Cumulate pyroxenite, Toad Lake gabbro, 1340-801
16. Cumulate pyroxenite, Toad Lake gabbro, 1400-601

Table 8: Representative Analyses of Orthopyroxene from the Trinity Peridotite and Associated Gabbroic Rocks

	1	2	3	4	5	6	7	8	9
SiO ₂	54.93	56.17	57.09	55.68	55.90	55.94	56.44	56.60	57.57
TiO ₂	0.07	0.05	0.04	0.10	0.11	0.12	0.09	0.05	0.07
Al ₂ O ₃	3.20	1.90	1.57	3.44	2.59	2.73	1.65	1.45	1.54
Cr ₂ O ₃	0.98	0.52	0.32	0.53	0.55	0.63	0.69	0.52	0.61
MgO	32.76	34.32	35.09	33.20	33.62	33.55	33.73	34.49	33.75
CaO	2.24	0.87	0.69	0.54	0.79	1.05	1.17	0.95	0.77
MnO	0.14	0.15	0.17	0.19	0.19	0.16	0.13	0.15	0.14
FeO	5.40	5.65	5.91	6.26	6.39	6.10	5.90	6.09	5.91
Na ₂ O	0.03	0.05	0.00	0.06	0.03	0.00	0.02	0.00	0.00
Sum	99.75	99.68	100.88	100.00	100.17	100.28	99.82	100.30	100.36
Catatoms Normalized to 4.0									
Si	1.903	1.938	1.946	1.923	1.927	1.927	1.952	1.945	1.983
Ti	0.002	0.001	0.001	0.003	0.003	0.003	0.002	0.001	0.002
Al	0.131	0.007	0.063	0.140	0.105	0.111	0.067	0.059	0.063
Cr	0.027	0.014	0.009	0.014	0.015	0.017	0.019	0.014	0.017
Mg	1.692	1.766	1.783	1.710	1.728	1.723	1.740	1.767	1.733
Ca	0.083	0.032	0.025	0.020	0.029	0.039	0.043	0.035	0.028
Mn	0.004	0.004	0.005	0.006	0.006	0.005	0.004	0.004	0.004
Fe	0.156	0.163	0.168	0.181	0.184	0.176	0.171	0.175	0.170
Na	0.002	0.003	0.000	0.004	0.002	0.000	0.001	0.000	0.000
Mg/Mg+Ca+Fe+Mn	87.41	89.84	89.98	89.23	88.75	88.71	88.87	89.18	89.53
Ca/Mg+Ca+Fe+Mn	4.30	1.64	1.27	1.04	1.50	2.00	2.22	1.77	1.47
FeMn/Mg+Ca+Fe+Mn	8.30	8.54	8.75	9.73	9.75	9.29	8.92	9.06	9.01
	10	11	12	13	14	15	16	17	
SiO ₂	56.28	55.91	56.22	56.52	56.68	55.85	56.48	54.68	
TiO ₂	0.09	0.10	0.07	0.16	0.09	0.05	0.06	0.15	
Al ₂ O ₃	2.10	2.41	2.00	1.70	2.01	1.29	1.02	1.65	
Cr ₂ O ₃	0.62	0.65	0.42	0.24	0.22	0.32	0.36	0.09	
MgO	34.01	33.49	33.86	33.90	33.77	32.80	34.19	27.91	
CaO	0.91	0.89	0.80	1.08	1.47	0.82	0.80	0.89	
MnO	0.16	0.14	0.17	0.12	0.17	0.16	0.16	0.31	
FeO	5.90	6.58	6.54	6.39	6.08	8.51	6.60	13.87	
Na ₂ O	0.02	0.00	0.00	0.03	0.04	0.01	0.00	0.01	
Sum	100.09	100.17	100.08	100.14	100.53	99.89	99.68	99.56	
Catatoms Normalized to 4.0									
Si	1.939	1.930	1.940	1.948	1.946	1.947	1.956	1.966	
Ti	0.002	0.003	0.002	0.006	0.002	0.001	0.002	0.004	
Al	0.085	0.098	0.081	0.069	0.081	0.053	0.042	0.070	
Cr	0.017	0.018	0.011	0.006	0.006	0.009	0.010	0.003	
Mg	1.747	1.724	1.742	1.742	1.729	1.705	1.765	1.496	
Ca	0.034	0.033	0.030	0.040	0.054	0.030	0.030	0.034	
Mn	0.005	0.004	0.005	0.004	0.004	0.005	0.005	0.009	
Fe	0.170	0.190	0.189	0.184	0.175	0.248	0.191	0.417	
Na	0.000	0.000	0.000	0.002	0.002	0.001	0.000	0.001	
Mg/Mg+Ca+Fe+Mn	89.35	88.36	88.64	88.43	88.08	85.76	88.65	76.47	
Ca/Mg+Ca+Fe+Mn	1.72	1.69	1.51	2.03	2.75	1.51	1.51	1.75	
FeMn/Mg+Ca+Fe+Mn	8.92	9.95	9.86	9.54	9.17	12.73	9.84	21.78	

1. Plag. lherzolite, porphyroclast core, 67-101
2. Plag. lherzolite, porphyroclast rim, 6723-106
3. Plag. lherzolite, matrix grain, 6723-1102
4. Lherzolite, porphyroclast core, 9030-3801
5. Lherzolite, porphyroclast rim, 9030-3804
6. Lherzolite, matrix grain, 9030-4501
7. Harzburgite, porphyroclast core, 9040-3101
8. Harzburgite, porphyroclast rim, 9040-3104
9. Harzburgite, matrix grain, 9040-4301

10. Ariegite band, 214-401
11. Poikilitic cpx clot in dunite, 120-301
12. Websterite dike, 4010-101
13. Plag-pyroxene vein, grain rim, 9210-301
14. Plag-pyroxene vein, grain core, 9210-302
15. Wehrlite layer in dunite, 7900-501
16. Oliv. Pyroxenite, Toad Lake Gb, 1340-501
17. Microgabbro dike, 1001-601

Table 9: Representative Analyses of Clinopyroxene from the Trinity Peridotite and Associated Gabbroic Rocks

	1	2	3	4	5	6	7	8	9	
SiO ₂	51.46	52.64	53.23	51.65	52.08	53.16	53.56	52.62	53.63	
TiO ₂	0.34	0.24	0.15	0.30	0.25	0.24	0.13	0.25	0.18	
Al ₂ O ₃	4.42	2.68	2.47	3.55	3.25	2.89	1.94	3.30	2.33	
Cr ₂ O ₃	1.32	0.86	0.93	1.06	1.08	1.02	0.88	1.43	0.97	
MgO	16.59	17.29	17.53	17.90	17.39	17.12	17.47	17.40	17.28	
CaO	22.17	22.62	22.76	22.31	22.65	22.34	22.34	22.66	23.89	
MnO	0.10	0.04	0.09	0.07	0.09	0.09	0.07	0.10	0.04	
FeO	2.49	2.51	2.36	2.68	2.67	2.65	2.17	2.65	2.21	
Na ₂ O	0.44	0.27	0.38	0.26	0.23	0.26	0.28	0.35	0.30	
Sum	99.31	99.16	99.93	99.78	99.69	99.77	98.84	100.76	100.83	
Catatoms Normalized to 4.0										
Si	1.880	1.925	1.931	1.873	1.895	1.936	1.965	1.896	1.931	
Ti	0.009	0.007	0.004	0.008	0.007	0.007	0.004	0.007	0.005	
Al	0.190	0.116	0.106	0.152	0.139	0.124	0.084	0.140	0.099	
Cr	0.038	0.025	0.027	0.030	0.031	0.029	0.026	0.041	0.028	
Mg	0.904	0.943	0.948	0.968	0.944	0.930	0.955	0.935	0.928	
Ca	0.868	0.887	0.884	0.867	0.883	0.872	0.878	0.875	0.922	
Mn	0.003	0.001	0.003	0.002	0.003	0.003	0.002	0.003	0.001	
Fe	0.076	0.077	0.072	0.081	0.081	0.081	0.067	0.080	0.067	
Na	0.031	0.019	0.027	0.018	0.016	0.018	0.020	0.024	0.021	
Mg/Mg+Ca+Fe+Mn	48.92	46.51	49.71	50.46	49.38	49.32	50.23	49.39	48.39	
Ca/Mg+Ca+Fe+Mn	46.97	49.45	46.39	45.19	46.22	46.25	46.16	46.23	48.08	
FeMn/Mg+Ca+Fe+Mn	4.11	4.04	3.90	4.35	4.40	4.43	3.61	4.38	3.53	
	10	11	12	13	14	15	16	17	18	19
SiO ₂	52.99	52.57	53.33	53.17	54.06	53.82	53.95	54.69	52.73	52.58
TiO ₂	0.15	0.17	0.32	0.09	0.11	0.12	0.12	0.11	0.27	0.40
Al ₂ O ₃	2.58	3.42	2.74	1.39	1.35	1.55	1.36	1.16	1.66	2.68
Cr ₂ O ₃	0.54	1.11	0.44	0.48	0.60	0.70	0.49	0.20	0.15	0.14
MgO	17.40	16.59	17.67	17.44	16.83	17.36	17.61	17.30	17.01	15.26
CaO	23.01	23.56	22.07	23.43	24.48	24.06	24.08	23.41	22.89	22.20
MnO	0.09	0.10	0.13	0.10	0.08	0.07	0.10	0.22	0.11	0.16
FeO	2.95	2.60	2.85	2.94	2.57	2.59	2.76	3.23	4.49	6.22
Na ₂ O	0.20	0.34	0.16	0.11	0.06	0.09	0.06	0.03	0.13	0.25
Sum	99.91	100.46	99.71	99.14	100.14	100.36	100.52	100.36	99.44	99.89
Catatoms Normalized to 4.0										
Si	1.925	1.903	1.940	1.949	1.968	1.951	1.952	1.986	1.935	1.938
Ti	0.004	0.005	0.009	0.002	0.003	0.003	0.003	0.003	0.007	0.011
Al	0.111	0.146	0.118	0.060	0.058	0.066	0.058	0.050	0.072	0.116
Cr	0.016	0.032	0.013	0.014	0.017	0.020	0.014	0.006	0.004	0.004
Mg	0.943	0.895	0.959	0.953	0.914	0.938	0.950	0.937	0.931	0.839
Ca	0.896	0.914	0.860	0.920	0.955	0.934	0.933	0.911	0.900	0.877
Mn	0.003	0.003	0.004	0.003	0.002	0.002	0.003	0.007	0.003	0.005
Fe	0.090	0.079	0.087	0.090	0.078	0.078	0.083	0.098	0.138	0.192
Na	0.014	0.024	0.011	0.008	0.004	0.006	0.004	0.002	0.009	0.018
Mg/Mg+Ca+Fe+Mn	48.82	47.35	50.21	48.47	46.90	48.05	48.25	47.98	47.20	43.86
Ca/Mg+Ca+Fe+Mn	46.39	48.32	45.03	46.80	49.00	47.85	47.38	46.65	45.64	45.84
FeMn/Mg+Ca+Fe+Mn	4.79	4.33	4.76	4.73	4.10	4.10	4.37	5.38	7.16	10.30

1. Plag. lherz., porphyroclast core, 9200-412
2. Plag. lherz., porphyroclast rim, 9200-401
3. Plag. lherz., matrix grain, 6723-302
4. Lherzolite, porphyroclast core, 9030-3501
5. Lherzolite, porphyroclast rim, 9030-3502
6. Lherzolite, matrix grain, 4031-402
7. Harzburgite, matrix grain, 9040-4601
8. Ariegite band, core or grain, 214-101
9. Ariegite band, rim of grain, 214-102

10. Websterite dike, 4010-202
11. Poikilitic cpx-rich clot in dunite, 120-101
12. Plag-pyroxene vein, 9210-201
13. Wehrlite layer in dunite, 7900-102
14. Poikilitic cpx in cumulate dunite, Toad Lake gabbro, 140-201
15. Cumulate wehrlite, Toad Lake gabbro, 1210-101
16. Cumulate pyroxenite, Toad Lake gabbro, 1400-301
17. Feldspathic pyroxenite, Toad Lake gabbro, 1090-101
18. Toad Lake gabbro, 220-901
19. Microgabbro dike, 1001-1002

Table 10: Representative Analyses of Spinel from the Trinity Peridotite and Associated Gabbroic Rocks

	1	2	3	4	5	6	7	8	9	10	11	12
SiO ₂	0.11	0.12	0.09	0.08	0.05	0.02	0.11	0.05	0.11	0.10	0.10	0.13
TiO ₂	0.15	0.44	0.25	0.21	0.26	0.15	0.09	0.36	0.25	0.37	0.26	0.39
Al ₂ O ₃	28.22	27.12	33.09	21.87	18.87	27.39	33.77	23.34	18.55	14.85	18.10	21.22
Cr ₂ O ₃	38.42	38.96	33.94	45.97	46.14	39.47	32.46	42.51	40.64	44.37	45.58	37.65
MgO	14.09	12.81	15.34	12.96	12.19	14.22	15.72	12.83	7.15	9.11	9.62	7.83
MnO	0.22	0.20	0.22	0.26	0.22	0.20	0.17	0.33	0.61	0.34	0.32	0.41
FeO	18.30	20.17	16.03	18.15	21.47	18.50	16.78	21.37	32.35	26.16	24.85	29.34
Nb ₂ O ₅	0.01	0.02	0.00	0.00	0.01	0.06	0.05	0.02	0.00	0.06	0.00	0.00
ZrO ₂	0.03	0.00	0.03	0.00	0.00	0.06	0.00	0.00	0.00	0.02	0.04	0.00
ZnO	0.10	0.08	0.28	0.02	0.10	0.10	0.00	0.07	0.10	0.10	0.27	0.32
Sum	99.65	99.92	99.27	99.52	99.30	100.17	99.15	100.88	99.76	95.47	99.13	97.29

Catatoms Normalized to 3.0

Si	0.003	0.004	0.003	0.002	0.002	0.001	0.003	0.002	0.004	0.004	0.003	0.004
Ti	0.003	0.010	0.005	0.005	0.006	0.003	0.002	0.008	0.006	0.009	0.006	0.010
Al	0.993	0.965	1.138	0.797	0.700	0.963	1.156	0.836	0.708	0.591	0.686	0.816
Cr	0.907	0.929	0.783	1.123	1.148	0.931	0.745	1.021	1.041	1.185	1.159	0.971
Mg	0.627	0.576	0.667	0.597	0.572	0.632	0.681	0.581	0.345	0.458	0.461	0.380
Mn	0.006	0.005	0.005	0.007	0.006	0.005	0.004	0.008	0.017	0.010	0.009	0.011
Fe	0.457	0.509	0.391	0.469	0.565	0.461	0.408	0.543	0.877	0.739	0.668	0.800
Nb	0.000	0.000	0.000	0.000	0.000	0.001	0.001	0.000	0.000	0.001	0.000	0.000
Zr	0.000	0.000	0.000	0.000	0.002	0.002	0.000	0.002	0.002	0.000	0.001	0.000
Zn	0.002	0.002	0.006	0.000	0.002	0.002	0.000	0.002	0.002	0.002	0.006	0.008
FMCr ₂ O ₄	45.42	46.53	39.20	56.20	57.41	46.57	37.32	51.07	52.11	59.35	58.03	48.60
FM ₂ TiO ₄	0.34	1.00	0.55	0.49	0.62	0.34	0.20	0.82	0.61	0.93	0.62	0.96
FMAI ₂ O ₄	49.74	48.29	56.97	39.86	35.01	48.18	57.89	41.80	35.46	29.61	34.35	40.85
FMFe ₂ O ₄	4.51	4.17	3.28	3.46	6.96	4.91	4.59	6.31	11.82	10.11	7.01	9.58
Cr/Cr+Al	0.477	0.491	0.408	0.585	0.621	0.491	0.392	0.550	0.595	0.667	0.628	0.543
Fe ⁺⁺ /Mg+Fe ⁺⁺	0.372	0.427	0.331	0.403	0.428	0.365	0.319	0.419	0.651	0.529	0.527	0.607

1. Plag. Iherz., 6721-202
2. Plag. Iherz., 9020-4301
3. Lherzolite, 9030-4401
4. Harzburgitè, 9040-4101
5. Dunite, 9060-1701
6. Ariegite, 0211-701
7. Websterite, 4010-1401
8. Large dunite body, 4010-1401
9. Cumulate dunite, Toad Lake gabbro, 140-101
10. Cumulate wehrilite, " " " " , 1210-401
11. Cumulate pyroxenite, " " " " , 1340-201
12. Cumulate pyroxenite, " " " " , 1400-1001

Table 11: Representative Analyses of Plagioclase from the Trinity Peridotite and Associated Gabbroic Rocks

	1	2	3	4	5	6	7	8	9
SiO ₂	47.09	46.24	46.73	46.63	46.07	45.17	44.69	45.70	43.81
TiO ₂	0.01	0.13	0.11	0.00	0.00	0.00	0.09	0.03	0.01
Al ₂ O ₃	33.39	33.69	34.22	34.59	34.15	34.68	35.03	34.52	35.68
MgO	0.00	0.00	0.00	0.01	0.06	0.00	0.02	0.00	0.03
CaO	16.89	17.83	17.55	17.99	18.16	18.76	18.26	18.47	19.66
FeO	0.10	0.18	0.08	0.12	0.08	0.11	0.16	0.32	0.24
Na ₂ O	2.10	1.60	1.87	1.61	1.43	0.95	1.23	0.88	0.49
K ₂ O	0.03	0.02	0.02	0.02	0.02	0.03	0.02	0.03	0.02
BaO	0.13	0.00	0.00	0.00	0.03	0.00	0.03	0.00	0.00
Sum	99.74	99.69	100.58	100.97	100.00	99.70	99.53	99.95	99.94

Cations Normalized to 8.0 Oxygens

Si	2.171	2.140	2.140	2.127	2.123	2.091	2.075	2.109	2.031
Ti	0.000	0.005	0.004	0.000	0.000	0.000	0.003	0.001	0.000
Al	1.815	1.838	1.848	1.860	1.856	1.893	1.918	1.878	1.951
Mg	0.000	0.000	0.000	0.001	0.004	0.000	0.001	0.000	0.002
Ca	0.834	0.884	0.861	0.879	0.897	0.931	0.909	0.913	0.977
Fe	0.004	0.007	0.003	0.005	0.003	0.004	0.006	0.012	0.009
Na	0.188	0.144	0.166	0.142	0.128	0.085	0.111	0.079	0.044
K	0.002	0.001	0.001	0.001	0.001	0.002	0.001	0.002	0.001
Ba	0.002	0.000	0.000	0.000	0.001	0.000	0.001	0.000	0.000
Ab	18.34	13.96	16.15	13.92	12.46	8.38	10.85	7.92	4.31
An	81.49	85.93	83.74	85.96	87.43	91.45	89.03	91.90	95.57
Or	0.17	0.12	0.11	0.11	0.12	0.17	0.12	0.18	0.12

1. Plagioclase lherzolite, 6730-101
2. Plagioclase lherzolite, 6730-732
3. Plagioclase lherzolite, rime of grain, 6730-1301
4. Core of above grain, 6730-1391
5. Ariegite band, 214-201
6. Websterite dike, 150-101
7. Plagioclase lherzolite around above websterite dike, 170-102
8. Microgabbro, 10-201
9. Toad Lake gabbro, 220-401

Table 12: Representative Analyses of Amphibole from the Trinity Peridotite and Associated Gabbroic Rocks

	1	2	3	4	5
SiO ₂	48.01	47.91	46.09	45.66	48.62
TiO ₂	0.68	0.84	0.94	2.48	1.74
Al ₂ O ₃	11.23	12.41	11.93	11.91	7.57
Cr ₂ O ₃	1.50	2.52	2.05	0.78	0.00
MgO	19.88	19.06	18.99	18.80	17.32
CaO	11.85	11.82	12.60	10.42	12.45
MnO	0.03	0.05	0.05	0.07	0.10
FeO	3.95	3.35	3.49	4.73	7.23
Na ₂ O	1.32	0.91	2.22	2.42	2.57
K ₂ O	0.00	0.05	0.00	0.13	0.01
F	0.00	0.15	0.00	0.22	0.10
Cl	0.00	0.01	0.00	0.03	0.05
Sum	98.45	99.01	98.36	97.55	97.71

Catatoms - (Na + K) = 15

Si	6.630	6.587	6.445	6.498	7.002
Ti	0.071	0.087	0.099	0.266	0.189
Al	1.829	2.012	1.967	1.999	1.285
Cr	0.164	0.274	0.227	0.088	0.000
Mg	4.093	3.907	3.960	3.989	3.719
Ca	1.754	1.741	1.888	1.589	1.921
Mn	0.004	0.006	0.006	0.008	0.012
Fe	0.456	0.385	0.408	0.563	0.871
Na	0.354	0.243	0.602	0.668	0.718
K	0.000	0.009	0.000	0.024	0.002
F	0.000	0.065	0.000	0.099	0.046
Cl	0.000	0.002	0.000	0.007	0.012

1. Plagioclase lherzolite, 6723-601
2. Plagioclase lherzolite, 6724-101
3. Ariegite band, 211-202
4. Plag-amphibole vein, 980-102
5. Pegmatitic gabbro dike, 190-401

BULK COMPOSITIONS

Major element, bulk compositions for selected samples of the Trinity peridotite were calculated from the results of automated electron microprobe analyses. These compositions are tabulated in Table 13. Figures 43-46 present some of these data graphically.

All peridotite samples were found to be high in MgO, and low in SiO₂, Al₂O₃, Na₂O, and K₂O. The plagioclase lherzolite has the least refractory composition in the sense that it is characterized by the highest SiO₂, Al₂O₃, Na₂O, TiO₂ and CaO concentrations and the lowest MgO and FeO concentrations. The dunite samples represent the opposite end of this limited compositional spectrum with the most refractory bulk compositions, and the harzburgite and the lherzolite samples lie in between these two extremes.

The variations in bulk compositions, for the most part, reflect variations in modal mineralogy. The plagioclase lherzolites have the least refractory compositions by virtue of the presence of plagioclase, amphibole, and greater amounts of clinopyroxene. The lherzolites contain more clinopyroxene and orthopyroxene than the harzburgites and are, therefore, less refractory. The dunites are essentially biminerally intergrowths of olivine and spinel and, consequently have the most refractory or depleted compositions of all.

The compositions of these peridotite lithologies are similar to compositions that have been determined for other peridotite bodies. A comparison of Tables 13 and 14 illustrates that the plagioclase lherzolite is very similar in composition to the plagioclase lherzolite of the Lanzo peridotite massif reported by Boudier (1978), the Tinaquillo peridotite reported by Green (1963), and the Lizard plagioclase peridotite reported by Green (1964), although it is slightly lower

Table 13: Major Element Abundances in Samples of the Trinity Peridotite Computed from Automated Electron Microprobe Analyses of Polished Thin Sections

	1	2	3	4	5	6	7	8	9	10	11
SiO ₂	43.21	43.22	42.77	49.23	50.37	43.49	43.40	42.97	43.22	51.63	49.96
TiO ₂	0.04	0.04	0.04	0.10	0.11	0.03	0.04	0.03	0.04	0.08	0.20
Al ₂ O ₃	2.08	0.73	0.69	1.74	2.00	2.30	2.47	0.71	0.90	3.09	6.08
Cr ₂ O ₃	0.57	0.39	0.39	0.43	0.49	0.72	0.64	0.48	0.51	0.71	1.32
MgO	43.77	45.81	45.85	30.67	27.42	43.49	42.86	45.66	45.39	24.40	23.86
CaO	1.77	1.00	1.19	12.11	14.57	2.24	1.76	0.65	0.91	15.56	13.95
MnO	0.12	0.16	0.12	0.09	0.09	0.12	0.14	0.14	0.14	0.14	0.09
FeO	8.12	8.51	8.81	5.56	4.83	7.68	8.47	9.26	9.13	4.38	4.05
Na ₂ O	0.06	0.01	0.02	0.16	0.19	0.09	0.07	0.01	0.01	0.19	0.43
K ₂ O	0.00	0.00	0.00	0.00	0.00	0.00	0.00	0.00	0.00	0.01	0.002
NiO	0.22	0.16	0.24	0.11	0.08	0.24	0.25	0.28	0.27	0.05	0.07
Sum	99.96	100.03	100.12	100.20	100.16	100.38	100.10	100.19	100.52	100.24	100.01
	12	13	14	15	16	17	18	19	20	21	22
SiO ₂	43.22	42.74	44.62	40.47	41.01	44.14	50.96	50.78	51.42	50.46	49.31
TiO ₂	0.06	0.03	0.03	0.01	0.00	0.02	0.20	0.22	0.24	0.12	0.12
Al ₂ O ₃	1.68	0.94	0.64	0.24	0.21	2.90	14.05	13.34	10.93	15.95	15.59
Cr ₂ O ₃	0.45	0.59	0.44	0.53	0.45	0.36	0.09	0.09	0.16	0.18	0.18
MgO	44.30	46.26	44.96	48.41	49.15	42.45	12.75	12.97	13.90	16.10	12.78
CaO	0.95	0.70	0.67	0.01	0.12	1.99	15.48	16.04	16.24	13.61	13.30
MnO	0.16	0.10	0.17	0.18	0.25	0.12	0.13	0.12	0.15	0.09	0.09
FeO	8.91	9.13	8.16	9.11	9.15	7.68	6.17	6.01	6.38	2.90	8.09
Na ₂ O	0.05	0.01	0.01	0.00	0.00	0.10	0.41	0.40	0.37	0.53	0.52
K ₂ O	0.00	0.00	0.00	0.00	0.00	0.00	0.01	0.01	0.00	0.02	0.02
NiO	0.32	0.28	0.75	0.32	0.38	0.23	0.00	0.00	0.00	0.01	0.01
Sum	100.10	100.78	100.45	99.28	100.72	99.99	100.25	99.98	99.79	99.93	100.01

1. 8W40D: plagioclase lherzolite
 2. 8W40F: lherzolite
 3. 8W40H: lherzolite
 4. 8W40I: websterite dike
 5. 8W40I4: websterite dike
 6. 8W67: plagioclase lherzolite
 7. 8W82A: plagioclase lherzolite
 8. 8W82B: lherzolite
 9. 8W82C: lherzolite
 10. 8W82D: websterite dike
 11. 8W69: ariegite band

12. 9W2: plagioclase lherzolite
 13. 9W3: lherzolite
 14. 9W4: harzburgite
 15. 9W5: dunite
 16. 9W6: dunite
 17. 9W20: plagioclase lherzolite
 18. 8W100: microgabbro dike
 19. 8W100A: " "
 20. 8W100B: " "
 21. 9W21: plag-rich vein (measured)
 22. 9W21: plag-rich vein, composition recalculated allowing for Fe-Mg exchange (see text)

Table 14: Major Element Composition of Feldspathic or Spinel Lherzolites and Model Compositions for the Mantle

	1	2	3	4	5	6	7
SiO ₂	44.14	43.86	44.8	44.9	45.2	44.9	46.1
TiO ₂	0.02	0.18	0.1	0.1	0.7	0.24	0.2
Al ₂ O ₃	2.90	2.86	4.2	3.2	3.5	4.3	4.3
Cr ₂ O ₃	0.36	0.26	0.4	0.5	0.4	0.4	
MgO	42.45	39.19	39.2	40.0	37.5	38.9	37.6
CaO	1.99	2.35	2.4	3.0	3.1	2.5	3.1
MnO	0.12	0.11	0.1	0.1	0.14	0.1	
FeO	7.68	6.50	8.2	7.6	8.4	8.2	8.2
Na ₂ O	0.10	0.20	0.2	0.2	0.6	0.23	0.4
K ₂ O	0.00	tr	0.05	0.02	0.13	0.02	0.03
NiO	0.23	0.18	0.2	0.3	0.2	0.2	
Sum	99.99	97.79	99.96	99.92	100.03	100.01	99.93

1. Trinity plagioclase lherzolite, 9W20
2. Lanzo plagioclase lherzolite (Boudier, 1978)
3. Lizard plagioclase lherzolite (Green, 1964)
4. Tinaquillo spinel lherzolite (Green, 1963)
5. Pyrolite (Ringwood, 1966)
6. Pyrolite (Ringwood, 1975)
7. Pyrolite (Ringwood, 1975)

in K_2O , Na_2O and FeO and slightly higher in MgO . The harzburgite, lherzolite, and dunite are similar to the compositions of lithologies from alpine-type peridotites and the basal ultramafic sections of peridotites.

The compositions of the plagioclase lherzolite, lherzolite, harzburgite and dunite are low in alkalis, Al_2O_3 and SiO_2 compared to model compositions for undepleted mantle (Table 14). Certainly, no bulk compositions were found that approach pyrolite. The least refractory plagioclase lherzolite (9W20) is lower in alkalis and SiO_2 and higher in MgO than any of the model pyrolite compositions (Ringwood, 1966; Ringwood, 1975; and Green *et al.*, 1980).

The bulk compositions of samples of ariegite, websterite and plagioclase-rich veins were also calculated from point count data and are compiled in Table 13. The ariegite and websterite are higher in CaO , SiO_2 , and Na_2O than the other peridotite lithologies, reflecting the higher abundance of clinopyroxene. The ariegite is also higher in Al_2O_3 reflecting a higher abundance of plagioclase. The plagioclase-rich veinlet is similar in composition to a tholeiitic basalt with a somewhat high Al_2O_3 content (about 16 wt. %) and low K_2O content.

EQUILIBRATION TEMPERATURES AND PRESSURES

Numerous attempts have been made to place constraints on the pressure and temperature histories of ultramafic xenoliths (e.g. Davis and Boyd, 1966; Boyd, 1973; MacGregor, 1974; Mercier and Nicolas, 1975; Mercier and Carter, 1975; Boyd and Nixon, 1975) and alpine or high-temperature type ultramafic bodies (e.g. Medaris, 1972; Dickey, 1970; Green, 1964; Boudier and Nicolas, 1977; Boudier, 1978). These constraints are of interest to the general problem of the origin of peridotite. Moreover, to the extent that these peridotites are representative of the upper mantle, estimates of pressure and temperature provide constraints on the vertical heterogeneity of the mantle, on the pressures and temperatures at which mantle processes occur, and on the depths and rates of vertical motions that occur in the mantle (e.g. diapirs, convection and kimberlite pipes).

Equilibration temperatures were calculated for the Trinity peridotite using the following methods. The geothermometers of Wells (1977), Wood and Banno (1973) and Mercier and Carter (1975) were used to calculate equilibration temperatures for coexisting pairs of orthopyroxene and clinopyroxene. These temperatures were compared to those obtained by fitting the clinopyroxene compositions to the pyroxene solvi determinations of Davis and Boyd (1966) and Lindsley and Dixon (1976) assuming an equilibration pressure of about 5 Kb and utilizing the pressure dependence of Lindsley and Dixon (1976). 5 Kb was selected as a first approximation to the equilibration pressure because the presence of plagioclase places an upper limit of about 10 Kb (Kushiro and Yoder, 1966) on the final equilibration pressure of the peridotite. Equilibration temperatures were also calculated using Mg-Fe partitioning between olivine-spinel mineral pairs (Evans and Frost, 1975).

The results of these calculations for 49 ortho- and clinopyroxene pairs and 53 olivine-spinel pairs are tabulated in Table 15 according to lithology. All pyroxene pairs and most of the olivine-spinel pairs yielded equilibration temperatures greater than 900 degrees C., indicating a high temperature history for the Trinity peridotite. All of the pyroxene geothermometers are in reasonably good agreement except that the Wood and Banno (1973) geothermometer calculates temperatures that are consistently higher than the others by about 50-100 degrees. The ortho- and clinopyroxene pairs were further subdivided as to whether they were cores of porphyroclasts (P), or rims of porphyroclasts or matrix grains (R). The most careful study of porphyroclast cores and rims and interstitial pyroxene compositions was made for plagioclase lherzolite sample 8W67. Using the geothermometer of Wells (1977), the porphyroclast cores yielded equilibration temperatures (1176-1203 deg. C) that were in good agreement with the calculated olivine-spinel equilibration temperatures (1150-1165 deg. C) that were about 100 degrees higher than the porphyroclast rims or matrix grains (963-1097 deg. C). These results are compatible with a model in which the cores of the pyroxene porphyroclasts and the olivine-spinel pairs equilibrated initially at temperatures greater than 1150 degrees centigrade. The results from sample 9W20 suggest that this initial temperature may have actually been over 1250 degrees centigrade. The matrix pyroxene and porphyroclast rims equilibrated to lower temperatures during cooling of the peridotite, but the porphyroclast cores failed to reequilibrate completely.

Spinel and olivine also appear to have preserved a high temperature record in most rocks. The local reequilibration of adjacent olivine

Table 15 : Calculated Equilibration Temperatures (°C) for
Pyroxene-Pyroxene and Olivine-Spinel Mineral Pairs

Lithology and Sample	Pyroxene Geothermometers					Spinel-Olivine E&F
	Wells	W&B	D&B	M&C	L&D	
Plagioclase Lherzolite	BW67 P	1176-1203	1242-1293	1098-1195	1122-1140	1026-1201
	R	963-1097	1064-1206	1025-1091	954-1037	865-1012
	BW40D P	998-1024	1086-1117	997-1011	848- 898	798- 833
R	1027-1034	1020-1127	1063	991- 993	951	
P	1274	1313	1278		1296	
Lherzolite						
9W3 P	1020-1099	1122-1188	1073-1129		973-1088	878- 965
Harzburgite						
9W4 P	1119-1133	1197-1248	1148-1165		1117-1153	812- 888
Websterite Dikes						
8W40I P	10004-1159	1103-1229	1054-1205		932-1215	1125-1226
8W82 P	996-1043	1085-1123	1027-1061	928- 988	870- 948	
Depleted Zones						
8W40H P	1009-1112	1101-1197	1024-1084	926-1070	865-1088	1150-1198
R	1057	1139	1095	1033	1021	
Plag-Pyx Vein						
8W69 P	1012-1077	1109-1168	1020-1096	915-1035	885-1022	1178
R	970-1092	1073-1171	1014-1075	900-1041	839- 977	

Geothermometers:

Wells = Wells (1977)

W&B = Wood and Banno (1973)

D&B = Davis and Boyd (1966)

M&C = Lindsley and Dixon (1976)

E&F = Evans and Frost (1975)

P = Pophyroblast cores

R = Recrystallized pyroxene

and spinel that is displayed in Figures 24 and 35 was investigated to determine its effect on the calculated equilibration temperatures. Temperatures were calculated for the following cases: (1) adjacent olivine and spinel rims; (2) spinel cores and olivine far removed (>75 microns) from the spinel; and (3) spinel and olivine compositions that were recalculated to the compositions that they must have had before the $Mg/Mg+Fe^{++}$ gradient was developed in the olivine. The latter case assumed that the compositions of the coexisting spinel and olivine had only changed by simple exchange of Fe and Mg with one another. The results of these calculations were the same within a few tens of degrees suggesting that the $Mg/Mg+Fe^{++}$ profile in the olivine grain was developed and trapped at relatively high temperatures.

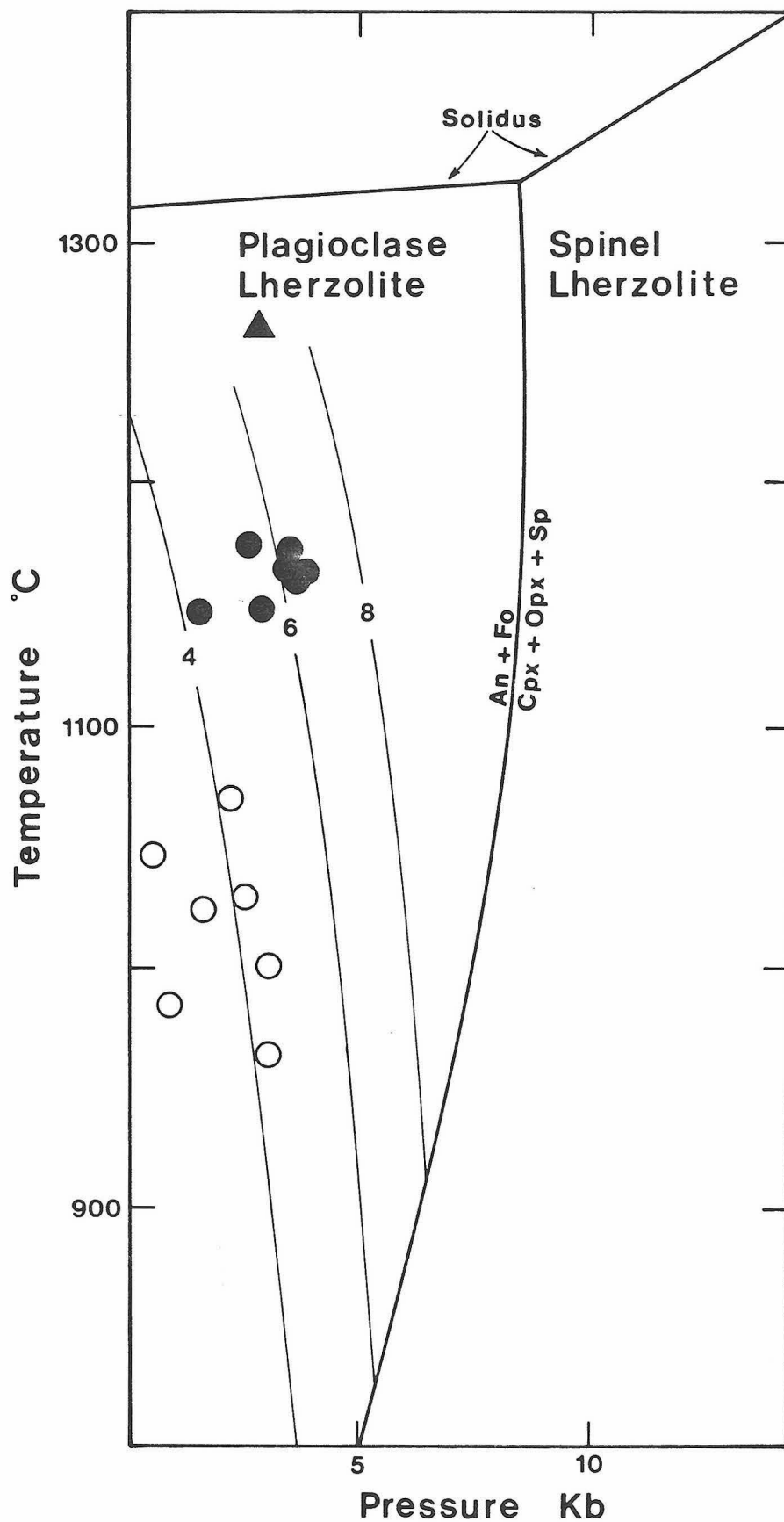
Serpentinization appears to have affected the spinel-olivine geothermometers much more than the pyroxene geothermometers. All of the samples included in Table 15 except 9W3 and 9W4 are less than 10 percent serpentinized, whereas 9W3 and 9W4 are about 50 percent serpentinized. The temperatures calculated for spinel-olivine pairs for these two samples (812-965 deg. C) are about 100-200 degrees lower than temperatures calculated for pyroxene pairs, and are about 200 degrees lower than the temperatures calculated from the olivine-spinel pairs from the unserpentinized samples. A possible explanation is that the spinel compositions were affected by addition of a magnetite component during the breakdown of olivine to form serpentine, brucite and magnetite. This suggests that the spinel-olivine geothermometer may be incapable of detecting the high temperature history of highly serpentinized peridotite.

Equilibration pressures were estimated for orthopyroxene coexisting

with plagioclase using the method of Obata (1976). Figure 42 shows the results of this calculation for pyroxenes from plagioclase lherzolite samples 8W67 and 9W20. Temperatures were calculated using the pyroxene-pyroxene geothermometer of Wells (1977) and the pressures were estimated based on the concentration of Al in the M1 site of orthopyroxene (Obata, 1976). The conclusions suggested by this diagram are: (1) the porphyroclast cores in samples 8W67 and 9W20 equilibrated at low pressures (<5 kb) and high temperatures (1150-1250 deg. C) in the plagioclase peridotite field; and (2) the porphyroclast rims and interstitial grains were reequilibrated during a episode of nearly isobaric cooling. It appears that the minerals of the Trinity peridotite preserve a record of high temperatures that were in the range of reasonable estimates of the solidus for plagioclase lherzolite.

Figure 42 also has important implications for the penultimate origin of the Trinity peridotite. The temperatures are much higher for the estimated pressures than are found along any estimated oceanic or continental geotherm (e.g. Clark and Ringwood, 1964; Mercier and Carter, 1975). Therefore, either the Trinity peridotite originated on an incredibly steep geotherm or originated on a more reasonable geotherm at great depth and ascended through the upper mantle without equilibrating thermally. These implications are discussed at length in a following section on the P-T trajectory of the Trinity peridotite.

Figure 42: Equilibration temperatures and pressures of pyroxenes in plagioclase lherzolite samples 9W20 and 8W67. Solid triangle, cores of porphyroclast pair in 9W20; solid circles, cores of porphyroclast pairs in 8W67; open circles, rims of porphyroclasts and matrix pyroxene. Temperatures are calculated using the geothermometer of Wells (1977) for Fe-Mg partitioning between ortho- and clinopyroxene pairs. Pressures are estimated graphically from catatom percent of Al in the M1 site of orthopyroxene using the calculated isopleths (contours) of Obata (1976). Isopleths for 4, 6 and 8 percent Al occupancy of M1 are shown as light lines. Also shown are the solidus and boundary between the plagioclase- and spinelbearing peridotite (heavy lines) for the system $\text{MgO-Al}_2\text{O}_3\text{-SiO}_2\text{-CaO}$ (Kushiro and Yoder, 1966).



DISCUSSION

INTRODUCTION

Whereas the preceding chapters are essentially descriptive, the goal of this chapter is to interpret the available data on and establish a petrogenetic model for the Trinity peridotite.

Most of the salient structural, petrographic, mineralogic and chemical characteristics of the Trinity peridotite in the study area can be explained by a model in which the peridotite ascended through the upper mantle to the base of the crust. Petrogenetic processes that are discussed include partial melting, fractional crystallization, and reaction between peridotite and transient melts. These processes and the structural events can be placed in the context of a loosely constrained, but feasible P-T trajectory that the Trinity peridotite followed through the upper mantle. Some speculations can be offered as to the possible tectonic setting of these events in light of what is known about the regional geology of the Klamath Mountains.

MANTLE ORIGIN OF THE TRINITY PERIDOTITE

A mantle origin for the Trinity peridotite has been previously suggested by other investigators. Irwin (1966) suggested, based on regional geologic mapping, that the Trinity was part of a huge sheet of ultramafic rocks that may be presently rooted in the mantle. Goullaud (1977) inferred a mantle origin for the Trinity on the basis of textural and mineralogic similarity to ultramafic xenoliths and structural and petrographic evidence for high temperature plastic flow. Lindsley-Griffin (1977) mapped the geology to the west of China Mountain and suggested that the Trinity was the ultramafic portion of a lower Paleozoic ophiolite and, as such, was a fragment of oceanic mantle.

The results of this thesis also indicate a mantle origin for the Trinity peridotite. The mineralogy and textures observed in the Trinity peridotite are also found in xenoliths of certain mantle origin (e.g. Mercier and Nicolas, 1975; White, 1966). Furthermore, the bulk compositions of the plagioclase lherzolite, lherzolite, harzburgite and dunite are within the range of compositions reported for mantle derived xenoliths (e.g. Carswell and Dawson, 1970; Danchin, 1979). The folds and foliation in the peridotite, as well as the preferred orientations of minerals and intragranular strain features suggest that the peridotite deformed plastically at high temperatures and pressures such as might be expected in the mantle (Mercier and Nicolas, 1975; Gueguen and Nicolas, 1980). The calculated densities of the different lithologies in the Trinity peridotite range from 3.25-3.35, which is consistent with estimated densities for the upper mantle based on isostatic (Woollard, 1970) and seismic (Dorman

and Ewing, 1962; Wang, 1970) considerations. Lastly, the estimated equilibration pressures are consistent with final equilibration of the peridotite in the region of the uppermost mantle near the base of the crust, and the calculated equilibration temperatures and evidence for the reaction, Spinel + Al-pyroxene = olivine + plagioclase, suggest that the peridotite may have ultimately come from much deeper in the mantle.

A mantle origin is also strongly suggested by the similarity of the Trinity peridotite to the Lanzo peridotite. Both massifs contain plagioclase lherzolite although it is less abundant in the Trinity. Both massifs contain structural and petrologic evidence for high temperature plastic deformation, and, as will be discussed, for partial melting. Both massifs contain petrologic evidence for having passed from the spinel peridotite stability field ($P >$ about 10 kb) to the plagioclase peridotite stability field ($P <$ about 10 kb), and for reaching the uppermost mantle while still at high temperatures ($T >$ 1100 degrees C.). These similarities, taken together suggest that the Lanzo and Trinity peridotites have experienced similar histories and, therefore, probably have similar origins. Boudier and Nicolas (1977) and Boudier (1978) presented a convincing argument for a mantle origin for the Lanzo peridotite based on structural analysis. Furthermore, geophysical studies demonstrated that the peridotite of the Lanzo massif is an ultramafic sheet that is rooted in the mantle (Berkhemer, 1968; Giese, 1962). Significantly, geophysical data for the Trinity peridotite (Griscom, 1977) suggest that it also is a sheet that extends to some depth, although a mantle connection has not been clearly demonstrated.

REGIONAL PARTIAL MELTING OF THE PLAGIOCLASE LHERZOLITE

EVIDENCE

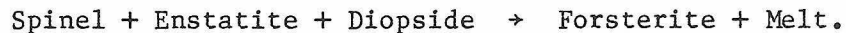
The plagioclase lherzolite displays ubiquitous evidence of partial melting. The evidence consists of (1) widespread feldspathic lenses that are interpreted to have been melt segregations, (2) plagioclase-rich veins, and (3) petrographic evidence for resorption of minerals and interstitial precipitation of other minerals.

The feldspathic lenses in the plagioclase lherzolite are similar in mineralogy and morphology to lenses that are described by Boudier and Nicolas (1977) and Boudier (1978) from the Lanzo massif in northern Italy. Experiments by Boudier and Nicolas (1977) on samples of the Lanzo peridotite demonstrated that these feldspathic lenses are, in fact, the lowest melting fraction of the peridotite. From this information, Boudier and Nicolas (1977) inferred that the lenses were zones of melt that were segregated and smeared-out during penetrative deformation of the peridotite. Boudier and Nicolas (1977) made detailed field measurements and suggested that the segregations that are at a high angle to the foliation formed during flow with a strong rotational shear. The experiments, coupled with the similarity between the descriptions of the lenses in the Lanzo peridotite and those in the Trinity peridotite, strongly suggest that the feldspathic lenses in the Trinity peridotite formed as melt segregations during partial melting and deformation.

Plagioclase-rich veins also appear to have formed from locally derived melts. The melt origin is indicated by their morphology and mineralogy. The small wispy tabular shapes must have formed by

injection and crystallization of a melt. The mineralogy is similar to that of the feldspathic segregations and, therefore, probably constitutes the lowest melting fraction of the plagioclase lherzolite.

There is abundant petrographic evidence for melting of orthopyroxene and clinopyroxene porphyroclasts and large spinel grains in these rocks. The embayments in the orthopyroxene and clinopyroxene porphyroclasts (Figure 17) are interpreted as resorption borders that were produced by incongruent melting of the pyroxenes. The deep embayments on the spinel grains (Figure 21) are also interpreted to be resorption borders. Kushiro and Yoder (1974) found the following reaction during experimental runs at 17 and 26 kb in the system $\text{MgSiO}_3\text{-CaSiO}_3\text{-Al}_2\text{O}_3$:



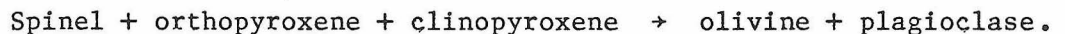
It is suggested that the apparent resorption borders on spinel, orthopyroxene and clinopyroxene, and the olivine that fills the embayments in the pyroxenes may be artifacts of this reaction.

Additional evidence comes from partial melting experiments on peridotite. Boudier and Nicolas (1977) performed melting experiments at 7 kb pressure on samples of plagioclase lherzolite from the Lanzo massif that were very similar in bulk composition to the Trinity plagioclase lherzolite (Table 14). Incipient melting occurred in these experiments at 1180 degrees centigrade. The solidus, plagioclase-out, clinopyroxene-out and orthopyroxene-out temperatures for these experiments were 1180, 1250 and 1400-1450 degrees centigrade respectively. These results are compatible with 5 Kb melting experiments on samples of the Tinaquillo spinel lherzolite by Green et al. (1979);

in these experiments the solidus and clino- and orthopyroxene-out temperatures were ~1180, ~1265 and ~1365 degrees centigrade, respectively. The similarity in bulk composition between the Trinity plagioclase lherzolite and the Lanzo and Tinaquillo lherzolites (Table 14) suggests similar solidus and clino- and orthopyroxene-out temperatures for the Trinity plagioclase lherzolite. The equilibration temperatures of the Trinity pyroxenes (Table 15) indicates that the Trinity peridotite was probably well above its solidus at some point in its history.

The interstitial plagioclase, amphibole and pyroxenes are suggested to have precipitated from the interstitial melt on the basis of textures. This is suggested by the cusped contacts of these minerals against the larger olivine grains and by their concentration along triple grain junctions between large olivine and pyroxene grains (Figures 19 and 20). This interpretation is reinforced by the occurrence of isolated interstitial grains of amphibole or pyroxene that are in optical continuity (Figure 19). Support for this hypothesis comes from melting experiments on samples of peridotite (Arndt, 1977), which found that partial melts tend to be concentrated along both triple grain junctions grain boundaries.

Green (1964) suggested that the textures of the spinel and plagioclase in the Lizard peridotite, which are similar to those in the Trinity, formed by the solid state reaction,



However, textural and mass balance considerations suggest that solid state reactions did not produce these textures. Plagioclase occurs as small grains that are isolated from pyroxene and spinel (Figure 20).

If plagioclase formed by the above solid state reaction it would probably be restricted to grain boundaries between pyroxene and spinel. The rims of the orthopyroxene porphyroclasts are depleted in Al, Cr and Ca relative to the cores. Likewise, the rims of the clinopyroxene porphyroclasts are depleted in Al, Cr, Ti, and Na relative to the cores. If the cores of the porphyroclasts are representative of the initial composition of the entire pyroxene, then these elements must have been removed from the rims of the porphyroclasts. Furthermore, if olivine is replacing pyroxene as suggested, then Si and Ca must have been removed from the vicinity of the pyroxenes during the replacement process. According to the above reaction, the Ca, Na, Al and Si could be concentrated in plagioclase and the Ti and Cr in spinel. However, in many cases, there is very little or no plagioclase or spinel in close proximity to the pyroxene porphyroclasts, and these elements would have to have been transported away from the pyroxenes for distances on the order of millimeters to centimeters. This transport of elements is difficult to understand if the reactions were constrained to occur by solid state diffusion. The most extensive examples of solid state diffusion that are documented in these rocks are 75 microns wide gradients in $Mg/Mg+Fe^{++}$ in olivine around spinel grains (Figure 24). Also, if extensive solid state diffusion had occurred, the pyroxene porphyroclasts would have been more thoroughly equilibrated and be more uniform in composition.

A cumulate origin for these textures might be considered as an alternative. The local development of layering in the plagioclase lherzolite suggests that some or all of the plagioclase lherzolite may have originated as cumulates from a fractionating silicate melt.

This possibility was suggested by Lindsley-Griffin (1977) based on field observations in the vicinity of Corey Peak and Bull Creek. If the textures were produced by cumulate processes, then the interstitial plagioclase, pyroxene and amphibole would have formed from the intercumulate melt, and the embayments on the pyroxene porphyroblasts and large spinel grains may have been produced by peritectic reaction with fractionated intercumulate melt. The textural evidence could have been somewhat obscured by post magmatic recrystallization and deformation. This is not unreasonable inasmuch as evidence for recrystallization and deformation of cumulates in the Troodos ophiolite has been described by George (1978).

However, the origin of these textures as cumulate features may be rejected on two grounds. First, the above textures and the plagioclase-rich segregations are ubiquitous features in the plagioclase lherzolite, whereas the prominent layering in these rocks is, for the most part, restricted to the vicinity of Bull Creek and adjacent ridges within the field area. Therefore, these features occur independently of the strongest evidence for a cumulate origin. Second, although peritectic reaction of spinel with a fractionating basaltic melt to produce plagioclase is possible, the analogous peritectic reactions of both orthopyroxene and clinopyroxene, simultaneously, to produce olivine during fractional crystallization are not. The normal fractionation courses involve peritectic reaction of melt and olivine to produce low-Ca pyroxene, and melt and low-Ca pyroxene or olivine to produce high-Ca pyroxene (Stolper, in press; Walker *et al.*, 1979; Kushiro and Schairer, 1963; Kushiro, 1964). The replacement of ortho- and clinopyroxene by olivine appears to be the reverse of these reac-

tions and suggests, therefore, incongruent melting of pyroxene. These arguments do not refute an ultimate origin for the plagioclase lherzolite as a cumulate. They do support the hypothesis, however, that the embayments on pyroxenes and spinel are produced by partial melting along grain boundaries and that the interstitial plagioclase, pyroxene, and amphibole crystallized from the partial melt.

The suggested conclusion is that many of the structural and petrographic features of the plagioclase lherzolite were produced by pervasive partial melting. The temperatures required to melt plagioclase completely and leave a residue of olivine, spinel, ortho- and clinopyroxene are in the range of 1180-1250 degrees centigrade (Boudier and Nicolas, 1977). This interpretation is consistent with the equilibrium temperatures and pressures that were calculated for the Trinity peridotite.

COMPOSITION OF THE MELT

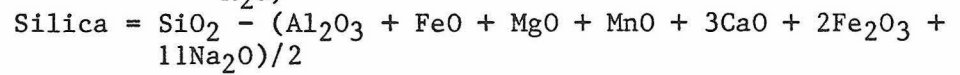
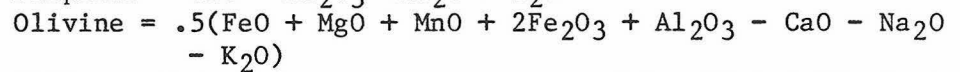
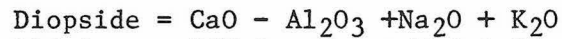
Determination of the composition of the partial melt is not straightforward. The feldspathic lenses and the plagioclase-rich veins are small and have indistinct boundaries so that physical separation of representative samples would be extremely difficult. The automated electron microprobe point count, of course, provides in situ determination of the bulk compositions of such small features. However, the indistinct boundaries make it difficult to assess how representative the point count is. Even if a composition is determined for one of these features, it is not certain that it is representative of the melt. The lense or vein could be a product of fractional crystallization and part of the melt may have migrated elsewhere. Therefore,

it is necessary to test if the determined composition is appropriate for a partial melt. The proposed melt composition should have been saturated with olivine, clinopyroxene and orthopyroxene since textural evidence indicates that these phases were not melted completely. One corollary to this requirement is that the melt composition must have the correct $Mg/Mg+Fe^{++}$ to be in equilibrium with the residual phases. A second corollary is that subtraction of this melt component from the plagioclase lherzolite should leave behind a residue essentially harzburgitic in composition since orthopyroxene and olivine are the most abundant residual phases.

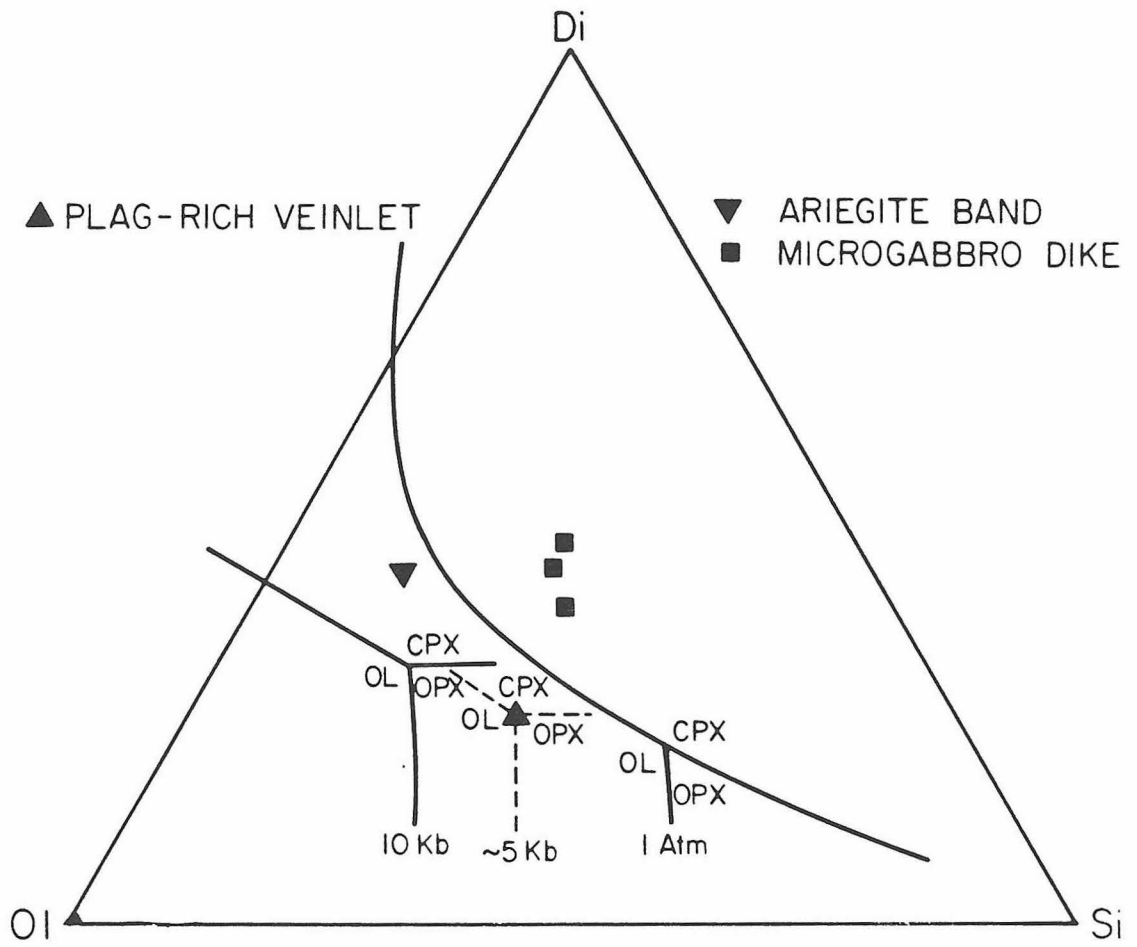
The composition of a plagioclase-rich dike, 9W21, was calculated (Table 13) from the results of an automated electron microprobe point count. The composition is essentially basaltic but is high in MgO and low in K_2O . This composition is plotted in Figure 43, which is a projection onto the normative olivine-diopside-silica plane using the scheme proposed by Walker et al. (1979). This projection is suitable for depicting relationships between a silicate and coexisting olivine, orthopyroxene, and clinopyroxene; it does not treat variations in $Mg/Mg+Fe^{++}$, nor is it appropriate for systems in which plagioclase or additional silicates are present as a phase. It is assumed in this discussion that the plagioclase and amphibole in the plagioclase lherzolite were completely incorporated into the partial melt. With this assumption in mind, note that the composition of the plagioclase-rich vein plots between the 10 kb ol-opx-cpx multiple saturation point for a midocean ridge basaltic melt (Stolper, in press) and the 1 atm ol-opx-cpx multiple saturation point (Walker et al., 1979). Stolper (in press) has demonstrated experimentally that this multiple saturation point

Figure 43: Projection onto the plane olivine-silica-diopside.

Points are plotted according to Walker et al. (1979):



where all values are formula proportions. Also plotted as solid lines are the 10 kb (Stolper, in press) and 1 atm (Walker et al., 1979) for basaltic melt in equilibrium with ol+opx, ol+cpx and opx+cpx.

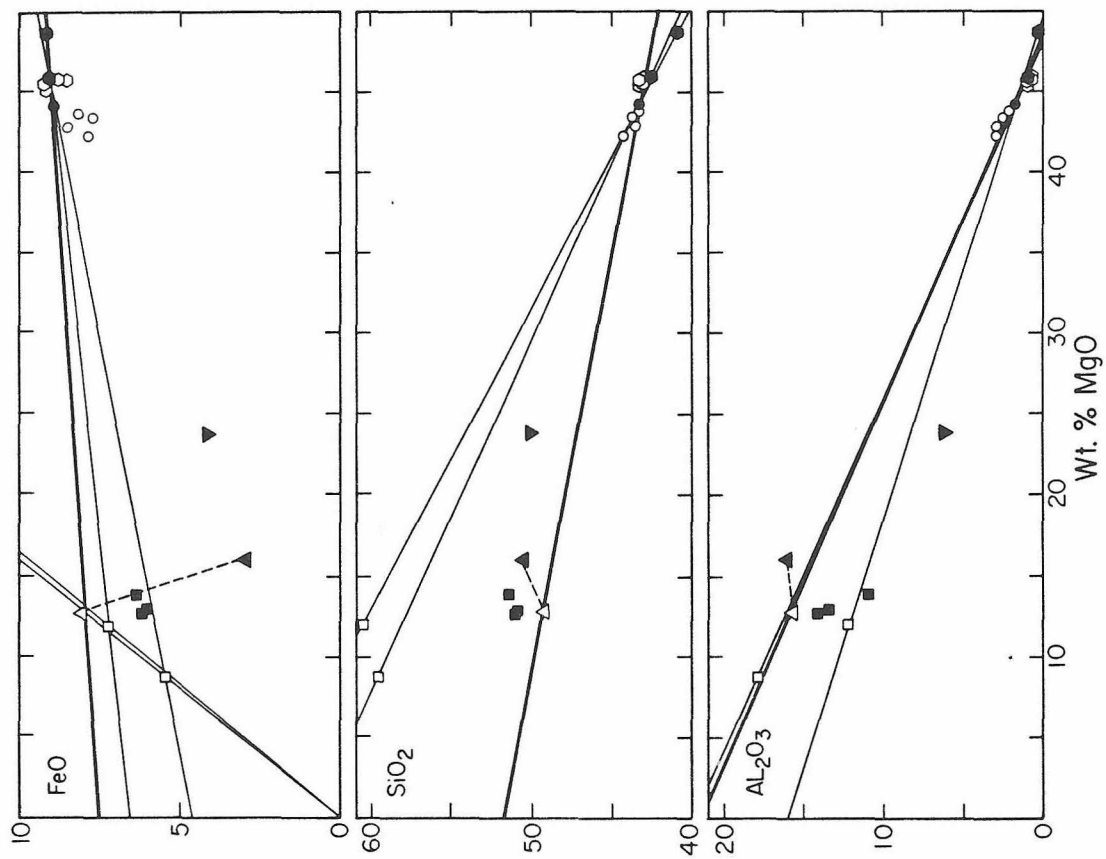
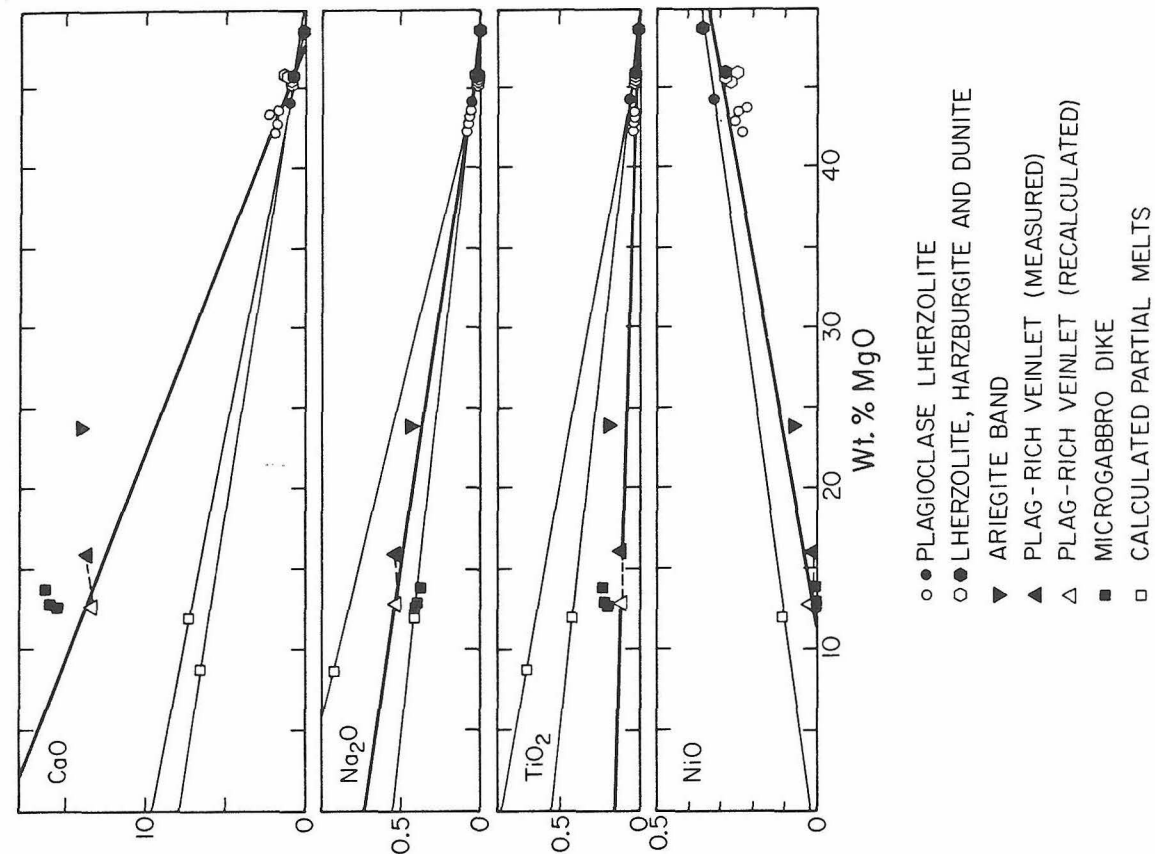


sweeps across the ternary diagram from left to right with decreasing pressure. Therefore, the composition of the plagioclase-rich vein could be appropriate for a melt that is saturated with olivine, orthopyroxene and clinopyroxene at a pressure between 10 kb and 1 atm. Approximate cotectics are indicated in Figure 43 by dashed lines to emphasize this point; the ~5 kb designation for these cotectic lines is somewhat arbitrary but is consistent with pressure estimates based on Al in orthopyroxene (Figure 15), and with the ultimate crystallization of plagioclase from the melt, which requires that the peridotite was in the plagioclase lherzolite stability field ($P < \text{about } 10 \text{ kb}$) when it solidified.

The $\text{Mg}/\text{Mg}+\text{Fe}^{++}$ of the plagioclase-rich vein is much too high for a melt in equilibrium with the olivine in the host plagioclase lherzolite. The $\text{Mg}/\text{Mg}+\text{Fe}^{++}$ of the vein is 0.9, whereas a melt in equilibrium with the olivine in the plagioclase lherzolite (Fo_{90-91}) should have an $\text{Mg}/\text{Mg}+\text{Fe}^{++}$ of about 0.74-0.75 (Roeder and Emslie, 1970). This disparity is illustrated in the FeO vs. MgO diagram in Figure 44. The compositions of the plagioclase lherzolites, lherzolites and harzburgites cluster in the upper right hand corner of the diagram, while the composition of the plagioclase-rich vein (solid triangle) plots to the lower left. Melts in equilibrium with olivine of Fo_{90-91} should plot along the faint lines that pass through the origin and corresponding to $\text{Mg}/\text{Mg}+\text{Fe}^{++}$ of 0.74 and 0.75, while the composition of the plagioclase-rich vein is far removed from these lines.

One possible explanation is that the $\text{Mg}/\text{Mg}+\text{Fe}^{++}$ of the vein was affected by exchange of Fe and Mg with the host peridotite. If the melt was in equilibrium with olivine and pyroxene with $\text{Mg}/\text{Mg}+\text{Fe}^{++} >$

Figure 44: Oxide vs. MgO diagrams for calculated bulk compositions of the rock types of the Trinity peridotite, a plagioclase-rich veinlet and a microgabbro dike. Solid circle and hexagons correspond to samples 9W2 (circle), 9W3 (hexagon) and the average of 9W5 and 9W6 (hexagon). Open squares are calculated compositions of partial melts that would have to be extracted from 9W2 to leave residues of 9W3 (lherzolite) and 9W5-6 (dunite). Open triangle is calculated from the composition of the plagioclase veinlet assuming Fe-Mg exchange with the host peridotite (see text).



0.9, then the first olivine and pyroxene that crystallize from the melt must be this magnesian. If the melt were chemically isolated, continued fractional crystallization would drive the melt to more Fe-rich compositions, which would not be in equilibrium with the minerals of the host peridotite. However, if the melt communicated and was in equilibrium with the host peridotite as it crystallized, exchange of Mg and Fe between the melt in the vein and the olivine and pyroxene of the wall rocks would maintain the crystallizing melt at an $Mg/Mg+Fe^{++}$ of about 0.74-0.75 so that it would always crystallize olivine and pyroxene with $Mg/Mg+Fe^{++} > 0.9$, and would lower the $Mg/Mg+Fe^{++}$ of the wall rock minerals. However, if the volume of the wall rock involved was much greater than the volume of the melt, then the $Mg/Mg+Fe^{++}$ would be only imperceptibly affected. The net result is that the ferromagnesian minerals that comprise the plagioclase-rich vein would all be deceptively Mg-rich and the FeO and MgO of the vein would no longer be representative of the melt that formed it.

The composition of the melt that formed the plagioclase-rich vein was estimated assuming that the composition vein is representative in all elements except Fe and Mg, which were affected by exchange with the host peridotite; this composition was constrained to have an $Mg/Mg+Fe^{++}$ of 0.74. The result of this calculation is tabulated in Table 14 and is plotted in Figure 44 by an open triangle. This composition will still plot at the solid triangle in Figure 43 because this projection ignores variation in $Mg/Mg+Fe^{++}$. Note that this composition plots near the compositions of the microgabbro dikes. This composition also plots along a trend defined by the plagioclase lherzolites, lherzolites and harzburgites for all the oxides in Figure 44

except FeO vs. MgO. Such a trend would be expected for all oxides if the lherzolites and harzburgites are the residues left behind by removal of a partial melt of fixed composition from a protolith of plagioclase lherzolite. Applying the lever rule to these graphs (except FeO vs. MgO), suggests that the melts were about 10 percent of the partially melted peridotite. The absence of a linear trend in Figure 44 for FeO and MgO suggests that some process other than simple partial melting may have been operating. Unfortunately, the data are biased; all of the harzburgite and lherzolite samples in Figure 44 were collected from depleted zones around websterite dikes and from the margins of large dunite bodies. As will be discussed in the following three sections, these are special situations that may have involved addition as well as subtraction of components. The possibility remains, however, that some of the lherzolite and harzburgite were produced by extraction of partial melt, but the data are not available to test this hypothesis.

Plagioclase-rich vein, 9W21, appears to meet some of the compositional tests for a partial melt in equilibrium with the olivine and pyroxene of the Trinity peridotite if appropriate adjustments are made to the FeO and MgO concentrations in the vein. This helps to confirm the interpretation that these features were formed from melts that were melted-out of the plagioclase lherzolite. Furthermore, this calculation suggests that a basaltic melt might be formed by partial melting of plagioclase lherzolite at pressures less than 10 kb. The conditions for this melting are estimated to be ~5 kb and 1180-1250 degrees centigrade. However, variations in FeO and MgO concentrations in the analyzed lherzolites and harzburgites cannot be explained by simple

subtraction of a small amount of partial melt from a protolith of plagioclase lherzolite.

PETROGENESIS OF LARGE DUNITE BODIES

The previous discussion demonstrated that the plagioclase lherzolite had undergone partial melting. Geothermometry suggests that temperatures in the peridotite were high enough to produce a lherzolithic and possibly harzburgitic residue by this mechanism. However, it was also pointed out that the FeO and MgO concentration of the analyzed lherzolites and harzburgites did not fit this model well, suggesting that some other process was operating. Another process is also required to explain the large dunite bodies. Experiments (Green *et al.*, 1979; Boudier and Nicolas, 1977) suggest that temperatures on the order of 1365-1450 degrees centigrade were required to produce a dunite residue by partial melting of a spinel or plagioclase lherzolite. Plagioclase lherzolite, showing effects of incipient melting at 1180-1250 degrees centigrade are found within 1 meter of large dunite bodies. This would require a temperature gradient of $\gg 100$ deg/m if the dunite was the residue of simple partial melting. Of course, gradients in volatile concentrations could have produced this steep apparent thermal gradient. Higher volatile (e.g. H₂O) concentrations where the dunite formed could have lowered the solidus and liquidus and, thereby, greatly increased the degree of partial melting. However, there is no mineralogic evidence for this process such as abundant amphibole or another hydrous phase. Instead, amphibole is restricted to trace abundances in the plagioclase lherzolite, which, according to this model, should have had the lowest volatile concentrations. Therefore, it appears that some process other than partial melting is required to explain the large dunite bodies.

It must be emphasized that there are at least two different types of dunite in the Trinity massif: large tabular bodies, and small irregular bodies. As discussed earlier, these two types of dunite appear to be related. Both are discordant to the foliation, and they grade into one another, and, therefore, these two types of dunite will be treated as equivalent and cogenetic. However, there may be some danger in this assumption. Duncan and Ave Lallemand (1977) studied small dunite bodies at Canyon Mountain, Oregon, and concluded that they formed by reaction of the orthopyroxene harzburgite with an aqueous vapor percolating along a system of brittle fractures. This hypothesis is discussed in greater detail below.

Several lines of evidence suggest that the large dunite bodies are igneous in origin. They have tabular, "dike-like" outcrop patterns. They contain clinopyroxene-rich lithologies, clumps of poikilitic clinopyroxene and concordant wehrlite bands. These features have igneous textures and the compositions of their constituent phases are similar to those of analogous phases in the lower cumulate rocks of the Toad Lake gabbro. The concordant wehrlite dikes are similar to the websterite dikes in that they parallel the dunite body and have a similar mineralogy although somewhat less orthopyroxene. Hopson et al. (1979) described tabular dunite bodies in the peridotite of the Semail ophiolite in Oman. They suggested that these bodies were formed by fractional crystallization of olivine on the walls of feeder dikes through which ascending basaltic melts were passing en route to a crustal magma chamber. The critical feature of this hypothesis is that dunite bodies are relicts of channels that were filled by essentially 100 percent melt at one time.

Other lines of evidence suggest that at least the margins of these large dunite bodies are residues left over from extraction of plagioclase and pyroxene from a plagioclase lherzolite protolith. Along the northern side of Vicki Bluff (Plate 2, Figure 13), an ariegite dike is crosscut by a salient of a large dunite body. The dike continues on strike on the opposite side of the dunite, and a trail of spinel grains is the relict of the dike within the dunite. This is conclusive evidence that at least the marginal few meters of the dunite formed by in situ removal of all minerals except spinel and olivine. This is consistent with evidence from the banding in the harzburgite, lherzolite and plagioclase lherzolite. The banding is the oldest structure in the Trinity massif and its continuity across the contacts between these lithologies suggests that the lherzolite and harzburgite also formed by in situ removal of plagioclase and pyroxene from a protolith of plagioclase lherzolite. The consistent lithologic zonation, plagioclase lherzolite, lherzolite, harzburgite and dunite demonstrates that removal of pyroxene and plagioclase was systematic and increased toward the dunite bodies. The contacts of the large dunite bodies are irregular in detail, deeply embayed and structurally complex in the Trinity peridotite, with isolated blocks of plagioclase lherzolite occurring in harzburgite and blocks of harzburgite in dunite. This is well illustrated in the map of Vicki Bluff, and is in contrast to the straight and abrupt contacts that would be expected if the dunite crystallized on the walls of a dike. Hopson et al. (1979) did observe harzburgite blocks in the tabular dunite bodies but interpreted them to be xenoliths of wall rock that were entrained in the dikes. However, this explanation is insufficient for the plagioclase lherzolite blocks

contained in the harzburgite unless the awkward position is assumed that the harzburgite is also a cumulate.

It appears that the simple mineralogy and simple gross structure of the large dunite bodies belie the complexity of the process that forms them. It is suggested that, as hypothesized by Hopson et al. (1979), these dunite bodies were formed along channels through which a melt was passing. At least the interiors of the bodies were deposited as crystal cumulates, explaining the igneous features found there. The size of the melt-filled channels can only be approximated, and must have been at least as wide as the wehrlite bands (1-3 m). In contrast, the margins of the dunite bodies, however, appear to be formed by some process that involved depletion of the wall rock peridotite in plagioclase and pyroxene. The contacts between the "igneous" and "replacement" dunite have not been located and their relative abundances are not known. Dunite formation by replacement may be restricted to the marginal few meters or involve replacement of much larger volumes of pyroxene- and plagioclase-bearing rock.

A hypothesis that could explain both the igneous and replacement textures is a reaction involving reaction between a silicate melt and the peridotite wall rocks. This hypothesis will be discussed in greater detail in the following section on the websterite dikes and associated depleted zones because it appears that these features formed by essentially the same mechanism.

An alternative explanation is that the dunite, at least, is metasomatic in origin. Duncan and Ave Lallemon (1977) studied small dunite bodies in the harzburgite of the Canyon Mountain peridotite and concluded that they formed by metasomatism involving dissolution of enstatite in an aqueous vapor that was diffusing through the

peridotite. This theory was based on the parallel fabrics that were observed in both lithologies and on the observation that amphibole was concentrated at the contacts between the lithologies. This theory is inadequate to explain the large dunite and harzburgite zones in the Trinity peridotite. First, it is hard to imagine diffusion producing the large scale features that are observed. Second, this process could not have produced the igneous-textured clinopyroxene-rich clots and wehrnite bands. Third, dissolution of only one phase, orthopyroxene, is required in the Canyon Mountain peridotite, but plagioclase, orthopyroxene, clinopyroxene, and amphibole are removed from the Trinity peridotite to leave behind a dunite residue. Third, the progressive compositional changes in the mangesiosilicates and spinel are difficult to explain by a simple dissolution model.

WEBSTERITE DIKES AND DEPLETED ZONES

The websterite dikes and associated depleted zones provide additional insight into the petrogenetic processes that affected the ultramafic rocks because they appear to be small scale analogs of the large dunite bodies and associated clinopyroxene-rich rocks. However, the small size of the websterite dikes and depleted zones makes them more tractable for detailed study.

Several observations that are critical to understanding the dikes and depleted zones will be reviewed. First, the progressive changes in the mineralogy (Figure 7) of the wall rock are as follows as the dikes are approached: (1) plagioclase-out; (2) amphibole-out; clinopyroxene porphyroblasts disappear, but clinopyroxene persists as an interstitial phase that is not visible in outcrop; (3) orthopyroxene-out. These changes correspond to the lithologic transitions--plagioclase lherzolite, lherzolite, harzburgite and dunite--as the dike is approached. It is important to remember that the orthopyroxene-out reaction and the corresponding dunite zone are not developed in all cases. Second, a progressive Fe-enrichment was found in olivine, orthopyroxene and clinopyroxene in a depleted zones as a websterite dike was approached. However, around a second dike, no significant variation was found (Figure 39). Third, spinel showed a progressive Al-enrichment as the dikes were approached (Figure 38). Fourth, the websterite dikes have igneous textures and appear to have crystallized from a melt.

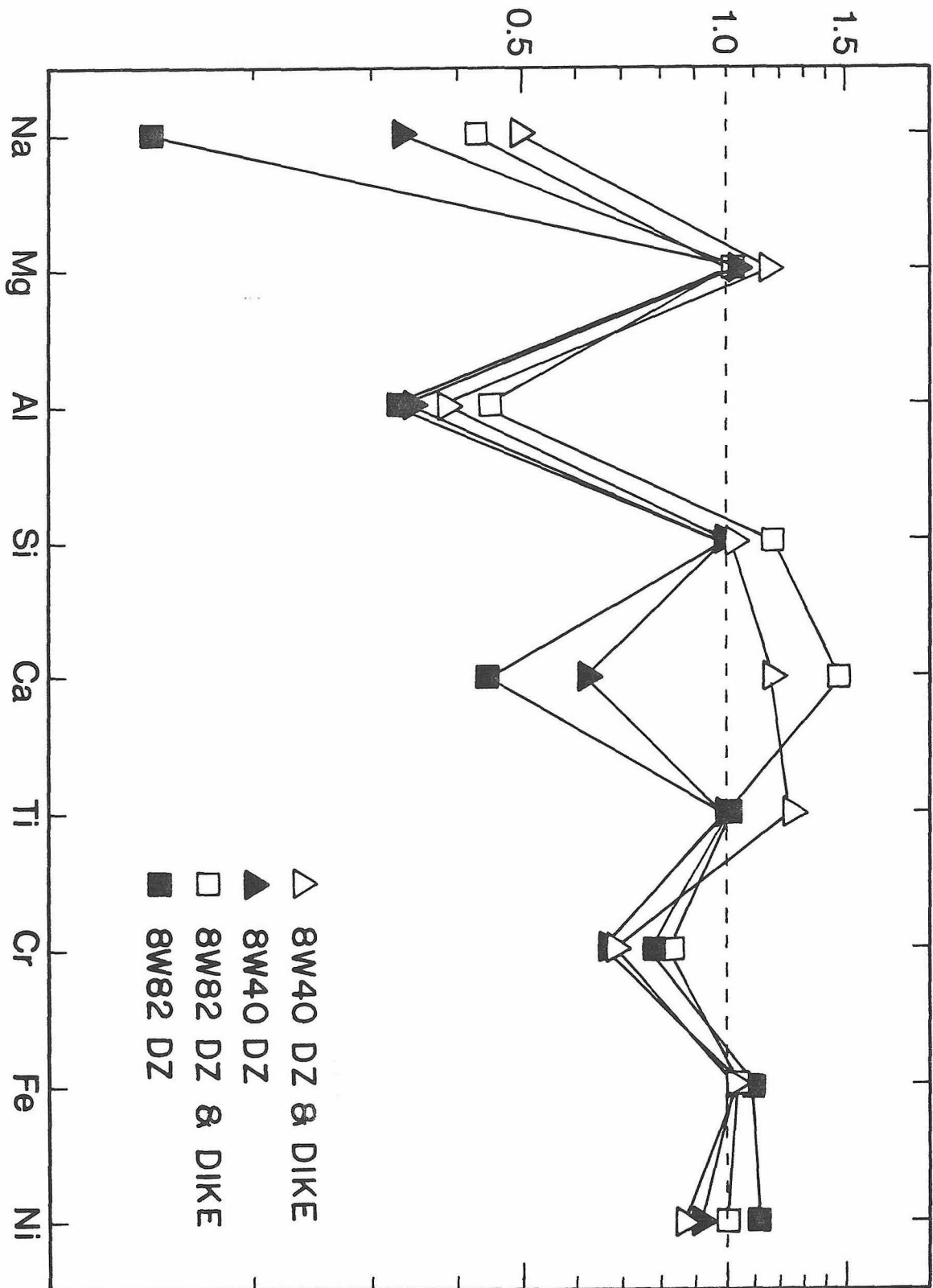
The bulk compositions of the dikes, depleted zones and host rocks provide powerful constraints and will, therefore, be discussed in greater detail. Figure 45 is a graph of the compositions of two sets

(8W40 and 8W82) of depleted zones (DZs) and depleted zones + dikes normalized to the composition of the host plagioclase lherzolite. If the composition of the depleted zone or the depleted zone + dike were the same as the host lherzolite, the plot would be a horizontal line at 1.0. For example, this would be expected if the dike was sweated out of the plagioclase lherzolite host, leaving behind the depleted zone as a residue, but no material was introduced or lost from the system. This mechanism was suggested by Dickey (1970) for similar dikes and depleted zones in the Ronda massif. However, as can be seen from Figure 45, this is clearly not the case for the Trinity peridotite. The depleted zones are depleted in Na, Al, Ca and Cr relative to the host plagioclase lherzolites and enriched in Mg and Fe. The depleted zones + dikes are depleted in Na, Al and Cr relative to the host plagioclase lherzolite and enriched in Mg, Si, Ca, Ti and Fe. These changes can be explained by removal of plagioclase from both depleted zones and dikes relative to the plagioclase lherzolite host, and addition of clinopyroxene to the dikes relative to the plagioclase lherzolite hosts. It appears then that the system was open and that components were added as well as subtracted.

A possible explanation of the above characteristics is that the websterite dikes and depleted zones were produced by the interaction of migrating silicate melts with the host peridotite. The postulated interaction removed plagioclase from the wall rocks to form the depleted zones in samples 8W40 and 8W82, and also removed both ortho- and clinopyroxene from the wall rocks of the dike shown in Figure 8. According to this model, the dikes were produced by fractional crystallization. This is consistent with the apparent igneous textures of the dikes.

Figure 45: Compositions of depleted zones and depleted zones plus associated websterite dikes normalized to the composition of the plagioclase lherzolite host rock. Elements that plot above the dashed line are enriched relative to the plagioclase lherzolite host and must have been added to the system. Elements that plot below the line are depleted relative to the plagioclase lherzolite host and must have been subtracted from the system.

Abundance / Abundance in LHZ Host



The normative plagioclase that must have been removed from the system could have been carried out by the fugitive melt after partial fractional crystallization formed the websterite dikes.

REACTION BETWEEN MELT AND WALL ROCKS

The previous discussion emphasized the analogy that can be drawn between the large dunite bodies with their associated clinopyroxene-rich lithologies and the much smaller depleted zones around the websterite dikes. Similar conclusions were reached regarding the characteristics of both sets of features. Igneous characteristics that are present in both are their tabular, dike-like shapes and the presence of igneous-textured clinopyroxene-rich rocks. However, the formation of both sets of features appears to have involved a reaction that removed components from the surrounding peridotite. It was concluded in both cases that this latter characteristic resulted from an interaction of the melt that precipitated the clinopyroxene-rich rocks with the wall-rocks. This discussion is directed toward the nature of these melts and the cause and effects of their interactions with the wall-rock peridotite.

Some loose but significant constraints may be placed on the nature of the transient melts. First, these melts must have been capable of fractionating olivine, clinopyroxene, orthopyroxene, plagioclase, spinel and minor amounts of amphibole if they precipitated the wehrlite bands and clinopyroxene-rich clumps in the dunite and the websterite dikes. This suggests that the magma had basaltic affinities and the presence of orthopyroxene in the cumulates suggests that it fractionated in the direction of a tholeiitic basalt rather than an alkaline basalt. If substantial portions of the large dunite bodies are cumulates, then the melts must have been capable of fractionating large amounts of olivine before other phases (except spinel) appeared on the liquidous. This suggests that these basalts may have been picritic. The $Mg/Mg+Fe^{++}$ of the melt can be estimated from the composition

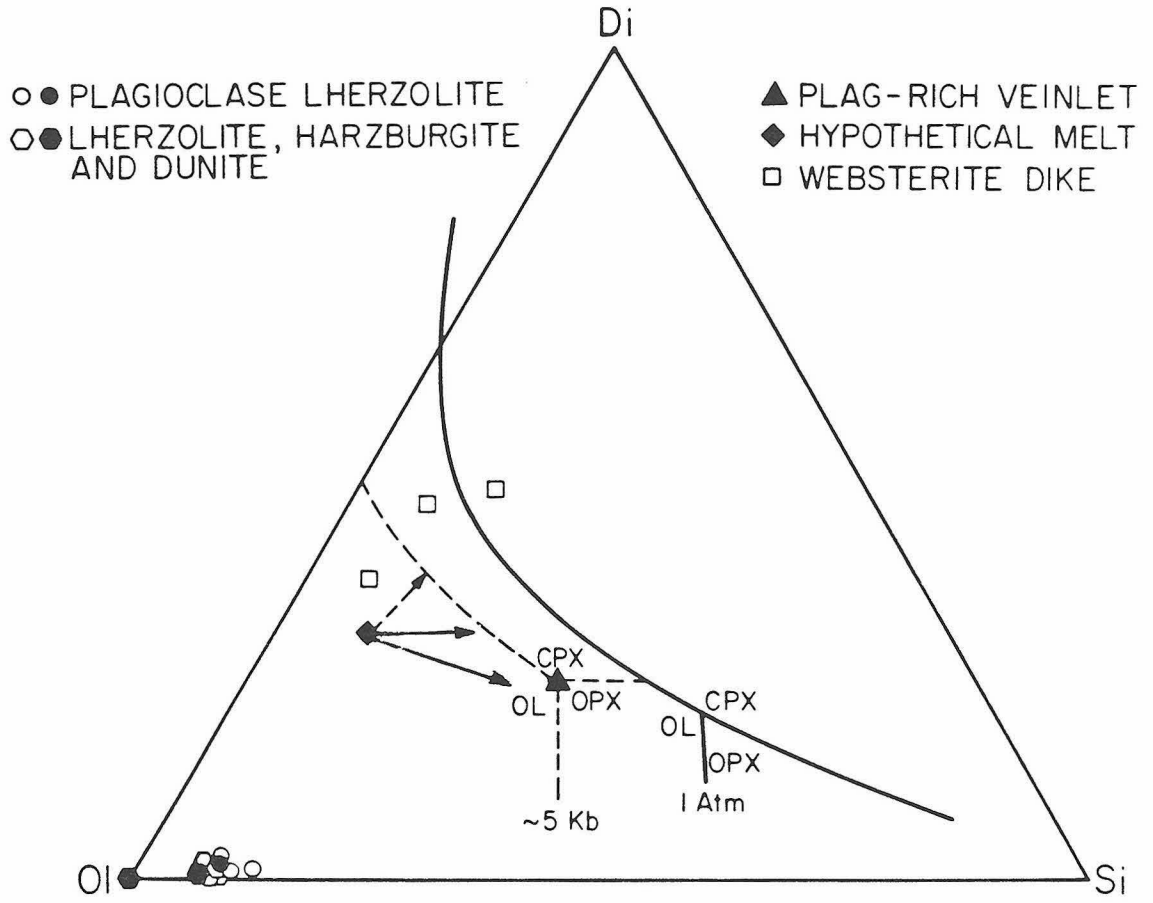
of the olivine in the large dunite bodies ($Fo_{90.5-92}$) and in the websterite dikes ($\sim Fo_{91}$) using the partition coefficients of Roeder and Emslie (1970) for coexisting olivine and basaltic melt. Basaltic melts coexisting with these olivines at a temperature of about 1200 degrees centigrade would have a $Mg/Mg+Fe^{++}$ of about 0.74-0.75. Therefore, it appears that the melt was primitive with respect to Mg and Fe.

Recent experiments by Walker et al. (1979) and Stolper (in press) on basaltic systems provide some possible explanations for some of the characteristics of the large dunite bodies and the dikes and depleted zones. Figure 46 is a projection onto the normative olivine-diopside-silica plane similar to Figure 43. Shown on this diagram are the 1 atm cotectics for a midocean ridge basalt determined by Walker et al. (1979) and a hypothetical set of ~ 5 kb cotectics from Figure 43. Stolper (in press) performed high pressure experiments on a primitive mid-ocean ridge basalt and found that basaltic melts generated by partial melting of peridotite at a pressure of 15 kb and multiply saturated with olivine, clinopyroxene and orthopyroxene plot as shown by the solid diamond. Assume for a moment that such a melt formed at a pressure of 15 kb and ascended through the upper mantle and passed through what is now the Trinity peridotite at some pressure less than 15 kb (e.g. 5 kb). This melt would no longer be multiply saturated because the cotectic paths shift to the right in Figure 46 with falling pressure (Stolper, in press). The melt would plot in the olivine field and, therefore, only be saturated with olivine. This melt would be capable of fractionating large amounts of olivine—one of the requirements for formation of the large dunite

bodies. Furthermore, if this melt came into contact with plagioclase- or pyroxene-bearing peridotite, these phases would be dissolved. This dissolution would continue until the melt became saturated in plagioclase and pyroxene or until these phases were completely removed from the wall rocks. Heat required for this dissolution could be provided by the heat in the melt or by the heat of crystallization of olivine. This provides a mechanism for formation of the depletion zones around the websterite dikes and the formation of dunite, harzburgite and lherzolite along the walls of the large dunite bodies.

Calculated compositions of the plagioclase lherzolites, lherzolites, harzburgites and dunites are plotted in Figure 46. Plagioclase lherzolites plot to the right of the lherzolites and harzburgites which, in turn, plot to the right of the average dunite analysis (hexagon at the Ol apex). The solid circles and hexagons are samples 9W2, 9W3 and 9W6 corresponding to plagioclase lherzolite, lherzolite and dunite along the margin of a large dunite body. It appears that with increasing reaction the wall rock composition is pushed toward the olivine apex of this diagram. It is important to remember, however, that this projection is effectively a projection from plagioclase and that some of the points, especially the plagioclase lherzolites, actually plot off of the Ol-Di-Si plane. A better statement of the reaction is as follows. If plagioclase lherzolite is converted to lherzolite, the bulk composition approaches the Ol-Di-Si plane from the direction of the plagioclase apex (not shown). With conversion of the lherzolite to harzburgite, clinopyroxene is dissolved and the bulk composition shifts down toward the Ol-Si join. With conversion of the harzburgite to dunite, orthopyroxene is dissolved and the bulk composition shifts toward the Ol apex. These changes

Figure 46: Compositions of peridotite compositions and hypothetical melt composition on to the Ol-Di-Si plane. See text and caption of Figure 43 for discussion.



in bulk composition of the wall rocks will be accompanied by conjugate changes in the bulk composition of the melt. The net effect will be to shift the melt in the general direction of the Si apex (solid arrow); if plagioclase lherzolite is involved, the melt will also be enriched in normative plagioclase. The exact direction of this shift depends on the modal mineralogy of the wall rocks and the relative rates at which plagioclase, orthopyroxene and clinopyroxene are dissolved into the melt.

Earlier discussions demonstrated that the plagioclase lherzolite was partially melted at one time. It is important to note that the proposed composition for that partial melt does not meet all of the above conditions. In particular, the proposed partial melt was multiply saturated with olivine, clinopyroxene and orthopyroxene. Such a melt would not react with the surrounding peridotite to leave residues of harzburgite and dunite. Therefore, the melt that formed the large dunite bodies and the smaller websterite dikes and depleted zones must have been unrelated to this partial melt. No definitive statement can be made about the timing of the partial melting of the plagioclase lherzolite and these reactions between melt and wall rocks. Both processes occurred prior to cessation of the plastic deformation of the peridotite. It is possible that the plagioclase lherzolite was partially melted at the same time a transient melt was passing through and reacting with the peridotite. Conceivably, the features preserved in the rocks reflect removal of partial melt coupled with dissolution of the residual pyroxenes.

The differences between the depleted zones with associated websterite dikes and the large dunite bodies with associated clinopyroxene-rich

rocks can be explained in terms of differences in melt to wall rock ratios. One significant difference is that the large dunite bodies contain a great deal of dunite whereas only a few of the smaller depleted zones contain dunite. The second difference is that orthopyroxene is relatively abundant in the websterite dikes (10-20 percent) but relatively rare in the wehrlite bands (<10 percent) and clinopyroxene-rich clumps (<<10 percent) in the large dunite bodies.

Consider the situation in which a large amount of melt saturated only in olivine is reacting with a small amount of peridotite. This scenario could describe a channel through which a large amount of melt was rapidly moving. New melt that is not saturated with respect to pyroxene and plagioclase would continually be supplied to react with the wall rocks. A large amount of pyroxene and plagioclase would be dissolved from the wall rocks producing wide zones of residual harzburgite and dunite. The composition of the melt would be only slightly affected by this process, and it seems likely that changes in the melt composition might be dominated by fractional crystallization of olivine. This process would drive the composition of the melt as shown by the dashed arrow in Figure 46; a melt that intersects the olivine-clinopyroxene cotectic will begin to crystallize a clinopyroxene-rich cumulate. Continued crystallization at pressures <10 kb will push the melt toward the orthopyroxene field and orthopyroxene will eventually crystallize (Stolper, in press). Such a crystallization sequence could explain the wehrlite bands and clinopyroxene-rich clumps in the dunitites if the melt left the system shortly after crystallization of orthopyroxene began.

Consider the other extreme case in which the wall rock is much more

abundant than the melt with which it is reacting. Such a scenario could describe a small amount of melt, which is saturated only with olivine, injected into a peridotite host rock and then becoming relatively stagnant. In this case, the composition of the wall rock would be much less affected because the melt might become saturated with respect to pyroxene before all the pyroxene is dissolved. This could explain why dunite is rare in the depleted zones of websterite dikes. The composition of the melt, however, would be much more greatly affected and would be pushed in the direction of pyroxene-saturation. The exact path that the melt composition would follow in Figure 46 would depend on the abundances of orthopyroxene, clinopyroxene and plagioclase in the wall rocks, the relative rates at which these phases are dissolved by reacting melt, and the amount of olivine that is fractionally crystallized. Possible paths are indicated by the solid arrows in Figure 46. These illustrate how the line of descent could diverge from the path the melt would follow by simple fractional crystallization of olivine. If the peridotite wall rocks are orthopyroxene-rich (as they are in the Trinity peridotite), the melt will be pushed in the direction of orthopyroxene saturation and will intersect either the olivine-clinopyroxene or olivine-orthopyroxene cotectic much nearer the olivine-orthopyroxene-clinopyroxene multiple saturation point than if it were driven only by olivine fractionation. This might result in precipitation of a more orthopyroxene-rich cumulate than makes up the websterite dikes.

The different Mg- and Fe-enrichment trends in Figure 39 might reflect the initial composition of the reacting melt. The Mg-enrichment trend in the plagioclase lherzolite-dunite transition suggests that the reacting melt was primitive with respect to $Mg/Mg+Fe^{++}$.

In contrast, the melt that produced the depleted zone and websterite dike in sample 8W40 must have been more Fe-rich and, therefore, more evolved with respect to $Mg/Mg+Fe^{++}$. Field relationships suggest that the websterite dikes appear to emanate from but post-date the large dunite bodies. It is possible that these dikes formed from melts that were trapped in pockets in the large dunite bodies where they evolved by fractional to more Fe-rich compositions. The olivine in the wehrlite bands, for example, is relatively Fe-rich (Fo₈₇) suggesting that some Fe-enrichment did occur in the melts. The melts may have then been injected into the surrounding country rock and produced an Fe-enrichment trend in the wall rock.

SUMMARY AND CONCLUSIONS

The Trinity peridotite contains a record of a complex igneous history. In addition to evidence for extensive partial melting of the plagioclase lherzolite, the peridotite reacted with transient melts. Two melts are required. The partial melts that formed in the plagioclase lherzolite would have been in equilibrium with two pyroxenes, olivine and spinel, and therefore, could not have reacted with the peridotite to form dunite and harzburgite by dissolution of pyroxenes. This suggests that a second melt, which was saturated only with olivine, passed through and reacted with the Trinity peridotite. Stolper (in press) demonstrated that cotectic paths of basaltic melts shift with pressure so that a melt composition that is saturated with two pyroxenes and olivine at high pressure may be saturated only with olivine at lower pressures. Therefore, the melts that reacted with the Trinity peridotite may have been generated by melting of peridotite at great depth and reacted with the wall rocks as they ascended through the

mantle. For example, these melts may have formed by partial melting of peridotite at a pressure of 15 kb and reacted with the Trinity peridotite at a pressure of about 5 kb. The timing of the passage of these transient melts relative to the pervasive partial melting of the plagioclase lherzolite is uncertain and it is possible that the plagioclase lherzolite was partially melted at the same time that melts generated at greater depth were passing through the Trinity peridotite.

The reaction of these transient melts with the peridotite wall rocks is significant because it suggests that a process in addition to fractional crystallization may be affecting the composition of basaltic melts as they ascend through the mantle. The net affect of the reaction with the wall rocks is to enrich the melt in K, Na, Ca, Al and Si more than would be expected from simple fractional crystallization of olivine. This process is analogous to zone refining (Harris, 1957) and provides a mechanism for generating a melt enriched in these and other incompatible elements although the source rocks and original melt may have been depleted in them.

ORIGIN OF THE GABBROIC ROCKS

It is tempting to speculate that the gabbroic and related rocks that intrude the Trinity peridotite crystallized from the transient melts that formed the large tabular dunite bodies and associated clinopyroxene-rich rocks. Certainly the mineralogies of the cumulate dunites, wehrlites, pyroxenites and olivine pyroxenites at the base of the Toad Lake gabbro (Table 5) are similar to those of the websterite dikes and associated depleted zones and the concordant wehrlite dikes and the associated dunites (Table 3). These cumulates record the crystallization sequence: olivine, olivine + clinopyroxene, olivine + clinopyroxene + orthopyroxene, olivine + clinopyroxene + orthopyroxene + plagioclase. Spinel is ubiquitous. Significantly, the sequence is identical to that inferred for the websterite dikes and the larger concordant wehrlite dikes. Furthermore, the olivine, orthopyroxene, and clinopyroxene in the basal cumulates of the gabbro are highly magnesian (Table 5), and very similar in composition to their counterparts in the wehrlite and websterite dikes (Table 3). This permits, although does not prove, that these lithologies are consanguineous.

Field relations, however, clearly indicate that the gabbro and related rocks cut the large dunite bodies and the small websterite dikes with depleted zones. There are no tabular dunite bodies in the study area that can be followed into the gabbros and demonstrated to have formed around feeder dikes that are directly related to the observed gabbros. If the gabbro bodies have feeder dikes, they are either covered by the gabbro bodies or younger rocks or feed the gabbro bodies from outside the study area. The latter possibility is quite likely because neither of the large gabbro bodies was completely

mapped in this study.

The crosscutting relationships suggest that there were multiple pulses of melts passing through the Trinity peridotite and that the melts that formed the gabbro bodies were not necessarily the same ones that formed the large dunite bodies and associated clinopyroxene-rich rocks or the websterite dikes and associated depleted zones. The similarities in mineralogy, crystallization sequence, and mineral chemistry, however, does suggest that all of the parental melts were similar in composition and crystallized phases under approximately the same conditions of pressure and temperature.

P-T TRAJECTORY

One of the principal goals of this investigation was to place constraints on the ultimate origin of the Trinity peridotite including its pressure and temperature history. The constraints that are available to work with consist of: (1) the petrologically-derived temperatures and pressures; (2) textural evidence for the peridotite passing from the spinel lherzolite stability field to the plagioclase lherzolite stability field; and (3) textural and structural evidence for widespread partial melting.

Figure 47 and Table 16 synthesize the mantle history of the Trinity peridotite. This cartoon relies heavily on the pyrolite melting experiments of Green and Ringwood (1967). All of the solidus and reaction lines must be considered as approximations because the composition of pyrolite is somewhat different than any of the bulk compositions encountered in the Trinity peridotite. Shown in the figure are: (1) the pyrolite dry solidus (Green and Ringwood, 1967) and wet solidus (0.1 wt. percent H₂O) determined by Green (1973); (2) the oceanic geotherm estimated by Clark and Ringwood (1964); (3) boundaries for the plagioclase pyrolite, spinel pyrolite and garnet pyrolite fields (Green and Ringwood, 1967); and (4) the equilibration temperatures and pressures calculated for pyroxenes from plagioclase lherzolite 8W67 (Figure 42). The fields labeled plagioclase, spinel, pyroxene or garnet pyrolite should, for the purposes of this discussion, be considered equivalent to plagioclase, spinel, pyroxene and garnet lherzolite, respectively.

The key to the following discussion is that the pyroxenes in the Trinity peridotite appear to have equilibrated at high temperatures

Figure 47: Possible P-T trajectory of the Trinity peridotite as it ascended through the upper mantle. Trajectory is indicated by shaded arrows. Heavy lines around stipple are envelopes encompassing calculated equilibration temperatures and pressures for pyroxene cores and rims and interstitial pyroxene grains in sample 8W67 in Figure 42. Dry solidus for pyrolite and boundaries between pyrolite assemblages from Green and Ringwood (1967). Wet solidus for pyrolite from Green (1973). Oceanic geotherm from Clark and Ringwood (1964).

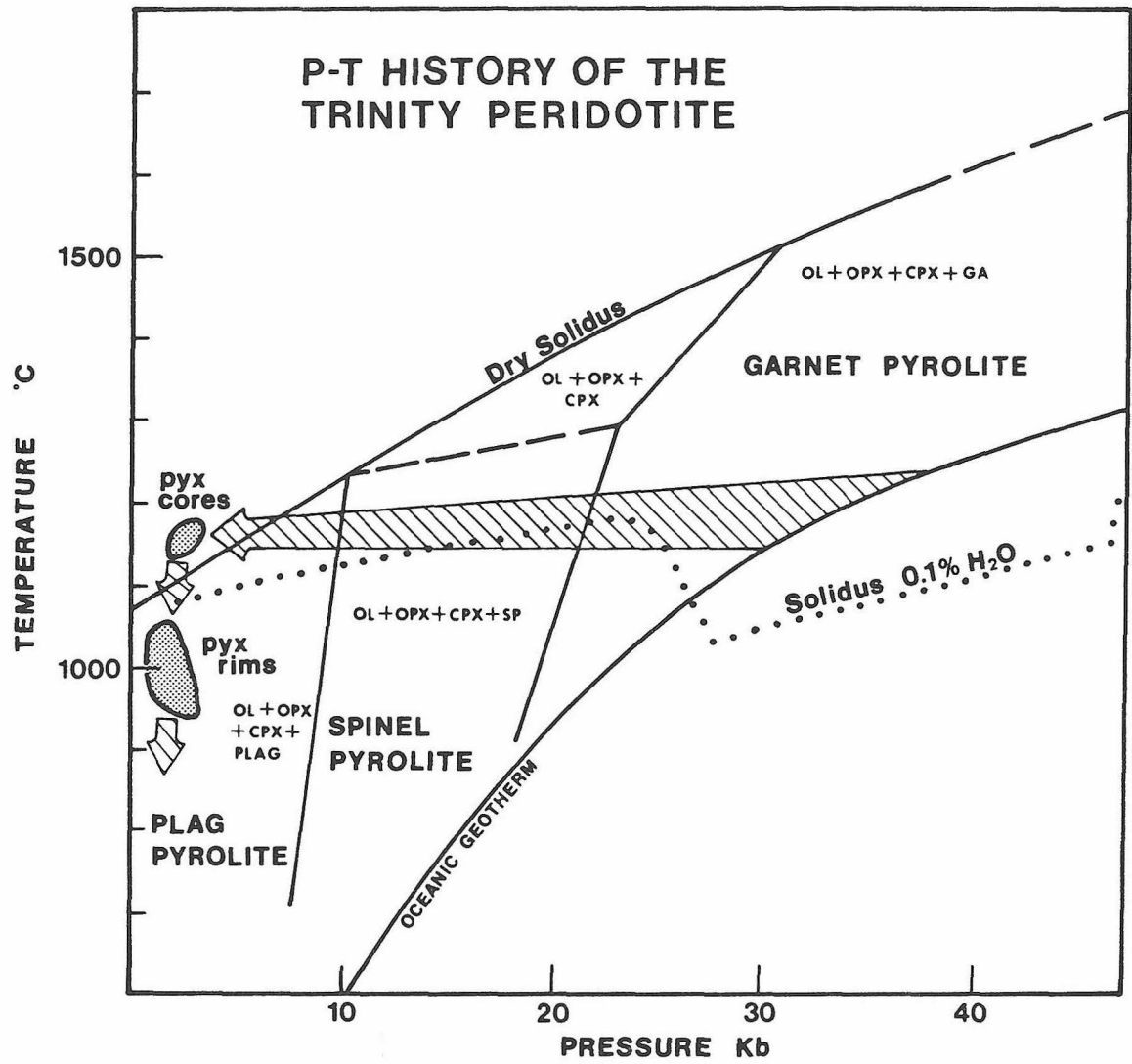
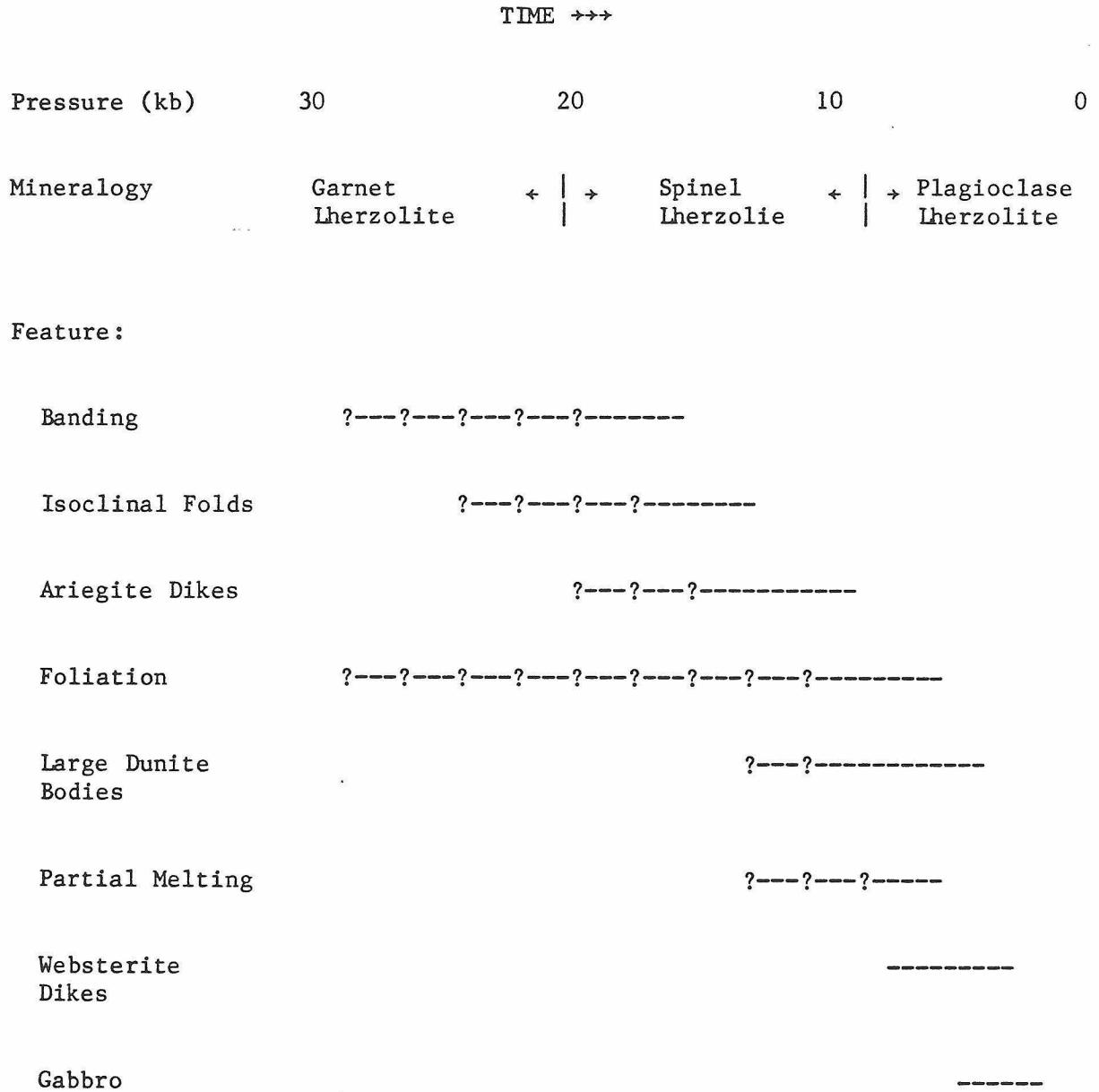


Table 16: Estimated Depth and Sequence of Events in the Mantle History of the Trinity Peridotite



----- estimated pressure range of occurrence;
 ? where uncertain of limits

and low pressures that are far removed from any reasonable geotherm. This suggests that the peridotite may have originated along a geotherm at greater depth and ascended through the upper mantle to reach the base of the crust while still at high temperatures. A similar interpretation was made by Boudier (1978) for the Lanzo peridotite. The arrow reaching from the pyroxene equilibration temperatures and pressures suggests two possible trajectories from the estimated geotherms. The base of the arrow is an isothermal trajectory, and the top of the arrow is an adiabatic trajectory. Both projections are essentially the same in that both intersect the model oceanic geotherms at pressures of about 30-40 kb, and both suggest that the Trinity peridotite passed through the spinel peridotite field and into the plagioclase peridotite field and, at some time, intersected the dry solidus. The final stages of the mantle P-T history are then characterized by essentially isobaric cooling as recorded by the recrystallized equilibration temperatures of the pyroxene porphyroblast rims and groundmass pyroxene. These inferences are compatible with the textural evidence for the reaction, spinel + orthopyroxene + clinopyroxene \rightarrow olivine + melt, corresponding to melting of spinel lherzolite, followed by precipitation of olivine + plagioclase, corresponding to crystallization in the plagioclase lherzolite field. The absence of garnet in the Trinity peridotite might be explained as follows. If present initially, all garnet may have been replaced as the peridotite passed through the spinel peridotite stability field. Alternatively, the Trinity peridotite may have originated on a steeper geotherm entirely within the spinel peridotite field.

The sequence of events that affected the Trinity peridotite may

be placed in the context of this P-T trajectory. All events that pre-date the formation of the ariegite bands and dikes must have occurred while the peridotite was in the spinel lherzolite stability field, because the primary aluminous phase in these dikes appears to have been spinel. These include the formation of the banding, isoclinal folding of the banding, and the emplacement of the ariegite dikes. The websterite dikes must have been emplaced after the peridotite entered the plagioclase peridotite field because these dikes contain plagioclase as the primary aluminous phase. The formation of the large dunite bodies is also assigned to this P-T range because some clinopyroxene pods in these dunites contain plagioclase. Of course, many episodes of dunite formation may have occurred and some dunite may have been formed while the peridotite was still in the spinel peridotite field. The extensive widespread partial melting would have occurred after the peridotite intersected the solidus. According to the reconstruction in Figure 47, this would have occurred at low pressures and temperatures after the peridotite had entered the plagioclase lherzolite field. This cannot be taken as a rigid constraint because the temperature of the solidus at any pressure is a function of the bulk composition. The wet solidus in Figure 47 illustrates that the temperature at which the peridotite first melts will be extremely sensitive to the volatile content of the system. Therefore, the peridotite could have crossed the solidus at any point during its ascent through the mantle. Gabbro dikes and plutons, and the plagiogranite and diabase dikes would have been emplaced late, after the peridotite had cooled sufficiently to be capable of brittle fracture.

SPECULATIONS ON THE TECTONIC SETTING

The preceding discussion suggests that the Trinity Peridotite originated at a depth of at least 30 km and possibly as much as 100 km in the upper mantle. During its passage upward to the base of the crust, it was intensely deformed, underwent partial melting on a regional scale, and reacted with ascending basaltic melts. The end of this chapter of its history was marked by the emplacement of the gabbro plutons at 455-480 m.y.. The peridotite was subsequently emplaced into the crust as an enormous thrust sheet with attending amphibolite grade metamorphism of the underlying Grouse Ridge Formation and Salmon Hornblende Schist. The age of this crustal emplacement is speculated to be about 380 m.y. based on the Rb-Sr age of the amphibolites (Lanphere et al., 1968). The tectonic setting in which these events could have occurred is the next question that will be addressed.

The Trinity Peridotite appears to have reached the base of the crust in an oceanic environment. Lindsley-Griffin (1977) mapped the northwestern margin of the Trinity Peridotite to the west of China Mountain and concluded that the Trinity Peridotite is, in fact, the base of an ophiolite. Within her field area, and structurally above the peridotite, she identified three types of gabbro, a sequence of diabase that contained some dikes, and an overlying sequence of mafic keratophyres and spilites. The types of gabbro were layered cumulate gabbro, amphibolitic gabbro associated with diorite, and a younger pegmatitic gabbro that intrudes the other two. The Penrose Conference on Ophiolites (1972) defined an ophiolite as a sequence of rocks consisting from bottom to top of peridotite, gabbro, a mafic sheeted dike complex, and a mafic volcanic complex. Rocks that may be associated

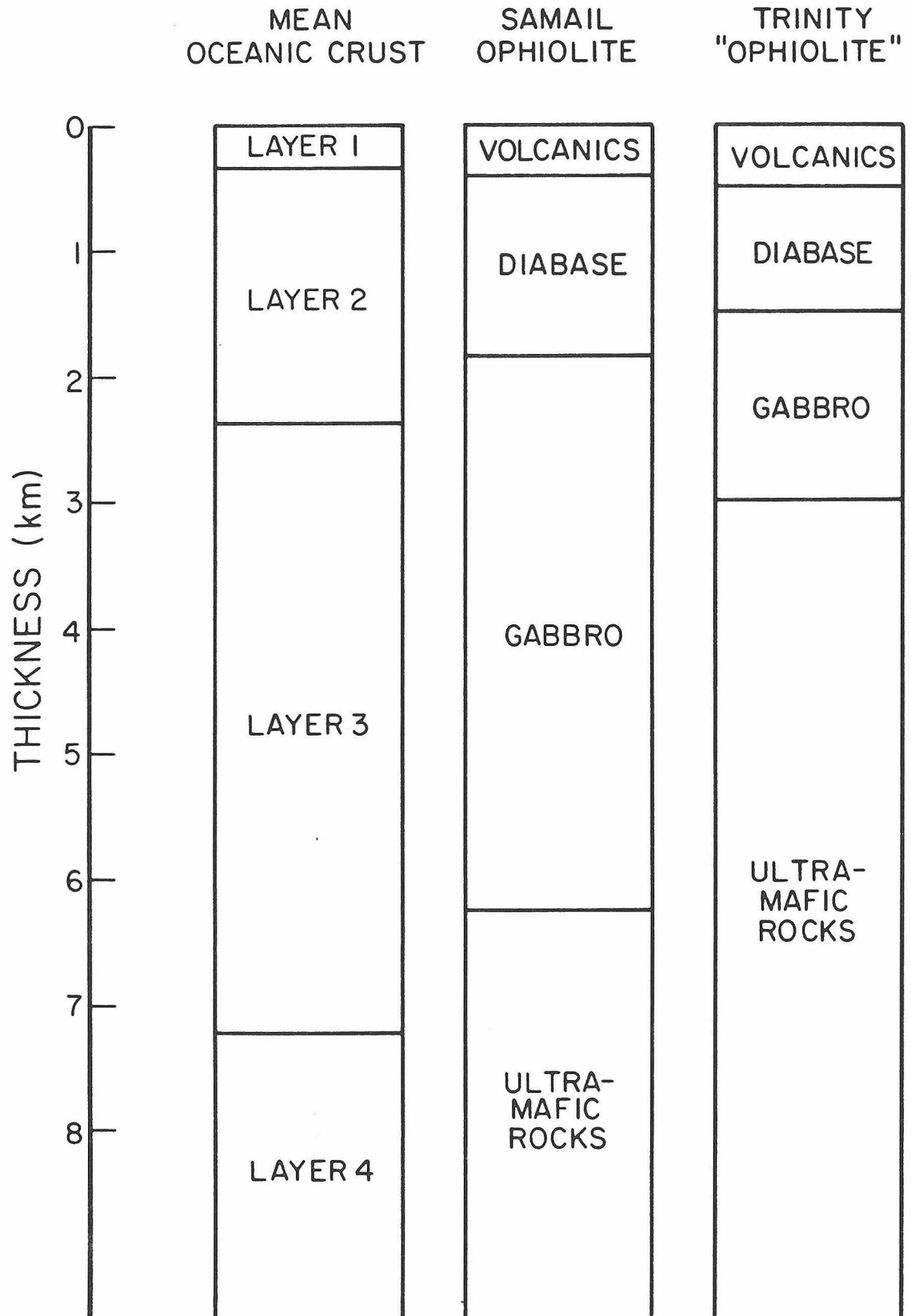
include pelagic sediments, chromitite bodies, and sodic felsic intrusive and extrusive rocks. The sequence described by Lindsley-Griffin (1977) does appear to meet the requirements of this definition, although it must be emphasized that the structural complexities in Lindsley-Griffin's field area obscure any clear evidence of a genetic link between the peridotite and overlying rocks (Lindsley-Griffin, oral communication, 1977). Therefore, the name, Trinity Ophiolite, introduced by Lindsley-Griffin (1977) will be used throughout the remainder of this discussion to encompass the Trinity peridotite and the overlying mafic rocks. Although the Penrose Conference on Ophiolites urged that the term "ophiolite" be employed independently of genetic connotations, it has become virtually dogmatic among geologists that ophiolites are fragments of oceanic crust that were generated at midocean ridges and transported by plate motions to continental margins where they were accreted to the continents (Coleman, 1977). Lindsley-Griffin (1977) concluded that:

"The Trinity Ophiolite presumably formed at an oceanic spreading center during early Ordovician time (480 to 455 m.y.). This spreading center which may have been located along a mid-ocean ridge or in a marginal basin was not immediately adjacent to a continent during the early Paleozoic."

The postulated oceanic affinity of the Trinity Ophiolite is supported by preliminary Nd-Sm isotopic measurements (Jacobsen, oral communication, 1979) which indicate that the plagioclase lherzolite has $^{143}\text{Nd}/^{144}\text{Nd}$ ($\epsilon\text{Nd} \sim 8-9$) in the range of oceanic and island arc values (DePaolo and Wasserburg, 1976a, 1976b, 1977) and similar to the early Paleozoic Bay of Island Ophiolite (Jacobsen and Wasserburg, 1979) and to the late Mesozoic Samail Ophiolite (McCulloch et al., 1980).

However, the gross thicknesses of the various units of the

Figure 48: Comparison of structural sections of the Samail ophiolite (Hopson et al., in press), the Trinity "ophiolite" (Lindsley-Griffin, 1977) and mean oceanic crust (Christensen and Salisbury, 1975).



Trinity Ophiolite as constructed by Lindsley-Griffin (1977) are quite different from those of classic ophiolite sections such as the Samail Ophiolite (Hopson et al., in press; Coleman, 1977) and the Bay of Islands Ophiolite (Malpas, 1977; Williams, 1971). A comprehensive review of the characteristics of these and other ophiolites is given by Coleman (1977). A simplified and schematic summary of the lithologic section of the Trinity Ophiolite is presented in Figure 48. The thicknesses for each of the units are the maximum estimates made by Lindsley-Griffin (1977). A similar section for the Samail ophiolite is also presented using thicknesses measured by Hopson et al. (in press) as well as the seismic structure of the "mean oceanic crust" determined by Christensen and Salisbury (1975). Figure 48 illustrates that the composite mafic section of the Trinity Ophiolite is a factor of 2-3 thinner than the mafic section of the Samail Ophiolite. Layers 1, 2 and 3 in the seismic structure of the oceanic crust correspond to sedimentary rocks, rocks with p-wave velocity = 5.1 km/sec and rocks with p-wave velocity = 6.8 km/sec, respectively. These presumably correspond to the sediments and underlying extensive rocks, diabases and gabbros of ophiolites, whereas layer 4 (p-wave velocity = 8.1 km/sec) presumably corresponds to the ultramafic portion of ophiolites (Christensen and Salisbury, 1975). The thicknesses the units of the Samail Ophiolite are very similar to the thicknesses of the seismic layers of the "mean oceanic crust", suggesting that the Samail Ophiolite is, indeed, a representative fragment of oceanic crust and mantle that formed at a spreading center as suggested by Coleman (1977) and Hopson et al. (in press). In contrast, the Trinity Ophiolite appears to have a mafic section that is much too thin to be a representative

section of oceanic crust.

The details of the rock associations and structures of the Trinity Ophiolite are also atypical of classical ophiolites. First, plagioclase hercynite is abundant in the Trinity but is totally absent or extremely rare in all well described ophiolites. Second, the gabbros in the Trinity Ophiolite appear to be intruded into the peridotite as discrete isolated plutons of different ages rather than forming a continuous sheet that rests on top of the peridotite. Third, the gabbroic rocks in the Trinity Ophiolite contain abundant orthopyroxene, which is rare in gabbros of classic ophiolites (Coleman, 1977). Fourth, the sheeted dike complex in the Trinity Ophiolite is, at best, poorly developed with individual dikes very difficult to discern (Lindsley-Griffin, 1977) whereas the sheeted dike complexes in the classic ophiolites are well developed arrays of subparallel dikes (Coleman, 1977). Fifth, there are no unequivocal pillow structures (Lindsley-Griffin, 1977) in contrast to the thick sequences of pillow lavas in most ophiolites. Sixth, rather than the pelagic cherts or shales that rest on most ophiolites, the Trinity Ophiolite is capped by immature volcanogenic graywackes and mudstones that are interbedded with mafic volcanic rocks and by massive sedimentary breccia. Many ophiolites, such as the Samail, the Troodos, the Papua and the Bay of Islands appear to have originated at midocean ridge-type spreading centers, by virtue of their gross structure, continuous sheet of gabbro, well developed sheeted dike complex, and overlying pillow basalts and pelagic sediments. The Trinity Ophiolite, on the other hand, must have originated in some other environment.

Alternative environments, such as marginal basins (Dewey and

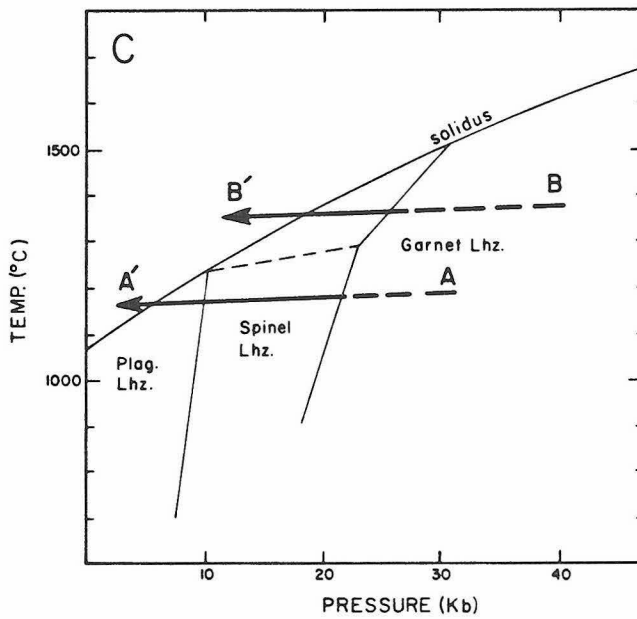
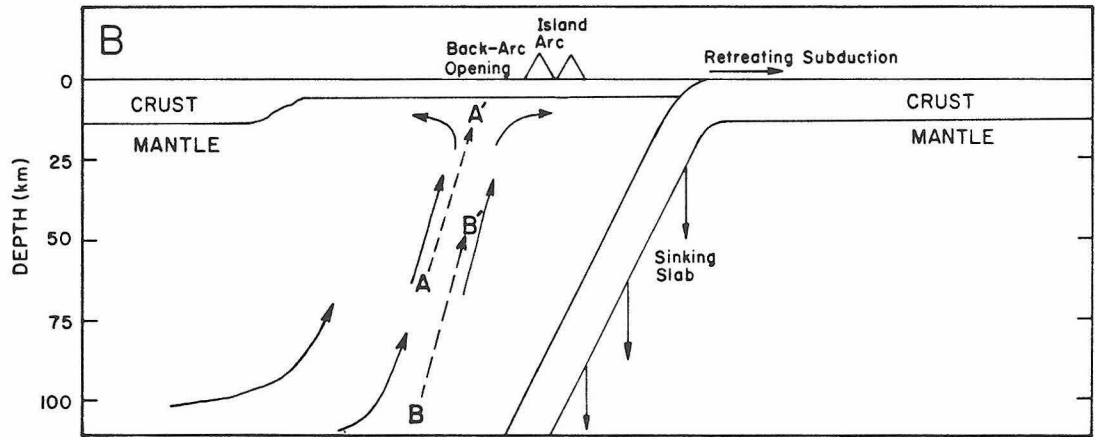
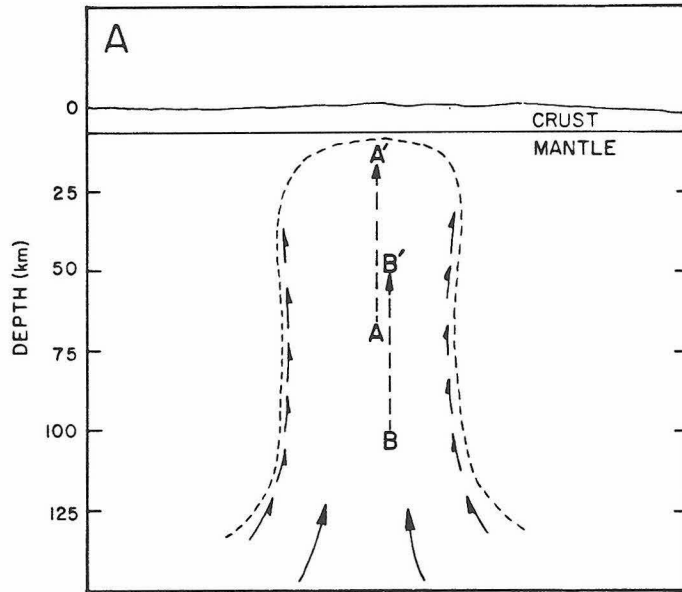
Bird, 1971) and island arcs (Miyashiro, 1973) have been suggested as sites of ophiolite genesis. Unfortunately, the unusual characteristics of the Trinity ophiolite make it difficult to draw an analogy to many other ophiolites. The only other ophiolitic section that contains abundant plagioclase lherzolite is the Othris ophiolite in northern Greece described by Menzies and Allen (1974). Like the Trinity, this ophiolite also has an anomalously thin mafic section (2-3 km), a poorly developed dike complex, and a limited amount of plutonic mafic rocks that formed within "small pockets of mafic liquid, or within feeders" (Menzies and Allen, 1974). Furthermore, systematic facies changes in the sediments associated with the ophiolite indicate continental margin deposition. Menzies and Allen (1974) concluded that the Othris Ophiolite formed in a near continental environment at the inception of rifting. There is no evidence, however, that the Trinity Ophiolite formed in a near continental environment, and indeed, there is no lower Paleozoic or Precambrian continental crust exposed in northern California.

The vicinity of an oceanic volcanic highland, such as an island arc or back-arc basin, is considered to be a reasonable alternative environment for the rise of the Trinity Peridotite through the mantle and the formation of the Trinity Ophiolite, based on the investigations of other workers and the regional geology of the Klamath Mountains. Such an environment could account for the coarse clastic sediments that overlie the Trinity Ophiolite. Furthermore, volcanic, volcani-clastic and intrusive rocks with calcalkaline affinities are found throughout the Klamath Mountains (Ando et al., 1977; Snoke et al., 1977; Snoke et al., in review; Irwin et al., 1977; Hamilton, 1978).

Potter (written communication, 1979) investigated some of the dikes from the dike complex of Lindsley-Griffin (1977) and found them to have REE, Ti, Zr, and Y concentrations similar to island arc volcanics. Potter inferred these rocks to be Silurian or younger, making them younger than the Trinity Ophiolite. Nevertheless, their presence suggests that calcalkaline volcanism did occur at some time in the vicinity of the Trinity Ophiolite. It is suggested that the Trinity Peridotite ascended through the upper mantle either beneath an active island arc or beneath a spreading back arc basin.

The ascent of the peridotite may have been diapiric and controlled by a density contrast with the surrounding upper mantle. Such an origin has been suggested by Avé Lallement (1976) for the Canyon Mountain Ophiolite based on the similarities between its structures and those of salt domes. A similar analogy might be made for the Trinity Peridotite. The multiple folding events observed in salt domes (Kupfer, 1962) are reminiscent of the folded folds in the Trinity Peridotite. However, an insufficient area of the peridotite has been mapped to determine if there is a radial symmetry to the foliation and multiple diapiric lobes as are found in salt domes (Kupfer, 1962). The density contrast required for the Trinity Peridotite to rise diapirically through the upper mantle could have been produced by the partial melting that is evidenced throughout the plagioclase lherzolite. This model provides a mechanism for relating the gabbroic melts that intrude the peridotite and the peridotite itself. Figure 49A is a cartoon illustrating possible paths of the Trinity peridotite (path A-A') and the source rocks for the gabbroic melts (path B-B') in an ascending mantle diapir. Possible P-T trajectories

Figure 49: Possible models for the tectonic setting in which the Trinity peridotite reached the base of the crust. (A) Mantle diapir. (B) Mantle upwelling below a zone of back-arc opening. (C) Hypothetical P-T paths for the Trinity peridotite (A-A') and for the source region for the melts that passed through and reacted with the Trinity peridotite (B-B'). Mantle trajectories for these paths are shown in (A) and (B).



for these two parts of the diapir are illustrated in Figure 49C. The greatest amounts of partial melting may have occurred in the interior of the diapir. If A-A' and B-B' originate on a geotherm that is steeper than the peridotite solidus and follow adiabatic paths toward the surface, path B-B' will intersect the solidus before A-A'. As the diapir continued to ascend, the deeper parts of the diapir (B-B') would cross further into the hypersolidus region (Figure 49C) than the leading edge (A-A') would. Also, the interior region could have been more insulated against the lower ambient temperature of the surrounding mantle through which the diapir was passing and more closely approximate an adiabatic ascent. The leading edge of the diapir might be expected to lose heat to the surrounding cooler mantle and, therefore, undergo less partial melting. Melts escaping the interior of the diapir could have reacted with the peridotite at the leading edge producing the tabular dunite bodies, clinopyroxene-rich dikes and bands, and further depleting the peridotite. Such a reaction would be expected if the escaping melts were generated at greater pressures (e.g. 15 kb) than the pressures at which they encountered the leading edge of the diapir (≤ 10 kb). These melts may have been involved in the formation of an island arc or new oceanic crust in a spreading back arc basin. The last magmas would be generated when the peridotite had reached the base of the crust and had ceased to rise; these melts may have formed the gabbros that intrude the Trinity Peridotite.

A somewhat different hypothesis is that the ascent of the Trinity Peridotite was driven by convection in the mantle wedge above a subduction zone. Such a process has been postulated by numerous authors (e.g. Sleep and Toksoz, 1971; Uyeda, 1977; Uyeda and Kanamori, 1979;

Irvine, 1980). As an alternative to convection driven by density contrast, convection in the mantle wedge has been postulated to be forced by coupling of the overlying mantle with the subducting slab (Sleep and Toksoz, 1973) or to be driven by the relative motions of the two lithospheric plate (Figure 49B; Uyeda and Kanamori, 1979). The partial melting of the peridotite may have resulted from decompression, and, as in the diapir model, the higher portions of the convecting peridotite (A') might be expected to react with ascending melts generated at greater depth (B').

The convection model has two advantages over the diapir model. First, it is not necessary to postulate an early melting event to produce the density contrast that drives a diapir; melting could have occurred at any time during the ascent of the peridotite. Second, the mantle convection provides for continuous mantle and crustal evolution in the Klamath Mountains. Uyeda and Kanamori (1979) suggested that the opening of back-arc basins above subduction zones is controlled by the geometry of the subduction zone and the relative motions of the plates. In a Chile or Alaska type subduction zone, the Benioff zones are shallow (10-20 degrees) and typified by major thrust events, and the plate motions are strongly convergent. These types of subduction zones do not have associated back-arc basins. In the Mariana type subduction zone, the Benioff zones are steep and devoid of great thrust event, and the plate motions are not strongly convergent. These types of subduction zones have associated active back-arc basins. Uyeda and Kanamori hypothesized that back-arc basins open when the descending slab of the subduction zone is no longer coupled to the hanging slab and sinks into the mantle

rather than being thrust under the hanging plate. This sinking causes the subduction zone to migrate away from the hanging plate, and produces a back-arc basin in the hanging plate. Magmatic activity and formation of new lithosphere will migrate, following the retreating subduction zone. This would be consistent with the general westward younging of the Klamath Mountains province. The Trinity Ophiolite may have formed with the initiation of subduction zone retreating. Continued westward retreating of the subduction zone intermittently could have produced the complex associations of ophiolitic and island arc affinity that young toward the west. Uyeda and Kanamori (1979) also suggest that the relative plate motions could shift back to strongly convergent periodically. Such an event could have caused the Trinity Peridotite to be thrust over the Central Metamorphic Belt and might also explain the other numerous easterly dipping thrusts in the Klamath Mountains.

CONCLUSIONS

The northeastern corner of the Trinity peridotite is underlain by a lithologically diverse suite of ultramafic rocks that preserve an excellent record of their mantle history. This diversity is unique among North American peridotites in that plagioclase lherzolite, in addition to harzburgite and dunite, is abundant. Furthermore, the rocks record a mantle history that included partial melting, reaction with transient melts and plastic deformation. Plastic deformation produced at least two generations of folds; the axial planes of the younger folds are coplanar with a penetrative foliation defined by preferred orientations of minerals and feldspathic segregations. Pervasive partial melting of the plagioclase lherzolite is evidenced by feldspathic segregations, plagioclase-rich veins and textures suggesting partial resorption of spinel, ortho- and clinopyroxene. The peridotite was apparently a spinel lherzolite at the inception of melting; subsequent crystallization of the partial melt occurred in the plagioclase lherzolite stability field. Calculated equilibration temperatures for ortho- and clinopyroxene pairs yield temperatures of >1150 degrees centigrade, which are compatible with the temperature requirements for partial melting of plagioclase or spinel lherzolite at pressures < 10 kb. Another melt, not in equilibrium with the peridotite, passed through and reacted with the ultramafic wall rocks to produce zones of lherzolite, harzburgite and dunite and crystallized websterite dikes, wehrlite bands in dunite, and other clinopyroxene-rich rocks.

The Trinity peridotite is inferred to have originated at a depth of not less than ~ 30 km and perhaps as deep as 100 km. The temperatures at which the pyroxene porphyroclase core equilibrated are high (>1150 deg. C.). This suggests that the peridotite ascended from a depth of

~100 km if it originated on a reasonable geotherm. This model is consistent with evidence that suggests the plagioclase lherzolite was produced by partial melting and recrystallization of a spinel lherzolite protolith.

The structural and petrogenetic record may be organized in the context of this model. Ariegite bands and dikes formed and isoclinal folding occurred while the peridotite was still in the spinel lherzolite stability field. Most of the large dunite bodies and associated clinopyroxene-rich rocks, as well as the websterite dikes and associated depleted zones, formed after the Trinity peridotite had passed from the spinel lherzolite field into the plagioclase lherzolite field. Deformation of the peridotite continued throughout this time producing a penetrative foliation and small, more open folds. At some time in its history, the Trinity peridotite passed above the plagioclase (or spinel) lherzolite solidus and partially melted. The composition of this partial melt seems to have been basaltic, but its chemistry has been obscured by exchange of Fe and Mg with the host peridotite during crystallization. It is not certain if the peridotite crossed the solidus from the spinel or the plagioclase lherzolite stability field. However, the Al-rich rocks appear to have been spinel lherzolite when they melted; subsequent crystallization of the melt precipitated plagioclase instead of spinel as the principal Al-phase and, therefore, occurred in the plagioclase lherzolite stability field.

Large, tabular dunite bodies cut the plagioclase lherzolite, lherzolite and harzburgite of the Trinity peridotite and are interpreted to mark channels along which melts passed through the peridotite en route to the surface. The mineralogy of the dunitites and the associated clinopyroxene-rich rocks suggest that the melts were picritic basalts.

These melts are hypothesized to have formed by partial melting of peridotite at a great depth (e.g. 15 kb pressure or ~45 km depth) and to have intersected the Trinity peridotite at lower pressures (<10 kb) at which they were no longer in equilibrium with pyroxene or plagioclase. Resorption of these phases into the melt left the marginal portions of the dunite bodies and the bordering harzburgite and lherzolite as residues. The reciprocal change in the composition of the transient melt is a greater enrichment in Al, Ca, Na, and Si than would be produced by simple fractionation of olivine. The interiors of the dunite bodies and the clinopyroxene-rich rocks in them appear to have formed as crystal cumulates from the transient melts. The reaction of the transient melts with the wall rocks is analogous to zone refining--incompatible elements are concentrated in the melt and refractory elements are concentrated in the residual peridotite. This is significant because it suggests that the compositions of basalts ascending through the upper mantle might be affected by other processes than simple fractional crystallization or magma mixing.

The websterite dikes and associated depleted zones appear to be small scale analogs of the large dunite bodies and associated clinopyroxene-rich rocks, with the websterite dikes forming as crystal cumulates and the depleted zones by reaction of the melt and wall rocks.

The clinopyroxene-rich rocks associated with the dunites and the websterite dikes are similar in mineralogy and mineral chemistry to the basal ultramafic cumulates of the gabbro plutons that intrude the Trinity peridotite. This suggests that all of these lithologies formed from melts of similar composition, and that the large dunite bodies could be marking the paths of channels that transported melts to the magma

chambers in which the gabbros crystallized.

The Trinity peridotite appears to have reached the base of the crust by 450-480 m.y. based on zircon age date of plagiogranites dikes that intrude gabbros that, in turn, intrude the Trinity peridotite. The Trinity was subsequently thrust into its present position in the crust and over the Central Metamorphic Belt with attending epidote to almandine amphibolite grade metamorphism of the rocks immediately below the peridotite. A second foliation was formed in the lower few thousand feet of the peridotite. This crustal emplacement is tentatively dated at ~380 m.y. based on Rb-Sr age dates on rocks from the Central Metamorphic Belt (Lanphere et al., 1968). Local metamorphism and deformation of the peridotite continued into the Mesozoic with the emplacement of granitic plutons.

The Trinity peridotite is intruded and overlain by lower Paleozoic mafic rocks. Lindsley-Griffin (1977) inferred that these rocks comprised an ophiolite and that they formed at a spreading center. However, there are significant differences between this package of rocks and classic ophiolites: the mafic section is extremely thin; gabbro forms isolated plutons rather than a continuous sheet; plagioclase lherzolite is abundant; pillow lavas are absent or extremely rare; a well developed sill and dike complex is not developed; rather than pelagic sediments, the mafic section is capped by volcanogenic graywackes, breccias and mudstones. In view of these contrasts with classic ophiolites, it is suggested that the Trinity peridotite did not ascend through the mantle beneath a midocean ridge spreading center. Instead, it is suggested that the Trinity peridotite may have ascended beneath an island arc or an active back-arc basin.

REFERENCES

- Albee, A.L., Beatty, D.W., Chodos, A.A. and Quick, J.E. (in press) Quantitative analysis of petrographic properties and of mineral compositions with a computer-controlled energy-dispersive system. Proc. 12th Nat'l. Conf. Electron Probe Anal.
- Albers, J.P. (1964) Geology of the French Gulch quadrangle, Shasta and Trinity Counties, California. U.S. Geol. Surv. Bull. 1141-J, J1-J70.
- Albers, J.P. and Robertson, J.F. (1961) Geology and ore deposits of east Shasta County, California. U.S. Geol. Surv. Prof. Paper 338, 107 p.
- Ando, C., Cashman P. and Davis G. (1977) Geologic summary and road log of portions of the central Klamath Mountains, California. In Geology of the Klamath Mountains, Northern California (eds. Lindsley-Griffin, N. and Kramer J.C.), prepared for 73rd annual meeting of the Cordilleran Section, Geol. Soc. Amer., 134-156.
- Arndt, N.T. (1977) The separation of magmas from partially molten peridotite. Yb. Carnegie Inst., Wash., 76, 424-427.
- Avé Lallemant, H.G. (1976) Structure of the Canyon Mountain (Oregon) ophiolite complex and its implication for sea-floor spreading. Geol. Soc. Amer. Spec. Paper 173, 49 p.
- Averill, C.V. (1931) Preliminary report on economic geology of the Shasta quadrangle. Calif. Div. Mines, Mining in California, 27, 3-65.
- Bennett, J.H., Sherburne, R.W., Cramer, C.H., Chesterman, C.W. and Chapman, R.H. (1978) Stephens Pass earthquakes, Mount Shasta -- August, 1978, Siskiyou County, Ca. Calif. Geol., 32, no. 2, 27-34.
- Benson, W.N. (1926) The tectonic conditions accompanying intrusion of basic and ultrabasic igneous rocks. Nat. Acad. Sci. Mem. 19, 90 p.
- Berkhemer, H. (1968) Topographie des "Ivrea Körpers" Abgeleitet aus seismischen und gravimetrischen Daten. Schweiz. Mineral. Petrogr. Mitt., 48, 235-254.
- Boettcher, A.L., O'Neil, J.R., Windom, K.E., Stewart, D.C., and Wilshire, H.G. (1979) Metasomatism of the upper mantle: the genesis of kimberlites and alkali basalts. In, The Mantle Sample: Inclusions in Kimberlites and Other Volcanics. (Boyd, F.R. and Meyer, H.O.A., eds.), Amer. Geophys. Un., 173-182.
- Bowen, N.L. (1928). The Evolution of the Igneous Rocks. Princeton Univ. Press, 332 p.

- Boudier, F. (1978) Structure and petrology of the Lanzo peridotite massif (Piedmont Alps). *Geol. Soc. Amer. Bull.*, 89, 1574-1591.
- Boudier, F. and Nicolas A. (1977) Structural controls on partial melting in the Lanzo peridotite. In *Magma Genesis, 1977* (ed. Dick, H.J.B.), Oregon Dept. Geol. Min. Ind. Bull. 96, 63-78.
- Boyd, F.R. (1973) A pyroxene geotherm. *Geochem. Cosmochem. Acta.*, 37, 2533-2546.
- Boyd, F.R. and Nixon, P.H. (1975) Origins of the ultramafic nodules from some kimberlites of northern Lesotho and the Monastery Mine, South Africa. In *Physics and Chemistry of the Earth*, 9, 431-454.
- Carswell, D.A. and Dawson, J.B. (1970) Garnet peridotite xenoliths in South African kimberlite pipes and their petrogenesis. *Contr. Min. Pet.*, 25, 163-184.
- Challis, G.A. (1965) The origin of New Zealand ultramafic intrusions. *J. Petrol.*, 6, 322-364.
- Champion, D.E., Albee, A.L. and Chodos A.A. (1975) Reproducibility and operator bias in a computer-controlled system for quantitative electron microprobe analysis. *Proc. 8th Nat'l. Conf. Electron Probe Anal.*, 45A.
- Chodos A.A., Albee A.L., Gancarz, A.J. and Laird J. (1973) Optimization of computer-controlled quantitative analysis of minerals. *Proc. 6th Nat'l. Conf. on Electron Probe Anal.*.
- Chodos A.A., Albee A.L. and Quick, J.E. (1977) The use of energy dispersive analysis for the study of phase aggregates (abstract). 12th Nat'l. Conf. on Electron Probe Anal, Boston, Massachusetts.
- Christensen, N.I. and Salisbury, M.H. (1975) Structure and constitution of the lower oceanic crust. *Rev. Geophys. Space Phys.*, 13, 57-86.
- Clark, S.P. and Ringwood, A.E. (1964) Density distribution and constitution of the mantle. *Rev. Geophys.*, 2, 35-88.
- Coleman, R.G. (1971) Plate tectonic emplacement of upper mantle peridotites along continental edges. *J. Geophys. Res.*, 76, 1212-1222.
- Coleman, R.G. (1977). *Ophiolites* (Eds. Wyllie, P.J., Engelhardt, W. and Hahn, T.), Springer-Verlag, New York, 229 p.
- Danchin, R.V. (1979) Mineral and bulk chemistry of garnet lherzolite and garnet harzburgite xenoliths from the Premier Mine, South Africa. *Proc. 2nd Internat'l. Kimberlite Conf.*, 2, 104-126.
- Davis, G.A. (1966) Metamorphic and granitic history of the Klamath Mountains, California. *Cal. Div. Mines and Geol. Bull.* 190, 39-50.

- Davis, B.T.C. and Boyd, F.R. (1966) The join $Mg_2Si_2O_6 - CaMgSi_2O_6$ at 30 kilobars pressure and its application to pyroxenes from kimberlites. *J. Geophys. Res.*, 14, 3567-3576.
- Davis, G.A., Holdaway, M.J., Lipman, P.W. and Romey, W.D. (1965) Structure, metamorphism, and plutonism in the south-central Klamath Mountains, California. *Geol. Soc. Amer. Bull.*, 76, 933-966.
- Davis, G.A., Monger, J.W.H. and Burchfield, B.C. (1978) Mesozoic construction of the Cordilleran "collage", central British Columbia to central California. In Mesozoic Paleogeography of the Western United States (eds. Howell, D.G. and McDougall, K.A.), Pacific Section of Economic Paleontologists and Mineralogists, Pacific Coast Paleogeography Symposium 2, 1-32.
- DePaolo, D.J. and Wasserburg, G.J. (1976a) Nd isotopic variations and petrogenetic models. *Geophys. Res. Lett.*, 3, 249-252.
- DePaolo, D.J. and Wasserburg, G.J. (1976b) Inferences about magma sources and mantle structure from variations of $^{143}Nd/^{144}Nd$. *Geophys. Res. Lett.*, 3, 743-746.
- DePaolo, D.J. and Wasserburg, G.J. (1977) The sources of island arcs as indicated by Nd and Sr isotopic studies. *Geophys. Res. Lett.*, 4, 465-468.
- Dewey, J.F. and Bird, J.M. (1971) Origin and emplacement of the ophiolite suite: Appalachian ophiolites in Newfoundland. *Jour. Geophys. Res.*, 76, 3179-3206.
- Dick, H.J.B. (1977) Evidence of partial melting in the Josephine Peridotite. In Magma Genesis, 1977 (ed. Dick, H.J.B.), Oregon Dept. Mines and Min. Ind. Bull., 96, 438-442.
- Dick, H.J.B. and Sinton, J.M. (1979) Compositional layering in alpine peridotites: evidence for pressure solution creep in the mantle. *Jour. Geol.*, 87, 403-416.
- Dickey, J.S. (1970) Partial fusion products in alpine-type peridotites: Serrania de la Ronda and other examples. *Min. Soc. Amer. Spec. Paper* 3, 33-49.
- Donato, M.M. and Coleman, R.G. (1979) Deformation and metamorphism of the schist of Condrey Mountain, Klamath Mountains, California and Oregon. *Geol. Soc. Amer. Abst. with Prog.*, 11(2), 75.
- Dorman, J. and Ewing M. (1962) Numerical inversion of seismic surface wave dispersion data and crust-mantle structure in the New York-Pennsylvania area. *J. Geophys. Res.*, 67, 5227-5241.
- Duncan, R.A. and Green, D.H. (1980) Role of multistage melting in the formation of oceanic crust. *Geology*, 8, 22-26.
- Duncan, M.A. and Avé Lallemant, H.G. (1977) Formation of small dunite

- bodies by metasomatic transformation of harzburgite in the Canyon Mountain ophiolite, northeast Oregon. In Magma Genesis, 1977 (ed. Dick, H.J.B.), Oregon Dept. of Mines and Min. Ind. Bull., 96, 109-128.
- Evans, B.W. (1977) Metamorphism of alpine peridotite and serpentinite. *Ann. Rev. Earth. Planet. Sci.*, 5, 397-447.
- Evans, B.W. and Frost, B.R. (1975) Chrome-spinel in progressive metamorphism -- a preliminary analysis. *Geochem. Cosmochem. Acta*, 39, 959-972.
- George, R.P. Jr. (1978) Structural petrology of the Olympus ultramafic complex in the Troodos ophiolite, Cyprus. *Geol. Soc. Amer. Bull.*, 89, 845-865.
- Giese, P. (1962) Die Struktur der Erdkruste im Bereich der Ivrea Zone. *Schweiz. Mineral. Petrog. Mitt.*, 48, 261-284.
- Goullaud, L. (1977) Structure and petrology in the Trinity mafic-ultramafic complex, Klamath Mountains, Northern California. In Geology of the Klamath Mountains, Northern California (eds. Lindsley-Griffin, N. and Kramer, J.C.), prepared for the 73rd annual meeting of the Cordilleran Section, *Geol. Soc. Amer.*, 112-133.
- Green, D.H. (1963) Alumina content of enstatite in a Venezuelan high-temperature peridotite. *Geol. Soc. Amer. Bull.*, 74, 1397-1402.
- Green, D.H. (1964) Petrogenesis of the high-temperature peridotite intrusion in the Lizard area, Cornwall. *Jour. Petrol.*, 5, part 1, 134-188.
- Green, D.H. (1973) Experimental melting studies on model upper mantle compositions at high pressure under both water-saturated and water-undersaturated conditions. *Earth. Planet. Sci. Lett.*, 19, 37-53.
- Green, D.H. and Hibberson, W. (1970) The instability of plagioclase in peridotite at high pressure. *Lithos*, 3, 209-221.
- Green, D.H., Hibberson, W.O. and Jaques, A.L. (1979) Petrogenesis of mid-ocean ridge basalts. In The Earth: Its Origin, Structure and Evolution (ed. McElhinney, M.W.), Academic Press, London.
- Green, D.H. and Ringwood, A.E. (1967) The stability fields of aluminous pyroxene peridotite and garnet peridotite and their relevance in the upper mantle structure. *Earth. Planet. Sci. Lett.*, 2, 41-52.
- Griscom, A. (1977) Aeromagnetic and gravity interpretation of the Trinity ophiolite complex, northern California. *Geol. Soc. Abst. with Prog.*, 9(4), 426-427.
- Grover, J.E. and Orville, P.M. (1969) The partitioning of cations between coexisting single- and multi-site phases with application

to the assemblages: orthopyroxene-clinopyroxene and orthopyroxene-olivine. *Geochim. Cosmochim. Acta*, 33, 205-226.

- Gueguen, Y. and Nicolas, A. (1980) Deformation of mantle rocks. In, Ann. Rev. Earth Planet. Sci., 8, 119-144.
- Hamilton, W. (1969) Mesozoic California and the underflow of Pacific Mantle. *Geol. Soc. Amer. Bull.*, 80, 2409-2430.
- Hamilton, W. (1978) Mesozoic tectonics of the western United States. In Mesozoic Paleogeography of the Western United States (eds. Howell, D.G. and McDougall, K.A.), Pacific Section of Economic Paleontologists and Mineralogists, Pacific Coast Paleogeography Symposium, 2, 33-70.
- Harris, P.G. (1957) Zone refining and the origin of potassic basalts. *Geochim. Cosmochim. Acta*, 12, 195-208.
- Himmelberg, G.R. and Coleman, R.G. (1968) Chemistry of primary minerals and rocks from the Red Mountain--Del Puerto ultramafic mass, California. U.S. Geol. Surv. Prof. Paper 600-C, C18-C26.
- Hess, H.H. (1938) A primary peridotite magma. *Am. J. Sci.*, 35, 321-344.
- Hess, H.H. (1955) Serpentes, orogeny and epeirogeny. Geol. Soc. Amer. Spec. Paper 62, 391-408.
- Hinds, N.E.A. (1935) Mesozoic and Cenozoic eruptive rocks of the southern Klamath Mountains, California. *Calif. Univ. Div. Geol. Sci. Bull.*, 23, 313-380.
- Hopson, C.A., Coleman, R.G., Gregory, R.T., Pallister, J.S. and Bailey, E.H. (in press) Geologic section through the Samail ophiolite and associated rocks along a Muscat-Ibra transect, southeastern Oman Mountains. Submitted to *Jour. Geophys. Res.*
- Hopson, C.A., Pallister, J.S. and Coleman R.G. (1979) Petrologic processes at oceanic crust-mantle boundary, southeastern Samail ophiolite, Oman. *Tans. Amer. Geophys. Union*, 60, 962.
- Hotz, P.E. (1973a) Blueschist metamorphism in the Yreka-Fort Jones area, northeastern Klamath Mountains, California. *U.S. Geol. Surv. Jour. Res.*, 1, 53-61.
- Hotz, P.E. (1973b) Blueschist metamorphism in the Yreka-Fort Jones area, northeastern Klamath Mountains, California. *Geol. Soc. Amer. Abst. with Prog.*, 5(1), 59-60.
- Irvine, T.N. (1967) Chromian spinel as a petrogenetic indicator; part 2, petrologic applications. *Can. Jour. Earth. Sci.*, 4, 71-103.
- Irvine, T.N. and Findlay, T.C. (1972) Alpine peridotite with particular reference to the Bay of Islands Complex. In The Ancient Ocean Lithosphere, Ottawa, Can. Dept. Energy, Mines and Resources,

Earth Physics Branch, 43, 97-126.

Irvine, T.N. (1980) Density current models of tectonic processes. Yb. Carnegie Inst., Wash., 78, 450-460.

Irwin, W.P. (1960) Geologic reconnaissance of the northern Coast Ranges and Klamath Mountains, California, with a summary of the mineral resources. Calif. Div. Mines. Bull. 179.

Irwin, W.P. (1963) Preliminary geologic map of the Weaverville quadrangle, California. U.S. Geol. Surv. Min. Invest. Field Studies Map MF-275. 1:62,500.

Irwin, W.P. (1966) Geology of the Klamath Mountains Province. Cal. Div. Mines. and Geol. Bull., 190, 19-38.

Irwin, W.P. (1972) Terranes of the western Paleozoic and Triassic belt in the southern Klamath Mountains, California. U.S. Geol. Survey Prof. Paper 800-C, C103-C111.

Irwin, W.P. (1977a) Review of Paleozoic rocks of the Klamath Mountains. In Paleozoic Paleogeography of the Western United States, Pacific Section, Society of Economic Paleontologists and Mineralogists, Pacific Coast Paleogeography Symposium 1.

Irwin, W.P. (1977b) Ophiolitic terranes of California, Oregon, and Nevada. In North American Ophiolites (eds. Coleman, R.G. and Irwin, W.P.), Oregon Dept. Geol. Min. Ind. Bull., 95, 75-92.

Irwin, W.P. and Bath, G.P. (1962) Magnetic anomalies and ultramafic rock in northern California. U.S. Geol. Surv. Prof. Paper 450-B, B65-B67.

Irwin, W.P., Jones D.L. and Pessagno, Jr., E.A. (1977) Significance of Mesozoic radiolarians from the pre-Nevadan rocks of the southern Klamath Mountains, California. Geology, 5, 557-562.

Irwin, W.P. and Lipman, P.W. (1962) A regional ultramafic sheet in the eastern Klamath Mountains, California. U.S. Geol. Surv. Prof. Paper 450-C, C18-C21.

IUGS Subcommittee of the Systematics of Igneous Rocks (1973) Classification and nomenclature of plutonic rocks: recommendations. N. Jb. Mineral. Mh., 4, 149-164.

Jacobsen, S.B. and Wasserburg G.J. (1979) Nd and Sr isotopic study of the Bay of Islands Ophiolite Complex and the evolution of the source of midocean ridge basalts. Jour. Geophys. Res., 84, 7429-7445.

Jackson, E.D. (1969) The cyclic unit in layered intrusions -- a comparison of repetitive stratigraphy in the ultramafic parts of the Stillwater, Muskox, Great Kyke and Bushveld complexes. In

Symposium on the Bushveld Igneous Complex and Other Layered Intrusions, Geol. Soc. S. Africa, Spec. Pub. 1.

- Juteau, T. Nicolas, A., Dubussey, J., Frichard, J.C. and Bouchez, J.L. (1977) Structural relationships in the Antalya ophiolite complex, Turkey: Possible model for an oceanic ridge. Geol. Soc. Amer. Bull., 88, 1740-1748.
- Kinkel, A.R. Jr., Hall, W.E. and Albers, J.P. (1956) Geology and base-metal deposits of West Shasta copper-zinc district, Shasta County, California. U.S. Geol. Surv. Prof. Paper 285, 156 p.
- Kornprobst, J. (1969) Le massif ultrabasic des Beni Bouchera (Rif Interne, Maroc). Contr. Mineral. Petrol., 23, 283-322.
- Kupfer, D.H. (1962) Structure of Morton Salt Company mine, Weeks Island salt dome, Louisiana: Am. Assoc. Petrol. Geol. Bull., 46, 1460-1467.
- Kushiro, I. (1964) The system diopside-forsterite-enstatite at 20 kilobars. Yb. Carnegie Inst., Wash., 63, 101.
- Kushiro, I. and Shairer, J.F. (1963) New data on the system diopside-forsterite-silica. Yb. Carnegie Inst., Wash., 62, 95.
- Kushiro, I. and Yoder, H.S. (1974) Formation of eclogite from garnet lherzolite; liquidous reactions in a portion of the system $MgSiO_3$ - $CaSiO_3$ - Al_2O_3 at high pressures. Yb. Carnegie Inst., 73, 26-269.
- Kushiro, I. and Yoder, H.S. (1966) Anorthite-forsterite and anorthite-enstatite reactions and their bearing on the basalt-eclogite transformation. Jour. Petrol., 7, 337-362.
- LaFehr, T.R. (1966) Gravity in the eastern Klamath Mountains, California. Geol. Soc. Amer. Bull., 77, 1177-1190.
- Lahee, F.H. (1961) Field Geology. McGraw-Hill Book Co., New York, 6th printing.
- Lanphere, M.A., Irwin, W.P. and Hotz, P.E. (1968) Isotopic age of the Nevadan orogeny and older plutonic and metamorphic events in the Klamath Mountains, California. Geol. Soc. Amer. Bull., 79, 1027-1052,
- Lindsley, D.H. and Dixon, S.A. (1976) Diopside-enstatite equilibria at 850 to 1400 C, 5 to 35 kb. Am. Jour. Sci., 276, 1285-1301.
- Lindsley-Griffin, N. (1977) The Trinity ophiolite, Klamath Mountains, California. In North American Ophiolites (eds. Coleman; R.G. and Irwin, W.P.), Oregon Dept. Geol. Min. Ind. Bull., 95, 107-120.
- Lipman, P.W. (1963) Gibson Peak pluton: A discordant composite intrusion in the southeastern Trinity Alps, northern California. Geol. Soc. Amer. Bull., 74, 1259-1280.

- Lipman, P.W. (1964) Structure and origin of an ultramafic pluton in the Klamath Mountains, California. *Amer. Jour. Sci.*, 262, 199-222.
- Loney, R.A., Himmelberg, G.R. and Coleman, R.G. (1971) Structure and petrology of the alpine-type peridotite and Burro Mountain, California, USA. *J. Petrol.*, 12, 245-309.
- Loomis, T.P. (1972) Diapiric emplacement of the Ronda ultramafic intrusion, southern Spain. *Geol. Soc. Am. Bull.*, 83, 2475-2496.
- Loomis, T.P. (1975) Tertiary mantle diapirism, orogeny, and plate tectonics east of the Strait of Gibraltar. *Am. J. Sci.*, 275, 1-30.
- MacGregor, I.D. (1974) The system $MgO-Al_2O_3-SiO_2$: Solubility of Al_2O_3 in enstatite for spinel and garnet peridotite compositions. *Amer. Min.*, 59, 110-119.
- Malpas, J. (1977) Petrologic and tectonic significance of Newfoundland ophiolites, with examples from the Bay of Islands. In *North American Ophiolites* (eds. Coleman, R.G. and Irwin, W.P.), Oregon Dept. Geol. Min. Ind. Bull., 95, 107-120.
- Maltman, A.J. (1978) Serpentinite textures in Anglesey, North Wales, United Kingdom. *Geol. Soc. Amer. Bull.*, 89, 972-980.
- Mattinson, J.M. and Hopson, C.A. (1972) Paleozoic ages of rocks from ophiolite complexes in Washington and northern California. *Trans. Amer. Geophys. Union*, 53(4), 543.
- McCulloch, M.T., Gregory, R.T., Wasserburg, G.J. and Taylor, H.P. (1980) A neodymium, strontium and oxygen isotopic study of the Cretaceous Samail Ophiolite and implications from the petrogenesis and seawater-hydrothermal alteration of oceanic crust. *Earth Planet. Sci. Lett.*, 46, 201-211.
- McTaggart, K.C. (1971) On the origin of ultramafic rocks. *Geol. Soc. Am. Bull.*, 82, 23-42.
- Medaris, L.G. (1972) High pressure peridotites in southwestern Oregon. *Geol. Soc. Amer. Bull.*, 83, 41-58.
- Medaris, L.G. (1975) Coexisting spinel and silicates in alpine peridotites of the granulite facies. *Geochim. Cosmochim. Acta*, 39, 947-958,
- Meeker, G.P. and Albee, A.L. (1979) Petrologic analysis of surfaces without sample preparation with midinfrared reflectance spectroscopy. *Geol. Soc. Amer. Abs. with Prog.*, 5(1), 97.
- Menzies, M. (1974) Mineralogy and partial melt textures within an ultramafic-mafic body, Greece. *Contr. Mineral. Petrol.*, 42, 273-285.
- Menzies, M. and Allen, C. (1974) Plagioclase lherzolite-residual mantle

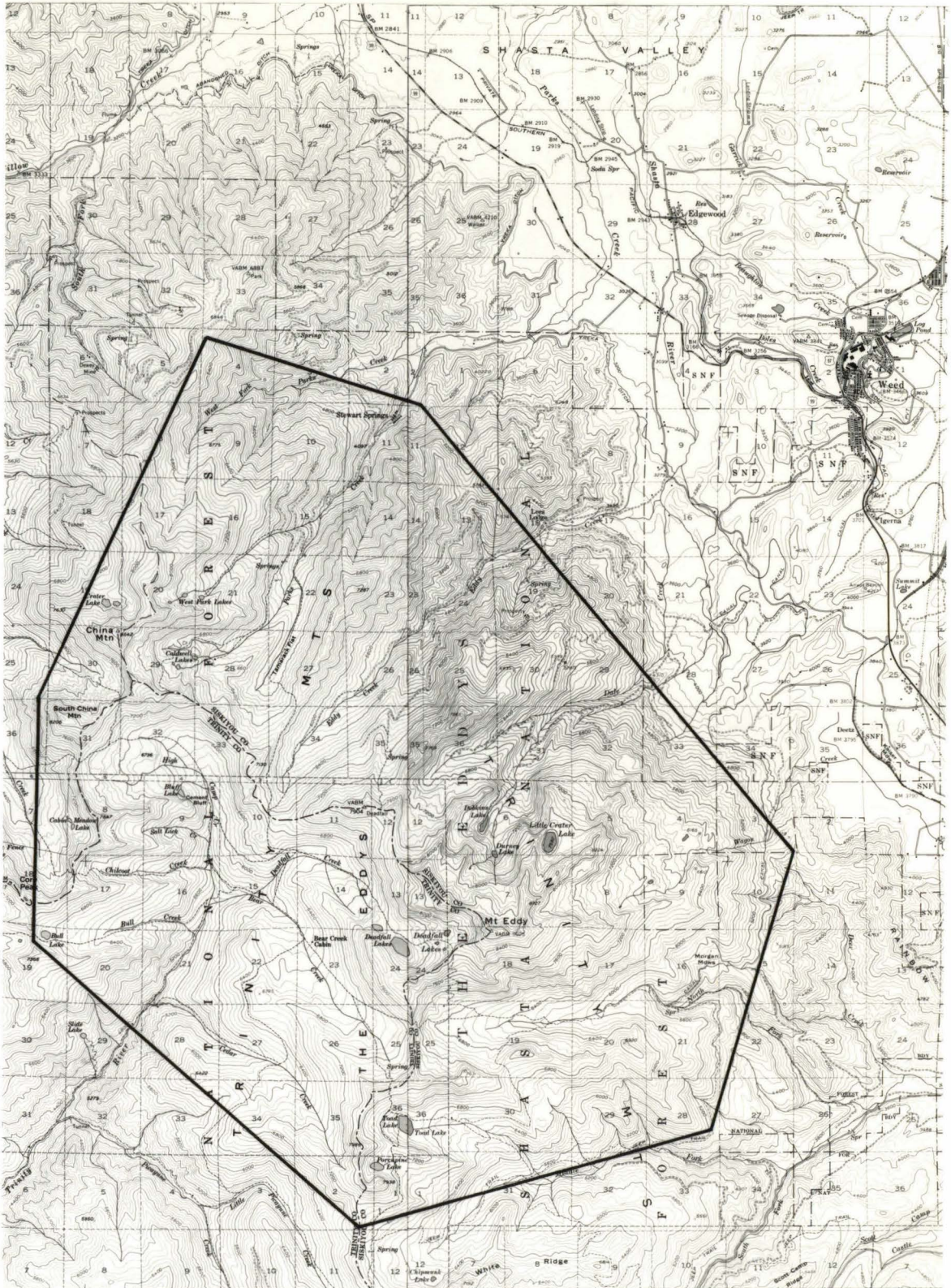
- relationships within two eastern Mediterranean ophiolites. *Contr. Min. Pet.*, 45, 197-213.
- Mercier, J.-C.C. and Carter, N.L. (1975) Pyroxene geotherms. *J. Geophys. Res.*, 80, 3349-3362.
- Mercier, J.-C.C. and Nicolas, A. (1975) Textures and fabrics of upper-mantle peridotites as illustrated by xenoliths from basalts. *J. Petrol.*, 16, 454-487.
- Miyashiro, A (1973) The Troodos ophiolite complex was probably formed in an island arc. *Earth Planet. Sci. Lett.*, 19, 218-224.
- Nehru, C.E. and Wyllie, P.J. (1974) Electron microprobe measurement of pyroxenes coexisting with H₂O-undersaturated liquid in the join CaMgSi₂O₆-Mg₂Si₂O₆-H₂O at 30 kb, with applications to geothermometry. *Contr. Min. Pet.*, 74, 221-228.
- Obata, M. (1976) The solubility of Al₂O₃ in orthopyroxene in spinel and plagioclase peridotites and spinel pyroxenite. *Am. Min.*, 61, 804-816.
- O'Hara, M.J. (1965) Primary magmas and the origin of basalts. *Scot. J. Geol.*, 1, 19-40.
- Penrose Field Conference on Ophiolites, report by the conference participants. In *Geotimes*, Dec., 1972, 24-25.
- Quick, J.E. and Albee, A.L. (1979a) Evidence for partial melting in the Trinity peridotite--A possible "high-temperature" peridotite in the eastern Klamath Mountains, northern California (abstract). *Geol. Soc. Am. Abst. with Prog.*, 11, 123.
- Quick, J.E. and Albee, A.L. (1979b) Dike-wall rock interactions in the Trinity peridotite, northern California--zone refining in the upper mantle (abstract). *Geol. Soc. Am. Abst. with Prog.*, 9, 123.
- Quick, J.E., Albee, A.L. and Quick, G.L. (1980) The structural and petrologic evolution of the Trinity peridotite, eastern Klamath mountains, California (abstract). *Geol. Soc. Am. Abst. with Prog.*, 12, 148.
- Reid, M.J., Gancarz, A.J. and Albee, A.L. (1973) Constrained least-squares analysis of petrologic problems with an application to lunar sample 12040. *Earth Planet. Sci. Lett.*, 17, 433-445.
- Ringwood, A.E. (1966) The chemical composition and origin of the earth. In *Advances in Earth Science* (ed. Hurley, P.M.), MIT Press, Cambridge, Mass., 287-356.
- Ringwood, A.E. (1975) Composition and Petrology of the Earth's Mantle. McGraw-Hill, New York.

- Roeder, P.L. and Emslie, R.F. (1970) Olivine-liquid equilibrium. *Contr. Min. Pet.*, 29, 275-289.
- Rohr, D.M. and Boucot, A.J. (1971) Northern California (Klamath Mountains) pre-late Silurian igneous complex. *Geol. Soc. Amer. Abst. with Prog.*, 3(2), 186.
- Rohr, D.M. and Potter, A.W. (1973) Paleozoic rocks of the Callahan-Gazelle area, Klamath Mountains, northern California. *Geol. Soc. Amer. Abst. with Prog.*, 5(1), 97.
- Sharp, R.P. (1960) Pleistocene glaciation in the Trinity Alps of northern California. *Am. Jour. Sci.*, 258, 305-340.
- Sleep, N. and Toksoz, M.N. (1971) Evolution of marginal basins. *Nature*, 233, 548-550.
- Snoke, A.W., Bowman, H.R. and Herbert A.J. (1977) The Preston Peak ophiolite, Klamath Mountains, California, an immature island arc: petrochemical evidence. *Calif. Div. Mines. Geol. Spec. Report 129*, 67-79.
- Snoke A.W., Quick, J.E. and Bowman H.R. (in review) Bear Mountain igneous complex, Klamath Mountains, California: an ultrabasic to silicic calcalkaline suite.
- Stolper, E. (in review) A phase diagram for mid-ocean ridge basalt: preliminary results and implications for petrogenesis.
- Strand, R.G. (1962) Geologic map of California, Redding Sheet. *Calif. Div. Mines Geol.*. Second printing, 1969.
- Strand, R.G. (1964) Geologic map of California, Weed Sheet. *Calif. Div. Mines Geology*. Second printing, 1973.
- Thayer, T.P. (1960) Some critical differences between alpine-type and stratiform peridotite-gabbro complexes. *21st Intern. Geol. Congr.*, Copenhagen, 13, 247-259.
- Uyeda, S. (1977) Some basic problems in the trench-arc--back-arc system. In Island Arcs, Deep Sea Trenches and Back-Arc Basins (eds. Talwani, M. and Pitman, III, W.C.). *Amer. Geophys. Union*.
- Uyeda, S. and Kanamori, H. (1979) Back-arc opening and the mode of subduction. *Jour. Geophys. Res.*, 84, 1049-1061.
- Vennum, W.R. (1980) Petrology of the Castle Crags pluton, Klamath Mountains, California. *Geol. Soc. Am. Bull.*, 91, 255-258.
- Wager, L.R. and Brown, G.M. (1967) Layered Igneous Rocks. W.H. Freeman and Co., San Francisco. 588 p.
- Walker, D., Longhi, J., and Hays, J.F. (1972) Experimental petrology

- and origin of Fra Mauro rocks and soil. Proc. Lunar Sci. Conf 3rd, 797-817.
- Walker, D., Shibata, T. and Delong, S.E. (1979) Abyssal tholeiites from the Oceanographer Fracture Zone II. Phase equilibria and mixing. Contr. Min. Pet., 70, 111-125.
- Wallawender, M.J. (1976) Petrology and emplacement of the Los Pinos pluton, southern California. Can. Jour. Earth Sci., 13, 1288-1300.
- Wang, C.Y. (1970) Density and constitution of the mantle. Jour. Geophys. Res., 75, 3264-3284.
- Warner, R.D. and Luth W.C. (1974) The diopside-orthoenstatite two phase region in the system $\text{CaMgSi}_2\text{O}_6\text{-Mg}_2\text{Si}_2\text{O}_6$. Am. Min., 59, 98-109.
- Wells, P.R.A. (1977) Pyroxene thermometry in simple and complex systems. Contr. Min. Pet., 62, 129-139.
- White, R.W. (1966) ultramafic inclusions in basaltic rocks from Hawaii. Contr. Mineral. Petrol., 12, 245-314.
- Williams, H. (1971) Mafic-ultramafic complexes in west Newfoundland Appalachians and the evidence for their transportation: a review and interim report. Geol. Ass. Can. Proc., 24, 9-25.
- Wood, B.J. and Banno S. (1973) Garnet-orthopyroxene and orthopyroxene-clinopyroxene relationships in simple and complex systems. Contr. Min. Pet., 42, 109-124.
- Woollard, G.P. (1970) Evaluation of the isostatic mechanism and role of mineralogic transformations from seismic and gravity data. Phys. Earth. Planet. Interiors, 3, 484-498.
- Yoder, H.S. Jr. (1976) Generation of Basaltic Magma. Natl. Acad. Sci., Washington, D.C., 265.

APPENDIX TO PART I

Figure 50: Topographic map of the study area showing the boundary of the study area, place names and location relative to the nearest city, Weed, California. North is toward the top of the map. The dashed square grid is in approximate square miles.



PART II:

PETROGENESIS OF LUNAR BRECCIA 12013

INTRODUCTION

Sample 12013 is unique among the returned samples of lunar breccia in both bulk chemistry and mineralogy. The rock is extremely rich in incompatible elements (K, REE, P, U, Th, Pb, Ba, Rb, Zr, and Nb) relative to other lunar samples, and it contains abundant "granitic" material composed of silica minerals and potassium feldspar. These characteristics were recognized during preliminary examination (LSPET, 1970), and because of the importance of the sample, it was designated for immediate study by a consortium of investigators. The preliminary results of this consortium were published in a special issue of Earth and Planetary Science Letters (EPSL) in September, 1970, less than 10 months after the Apollo 12 samples were removed from their sample return containers in Houston. Later Apollo missions returned other rocks with high incompatible-element abundances (e.g., 72255, 15405, 73215). Only a few of these rocks, however, have incompatible-element concentrations approaching those in 12013, and none contain more "granitic" material. As a result, 12013 has come to be regarded as the type specimen of highly evolved lunar rocks, and is certainly one of the most significant samples for placing constraints on the origin of lunar "granite."

Previous investigations of 12013 employed a wide spectrum of methods. The papers published by the 12013 consortium in the EPSL special issue report data in the following fields: petrology and mineralogy (Drake et al., 1970; Albee et al., 1970; Gay et al., 1970); charged particle tracks (Burnett et al., 1970; Schnetzler et al., 1970); instrumental neutron activation analyses for major-, minor-, and trace-element abundances (Wakita and Schmitt, 1970); instrumental neutron activation analyses for O, Si, Al, and Fe abundances (Morgan and Ehmann, 1970);

^{40}Ar - ^{39}Ar stepwise heating (Turner, 1970); atomic absorption and/or isotopic dilution analyses for major-, minor-, and trace-element abundances (Hubbard et al., 1970; Schnetzler et al., 1970); U-Th-Pb isotopic systematics (Tatsumoto, 1970); rare gas isotopic ratios and abundances (Alexander, 1970; Albee et al., 1970); O and Si isotopic ratios (Taylor and Epstein, 1970); and siderophile-element abundances (Laul et al., 1970). Other studies published shortly after the EPSL report are as follows: a petrographic description (James, 1970); charged particle track studies (Burnett et al., 1971; Haines et al., 1971); and additional ^{40}Ar - ^{39}Ar stepwise heating data (Turner, 1971). More recently, attempts have been made to determine the Pb-Pb ages of zircon and apatite grains in 12013,14 using ion microprobe mass analysis (Hinthorne and Anderson, 1974; Anderson and Hinthorne, 1973).

Since 1970-71, much has been learned about lunar breccia-forming processes and about the fragments of lunar "granites" that are found in other breccias. We have restudied 12013 in light of this information. This paper presents detailed petrologic and mineralogic descriptions of the rock and a discussion of its genesis and history. Summaries and preliminary reports of some of the data given herein were presented by Quick and Albee (1976), Ma et al. (1977), and Quick et al. (1977). Another aspect of our restudy of the rock, an estimation of trace-element abundances in melt-derived lithologies by combined instrumental neutron activation analysis and petrographic study, was presented by Quick et al. (1977).

GEOLOGY OF THE LANDING SITE

The geology of the Apollo 12 landing site is discussed in detail by Shoemaker *et al.* (1970) in the Apollo 12 Preliminary Science Report. The mission landed in the eastern part of Oceanus Procellarum at 23.4°W and 3.2°S. The site is without striking topographic features, the largest being craters 50-400 m wide and small mounds a few meters high. It is underlain by a regolith of fragmental material derived, for the most part, from mare basalt of Oceanus Procellarum.

Two observations are particularly significant to sample 12013. First, the landing site was located on a broad, high albedo ray emanating from the Crater Copernicus approximately 370 km to the north. Second, the regolith underlying the site was layered with light gray material covered by a thin veneer of lower-albedo material. Locally, patches of the light gray material were exposed at the surface and may be the same material that defines the ray seen from space. Therefore, although the landing site is underlain by mostly mare basalt of Oceanus Procellarum, it is possible that ejecta from Crater Copernicus was also sampled. No record of the actual collection of 12013 exists, so that it is not possible to determine if it was sampled from the light gray layer.

EXPERIMENTAL TECHNIQUES

Four types of data are presented in this paper. These are: (1) petrographic descriptions; (2) volume proportions of clasts, derived from point-count data, graciously supplied by Odette James; (3) the results of more than 1000 electron microprobe analyses on individual phases; and (4) "whole-rock" chemical compositions obtained by over 100 defocused-beam electron microprobe analyses of fine grained rock fragments and by automated electron microprobe analysis of 4 coarse grained rock fragments. All data were collected from polished thin sections 12013,13, 12013,14, and 12013,15.

The microprobe investigations were conducted with an automated MAC-5-SA3 electron microprobe equipped with three crystal spectrometers and an ORTEC Si(Li) solid state detector. For control and on-line data processing, the crystal spectrometers are interfaced to a PDP-8/L computer, and the solid-state detector is interfaced to an NS880 multichannel analyzer and a PDP-11 computer. The compositions of individual mineral grains were obtained by wave length dispersive analysis, using the crystal spectrometers and the procedures described by Chodos *et al.* (1973); all analyses were made for 9 to 15 elements. Operating conditions were 15kV accelerating voltage, 0.05 μ A sample current on brass and spot diameters of 2-15 μ m, except where analyses of very small grains were required; in these cases, analyses were performed at 0.005 μ m sample current to minimize spot size.

Defocused-beam "whole-rock" analyses were performed using spot diameters ranging from 30 μ m to 300 μ m. The areas smaller than 50 μ m across were analyzed with both the crystal spectrometers and the solid-state detector, and the areas larger than 50 μ m across were analyzed using only

the solid-state detector. The data reduction procedures for the defocused-beam analyses were as outlined by Albee et al. (1977). Defocused-beam analyses run simultaneously with both the crystal spectrometers and the solid-state detector agree within the uncertainties inherent in broad beam analyses (Albee et al., in press).

HAND SPECIMEN DESCRIPTION

Breccia 12013 is a small subangular rock about 3x4x5 cm in size. Its exterior surface is mottled black, white, and light gray, and is somewhat vuggy. Micrometeorite pits are present on all but one surface.

Figures 1 and 2 illustrate the relationships between the various materials that make up the rock. Figure 1 is a photograph of one of the sawed surfaces of slab 12013,10; this is the slab that was dissected to yield subsamples for chemical and isotopic studies. Figure 2 is a composite photograph of the three polished thin sections that were made from the adjacent slab, 12013,9. As can be seen in Figures 1 and 2, the sample is made up of two lithologies: a mottled gray and white lithology, and a black lithology. Previous authors regarded the gray and white materials within the mottled lithology as separate lithologies because small amounts of white material are also present within the black lithology. The black lithology, the gray material within the mottled lithology, and the white material, respectively, were given the following names in earlier publications: dark, gray, and light lithologies (Albee et al., 1970); dark lithology, light lithology, and granitic component (Drake et al., 1970); black material, gray material, and white material (Hubbard et al., 1970; Schnetzler et al., 1970); and dark gray fragment aggregate, gray fragment aggregate, and felsite (James, 1970). This reexamination indicates that the white material is an essential component of the mottled lithology. Therefore, the old three-fold lithologic description of 12013 is abandoned in favor of a description in terms of two lithologies: a gray breccia, corresponding to the mottled gray and white lithology; and a black breccia, corresponding to the black lithology.

12013 is a complex mixture of these two breccias. The gray breccia

Figure 1: Sawed surface of slab 12013,10, which was dissected at the California Institute of Technology for chemical and isotopic studies. The slab is about 5 cm long and about 4 mm thick. Note distribution of black and gray breccias.

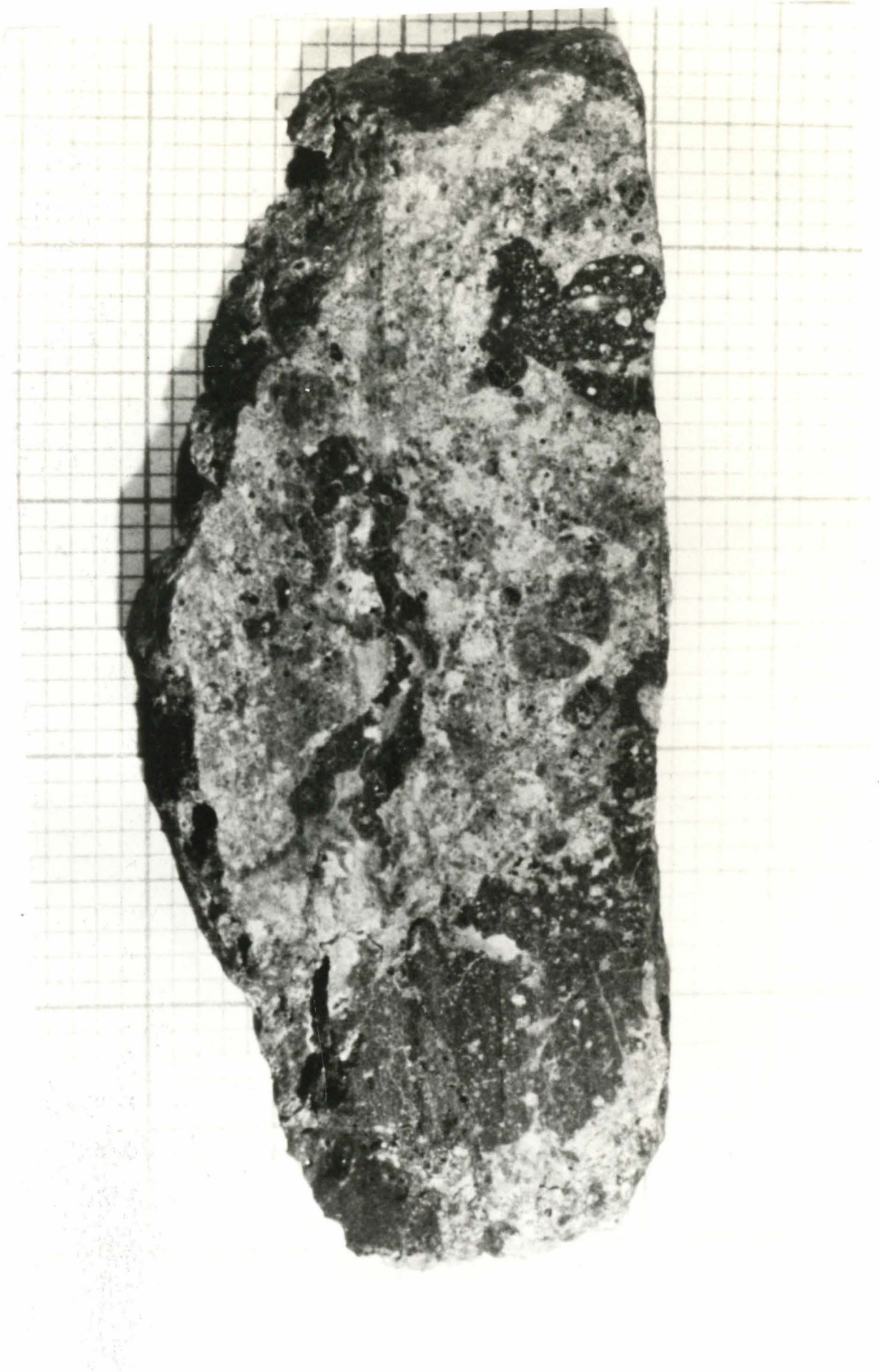


Figure 2: Thin sections made from slab 12013,9. This slab was facing slab illustrated in Figure 1. From top to bottom, the thin sections are numbered 12013,13, 12013,15 and 12013,14. The composite is approximately 4.5 cm long.



is the dominant lithology in the hand specimen; it constitutes approximately 80 percent of slabs 12013,10 and 12013,9. The black breccia forms irregular patches and globules that are partly to completely enclosed by the gray breccia and are concentrated near the edges of the hand specimen. Because of the small size of the sample, it is not possible to determine whether a large sample would consist predominantly of gray breccia or of black breccia. As some isolated black breccia patches are completely surrounded by gray breccia, but the reverse is not observed, we consider the former alternative to be more likely.

The forms and internal structures of the black breccia bodies are variable. One black breccia patch, 6mm across, has smooth cusped contacts with the surrounding gray breccia and contains abundant tiny vesicles and globules of white material. The largest black breccia patch, 1cm across, has irregular contacts with the gray breccia, contains abundant angular to subangular clasts, and is cut by a veinlet of white material about 8mm long. A third black breccia patch forms an irregular streak almost 2cm long and about 3mm thick that is bisected by a stringer of white material.

PETROGRAPHY

PETROGRAPHIC OVERVIEWIntroduction

An overview prefaces the detailed petrographic description because of the complexity of sample 12013. This overview is intended to distill the salient points of the petrography and to provide a background for the following details.

The clasts that comprise 12013 are divided in the following description into mineral and lithic clasts, depending on whether they are composed of more than one mineral. It is emphasized that the term, lithic clast, is applied to all phase aggregates regardless of size, and that these aggregates are assigned lithologic names although they may be too small to be representative of the protolith from which they were derived.

Gray Breccia

The bulk gray breccia (Figure 2 and 4) is made up of a patchy mixture of two components: (1) a white material consisting of a melt-derived intergrowth of K-feldspar and silica materials; and (2) a gray material consisting of an aggregate of lithic and mineral fragments. The white material is termed felsite. In most places the silica mineral is quartz, but locally it is tridymite. The silica minerals form needle-like grains and the K-feldspar forms anhedral grains that envelop these needles (Figure 6). The bulk of the gray aggregate is made up of fragments ranging from $\sim 10 \mu\text{m}$ to $\sim 8\text{mm}$ across and having a seriate size distribution. The interstices between the fragments are filled by a fine-grained intergrowth of K-feldspar and silica minerals that is identical to the felsite patches.

The gray breccia, taken as a whole, is a patchy but intimate mixture of the above two components. For the most part, it consists of

20-200 μ m irregular patches of felsite and gray aggregate. Locally, however, larger patches of each of the two components are present. In some areas, patches of gray aggregate as much as 500 μ m across are completely free of felsite (Figure 5). In other areas, felsite forms 200-500 μ m sharply bounded patches with subangular outlines (Figure 5); these patches are completely devoid of fragmental material. Locally, patches of felsite that contain no fragmental material grade into interstitial felsite, so that in many areas (e.g., most of 12013,13) the two types of felsite cannot be easily distinguished.

Most of the fragments in the gray breccia were derived from a suite of related gabbros and basalts. For the purposes of description and mapping, these fragments are divided into two size fractions: clasts ($\geq 140\mu$ m) and matrix ($< 140\mu$ m). The population of $> 140\mu$ m clasts is dominated by fragments of gabbroic and basaltic rocks; fragments of plagioclase, pyroxene, tonalite, and ANT-suite rocks are present but subordinate in abundance. In the matrix size fraction, plagioclase is the most abundant type of fragment; less abundant types are low-Ca pyroxene, high-Ca pyroxene, ilmenite and Cr-spinel. The grain sizes and mineral compositions are compatible with derivation of most of the mineral fragments from the same basaltic and gabbroic rocks that were the source of the $> 140\mu$ m lithic clasts.

Primary clast textures and outlines have been obscured by reaction with interstitial felsite and by recrystallization. Felsite has reacted with olivine to produce orthopyroxene, and with ilmenite to produce high-Nb ilmenite. Plagioclase fragments in contact with felsite are rimmed by K-feldspar, and some plagioclase grains have been largely replaced by K-feldspar.

Black Breccia

The black breccia is an aggregate of mineral and lithic fragments set in a groundmass of minute grain size (Figures 21,22). Lithic clasts in the black breccia are mostly ANT-suite rocks, quartzofeldspathic rocks, and basalt. Mineral clasts are plagioclase, pyroxene, olivine, devitrified maskelinite, ilmenite, zircon, apatite, and whitlockite. The term groundmass, as used by James (1976), describes a very fine-grained component of a breccia that is texturally distinct from the lithic and mineral fragments that it encloses. The groundmass of the 12013 black breccia is a equigranular intergrowth of $\leq 5\mu\text{m}$ grains of plagioclase and low-Ca pyroxene, with minor amounts of other phases (Figure 22). Locally abundant vesicles indicate that this intergrowth crystallized from a melt. This intergrowth makes up approximately 50% by volume of the black breccia.

The fragments in the black breccia range from 2mm to $< 10\mu\text{m}$ across and have a seriate size distribution. Primary fragment textures and fragment boundaries are not greatly obscured by post-consolidation recrystallization and reaction.

Felsite, which is mineralogically and texturally like the felsite in the gray breccia, is present in the black breccia, but it is less abundant and it has a different mode of occurrence. It forms bodies that have sharp, well-defined contacts with the clasts and groundmass, and nowhere does it pervade the surrounding material as it does in the gray breccia. The mode of occurrence of the felsite is different in different parts of the black breccia. In one area, it forms isolated spheroidal blebs; in another area, it forms isolated patches that have subangular

outlines. It also forms thin veinlets that intrude the breccia, cutting both groundmass and clasts.

Major distinctions between the black and gray breccias

There are several important differences between the clast populations of the black and gray breccias. First, the relative proportions of different types of clasts are different in the two breccias. Fragments of plagioclase are the most abundant clasts in the black breccia, but lithic fragments are the most abundant clasts in the gray breccia. In the gray breccia, the most abundant lithic clasts are of gabbro and basalt, and clasts of quartzofeldspathic rocks and norite are rare; in the black breccia, the reverse is true. Fragments of apatite and zircon are important, though minor, constituents of the clast suite in the black breccia but are absent from the gray breccia. Second, as will be detailed in the next section, there are systematic differences in composition between the mineral clasts in the two breccias. Clasts of relatively sodic plagioclase, An_{50-70} , are abundant in the black breccia but are rare in the gray breccia. Clasts of high-Ca pyroxene clasts are much more abundant, and tend to have more Fe-rich compositions, in the black breccia than in the gray breccia. Clasts of olivine in the black breccia have a much wider range in Fo content than in the gray breccia. Third, almost all plagioclase in the gray breccia is turbid, due to the presence of abundant minute inclusions of pyroxene, but most of the plagioclase in the black breccia is clear and inclusion free. These contrasts demonstrate that the black and the gray breccias do not differ simply by degree of infiltration by felsite as suggested previously (Albee et al., 1970).

The color difference between the two breccias is a function of their mineralogies and grain sizes. The black breccia is darker than the gray breccia because its groundmass is finer grained than the matrix of the gray breccia and contains abundant disseminated $< 5\mu\text{m}$ grains of ilmenite and FeS.

DETAILED PETROLOGY OF THE GRAY BRECCIA

Introduction

To facilitate description of this complex lithology, the results of our microprobe and petrographic study are condensed in tables and graphs, and a discussion of these tables and graphs is offered in the text. The clasts $> 140\mu\text{m}$ across have been studied in detail, and have been classified as mineral clasts or as belonging to one of nine categories of mineralogically and/or texturally distinct lithic clasts. The modal proportions of the various types of $> 140\mu\text{m}$ clasts have been determined by point counting, and the results are presented in Table 1. The different types of lithic clasts are briefly described in Table 2, their textures are illustrated in Figure 3, and the whole-rock compositions derived from defocused-beam microprobe analyses and electron microprobe point count analyses are compiled in Table 3 and presented graphically in Figures 14 and 15. Representative compositions of their minerals are listed in Tables 5-9 and all mineral analyses are presented graphically in Figures 7-11. The mineral clasts are briefly described in Table 4, representative analyses compiled in Tables 5-9, and all analyses are presented graphically in Figures 7-11.

Lithic Clasts $> 140\mu\text{m}$

Lithic clasts comprise about 80 volume percent of the $> 140\mu\text{m}$

clasts in the gray breccia. The most abundant types are basalts, gabbros, and granulated olivine gabbros. The basalts have been subdivided into subophitic basalts, bladed basalts, basaltic "chondrules," and basaltic aphanites. The basalts comprise about 50 volume percent of the clasts, the gabbros about 15 volume percent, and the granulated olivine gabbros about 15 volume percent. Lithic clasts present in minor amounts are of tonalite, granulated norite, and ANT-suite hornfels.

No statistical treatment of lithic clast size has been made because of uncertainties in identifying the boundaries of granulated and recrystallized clasts. Gabbro, granulated olivine gabbro, and granulated norite form the largest clasts, which are as much as 4mm across. Basalt forms the next largest clasts, most ranging from ~ 250 μ m to ~ 500 μ m across. Tonalite and ANT-suite hornfels make up the smallest lithic fragments, < 250 μ m across.

Gabbro and basalt: These clasts form a gradational series in terms of grain size, clast size, and abundance (Figure 3). The members of this series are, in order of decreasing average grain size, clast size, and abundance: gabbros and granulated olivine gabbros; subophitic basalts; bladed basalts; basaltic "chondrules"; and basaltic aphanites. The most abundant minerals in all of these rocks are plagioclase and pyroxene, but some of the rocks also contain abundant olivine. Cr-spinel and ilmenite are ubiquitous accessory minerals. The major- and trace-element compositions of these minerals are similar in all these rocks, but there are some minor systematic variations in mineralogy and mineral chemistry that correlate with changes in grain size. First, the modal abundance of olivine decreases with decreasing grain size. Olivine constitutes as

much as 30 percent of the granulated olivine gabbros, makes up 0-20 percent of the gabbros, is present in trace amounts in the subophitic basalts, and is absent in the finer-grained basalts. Second, the plagioclase tends to be slightly more calcic in the coarser-grained clasts (Figure 7). Third, there is a tendency for the pyroxene to be slightly more Fe-rich in the basalts than in the gabbros (Figure 8).

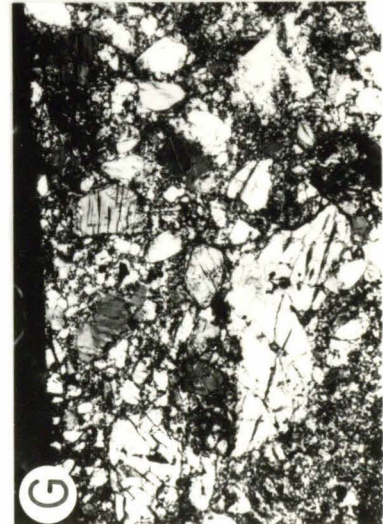
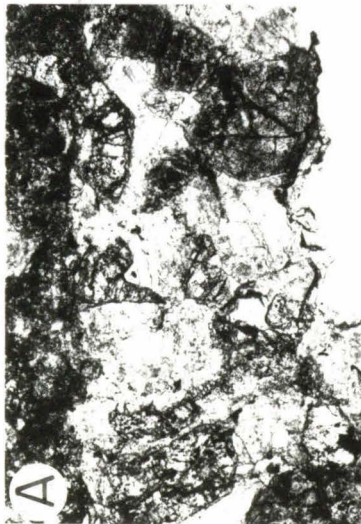
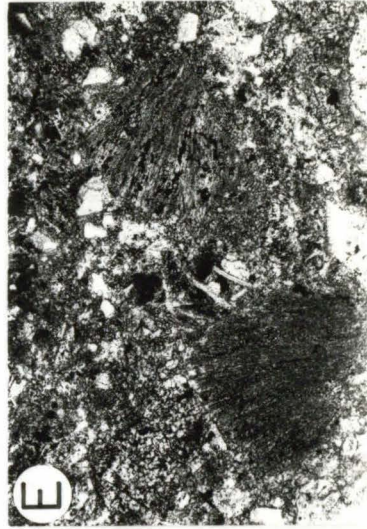
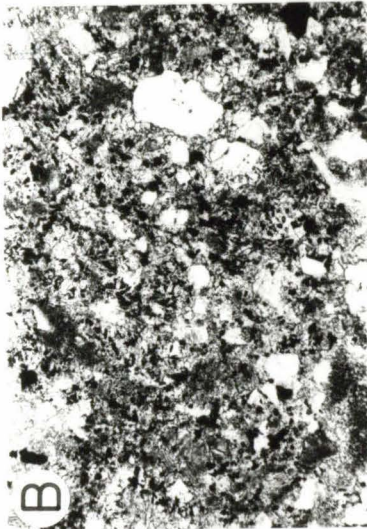
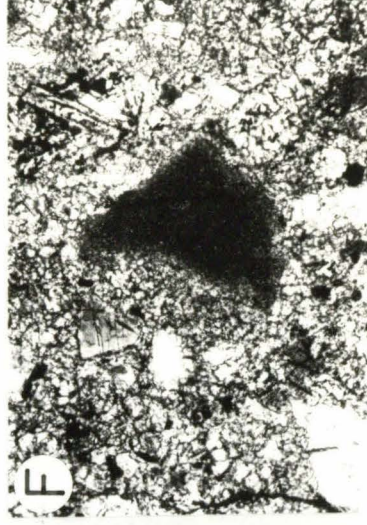
Most of the basalt clasts are similar in bulk composition (Table 3). Figure 15 illustrates that most are slightly quartz-normative; the single basalt clast that is olivine-normative is a relatively coarse-grained subophitic basalt. In contrast, the gabbro clasts are strongly olivine-normative. However, Figure 15 illustrates that the compositions of the basalts could be derived from that of the gabbros by removal of olivine similar in composition to the olivine in the gabbro clasts.

Granulated Norite: One large (~ 2mm) clast of granulated norite is in the gray breccia (Figure 3). Its primary textures have been completely destroyed by cataclasis, and it consists of a porous aggregate of angular fragments. It has a 250 μ m rim that is recrystallized to a nonporous inequigranular mosaic. The rock is virtually bimineralic and is made up almost entirely of plagioclase and pyroxene with only trace amounts of olivine. The plagioclase is extremely Ca-rich and homogeneous (Figure 7), and the orthopyroxene is relatively Mg-rich (Figure 8).

This clast is texturally and mineralogically distinct from all other lithic clasts in the gray breccia, but it is similar to granulated norite clasts that are common in the black breccia. The similar clasts that are abundant in the black breccia are concentrated near the black breccia-gray breccia contacts. Although this clast has no apparent

Figure 3: Photomicrographs illustrating textures of lithic clasts in the gray breccia. Numbers in parentheses refer to the length of the long axis of the photomicrographs. All photos taken with plane transmitted light unless otherwise indicated. (Photography by O. B. James.)

- (A) Gabbro (2.2 mm).
- (B) Granulated olivine gabbro (1.75 mm).
- (C) Subophitic basalt (2.2 mm).
- (D) Bladed basalt (1.75 mm).
- (E) Basaltic chondrules (2.2 mm).
- (F) Basaltic aphanite (0.79 mm).
- (G) Granulated norite (1.75 mm).
- (H) Tonalite (1.75 mm). Crossed nicols.
- (I) ANT-suite hornfels (0.88 mm). Crossed nicols.



contacts with black breccia in the thin section, it may be a component of the black breccia that penetrated the gray breccia during the breccia-forming process.

Tonalite: One small $\sim 250\mu\text{m}$ tonalite clast occurs in the gray breccia (Figure 3). This clast consists of two phases not present in other lithic clasts in the gray breccia: quartz, and inclusion-free, relatively sodic plagioclase. Like the clast of granulated norite, it is mineralogically distinct from all other lithic clasts in the gray breccia but is similar to clasts present in greater abundance in the black breccia. Unlike the granulated norite, however, the tonalite clast is far removed from patches of black breccia and is clearly a component, although a minor one, of the gray breccia.

ANT-suite melt-rock: One small ($\sim 250\mu\text{m}$) clast of ANT-suite hornfels occurs in the gray breccia. This clast differs texturally from the other lithic clasts in the gray breccia; interstices between blocky grains of plagioclase and plagioclase laths are filled by mosaic-textured pyroxene grains, K-rich mesostasis, and whitlockite grains (Figure 3).

Mineral Clasts $> 140\mu\text{m}$

The textures and compositions of most mineral clasts suggest that they were derived from rocks of the basalt-gabbro lithic clast suite. The largest mineral clasts are about the same size as the largest mineral grains in the gabbro clasts, and the relative proportions of the clasts of the different minerals are similar to the relative proportions of the same phases in the gabbro and basalt clasts (Table 1). Most of the mineral clasts are turbid, as are the mineral grains in the basalt and gabbro clasts. Most of the silicate mineral clasts have compositions

that fall within the ranges shown by the same minerals in the basalt and gabbro clasts (Figures 7 and 8).

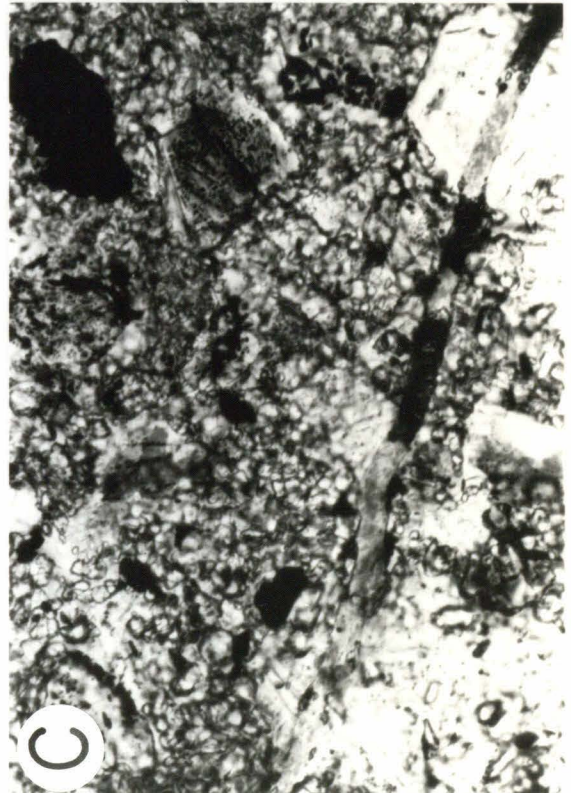
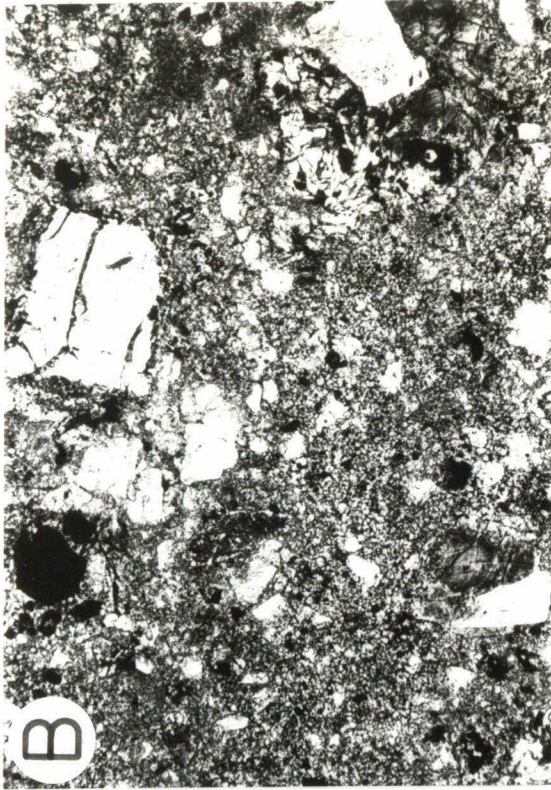
A small proportion of the mineral clasts have compositions that indicate they were derived from source rocks other than those of the basalt-gabbro suite. These are: plagioclase clasts that are more sodic than $\sim \text{An}_{70}$, and low-Ca pyroxene clasts that are more magnesian than $\sim \text{En}_{70}$. The plagioclase clasts are small ($< 200\mu\text{m}$) and inclusion free, suggesting that they may have been derived from the same source rocks as the tonalite clast. The low-Ca pyroxene clasts are also clear and inclusion free, and their compositions suggest derivation from rocks related to the granulated norite clast.

Deformation Textures in Clasts

Many lithic clasts and some mineral clasts were deformed prior to being incorporated into the breccia. The most common intragranular deformation features in plagioclase are shock-induced undulatory extinction, fractures and small faults offsetting twin lamellae. The most common intragranular deformation features in pyroxene and olivine are healed fractures; pyroxene also contains rare kink bands. In clasts of the basalt-gabbro suite, the extent of deformation increases with increasing grain size. Basaltic aphanites and "chondrules" show no evidence of deformation. Most clasts of variolitic and subophitic basalt contain crushed pyroxene grains intruded by finely granulated plagioclase; and, in many of these clasts, the plagioclase laths are bent or broken or show undulatory extinction. Clasts of gabbro show deformation features like those of the basalts, but also have undergone more intense cataclasis. Clasts of granulated olivine gabbro have undergone extreme cataclasis so

Figure 4: Textures of matrix and interstitial felsite in the gray breccia. Numbers in parentheses refer to the field of view along the long axis of the photo. (Photography by O. B. James.)

- (A) Representative texture of felsite (0.88 mm). Crossed nicols.
- (B) Representative texture of the gray breccia: large angular clasts set in a matrix of smaller clasts and felsite (2.2 mm). Plane polarized light.
- (C) Matrix of gray breccia showing clasts and interstitial felsite (and a crack) (0.48 mm). Plane polarized light.
- (D) Matrix of gray breccia showing clasts and interstitial felsite (0.35 mm). Plane polarized light.



that primary textures have been nearly obliterated. In the clast of granulated norite, the effects of deformation are somewhat different than those in the clasts of basalt and gabbro; cataclasis has destroyed the primary texture, but the mineral fragments that make up the clast show no intragranular deformation. Detailed descriptions of the deformation and recrystallization features that are typical of individual types of clasts are given in Tables 2 and 4.

Matrix (Clasts < 140 μ m and interstitial felsite)

The matrix is a recrystallized, inequigranular mosaic of subangular to rounded grains that are mostly plagioclase and low-Ca pyroxene (Figure 4). HighCa pyroxene, ilmenite, and Cr-spinel are also present in minor amounts. The grain size ranges from $\sim 1\mu$ m to 140 μ m and averages about 20-30 μ m. In most places the larger fragments touch one another and interstices between them are filled with the smaller fragments and felsite. Locally, the interstitial felsite is abundant, and the fragments appear to "float" in felsite.

The compositions of most of the mineral fragments in the matrix are similar to the compositions of the corresponding phases in the lithic clasts of the basalt-gabbro suite. Therefore, it appears that most of the < 140 μ m mineral fragments in the matrix, like the > 140 μ m mineral fragments, were derived from the same source rocks as the basalt-gabbro lithic clasts. Compositions of low-Ca pyroxenes and high-Ca pyroxenes (Figure 8) are slightly more Fe-rich than the compositions of clasts of > 140 μ m mineral clasts and of pyroxenes in the clasts of gabbro and granulated olivine gabbro, but are nearly identical to the compositions of pyroxenes in the clasts of basalt. These observed variations are

compatible with derivation of the mineral fragments in the matrix from rocks of the basalt-gabbro suite, the larger mineral clasts reflect a greater contribution from the coarse-grained rocks of the suite, and the $< 140\mu\text{m}$ fragments in the matrix reflect a greater contribution from the finer-grained rocks. About 75 percent of the plagioclase grains in the matrix have compositions more calcic than An_{70} , suggesting that they were derived from the same source as the basalts and gabbros. The compositions of most of the fragments of ilmenite (Figure 10) and the fragments of Cr-spinel (Figure 11) suggest that they were also derived from the same source of the basalts and gabbros.

Some of the mineral clasts, however, have compositions that suggest they were not derived from rocks similar to the observed basalts and gabbros. About 25 percent of the fragments of plagioclase have compositions that are too sodic, An_{50-70} , to have been derived from this source. The clast of tonalite is the only lithic clast that contains plagioclase with a similar range of compositions, but it is unlikely that the tonalite and the fragments of relatively sodic plagioclase in the matrix were derived from the same source because disaggregation of the tonalite should also have produced fragments of quartz, and these are not observed in the matrix. It seems more likely that the smaller plagioclase grains in the matrix were originally more calcic and became enriched in Na due to reaction with interstitial feldspar; this hypothesis is discussed more fully in a later section. The smaller fragments of ilmenite are preferentially enriched in Nb_2O_5 (Figure 10). This enrichment is also probably due to reactions with interstitial feldspar.

The interstitial feldspar is composed of needles of a silica

Figure 5: Texture of felsite patches in the gray breccia. Plane polarized light. Numbers in parentheses refer to horizontal scale. (photography by O. B. James.)

(A) Felsite patch with gradational contacts with surrounding aggregate (2.2 mm).

(B) Felsite patch with mostly sharp, angular contacts with surrounding aggregate (2.2 mm).

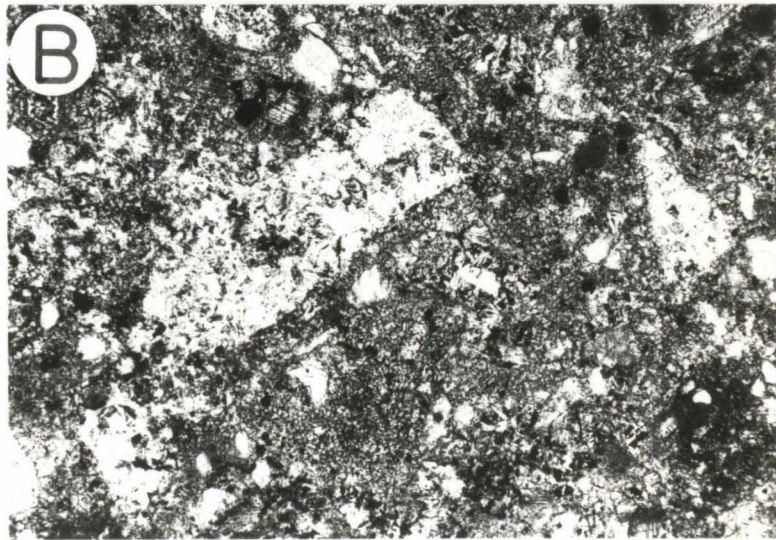
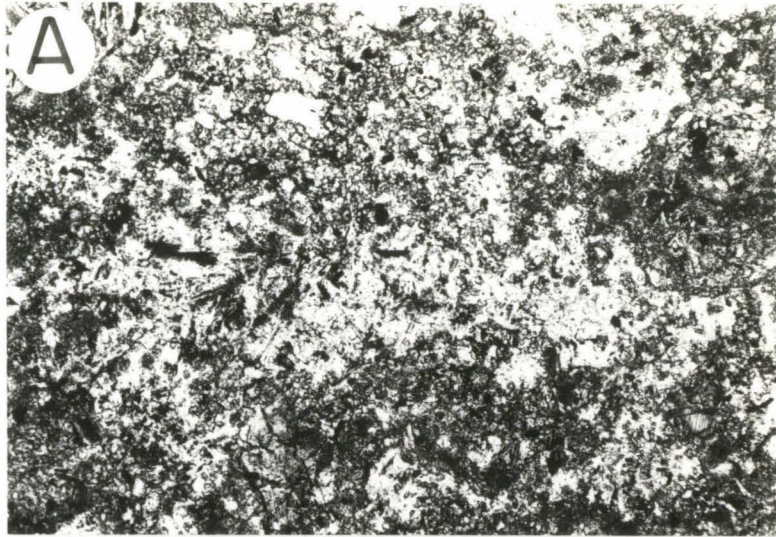


Figure 6: Felsite textures in the gray breccia. Numbers in parentheses refer to horizontal field of view. Both photomicrographs were taken with crossed nicols. (Photography by O. B. James.)

(A) Felsite with K-feldspar microphenocrysts (1.41 mm).

(B) Felsite replacing plagioclase (0.55 mm).

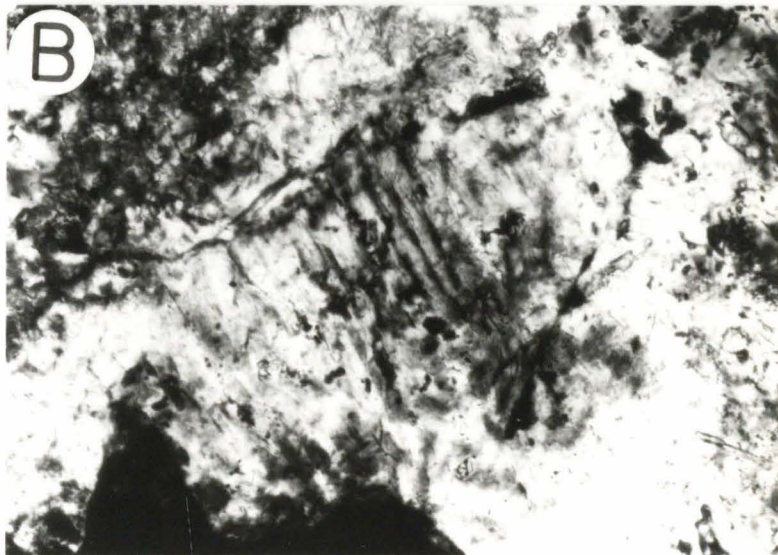
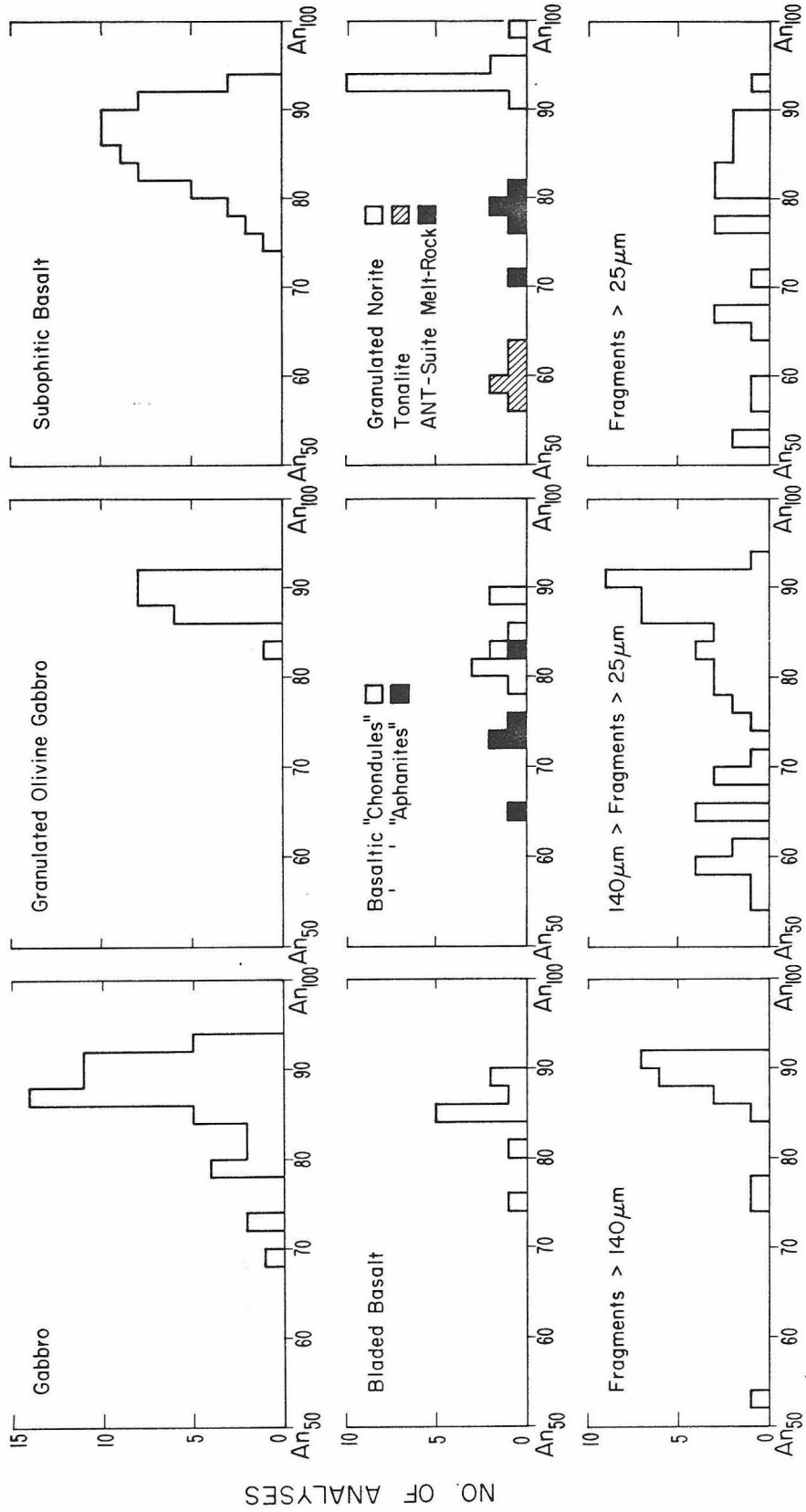


Figure 7
GRAY BRECCIA PLAGIOCLASE



mineral (up to 200 μm long and <5-10 μm wide)) enclosed by anhedral grains of K-feldspar (Figure 4). The silica polymorph has low reflectivity; this and its habit suggest that it is tridymite. Locally, the intergrowth contains small ($\sim 30\mu\text{m}$) equant microphenocrysts of K-feldspar. K-feldspar has an overall range of composition from $\text{An}_{14.1}\text{Ab}_{29.8}\text{Or}_{54.1}\text{Cel}_{2.0}$ to $\text{An}_{1.4}\text{Ab}_{14.8}\text{Or}_{80.9}\text{Cel}_{3.0}$; celsian content increases with increasing Or content (Figure 12). Both the range and the trend of these compositions are similar to those of K-feldspar in the large patches of felsite in the gray breccia.

Felsite

The felsite that forms large patches in the gray breccia (Figure 5) is composed mostly of silica minerals and K-feldspar. Minor amounts of ferroaugite, ilmenite and plagioclase, and trace amounts of apatite, whitlockite, zircon, zirconolite, troilite, Fe-Ni metal and K-rich glass are also present. A typical mode is ~ 40 percent silica minerals, ~ 50 percent K-feldspar, ~ 5 percent ferroaugite, $\sim 1-2$ percent plagioclase, ~ 1 percent ilmenite, and less than 1 percent other phases.

Texture. Silica minerals form needles (50 μm to 2mm long and 4-15 μm thick), which are enclosed by large (1mm) anhedral grains of K-feldspar. In most places, the silica polymorph has a higher refractive index than the enclosing feldspar suggesting that it is quartz. Its acicular habit, however, suggests that the primary silica phase was tridymite, and that the quartz formed by inversion from tridymite. Locally, tridymite (identified by its low refractive index) is still preserved. In some areas, the anhedral K-feldspar grains contain blocky, zoned K-feldspar microphenocrysts as much as 600 μm across; some of these

Figure 8

GRAY BRECCIA PYROXENES

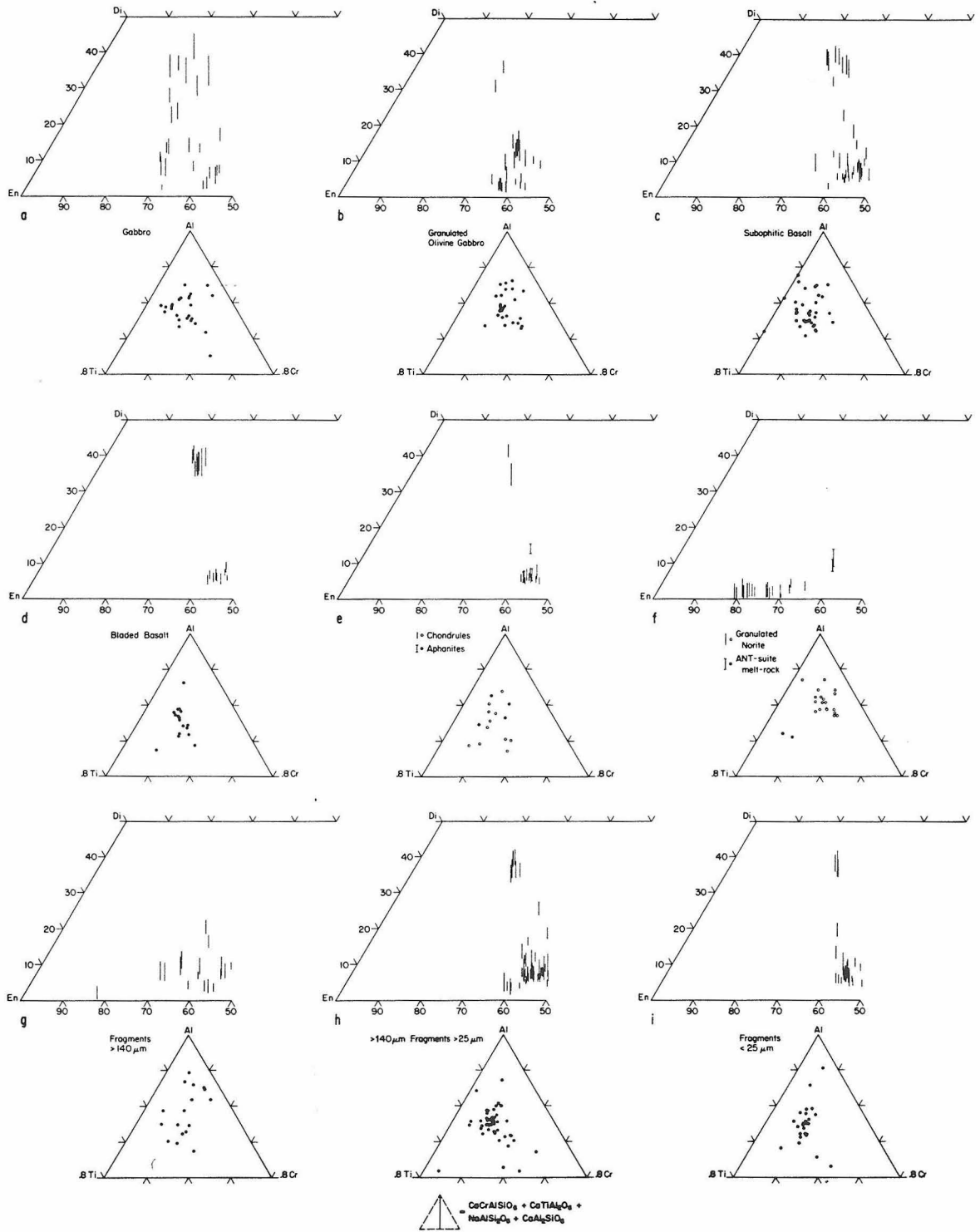


Figure 9

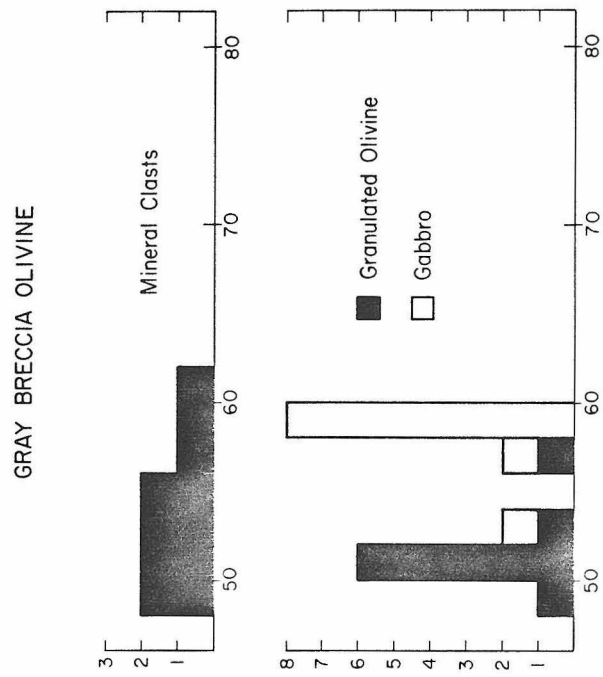


Figure 10

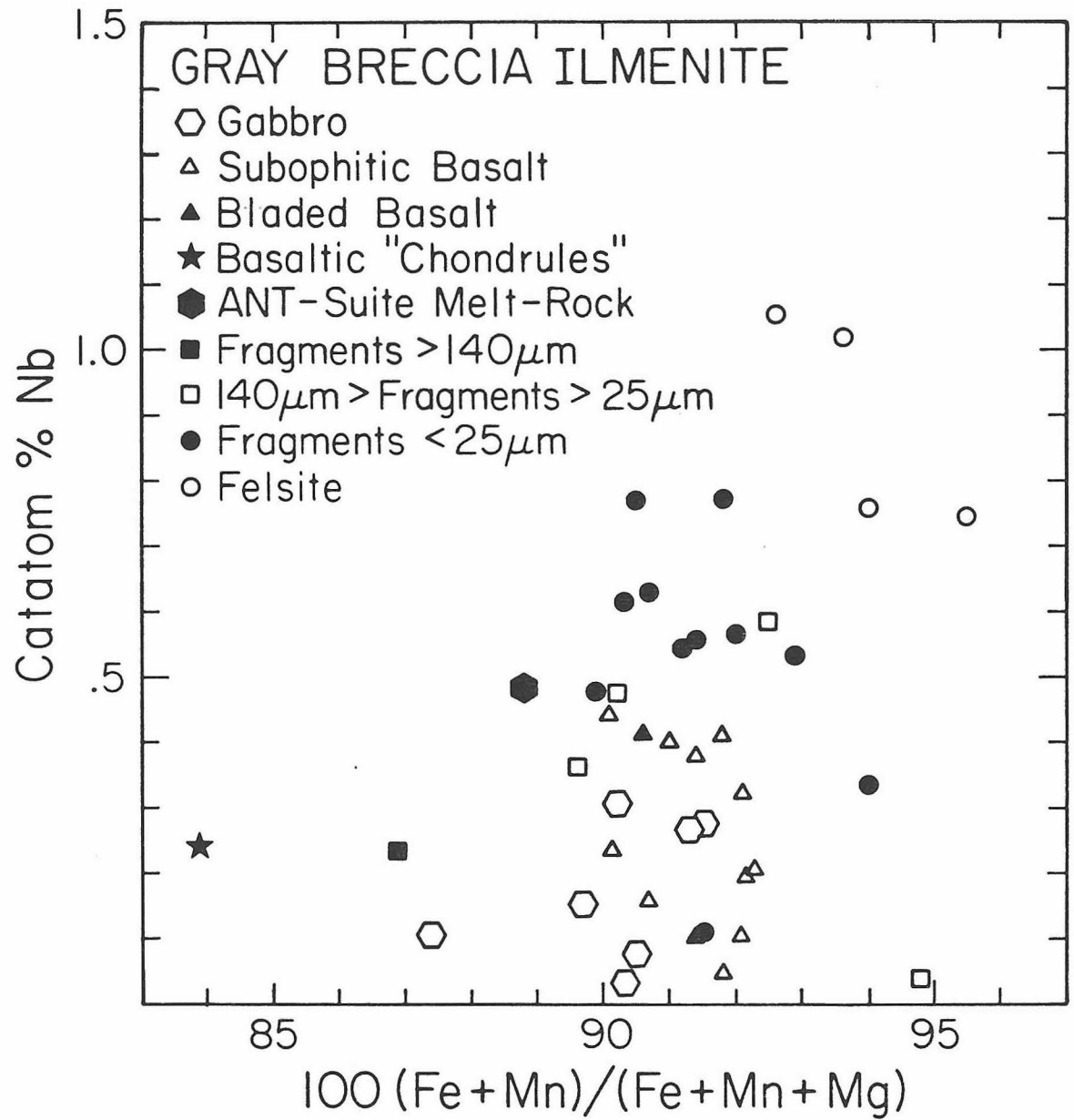
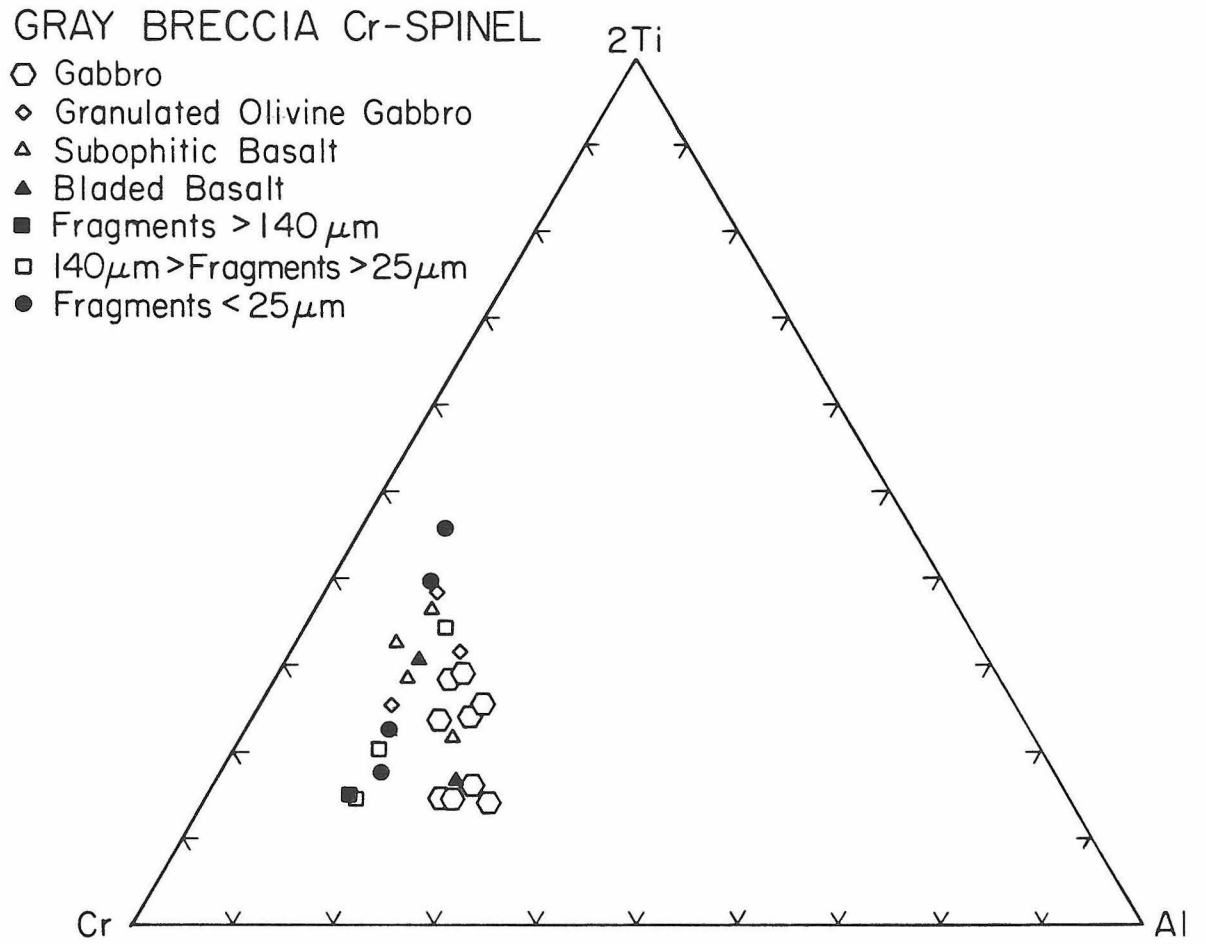


Figure 11



microphenocrysts contain anhedral cores of plagioclase 10-20 μ m across. Plagioclase also occurs as small (\leq 20 μ m) interstitial grains and as clusters of anhedral grains. The clustered grains are in optical continuity over large areas (\sim .5mm across) and have interstices filled with a fine-grained intergrowth of quartz and K-feldspar; the texture suggests that the entire cluster represents a single large plagioclase grain that was partly replaced by quartz and K-feldspar. Ferroaugite forms large acicular skeletal crystals (\sim 100 μ m wide and 0.5-6mm long), and small subhedral, equant grains (5-20 μ m across). Low-Ca pyroxene occurs as small (\leq 50 μ m) equant grains. Ilmenite occurs as tiny euhedral plates, 5-20 μ m long and \leq 3 μ m thick. Apatite, whitlockite, zircon, zirconolite, troilite, and Fe-Ni metal form tiny (\leq 10 μ m) interstitial anhedral grains that tend to occur in clusters. Locally, K-rich glass fills interstices.

Mineral Chemistry. Representative compositions for the phases in the felsite are presented in Tables 5, 6 and 8, and graphical representations of the data are presented in Figures 10, 12 and 13. The bulk composition of the felsite (Quick *et al.*, 1977) is given in Table 15.

The compositions of pyroxene, plagioclase and ilmenite in the felsite are distinct from the compositions of the corresponding minerals in all the lithic clasts in the gray breccia except the tonalite clast. Pyroxene in the felsite is more Fe-rich and lower in Cr (Figures 8 and 13) than pyroxene in the lithic clasts. Plagioclase (Figure 12) in the felsite is similar in composition to the plagioclase in the clast of tonalite, but is much more sodic than the plagioclase in the other lithic clasts. The ilmenite plates in the felsite are remarkably Nb-rich (1.1-1.9 wt. percent) and are thus compositionally distinct from the ilmenite

Figure 12

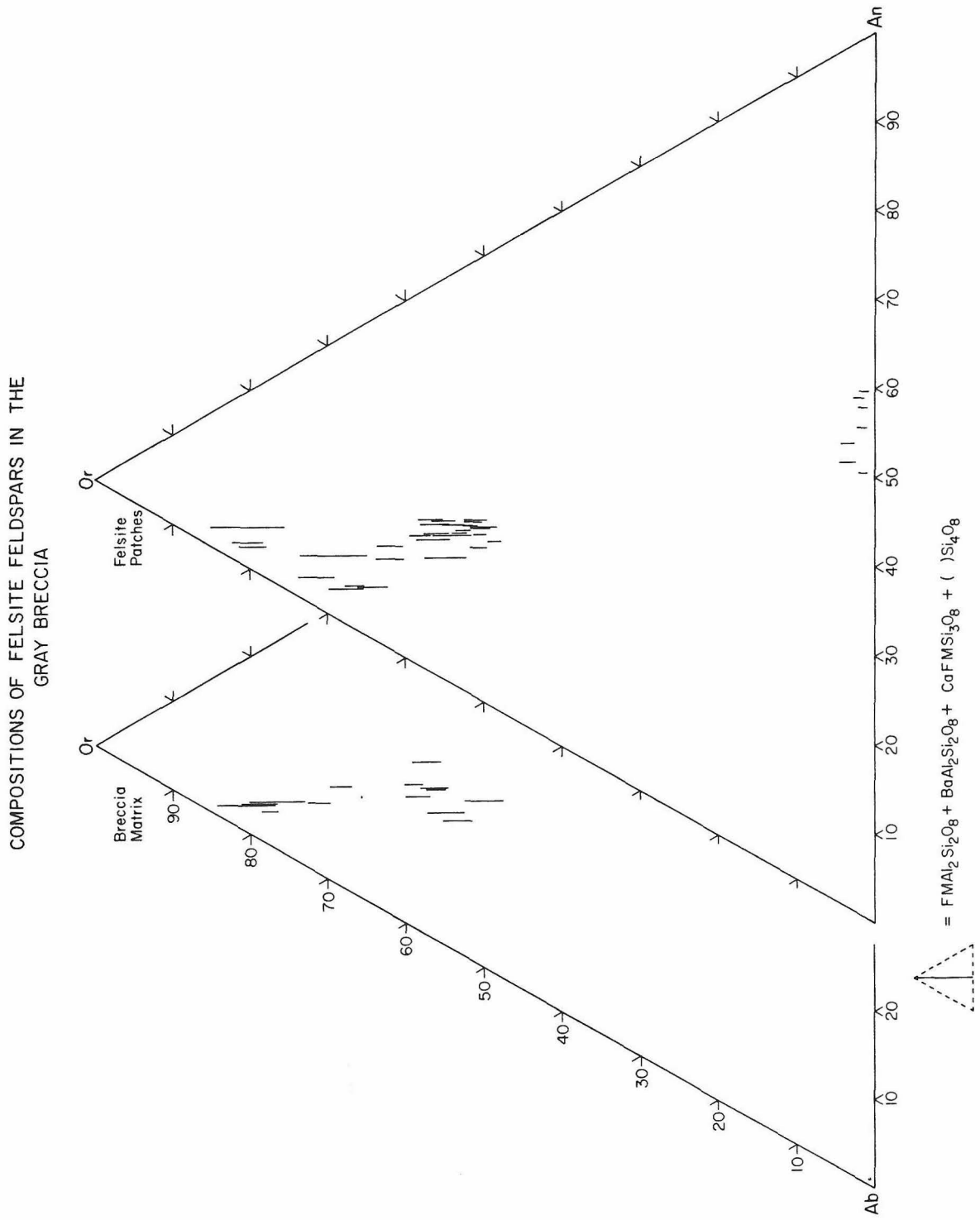


Figure 14

12013 - COMPOSITIONS OF LITHIC CLASTS, FELSITE
AND BLACK BRECCIA GROUNDMASS

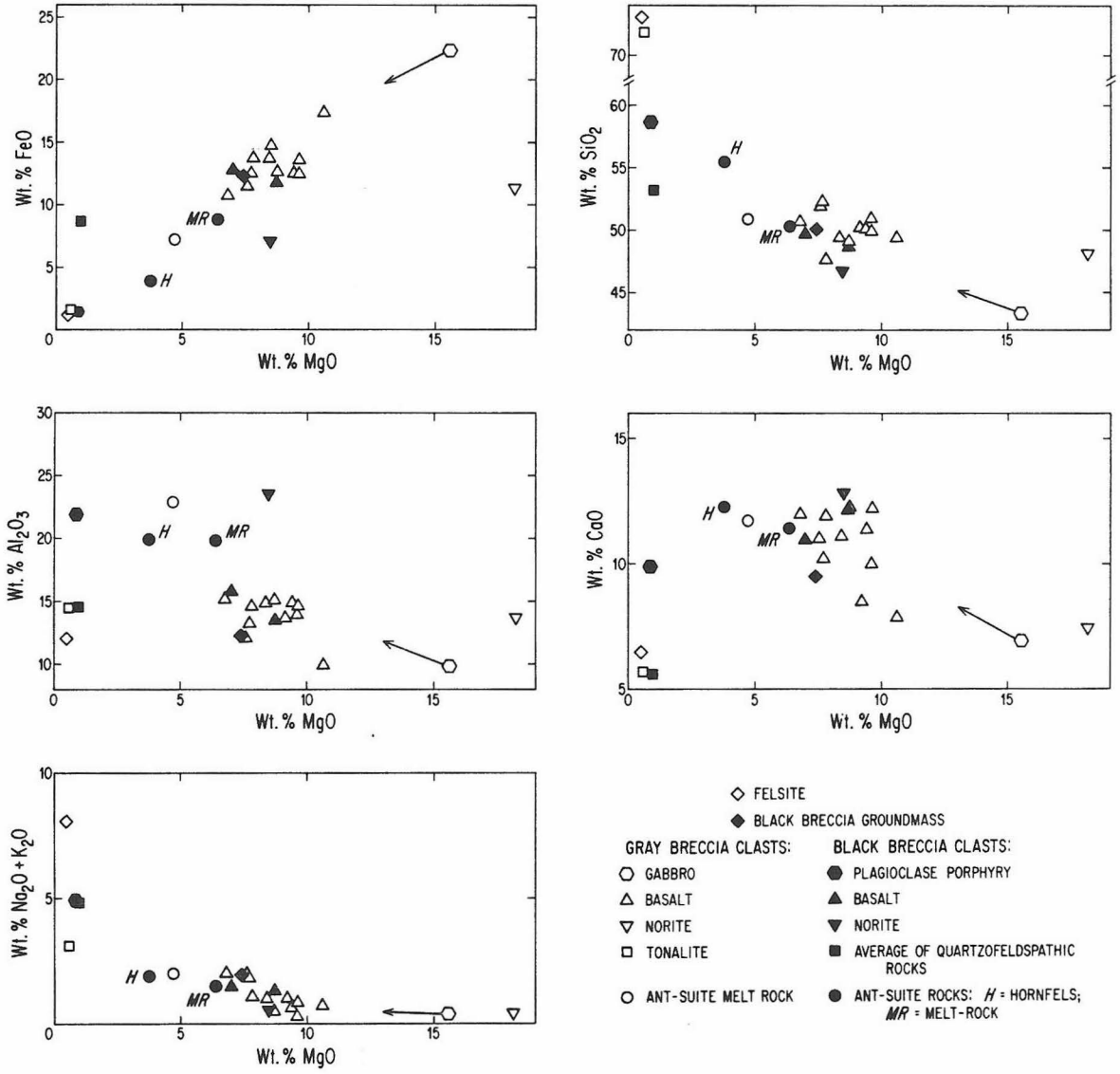
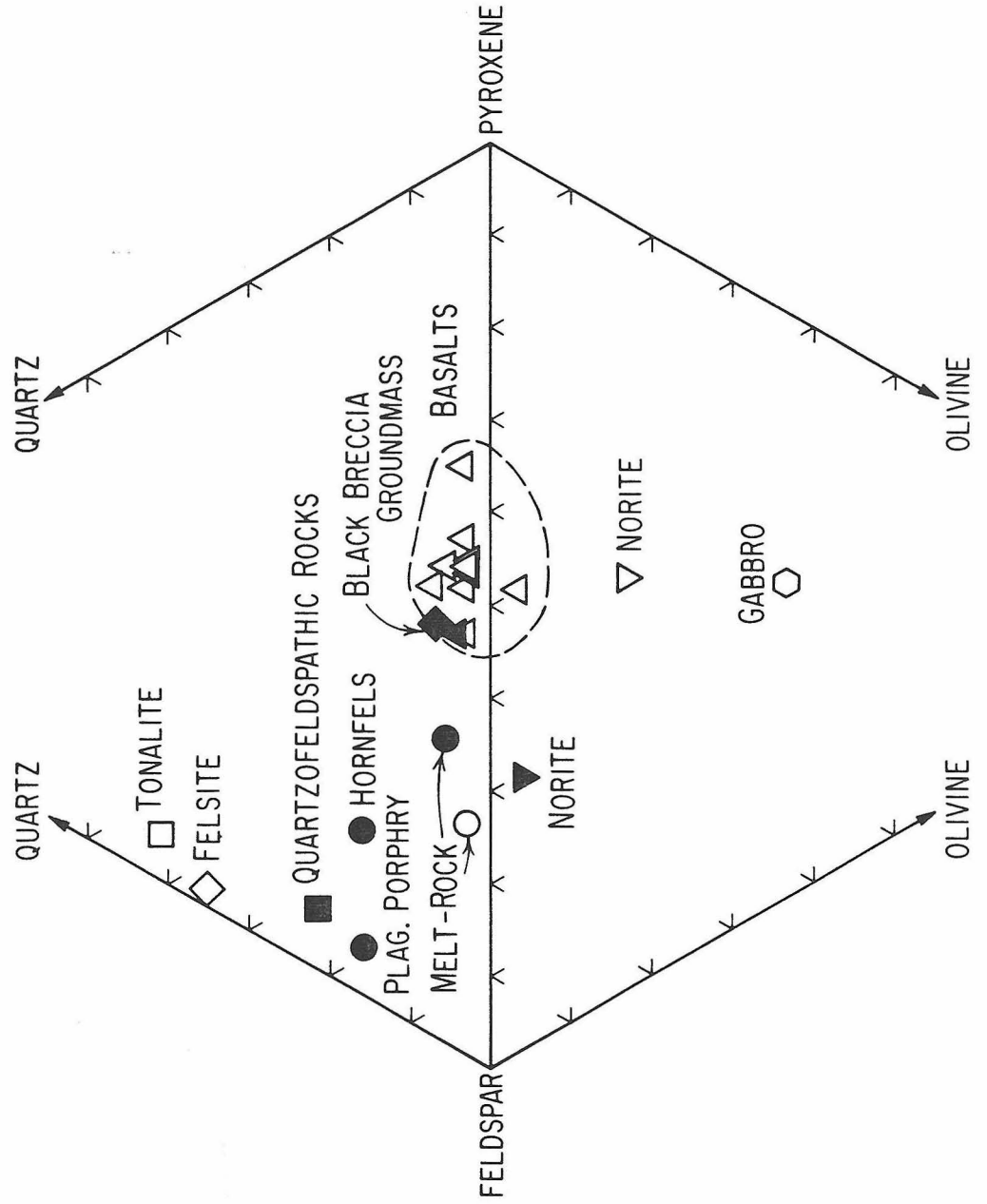


Figure 15

12013-NORMATIVE MINERALOGY OF LITHIC CLASTS,
FELSITE AND BLACK BRECCIA GROUNDMASS



grains in the clasts of basalt and gabbro. The range in composition of K-feldspar is similar to that of K-feldspar grains in the matrix of the gray breccia (Figure 12); analyses range from $\sim \text{An}_{18.3}\text{Ab}_{30.7}\text{Or}_{50.2}\text{Cel}_{.9}$ to $\text{An}_{1.9}\text{Ab}_{16.2}\text{Or}_{79.0}\text{Cel}_{2.9}$, with celsian content increasing with Or content.

Apatite, whitlockite, zircon and zirconolite in the felsite are difficult to analyze because of their small grain sizes. Nevertheless, considerable effort has been invested to obtain analyses of these minerals because they concentrate most of the REE, U, Th and Pb in the felsite. Fission track studies (Burnett et al., 1971; Haines et al., 1971) and electron microprobe analyses (Haines et al., 1971; Quick et al., 1977) indicate that U is concentrated in these phases as follows: zirconolite > zircon > whitlockite > apatite.

BLACK BRECCIA

Introduction

Many of the same types of mineral and lithic clasts are present in both the gray breccia and the black breccia. However, there are significant differences between the two breccias in terms of relative abundances of clasts, compositions of mineral clasts, modes of occurrence of felsite and structural relations. The following description of the black breccia is presented as a comparison with the gray breccia in order to emphasize differences.

In order to simplify this comparison, the data for the black breccia are condensed in tables and graphs similar to those used to present the data for the gray breccia. Clast boundaries are more easily

delineated in the black breccia than in the gray breccia, so that smaller fragments ($\geq 100 \mu\text{m}$) have been mapped and point counted. Volume percentages of clasts both $>100 \mu\text{m}$ and $>140 \mu\text{m}$ were determined by point counting polished thin section 12013,14 (written communication, O. James, 1977) and are presented in Table 11. Lithic clasts are described in Table 12, their textures are illustrated in Figure 21 and their whole-rock compositions derived from defocused-beam analyses of clasts are tabulated in Table 13. Mineral clasts are described in Table 14. Representative analyses of mineral clasts and of minerals in lithic clasts, felsite and groundmass are given in Tables 5-10 and all analyses are presented graphically in Figures 16-20.

Lithic Clasts $> 140 \mu\text{m}$

In contrast to the gray breccia, where lithic clasts make up about 80 percent of the $>140 \mu\text{m}$ clasts, lithic clasts comprise only about 40 percent of the $>140 \mu\text{m}$ clasts. Also, the relative abundances of the lithic clasts are strikingly different. The lithic clasts in the black breccia are, in order of decreasing abundance, quartzofeldspathic rocks, granulated norite, ANT-suite hornfels, ANT-suite melt-rock, basalt and mosaic-textured anorthosite. Clasts of gabbro and basalt, which are abundant in the gray breccia, are absent or rare, whereas clasts of granulated norite and quartzofeldspathic rocks, which are scarce in the gray breccia, dominate the lithic clast suite in the black breccia. Furthermore, clasts of ANT-suite hornfels and mosaic-textured anorthosite do not occur in the gray breccia.

In general, the lithic clasts in the black breccia are smaller than those in the gray breccia. Quartzofeldspathic rocks and granulated norite form the largest clasts, which are highly elongate and about 1-2 mm

BLACK BRECCIA PLAGIOCLASE

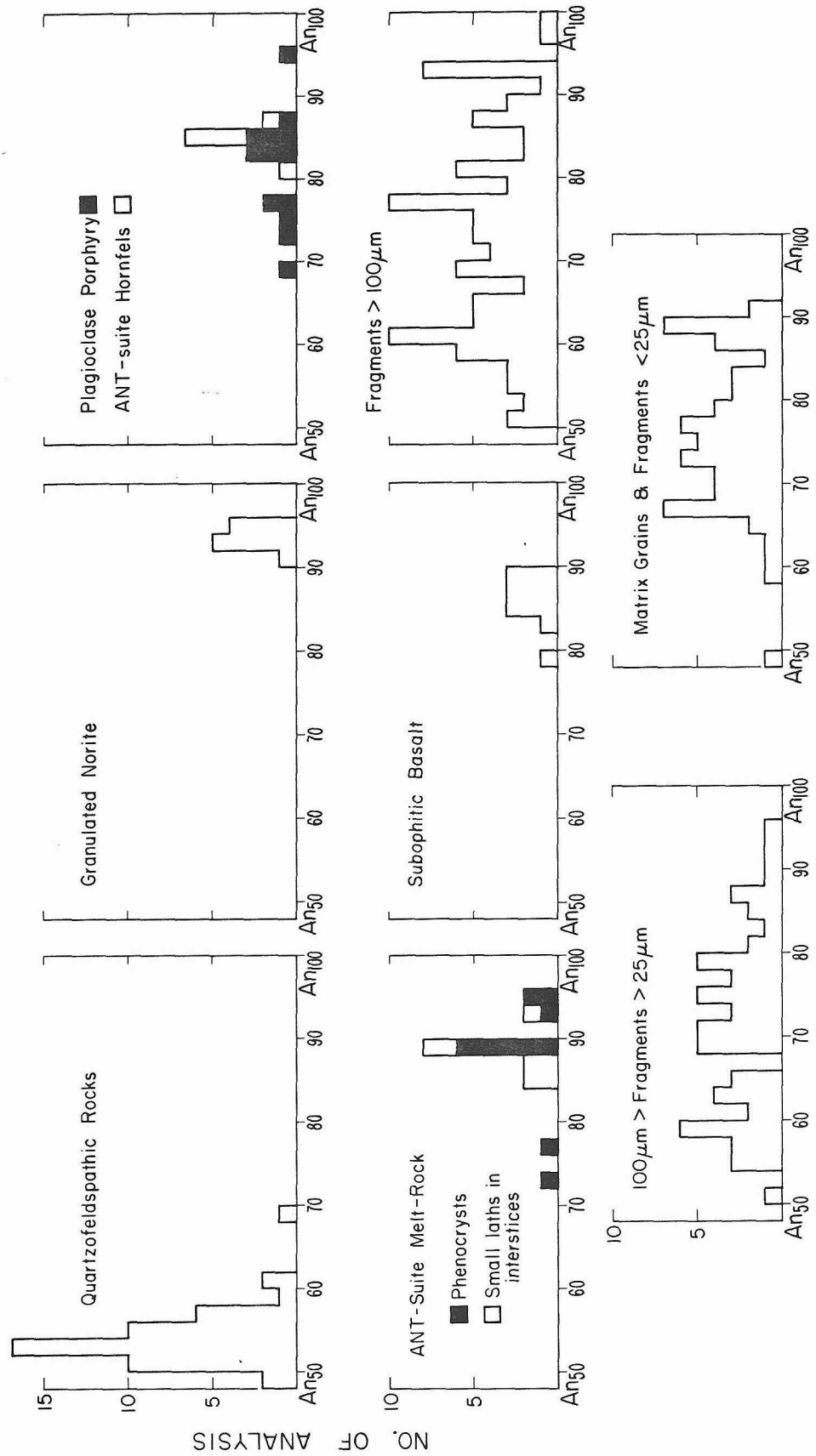


Figure 16

Figure 17

BLACK BRECCIA PYROXENES

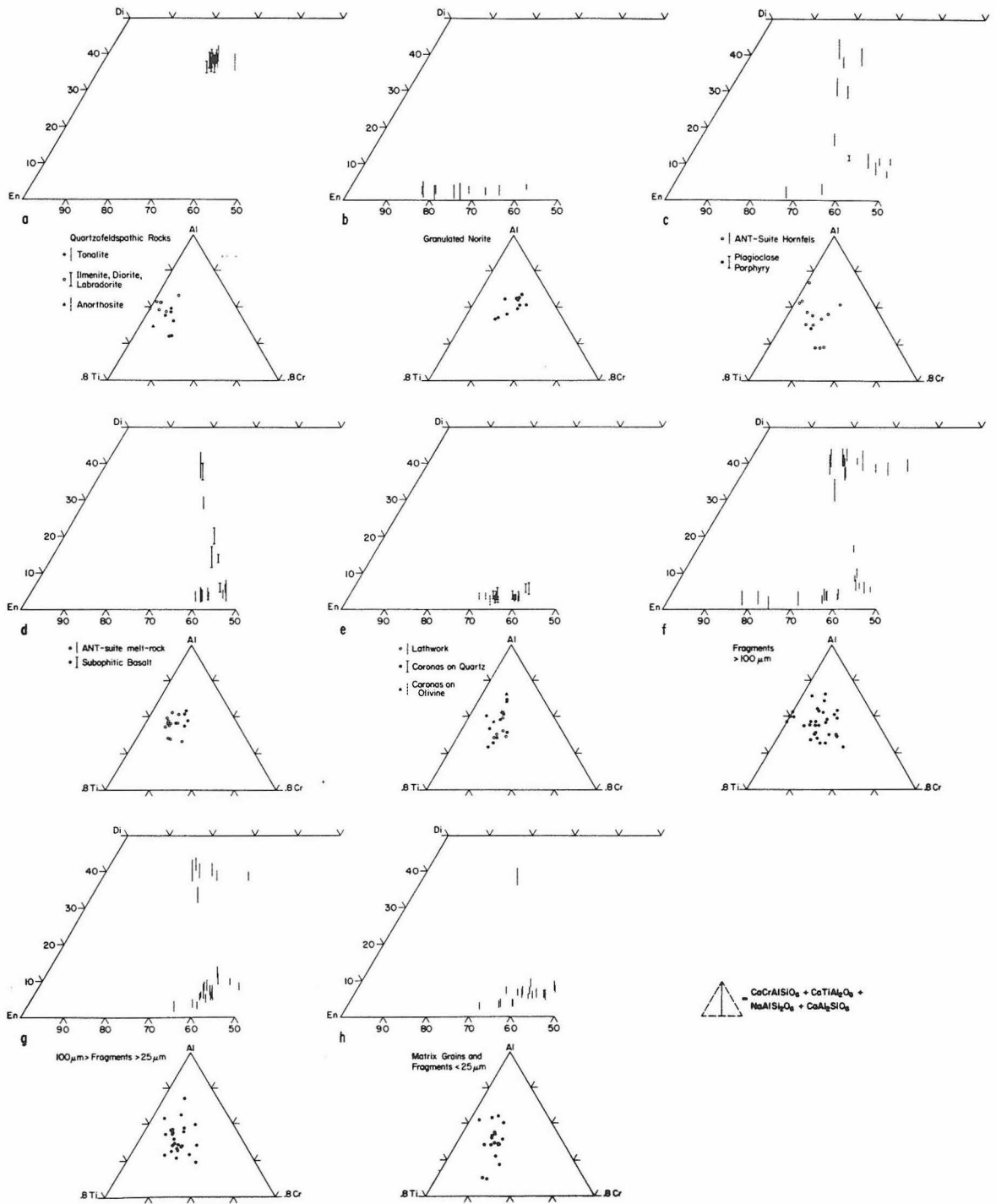


Figure 18

BLACK BRECCIA
OLIVINE

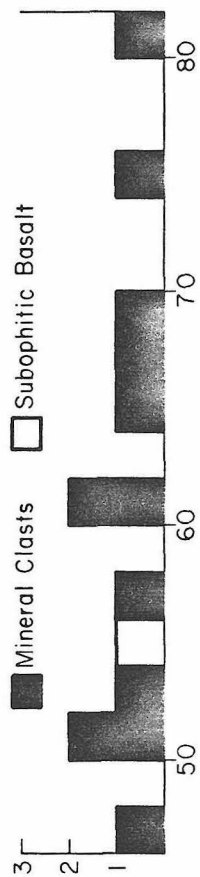
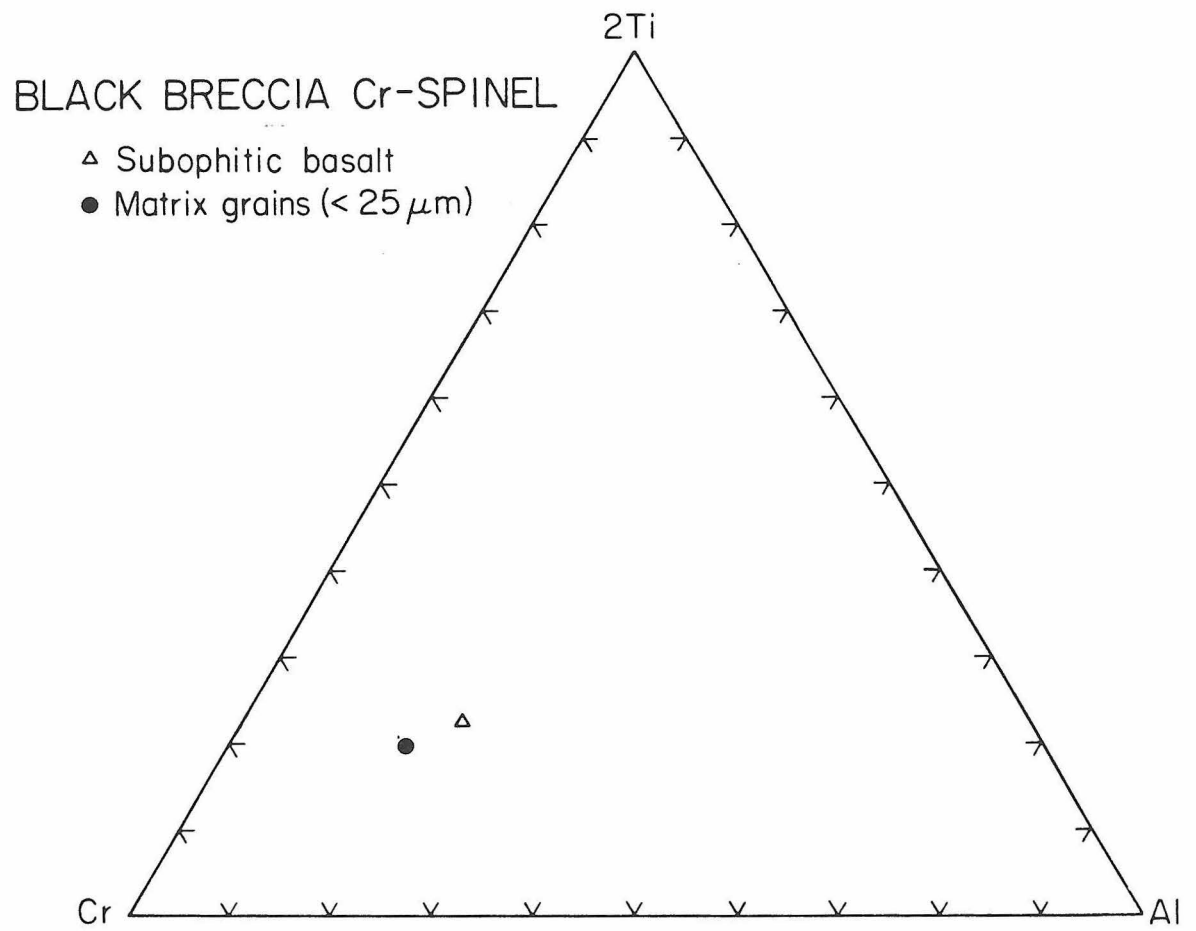


Figure 20



long. Clasts of ANT-suite hornfels and ANT-suite melt-rock are mostly equant and 250 μm to 1 mm across; one clast is ~ 2 mm across. Clasts of basalt and mosaic-textured anorthosite are equant and <250 μm across.

Quartzofeldspathic Rocks. Lithic clasts of tonalite, labradorite, anorthosite and ilmenite diorite occur in close association within the black breccia (Figure 21). These clasts have similar mineralogies, textures and mineral compositions suggesting that they were derived from the same source, possibly by comminution of a single, large rock. Furthermore, all these clasts are intimately associated with felsite. Therefore, they are discussed collectively as quartzofeldspathic rocks.

Many of the same types of minerals occur in all the quartzofeldspathic rocks. Relatively sodic plagioclase, high-Ca pyroxene, ilmenite, tridymite, K-feldspar and K-rich glass are essential components in all the clasts. Quartz only occurs in the clast of tonalite, but it is the only major phase restricted to one quartzofeldspathic lithology. Phases present in trace amounts are phosphate minerals, zircon, troilite and metal. The modal abundance of the major and trace phases are extremely variable from one quartzofeldspathic clast to another; but, if the labradorite anorthosite, ilmenite diorite and tonalite clasts represent one highly sheared and dismembered clast, its approximate modal mineralogy would be about 35 percent plagioclase, 10 percent ilmenite, 3 percent high-Ca pyroxene, 22 percent silica minerals, 27 percent K-feldspar, 1 percent phosphate minerals and trace amounts of low-Ca pyroxene, zircon and glass.

The primary textures of all the quartzofeldspathic rocks have been mostly obliterated by cataclasis and recrystallization. All of these lithic clasts are predominately inequigranular aggregates of mineral

fragments. The interstices between fragments are filled by smaller fragments and an intergrowth of tridymite needles and K-feldspar. Patches of felsite as much as 300 μm across are found in all of the quartzofeldspathic rocks; some plagioclase grains, in contact with these patches, have been mostly replaced by K-feldspar, producing large K-feldspar pseudomorphs after plagioclase that contain scattered, but optically continuous plagioclase inclusions.

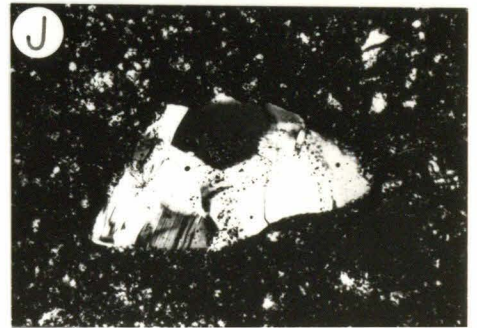
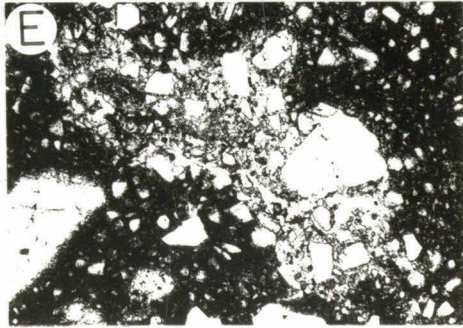
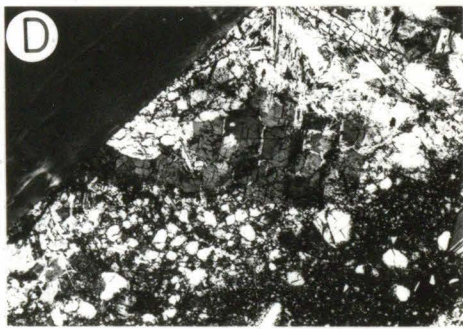
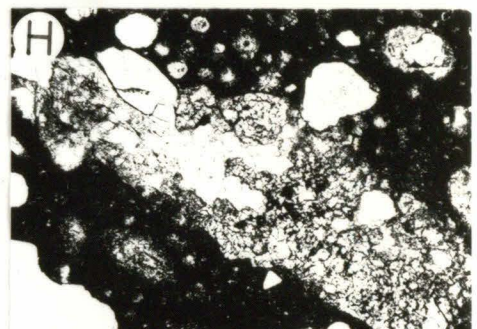
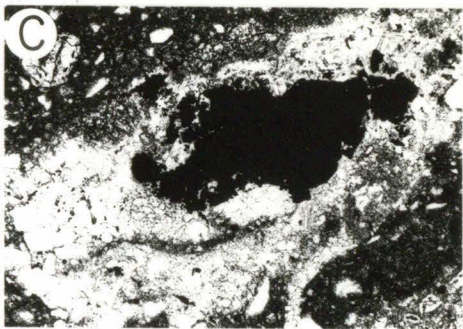
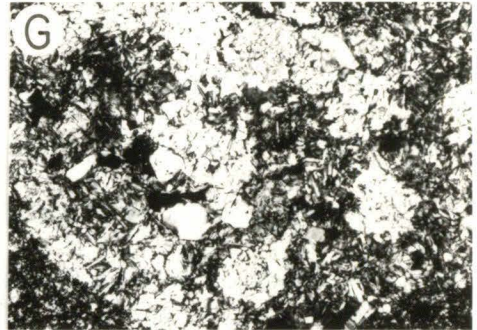
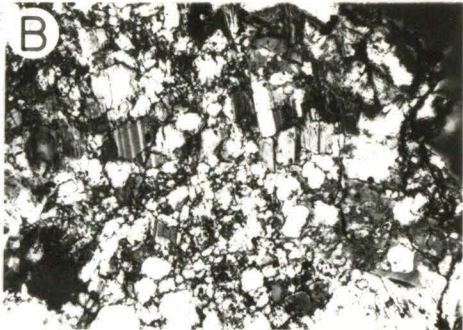
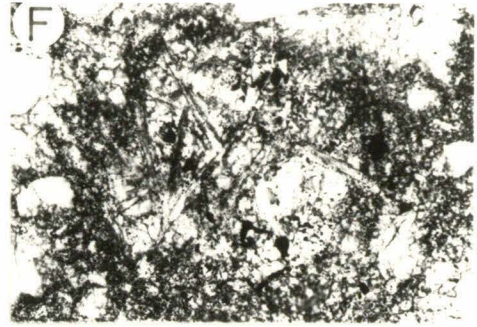
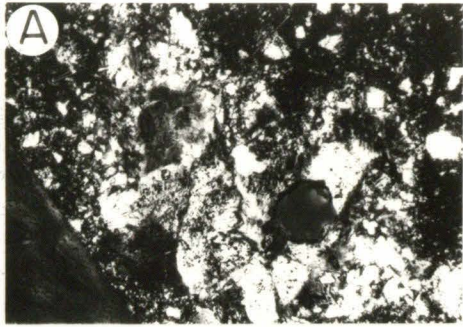
Some relicts of coarse-grained xenomorphic-granular texture are preserved in all the quartzofeldspathic lithologies. The presence of large mineral fragments, as well as the coarse-grain size of the areas with relict textures, suggests that the predeformation grain size of the quartzofeldspathic rocks was 0.2-1 mm. Significantly, this range in grain size and the relict textures are similar to those of the tonalite clast in the gray breccia.

The compositions of the minerals in the different quartzofeldspathic clasts are almost identical. Plagioclase compositions (Figure 16) have essentially the same range in $\text{Ca}/\text{Ca}+\text{Na}$, and pyroxene grains in the different lithologies have essentially the same composition (Figure 17) except that the single grain in the clast of labradorite anorthosite is slightly more Fe-rich. The similarity in mineral compositions is enhanced by the fact that the only other lithologies with similar mineral compositions are the felsite and the single clast of tonalite in the gray breccia.

Granulated Norite. These clasts tend to occur as streaks near the contacts with the gray breccia in thin section 12013,15 and in thin section 12013,14. Length to width ratios for these clasts range from 3:1 to 7:1 suggesting they have been intensely deformed.

Figure 21: Photomicrographs of lithic clasts in the black breccia. All photographs taken in plane polarized light unless noted otherwise. Numbers in parentheses refer to horizontal scale of photo. (Photography by O. B. James.)

- (A) Tonalite (1.41 mm). Crossed nicols.
- (B) Labradorite anorthosite (0.88 mm). Crossed nicols.
- (C) Ilmenite diorite (2.2 mm).
- (D) Quartzofeldspathic clast with extensive replacement of plagioclase by K-feldspar (2.2 mm). Crossed nicols.
- (E) Granulated norite (2.2 mm).
- (F) Subophitic basalt (0.70 mm).
- (G) ANT-suite melt-rock (0.88 mm). Crossed nicols.
- (H) ANT-suite hornfels (1.75 mm).
- (I) Plagioclase porphyry (0.70 mm).
- (J) Mosaic anorthosite (0.57 mm). Crossed nicols.



These clasts are essentially identical in texture, mineralogy and mineral chemistry to the clast of granulated norite in the gray breccia, except that they do not have recrystallized rims and that they contain trace amounts of ilmenite. The similarity in mineralogy and mineral chemistry is particularly pronounced because no other types of lithic clasts in 12013 contain both extremely calcic plagioclase (An_{90}) and magnesian (En_{56}) low-Ca pyroxene and magnesian (Fo_{60}) olivine.

Basalt. Two small basalt clasts occur in the black breccia that are texturally and mineralogically similar to basalt clasts in the gray breccia (Figure 21). One clast is a fine-grained subophitic basalt composed of subequal amounts of plagioclase and pyroxene, with minor amounts of olivine, ilmenite and Cr-spinel. The compositions of plagioclase (Figure 16), pyroxene (Figure 17) and olivine (Figure 18) fall within the ranges in composition of the corresponding minerals in the basalt-gabbro suite in the gray breccia. The other clast is an extremely fine-grained basaltic "chondrule" composed of subequal amounts of acicular plagioclase and pyroxene, and minor amounts of ilmenite.

ANT-suite melt-rock. This clast (Figure 21) is texturally similar to the clast of ANT-suite melt-rock in the gray breccia. Both lithic clasts contain blocky grains of plagioclase, plagioclase laths, interstitial to sieve-textured pyroxene, phosphate minerals and K-rich glass. Both clasts appear to have formed by crystallization of a mixture of mineral grains and silicate melt prior to their incorporation into 12013. However, the ANT-suite melt-rock in the gray breccia is finer-grained, more feldspathic and contains plagioclase that is more sodic. Also, the pyroxene in the clast in the black breccia is not recrystallized to a mosaic texture.

ANT-suite Hornfels. There are three clasts of ANT-suite hornfels in the black breccia (Figure 21). All three clasts are composed mostly of fragments of plagioclase and pyroxene which have recrystallized to a tight mosaic. The interstices of this mosaic are filled by ilmenite, troilite, phosphate minerals, metal and K-rich glass. Primary textures have been virtually obliterated by brecciation and recrystallization, but traces of primary, coarse-grained xenomorphic-granular texture are preserved in one clast. There are no other types of clasts that are texturally similar to the ANT-suite hornfels in either the black breccia or the gray breccia.

The plagioclase and pyroxene compositions in the different hornfels clasts are dissimilar. One clast contains pyroxene that is more Fe-rich and plagioclase that is more sodic than the other two clasts; most of the pyroxene in one of the remaining clasts is high-Ca pyroxene, and all of the pyroxene in the other is low-Ca pyroxene.

The only other type of clast in the black breccia that has similar mineral compositions is the ANT-suite melt-rock. However, the plagioclase grains in the clasts of hornfels have a considerably greater range in composition, and the compositions of pyroxenes in the hornfels rocks and melt-rocks do not define overlapping fields on the pyroxene quadrilateral (Figure 17).

Plagioclase Porphyry. Two clasts of plagioclase porphyry (Figure 21) occur in the black breccia. They are composed of extremely calcic plagioclase laths, pyroxene grains and a mesostasis of pyroxene crystallites and K-rich glass. This texture is not found in any other clasts in 12013.

Pyroxene Lathwork. Patches of randomly oriented pyroxene laths are scattered throughout the black breccia. The similarity in the texture

and pyroxene compositions in reaction rims around olivine fragments suggest that these patches formed by complete reaction of olivine with the black breccia groundmass.

Mineral Fragments >10 μm

Mineral clasts dominate the clast population of the black breccia, making up about 60 percent of the >140 μm , and essentially all fragments <100 μm . The most abundant of these are clear, inclusion-free fragments of plagioclase, which make up more than half the total clast population. Other mineral clasts, in order of decreasing abundance, are pyroxene, tridymite and cristobalite, olivine, ilmenite, devitrified maskelynite, phosphate minerals, K-feldspar and zircon; significantly, all of these are absent from the clast population of the gray breccia except pyroxene, olivine and ilmenite.

There are systematic differences in composition between the mineral clasts in the black and the gray breccias. Clasts of relatively sodic plagioclase (Figures 7 vs. 16), high-Ca pyroxene and Mg-rich low-Ca pyroxene (Figure 8 vs. 17) are much more abundant in the black breccia than in the gray breccia, and clasts of high-Ca pyroxene in the black breccia (Figure 8 vs. 17) reach much more Fe-rich compositions and are less Ca-rich than those in the gray breccia. Also, olivine clasts in the black breccia (Figure 9 vs. 18) have a much wider range in Fo-content.

As in the gray breccia, the compositions of mineral fragments are somewhat dependent on grain size. In particular, the compositions of small (<25 μm) fragments of pyroxene and plagioclase are somewhat different from those of the larger fragments. The entire range in composition for

plagioclase fragments in the black breccia is about An₅₀₋₁₀₀, but plagioclase fragments that are more sodic than about An₆₅ or more calcic than about An₉₀ are rare in the <25 μm size fraction and relatively abundant in the >25 μm size fraction. Similarly, fragments of high-Ca pyroxene, and fragments of low-Ca pyroxene that are more magnesian than about En₆₆ are rare in the <25 μm size fraction but are abundant in the >25 μm size fraction. These differences in composition are interpreted as resulting from reactions between mineral clasts and the black breccia groundmass, and will be discussed in detail in a later section.

Most of the mineral clasts have composition, textures and grain sizes that suggest that they were derived from the same rocks as the clasts of granulated norite, ANT-suite hornfels and quartzofeldspathic rocks. The other types of clasts in the black breccia are either too fine-grained, do not contain clear, inclusion-free plagioclase or have inappropriate mineral compositions to be representative of the source rocks. The clasts of the basalt-gabbro suite in the gray breccia are also not representative of the source rocks because most of their plagioclase and pyroxene grains are turbid.

Some mineral clasts in the black breccia cannot be derived from the observed lithic clasts because appropriate mineral grains of similar size and/or composition are not found in the lithic clasts. These mineral clasts are Fe-rich, high-Ca pyroxene, large apatite clasts, large zircon clasts and clasts of devitrified maskelinite.

Deformation Textures

As in the gray breccia, the degree of deformation in lithic clasts correlates with grain size. Coarse-grained lithic clasts are elongate

and most primary textures in them have been destroyed by cataclasis (Figure 21), while fine-grained lithic clasts show little or no internal deformation. However, unlike in the gray breccia, there is little evidence of intragranular deformation in either the lithic clasts or in the mineral clasts of the black breccia; undulatory extinction, kink bands and bent or offset twin lamellae are present but more scarce than in the gray breccia.

Groundmass

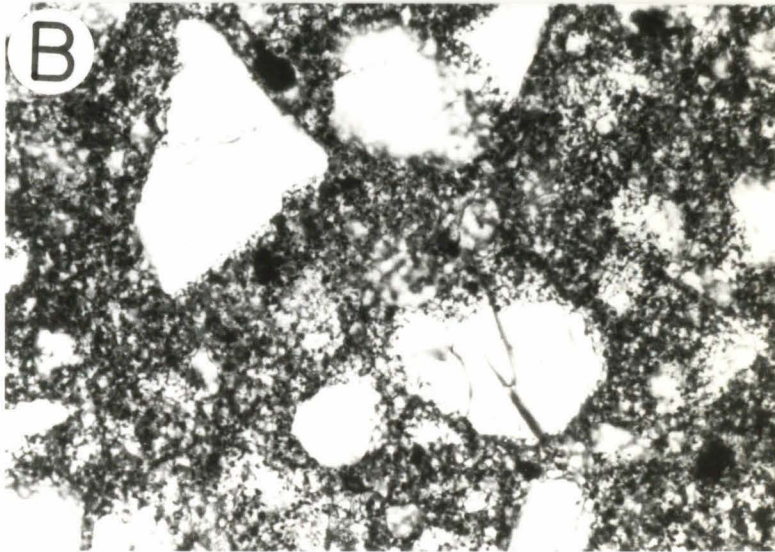
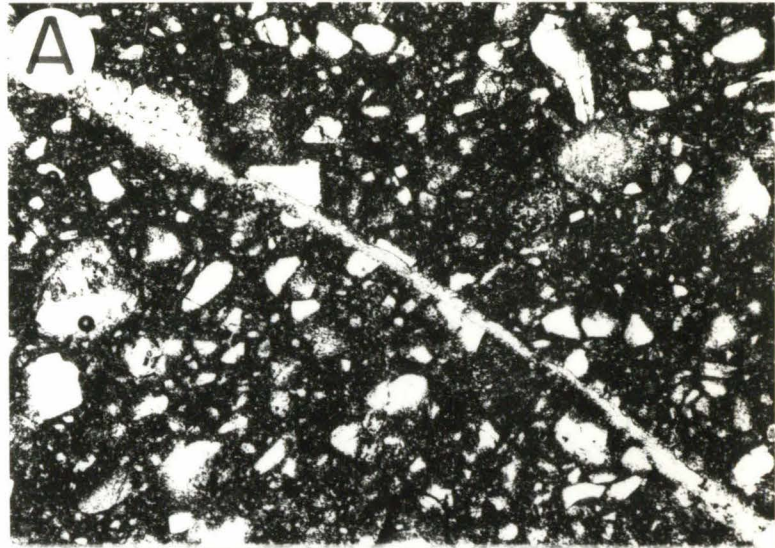
Approximately 50 percent of the black breccia is groundmass, which fills the interstices between clasts (Figure 22). It consists of an equigranular mosaic of mostly 1 to 5 μm -sized grains of pyroxene and plagioclase, and micron-sized ilmenite (Figure 27). The mode is consistently around 40-50 percent plagioclase, 45-55 percent pyroxene and about 5 percent ilmenite. Minor or trace amounts of interstitial, submicron-sized grains of apatite, whitlockite, Zr-bearing minerals, sulfides and metal are also present. The only void spaces are spherical vesicles, which range in diameter from 25 μm to 200 μm , and locally comprise as much as 25 percent by volume of the groundmass (Figure 27). These vesicles demonstrate that the groundmass crystallized from a melt.

The compositions of the groundmass minerals are difficult to determine because of their small size, and because they are difficult to distinguish from the smallest mineral fragments. Qualitative analysis of ilmenite indicates that it has low Nb concentrations, and both whitlockite and apatite were identified in the groundmass by the absence or presence of Cl. However, groundmass ilmenite, phosphate minerals, Zr-bearing minerals, metal and sulfide grains are too fine-grained for quantitative

Figure 22: Photomicrographs illustrating the texture of the black breccia. Numbers in parentheses refer to horizontal scale. (Photography by O. B. James.)

(A) Representative appearance of black breccia (2.2 mm). Note felsite vein cutting both clasts and groundmass. Plane polarized light.

(B) Closer view of the black breccia showing groundmass between clasts (0.48 mm). Plane polarized light.



analysis by the electron microprobe. The total range in composition of 28 plagioclase grains that are $\leq 10 \mu\text{m}$ is $\text{An}_{61.3}\text{Ab}_{37.7}\text{Or}_{1.0}$ to $\text{An}_{90.6}\text{Ab}_{9.2}\text{Or}_{.2}$ and the compositions of 26 analyzed pyroxene grains of similar size range from $\text{En}_{66}\text{Wo}_3\text{Fs}_{31}$ to $\text{En}_{46}\text{Wo}_7\text{Fs}_{47}$. The variability is greater than would be expected for phases that had crystallized from a quenched melt or an annealed glass. It is possible that tiny mineral fragments of plagioclase and pyroxene are biasing these results. Defocused beam analyses of very fine-grained ($< 5 \mu\text{m}$) patches of the groundmass suggest that the composition of the plagioclase and pyroxene are, in fact, much more uniform. Within these areas, the compositions of normative plagioclase are restricted to about An_{58-68} and the compositions of the normative pyroxene are restricted to about En_{46-54} . These ranges are more consistent with formation from a quenched melt or annealed glass.

Felsite in the Black Breccia

The felsite that occurs in the black breccia is similar to the felsite in the gray breccia in texture, mineralogy, mode and mineral chemistry. The felsite in the black breccia, however, is much less abundant and has different modes of occurrence than in the gray breccia.

Felsite occurs in the black breccia as: (1) discrete rounded blebs, some of which are vesicular (Figure 23); (2) discrete subangular to angular inclusions (Figure 23); (3) vein fillings that crosscut both clasts and groundmass (Figure 22); (4) irregular patches associated with and filling the interstices of quartzofeldspathic clasts; (5) rims on tridymite or quartz clasts; and (6) thin selvages on plagioclase clasts.

As in the gray breccia, most of the felsite is composed of needles of silica minerals, 50-300 μm long and about 10 μm wide, enclosed in anhedral grains of K-feldspar, about 100-500 μm across. Unlike in the

Figure 23: Photomicrographs of felsite in the black breccia. Photos taken in plane polarized light. Numbers in parentheses refer to horizontal scale. (Photography by O. B. James.)

(A) Globular felsite in black breccia (2.2 mm). Note smooth rounded contacts and a vesicle shared by the felsite and the black breccia groundmass.

(B) A more angular "fragment" of felsite (1.75).

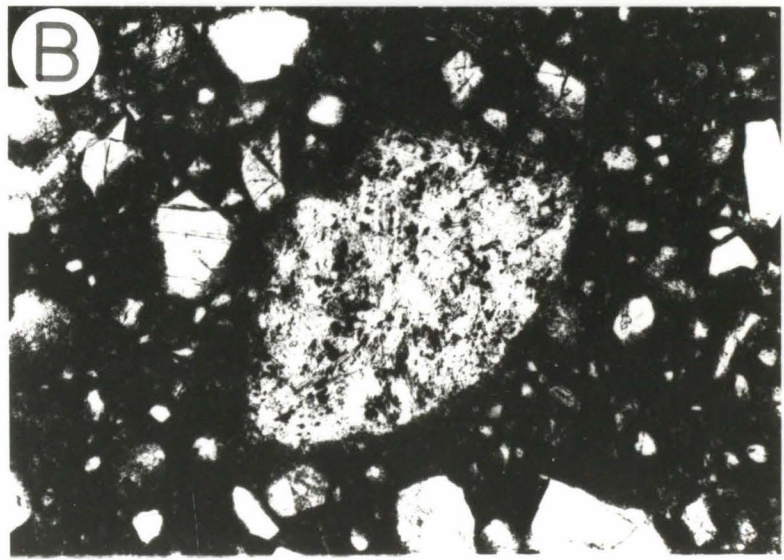
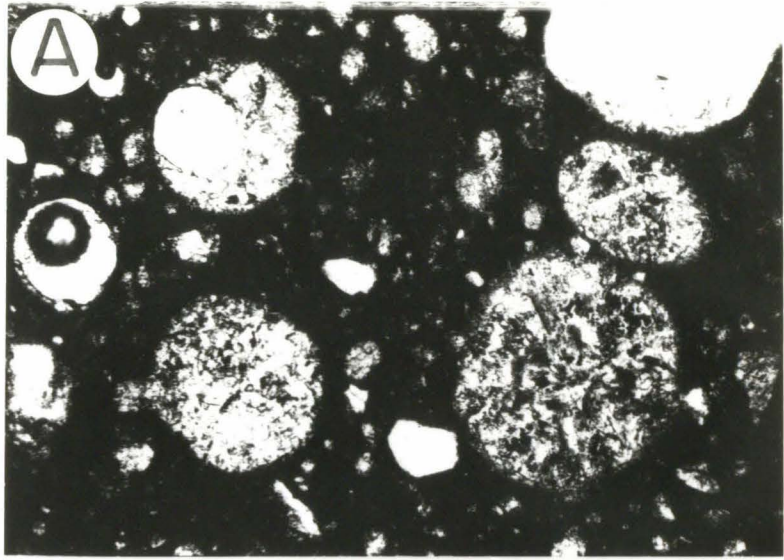


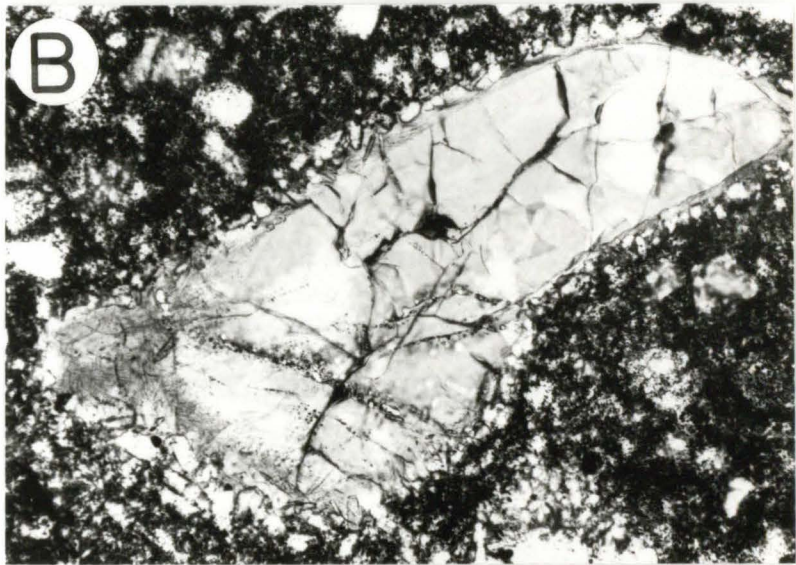
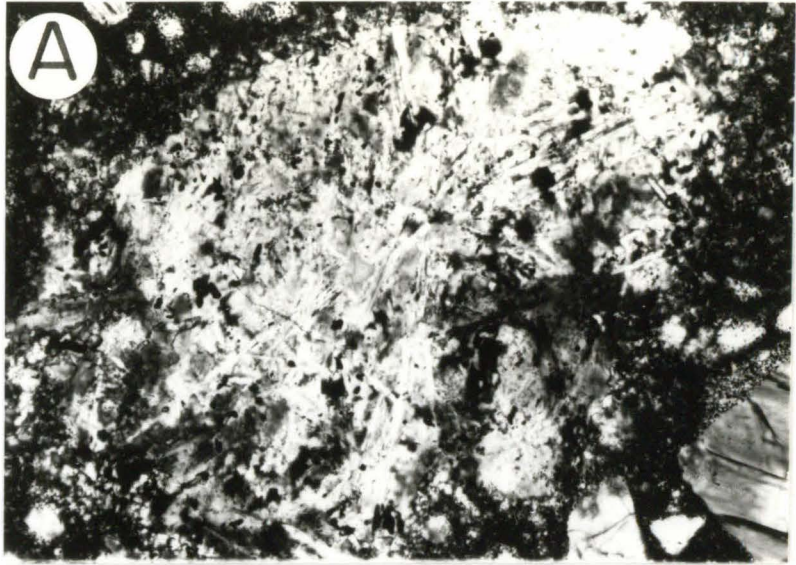
Figure 24: Texture and morphology of felsite in the black breccia.

All photos taken with crossed nicols. Numbers in parentheses refer to horizontal scale of photos. (Photography by O. B. James.)

(A) Representative texture (0.88 mm).

(B) Tridymite clast with thin rim of felsite (0.88 mm).

(C) K-feldspar microphenocrysts with plagioclase cores in felsite (0.88 mm).



gray breccia, however, tridymite is the more abundant silica polymorph, and only locally, in the larger blebs and in wide spots in the vein fillings, is the silica polymorph quartz. In most places, the silica needles are randomly oriented. However, a well developed preferred orientation of silica needles exists in some blebs, in the felsite rings on tridymite and quartz clasts and in the selvages on plagioclase clasts. In some blebs and vein fillings, the K-feldspar grains contain blocky 15-25 μm K-feldspar microphenocrysts. Ferroaugite forms subhedral, equant grains about 10-20 μm across. Ilmenite occurs as tiny (<10 μm) ubiquitous plates; and zircon, zirconolite, apatite, whitlockite, troilite and Fe-Ni metal form tiny (<5 μm) interstitial grains. In some of the blebs of felsite, interstices are also filled by red-brown glass.

The compositions of phases in the felsite in the black breccia are similar to those of equivalent phases that comprise the felsite in the gray breccia. K-feldspar ranges in composition from about $\text{An}_{18.6}\text{Ab}_{41.3}\text{Or}_{39.4}\text{Cel}_{1.7}$ to $\text{An}_{1.8}\text{Ab}_{21.2}\text{Or}_{72.6}\text{Cel}_{4.5}$ (Figure 25). K-feldspar grains in veins are more enriched in both Or and Cel components than are the K-feldspar grains in the felsite blebs. The entire range in composition overlaps that of K-feldspar in the felsite of the gray breccia, but extends to lower Or-contents and does not reach as high Or-contents. The zoning trend is less well-defined because K-feldspar microphenocrysts are smaller and less abundant, but core and rim compositions on small (20-30 μm) K-feldspar microphenocrysts indicate that the zoning has the same sense as in the felsite of the gray breccia. The composition of plagioclase (Figure 25) is about $\text{An}_{58}\text{Ab}_{41}\text{Or}_1$, and within the compositional range of plagioclase in the felsite in the gray breccia. Low-Ca pyroxenes (Figure 13) range in composition from about $\text{En}_{51}\text{Wo}_6\text{Fs}_{43}$ to about En_4 and Fs_{50} and

high-Ca pyroxenes range in composition from about $\text{En}_{39}\text{Wo}_{39}\text{Fs}_{22}$ to about $\text{En}_{36}\text{Wo}_{30}\text{Fs}_{34}$; these compositions are similar to those of the pyroxenes in the felsite of the gray breccia, except that the high-Ca pyroxenes in the black breccia felsite are slightly less Fe-rich.

POST CONSOLIDATION RECRYSTALLIZATION AND REACTION FEATURES

Clasts in both breccias have been affected by analogous types of recrystallization and reactions with felsite and/or the breccia groundmass. In both breccias, the effects are more pronounced at the clast margins than in the clast interiors indicating these features post-date brecciation. This is obviously the case in the black breccia where the effects of recrystallization and reaction are mostly limited to the outer 1-10 μm of clast margins. In contrast, recrystallization in the gray breccia has been more pervasive and even the interiors of the largest clasts have been somewhat affected.

Recrystallization effects are pervasive throughout the gray breccia. However, the following features are more developed at clast margins than in clast interiors. Pyroxene grains in many lithic clasts are recrystallized to an equigranular mosaic. Turbid, high-Ca pyroxene is rimmed by clear, inclusion-free pigeonite, and turbid plagioclase is rimmed by clear, inclusion-free plagioclase of similar composition. Highly granulated margins of lithic clasts are recrystallized to an inequigranular, nonporous mosaic of plagioclase and pyroxene.

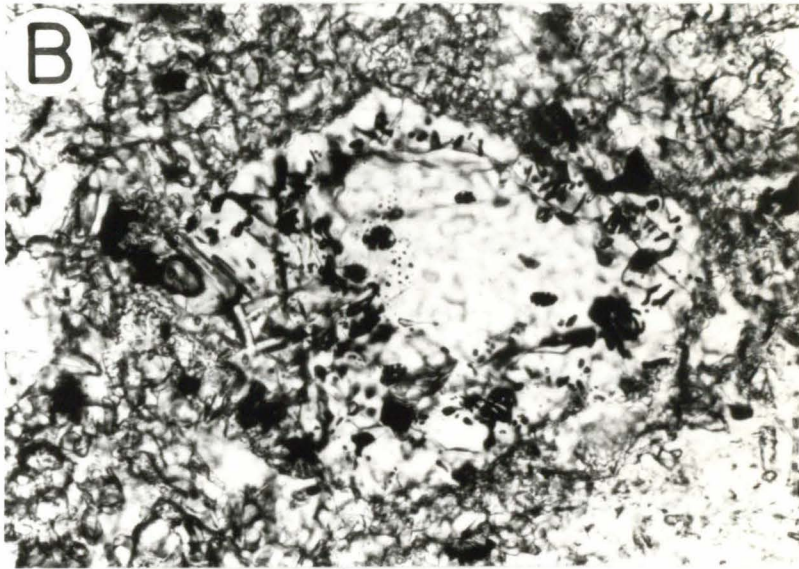
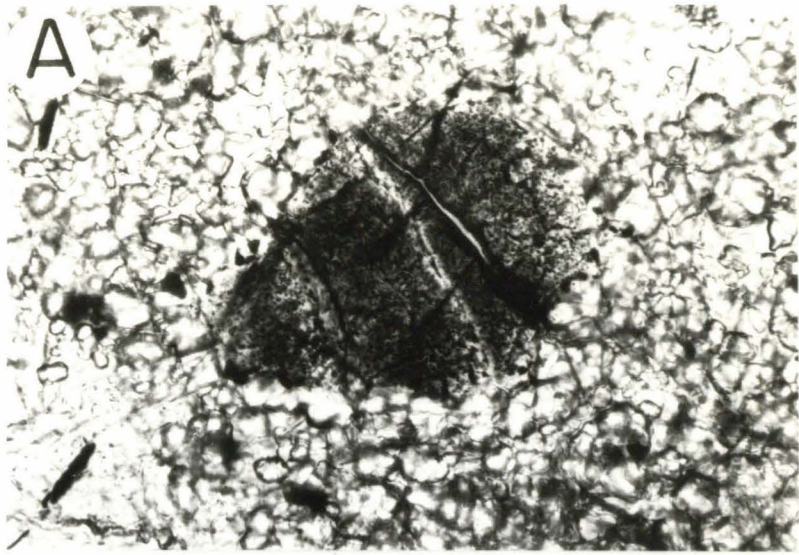
Olivine and felsite have reacted to produce continuous rims of orthopyroxene 3-15 μm thick around the olivine; the Fs-content of the orthopyroxene of the rim is generally about 5-7 mole percent less than

Figure 26: Recrystallization and reaction textures. All photomicrographs taken in plane polarized light. Numbers in parentheses refer to the horizontal scale. (Photography by O. B. James).

(A) High-Ca pyroxene in the gray breccia rimmed by low-Ca pyroxene (0.88 mm).

(B) Olivine in gray breccia with rim of low-Ca pyroxene and opaques (0.48 mm). Lath network developed locally.

(C) Olivine in black breccia with rim of low-Ca pyroxene (0.70 mm).



the Fo-content of the unreacted olivine, and orthopyroxene becomes increasingly Fe-rich with increasing distance from olivine grains. In many places, these rimmed grains are surrounded by an open network of orthopyroxene laths ($\sim \text{En}_{64}\text{Wo}_2\text{Fs}_{34}$). The orthopyroxene laths are 10-30 μm long and 2-10 μm wide and interstices between them are void. In some areas, such as in granulated olivine gabbro clasts, the olivine has been extensively replaced and the orthopyroxene network pervades the interstices between the grains and is the cementing agent holding the grains together.

Some plagioclase clasts have reacted with feldspar and have been largely replaced by K-feldspar (Figure 6). The original fragmental outlines of the clasts are preserved, but only a few isolated plagioclase relicts, in optical continuity, remain within the K-feldspar. Other plagioclase grains in contact with feldspar are rimmed by K-feldspar but show no internal replacement.

Ilmenite in contact with the feldspar has Nb-rich margins, and small ilmenite fragments in the matrix tend to be more Nb-rich than cores of larger ilmenite fragments. This Nb-enrichment could be explained by an exchange reaction between feldspar and low-Nb ilmenite to produce high-Nb ilmenite, or by precipitation of high-Nb ilmenite from the feldspar as rims on preexisting low-Nb ilmenite.

Postconsolidation recrystallization is volumetrically less significant in the clasts in the black breccia, and for the most part, is limited to narrow zones at clast margins. Recrystallization features are: (1) devitrification of maskelynite clasts; (2) enlargement of exsolution lamellae at the margins of pyroxene clasts; (3) healing of fractures in plagioclase, pyroxene and olivine; and (4) minor sintering of small

fragments within granulated lithic clasts. Excluding the last point, no post-consolidation recrystallization features are found more than 5-10 μm from clast margins.

Reaction of olivine with the black breccia groundmass has produced orthopyroxene rims around olivine clasts. Thin (5-10 μm) continuous rims of orthopyroxene, which contain micron-sized inclusions of ilmenite and plagioclase, mantle all olivine grains that are in contact with the black breccia groundmass. These rims grade outward into coronas ≤ 100 μm wide that have a pyroxene-microphyric texture. In these coronas, orthopyroxene laths 10-30 μm long and 2-10 μm wide form an interlocking network, with interstices filled by plagioclase, ilmenite, phosphate minerals and accessory phases. Contacts between the pyroxene-microphyric coronas and the equigranular groundmass are gradational. Orthopyroxene rims are 4-10 mole percent higher in Fs-content than the Fo-content of the host olivine. With increasing distance from the olivine, the orthopyroxene is more magnesian and less abundant.

Tridymite clasts are surrounded by coronas of tridymite-bearing felsite 10-30 μm wide (Figure 24); and these coronas are, in turn, rimmed by discontinuous halos of mosaic-textured pyroxene grains. The felsite coronas could be associated with tridymite clasts because both were associated in the protolith. However, continuous felsite rims are found on every tridymite clast in the black breccia suggesting that these rims formed after incorporation of the tridymite clasts and involved reaction with the groundmass. In support of this interpretation, the well-rounded shapes of the tridymite clasts suggest resorption of tridymite has occurred. However, the source for K_2O to make the K-feldspar in the coronas is

problematic because of the low K_2O concentration in the black breccia groundmass. The compositions of the pyroxenes that rim the feldspar range from $En_{63}Wo_3Fs_{34}$ to $En_{54}Wo_5Fs_{41}$, within the range of typical compositions for groundmass pyroxenes.

The margins (1-3 μm) of plagioclase fragments tend to approach compositions of about An_{65-75} regardless of the interior composition of the fragment. The actual An values that rim compositions approach varies from place to place in the black breccia. The small size of the rims makes it difficult to determine if they are produced by an exchange reaction between plagioclase clasts and the groundmass or by overgrowth by thin layers of groundmass plagioclase on clasts.

Some clasts appear highly corroded and embayed. Isolated, ragged plagioclase grains, separated by K-rich mesostasis, are in optical continuity suggesting replacement of plagioclase by K-rich mesostasis. Elsewhere, thin selvages of feldspar coat ragged edges of some plagioclase grains. The morphology of zircon and phosphate mineral clasts is suggestive of resorption by the black breccia groundmass. Both types of clasts are well-rounded, and one large, apatite clast is deeply embayed and ragged on one side.

Table 1: Relative Abundances of Fragments Larger than 0.14 mm
in the Gray Breccia (Data Courtesy of O. B. James)

Lithic Fragments			Mineral Fragments		
	Vol. % Abundances			Vol. % Abundances	
	Relative to Lithic Frags.	Relative to All Frags.		Relative to Min. Frags.	Relative to All Frags.
Gabbro	21.0	17.3	Plagioclase	51.7	9.0
Granulated Ol-gabbro	16.6	13.7	Pyroxene	17.2	3.0
Ophitic Basalt	27.4	22.6	Olivine*	29.6	5.2
Bladed Basalt	19.2	15.8	Opaque minerals	1.4	0.2
Misc. Basalt and Gabbro	7.2	5.9		100.0	17.5
Basaltic Chondrules	3.1	2.6			
Basaltic Aphanite	2.8	2.3			
Quartzo- feldspathic rock	0.4	0.3			
ANT-Suite Melt-Rock	2.3	1.9			
	100.0	82.5			

*Includes pyroxene rims

Table 2: Gray Breccia Lithic Clasts

Clast Lithology	Texture		Assemblage and Mode	Compositions
	Primary	Secondary		
Gabbro	Hypidiomorphic to Xenomorphic granular; subhedral pyroxene and olivine are enclosed by anhedral poikilitic plagioclase. Anhedral pyroxene and plagioclase form a mosaic. Chromite occurs as inclusions in olivine and as sparse, large subhedral crystals. Ilmenite is interstitial to plagioclase and pyroxene or included in pyroxene	Deformation Features: Plagioclase and olivine show undulatory and patchy extinction. Some plagioclase, pyroxene and olivine have been crushed. Recrystallization Features: Primary pyroxene has been converted to a mosaic of turbid pyroxene. Grains at the margins of the pyroxene mosaics are, in many places, inclusion-free. Olivine is locally a mosaic of minute grains. Plagioclase is turbid; grain margins are locally clear and inclusion-free. Reaction Features: Olivine is partly or completely converted to orthopyroxene at clast margins.	Variable from clast to clast Plagioclase: 30-50% Pyroxene: 50-60% Olivine: 0 to 20% Cr-spinel: 0 - 10% Ilmenite: 1 to 5%	Plagioclase: An ₇₈₋₉₃ (Or content up to 8-8% in more sodic plagioclase.) Pyroxene: Low-Ca; ~En ₅₃ Wo ₄₇ Fs ₂₉ to ~En ₅₀ Wo ₄₇ Fs ₄₃ ; High-Ca; En ₄₇ Wo ₃₅ Fs ₁₈ to En ₃₉ Wo ₃₇ Fs ₂₈ Olivine: Fo ₅₂₋₆₀ but most are Fo ₅₈₋₆₀ Cr-spinel: 5.1 to 14.4 wt.% TiO ₂ Ilmenite: Fe/Fe+Mg = 0.87-0.92 Catatom % Nb = 0.02-0.3
Granulated olivine-gabbro	Xenomorphic-granular intergrowth of olivine, pyroxene, plagioclase, and minor interstitial ilmenite. Cr-spinel forms tiny inclusions in olivine.	Deformation Features: Olivine, plagioclase and pyroxene are granulated; and the rock is an inequigranular, porous mosaic of subangular fragments of these minerals. Recrystallization Features: Mineral fragments are welded together by low-Ca pyroxene. K-rich mesostasis occurs in healed fractures of some plagioclase grains. Both plagioclase and large pyroxene grains are turbid. Reaction Features: Olivine is replaced by a porous lathwork of low-Ca, Mg-rich pyroxene.	Plagioclase: ~40% Pyroxene: ~30% Olivine+pyroxene lathwork ~30% Cr-spinel: trace Ilmenite: trace	Plagioclase: An ₈₃₋₉₁ (Or content up to 0.6 in more sodic plagioclase.) Pyroxene: Low-Ca; En ₆₁ Wo ₃₉ Fs ₃₄ to ~En ₄₈ Wo ₃₈ Fs ₄₃ ; High-Ca; ~En ₄₃ Wo ₃₆ Fs ₂₁ Olivine: Fo Cr-spinel: 11.8 wt. % TiO ₂ Pyroxene Lathwork: En ₆₀ Wo ₃₃ Fs ₃₇ to En ₅₄ Wo ₃₃ Fs ₄₃
Subophitic basalt	Subophitic to intergranular; anhedral pyroxene, ilmenite and Cr-spinel fill interstices between plagioclase laths. Rare olivine and plagioclase phenocrysts are present. Ilmenite is interstitial or included by pyroxene. Grain size is uniform in each clast but variable from clast to clast.	Deformation Features: Variable. Some clasts show no internal deformation. In others, plagioclase laths have been bent or broken, and some pyroxene grains have been broken. Recrystallization Features: Pyroxene is recrystallized to a fine-grained turbid mosaic. Locally, rims of pyroxene mosaics are clear. Some pyroxene grains have micron-sized exsolution lamellae. Plagioclase is turbid. Reaction Features: Olivine is partially to completely converted to a network of low-Ca pyroxene laths. Melting Features: Fractures in pyroxene are filled by glass.	Plagioclase: 40-50% Pyroxene: 50-60% (mainly pigeonite) Olivine+pyroxene lathwork: as much as % in some clasts Cr-spinel: <2% Ilmenite: 1-5%	Plagioclase: An ₇₄₋₉₄ (Or content up to 0.8 in more sodic plagioclase.) Pyroxene: Low-Ca; En ₅₇ Wo ₃₅ Fs ₂₁ to En ₄₄ Wo ₃₂ Fs ₄₄ ; High-Ca; En ₄₀ Wo ₃₉ Fs ₂₁ to En ₃₆ Wo ₃₆ Fs ₃₈ Olivine: Fo Pyroxene laths: as much as % in some clasts Cr-spinel: 8.3-13 wt. % TiO ₂ Ilmenite: Fe/Fe+Mg = .90-.92 Catatom % Nb = .05-.45
Bladed basalt	Intergrowth of subparallel blades of pyroxene and plagioclase. Ilmenite and Cr-spinel form interstitially or equant inclusions in pyroxene. K-rich mesostasis fills tiny interstices.	Deformation Features: Some plagioclase grains show undulatory extinction. Recrystallization Features: Pyroxene is recrystallized to a fine-grained, turbid mosaic. Felsite has permeated some clasts.	Plagioclase: 40-50% Pyroxene: 50-60% Cr-spinel: 1-2% Ilmenite: 2-4% Plagioclase: 40-50% Pyroxene: 50-55% Cr-spinel: trace Ilmenite: 1-5%	Plagioclase: An ₈₂ Ab ₁₃ Or ₃ to An ₈₉ Ab ₁₀ Or ₇ Pyroxene: Low-Ca; En ₅₃ Wo ₃₅ Fs ₄₂ to En ₄₇ Wo ₃₉ Fs ₄₄ ; High-Ca; En ₄₀ Wo ₃₉ Fs ₂₁ to En ₃₇ Wo ₃₉ Fs ₂₄ Cr-spinel: 11.8 wt. % TiO ₂ Ilmenite: Fe/Fe+Mg = .90-.92 Plagioclase: An ₇₆ Ab ₁₉ Or ₆ to An ₇₆ Ab ₁₉ Or ₆ Pyroxene: Low-Ca; En ₅₄ Wo ₃₆ Fs ₄₀ to En ₃₉ Wo ₄₁ Fs ₂₀ to En ₄₂ Wo ₃₃ Fs ₂₅ Ilmenite: Fe/Fe+Mg = .84 Catatom % Nb = .25
Basaltic "chondrules"	Intergrowth of subparallel to skeletal radiating acicular and an interstitial fine-grained mosaic of pyroxene and ilmenite and Cr-spinel. Similar to some clasts of "bladed basalt", except the "chondrules" are much finer-grained and have more acicular plagioclase grains.	Deformation Features: None. Recrystallization Features: None.	Plagioclase: 40-45% Pyroxene: 50-55% Ilmenite: 1-2%	Plagioclase: An ₆₄ Ab ₃₅ Or ₄ to An ₈₃ Ab ₁₆ Or ₅ Pyroxene: Low-Ca, En ₅₃ Wo ₃₅ Fs ₄₁ to En ₅₁ Wo ₃₆ Fs ₄₃ High-Ca; ~En ₄₆ Wo ₃₄ Fs ₂₀ to En ₄₂ Wo ₃₃ Fs ₂₅ Ilmenite: Fe/Fe+Mg = .84 Catatom % Nb = .25
Basaltic aphanites	Equigranular, to pyroxene phyrlic, to plagioclase-phyric. Most clasts are an extremely fine-grained equigranular intergrowth of plagioclase, pyroxene, and ilmenite. In some clasts, the pyroxene grains are skeletal and acicular. In one clast, a plagioclase-phyric texture is developed; acicular micro-phenocrysts of plagioclase are set in a matrix of micro-meter-sized, equigranular plagioclase, pyroxene and ilmenite.	Deformation Features: Cataclasis has produced a porous aggregate of inequigranular fragments of plagioclase and orthopyroxene. Recrystallization Features: The outer 100µm of the clast is a nonporous recrystallized aggregate. Recrystallization in the clast interior has welded grains. Reaction Features: Large pyroxene fragments are compositionally and optically zoned. Zoning parallels fragment edges; suggesting that it post dates granulation.	Plagioclase: 30-40% Orthopyroxene: 60-70% High-Ca pyroxene: trace Plagioclase: ~60% Quartz: ~40%	Plagioclase: An ₉₁ Ab ₈ Or ₃ to An ₈₀ Ab ₁ Fs ₁₉ to En ₆₂ Wo ₃₅ Fs ₃₅ ; High-Ca; ~En ₄₆ Wo ₃₄ Fs ₂₀ Plagioclase: An ₅₆ Ab ₄₂ Or ₁ to An ₆₂ Ab ₃₅ Or ₆ Quartz: ~40%
Granulated norite	Primary textures have been destroyed by cataclasis. The size of the mineral fragments indicate that the parent rock was very coarse-grained. Both plagioclase and pyroxene are clear and inclusion-free.	Deformation Features: Plagioclase grains have been broken and intruded by felsite. Plagioclase and quartz exhibit patchy extinction.	Plagioclase: ~70% Pyroxene: ~30% Ilmenite: ~5% Whitlockite: trace	Plagioclase: An ₇₀ Ab ₂₉ Or ₅ to An ₇₉ Ab ₂₀ Or ₅ Pyroxene: ~En ₅₂ Wo ₃₈ Fs ₃₈ Ilmenite: Fe/Fe+Mg = 0.89 Catatom % Nb = 0.5
Granulated tonalite	Hypidiomorphic-granular; interlocking anhedral grains of quartz and subhedral to euhedral grains of plagioclase. Quartz contains abundant submicron-sized, elongate voids. Plagioclase shows normal progressive zoning and is free of inclusions.	Deformation Features: None. Recrystallization Features: None.	Plagioclase: ~60% Quartz: ~40%	Plagioclase: An ₅₆ Ab ₄₂ Or ₁ to An ₆₂ Ab ₃₅ Or ₆
ANT-suite hornfels	Recrystallized microsubophitic; blocky and lath-shaped plagioclase are enclosed by mosaic intergrowths of tiny pyroxene grains. K-rich mesostasis and Whitlockite fill interstices.	Deformation Features: None. Recrystallization Features: None.	Plagioclase: ~70% Pyroxene: ~30% Ilmenite: ~5% Whitlockite: trace	Plagioclase: An ₇₀ Ab ₂₉ Or ₅ to An ₇₉ Ab ₂₀ Or ₅ Pyroxene: ~En ₅₂ Wo ₃₈ Fs ₃₈ Ilmenite: Fe/Fe+Mg = 0.89 Catatom % Nb = 0.5

TABLE 3 : BULK COMPOSITIONS OF LITHIC CLASTS IN THE GRAY BRECCIA DETERMINED BY ELECTRON MICROPROBE POINT COUNT ANALYSIS (PCA) OR DEFOCUSED BEAM ANALYSIS (DBA)

	1	2	3	4	5	6	7	8	9
SiO ₂	43.87	47.66	49.2	49.4	50.1	50.2	48.06	71.9	50.9
TiO ₂	0.45	2.48	0.5	2.2	0.8	1.0	0.30	0.1	0.2
Al ₂ O ₃	9.80	14.63	15.1	14.8	14.8	13.7	13.65	14.4	22.9
Cr ₂ O ₃	0.42	0.14	0.2	0.2	0.2	0.2	0.42	0.0	0.1
MgO	15.57	7.81	8.7	8.4	9.4	9.2	18.16	0.6	4.7
CaO	6.89	11.93	12.2	11.1	11.4	8.5	7.45	5.7	11.7
MnO	0.22	0.20	0.2	0.2	0.2	0.2	0.18	0.0	<0.1
FeO	22.40	13.81	12.8	13.7	12.6	14.8	11.34	1.6	7.2
Na ₂ O	0.38	1.02	0.4	0.8	0.6	1.0	0.37	2.4	1.8
K ₂ O	0.02	0.06	0.0 ₁	0.2	0.0 ₃	0.0 ₂	0.01	0.6	0.2
P ₂ O ₅	0.09	0.12	0.1	0.1	0.1	0.1	0.07	0.1	0.3
ZrO ₂	<0.01	0.02	-	-	-	-	-	-	-
SO ₃	0.02	0.02	<0.1	0.1	0.1	0.2	-	0.0	0.0
NiO	0.01	-	0.0	0.1	<0.1	0.0	<0.01	0.1	0.0
BaO	<0.01	-	-	-	-	-	<0.01	-	-
Total	100.14	99.90	99.4	101.3	100.3	99.1	100.01	97.5	99.91
Catonom % Normative Minerals									
An	25.33	36.09	40.1	36.7	38.2	34.0	34.85	28.0	53.9
Ab	3.46	9.40	4.1	7.3	5.2	9.1	3.26	22.7	16.4
Or	0.12	0.36	0.1	1.1	0.2	0.1	0.06	4.0	1.1
Cel	0.00	0.00	-	-	-	-	<0.01	-	-
En	17.04	21.83	24.7	23.3	26.2	26.1	32.88	1.7	13.0
Fs	13.51	18.35	19.6	18.4	18.6	22.0	11.23	2.5	10.8
Wo	3.50	9.54	8.7	7.3	7.3	3.5	0.37	0.4	0.9
Fo	19.92	0.22	0.0	0.0	0.0	0.0	12.19	0.0	0.0
Fa	15.79	0.19	0.0	0.0	0.0	0.0	4.16	0.0	0.0
Qtz	0.00	0.00	1.6	2.1	2.5	3.0	0.00	40.3	2.8
Ilm	0.64	3.54	0.8	3.1	1.2	1.4	0.41	0.2	0.3
Chr	0.47	0.16	0.2	0.3	0.3	0.3	0.42	0.0	0.1
Zir	0.00	0.02	-	-	-	-	-	-	-
Ap	0.19	0.26	0.1	0.3	0.3	0.2	0.14	0.2	0.7
FeS	0.03	0.03	<0.1	0.1	0.1	0.3	0.00	0.0	0.0
NiO	0.01	0.00	0.0	0.1	<0.1	0.0	0.00	0.1	0.0

- 1) Gabbro, PCA
- 2) Coarse grained subophitic basalt, PCA
- 3) Fine grained subophitic basalt, DBA
- 4) Bladed basalt, DBA
- 5) Basaltic chondrules, DBA
- 6) Basaltic aphanite, DBA
- 7) Norite, PCA
- 8) Tonalite, DBA
- 9) ANI-suite melt-rock, DBA

Table 4
Gray Breccia Mineral Clasts > 140 μ m

Type	Textural Features	Grain Size	Composition
Plagioclase	Clasts are angular to subangular and generally cloudy; rare small, clear clasts, similar to those in black breccia. Cloudiness due to abundant pyroxene inclusions. Deformation features rare but include undulatory extinction, healed fractures, and bent lamellae. Some plagioclase is extensively replaced by K-spar. Clasts in contact with felsite have K-spar rims.	Up to 300 μ m	An50-94
Pyroxene	Clasts are angular to subangular and cloudy due to tiny ilmenite and plagioclase inclusions. Sub-micron exsolution lamellae in some grains.	Up to ~200 μ m	High-Ca: no analyses Low-Ca: En81-47 Wo < 2-10Fs19-46
Olivine	Clasts are angular. The only deformation features are healed fractures. Reaction with felsite resulted in replacement by low-Ca pyroxene.	Up to ~500 μ m	Fo48-62
Ilmenite	Subangular to subrounded.	Up to ~200 μ m	Nb ₂ O ₅ < 1.0 wt. % MgO: 1.5-3.5 wt. %

Table 5: Representative Analyses of Feldspars in 12013

	1	2	3	4	5	6	7	8	9	10	11	12	13	14	15
SiO ₂	54.45	44.38	46.70	47.47	45.63	46.94	45.50	49.48	54.76	45.27	46.08	46.62	48.86	46.62	48.54
TiO ₂	0.04	0.00	0.01	0.11	0.08	0.16	0.00	0.06	0.16	0.02	0.00	0.10	0.08	0.02	0.08
Al ₂ O ₃	28.50	36.03	34.15	33.13	34.95	34.25	35.12	31.72	27.75	34.57	34.86	33.80	34.03	34.58	31.33
MgO	0.04	0.02	0.04	0.09	0.01	0.05	0.00	0.07	0.07	0.02	0.12	0.00	0.07	0.02	0.06
CaO	11.19	18.97	17.09	17.58	18.14	17.65	18.26	15.39	10.29	18.52	17.28	17.77	17.47	17.54	14.80
FeO	0.13	0.14	0.36	0.24	0.30	0.17	0.12	0.27	0.25	0.16	0.35	0.58	0.30	0.44	0.47
Na ₂ O	4.82	0.66	1.55	1.62	1.21	1.32	0.22	2.65	5.32	1.25	1.28	1.56	1.70	1.66	3.04
K ₂ O	0.29	0.04	0.06	0.03	0.02	0.03	0.02	0.14	0.57	0.07	0.06	0.03	0.05	0.04	0.09
BaO	0.43	0.13	0.08	0.00	0.00	0.44	0.00	0.18	0.40	0.02	0.08	0.00	0.00	0.20	0.06
Total	99.89	100.37	100.04	100.27	100.34	101.01	99.24	99.96	99.57	99.90	100.11	100.46	100.56	101.12	98.47

Number of Cations Normalized to 16 Oxygens

Si	2.468	2.044	2.147	2.179	2.098	2.145	2.104	2.267	2.495	2.094	2.117	2.142	2.188	2.127	2.260
Ti	0.001			0.004	0.003	0.006		0.002	0.005	0.001		0.003	0.003	0.001	0.003
Al	1.523	1.957	1.851	1.793	1.895	1.846	1.915	1.714	1.490	1.885	1.889	1.832	1.797	1.861	1.720
Mg	0.003	0.001	0.003	0.006	0.001	0.003		0.005	0.005	0.001	0.008		0.005	0.001	0.004
Ca	0.543	0.936	0.842	0.865	0.894	0.864	0.905	0.756	0.502	0.918	0.851	0.875	0.838	0.858	0.738
Fe	0.005	0.005	0.014	0.009	0.012	0.006	0.005	0.010	0.010	0.006	0.013	0.022	0.011	0.017	0.018
Na	0.424	0.059	0.138	0.144	0.108	0.117	0.020	0.235	0.470	0.112	0.114	0.139	0.148	0.147	0.274
K	0.017	0.002	0.004	0.002	0.001	0.002	0.001	0.008	0.033	0.004	0.004	0.002	0.003	0.002	0.005
Ba	0.008	0.002	0.001			0.008		0.003	0.007		0.001			0.004	0.001
Ab	42.37	5.86	13.82	14.27	10.70	11.70	1.97	23.49	46.42	10.84	11.41	13.69	14.76	14.45	26.89
An	53.59	93.00	83.91	84.04	87.97	85.50	90.47	73.86	48.20	88.00	85.08	83.94	82.27	83.18	70.28
Or	1.68	0.23	0.35	0.17	0.12	0.18	0.12	0.82	3.27	0.40	0.35	0.17	0.29	0.23	0.52
Others*	2.36	0.91	1.92	1.52	1.21	2.62	7.44	1.83	2.11	0.76	3.16	2.20	2.68	2.14	2.31

	16	17	18	19	20	21	22	23	24	25	26	27	28	29	30
SiO ₂	44.72	48.68	54.65	45.50	46.95	50.30	55.60	62.29	66.08	61.88	63.29	52.77	60.90	65.47	61.55
TiO ₂	0.20	0.09	0.06	0.02	0.01	0.10	0.09	0.09	0.10	0.06	0.00	0.00	0.00	0.00	0.00
Al ₂ O ₃	34.78	32.91	28.90	34.74	34.38	31.47	27.24	21.97	17.80	21.12	19.66	30.37	22.23	19.16	21.57
MgO	0.02	0.02	0.07	0.42	0.05	0.00	0.02	0.00	0.03	0.00	0.00	0.02	0.01	0.02	0.00
CaO	18.93	15.64	11.80	17.90	16.34	12.38	10.20	3.48	0.80	2.77	0.49	12.16	3.96	1.28	2.39
FeO	0.16	0.31	0.21	0.93	0.13	0.41	0.39	0.10	0.00	0.11	0.16	0.22	0.11	0.05	0.14
Na ₂ O	0.82	2.41	4.47	1.07	2.25	4.64	5.25	3.27	3.02	3.42	1.60	4.68	4.73	2.50	2.86
K ₂ O	0.02	0.05	0.30	0.05	0.10	0.10	0.49	9.03	10.68	8.67	12.13	0.16	6.85	10.09	10.16
BaO	0.64	0.04	0.00	0.21	0.11	0.00	0.08	0.86	1.17	1.85	1.71	0.11	0.38	1.39	1.67
Total	100.29	100.15	100.46	100.84	100.32	99.40	99.36	101.09	99.68	99.88	99.04	100.49	99.17	99.96	100.34

Number of Cations Normalized to 16 Oxygens

Si	2.074	2.225	2.458	2.090	2.150	2.307	2.526	2.823	3.025	2.849	2.944	2.383	2.791	2.981	2.833
Ti	0.007	0.003	0.002	0.001		0.003	0.003	0.003	0.003	0.002					
Al	1.902	1.774	1.533	1.881	1.856	1.702	1.459	1.174	0.961	1.147	1.078	1.617	1.201	1.029	1.170
Mg	0.001	0.001	0.005	0.029	0.003	0.001	0.001	0.002	0.002			0.001	0.001	0.001	
Ca	0.941	0.766	0.569	0.881	0.802	0.608	0.497	0.169	0.039	0.137	0.024	0.588	0.194	0.062	0.118
Fe	0.006	0.012	0.008	0.036	0.005	0.016	0.015	0.004		0.004	0.006	0.008	0.004	0.002	0.005
Na	0.074	0.214	0.390	0.095	0.200	0.413	0.463	0.287	0.268	0.305	0.144	0.410	0.420	0.221	0.255
K	0.001	0.003	0.017	0.003	0.006	0.006	0.028	0.522	0.624	0.509	0.720	0.009	0.401	0.586	0.597
Ba	0.012	0.001		0.004	0.002		0.001	0.015	0.021	0.033	0.031	0.002	0.007	0.025	0.030
Ab	7.18	21.37	38.99	9.36	19.63	39.58	46.25	28.74	26.81	30.54	14.44	40.24	41.13	22.08	25.39
An	90.84	76.54	55.94	83.65	78.78	58.35	48.15	16.90	3.92	13.67	2.44	57.72	18.54	6.25	11.72
Or	0.12	0.29	1.72	0.29	0.57	0.56	2.84	51.92	62.38	50.52	71.99	0.90	39.18	58.62	59.35
Others*	1.86	1.80	3.35	6.70	1.02	1.51	2.76	2.44	6.89	5.27	11.13	1.14	1.15	13.05	3.54

*BaAl₂Si₂O₈ + PMAl₂Si₂O₈ + CaFMSi₃O₈ + []Si₄O₈

- | | | | |
|------|---|--------|--|
| 1) | Plagioclase in quartzofeldspathic rock, black breccia | 16) | Plagioclase in granulated norite clast, gray breccia |
| 2) | Plagioclase in granulated norite clast, black breccia | 17) | Plagioclase in ANI-suite melt-rock, gray breccia |
| 3) | Plagioclase in plagioclase porphyry, black breccia | 18) | Plagioclase in tonalite clast, gray breccia |
| 4) | Plagioclase in ANI-suite hornfels, black breccia | 19-21) | Plagioclase mineral fragments, gray breccia |
| 5) | Plagioclase in ANI-suite melt-rock, black breccia | 22) | Plagioclase in felsite patch, gray breccia |
| 6) | Plagioclase in subophitic basalt, black breccia | 23) | Alkali feldspar in felsite patch, gray breccia |
| 7-9) | Plagioclase mineral fragments, black breccia | 24) | Alkali feldspar in felsite patch, gray breccia |
| 10) | Plagioclase in gabbro clast, gray breccia | 25) | Alkali feldspar in groundmass, gray breccia |
| 11) | Plagioclase in olivine gabbro clast, gray breccia | 26) | Alkali feldspar in groundmass, gray breccia |
| 12) | Plagioclase in subophitic basalt clast, gray breccia | 27) | Plagioclase in felsite bleb, black breccia |
| 13) | Plagioclase in bladed basalt clast, gray breccia | 28) | Alkali feldspar in felsite bleb, black breccia |
| 14) | Plagioclase in basaltic "chondrule", gray breccia | 29) | Alkali feldspar in felsite bleb, black breccia |
| 15) | Plagioclase in aphanite clast, gray breccia | 30) | Alkali feldspar in felsite vein, black breccia |

Table 6: Representative Analyses of Pyroxenes in 12013

	1	2	3	4	5	6	7	8	9	10	11	12	13	14	15
SiO ₂	51.26	51.45	50.50	54.75	53.22	53.63	51.37	52.29	52.18	50.82	50.74	52.14	52.50	52.33	52.21
TiO ₂	0.95	0.87	0.96	0.47	0.50	0.47	0.39	0.61	0.52	0.83	1.27	0.44	0.84	0.33	0.43
Al ₂ O ₃	1.08	1.07	0.68	1.38	1.43	1.14	0.25	0.89	0.44	0.97	1.85	0.62	1.06	0.40	0.41
Cr ₂ O ₃	0.03	0.28	0.14	0.86	0.66	0.61	0.25	0.45	0.21	0.33	0.43	0.33	0.40	0.23	0.25
MgO	12.54	12.58	10.89	31.07	27.09	26.23	15.13	13.83	18.21	19.33	13.11	18.02	13.59	20.12	20.93
CaO	18.62	18.19	17.76	1.38	1.22	1.21	4.92	18.88	5.37	1.92	18.60	2.95	18.45	1.55	1.74
MnO	0.26	0.27	0.18	0.13	0.18	0.26	0.41	0.00	0.32	0.36	0.18	0.45	0.21	0.35	0.31
FeO	15.11	14.40	18.45	10.91	15.66	17.50	26.75	14.10	23.44	25.73	12.98	27.06	14.14	24.73	24.17
Na ₂ O	0.00	0.09	0.20	0.14	0.00	0.01	0.00	0.00	0.02	0.01	0.13	0.00	0.17	0.02	0.00
Total	99.85	99.20	99.76	101.09	99.96	101.06	99.46	101.05	100.71	100.30	99.29	102.01	101.36	100.06	100.45

Number of Cations Normalized to 4.0

Si	1.957	1.973	1.954	1.909	1.922	1.931	2.000	1.958	1.968	1.925	1.934	1.958	1.961	1.976	1.956
Ti	0.027	0.025	0.028	0.012	0.014	0.013	0.011	0.017	0.015	0.024	0.036	0.012	0.024	0.009	0.012
Al	0.049	0.048	0.031	0.057	0.061	0.048	0.011	0.039	0.020	0.043	0.083	0.027	0.047	0.018	0.018
Cr	0.001	0.008	0.004	0.024	0.019	0.017	0.008	0.013	0.006	0.010	0.013	0.010	0.012	0.007	0.007
Mg	0.714	0.719	0.628	1.615	1.459	1.408	0.879	0.772	1.024	1.092	0.745	1.009	0.757	1.133	1.169
Ca	0.762	0.748	0.736	0.052	0.047	0.047	0.205	0.758	0.217	0.078	0.760	0.119	0.739	0.063	0.070
Mn	0.008	0.009	0.006	0.004	0.006	0.008	0.014	0.000	0.010	0.012	0.006	0.014	0.007	0.011	0.010
Fe	0.483	0.462	0.597	0.318	0.473	0.527	0.872	0.442	0.739	0.815	0.414	0.850	0.442	0.781	0.758
Na	0.000	0.007	0.015	0.009	0.000	0.001	0.000	0.000	0.001	0.001	0.010	0.000	0.012	0.001	0.000

Fe ₂ Si ₂ O ₆	24.57	23.61	29.39	15.75	23.64	26.43	44.30	22.01	37.05	40.55	20.99	42.83	22.24	39.38	37.75
Mg ₂ Si ₂ O ₆	35.72	36.09	30.61	79.00	72.05	69.57	43.98	38.49	50.60	53.54	37.26	50.00	37.53	56.30	57.51
Ca ₂ Si ₂ O ₆	36.88	36.24	35.38	0.78	0.36	0.69	9.79	36.45	10.12	2.53	35.83	4.95	35.48	2.54	2.80
Others*	2.83	4.06	4.62	4.47	3.95	3.31	1.93	3.05	2.23	3.38	5.92	2.22	4.75	1.78	1.94

	16	17	18	19	20	21	22	23	24	25	26	27	28	29	30
SiO ₂	53.21	53.95	51.79	52.00	51.52	51.63	52.62	50.91	50.54	50.46	51.80	51.87	50.97	51.54	52.00
TiO ₂	0.40	0.62	0.52	0.54	0.49	0.58	0.47	0.47	1.58	0.70	0.27	0.54	0.49	0.80	0.54
Al ₂ O ₃	0.97	1.34	0.87	0.60	0.50	0.57	0.95	0.53	2.02	1.30	0.82	0.77	0.49	0.76	0.43
Cr ₂ O ₃	0.30	0.67	0.25	0.00	0.11	0.00	0.41	0.14	0.63	1.17	0.24	0.52	0.25	0.34	0.35
MgO	23.48	28.41	21.43	17.56	7.54	13.23	21.21	17.10	15.14	16.98	21.23	15.17	16.23	12.90	17.59
CaO	1.31	1.75	1.83	3.08	18.04	19.80	6.72	3.42	17.07	7.63	1.49	18.00	4.41	19.09	2.70
MnO	0.27	0.11	0.24	0.51	0.48	0.29	0.29	0.32	0.21	0.38	0.38	0.06	0.45	0.31	0.38
FeO	21.44	13.27	22.99	25.80	22.06	13.49	17.25	26.30	12.64	20.99	23.14	12.92	26.63	14.37	25.30
Na ₂ O	0.00	0.00	0.00	0.00	0.21	0.17	0.03	0.07	0.12	0.00	0.00	0.06	0.01	0.14	0.00
Total	101.38	100.12	99.92	100.09	100.95	99.76	99.95	99.26	99.95	99.61	99.37	99.91	99.93	100.25	99.29

Number of Cations Normalized to 4.0

Si	1.944	1.928	1.941	1.988	2.012	1.957	1.949	1.966	1.899	1.926	1.953	1.949	1.966	1.953	2.004
Ti	0.011	0.017	0.015	0.016	0.014	0.017	0.013	0.014	0.045	0.020	0.008	0.015	0.014	0.023	0.016
Al	0.042	0.056	0.038	0.027	0.023	0.025	0.041	0.024	0.089	0.058	0.036	0.034	0.022	0.034	0.020
Cr	0.009	0.019	0.007	0.003	0.003	0.012	0.004	0.019	0.035	0.007	0.015	0.008	0.010	0.011	0.011
Mg	1.279	1.513	1.197	1.001	0.439	0.748	1.172	0.985	0.848	0.966	1.193	0.850	0.933	0.729	1.011
Ca	0.051	0.067	0.073	0.126	0.755	0.804	0.267	0.142	0.687	0.312	0.060	0.725	0.182	0.775	0.111
Mn	0.008	0.003	0.008	0.017	0.016	0.009	0.009	0.010	0.007	0.012	0.012	0.002	0.015	0.010	0.012
Fe	0.655	0.397	0.721	0.825	0.721	0.428	0.535	0.850	0.397	0.670	0.730	0.406	0.859	0.456	0.816
Na				0.016	0.012	0.002	0.005	0.009				0.004	0.001	0.010	

Fe ₂ Si ₂ O ₆	32.86	19.81	36.01	42.37	36.96	21.41	27.02	42.55	19.86	33.70	36.77	20.09	43.26	22.82	41.65
Mg ₂ Si ₂ O ₆	63.34	74.99	59.21	50.39	22.03	36.64	58.22	48.71	41.70	47.72	59.15	41.86	46.20	35.74	50.84
Ca ₂ Si ₂ O ₆	1.29	1.45	2.50	5.67	37.62	39.09	11.98	6.42	31.34	13.09	1.90	34.58	8.30	37.18	4.84
Others*	2.51	3.75	2.28	1.57	3.39	2.86	2.78	2.32	7.10	5.49	2.18	3.47	2.24	4.26	2.67

	31	32	33	34	35	36	37	38	39	40	41	42
SiO ₂	51.93	51.76	52.07	51.32	52.04	53.49	51.79	51.70	49.47	51.33	50.17	50.99
TiO ₂	0.92	0.41	0.66	0.51	0.73	0.43	0.43	0.74	1.26	0.67	0.76	0.51
Al ₂ O ₃	1.27	0.39	0.80	0.44	0.47	1.06	0.47	0.69	0.88	0.40	0.93	0.47
Cr ₂ O ₃	0.53	0.47	0.30	0.17	0.26	0.57	0.21	0.37	0.14	0.21	0.32	0.06
MgO	13.86	17.58	13.51	18.66	18.54	28.36	16.69	13.66	9.54	17.97	12.22	14.17
CaO	18.28	3.43	20.02	2.68	4.22	1.07	4.14	19.26	17.08	3.06	17.95	4.30
MnO	0.20	0.29	0.22	0.30	0.22	0.00	0.33	0.26	0.37	0.43	0.27	0.35
FeO	13.65	26.03	11.77	25.50	23.55	14.76	25.26	13.32	20.19	26.47	16.77	30.27
Na ₂ O	0.28	0.00	0.11	0.10	0.06	0.13	0.10	0.17	0.17	0.07	0.16	0.12
Total	100.92	100.36	99.46	99.68	100.09	99.87	99.42	100.17	99.18	100.61	99.55	101.24

Number of Cations Normalized to 4.0

Si	1.943	1.975	1.973	1.958	1.973	1.918	1.997	1.950	1.947	1.952	1.928	1.969
Ti	0.026	0.012	0.019	0.015	0.021	0.012	0.012	0.021	0.037	0.019	0.022	0.015
Al	0.056	0.018	0.036	0.020	0.021	0.045	0.021	0.031	0.041	0.018	0.042	0.021
Cr	0.016	0.014	0.009	0.005	0.008	0.016	0.006	0.011	0.004	0.006	0.010	0.002
Mg	0.773	1.000	0.763	1.062	1.048	1.516	0.959	0.768	0.560	1.019	0.700	0.816
Ca	0.733	0.140	0.813	0.110	0.171	0.041	0.171	0.778	0.720	0.125	0.739	0.178
Mn	0.006	0.009	0.007	0.010	0.007	0.000	0.011	0.008	0.012	0.014	0.009	0.011
Fe	0.427	0.831	0.373	0.814	0.747	0.463	0.815	0.420	0.665	0.842	0.539	0.978
Na	0.020		0.008	0.007	0.004	0.009	0.007	0.012	0.013	0.005	0.012	0.009

Fe ₂ Si ₂ O ₆	21.27	41.66	18.91	40.36	37.19	21.62	41.30	20.91	33.02	41.72	26.66	48.80
Mg ₂ Si ₂ O ₆	37.94	49.59	37.97	52.02	51.69	74.04	48.00	37.48	27.30	49.67	34.08	40.24
Ca ₂ Si ₂ O ₆ </												

TABLE 7 : REPRESENTATIVE ANALYSES OF OLIVINES IN 12013

	1	2	3	4
SiO ₂	36.54	34.27	35.43	36.16
TiO ₂	0.03	0.14	0.07	0.07
Al ₂ O ₃	0.00	0.01	0.00	0.00
Cr ₂ O ₃	0.10	0.25	0.00	0.00
MgO	32.58	20.75	23.59	28.15
CaO	0.06	0.08	0.08	0.08
MnO	0.39	0.35	0.36	0.28
FeO	29.99	46.34	40.37	35.20
NiO	0.09	0.01	0.09	0.00
Total	99.78	102.20	99.99	99.94
Number of Catatoms Normalized to 3.0				
Si	0.990	0.982	1.013	1.005
Ti	0.001	0.003	0.002	0.001
Al				
Cr	0.002	0.006		
Mg	1.316	0.887	1.006	1.166
Ca	0.002	0.002	0.002	0.002
Mn	0.009	0.008	0.009	0.007
Fe	0.679	1.111	0.966	0.818
Ni	0.002	0.000	0.002	
Fa	34.35	55.80	49.21	41.43
Fo	65.65	44.20	50.79	58.57

- 1) Olivine fragment, black breccia
- 2) Subophitic basalt clast, black breccia
- 3) Olivine fragment, gray breccia
- 4) Gabbro clast, gray breccia

Table 8 : REPRESENTATIVE ANALYSES OF ILMENITES IN 12013

	1	2	3	4	5	6	7	8	9	10
SiO ₂	0.02	0.10	0.04	0.03	0.10	0.11	0.09	0.05	0.03	0.06
TiO ₂	52.58	52.52	53.13	52.44	51.08	53.62	52.84	52.38	53.43	50.50
Al ₂ O ₃	0.00	0.00	0.01	0.00	0.00	0.10	0.00	0.00	0.00	0.00
Cr ₂ O ₃	0.38	0.41	1.26	0.38	0.66	0.22	0.32	0.23	0.35	1.29
MgO	2.07	2.92	3.22	3.33	1.76	2.83	2.65	2.33	3.57	2.01
MnO	0.39	0.33	0.28	0.46	0.28	0.00	0.41	0.40	0.34	0.27
FeO	43.93	42.85	42.98	42.19	44.95	43.76	43.32	43.78	41.85	44.23
Nb ₂ O ₅	1.43	0.57	0.28	0.66	1.09	0.28	0.44	0.11	0.42	1.87
ZrO ₂	0.00	0.00	0.00	0.06	0.03	0.19	0.00	0.01	0.00	0.00
V ₂ O ₅	0.00	0.00	0.00	0.00	0.00	0.06	0.01	0.00	0.00	0.08
Total	100.80	99.70	101.16	99.55	99.95	101.17	100.08	99.29	99.99	100.31
Number of Cations Normalized to 2.0										
Si	0.000	0.002	0.001	0.001	0.002	0.003	0.002	0.001	0.001	0.001
Ti	0.981	0.980	0.974	0.977	0.961	0.986	0.984	0.984	0.989	0.947
Al	0.000	0.000	0.000	0.000	0.000	0.003	0.000	0.000	0.000	0.000
Cr	0.007	0.008	0.024	0.007	0.013	0.004	0.006	0.005	0.007	0.025
Mg	0.076	0.108	0.117	0.123	0.066	0.103	0.098	0.087	0.131	0.075
Mn	0.008	0.007	0.006	0.010	0.006	0.000	0.009	0.008	0.007	0.006
Fe	0.911	0.889	0.875	0.874	0.940	0.895	0.897	0.914	0.861	0.923
Nb	0.016	0.006	0.003	0.007	0.012	0.003	0.005	0.001	0.005	0.021
Zr	0.000	0.000	0.000	0.001	0.000	0.002	0.000	0.000	0.000	0.000
V	0.000	0.000	0.000	0.000	0.000	0.001	0.000	0.000	0.000	0.002

- 1) Ilmenite diorite, black breccia
- 2) ANT-suite melt-rock, black breccia
- 3) Ilmenite fragment >100µm, black breccia
- 4) Ilmenite grain in matrix, black breccia
- 5) Ilmenite in felsite bleb, black breccia
- 6) Ilmenite in gabbro, gray breccia
- 7) Ilmenite in subophitic basalt, gray breccia
- 8) Ilmenite in bladed basalt, gray breccia
- 9) Ilmenite fragment, gray breccia
- 10) Ilmenite in felsite, gray breccia

Table 9 : REPRESENTATIVE ANALYSES OF CR-SPINEL IN 12013

	1	2	3	4	5	6	7
SiO ₂	0.10	0.13	0.02	0.05	0.11	0.02	0.01
TiO ₂	8.35	7.47	9.06	9.39	12.71	6.06	5.49
Al ₂ O ₃	10.47	8.45	10.32	6.29	5.34	12.94	7.66
Cr ₂ O ₃	39.80	45.35	38.94	43.37	34.25	43.42	51.76
MgO	2.45	2.42	2.68	1.65	2.15	3.27	2.59
MnO	0.22	0.11	0.57	0.20	0.31	0.21	0.12
FeO	38.46	36.81	37.26	38.71	43.72	34.78	33.18
Nb ₂ O ₅	0.00	0.00	0.00	0.00	0.00	0.16	0.01
ZrO ₂	0.00	0.00	0.00	0.02	0.00	0.00	0.00
V ₂ O ₅	0.60	0.46	0.46	0.48	0.63	0.47	0.43
Total	100.45	101.20	99.31	100.16	99.22	101.33	101.25
Number of Cations Normalized to 3.0							
Si	0.003	0.005	0.001	0.002	0.004	0.001	0.000
Ti	0.217	0.195	0.238	0.252	0.343	0.154	0.144
Al	0.427	0.346	0.425	0.264	0.226	0.516	0.314
Cr	1.089	1.245	1.077	1.222	0.972	1.160	1.425
Mg	0.126	0.125	1.140	0.088	0.115	0.165	0.134
Mn	0.006	0.003	0.017	0.006	0.009	0.006	0.004
Fe	1.113	1.069	1.090	1.153	1.312	0.983	0.966
Nb	0.000	0.000	0.000	0.000	0.000	0.002	0.000
Zr	0.000	0.000	0.000	0.000	0.000	0.000	0.000
V	0.017	0.013	0.013	0.014	0.018	0.013	0.012

1) Subophitic basalt, black breccia

2) Cr-Spinel grain in matrix, black breccia

3) Gabbro, gray breccia

4) Granulated olivine gabbro, gray breccia

5) Subophitic basalt, gray breccia

6) Bladed basalt, gray breccia

7) Cr-Spinel fragment, gray breccia

Table 10: Representative Compositions of Accessory Phases in 12013

	1	2	3	4	5
Na ₂ O	0.29	0.14	0.00	0.00	
MgO	3.14	3.16	0.04	BDL	
Al ₂ O ₃	0.11	0.24	0.08	0.20	
SiO ₂	0.27	0.48	32.42	33.04	2.0
CaO	40.88	38.66	0.03	0.02	2.9
TiO ₂	0.00	0.00	0.05	0.09	22.1
Nb ₂ O ₅	0.00	0.00	0.00	0.00	7.9
Cr ₂ O ₃	0.00	0.00	0.00	0.11	0.0
MnO	0.00	0.00	0.09	0.12	0.0
FeO	1.07	1.47	0.40	0.14	13.8
P ₂ O ₅	43.15	37.29	0.00	0.00	0.0
ZrO ₂	0.00	0.00	64.11	63.73	17.2
F	BDL	0.54	0.00	0.00	0.0
Cl	BDL	0.01	0.00	0.00	0.0
La ₂ O ₃	1.19	1.41	BDL	BDL	0.2
Ce ₂ O ₃	2.97	3.53	BDL	BDL	1.6
Pr ₂ O ₃	0.39	0.25	0.24	0.30	
Nd ₂ O ₃	1.64	1.78	0.14	0.17	8.9
Sm ₂ O ₃	0.61	0.52	BDL	BDL	0.9
Gd ₂ O ₃	0.99	0.58	BDL	0.65	
Tb ₂ O ₃	0.16	0.13	BDL	BDL	
Dy ₂ O ₃	0.44	0.67	BDL	BDL	
Ho ₂ O ₃	BDL	0.26	BDL	BDL	
Er ₂ O ₃	2.98	4.05	BDL	BDL	
Yb ₂ O ₃	BDL	0.14	0.54	BDL	
Lu ₂ O ₃	0.26	0.35	BDL	BDL	
ThO ₂	0.18	0.08	0.00	0.00	3.5
UO ₂	BDL	0.12	0.36	BDL	3.6
PbO	BDL	0.05	BDL	0.00	4.2
Ta ₂ O ₅	0.00	0.00	0.11	0.00	
Sum	100.72	95.91	98.61	98.47	88.80

1. whitlockite clast, black breccia
2. whitlockite clast, black breccia
3. zircon clast, black breccia
4. zircon clast, black breccia
5. zirconolite, feldspar, gray breccia
(Haines et al., 1971)

BDL = below detection limit

Table 11: Relative Abundances of Fragments in the Black Breccia

Fragments > 0.14 mm

	Lithic Fragments		Mineral Fragments		
	Vol. %		Vol. %		
	Relative to Lithic Frags.	Relative to All Frags.	Relative to Min. Frags.	Relative to All Frags.	
ANT-Suite Hornfels	6.2	2.8	Plagioclase	64.9	35.4
Felsite*	3.3	1.5	Pyroxene	15.6	8.5
			Olivine	4.4	2.4
ANT-Suite Melt-Rock	0.9	0.4	Pyx Replac- ing Ol	1.5	0.8
Mosaic- Textured Anorthosite	0.4	0.2	Ilmenite	2.7	1.5
Quartzo- feldspathic rocks	32.1	14.6	Quartz	0.2	0.1
Labradorite Anorthosite	18.3	8.3	Tridymite	8.3	4.5
Granulated Norite	27.6	12.5	K-feldspar	0.7	0.4
Felsite Qtz+Ksp	7.5	3.4	Zircon	0.4	0.2
Trid+Ksp	3.5	1.6	Phosphate Minerals	1.3	0.7
	100.0	45.4		100.0	54.6

Fragments > 0.10 mm

	Lithic Fragments		Mineral Fragments		
	Vol. %		Vol. %		
	Relative to Lithic Frags.	Relative to All Frags.	Relative to Min. Frags.	Relative to All Frags.	
ANT-Suite Hornfels	6.2	2.6	Plagioclase	63.7	36.6
Felsite*	3.4	1.4	Pyroxene	18.0	10.4
ANT-Suite Melt-Rock	0.9	0.4	Olivine ^ψ	5.8	3.3
Mosaic- Textured Anorthosite	0.4	0.2	Ilmenite	2.6	1.5
Quartzo- feldspathic Rocks	31.6	13.4	Quartz	0.1	0.1
Labradorite Anorthosite	18.0	7.7	Tridymite	7.2	4.1
Granulated Norite	27.1	11.5	K-feldspar	1.0	0.6
Felsite Qts+Ksp	7.6	3.2	Zircon	0.4	0.2
Trid+Ksp	4.5	1.9	Phosphate Minerals	1.2	0.7
	100.0	42.5		100.0	57.5

*Associated with quartzofeldspathic rocks

^ψIncludes olivine that is totally converted to pyroxene lathworks

Table 12:	Black Breccia Lithic Clasts	Texture	Secondary	Grain Size	Mineralogy	Compositions
Lithology	Primary	Texture	Secondary	Grain Size	Mineralogy	Compositions
Quartzofeldspathic rocks						
Labradorite Anorthosite	Hydromorphic-granular: A coarse-grained intergrowth of subhedral to anhedral clear plagioclase grains showing slight normal progressive zoning. Accessory phases (high-Ca pyroxene, zircon and phosphate-minerals) form small interstitial grains.	Deformation Features: Cataclasis has destroyed the primary texture in most places. The clast is now a slightly porous aggregate of equant subangular fragments having a seriate size distribution. The lithic clasts are elongate and form schlieren; elongate mineral fragments in each clast tend to be aligned parallel to the long axis of the clast. Recrystallization Features: Locally, plagioclase is extensively replaced by K-feldspar. Trains of submicrometer-sized ilmenite and sulfide grains, and blebs of K-rich mesostasis mark healed fractures in plagioclase. Melting Features: Felsite fills the larger interstices and K-rich mesostasis fills the smaller interstices. Deformation Features: Cataclasis has destroyed most of the primary textures. The clast is an aggregate of equant plagioclase, pyroxene and ilmenite fragments. Recrystallization Features: Locally, plagioclase is extensively replaced by K-feldspar. Interstices between granulated mineral fragments are filled by K-rich mesostasis or felsite.	Plagioclase: 5 μ m-1.2mm Pyroxene: <50 μ m Zircon: <20 μ m Phosphate minerals: <20 μ m Trace	Plagioclase: An ₄₉ Ab ₅₁ Or _{3.5} to An _{61.4} Ab ₃₈ Or ₆ One grain is An _{68.9} Ab _{30.6} Or ₅ Pyroxene: En ₇₂ Wo ₃₇ Fs ₃₁		
Ilmenite Diorite	Hydromorphic-granular: An intergrowth of anhedral ilmenite and subhedral to anhedral pyroxene and plagioclase grain. Sulfide-minerals and metal form tiny, equant inclusions in ilmenite, plagioclase and pyroxene. Plagioclase is clear and inclusion free, and pyroxene contains abundant submicrometer-sized exsolution lamellae.	Deformation Features: Cataclasis has destroyed most of the primary textures. The clast is an aggregate of equant plagioclase, pyroxene and ilmenite fragments. Recrystallization Features: Locally, plagioclase is extensively replaced by K-feldspar. Interstices between granulated mineral fragments are filled by K-rich mesostasis or felsite.	Plagioclase: 5-400 μ m Pyroxene: 5-400 μ m Ilmenite: ~1mm Sulfide Minerals: 1-5 μ m Metal: 1-5 μ m	Plagioclase: An _{47.9} Ab _{51.2} Or ₉ to An _{57.9} Ab _{41.1} Or _{1.0} Pyroxene: En ₇₀ Fs ₂₅ to En ₃₇ Wo ₃₇ Fs ₂₆ Ilmenite: Fe/Fe+Mg = .92-.93 Catatomb % Nb = .65-.80 Metal: trace		
Tonalite	Hydromorphic-granular: An intergrowth of anhedral quartz and subhedral to anhedral plagioclase grains. Subhedral to anhedral acicular grains of high-Ca pyroxene are enclosed in both quartz and plagioclase. Quartz contains numerous, tiny oriented "inclusions" (~1 μ m) which locally form a herringbone pattern. Plagioclase is inclusion free. High-Ca pyroxene contains abundant submicrometer-sized exsolution lamellae.	Deformation Features: The clast is a porous aggregate of granulated inequigranular plagioclase and orthopyroxene grains. Recrystallization Features: Welded grains. Reaction Features: Large pyroxene fragments show continuous, concentric zoning. This zoning parallels fragment edges, suggesting post-granulation formation.	Plagioclase: 20-50 μ m Pyroxene: 10-50 μ m long, 5-25 μ m wide Quartz: 200-300 μ m	Plagioclase: An _{49.3} Ab _{49.4} Or _{1.3} to An _{53.5} Ab _{45.3} Or _{1.4} Pyroxene: En ₃₇ Wo ₃₈ Fs ₂₅ to En ₃₅ Wo ₃₉ Fs ₂₆ Quartz: ~50 μ m		
Granulated Norite	Most primary textures have been obscured by cataclasis. In a few places, mineral contacts are preserved and suggest the rock was originally a hypidomorphic or xenomorphic-granular intergrowth of plagioclase and pyroxene. Ilmenite forms inclusions in plagioclase and pyroxene and equant interstitial grains. Zircon and apatite form interstitial grains.	Deformation Features: The clast is a porous aggregate of granulated inequigranular plagioclase and orthopyroxene grains. Recrystallization Features: Welded grains. Reaction Features: Large pyroxene fragments show continuous, concentric zoning. This zoning parallels fragment edges, suggesting post-granulation formation.	Plagioclase: ~10-400 μ m Pyroxene: ~10-400 μ m Ilmenite: <10 μ m Zircon: < 10 μ m Apatite: < 10 μ m	Plagioclase: Zoned from An _{90.2} Ab ₉ Or ₁ to An _{53.3} Ab _{5.0} Or ₂ Pyroxene: Zoned from En ₈₁ Wo ₁₇ Fs ₄₁ at core to En ₅₆ Wo ₃ Fs ₄₁ at edges		
ANF-Suite Hornfels	Complex and highly variable in detail, but basically all fragments have cataclastic textures consisting of inequigranular mosaics of anhedral equant pyroxene and plagioclase grains. Possible relic textures are: ophitic, medium-grained hypidomorphic granular and breccia.	Deformation Features: None Recrystallization Features: None Melting Features: Interstices are filled by K-rich mesostasis.	Plagioclase: 10-300 μ m Pyroxene: 10-50 μ m Ilmenite: 5-20 μ m Troilite: <15 μ m Phosphate minerals: 2-5 μ m	Plagioclase: An _{69.3} Ab _{29.9} Or ₈ to An _{94.3} Ab _{5.6} Or ₁ Pyroxene: Low Ca; En ₇₀ Wo ₃₀ Fs ₂₇ to High Ca; En ₃₅ Wo ₃₈ Fs ₂₇		
Plagioclase porphyry	Porphyritic: interstices between large plagioclase laths and, in one clast, anhedral pyroxene grains, are filled by mesostasis composed of K-rich glass, acicular pyroxene needles, and ilmenite.	Deformation Features: None Recrystallization Features: None Melting Features: None Recrystallization Features: None	Plagioclase: 10-25 μ m Pyroxene: anhedral grains, 25-50 μ m; needles, <5 μ m wide, 50 μ m long Ilmenite: < 10 μ m	Plagioclase: An _{90.0} Ab ₁₀ Or ₆ to An _{86.0} Ab _{13.7} Or ₃ Pyroxene: En ₅₁ Wo ₁₂ Fs ₃₇		
Mosaic-textured anorthosite	Inequigranular mosaic of plagioclase and pyroxene.	Deformation Features: None Recrystallization Features: None Melting Features: None Recrystallization Features: None	Plagioclase: 20-100 μ m Pyroxene: < 20 μ m	Plagioclase: An _{90.0} Ab ₁₀ Or ₆ to An _{86.0} Ab _{13.7} Or ₃ Pyroxene: En ₅₁ Wo ₁₂ Fs ₃₇		
ANF-Suite Met-Rock	Poikilitic: Ilmenite, troilite and phosphate minerals form interstitial grains. Many euhedral plagioclase grains are poikilitically enclosed by anhedral pyroxene grains. Locally, plagioclase laths form networks with K-rich mesostasis filling interstices. Anhedral zircon, ilmenite, and trace amounts of phosphate and sulfide minerals occur in interstices in these networks.	Deformation Features: None Recrystallization Features: None Melting Features: None Recrystallization Features: None	Plagioclase: laths, 10-15 μ m long and ~5-10 μ m wide; blocky, ~50 μ m Pyroxene: 75-150 μ m Ilmenite: 1-50 μ m Zircon: <20 μ m Phosphate minerals: <20 μ m Sulfide minerals: <10 μ m Plagioclase: ~150 μ m long, 10-20 μ m wide. Pyroxene: 25-50 μ m Olivine: 25-50 μ m Cr-spinel: 5-10 μ m Ilmenite: 5-10 μ m Sulfide minerals: <10 μ m Metal: <10 μ m	Plagioclase: An ₈₉ Ab ₁₀ Or ₁ to An ₉₄ Ab ₅ Or ₁ laths An _{85.4} Ab ₁₄ Or ₂ An _{92.2} Ab _{7.6} Or ₂ Pyroxene: Low-Ca; En ₅₄ Wo ₃₉ to En ₅₀ Wo ₃₉ Fs ₄₄ / High-Ca; En ₃₉ Wo ₃₈ Fs ₂₃ Ilmenite: Fe/Fe+Mg = .89-.91 Catatomb % Nb = ~.3		
Subophitic Basalt	Subophitic: Turbid acicular grains of plagioclase are enclosed by turbid pyroxene and olivine; minor Cr-spinel and ilmenite fill interstices. Sulfide and metal grains are included in pyroxene.	Deformation Features: None Recrystallization Features: Pyroxene is a mosaic of minute grains.	Plagioclase: ~45% Pyroxene: ~5% Ilmenite: 4-5% Zircon: trace K-rich mesostasis: 2-3% Phosphate minerals: trace Sulfide minerals: trace Plagioclase: ~40% Pyroxene: ~45% Olivine: ~5% Cr-spinel: ~5% Ilmenite: ~5% Sulfide minerals: trace Metal: trace	Plagioclase: An _{78.9} Ab _{20.6} Or ₅ to An _{88.4} Ab _{11.4} Or ₂ Pyroxene: Low-Ca, En ₅₁ Wo ₃₉ Fs ₄₃ to High-Ca, En ₄₅ Wo ₃₉ Fs ₃₆ / High-Ca, En ₃₉ Wo ₃₇ Fs ₂₄ Olivine: Fo ₅₆ Cr-spinel: Fe/Fe+Mg = 0.90 Ilmenite: Fe/Fe+Mg = 0.90 Catatomb % Nb =		

Table 13 : BULK COMPOSITIONS OF LITHIC CLASTS IN THE BLACK BRECCIA DETERMINED BY ELECTRON MICROPROBE POINT COUNT ANALYSIS (PCA) OR DEFOCUSED BEAM ANALYSIS (DBA)

	1	2	3	4	5	6	7	8
SiO ₂	53.22	46.73	50.3	55.5	51.43	58.5	49.8	48.7
TiO ₂	8.84	0.25	0.8	0.6	0.33	0.4	1.2	2.6
Al ₂ O ₃	14.54	23.46	19.8	19.9	16.71	21.9	15.7	13.6
Cr ₂ O ₃	0.06	0.38	0.1	<0.1	0.12	0.1	0.2	0.4
MgO	1.03	8.47	6.4	3.8	6.54	0.9	7.0	8.7
CaO	5.63	12.77	11.4	12.3	11.36	9.9	11.0	12.2
MnO	0.05	0.09	0.1	0.1	0.14	0.1	0.1	0.2
FeO	8.72	7.06	8.8	3.9	10.84	1.5	12.8	11.8
Na ₂ O	2.13	0.55	1.2	1.6	1.82	1.8	1.0	1.3
K ₂ O	2.70	0.02	0.3	0.3	0.35	3.1	0.4	<0.1
P ₂ O ₅	0.60	0.28	0.6	0.1	0.13	0.6	0.4	0.1
ZrO ₂	0.06	-	-	-	-	-	-	-
SO ₃	0.14	-	0.1	0.5	0.07	0.6	<0.1	0.4
NiO	0.02	-	<0.1	0.1	-	<0.1	<0.1	0.1
BaO	1.19	0.01	-	-	-	-	-	-
Total	98.93	100.07	99.90	98.7	99.84	99.4	99.6	100.1
Catatom % Normative Minerals								
An	21.43	61.18	48.4	47.4	36.83	43.3	37.9	32.0
Ab	20.52	4.91	10.6	14.8	16.53	16.2	9.7	11.5
Or	17.11	0.12	2.0	1.6	2.09	18.8	2.5	0.1
Cel	2.32	0.02	-	-	-	-	-	-
En	3.05	19.75	17.7	10.6	18.27	2.4	19.7	24.4
Fs	1.11	8.83	12.6	4.8	16.56	0.9	18.6	14.4
Wo	1.73	0.02	2.0	5.6	7.34	1.0	6.1	11.4
Fo	0.0	2.64	0.0	0.0	0.0	0.0	0.0	0.0
Fa	0.0	1.18	0.0	0.0	0.0	0.0	0.0	0.0
Qtz	17.82	0.0	4.0	13.2	1.00	14.5	2.7	1.0
Ilm	13.21	0.35	1.1	0.8	0.46	0.5	1.7	3.7
Chr	0.07	0.41	0.2	<0.1	0.13	0.1	0.2	0.4
Zir	0.06	-	-	-	-	-	-	-
Ap	1.34	0.58	1.2	0.3	0.28	1.2	0.9	0.3
FeS	0.21	0.0	0.2	0.7	0.10	0.9	0.1	0.6
NiO	0.02	0.0	<0.1	0.1	0.0	<0.1	<0.1	0.1

1) Average of all quartzofeldspathic clasts, PCA
 2) Norite, PCA
 3) ANT-suite melt-rock, DBA
 4) Small, fine grained clast of ANT-suite hornfels, DBA

5) Large, coarse grained clast of ANT-suite hornfels, PCA
 6) Plagioclase porphyry, DBA
 7) Subophitic basalt, DBA
 8) Basaltic chondrule, DBA

Figure 14

Black Breccia Mineral Clasts > 0.10 mm

Type	Textural features	Grain Size	Composition
Plagioclase	Clasts are subangular and clear. Minor deformation features include bent or offset twin lamellae, undulatory extinction, and healed fractures. Abundant pyroxene inclusions. Reaction with groundmass produced narrow rims with compositions of An ₆₅₋₇₅ . Shocked clasts reacted more strongly than unshocked clasts.	<10-500 μm	An ₄₈₋₉₆ FeO < 0.5 %
Devitrified Maskelinite	Clasts are rounded. Devitrification produced very fine-grained spherulitic or granular texture.	Up to 1 mm	1 clast: An ₇₄
Pyroxene	Subangular to rounded. Deformation features include healed fractures and deformation lamellae. High-Ca pyroxenes and pigeonites(?) have low-Ca rims. Exsolution lamellae wider at rim of one Low-Ca pyroxene grain than at core.	Up to 700 μm	Low-Ca: En ₇₉ Wo ₅ Fs ₁₆ to En ₄₆ Wo ₈ Fs ₄₆ High-Ca: En ₃₈ Wo ₄₂ - Fs ₂₀ to En ₃₃ Wo ₃₉ - Fs ₂₀
Olivine	Equant, single crystal or mosaic-textured clasts. Reaction with groundmass produced low-Ca pyroxene lathwork ~En ₅₆ Wo ₄ Fs ₄₀ . Interstices of lathwork filled with plagioclase, An ₇₈₋₉₀ , and ilmenite.	Up to ~500 μm	Fo ₄₄₋₈₁
Ilmenite	Equant, anhedral.	Up to ~500 μm	Nb ₂ O ₅ < 0.7 % MgO: 2.0- 3.5 %
Zircon	Equant, rounded.	10-50 μm	
Phosphate Minerals	Equant, rounded. Roundness suggest resorption?	10-50 μm; some >1 mm.	

CHEMICAL COMPOSITIONS OF THE FELSITE
AND THE BLACK BRECCIA GROUNDMASS

INTRODUCTION

The preliminary chemical, isotopic and petrologic studies that were published in 1970 (Earth Planet. Sci. Lett., v. 9, 1970) were conducted without significant interchange of data between consortium members. It is now apparent that the samples analyzed were, in fact, heterogeneous mixtures involving both clastic and melt components. Therefore, chemical and isotopic data published to date report the chemistry of complex mixtures. Nevertheless, the preliminary chemistry studies showed the presence in 12013 of two distinct chemical components highly enriched in incompatible trace elements, but having different REE patterns (Wakita and Schmitt, 1970; Schnetzler et al., 1970; Hubbard et al., 1970). Quick et al. (1977) demonstrated that both the felsite and black breccia groundmass have highly evolved trace element chemistry, and it is the abundance of these two components which gives 12013 its high whole-rock enrichments in the incompatible elements. Clearly, the compositions of these components are data critical to the petrogenesis of 12013.

Quick et al. (1977) performed a combined petrographic, microprobe and instrumental neutron activation analysis study to determine the compositions of these two trace element-enriched lithologies. The following discussion describes the techniques used in that investigation and summarizes the results.

SAMPLE PROCESSING AND ANALYTIC TECHNIQUE

During the preliminary studies on 12013, the rock was cut into

slabs, and slab 12013,10 was sent to the California Institute of Technology. There it was broken into small fragments, many of which were distributed for chemical and isotopic studies (Anderson, 1970). From the remaining fragments of slab 12013,10 three black breccia samples and three gray breccia samples were handpicked, taking care to minimize the clast components and maximize melt components. Black breccia samples were taken from slab fragments 12013,10,09, 12013,10,16B and 12013,10,01A. Gray breccia samples were taken from slab fragments 12013,10,16B, 12013,10,28 and 12013,10,12A and consisted of 5 and 9 tiny fragments, respectively. These samples will be referred to herein as black breccia samples 09, 16B and 01A and gray breccia samples 16B, 28 and 12A.

All samples were sent to the Oregon State University Radiation Center for determination of 29 major, minor and trace element abundances by instrumental neutron activation analysis (INAA). Sample preparation and the detailed INAA procedures are the same as reported by Wakita et al. (1970) and Laul and Schmitt (1973).

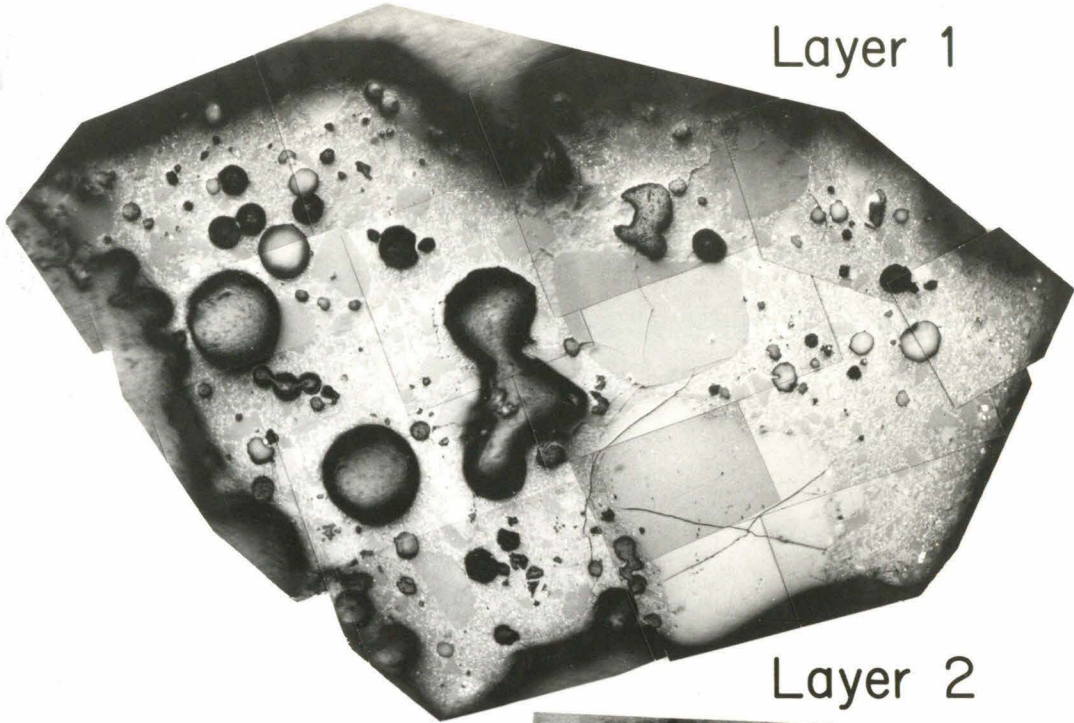
Four samples (black breccia 16B and 09, and gray breccia 16B and 28) were returned to the California Institute of Technology for detailed petrographic and electron microprobe study. Each fragment was mounted in epoxy and ground down. At evenly spaced intervals, surfaces were polished, photographed, mapped and point counted. Two of the surfaces studied within black breccia sample 16B and one surface within one fragment of gray breccia sample 16B are illustrated in Figures 27, 28 and 29. This phase of the project was designed to: (1) identify clasts with high trace element concentrations; (2) determine the mineralogy and mineral chemistry of the most abundant clasts; and (3) determine approximate modal abundance

Figure 27: Reflected light photomosaics of two sequential surfaces of black breccia sample 12013,10,16B that have been mapped and point-counted. Maps of these layers are illustrated in Figure 28. Note abundant vesicles. A tridymite clast with a continuous felsite rim occurs near the top edge of Layer 2.

12013, 10, 16b
BLACK BRECCIA

┌───┐ .25 mm

Layer 1



Layer 2

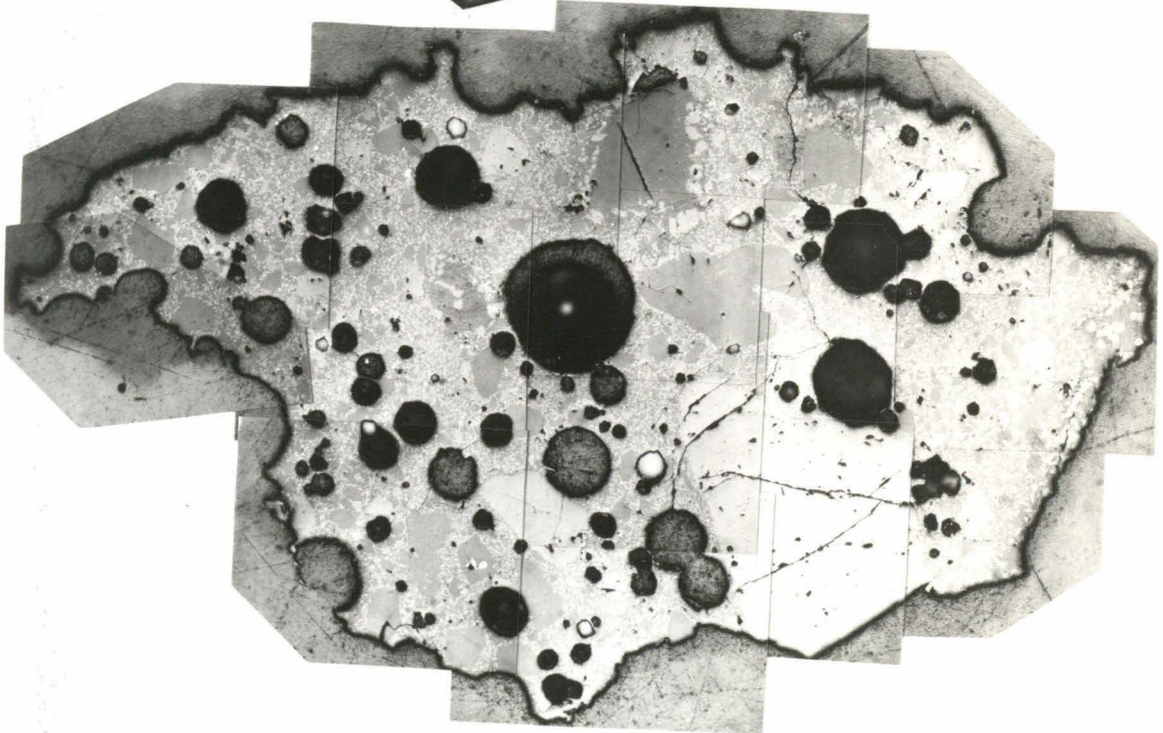


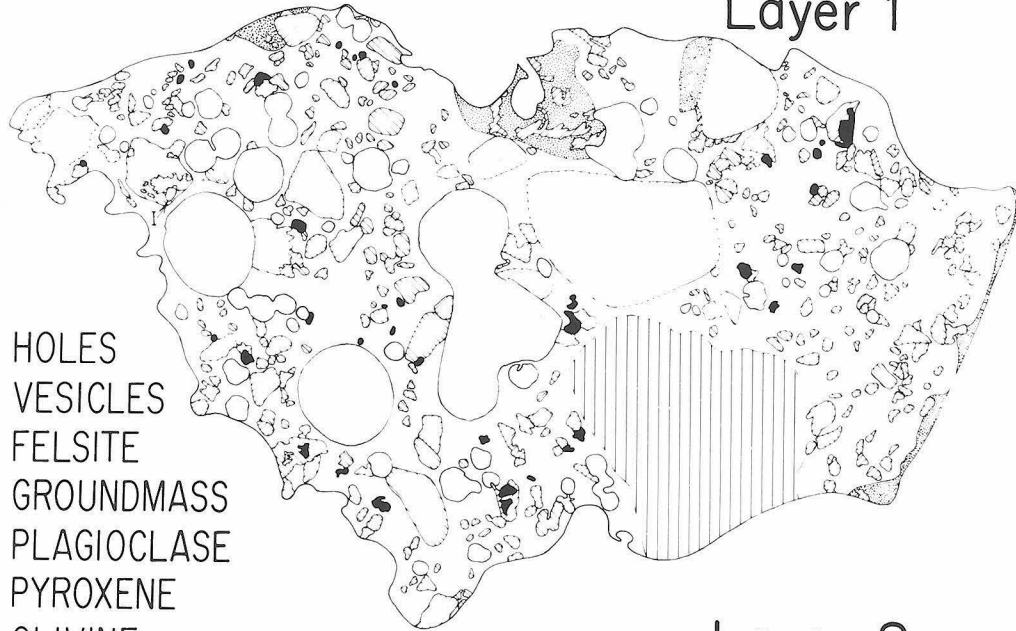
Figure 28: Maps of the sequential surfaces of black breccia sample 12013, 10,16B that are illustrated in Figure 27. Holes are formed by plucking during polishing.

12013, 10, 16b
BLACK BRECCIA

—|—| .25 mm

Layer 1

-  HOLES
-  VESICLES
-  FELSITE
-  GROUNDMASS
-  PLAGIOCLASE
-  PYROXENE
-  OLIVINE
-  ILMENITE
-  SiO₂



Layer 2

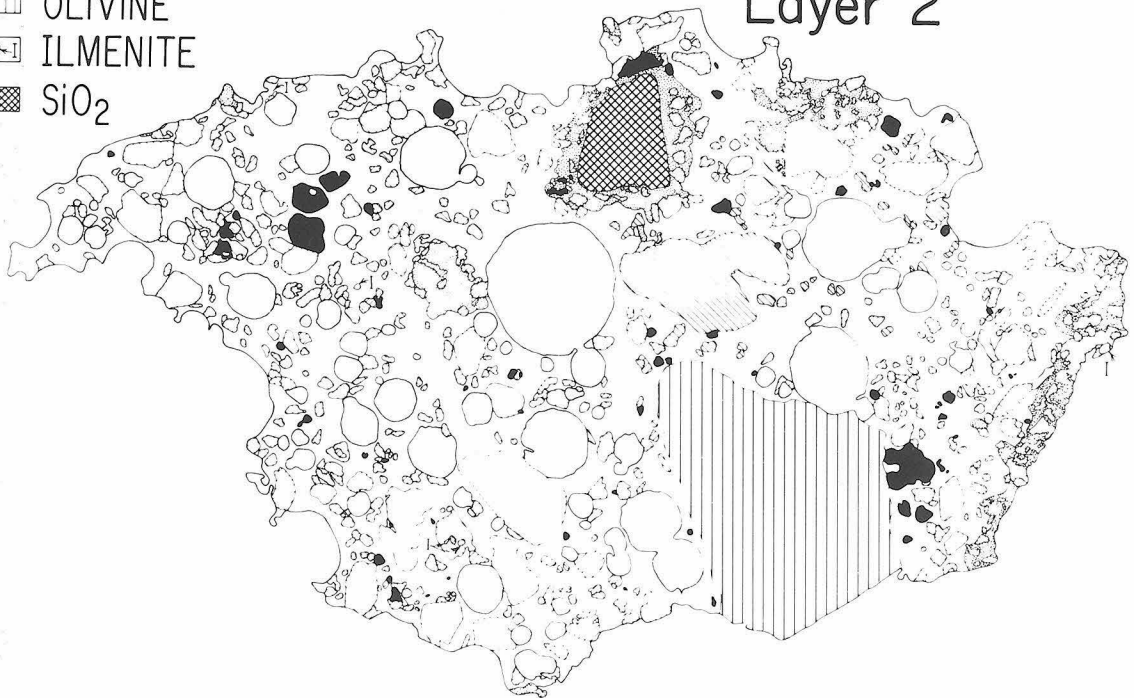





Figure 29: Reflected light photomosaic and map of one point-counted surface of one fragment of gray breccia sample 12013,10,16B.

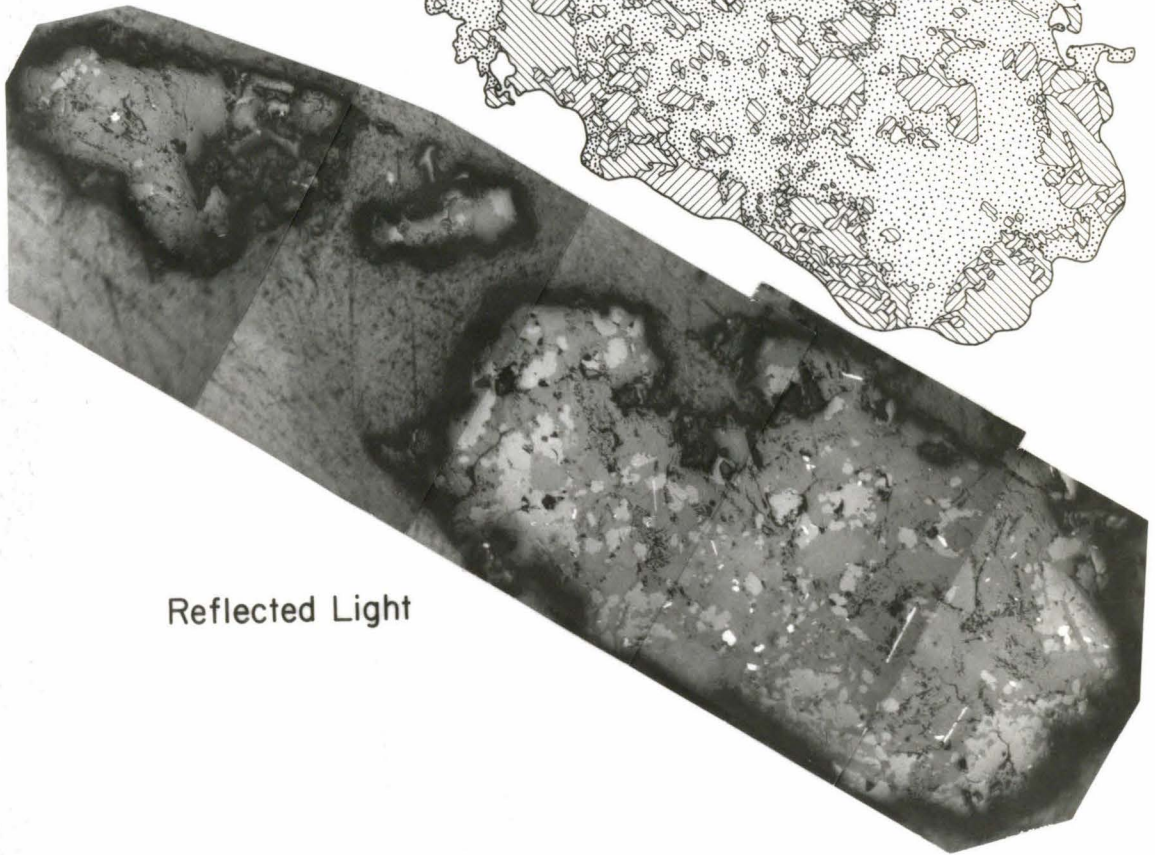
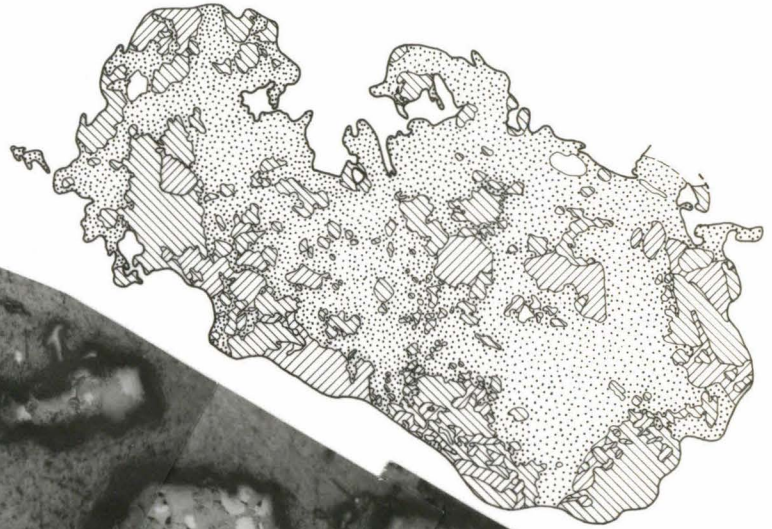
12013, 10, 16B
GRAY BRECCIA

— .25 mm



Layer 1, Frag.1

-  PYROXENE
-  PLAGIOCLASE
-  FELSITE



Reflected Light

of clasts, felsite and black breccia groundmass.

Microprobe point counts were performed on gray breccia samples using the technique described by Chodos et al. (1977). The fine grain size of the black breccia groundmass, and the occurrence of plagioclase clasts and groundmass plagioclase with similar compositions prohibits the use of microprobe point counting as a means of discriminating groundmass and the black breccia samples. These samples were point counted by placing a grid over a mapped photomosaic of each layer and counting the phase under each grid point. Clasts were distinguished from groundmass on the basis of grain size and morphology. In general, there is a distinct gap in grain size between the groundmass ($\leq 5 \mu\text{m}$) and clasts ($\geq 10 \mu\text{m}$), and clasts are less equant and more angular than groundmass phases. Major element chemistry of the black breccia groundmass and felsite was determined by defocused beam analysis (DBA) of 25-200 μm diameter, clast-free areas using data reduction procedures described by Albee et al. (1977).

Final estimates of felsite and black breccia groundmass abundance in each sample were based on weighted, least-squares, mass balance calculations (Reid et al., 1973). The abundance of the two melt-derived lithologies and clasts in each sample were calculated by balancing the whole-sample composition, determined by INAA, with representative compositions of the melt-derived lithologies and clasts. The calculations were performed solely with elements routinely analyzed by microprobe. The least-squares calculations were checked by comparing calculated mineral modes with modes determined from point-count data. Trace element abundances of felsite and black breccia groundmass were calculated assuming the incompatible trace elements (REE, U, Th, etc.) are concentrated in these

two components. The validity of this assumption, i.e., that the trace element contribution of the clasts is negligible, was confirmed by electron microprobe analyses of the mineral and lithic clasts, and by mass balance calculations for K and Ba.

RESULTS

The "whole rock" INAA data for the gray breccia and black breccia samples are listed in Table 16. The pattern of incompatible elements, normalized to chondritic abundances, of the 6 samples are illustrated in Figure 30. Microprobe analyses of felsite and black breccia groundmass are tabulated in Table 15. The results of the constrained least-squares analyses applied to the trace elements are presented in Table 17, and are illustrated in Figure 31. Tables 18 and 19 summarize the compositional data input into the least-squares calculation for black breccia sample 16B and gray breccia sample 16B, along with the point-count determined modal mineralogy and the modal mineralogy and bulk composition calculated by constrained least-squares.

The constrained least-squares calculations were performed using several constraints from the measured modal mineralogy of each sample to prevent negative mineral abundances from appearing in the solution. In the analysis of black breccia 16B, black breccia groundmass was constrained to be 50 ± 5 wt. percent and augite was constrained to be 1 ± 1 wt. percent. Similarly, tridymite was constrained to be 0.5 ± 0.5 wt. percent in the analysis of gray breccia 16B. Simultaneous solution for olivine, pyroxene and tridymite abundances is possible because the average pyroxene

TABLE 15: DEFOCUSED BEAM MICROPROBE ANALYSES OF MAFITE AND FELSITE

	MAFITE		FELSITE*			
	(1)		(2)		(3)	
	Wt. %	S.D.	Wt. %	S.D.	Wt. %	S.D.
Na ₂ O	1.9	0.3	1.4	0.2	1.4	0.4
MgO	7.4	1.4	0.5	0.5	0.7	1.1
Al ₂ O ₃	13.2	1.8	12.1	0.8	11.9	1.8
SiO ₂	50.1	1.7	73.1	1.5	73.0	3.6
K ₂ O	0.06	0.03	6.7	0.6	6.8	1.1
CaO	9.5	1.1	1.5	0.6	1.4	1.1
TiO ₂	2.2	0.5	N.A.		0.6	0.9
Cr ₂ O ₃	0.13	0.04	<0.1		<0.1	
MnO	0.15	0.07	<0.1		<0.1	
FeO	12.3	1.9	1.3	0.9	1.4	1.8
BaO	0.03	0.03	N.A.		0.73	0.24
NiO	0.02	0.03	<0.1		<0.1	
P ₂ O ₅	1.2	0.2	0.2	0.2	0.13	0.26
SO ₃	0.1	0.1	<0.1		<0.1	
ZrO ₂	0.3	0.6	N.A.		<0.1	
Sum	98.6		96.8		98.2	

(1) Average of 23 WDA analyses. Spot size 30 m.

(2) Average of 15 EDA analyses. Spot size 200 m.

(3) Average of 45 WDA analyses. Spot size 40 m.

*Column (2) is our preferred estimate of the felsite composition for all oxides except BaO and TiO₂ for which we use the results in column (3).Table 16: Elemental abundances in 12013,10 rock fragments determined by INAA^a

Element	12013,10,16 Black breccia (1.52 mg)	12013,10,09 Black breccia (2.04 mg)	12013,10,01A Black breccia (6.16 mg)	12013,10,16b Gray breccia (1.21 mg)	12013,10,28 Gray breccia (0.98 mg)	12013,10,12A Gray breccia (5.25 mg)
TiO ₂ (%)	1.9	4.6	3.3	0.75	0.86	0.3
Al ₂ O ₃	12.5	11.9	14.6	11.1	9.8	10.1
FeO	14.2	13.3	13.7	9.6	6.0	14.0
MgO	10.7	8.6	9.0	6.3	5.5	8.5
CaO	7.3	8.9	9.7	4.1	3.8	4.6
Na ₂ O	1.45	1.47	1.45	1.28	1.17	1.12
K ₂ O	0.37	0.50	0.40	3.74	3.03	2.6
MnO	0.158	0.164	0.166	0.122	0.077	0.150
Cr ₂ O ₃	0.130	0.144	0.162	0.151	0.086	0.252
Sc (ppm)	23	30	28	21	17	25
V	33	46	34	47	42	61
Co	29	24	27	12	8.6	24
Zr	940±310	1140±280	2370±200	1130±310	720±310	690±150
Hf	32	38	63	23	25	27
Th	17.2	17.0	24.5	44.8	35.6	47.5
U	5.3±0.9	6.2±0.3	10.4±2.3	12.1±1.4	10.4±0.9	14.2±1.0
Ba	660±190	1430±140	390±150	4150±200	4160±290	3760±160
La	135	130	135.7	64	39	56.5
Ce	333	344	347	170	100	151
Nd	242	219	215±46	91	59	74±23
Sm	53	53	59.0	20	13	19.0
Eu	2.52±0.37	3.29±0.30	3.89	1.85±0.04	1.74±0.11	2.14
Tb	10.6	11.4	12.5	4.9	3.7	5.2
Dy	67	70	75	38	23	33
Yb	36	37	39	35	25	30
Lu	4.8	4.5	5.2	5.2	3.0	4.2
Ta	3.9	9.1	5.3	6.6	5.0	7.1
Rb	16±13	33±17	10±7	124±21	101±21	87±11
Cs	1.8±0.8	2.1±0.6	1.7±0.4	4.0±0.7	4.3±0.3	3.1±0.6

^a Estimated errors due to counting statistics are: Al₂O₃, Na₂O, MnO, Sc, La and Sm, ~±1-3%; FeO, K₂O, Cr₂O₃, Co, Ce, Tb, Yb, Th and Hf, ~±5%; TiO₂, CaO, Dy, Lu and Ta, ~±5-15%; MgO, V, Ba, Cs, Eu and U, ~±10-30%; Zr ~±30-40%; Nd and Rb ~±20-60%.

Figure 30: Chondritic-normalized K, Rb, Cs, Ba, REE, Sc, Hf, Ta and U abundances in six black breccia and gray breccia samples from 12013,10.

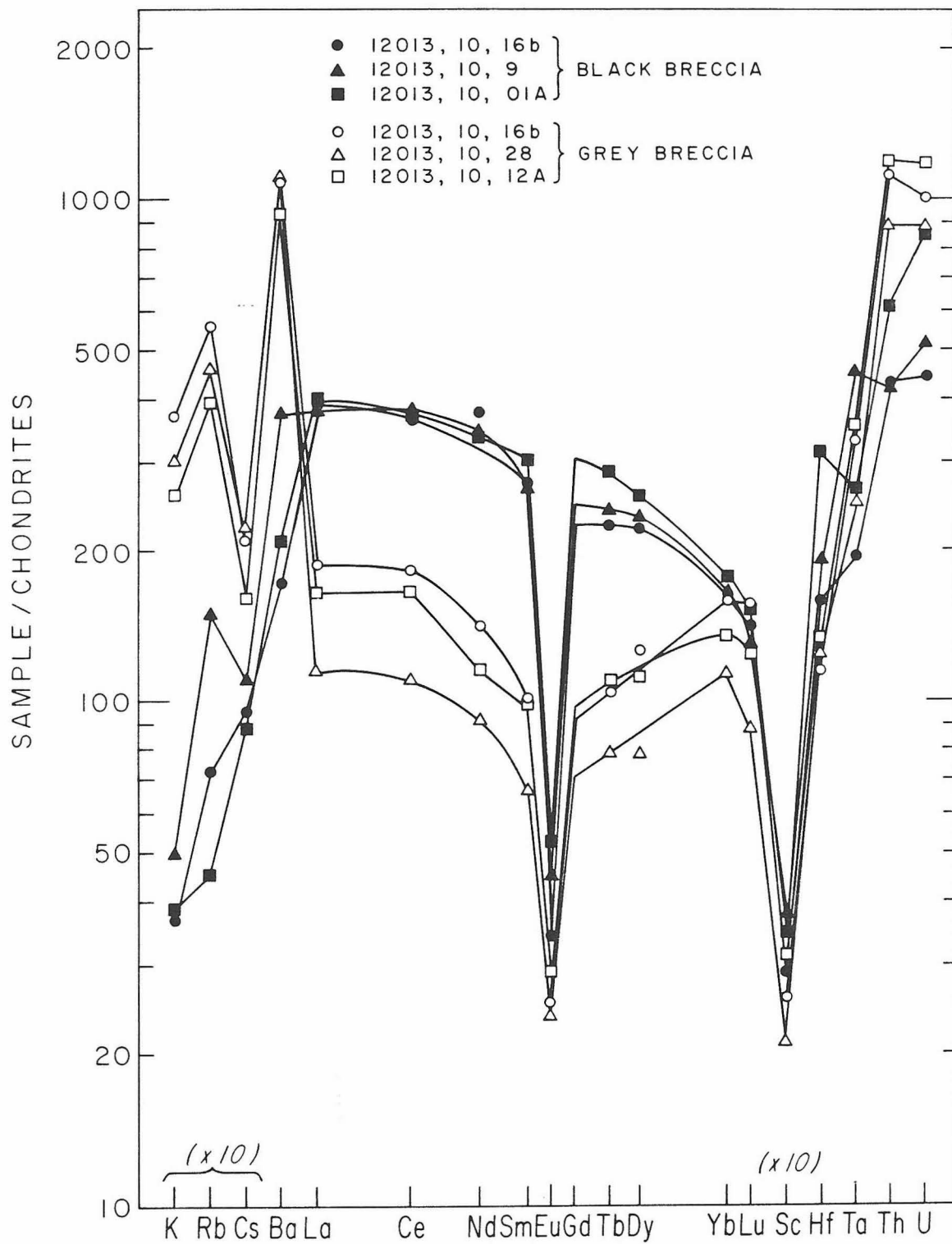


Figure 31: Chondritic-normalized K, Rb, Cs, Ba, REE, Sc, Hf, Ta and U abundances in the black breccia groundmass and the felsite of the gray breccia.

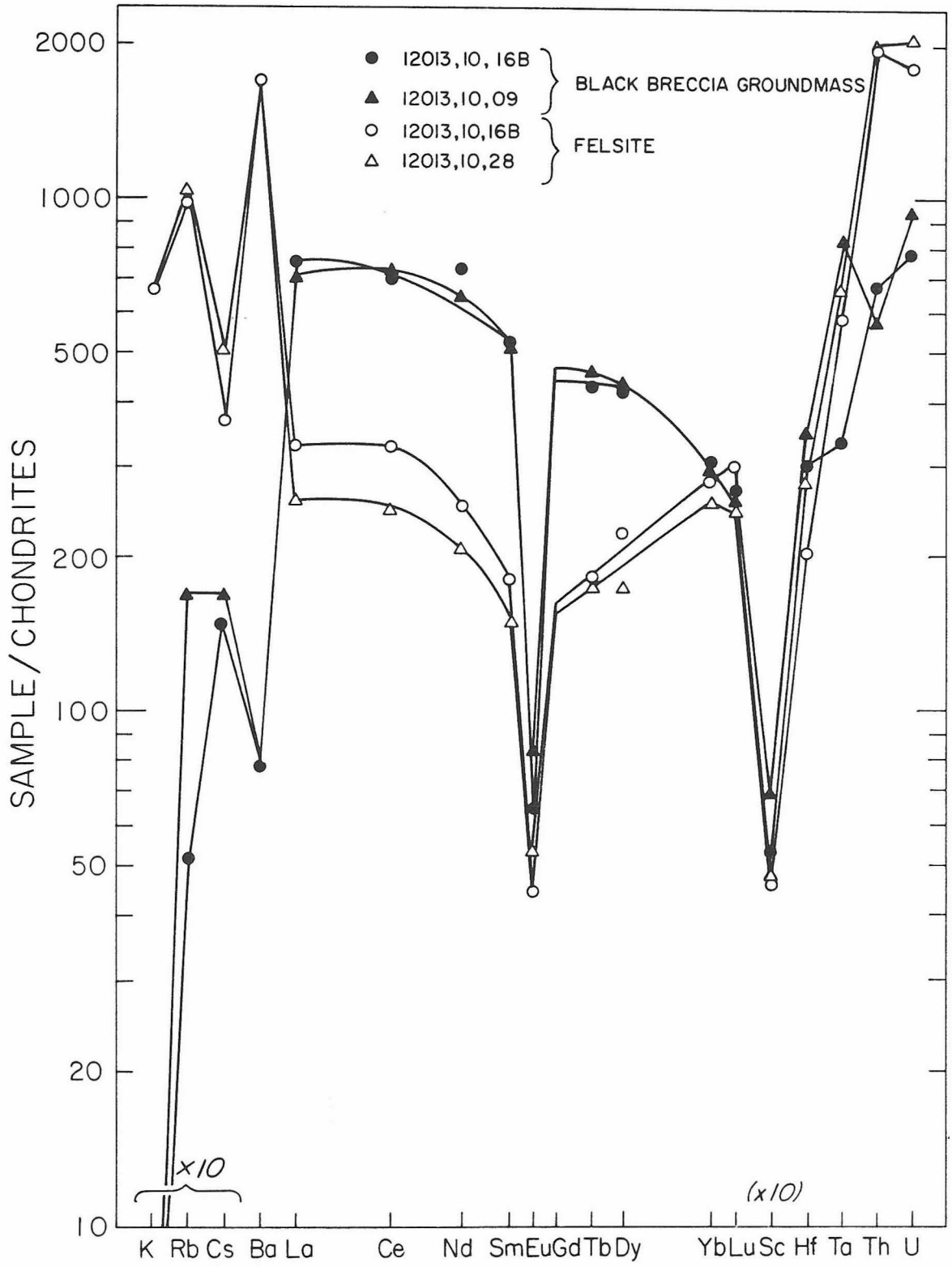


Table 17a: Comparison of point count results with least-squares solutions for two 12013 fragments.

	12013,10,16b Black Breccia		12013,10,16b Gray Breccia		
	Measured ^a	Least-Squares	Measured	Least-Squares	
	Wt. %	Wt. %	Wt. %	Wt. %	
B.B. Gdms	49.89	49.76±0.72	0.0	0.0	
Felsite	4.42	4.72±0.22	57.00	56.67±1.65	
CLASTS {	Plagioclase	15.76	16.46±0.97	12.98	13.87±1.41
	Pyroxene	15.49	14.21±1.58	29.17	23.79±3.64
	Olivine	12.61	11.96±0.99	0.13	3.86±2.04
	Ilmenite	0.14	1.35±0.17	0.71	1.20±0.18
	Apatite	0.06	N.D.	0.0	0.0
	Tridymite	1.62	1.62±2.29	tr.	0.43±0.34
	Zircon	<0.01	N.D.	0.0	0.0
	Chromite	0.02	0.04±0.02	0	0.18±0.03
Na ₂ O	1.45±0.03	1.45	1.28±0.04	1.28	
MgO	10.7±1.1	10.2	6.3±1.2	5.5	
Al ₂ O ₃	12.5±0.1	12.5	11.1±0.1	11.1	
SiO ₂	N.A.	49.8	N.A.	62.8	
K ₂ O	0.37±0.02	0.37	3.74±0.19	3.82	
CaO	7.3±0.7	8.0	4.1±0.62	3.62	
TiO ₂	1.9±0.1	1.9	0.75±0.11	0.75	
Cr ₂ O ₃	0.13±0.004	0.13	0.151±0.005	0.151	
MnO	0.158±0.002	0.157	0.122±0.001	0.122	
FeO	14.2±0.4	14.3	9.6±0.29	9.4	
BaO	0.07±0.02	0.05	0.463±0.022	0.414	

^a Mineral wt. % were determined from point count vol. % assuming phase densities.
Oxide wt. % were determined by INAA.

N.A. = Not analyzed for

tr. = trace

Table 17b: TRACE ELEMENT ABUNDANCES^a IN FELSITE AND B. B. Groundmass

Element	12013,10,16b Groundmass	12013,10,09 Groundmass	12013,10,16b Felsite	12013,10,28 Felsite
Sc	43	55	37	38
V	58	81	83	95
Co	56	45	21	19.4
Zr	1700	2010	1990	1620
Hf	60	71	41	56
Th	27	23	79.1	80.2
U	9.4	11.3	21.9	24.8
La	261	245	113	88
Ce	640	648	300	225
Nd	471	416	161	133
Sm	103	101	35	29
Eu	4.75	6.14	3.26	3.92
Tb	20.5	21.6	8.6	8.3
Dy	128	131	67	52
Yb	66	66	62	56
Lu	9.1	8.6	10.2	8.3
Ta	6.7	16.6	11.6	11.3
Rb	11	37	219	228
Cs	2.9	3.3	7.1	9.7

^a All abundances in ppm.

Table 18: Least-squares analysis of black breccia sample 16B: Compositional data used in the calculation, the modal mineralogy determined by visual point-counting, and the modal mineralogy calculated by least-squares. For discussion, see text.

Wt. % (point-count) ^a	Calcic Plag.	Sodic Plag.	High-Ca Pyx.	Low-Ca Pyx.	Tridymite	Olivine	Ilmenite	Chromite	Felsite	Ground-mass	Bulk Composition		
											(INAA)	Least-squares ^c	
	15.7 ₃		15.4 ₆		1.6 ₂	12.6 ₁	0.1 ₄	0.0 ₂	4.4 ₁	49.7 ₉			
Wt. % (least-squares) ^b	10.1 ₀	6.2 ₄	0.8 ₄	13.3 ₇	1.6 ₂	11.9 ₆	1.3 ₅	0.0 ₄	4.7 ₂	49.7 ₆			
Data for least-squares calculation	Na ₂ O	0.74	5.45	0.15	0.04	0.0	--	--	1.3 ₅	1.9 ₄	1.45±0.03	1.4 ₅	
	MgO	0.02	0.08	12.34	18.77	0.02	31.83	3.22	2.68	0.5	7.4 ₅	10.7 ±1.1	10.2 ₁
	Al ₂ O ₃	35.76	26.32	0.71	0.38	0.72	0.0	0.01	10.32	12.0 ₅	13.2 ₄	12.5 ±0.1	12.4 ₈
	SiO ₂	44.06	56.75	51.81	51.48	98.22	37.96	0.04	0.0	73.1 ₄	50.1	--	49.8 ₃
	K ₂ O	0.03	0.37	--	--	0.06	--	--	--	6.6 ₉	0.0 ₆	0.37±0.02	0.3 ₇
	CaO	19.31	10.43	19.79	2.74	0.04	0.09	--	--	1.5 ₄	9.5 ₂	7.3 ±0.7	7.9 ₆
	TiO ₂	0.01	0.0	0.69	0.39	0.15	0.06	53.12	9.06	0.0	2.2 ₂	1.9 ±0.1	1.8 ₉
	Cr ₂ O ₃	--	--	0.21	0.20	--	0.04	1.26	38.94	0.0 ₁	0.1 ₃	0.13±0.01	0.1 ₃
	MnO	--	--	0.25	0.44	--	0.12	0.28	0.57	0.0 ₆	0.1 ₅	0.158±0.005	0.1 ₆
	FeO	0.14	0.0	14.78	25.71	0.08	33.28	42.94	37.26	1.3	12.2 ₈	14.2 ±0.4	14.3 ₄
BaO	0.0	0.0	--	--	0.0	--	--	--	0.73	0.0 ₃	0.07±0.02	0.0 ₅	
Sum	100.07	99.40	100.73	100.15	99.29	103.38	100.87	98.83	97.37	97.12			

^a Calculated from point-count data (Vol. %; 23,909 points) using phase densities.

^b Solution to least-squares calculation.

^c Calculated from the least-squares-determined modal mineralogy using the compositional data for each phase.

Table 19: Least-squares analysis of gray breccia sample 16B: Compositional data used in the calculation, the modal mineralogy determined by microprobe point-counting, and the modal mineralogy calculated by least-squares. For discussion, see text.

Wt. % (point-count) ^a	Calcic Plag.	Sodic Plag.	High-Ca Pyx.	Low-Ca Pyx.	Tridymite	Olivine	Ilmenite	Chromite	Felsite	Bulk Composition		
										(INAA)	Least-squares ^c	
	12.9 ₈		29.1 ₇		<0.1	0.1 ₃	0.7 ₁	0.0	57.0			
Wt. % (least-squares) ^b	5.2 ₄	8.3 ₅	0.8 ₂	21.7 ₄	0.4 ₀	4.5 ₈	1.2 ₂	0.1 ₉	57.4 ₆			
Data for least-squares calculation	Na ₂ O	0.74	5.45	0.15	0.0	--	--	--	1.3 ₅	1.28 ±0.04	1.2 ₇	
	MgO	0.02	0.08	13.10	16.69	0.02	31.83	3.22	2.68	0.5	6.3 ±1.2	5.5 ₃
	Al ₂ O ₃	35.76	26.32	0.81	0.31	0.72	0.0	0.01	10.32	12.0 ₅	11.1 ±0.1	11.0 ₉
	SiO ₂	44.06	56.75	51.64	51.38	98.22	37.96	0.04	0.0	73.1 ₄	--	62.8 ₀
	K ₂ O	0.03	0.37	--	--	0.06	--	--	--	6.6 ₉	3.74 ±0.19	3.8 ₈
	CaO	19.31	10.43	19.30	2.21	0.04	0.09	--	--	1.5 ₄	4.1 ±0.6	3.4 ₁
	TiO ₂	0.01	0.0	0.68	0.36	0.15	0.06	53.12	9.06	0.0	0.75 ±0.11	0.7 ₅
	Cr ₂ O ₃	--	--	0.42	0.24	--	0.04	1.26	38.94	0.0 ₁	0.151±0.005	0.1 ₅
	MnO	--	--	0.05	0.35	--	0.12	0.28	0.57	0.0 ₆	0.122±0.002	0.1 ₂
	FeO	0.14	0.0	13.54	29.91	0.08	33.28	42.94	37.26	1.3	9.6 ±0.3	9.5 ₀
BaO	0.0	0.0	--	--	0.0	--	--	--	0.73	0.46 ±0.02	0.4 ₂	
Sum	100.07	99.40	99.69	101.45	99.29	103.38	100.87	98.83	97.37			

^a Calculated from point-count data (Vol. %; 4969 points) using phase densities.

^b Solution to least-squares calculation.

^c Calculated from the least-squares-determined modal mineralogy using the compositional data of each phase.

composition in the samples studied are not colinear with the olivine and tridymite compositions. Abundant tiny ilmenite inclusions occur in some pyroxene clasts in the black breccia sample, but were not point counted because of their small size. As a result, the abundance of ilmenite is much lower in the point-count results than in the least squares solution for this sample. In the gray breccia sample, pyroxene is higher and olivine is lower in the point-count results than in the least-square solution because the reaction, melt + olivine = orthopyroxene, has replaced olivine xenocrysts with orthopyroxene. Taking these observations into consideration, the calculated mineralogy and point-counted mineralogy are in excellent agreement. This strongly supports the methodology used in this project and suggests the abundance of the phases and the compositions of the melt-derived lithologies in each sample have been accurately determined.

The REE patterns in Figure 9 form two distinct groups. Black breccia fragments have tightly-grouped REE patterns with the highest total REE abundances and a negative Eu anomaly. Gray breccia fragments show a greater range in REE abundances than do the black breccia fragments, and possess a negative Eu anomaly superimposed on a distinctive, V-shaped REE pattern. These results are similar to those from the preliminary investigations of 12013. The black breccia REE patterns are similar to those of the "dark-colored portions" (12013,10-10, -15 and -8 matrix) analyzed by Schnetzler et al. (1970) and the "black material" (12013, 10-05D) analyzed by Hubbard et al. (1970). The gray breccia REE patterns are similar to those of the "light-colored portions" (12013,10-37+24, -8, and -15) analyzed by Schnetzler et al. (1970) and "white material" (12013,10-05L) analyzed by Hubbard et al. (1970).

The REE patterns calculated for the felsite in gray breccia samples 16B and 28, and for the black breccia groundmass in black breccia samples 16B and 09 (Fig. 10) are basically similar to the "whole-rock" breccia patterns, but enriched in REE by a factor of about 2. The close grouping of the REE patterns indicates that the black breccia groundmass is homogeneous on a scale of about 1 mg. These two patterns are similar to those of KREEP (Laul and Schmitt, 1973), but the absolute REE abundances are similar to those observed in 15405,85, a quartz monzodiorite sample (Nyquist et al., 1977) and are the highest ever observed in any lunar lithology. The spread between the felsite patterns suggests that the felsite is not homogeneous on a scale as small as 1.0 mg. Furthermore, K and Ba abundances do not correlate with REE abundance in the gray breccia. This may be explained by different amounts of Ba-rich K-feldspar in each of the gray breccia samples. The distinctive V-shaped REE pattern is similar to the pattern reported by Blanchard et al. (1977) for a felsite clast from 73215.

DISTRIBUTION OF ELEMENTS BETWEEN PHASES

The distribution of elements among the phases in 12013 must be understood before possible genetic relationships can be discussed. Microprobe analyses of gray breccia phases demonstrate that K and Ba are concentrated in K-feldspar microphenocrysts, interstitial K-feldspar, and trace amounts of glass, all of which formed from the felsite melt. Rb-Sr isotopic studies (Albee et al., 1970) on heavy liquid separates of felsite demonstrated that the highest Rb concentrations were in separates rich in K-feldspar. Therefore, the K, Ba and Rb concentrations in the gray breccia and felsite are controlled by the modal abundance of K-feldspar.

The remaining incompatible elements are more difficult to assign to phases in the felsite. Candidates for concentrating REE, U and Th are whitlockite, apatite, zircon, zirconolite and possibly residual glass. The occurrence of these phases was discussed above. Clastic phosphate and zircon are extremely rare in the gray breccia, and absent in gray breccia samples #16B and #28.

Therefore, the abundances of most trace elements in the gray breccia are exclusively controlled by phases which crystallized from the felsite melt, and understanding the distribution of these elements in the gray breccia is equivalent to understanding their distribution in the felsite. Given the compositions of these phases, the modal abundances may be estimated that are required to produce the observed whole-sample trace element concentration, or estimate the whole-sample concentration from measured modes. By comparing these estimates with observed modal abundances or element concentrations, it is possible to determine which phases control the trace element chemistry of the gray breccia and felsite. The compositions, including some trace element data, of zircon, apatite, whitlockite, and zirconolite (phase β) in 12013 have been documented by Haines et al. (1971). The highest REE concentrations occur in whitlockite ($\text{REE}_2\text{O}_3 \sim 4.9 \text{ wt. } \%$) and zirconolite ($\text{REE}_2\text{O}_3 \sim 2.3 \text{ wt. } \%$). By comparison, apatite and zircon have negligible REE concentrations ($\text{REE}_2\text{O}_3 < 0.5 \text{ wt. } \%$). The highest U and Th concentrations occur in zirconolite, which contains about 3.4 wt. percent UO_2 and about 4.1 wt. percent ThO_2 . Zircon, apatite and whitlockite all contain less than 300 ppm U; Th concentrations for these phases are not known. Whitlockite is the most abundant phosphate mineral in the gray breccia, and the gray breccia REE concentrations may

be explained primarily in terms of whitlockite abundance. Point-count results on gray breccia sample 28 indicate that it contains 0.28 ± 0.07 wt. percent phosphate-rich phases. Assuming these phosphates to be entirely whitlockite, we calculate whole-sample La, Ce and Nd concentrations of 29 ± 7 , 88 ± 22 and 48 ± 12 ppm, respectively. These compare favorably with the whole-sample abundances determined by INAA (Table 16).

U and Th concentrations are controlled by the abundance of zirconolite. Based on point count data, zircon, apatite and whitlockite could contribute no more than 10 percent of the observed U abundance in gray breccia sample 28. The U and Th content of gray breccia sample 28 could be explained by 0.03 to 0.09 wt. percent zirconolite. This is compatible with our point count results which determined the abundance of Zr-rich phases (zircon + zirconolite) to be approximately 0.22 ± 0.08 wt. percent. Analyses from Haines *et al.* (1971) indicate Hf is almost exclusively partitioned into zircon. Using these data, the amount of zircon required to explain the Hf abundance in gray breccia sample 28 is ~ 0.09 wt. percent. Therefore, our computed values for zircon + zirconolite are 0.12-0.18 wt. percent, which is close to the measured amount.

A good estimate of the abundance of zirconolite in 12013 is important because of its high U and Th concentrations. Haines *et al.* (1971) noted a high Nb concentration in 12013 zirconolite (~ 8 wt. % Nb_2O_5) and suggested that if most of the Nb were concentrated in zirconolite, up to 0.3 wt. percent zirconolite would be required to account for the 12013 whole-rock Nb abundance of 170 ppm (LSPET, 1970). As a result of this study, we now know that Nb_2O_5 ranges from 0.5 wt. percent in clastic ilmenite to >1.5 wt. percent in ilmenite which crystallized from felsite.

Using the 12013 whole-rock Ti abundance of 1.2 wt. percent (LSPET, 1970), and assuming all Ti to be in ilmenite, we calculate ~ 4 wt. percent ilmenite in 12013. Taking 0.5 wt. percent Nb₂O₅ as a conservative estimate of Nb abundance in 12013 ilmenite, we calculate a contribution of 140 ppm Nb to the 12013 whole rock composition. The remaining 30 ppm Nb can be accounted for by only 0.05 wt. percent zirconolite, which is in agreement with estimate based on U and Th abundances.

In the felsite and gray breccia, K, Ba and Rb concentrations reflect K-feldspar abundance, REE concentrations reflect mainly whitlockite abundance, and U and Th reflect mainly zirconolite abundance.

The minute grain size of the 12013 black breccia groundmass make a detailed analysis of incompatible element distributions difficult. The K in this lithology (0.06 wt. % K₂O) is probably concentrated in plagioclase which is 40 to 50 wt. percent of the groundmass and contains 0.1 to 0.3 wt. percent K₂O. No other K-bearing phases have been identified with the microprobe. Rb and Ba are also inferred to be concentrated in this phase because their chemistries are similar to that of K. REE, U, and Th are concentrated in submicron to ~ 5 μm diameter phosphate-bearing phases and submicron diameter Zr-bearing phases. Both apatite and whitlockite have been identified on the basis of presence or absence of Cl, but the compositions of these phases have not been determined. The nature of the Zr-bearing phases has not been determined and they could be zirconolite and/or zircon. If the analyses of apatite, zircon, whitlockite and zirconolite by Haines et al. (1971) were applicable, whitlockite would have to be the most abundant phosphate in order to account for the extremely high REE abundances in the groundmass, and zirconolite would

have to be present to account for the high U and Th abundances. However, Burnett et al. (1971) demonstrated that U concentrations in 12013 phosphate minerals increase dramatically with decreasing grain size. Presumably, other incompatible elements also have the highest concentrations in the smallest accessory phases. Therefore, it is premature to speculate on the exact nature of the phosphate and Zr-bearing phases in the black breccia groundmass.

AGE CONSTRAINTS

RB-SR SYSTEMATICS

Rock 12013 was the first lunar breccia that was carefully dissected for Rb-Sr isotopic analysis. Three groups of investigators (Albee et al., 1970; Schnetzler et al., 1970; Hubbard et al., 1970) performed Rb-Sr isotopic measurements on samples of 12013 that were carefully selected by G.J. Wasserberg and coworkers at the California Institute of Technology (Anderson, 1970). These three investigations produced essentially compatible results, but by far the most detailed investigation was conducted by the Lunatic Asylum (Albee et al., 1970) who determined two "internal isochrons" for the gray breccia by means of density separates and numerous "whole" fragment analyses. Schnetzler et al. (1970) performed fewer analyses but these included both density separates and "whole" fragments. The added value of these data and those of Hubbard et al. (1970) is that additional trace element and some minor and major element analyses were performed on the same samples for which isotopic measurements were made. Figure 32 is a compilation of the Rb-Sr data from the Lunatic Asylum and selected data points from Schnetzler et al. (1970) and Hubbard et al. (1970); a sample description for each data point is given in Table 20. These investigations together represent the most thorough Rb-Sr study of a lunar rock, and present some age constraints that must be reconciled in any petrogenetic model of 12013.

The Lunatic Asylum (Albee et al., 1970) tested several models to explain the Rb-Sr isotopic evolution of 12013. Two internal isochrons were determined for fragments of gray breccia. These yielded ages of 4.01 ± 0.09 and 3.99 ± 0.05 AE with initial $^{87}\text{Sr}/^{86}\text{Sr}$ of 0.7085 ± 0.0008

Figure 32

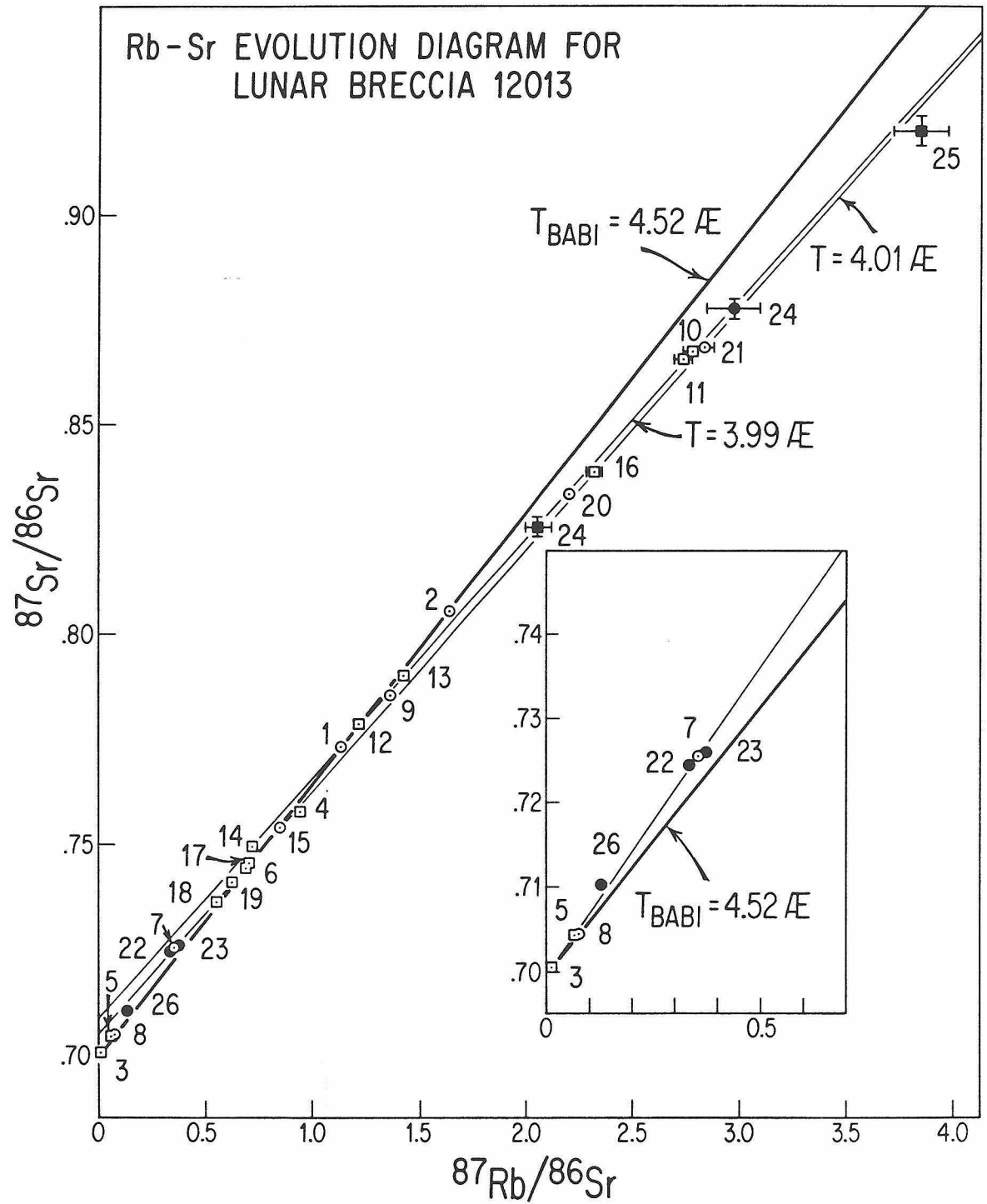


Table 20 : Sample Descriptions

<u>Analysis</u>	<u>Location</u>	<u>Description</u>
Analyses by the Lunatic Asylum (1970)		
1	?	"Light Fragment A": 2.1 mg of white to gray material. Exact nature unknown but probably a mixture of clasts and felsite from the gray breccia.
2	?	"Light Fragment B": 1.5 mg of gray material. Exact nature unknown. Taken from same 18 mg fragment as Light Fragment A and probably a mixture of clasts and felsite.
3	3	Plagioclase fragment (0.3 mg) from black breccia. Composition (An_{95}) suggests that it is related to the granulated norite.
4	9 & 10	"Composite A" (0.8 mg): Handpicked pinkish grains from black breccia. Split is mostly K-rich mesostasis and plagioclase.
5	9 & 10	"Composite B" (1.1 mg): Plagioclase grains (0.2-0.5 mm) handpicked from the black breccia.
6	10	"Composite C" (5.8 mg): A large ilmenite grain with minor amounts of K-rich mesostasis. Low Nb_2O_5 suggests that the ilmenite is not related to the quartzofeldspathic rocks or felsite, but may be related to the basalt-gabbro suite.
7	35	Black breccia fragment (1.8 mg).
8	09	Black breccia fragment (6.0 mg).
9	40	Mixture of clasts and felsite from the gray breccia (58 mg).
10	40	Density separate, $\rho < 2.65$ (2.6 mg). Sample dominated by felsite.
11	40	Density separate, $\rho < 2.65$ (2.8 mg). Sample dominated by felsite.
12	40	Density separate, $2.65 < \rho < 2.8$ (3.1 mg). Sample was a mixture of felsite and plagioclase and pyroxene clasts.
13	40	Density separate, $2.8 < \rho < 2.9$ (2.0 mg). Sample was a mixture of felsite and plagioclase and pyroxene clasts.
14	40	Density separate, $\rho > 3.3$ (6.2 mg). Sample was mostly pyroxene clasts with some plagioclase and minor felsite.
15	29	Mixture of clasts and felsite from the gray breccia (38 mg).
16	29	Density separate, $\rho < 2.65$ (1.1 mg). Sample dominated by felsite.
17	29	Density separate, $2.70 < \rho < 2.8$ (2.8 mg). Mostly plagioclase clasts; some felsite.
18	29	Density separate, $2.9 < \rho < 3.3$ (10.2 mg). Mostly pyroxene clasts with some plagioclase clasts and minor felsite.
19	29	Density separate, $\rho > 3.3$ (8.9 mg). Mostly pyroxene clasts and minor plagioclase clasts and felsite.
20	45	Mixture of clasts and felsite from the gray breccia (6.0 mg).
21	42	Mixture of clasts and felsite from the gray breccia (2.4 mg).
Analyses by Schnetzler <u>et al.</u> (1970)		
22	10	Black breccia fragment (10.0 mg). Constrained least squares analysis using trace element abundances suggests that the sample was ~50% groundmass melt, ~15% felsite and ~35% mineral clasts by weight.
23	15	Black breccia fragment (5.2 mg). Constrained least squares analysis using trace element abundances suggests that the sample was ~55% groundmass melt, ~12% felsite and ~33% mineral clasts by weight.
24	15	Gray breccia fragment (14.5 mg). Constrained least squares analysis using trace element abundances suggests that the sample was ~50% felsite and ~50% clasts by weight.
25	15	Density separate, $\rho < 2.62$ (1.3 mg). Sample was predominantly felsite.
Analyses by Hubbard <u>et al.</u> (1970)		
26	05	Black breccia fragment (41.45 mg).

and 0.7050 ± 0.0009 , respectively. A "whole rock isochron" corresponding to an age of 4.52 AE with an initial of BABI was suggested based on selected fragments of the breccias. Two isotopically indistinguishable scenarios were offered as their conclusion. One possibility was that at 4.5 AE 12013 was formed as a mixture of components with extreme variation in Rb/Sr and that this mixture was subsequently metamorphosed at about 4.0 AE. A second possibility was that separate high Rb/Sr and low Rb/Sr reservoirs were formed at 4.5 AE and later mixed at about 4.0 AE. Using the terminology of this paper, the high Rb/Sr material corresponds to the felsite, the low Rb/Sr material was considered to be the black breccia, and the gray material or gray breccia was interpreted to have formed by partial assimilation of the black breccia by the felsite. The critical point in these conclusions was that the felsite, or a high Rb/Sr progenator, must have formed very early in the moon's evolution to account for the high initial $^{87}\text{Sr}/^{86}\text{Sr}$ of the felsite and the 4.52 AE "whole rock isochron". Since isotopic studies on other lunar "granites" have yielded ambiguous results (Nyquist et al., 1977) or ages close to 4.0 AE (Compston et al., 1977; Tatsumoto and Unruh, 1976), 12013 was the sole evidence for an early ($\gg 4.0$ AE) episode of "granite" generation.

OTHER ISOTOPIC DATA

Turner (1970, 1971) performed ^{40}Ar - ^{39}Ar age determinations on a sample of gray breccia (12013,10,26) and a sample of black breccia (12013, 10,43). The release patterns for both samples were constant over most of the gas release suggesting that the samples were uniform in $^{40}\text{Ar}/\text{K}$. The most recently determined apparent ages were 4.06 ± 0.07 AE for the gray

breccia and 4.01 ± 0.07 AE for the black breccia. These ages are essentially identical to the Rb-Sr internal isochron ages determined by the Lunatic Asylum (Albee et al., 1970) and suggest that the last event causing extensive reequilibration of the phases was at approximately 4.0 AE.

Tatsumoto (1970) measured U-Th-Pb isotopic abundances in three samples. These were black breccia sample 12013,10,09 and gray breccia sample 12013,10,42 and 12013,10,45. Inspection of the photographs of slab 12013,10 suggests that sample 12013,10,45 contained a large fragment of basalt in a matrix of breccia. The other samples were less distinctive. The analyses produced three discordant points on a $^{226}\text{Pb}/^{238}\text{U}$ vs. $^{207}\text{Pb}/^{235}\text{U}$ plot that formed an array projecting from an upper concordia intercept of about 4.3-4.4 AE and a lower intercept of 0-1 AE. These results are difficult to understand in the context of the Rb-Sr and ^{40}Ar - ^{39}Ar studies (Albee et al., 1970; Turner, 1970). Tatsumoto (1970) considered the possibility that the samples might have been contaminated or incompletely decomposed during preparation, and reached the unspecific conclusion that "either the parental material of the.....breccia, if not the brecciation itself, formed quite early in the moon's history, possibly 3.9 to 4.3 b.y. ago."

Hinthorne and Andersen (1974) determined Pb-Pb and U-Pb ages for a single zirconolite grain in the felsite. The raw datum was slightly discordant. Hinthorne and Andersen (1974) employed a modern lead correction and drew discordia from the origin through the corrected point to produce an upper intercept with the concordia corresponding to an age of 3.87 AE. This was their favored estimate for the age of the grain.

The Lunatic Asylum (Albee et al., 1970) measured Xe isotopic abundances in black breccia sample 12013,10,10 and gray breccia samples

12013,10,35 and 12013,10,38. An exposure age of 55 m.y. was calculated for samples 12013,10,10 and 35 based on concentrations of spallogenic ^{126}Xe . The abundance of fissionogenic ^{136}Xe in sample 12013,10,35 was used to estimate a Xe retention age. No precise determination was possible because ^{136}Xe is a decay product of both ^{238}U and ^{244}Pu and the initial ratios of these isotopes in 12013 are not known. Assuming no initial ^{244}Pu yielded an estimated Xe-retention age of $4.1 \pm 0.5 - 0.7$ AE.

Burnett et al. (1971) examined fossil particle tracks in minerals from a sample (12013,10,44) from the interior of 12013. U fission-tracks in apatite grains ranged from 1.0 ± 0.2 to 3.2 ± 0.6 AE with most less than 1.7 ± 0.4 AE. This suggests that 12013 was affected by a post-3.9 AE thermal or shock event capable of annealing fission tracks. Fossil tracks in pyroxenes and feldspars were attributed to galactic cosmic rays. Track densities were higher in the feldspars than in the pyroxenes suggesting that the tracks in the later had been annealed; track densities in the feldspars suggested an exposure age of 15 ± 3 m.y..

SUMMARY

A detailed study of the Rb-Sr isotopic systematic of 12013 by the Lunatic Asylum (Albee et al., 1970) suggested that 12013 is composed of materials older than 4.0 AE but which suffered a major reequilibration at about 4.0 AE. The Lunatic Asylum also suggested that the protolith(s) of the breccia were formed at about 4.5 AE based on a "whole rock isochron" for 12013. This interpretation is discussed in greater detail in the discussion section of this thesis. Whereas the 4.5 AE age is based solely

on interpretation of the Rb-Sr data, there are considerable supporting data for the 4.0 AE event. ^{40}Ar - ^{39}Ar measurements on both the black and gray breccias (Turner, 1970) yield ages of about 3.87 AE. U-Th-Pb studies (Tatsumoto, 1970) and Xe isotopic studies (Albee et al., 1970), while yielding ages that are less well constrained, are consistent with a major recrystallization event at about 4.0 AE. Therefore, it seems certain that all of the components of 12013 suffered a major reequilibration at about 4.0 AE. This age is best interpreted, in light of the petrography of the rock, as the age of the breccia forming event.

Several events have been dated that are younger. Burnett et al. (1970) found that U fossil fission tracks in apatite yield an age of ≤ 1.4 AE suggesting a mild thermal or shock event at that time. Exposure ages are on the order of 55 ± 3 m.y. (Albee et al., 1970; Burnett et al., 1970).

DISCUSSION

INTRODUCTION

Lunar rock 12013 is an extremely complex breccia for which a large body of experimental and observational data exist. The following discussion is aimed at a synthesis of petrographic, chemical, and isotopic data. The primary goals of this discussion are to present a feasible model for the formation of the breccia, evaluate the possible genetic relationships between the various components, and place some constraints on the nature of the source area(s). Conclusions on the nature and petrogenesis of the various lithologies in 12013 based on the preceding petrographic and electron microprobe study are presented first to establish constraints for interpretation of the chemical and isotopic data.

BRECCIA GENESIS

Previous petrographic studies produced three somewhat divergent interpretations on the nature and petrogenesis of 12013. Drake et al. (1970) interpreted the main features of 12013 to be volcanic in origin, and suggested that the black breccia, and possibly the gray breccia, were formed as ignimbrites laid down by lunar base surge clouds during explosive volcanic eruption. Albee et al. (1970) suggested that 12013 was a brecciated rock that may have formed by injection of a "granitic" magma, which ultimately crystallized to form the felsite, into the lunar regolith. A possible process for formation of the magma was postulated to be removal of a high-K residual melt from highly fractionated Apollo 11 or 12 basalts by filter pressing. Many of the structures and textures were explained by extensive reaction of the regolith components with the granitic magma. James (1970) suggested that most of the petrography of 12013 could be

explained in terms of impact related processes. Mineral and lithic clasts were suggested to be products of impact brecciation and the black breccia groundmass and felsite were interpreted to be crystallized melts or glasses initially produced by impact melting. These preliminary petrographic studies of 12013 were conducted without benefit of what has since been learned from the investigations of Highlands samples, and the discrepancies between their final conclusions on the nature of 12013 arise, at least in part, from the fact that these were the first detailed petrographic studies of a complex lunar breccia.

Based on comparison with the Highlands samples, 12013 is best interpreted as a mixture of two polymict breccias, both of which were produced by impact related processes and are petrologically more similar to Highlands breccias than to rocks of mare affinity. Clast and melt components in both breccias appear to have formed by fragmentation and melting of mainly basalt, gabbro, "granitic," and ANT-suite protoliths during impact, and the final breccia consolidation with attending recrystallization of clasts probably took place in an ejecta blanket. The two breccias are, however, sufficiently different in their clast populations and in conditions that prevailed during their formations to warrant separate discussion.

Black Breccia

The results of this petrologic study indicate that the black breccia of 12013 is a member of a class of lunar breccias that have been variously termed fragment-laden melt-rocks (James, 1976) or clast-laden melt-rocks (Dymek et al., 1976). Although texturally diverse, all of these rocks are inferred to have formed by mixing of cold, impact-derived

mineral and lithic clasts with superheated, impact-generated melts during major impact events (Grieve et al., 1974; Simonds et al., 1976; Simonds, 1975; James, 1976; Dymek et al., 1976). Many of the features of the black breccia are compatible with this model.

Textures indicate that the groundmass of the black breccia crystallized from a melt. The groundmass contains abundant vesicles and has formed igneous-textured coronas around olivine clasts. The extremely fine-grained, equigranular texture of most of the groundmass was most likely produced by rapid quenching of the melt. Furthermore, the relatively monotonous composition of the groundmass throughout the black breccia suggests that it introduced into the black breccia from a single homogeneous melt, rather than formed in situ by partial melting of clastic material.

It is more difficult, however, to establish that this melt was produced by impact melting of target rocks. An igneous origin for the black breccia (Drake et al., 1970), and more generally, for all fragment-laden melt rocks (Crawford and Hollister, 1974; Hollister, 1975) has been postulated previously. However, recent detailed studies of terrestrial analogs at Manicougan Crater (Simonds et al., 1976) have clearly supported an impact origin for the melt components of this type of breccia, and it, therefore, is no longer necessary to postulate volcanic events in order to explain these melts. In the specific case of the black breccia of 12013, the evidence for impact-production of the melt is indirect. Although clasts are uniformly distributed, they obviously did not equilibrate chemically with the melt; many clasts are only partially resorbed and clast compositions vary greatly, but groundmass phase compositions are

restricted to narrow compositional ranges. These characteristics and the monotonous bulk composition of the groundmass are compatible with rapid, violent mixing of a homogeneous melt with a diverse clast suite, followed by cooling at a rate too rapid to allow attainment of chemical equilibrium. Such conditions are compatible with current models for an impact ejecta cloud (Simonds, 1975; Simonds et al., 1976) but are almost certainly not realized in a basaltic intrusion or flow.

An impact origin for the clasts in the black breccia seems less equivocal. Intergranular deformation features are common in lithic clasts and intragranular deformation features are present although less abundant. The strong granulation of the lithic clasts indicates that they were already broken up at the time they were mixed with the groundmass melt. This is obviously consistent with an origin by brecciation during the early stages of an impact event followed immediately by mixing with impact melt. The scarcity of intragranular shock features could be explained by derivation of most of the fragmental material from a considerable distance from the center of the impact. Of course, some of the evidence of intragranular shock deformation may have been destroyed by annealing subsequent to breccia formation. The presence of spherulitic-textured plagioclase that probably formed by devitrification of maskelinite suggests that some annealing did, in fact, occur.

The fragmental material in the black breccia appears to have been cold when it was mixed with the melt. Some low-Ca pyroxene clasts have high-Ca exsolution lammellae that are much wider ($\sim 4\mu\text{m}$) within about 10 micrometers of the clast margins than in the interior ($\sim 1\mu\text{m}$) of the clasts of the grain. This texture suggests that the outer few micrometers

of the pyroxene clasts were heated to temperatures sufficiently high to promote growth of the exsolution lamellae but that the interiors were cold and did not reach temperatures sufficiently high to recrystallize. Such a thermal history is consistent with sudden mixing of superheated melt and cold clasts. Furthermore, the scarcity of intragranular shock deformation features in the clasts suggests that most of the clasts were exposed to low shock pressures during the breccia forming process, certainly less than the 100 kb required to form maskelynite, and, therefore, were probably not heated to temperatures of more than 200-300° (Ahrens and O'Keefe, 1972).

To summarize, the formation of the black breccia appears to have been as follows. Both a mafic silicate melt and crushed and granulated lithic and mineral clasts were produced during an impact event. The scarcity of intragranular deformation features and isotropized grains indicate that the clasts were derived a considerable distance from the point of impact. These clasts and the melt were rapidly and thoroughly mixed in the ejecta cloud. The smeared-out form of the lithic clasts indicates that this mixing was violent.

The origin of the felsite in the black breccia is problematic. The only statement that can be made with certainty is that the presence of rare vesicles in the felsite, the igneous texture of the felsite, and the occurrence of felsite veins indicate that this material was molten at some time after it was incorporated into the black breccia. Albee et al. (1970) and Drake et al. (1970) suggested that the felsite was intruded into the black breccia after that lithology had solidified, and that the felsite blebs in the black breccia represent vesicles that were filled by

felsite. This interpretation, however, is inconsistent with the observation that most of the felsite blebs are large ($\gg 100\mu\text{m}$) and ovoid, and essentially all the vesicles are small ($< 100\mu\text{m}$) and spherical. The smooth rounded shape of the felsite blebs is readily explained if the felsite melt and black breccia groundmass melt coexisted but failed to mix prior to the lithification of the black breccia. The smooth ovoid contacts would have then been fluid-fluid interfaces. This interpretation is strongly supported by the occurrence of a vesicle at the edge of a bleb that is shared by both the felsite and black breccia groundmass. The apparent immiscibility of these two melts will be discussed in a later section; however, it is clear that the felsite existed as a melt in the black breccia while the groundmass was also still molten.

Several possibilities exist for the penultimate origin of the felsite. First, the felsite melt may have formed by complete impact melting of a crystalline precursor and was incorporated into the black breccia as melt droplets or glass fragments that were subsequently remelted. Indeed, some patches of felsite in the black breccia are angular in outline suggesting that they may have been incorporated as glass clasts. The significant consequence of this hypothesis is that essentially all petrographic record of the felsite's progenitor would have been lost. However, the quartzofeldspathic rocks are mineralogically very similar to the felsite. Particularly striking are the similar Nb_2O_5 contents of the ilmenite and the An contents of the plagioclase in both lithologies. Therefore, a second and more probable hypothesis is that the felsite formed by partial melting of a crystalline precursor that is represented in the clast population as quartzofeldspathic rocks

and fragments of plagioclase (An_{50-60}) and silica. This hypothesis is particularly attractive since many of these clasts are intimately associated with felsite, and a similar spatial relationship between a fine-grained felsite and a coarse-grained "granitic" clast has been described in 73215 by James and Hammarstrom (1977) and interpreted as the result of partial melting. The heat required for partial melting may have come directly from an impact event, but this seems unlikely since isotropized feldspar is not found in the quartzofeldspathic clasts, indicating they were exposed only to low shock pressures and temperatures. Alternatively, the necessary heat may have come from the superheated groundmass melt, or, more generally, from other hot material in the same part of the ejecta cloud or blanket. A third possibility for the origin of the felsite is that it is related to the black breccia through liquid immiscibility, and either exsolved directly from the more Fe-rich groundmass melt, or was produced by a reaction between the black breccia groundmass and the quartzofeldspathic rocks. The latter possibility could explain the close association between the felsite and the quartzofeldspathic rocks, but the liquid immiscibility hypothesis does not explain the abundance of felsite in the gray breccia and well removed from the black breccia. Silicate liquid immiscibility was suggested previously (Quick *et al.*, 1977) as one possible way to explain the unusual bulk compositions of both the black breccia groundmass and the felsite. However, if the black breccia groundmass and felsite were genetically related through liquid immiscibility, the distribution of these two materials in 12013 requires that relationship to predate the formation of the breccia.

Of the three hypotheses advanced above, the second seems most

likely, based on both mineralogical and textural constraints. The felsite appears to have been incorporated into the black breccia as some combination of glass fragments, blobs of melt, and perhaps melt associated with the quartzofeldspathic rocks. Continued melting of the quartzofeldspathic rocks, then in contact with the superheated impact melt, may have produced more felsite. Thermal equilibrium between the impact melt and the clasts is estimated to be reached within a few seconds (Simonds et al., 1976) in breccias of this type, and subsequent cooling of the clast-melt mixture would be slower. Ultimately, the impact melt crystallized to form the black breccia groundmass. The felsite must have remained molten longer since it forms veins that crosscut both the groundmass and clasts.

Gray Breccia

The petrography of the gray breccia indicates that it also formed as a mixture of silicate melt and impact-derived lithic and mineral clasts. However, the gross texture of this breccia is unlike that of the black breccia and other clast-laden melt-rocks, and the abundance of granitic-compositioned felsite in the matrix sets it apart from other types of lunar breccias that have been described in the literature.

The first petrographic studies of 12013 (Drake et al., 1970; Albee et al., 1970) concluded that the pervasive distribution of the felsite in the gray breccia is best understood if the felsite formed from a granitic composition melt with a sufficiently low viscosity to permeate the interstices between the mineral and lithic clasts. The conclusions of this study are in agreement on a melt origin for the felsite. The hypidiomorphic granular and microporphyritic texture of the felsite must

have formed by crystallization of minerals from a melt. This interpretation is reinforced by the similarity in texture and mineralogy between the felsite in the gray breccia and the felsite blebs and veins in the black breccia that certainly crystallized from melts. The distribution of the felsite in the gray breccia, however, is probably due mostly to violent mixing of very small felsite glass fragments and/or blobs of melt with the clasts of the gray breccia during the accretion of the breccia in an ejecta cloud, and subsequent permeation of the felsite through the interstices of the gray breccia probably only occurred on a very local scale of a few tens of micrometers. Permeation over greater distances would have required a very low melt viscosity, which in turn would suggest that either the felsite melt was greatly superheated or that the clasts in the gray breccia were very hot during the formation of the breccia. Since there is no evidence for either a superheated melt or very hot clasts, intimate mixing of melt and clasts in an ejecta cloud seems more probable.

However, it is not clear if the felsite was incorporated into the gray breccia as blobs of rhyolitic melt, as fragments of glass that subsequently melted, as fragments of crystalline protolith that were mostly destroyed by melting, or as some combination of these. The large clast-free, angular patches of felsite in the gray breccia may represent glass fragments that never melted or remained too viscous to mix with mineral and lithic clasts when they were incorporated into the breccia. Similarly, the tonalite clast may represent a fragment of a protolith that survived melting after it was incorporated into the gray breccia.

Therefore, all the felsite in the gray breccia may not have crystallized from an impact melt, but rather some may have crystallized from a melt that formed by in situ melting of rock and/or glass fragments after incorporation into the breccia. There is insufficient petrographic evidence to determine which of these scenarios was dominant. However, the relative scarcity of suitable fragments of a crystalline protolith suggests that the felsite was mostly a melt or a glass when it was introduced into the gray breccia.

The impact origin of the mineral and lithic clasts is recorded by both intracrystalline and intercrystalline deformation features. The intense granulation of the coarse-grained lithic clasts, and the plastic deformation of minerals in the basalt clasts were almost certainly produced by shock deformation. However, as in the black breccia, there are very few clasts of devitrified maskelynite indicating that shock pressures did not exceed 100 Kb (Ahrens and O'Keefe, 1972) in the terrane from which most of the clasts were derived.

The major conclusions about the genesis of the gray breccia are as follows. Shock deformation features indicate that the clastic component of the gray breccia was produced by an impact but the absence of abundant isotropized grains indicate that the clasts never experienced high shock pressures. The distribution of the felsite throughout the gray breccia suggests that it was violently mixed with the clastic component in an ejecta cloud. Portions of the felsite may have been mixed in as blobs of melt, or as fragments of glass or protolith that were subsequently melted. The gray breccia is not a clast-laden melt-rock but, instead, is better characterized as a clastic or fragmental breccia into which a large amount

of molten and/or low melting point, granitic-compositioned material was mixed during the breccia-forming event.

Relationships between the Breccias

It is not possible to determine with absolute certainty which if either of the breccias is included in the other. In many Highlands breccias (e.g., 73215 and 66075), breccia fragments with black aphanitic groundmass occur as angular or rounded clasts in light colored breccias. By analogy to these rocks, the black breccia of 12013 could be interpreted as clasts that were incorporated into a larger piece of gray breccia. Certainly, the gray breccia constitutes the bulk of 12013. This fact and the occurrence of small isolated patches of black breccia, which appear in saw cut surfaces to be completely surrounded by gray breccia, support this interpretation.

Many of the structures in 12013 were probably formed after juxtaposition of the two breccias but while they were both lubricated by silicate melts still deforming plastically. As a result many of these features are confusing and sometimes appear contradictory. The general appearance of the smooth, cusped contact between the gray breccia and the larger blob of black breccia in thin section 12013,13 (Figure 2) is suggestive of an interface between two fluids. Significantly, this contact is adjacent to a portion of the gray breccia in which the feldspar/clast ratio is $\gg 1$. Therefore, this part of the gray breccia must have behaved as a viscous fluid at the time this meniscus-like feature formed. In contrast, contacts between the black breccia and portions of the gray breccia that are dominated by clasts tend to be much more irregular and ragged suggesting that these portions of the gray

breccia were less fluid due to the greater abundance of clasts. The schlieren of black breccia that crosscuts the gray breccia in 12013,15 (Figure 2) suggests that the black breccia intruded the gray breccia. Indeed, this feature is best explained as an apophysis of black breccia that was injected into the gray breccia while still molten. The extreme shearing that occurred during this injection is evidenced by the intensely smeared-out norite and quartzofeldspathic clasts in the schlieren. It would, therefore, appear that the black breccia intruded the gray breccia during the formation of 12013 and is the younger lithology. However, the black breccia probably solidified before the gray breccia. The felsite veins that crosscut the black breccia clearly indicate that the felsite was still molten after the groundmass melt of the black breccia had crystallized and become capable of brittle fractures. Therefore, by analogy, the felsite in the gray breccia must also have still been capable of flow.

The schlieren, cusped black breccia-gray breccia contacts, and the felsite veins indicate that deformation of 12013 continued well after juxtaposition of the two breccias. One possible environment in which these features may have been produced is within an ejecta blanket collapsing under its own weight.

TEMPERATURE HISTORY

Black Breccia

The most comprehensive model for the thermal history of fragment-laden melt rocks has been developed by Simonds (1975) and Simonds et al. (1976) who suggested that the textural variation in these rocks is explainable in terms of differences in initial fragment/melt ratio and

the degree of superheating of the melt at the time of mixing. Clasts are presumed to have been cold ($< 300^{\circ}\text{C}$) when initially introduced into these mixtures because of the general scarcity of shock features indicating high impact pressures and temperatures (Simonds, 1975). Melts are presumed to have been superheated, based on experimental shock studies (Gibbons et al., 1975), analogies to terrestrial impact melts (Simonds et al., 1976) and simple thermodynamic calculations of the heat required to resorb cold clasts (Simonds et al., 1976). Mixing of these components was probably tumultuous and rapid in the ejecta cloud of an impact and, therefore, Simonds et al. (1976) suggest that the thermal histories of these rocks are adequately described by a two stage model involving (1) rapid attainment of thermal equilibrium between the clasts and the melt followed by (2) a period of slower cooling of the entire mixture.

It is possible to place some semiquantitative limits on the pressure and temperature conditions that existed in the black breccia during the early stages of its formation. The vesicles in the groundmass indicate that the environment was low pressure. Based on the scarcity of intragranular shock features, the clasts were apparently cold when they were mixed with the impact melt. Experiments by Rutherford and Hess (1978) determined that the liquidus temperature of the black breccia groundmass is slightly above 1180°C . Simonds et al. (1976) has presented calculations that allow rough approximations of initial melt temperature and the temperature at which clasts and melt first reach thermal equilibrium if the initial clast/melt ratio is known. The observed clast/melt ratio in the black breccia of 12013 is essentially 1:1. There is evidence for clast melt reactions and partial resorption of clasts by

the melt, but for the most part these effects are limited to narrow coronas around rare clasts of olivine, silica, and some plagioclase. It seems likely, therefore, that extensive assimilation of clasts by melt has not occurred. This is further supported by the very uniform composition of the groundmass throughout most of the black breccia. If extensive assimilation of clasts had occurred, the local composition of the groundmass would be highly variable and dependent on the mineralogy of initial local clast population. Nevertheless, the observed clast/melt ratio must be regarded as a minimum, especially in view of the difficulty in distinguishing very small mineral clasts from phases that crystallized from the groundmass melt. An additional constraint may be placed on the equilibration temperature since there is textural evidence that the felsite and black breccia groundmass crystallized from melts that coexisted. The well-rounded shapes of many of the felsite blebs in the black breccia resemble equilibrium fluid-fluid contacts and, therefore, suggest that thermal equilibrium between clasts and impact melt was first reached at temperatures above both the granite minimum and the solidus temperature of the groundmass melt. Applying these constraints to Figures 6 and 7 of Simonds et al. (1976) yields an estimate for initial melt temperature of about 1700-2000°C, an estimated initial breccia composed of about 50-60 weight percent melt and 50-40 weight percent clasts, and an initial equilibration temperature of ~ 1150-1180°C. The elapsed time between mixing and thermal equilibrium for similar breccias was probably on the order of ~ 1 sec based on heat flow modeling of similar breccias (Simonds et al., 1976).

Gray Breccia

The early thermal history of the gray breccia appears to have been somewhat different than that of the black breccia. Clasts are more pervasively recrystallized suggesting that their interiors were raised to higher temperatures or heated longer than the clast interiors in the black breccia. Most of the basalt and gabbro clasts, however, show no evidence of partial melting indicating that most of them were never heated to supersolidus temperatures. The solidus temperature for basalts of roughly similar composition is about 1100°C (Walker et al., 1972) and, therefore, this temperature can be used as an approximate upper limit for the maximum temperature to which clasts in the gray breccia were exposed. The relatively coarse-grain size of the felsite, the absence of glass and its well developed igneous texture supports that the felsite and clasts in the gray breccia reached thermal equilibrium at a temperature above the felsite solidus and then cooled sufficiently slowly to allow nucleation of and growth of large K-feldspar and pyroxene grains. This solidus temperature can be approximated as the dry granite minimum melting temperature (Schaire and Bowen, 1947) of about 990°C for a K-feldspar and quartz eutectic melt. Therefore, most of the material in the gray breccia was probably heated to temperatures between 1000 and 1100°C.

The gray breccia appears to have cooled more slowly than the black breccia. Most of the felsite in the black breccia contains tridymite as the dominant silica mineral suggesting that the black breccia cooled rapidly through the tridymite to quartz transition and preserved metastable tridymite. In contrast, quartz is the dominant silica-bearing phase in the felsite of the gray breccia. However, the acicular habit of these

quartz needles is identical to that of the tridymite in the black breccia, suggesting that it first crystallized as tridymite and then inverted to quartz. A slower cooling rate for the gray breccia might be partially explained in terms of the continued existence of a melt component at lower temperatures. The crystallization of the felsite would tend to buffer the temperature of the gray breccia at about 1000°C by gradually releasing latent heat of fusion. The black breccia groundmass would have crystallized completely at a higher temperature, releasing all its latent heat of fusion and, therefore, could have cooled rapidly at subsolidus temperatures.

Single vs. Multiple Impact Events

A model for the formation of 12013 by a single major impact event is supported by several observations. First, the rock as a whole has a relatively simple clast population. The lithic clast suites of both breccias are dominated by basalt-gabbro-suite rocks, quartzofeldspathic rocks and norite, although the relative abundances are grossly different in the two breccias. Only minor amounts of other lithologies are found. Furthermore, textures, grain sizes, and compositions of most mineral clasts in both breccias are compatible with derivation from rocks similar to these three lithologic groups. The rather limited overall diversity of clast types suggests that both the black breccia and the gray breccia were derived from similar terranes and experienced very little reworking. Second, neither of the two breccias are similar to regolith breccias as would be expected if they had been gardened by multiple impact events while in the lunar regolith. Glass spheres, which are important constituents

of regolith breccias, are absent from 12013. The clast sizes, especially in the gray breccia, are larger than clasts in regolith breccias as exemplified by 15205 (Dymek et al., 1974). Devitrified glass clasts are abundant in regolith breccias, but only a minute percentage of the clasts in 12013 (basaltic aphanites and "chondrules," and devitrified maskelynites) could be interpreted as devitrified glass fragments. Most of the recrystallization in 12013 occurred during and after breccia consolidation, but many clasts in regolith breccias typically record earlier and even multiple recrystallization events. A few clasts apparently recrystallized prior to their incorporation into 12013, but such clasts constitute only a very minor component of the black breccia and are extremely rare in the gray breccia. Third, the internal structures of both breccias suggest that they formed by violent mixing in an environment similar to that postulated for an ejecta cloud (Simonds et al. 1976), and the contact relationships between the breccias suggests that they were both hot and plastic when juxtaposed. Certainly many models can be postulated to explain these features, but they are most easily explained by simultaneous formation of the gray and black breccias in different parts of an ejecta cloud of a single impact event, followed by a collision of the still plastic breccias while in flight or during burial in an impact blanket.

An analogy may be drawn with the ejecta from the West Clearwater Crater, Quebec. Detailed field studies of these rocks by Simonds et al. (1978) determined that they are made up of a basal unit of $\leq 20\text{m}$ of impact-melt-bearing fragmental breccia, overlain by $\sim 15\text{m}$ of clast-rich melt rock that grades upward into clast-poor melt rock. The contact between

the melt rock and the fragmental breccia is marked by a chilled margin and is extremely irregular. Dikes of melt rock intrude downward into the fragmental breccia and blobs of smeared-out impact generated glass are mixed into the fragmental breccia. Apparently, during the impact, a large volume of impact melt was produced by complete melting of the target rocks at and near ground zero. This melt incorporated clastic material as it flowed with great turbulence along the floor of the excavated crater. The fragmental breccia, which was derived farther from the point of impact, was deposited first and then covered by the clast-laden melt. Although the features of the contact between the fragmental breccia and melt-rock are much larger in size, they are reminiscent of the structures in 12013. The black breccia is analogous to the chilled melt-rock and felsite to the fragmental breccia. 12013 may then be a sample from a portion of an impact sheet that is very near the contact of the fragmental breccias and the overlying melt-rocks.

MELT COMPONENTS

Introduction

The chemical composition of the felsite and the black breccia groundmass have been discussed in detail by Quick et al. (1977). Both lithologies show extreme enrichments in some incompatible elements but are depleted in others, and it is the relative abundances of these two lithologies that control the incompatible element balance of 12013. The black breccia groundmass (Tables 15 and 16) has essentially the bulk composition of a feldspathic basalt or a low-K Fra Mauro basalt that is enormously enriched in P, U, Th, and REE, but depleted in K. The low-K concentration ($K_2O < 0.1$ weight percent) is particularly unusual considering that U,

Th, and REE range from 300 to 800 times chondritic abundances. The REE pattern resembles the pattern that is conventionally associated with the so-called KREEP component (Figure 10 in Quick et al., 1977) and is characterized by a light REE enrichment and strong negative Eu anomaly. However, the low-K content of this lithology clearly indicates that it is not related to KREEP by conventional petrologic processes. The felsite (Figure 15 and 16) is essentially granitic in bulk composition and also is strongly enriched in U, Th, and REE but, in contrast to the black breccia groundmass, has a low P concentration and a high K and Ba concentration. U, Th, and REE abundances reach 200 to 2000 times chondritic, K₂O is approximately 6.7 weight percent but P₂O₅ is only about 0.2 weight percent. In spite of the high abundances of most of the incompatible elements, K, Ba, and Rb are strongly enriched relative to REE (Hess et al., 1975; Quick et al., 1977). The REE pattern is bowl-shaped, with intermediate REE depleted relative to light and heavy REE elements, and has a pronounced negative Eu anomaly. The REE pattern and low P content of this lithology indicate that it is also not obviously related to KREEP.

This occurrence of two distinct lithologies, both showing extreme enrichments in some incompatible elements but unusual depletions in others, is a unique property of 12013 that is not duplicated in any other lunar samples. Furthermore, the splitting of incompatible elements indicates that some process other than or in addition to simple crystal fractionation of a melt must have been involved in the petrogenesis of these two lithologies; otherwise, a more uniform enrichment in incompatible elements would be anticipated in both lithologies (Quick et al., 1977). How are such high concentrations of U, Th, P, and REE produced in a basalt

with a relatively unevolved major element chemistry, and how can these enrichments form without a corresponding enrichment in K? Similarly, how can extreme enrichments in K, Rb, and Ba be produced in the felsite without corresponding enrichments in P and REE? The origins of these unusual melt compositions are problematic but clearly of paramount importance to the understanding of 12013.

Criteria for Silicate Liquid Immiscibility (SLI)

Roedder and Weiblen (1970) first documented evidence for SLI in lunar basalts. The examples cited were late-stage, coexisting, high-Fe and high-Si glasses in the interstices of Apollo 11 mare basalts. Numerous examples of SLI have since been recognized in lunar basalts returned by subsequent missions (Roedder and Weiblen, 1971, 1972; Powell et al., 1975). Hess et al. (1975) and Rutherford et al. (1976) demonstrated experimentally that continued fractional crystallization of melts representing a wide range of lunar basalt compositions leads to the production of co-existing high-Fe and high-Si melts by SLI.

As a result of these observations and experiments, we now know that SLI is common in lunar basaltic magmas, and that SLI leaves a distinctive chemical signature on the conjugate immiscible melts. Normal incompatible element associations are disrupted by SLI; the effects most easily determined by electron microprobe analysis are that Ti and P are strongly partitioned into the high-Fe melt and K is strongly partitioned into the high-Si melt. Hess and Rutherford (1974) advanced a theoretical model for element partitioning between immiscible silicate melts based on ionic field strength (cation charge/cation radius). According to this hypothesis, cations with the highest ionic field strength and which cannot

tetrahedrally coordinate oxygen (e.g., U, Th, REE, P, Zr, Ti) are partitioned into the high-Fe immiscible melt, and low-ionic field strength cations (e.g., K, Ba, Rb) are partitioned into the high-Si immiscible melt. Partial confirmation of this hypothesis comes from experimental investigations by Ryerson and Hess (1975) and Watson (1976) on cation partitioning (specifically Mg, P, Ca, Ti, Cr, Mn, Sr, Zr, Cs, Ba, La, Sm, Yb, Lu, and Ta) between immiscible silicate melts. As common incompatible element associations are strongly disrupted by the onset of SLI, it should be possible to recognize the effects of SLI in a given lithology by measuring certain key element ratios such as K/La and K/P.

Felsite as a Product of SLI

Hess et al. (1975) suggested that the felsite in 12013 was a direct result of SLI, and that the felsite crystallized from a high-Si melt that had completely separated from the conjugate high-Fe melt. The critical point of their argument was that K/La, Rb/Yb, and Ba/La ratios were approximately an order of magnitude higher than the "average" lunar element ratios (Taylor and Jakes, 1974) of K/La = 70, Rb/Yb = 0.8, and Ba/La = 13. Using published data on 12013 (Drake et al., 1970; Hubbard et al., 1970), Hess et al. (1975) inferred that these ratios in the felsite were K/La = 520, Rb/Yb = 3, and Ba/La = 90. Our data on the felsite composition yield ratios of K/La = 554, Rb/Yb = 3.8, and Ba/La = 65, which are in close agreement and clearly demonstrate that the normal associations of K, Rb, and Ba with REE do not exist in the felsite. This "splitting up" of incompatible elements is a characteristic feature of SLI. Hess et al. (1975) argued that crystal fractionation was an improbable mechanism for producing the felsite composition, since fractionation of

> 6 wt. percent whitlockite from a parent granitic melt would be required to produce the observed feldsite composition. This would constrain the parent melt to have at least 4 wt. percent P_2O_5 . Inasmuch as no lunar granite has been reported with P_2O_5 contents this high, they rejected fractional crystallization for lack of a suitable parent. Furthermore, an origin of the 12013 feldsite by SLI is supported by compositional similarities with experimentally produced high-Si melts (Hess et al., 1975), and late-stage high-Si immiscible melts in lunar basalts.

Black Breccia Groundmass as a Product of SLI

Compositionally, the 12013 black breccia groundmass is a low-K feldspathic basalt. However, it is distinguished from all other lunar feldspathic basalts by extremely high concentrations of REE, Th, U, and P. Our calculated K/La, Rb/Yb, and Ba/La ratios for the black breccia groundmass are 2.4, 0.2, and 1.2, respectively. These values are approximately an order of magnitude lower than the "average" lunar ratios (Taylor and Jakes, 1974), suggesting that, as in the case of the feldsite, normal incompatible element associations have been disrupted by SLI. The major element chemistry of the black breccia groundmass is not typical of late-stage, high-Fe immiscible melts commonly observed in lunar basalts (Roedder and Weiblen, 1970, 1971, 1972; Powell et al., 1975) but high-Fe immiscible melts with similar major element chemistries have been produced experimentally (Hess et al., 1975).

James (1976) classified the 12013 black breccia as one member of a "gradational series of highlands breccias" which included: Apollo 17 light-gray breccias, blue-gray breccias, and green-gray breccias; Apollo 16 poikilitic rocks; Apollo 15 and 16 "black and white" rocks; and dark

clasts in Apollo 14 thermally metamorphosed breccias. James (1976) noted that these were all "fragment-laden melt rocks" with similar textures, major element compositions, and REE element patterns. Using published data, we calculated the K/La, Rb/Yb, and Ba/La ratios for the following members of the series: 73215,161 and 73215,184 (James et al., 1975b); 73215,46 (Blanchard et al., 1976); 64015 (Bansal et al., 1973); 15455 black (Taylor et al., 1973); and 14306 dark (Taylor et al., 1972). The range in K/La values for these samples is 44 to 133, the range in Rb/Yb values is 0.3 to 0.6, and the range in Ba/La values is 10 to 12. These values are close to the "average" lunar element ratios, and K/La and Ba/La are an order of magnitude higher than the respective ratios for the 12013 black breccia groundmass. While the 12013 black breccia may be classified as a member of this "gradational series of highlands breccias," we feel that the unusual composition of the black breccia groundmass strongly suggests an episode of SLI occurred at some time in its history.

Felsite-Black Breccia Groundmass Relationship

As discussed above, many of the textural and chemical attributes of the black breccia groundmass and felsite in 12013 are compatible with a cogenetic relationship involving SLI. Abundant textural evidence suggests that these two lithologies crystallized from melts which co-existed but failed to mix. Diffusion zones should exist at the contacts of the felsite and black breccia groundmass if they crystallized from miscible melts. For example, in one experiment by Yoder (1973), diffusion zones 60 μ m wide were produced between basaltic- and granitic-compositioned melts in contact for one hour at 1200°C. Coronas around olivine clasts in the black breccia indicate that diffusion occurred in the groundmass

melt over distances on the order of 100 μ m. However, compositional changes across the felsite-black breccia groundmass contacts are abrupt (Figures 33), and similar to compositional changes across the interface of co-existing high-Fe and high-Si glasses in the interstices of lunar basalts (Figure 34). The similarity of the felsite and black breccia groundmass to conjugate high-Si and high-Fe melts is even more striking on inspection of the major element chemistry. P is enriched in the black breccia groundmass ($P_2O_5 > 1$ wt. %) and K is only present at trace levels (< 0.1 wt. %), while the felsite is strongly enriched in K and depleted in P. Furthermore, the major element compositions of both felsite and black breccia groundmass are similar to those of experimentally produced conjugate high-Si and high-Fe immiscible melts (Hess et al., 1975). The textural relations and major element chemistries of the black breccia groundmass and felsite argue strongly for a cogenetic relationship involving SLI.

Some of the compositional characteristics of the felsite and black breccia groundmass are somewhat problematic. To test the trace elements for compatibility with SLI we have compared the interelement ratios between the felsite and black breccia groundmass from sample 16B. The enrichment factors, i.e., ratios of the interelement felsic ratios to the interelement mafic ratios, e.g., $(K/La)_{\text{felsic}}/(K/La)_{\text{mafic}}$, abbreviated hereafter as $(K/La)_{f/m}$, are inconsistent with the theoretical predictions (Hess and Rutherford, 1974) and the experimental data (Ryerson and Hess, 1975; Watson, 1976) for trace element partitioning between two immiscible melts. The observed enrichment factors are: $(K/La)_{f/m} = 246$, $(K/Lu)_{f/m} = 94$, $(K/U)_{f/m} = 37$, $(K/Ta)_{f/m} = 63$, and $(La/Lu)_{f/m} = 0.4$. Based upon the

Figure 33: 12013,09,13 -- Photomicrographs and X-ray scans of the boundary between a felsite "bleb" and surrounding black breccia groundmass illustrating the abrupt compositional transitions across the black breccia groundmass-felsite contact. Field of view is the same for all photos and scans.

(A) Reflected light.

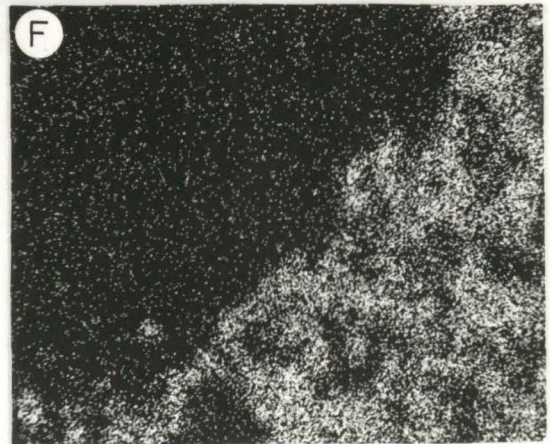
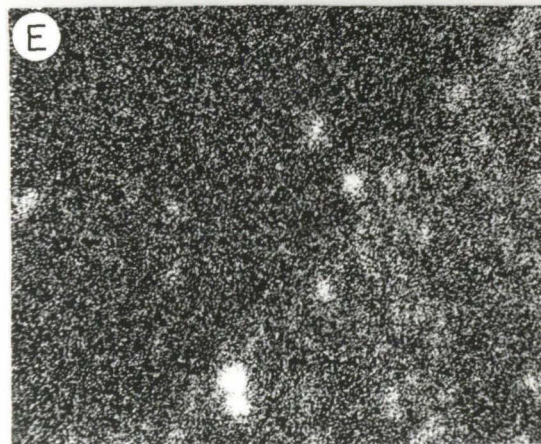
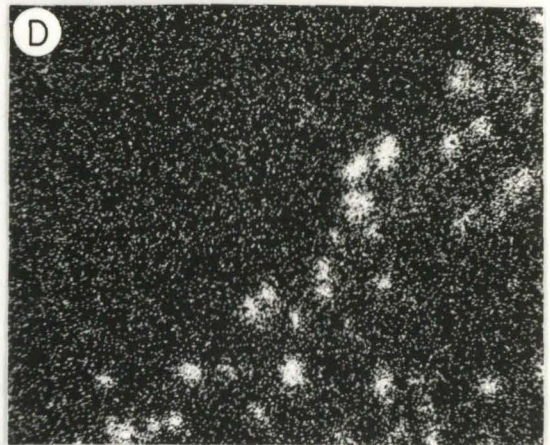
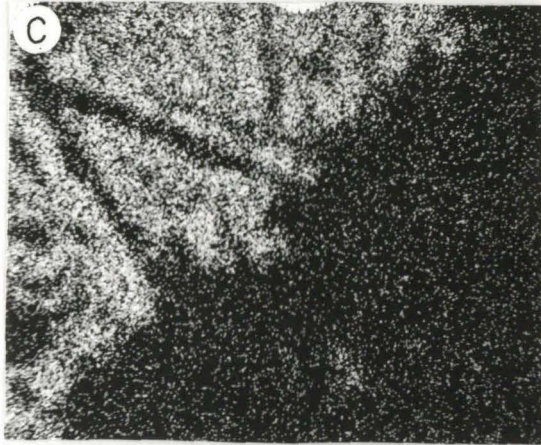
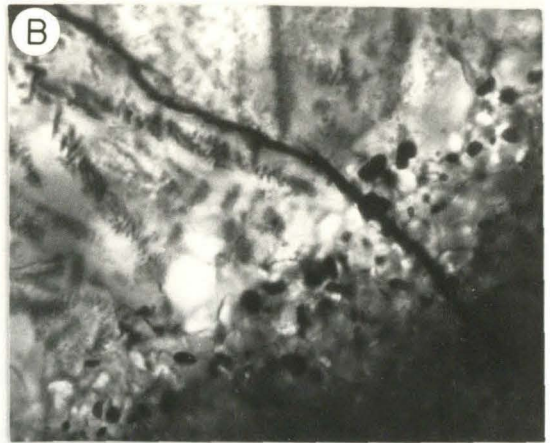
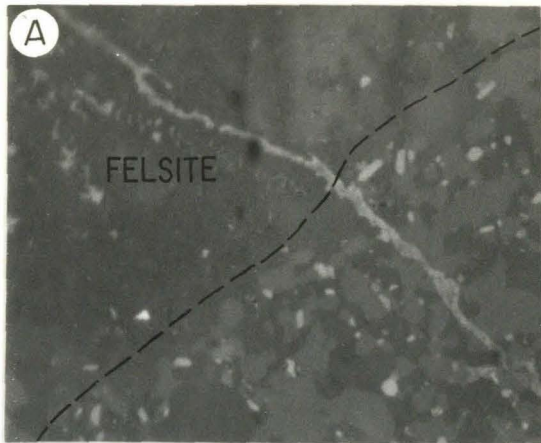
(B) Transmitted light. The felsite-groundmass contact appears gradational because it dips gently to the lower right.

(C) K X-ray scan.

(D) Ti X-ray scan.

(E) P X-ray scan.

(F) Fe X-ray scan.



12013, 09, 13

0.05 mm

Figure 34: 14310,6 -- Photomicrographs and X-ray scans of late-stage, coexisting, immiscible silicate glasses. The bar scale in (A) is 25 μm . All photos and scans are approximately the same scale.

(A) Reflected light.

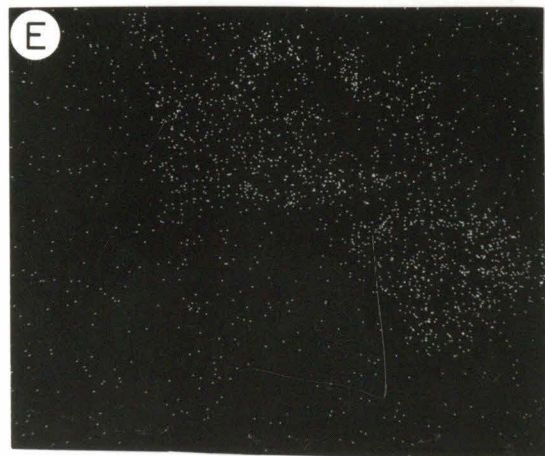
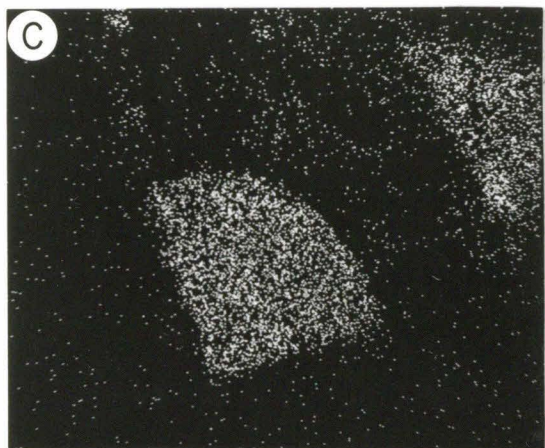
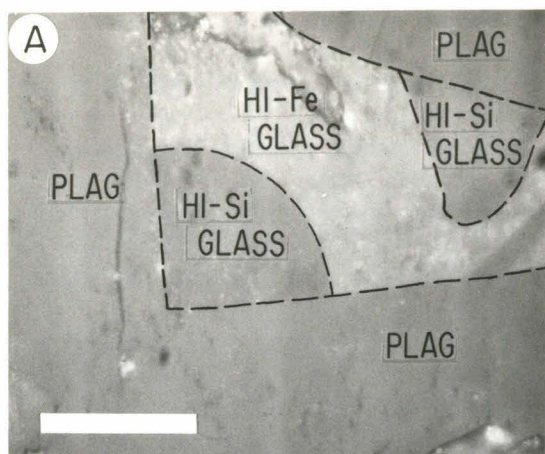
(B) Transmitted light.

(C) K X-ray scan.

(D) Ti X-ray scan.

(E) P X-ray scan.

(F) Fe X-ray scan.



14310,6

theoretical predictions and the experimental results, the relative values of the enrichment factors should be $(K/Th)_{f/m} \sim (K/U)_{f/m} > (K/Lu)_{f/m} > (K/La)_{f/m}$ which is inconsistent with our observations on 12013. Furthermore, $(La/Lu)_{f/m}$ should be > 1 for an immiscible melt pair since both La and Lu have the same charge (+3) but Lu has a smaller ionic radius and therefore greater ionic field strength. In addition to the enrichment factor argument, experimental evidence (Watson, 1976) indicates that the REE patterns for two equilibrium immiscible melts should be similar because only small differences exist between melt-melt partition coefficients for different REE. This is clearly not the case for the patterns in Figure 31. In addition, Rutherford and Hess (1978) demonstrated experimentally that intermediate melt compositions in the binary system felsite-black breccia groundmass did not exsolve immiscible melts that were similar in composition to those of the felsite and black breccia groundmass. Furthermore, they pointed out that the Al_2O_3 concentration is higher in the black breccia groundmass than in the felsite, in contrast to the results of experimentally produced immiscible melts in which Al is partitioned into the high-Si melt.

We conclude that the details of the bulk compositions of the felsite and the black breccia groundmass evaluated independently of petrographic constraints do not support a genetic relationship involving SLI. The probability still remains that SLI played a role in the evolution of one or both of these lithologies prior to the breccia forming event but that they are not genetically related. However, some alternatives to SLI will be discussed.

One alternative to the SLI hypothesis for the black breccia

groundmass is that its unique composition was produced by modification of some more mundane source material by addition and/or subtraction of components and/or elements during and after the impact event that formed 12013. The major element composition of the black breccia groundmass is essentially that of a basalt, suggesting that it may be mostly the product of impact melting of a basaltic protolith. In particular, the compositional similarity of the groundmass (Table 15) and the clasts of the basalt-gabbro suite (Table 3) is noteworthy. The abundance of all major elements in the groundmass fall within the ranges found in the basalt-gabbro suite except for Na and P, which are much more abundant in the groundmass, and Ti, which is somewhat more abundant in the groundmass. Therefore, the clasts of the basalt-gabbro suite could be samples of the protolith from which the black breccia groundmass was derived. Due to the lack of data for the basalt-gabbro suite, no comparison of trace element abundances can be made. However, the low modal and normative abundances of phosphate minerals and other phases that concentrate incompatible elements suggest that U, Th, and REE must be much less abundant in the clasts of the basalt-gabbro suite. Therefore, if the groundmass melt was derived by melting of a protolith similar to the members of the basalt-gabbro suite, some enigmatic component must have been added to the impact melt to account for its high P, U, Th, and REE abundances. The low Si and extremely low K contents of the groundmass require that the hypothetical enigmatic component be composed essentially of phosphate- and Zr-bearing minerals. However, the uniformity of the groundmass composition and the sparseness of phosphate- and Zr-bearing minerals suggest that the trace element abundances of the groundmass

predate its incorporation into black breccia.

Based on the intimate relationship between the felsite and quartzofeldspathic rocks, as well as mineralogic similarities, it was suggested that the felsite may be derived by partial melting of these quartzofeldspathic rocks. It is possible that the high K/REE ratios in the felsite may be the result of partial melting, either under equilibrium or disequilibrium conditions. If the felsite melt was removed from a residue of refractory silicate minerals and phosphate-bearing minerals, then the melt might be expected to be enriched in K and Rb relative to REE, which would remain in the phosphate-bearing minerals. Ma (personal communication, 1977) suggested that such a process could explain the middle REE depletion pattern of the felsite since middle REE are preferentially partitioned into phosphate minerals (Nagasawa, 1970). The uncertainty is how much phosphate minerals is required in the parent. In arguing against fractional crystallization, Hess et al. (1975) calculated that fractionation of more than 6 weight percent whitlockite from a parent granitic melt would be required to produce the observed K/REE ratios, constraining the parental magma to be ≥ 4 weight percent P_2O_5 . Inasmuch as no lunar granite has been found with P_2O_5 contents this high, Hess et al. (1975) reject the fractional crystallization process for lack of a suitable parent. Partial melting is, of course, quite a different process, and it is not clear what modal abundances of phosphate minerals are required in the pre-impact protolith to produce the observed K/REE. Certainly, the smaller the amount of partial melting, the less apatite and/or whitlockite would be required to remain in the residue. Therefore, the contribution of partial melting to the

unusual composition of the felsite cannot be discounted on compositional grounds alone. The very low modal abundance of phosphate minerals in the quartzofeldspathic rocks does, however, argue against this hypothesis, and it would seem necessary to postulate more whitlockite or apatite in the felsite protolith than is found in these clasts.

Clearly, the felsite and the black breccia groundmass represent extreme lunar compositions, but, unfortunately, the complexities and vagaries of the processes attending impact events makes the relative significance of SLI, impact mixing, volatilization, and partial melting extremely difficult to evaluate. SLI may well have played a significant role in the petrogenesis of either or both the black breccia groundmass and felsite, but its chemical signature may have been overprinted by subsequent impact-related processes.

Rb-Sr SYSTEMATICS

Although some petrographic data were employed by the Lunatic Asylum in their interpretation of the Rb-Sr systematics of 12013, strong petrographic and compositional constraints on the natures and inter-relationships of the various lithologies did not yet exist. It is now possible to reassess the isotopic data in view of the following observations. (1) The black and the gray breccias are extremely different in terms of dominant clastic and melt components, and thermal histories, and, therefore, must be considered separately in evaluating the Rb-Sr isotopic systematics of 12013. (2) Chemical equilibrium was achieved on only a local scale in both breccias. In the black breccia, chemical equilibration between the clasts and groundmass melt has only affected

the outer few microns of clasts, and, therefore, the black breccia must be considered a mixture of chemically and isotopically unequilibrated clasts and groundmass. Recrystallization in the gray breccia is more extensive, but incomplete reactions of large olivine clasts and feldspar indicate that chemical disequilibrium in places exists over distances greater than 50-100 μ m. Therefore, chemical and isotopic equilibrium between feldspar and clasts may have been approached, but cores of larger clasts may never have equilibrated with the feldspar. (3) Mixing of clastic and melt components is extremely thorough in both breccias so that it is impossible to handpick fragments that are \geq 500 mg in size and that sample exclusively feldspar or black breccia groundmass. Therefore, there are probably no isotopic data for either of the two melt components in 12013, and most analyses, excluding handpicked mineral separates, were probably made on mixtures of clasts and feldspar or black breccia groundmass.

The following discussion will be directed at Figure 32, which is an Rb-Sr evolution diagram for 12013 including all the Lunatic Asylum data and selected analyses by Hubbard et al. (1970) and Schnetzler et al. (1970). No attempt was made to correct interlaboratory biases. The data by Hubbard et al. (1970) and Schnetzler et al. (1970) were included only to underscore specific points presented below, and the discussion of the Rb-Sr systematics will be based almost entirely on the data of the Lunatic Asylum. Each data point is numbered corresponding to a description offered in Table 20; the first 23 points also have sample descriptions published by the Lunatic Asylum (Albee et al., 1970).

Black Breccia

The data for the black breccia consist of points 3, 4, 5, 6, 7,

8, 22, 23, and 26, and are similar to data for aphanite clasts for other breccias. Points 3, 4, 5, and 6 are mineral separates. The higher $^{87}\text{Sr}/^{86}\text{Sr}$ of points 4 and 5 relative to the other black breccia points is due to the presence of small amounts of feldspar. It is noteworthy that all the other data, excluding point 3, which is very near the vertical axis, plot far to the left of the 4.52 AE "isochron." These points define a linear array with a slope that would correspond to an age of > 5.0 AE if they defined an internal isochron for the black breccia. Similar, impossibly old "isochrons" have been measured for aphanite clasts associated with feldspars in breccia 83215 by Compston et al. (1977), who suggested that the arrays were mixing lines between a low-Rb component with a primitive $^{87}\text{Sr}/^{86}\text{Sr}$ and a high-Rb "excess-age" component. The low-Rb component was suggested to be the ANT-suite clasts that comprise a large portion of the aphanite clasts in 83215. The "excess-age" component was suggested to be either the groundmass melt or plagioclase mineral clasts from a "crystalline" feldspar that were relatively abundant in the aphanites. In the first case, a high $^{87}\text{Sr}/^{86}\text{Sr}$ ratio but low-Rb content could have been produced in the groundmass melt by Rb loss during the impact event(s) that formed the aphanites or by preferential melting of a portion of the target material that was "enriched in a low Rb/Sr mineral such as plagioclase by normal crystal fractionation" (Compston et al., 1977). In the second case, the plagioclase clasts could have been the low Rb/Sr portion of a feldspar with a high initial $^{87}\text{Sr}/^{86}\text{Sr}$.

In the specific case of the 12013 black breccia, there is evidence that both plagioclase fragments related to the quartzofeldspathic clasts and the groundmass contribute to the "excess-age" component. Calcic

plagioclase and pyroxene mineral clasts, which dominate the clast population, would be expected to have low Rb and low $^{87}\text{Sr}/^{86}\text{Sr}$ ratios and are, therefore, likely candidates for the low Rb end-member of the mixing line. The two analyses of plagioclase separates, points 3 and 5, fall at the low-Rb end of the mixing line, and are consistent with this inference. The slightly higher $^{87}\text{Sr}/^{86}\text{Sr}$ of point 5 is readily explained by mixing of two chemically and isotopically different types of plagioclase; a split of the separate is composed of two compositions of plagioclase, $\sim \text{An}_{85}$ and $\sim \text{An}_{50}$. The $\sim \text{An}_{85}$ plagioclase would be expected to plot closer to point 3, which is a higher purity separate of calcic plagioclase. The $\sim \text{An}_{50}$ plagioclase is almost certainly derived from the quartzofeldspathic rocks and must have a higher $^{87}\text{Sr}/^{86}\text{Sr}$ than point 5 if that sample is indeed a mixture of two end-members. Therefore, plagioclase (An_{50-60}) from the quartzofeldspathic rocks is contributing to the "excess-age" component. The close grouping of points 7, 22, and 23, which represent analyses of black breccia fragments that are $\gg 1$ mg in size, suggests that these fragments are mixtures of similar amounts of low-Rb and high-Rb end-members. Considering that the three fragments were selected from different parts of the black breccia and that the mineral and lithic clast population of the black breccia is extremely variable, it seems unlikely that the high-Rb end-member in these samples is part of the clast population. The fact that black breccia samples of this size are uniform mixtures of essentially equal amounts of clasts and groundmass suggests that the groundmass is the dominant high-Rb end-member. Dispersion in the data points from a perfect linear array is attributable to isotopic variation among the mineral and lithic clasts at the low-Rb/Sr end of the mixing

line, and by variations in the relative abundance of groundmass and An₅₀₋₆₀ plagioclase clasts. Admixing of very small but locally variable amounts of felsite would also greatly increase the scatter.

A precise determination of the isotopic composition of the black breccia groundmass is not possible at this time. Detailed calculations that take into account the abundances of clasts, felsite, and groundmass in each sample are not justified because of the large uncertainties in the Rb and Sr concentrations and isotopic ratios of these end-members. In the absence of better data, a crude estimate of the isotopic composition of the groundmass may be made assuming that point 7 represents a fragment that is essentially 50 percent groundmass and 50 percent clasts, that the Sr concentrations in the two end-members are approximately equal, and that the low Rb/Sr end-member is represented by point 3. These assumptions lead to an estimated $^{87}\text{Rb}/^{86}\text{Sr} \cong 0.71$ and $^{87}\text{Sr}/^{86}\text{Sr} \cong 0.75$ for the black breccia groundmass.

Several explanations may be considered to explain why the black breccia groundmass plots to the left of the 4.52 AE "isochron". First, the groundmass may have formed by non-representative impact melting of a differentiated body, during which only low-Rb material was incorporated into the melt. This hypothesis is neither supported nor refuted by any existing data. However, it suffers from being rather ad hoc. Certainly, the unusual isotopic composition of the 12013 black breccia and all the 73215 aphanites could not all be the result of such serendipity. Second, the groundmass melt may have assimilated clastic materials that acquired a low Rb content and high $^{87}\text{Sr}/^{86}\text{Sr}$ by normal fractionation processes. Considering the homogeneity of the black breccia groundmass, however,

and the lack of petrographic evidence for extensive assimilation, this process also seems unlikely. Third, the black breccia groundmass may have suffered Rb-loss while a melt. Gibson and Hubbard (1972) have shown that substantial Rb-loss can occur in breccias that were heated for 1-6 hours at 1050°C. This loss may have occurred by volatilization during and after the impact event, or by partitioning of Rb into the felsite of the gray breccia during a period of liquid immiscibility. Of these two processes, Rb-loss by volatilization appears more likely since the same Rb-Sr signature is found in other aphanites, and the felsite and black breccia groundmass have some elemental abundances that are grossly in contrast to those of coexisting immiscible silicate melts.

Gray Breccia

The Lunatic Asylum data points for the gray breccia consist of "whole rock" points 1, 2, 9, 15, 20, and 21, and density separates 10-14 and 16-19, which were made from the same fragments as 9 and 15, respectively. "Whole rock" datum #9 and density separates 9-14 define an isochron with a slope corresponding to 3.99 ± 0.05 AE and an initial $\text{Sr}^{87}/\text{Sr}^{86}$ of 0.7085 ± 8 , while "whole rock" datum #15 and density separates yield an isochron of 4.01 ± 0.09 AE with an initial $\text{Sr}^{87}/\text{Sr}^{86}$ of 0.7050 ± 9 . The preferred interpretations of the Lunatic Asylum (Albee *et al.*, 1970) are that these are two statistically distinct internal isochrons for two areas of 12013 that evolved from slightly different initial Sr compositions, and that the two ages, which are equivalent, date the time of mixing and crystallization of 12013. These results are in close agreement with an ^{40}Ar - ^{39}Ar age determination of 3.90 ± 0.03 AE for the gray breccia (Turner, 1970), and the interpretations are consistent with the petrographic

constraints discussed above. The portions of the gray breccia from which these data were collected were probably composed of felsite and relatively small clasts so that local isotopic equilibration between clasts and felsite was probably virtually complete at the formation of 12013.

Evolved Rocks at 4.5 AE?

The Lunatic Asylum (Albee et al., 1970) concluded that a highly-evolved high Rb/Sr reservoir (i.e., felsite or felsite progenitor) existed at ~ 4.5 AE based on the high initial $^{87}\text{Sr}/^{86}\text{Sr}$ of the gray breccia internal isochrons (points 9-19) and on a best fit model isochron for "whole samples of light-colored fragments." However, a reconsideration of the existing data suggests that a 4.5 AE age for the felsite or a progenitor of the felsite is not required.

The critical points leading to the Lunatic Asylum's conclusions were as follows. First, 12013 was assumed to have been isotopically inhomogeneous at 4.0 AE. Second, "whole rock" points which plot on or near the 4.52 AE "isochron" were inferred to be measurements made on closed systems that define a whole rock isochron. These consist of four points, 1, 2, 9 and 15. Third, breccia "whole rock" fragments for which the data plot off the 4.52 AE "isochron" (points 20, 21, 7 and 8) were inferred to be isotopically inhomogeneous samples that probably do not represent whole systems due to complex heterogeneties over a scale comparable to the size of these samples. Fourth, density separates on the same samples as "whole rock" points 9 and 15 define statistically distinct "internal isochrons" that are true isochrons recording an event at about 4.0 AE. Fifth, the high initial $^{87}\text{Sr}/^{86}\text{Sr}$ of these isochrons argues for the existence of an old ($\gg 4.0$ AE) Rb-rich reservoir, i.e.,

progenitor to the felsite, at the time 12013 was formed.

Although some petrographic data were employed by the Lunatic Asylum in their interpretation of 12013, strong petrographic and compositional constraints on the natures and relationships of the various lithologies did not yet exist. It is now possible to reassess the isotopic data in view of the following observations. The black and the gray breccias are extremely different in terms of dominant clastic and melt components, and thermal histories, and, therefore, must be considered separately in evaluating the Rb-Sr isotopic systematics of 12013. Chemical equilibrium was achieved on only a local scale in both breccias. In the black breccia, chemical equilibration between the clasts and groundmass melt has only affected the outer few microns of clasts, and, therefore, the black breccia must be considered a mixture of chemically and perhaps isotopically unequilibrated clasts and groundmass. Recrystallization in the gray breccia is more extensive, but incomplete reactions of large olivine clasts and felsite indicate that chemical disequilibrium in places exists over distances greater than 5-100 μm . Therefore, chemical and isotopic equilibrium between felsite and clasts may have been approached, but cores of larger clasts may never have equilibrated with the felsite. Mixing of clastic and melt components is extremely thorough in both breccias so that it is impossible to handpick fragments that are ≥ 500 mg in size and that sample exclusively felsite or black breccia groundmass. Therefore, there are probably no isotopic data for either of the two melt components in 12013. Furthermore, most analyses, excluding handpicked mineral separates 3, 4, 5 and 6, were probably made on mixtures of clasts and felsite or black breccia groundmass.

The Lunatic Asylum (Albee et al., 1970) noted that the high initial Sr of the two internal isochrons defined by data points 9-19 required that the felsite had to be highly evolved at the time it was mixed into the gray breccia. The Lunatics calculated a minimum age for the felsite or its progenitor of >4.3 AE to account for this high initial Sr, assuming that the $^{87}\text{Rb}/^{86}\text{Sr}$ of the felsite was equal to that (~ 2.8) of their highest $^{87}\text{Rb}/^{86}\text{Sr}$ datum, point 21. The error in this calculation is that the fragment on which datum 21 was determined was a mixture of roughly equal amounts of felsite and unrelated low $^{87}\text{Rb}/^{86}\text{Sr}$ material, and the appropriate $^{87}\text{Rb}/^{86}\text{Sr}$ of the felsite is probably about twice that determined for fragment 21. A rough estimate of the appropriate $^{87}\text{Rb}/^{86}\text{Sr}$ may be made using the data of Schnetzler et al. (1970) for point 25 (12013, 10,15). These data include analyses for REE and other minor elements, thus allowing an estimation of the amount of clasts and felsite in the sample by a least-squares balance calculation using a program developed by Reid et al. (1973). Using the estimation of the composition of the felsite in fragment 12013,10,16B by Quick et al. (1977), and assuming the REE, K and Ba concentrations in the clastic component of 12013,10,15 to be negligible, fragment 12013,10,15 is calculated to have been ~ 51 percent felsite and ~ 49 percent clasts. If the $^{87}\text{Rb}/^{86}\text{Sr}$ of the clastic component is taken as the average of high density separate points 14, 17, 18 and 19, the $^{87}\text{Rb}/^{86}\text{Sr}$ of the felsite is estimated to be about 5.1. A reservoir with this $^{87}\text{Rb}/^{86}\text{Sr}$ would only require ~ 0.14 AE to evolve an $^{87}\text{Rb}/^{86}\text{Sr}$ of 0.7085 starting from BABI, and, therefore, the progenitor of the felsite could have formed from a primitive source as recently as 4.14 AE. Clearly, this calculation is strongly dependent on the estimated $^{87}\text{Rb}/^{86}\text{Sr}$ of the

felsite, and the above estimation is approximate at best. However, this calculation probably overestimated the $^{87}\text{Rb}/^{86}\text{Sr}$ of the clastic component because the density separates on which it was based are all contaminated by felsite (Table 21). If the clastic component in 12013,10,15 had a lower $^{87}\text{Rb}/^{86}\text{Sr}$, the estimated $^{87}\text{Rb}/^{86}\text{Sr}$ for the felsite would be >5.1 and the time required to generate $^{87}\text{Sr}/^{86}\text{Sr} = 0.7085$ would be <0.14 AE. Furthermore, an $^{87}\text{Rb}/^{86}\text{Sr} = 5.1$ should be regarded as a lower limit for this calculation because, if the decay of ^{87}Rb is considered, the $^{87}\text{Rb}/^{86}\text{Sr}$ of the felsite must have been closer to 5.4-5.5 at the time of breccia genesis, 4.0 AE ago. On the other hand, the Rb-Sr systematics of the gray breccia is partly controlled by the mixing of unrelated high Rb/Sr felsite and low Rb/Sr clasts. The Lunatic Asylum (Albee et al., 1970) noted that, if the initial Sr of the felsite was higher than that of the clasts, as would be reasonable, then 0.7085 is a minimum initial Sr value for the felsite. If one assumes that complete equilibration of clasts and felsite occurred at the time of mixing, 4.0 AE, then the highest minimum initial Sr for the felsite that can be calculated from the data would be given by the intercept of a line with a slope equivalent to 4.0 AE and passing through point 2. This intercept is $^{87}\text{Sr}/^{86}\text{Sr} = 0.71105$. However, even this initial Sr could be generated by a Rb-rich source with an $^{87}\text{Rb}/^{86}\text{Sr} = 5.1$ in only 0.17 AE. In fact, given an $^{87}\text{Rb}/^{86}\text{Sr} \sim 5.1$, the progenitor of the felsite could evolve a $^{87}\text{Sr}/^{86}\text{Sr} > 0.72$ in 0.3 AE starting from BABI. It, therefore, appears that the felsite, or its progenitor need not have formed prior to ~ 4.17 AE to explain the Rb-Sr data, and that, based on initial Sr considerations, 4.3 AE should probably be regarded as a maximum age for the Rb-rich reservoir from which the

felsite formed rather than a minimum age as suggested by the Lunatic Asylum (Albee et al., 1970).

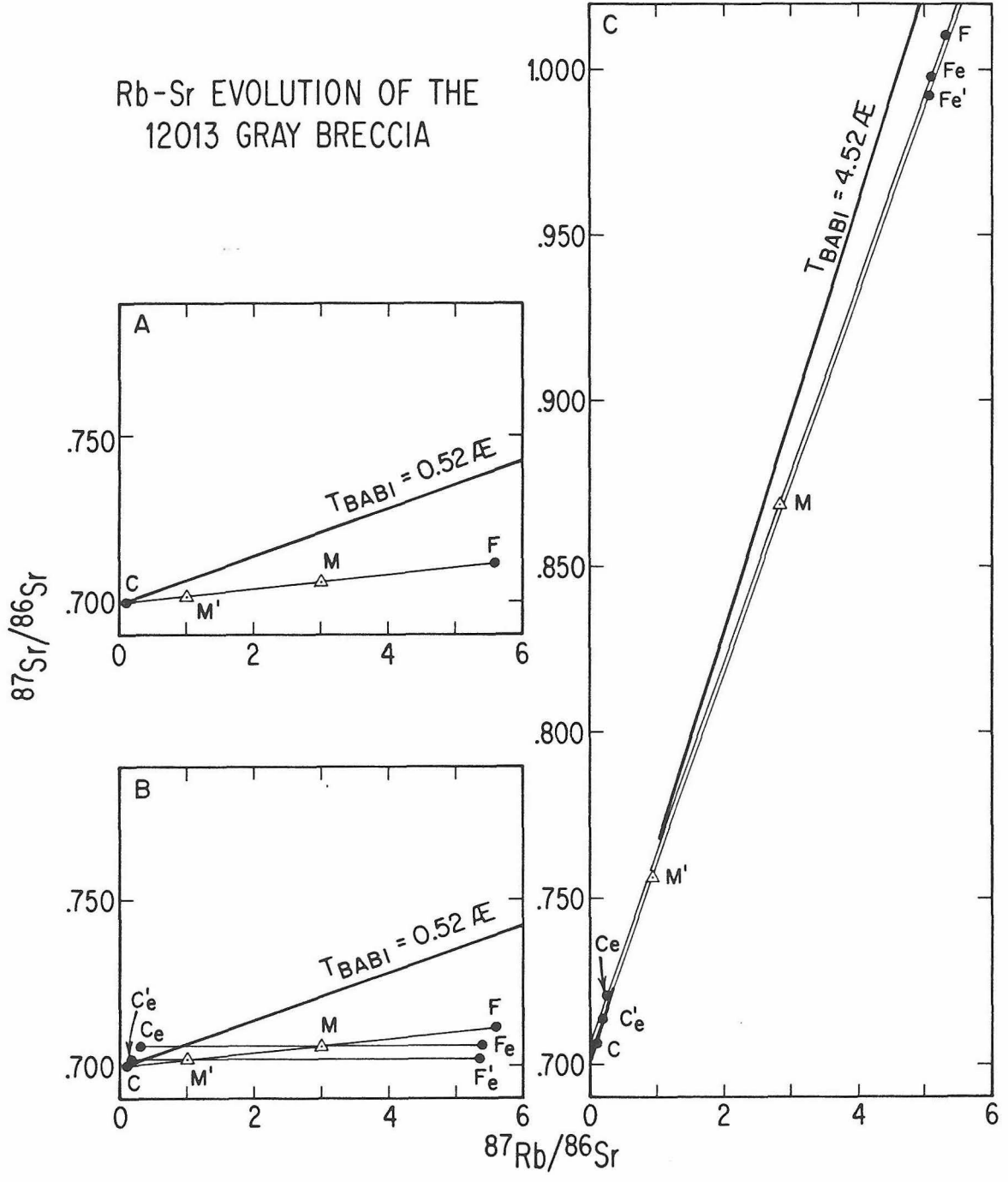
The "whole rock" model isochron for 12013 corresponds to an age of 4.52 ± 0.06 AE and is a least-squares fit to points 1, 2, 9 and 15 that is constrained to pass through BABI. The fact that point 4, a composite sample of handpicked plagioclase grains (Table 21), also falls on this "isochron" was considered as additional evidence in support of a 4.5 AE age. Close inspection of the individual points that define this "isochron", however, suggests that the the data do not warrent a 4.5 AE age interpretation. First, point 4 was measured on grains that were handpicked from black breccia, and, therefore, should not be considered in evaluating an isochron for the gray breccia. Second, points 1 and 9 do not fall on the 4.52 AE "isochron" within the errors for each point (Albee et al., 1970) so that points 15 and 2 are the only "whole rock" points that actually define the "isochron". Third, points 1, 2, 9 and 15 are all mixtures of materials that could be totally unrelated since there is no evidence to link them and their proximity to the 4.52 AE "isochron" is probably fortuitous. Based on their Rb contents, it appears that they are not even representative sample of the gray breccia. The best estimate for the Rb-content of the felsite is ~219 ppm (Quick, et al., 1977). Assuming that the Rb balance of these gray breccia samples is dominated by the felsite, and using the Rb concentration reported by the Lunatic Asylum (Albee, et al., 1970) for points 1, 2, 9 and 15, these samples are all calculated to be composed of <35 percent felsite and >65 percent clasts. Considering that the gray breccia is essentially a 50/50 mixture of clasts and felsite (Quick et al., 1977), points 1, 2, 9 and 15 cannot be considered representative of

the breccia. In fact, points 20 and 21 are measured on samples that are about 50-60 percent felsite by the above lines of reasoning. These points are, therefore, better approximations of "whole rock" samples of the gray breccia. Significantly, these data points plot far off the 4.52 AE model isochron of the Lunatic Asylum. The conclusion that must be reached is that a 4.52 AE age is not required by the data and could be an artifact produced by careful selection and omission of data points.

An alternative explanation, based on the results of this petrographic study, is presented in Figure 35. The isotopic compositions of the components of the gray breccia are estimated in these diagrams for illustrative purposes, but are not presented as unique or even preferred values. The isotopic conditions at ~4.0 AE, at the time of the formation of 12013, are represented in Figure 35A. A felsite melt (F), glass or protolith existed with an inferred isotopic composition of $^{87}\text{Rb}/^{86}\text{Sr}$ of ~5.6 and $^{87}\text{Sr}/^{86}\text{Sr}$ ~0.711 and an unrelated suite of clasts (C) with primitive Sr and a very low $^{87}\text{Rb}/^{86}\text{Sr}$ are mixed together to form mixtures (e.g. M and M1) along the CF join. The mixtures differ only in clast/felsite ratio. Note that the Sr composition of the felsite could have evolved in ~.15 AE from BABI. The clastic component is, in fact, a collection of low Rb/Sr phases and/or rock fragments, dominated by the basalt-gabbro suite and perhaps derived from several unrelated sources. The ages of these materials in this model are constrained only to be <0.52 AE at the time of mixing. Mixtures of clasts and felsite could plot anywhere along the CF join; in the actual case of 12013, there must be some scatter off of a perfect linear array due to isotopic inhomogeneities in the clastic component. At some later time, represented in Figure 35B, isotopic

Figure 35: Model for the Rb-Sr isotopic evolution of the gray breccia of 12013. See text for discussion.

Rb-Sr EVOLUTION OF THE
12013 GRAY BRECCIA



equilibration between the felsite and clasts occurs on a local scale moving clast compositions to C_e and C_e^1 and felsite compositions to F_e and F_e^1 . Complete equilibration in subsystems M and M^1 would result in horizontal joins C_e-F_e and $C_e^1-F_e^1$, respectively, while incomplete equilibration would result in joins with a slight positive slope constrained only to be less than the CF join. If the individual subsystems then evolve as closed systems to the present time, an Rb-Sr evolution diagram (Figure 35C) is produced that is very similar to that determined by the Lunatic Asylum (Albee et al., 1970) for 12013 (Figure 32). The 0.52 AE reference isochron in Figures 35A and 35B has evolved to a 4.52 AE isochron and the modal data points, which retain the same labels, have evolved to new isotopic compositions. Small samples or density separates of subsystems M and M^1 will plot on the C_e-F_e and $C_e^1-F_e^1$ joins respectively and will define statistically distinct, parallel isochrons. Subsystems that are dominated by the elastic component (e.g. M^1) will plot near to the 4.52 AE reference isochron and could fall to the left, right or directly on that line depending on the clast/felsite ratio. These model points would be analogous to data points 1, 2, 9 and 15 in Figure 32. Subsystems that contain more felsite (e.g. M) will plot well off to the right of the 4.52 AE reference isochron and are analogous to points 20, 21 and 25 in Figure 32. Samples of pure felsite (F, F_e and F_e^1) will plot at extremely high $^{87}\text{Rb}/^{86}\text{Sr}$ and are not represented in Figure 32.

The preceding interpretation is essentially that reached by Albee et al. (1970) except that the Rb-Sr isotopic data were explained without resorting to a 4.5 AE "granitic" system. The salient features of the Rb-Sr systematic of the gray breccia may be explained in terms of

mixing and partial equilibration of two or more end members that are not much older than 4.0 AE--say ~4.2 AE for example. This removes some constraints from the source terrane. The clastic and melt components do not have to be consanguineous and the terrane does not have to be extremely ancient. However, neither of these possibilities is completely ruled out.

SOURCE TERRANE

Rock 12013 appears to be exotic to the Apollo 12 landing site. The clast suite is characterized by an abundance of lithologies common in Highlands breccias and a complete absence of mare components. The minimum ages on samples from 12013 are >3.9 AE (Albee et al., 1970; Turner, 1970), which are considerably older than the <3.3 AE ages determined for samples of Apollo 12 mare basalts (Papanastassiou and Wasserburg, 1971; Turner, 1971). The Apollo 12 landing site is located on a high albedo ray that can be seen from outer space and that emanates from the crater Copernicus ~370 km to the north (Shoemaker et al., 1970). It is suggested that 12013 is a sample of Copernican ejecta and that it was transported to the Apollo 12 site.

The rock and mineral fragments and the melt derived lithologies are most similar to materials found in Highlands breccias. Most of the clasts in both breccias were derived from basalt, gabbro norite and "granitic" rocks. The basalt and gabbro clasts are more plagioclase-rich and less Fe-rich than Apollo 12 mare basalts (Beaty et al., 1979; Baldrige et al., 1979); they are texturally and compositionally more similar to Apollo 14 KREEP basalts (e.g. McKay et al., 1979) and to feldspathic basalts in breccia 15205 (Dymek et al., 1974). The quartzofeldspathic

rocks are most similar to the quartz-monzodiotite clast in breccia 15405 (Ryder et al., 1976) and the felsite clasts in Apollo 17 breccias (Ryder et al., 1976; James and Hammastrom, 1977). The norite clasts are mineralogically and compositionally similar to fragments that are common components of Highlands breccias (e.g. 73255; James and McGee, 1979). The ANT-suite melt-rocks and hornfels and the plagioclase porphyries are similar to clasts in Highlands regolith breccias such as 66075 (Quick et al., 1978). The clast populations of both breccias are dominated by fragments of coarse-grained rocks that have apparently experienced only one major episode of impact deformation and one recrystallization event. These rocks may have been derived from a complex crystalline basement in the lunar crust at the time of the impact that formed 12013.

The clasts of the basalt-gabbro suite may represent samples of different basaltic intrusions or flows. This would explain the systematic variation in mineralogy and mineral chemistry in the suite. Figure 11 illustrates that the major element composition of the basalts can be derived from that of the gabbros by subtraction of olivine. Therefore, the clasts of gabbro and olivine gabbro may be samples of a basaltic body that were enriched in cumulate olivine, and the finer grained clasts may have been derived from the more rapidly cooled parts of the same intrusion or flow. Indeed, large variations in grain size and texture have been recognized in samples from single flows from the Apollo 11 site (Beaty and Albee, 1978).

The quartzofeldspathic rocks in the black breccia and the tonalite clast in the gray breccia may have been derived from a single "granitic" body or from unrelated but similar "granitic" intrusions. The actual bulk composition of the protolith is uncertain because the rock fragments are

only slightly larger than the grain sizes of the constituent minerals. This introduces a problem of considerable sampling error that is reflected by the great modal diversity of these clasts (Table 13). Also, if the felsite in these clasts was formed by in situ partial melting, it is not clear how much felsite melt may have been removed, thereby biasing the bulk composition toward that of the more refractory plagioclase-rich residue. Therefore, the protolith may have been any of a wide spectrum of "granitic" rocks, including granite, tonalite and quartz monzonite.

The norite clasts are also small relative to the grain sizes of their constituent minerals and, therefore, may be biased samples of their protolith. The two norite clasts that were analyzed (Tables 3 and 14, Figures 10 and 11) have significantly different bulk compositions although the similarities in mineral compositions indicate that they were derived from similar sources. The bulk analyses fall close to a mixing line between plagioclase and low-Ca pyroxene indicating that the observed differences in bulk composition are essentially due to differences in modal abundances of pyroxene and plagioclase. An additional sampling error may have resulted from nonrepresentative sampling of olivine by these clasts. Olivine ($Fo_{>60}$) occurs in trace amounts as small ($<100 \mu\text{m}$) grains in the norite clasts, but much larger olivine mineral clasts with similar compositions occur in the black breccia as mineral clasts. If these mineral clasts were derived from the same protolith as the norite, than protolith may have contained substantially more olivine that is preserved in the lithic clasts. Such a protolith would still be essentially noritic rock composed mostly of plagioclase and pyroxene with only minor amounts of olivine.

There is some evidence that suggests that the clasts of the basalt-gabbro suite, the quartzofeldspathic rocks and the norite clasts were derived from intrusive bodies in the lunar crust at the time of the impact event that formed 12013. The coarse-grain size of the quartzofeldspathic rocks and the norite suggests that the protoliths were plutonic. Similarly, the coarse-grain size of the gabbro could indicate a plutonic origin or, perhaps, formation in the slowly cooled interior of a thick dike or flow; the finer-grained basalts could have been derived from chilled border zones. All of these lithic clasts appear to have undergone one episode of shock deformation, dominated by crushing, followed by one episode of recrystallization and/or partial melting. FeNi metal is totally absent from the basalt, gabbro and norite clasts are extremely rare in the quartzofeldspathic rocks, suggesting that admixing of meteoritic material, as would be expected in a regolith, was not significant. It is tempting to speculate that the protoliths of these lithic clasts were all genetically related rocks that formed part of a single, large differentiated body.

Such a model has been proposed by Ryder (1976) for the lithic clast population in 15405. Ryder (1976) suggested that the clasts of medium-K KREEP basalt in 15405 were derived from KREEP basalt flows or sills that capped a large "KREEP norite pluton" or from a basaltic unit that was analogous to the upper border group of the Skaergaard intrusion. The clasts of quartz monodiorite in 15405 were postulated to be late stage "granitic" differentiates produced by normal process of fractional crystallization, and the bulk of the complex was postulated to be a KREEP norite, although no clasts of this lithology were found in 15405. On first consideration, the lithic clast population in 12013 appears to fit a similar model for all three lithologies, basalt, norite and granitic

rocks, are present. However, these three groups of rocks appear to be distinct and unrelated on the basis of mineral and bulk compositions.

The quartzofeldspathic rocks appear to be unrelated to either the basalt-gabbro suite or the norites. This is strongly suggested by the absence of clasts with intermediate compositions and the low-K contents of the basalts, gabbros and norites (Tables 3 and 14). Extreme fractionation of the parental magmas of the basalt-gabbro suite and the norites would be required to produce a K-rich granitic melt. Furthermore, substantial compositional gaps exist between the plagioclase in the quartzofeldspathic rocks and the plagioclase in the basalts, gabbros and norites. This observation and virtual absence of K-rich mesostasis in the basalt, gabbro and norite clasts, suggests that the parental magmas of these rocks crystallized completely before they evolved to alkali and silica-rich compositions.

A genetic relationship between the norites and the basalt-gabbro suite is more difficult to evaluate because of the uncertainties in the bulk composition of the norite protolith. This problem is further complicated by the fact that the norites could be fragments of cumulate rocks and, therefore, not representative of melt compositions. Some arguments can be made, however, on the basis of mineral chemistry. Olivine in the norite is much more magnesian than olivine in the basalt-gabbro suite. Also, although there is some compositional overlap, the plagioclase and pyroxene in the norite are generally much more Ca-rich and Mg-rich, respectively, than their counterparts in the basalt-gabbro suite. Therefore, these two groups of rocks appear mineralogically distinct and unrelated. Furthermore, Figure 14 illustrates that the norite

clasts have bulk compositions that are distinct from those of the basalt-gabbro suite in the Al_2O_3 vs. MgO and FeO vs. MgO diagrams. Since the compositions of the basalts and gabbros may be related by olivine fractionation, it is logical to look for a similar fractionation scheme to relate the norites to these rocks. From the oxide-oxide diagrams, however, it is clear that addition or subtraction of olivine from the norite clasts will not move their bulk compositions into the basalt-gabbro field or even on trend with the basalts and gabbros. Similarly, addition or subtraction of plagioclase or pyroxene of the composition measured in the norite will not move the bulk compositions into the trend of the basalts and gabbro. No petrographic or chemical evidence exists for evolution of the norite or the basalt-gabbro parental magmas controlled by fractionation of another phase such as chromite or ilmenite. It seems unlikely that the norite and basalt-gabbro clasts are genetically related.

Clastic materials that are apparently "exotic" to the 12013 source terrane make up small amounts of both breccias. These fragments include devitrified maskelynite, ANT-suite rocks and hornfels, and plagioclase porphyry rocks. All of these are common constituents of regolith breccias, such as 66075 (Quick *et al.*, 1978) and 61175 (Winzer, *et al.*, 1977), and have textures that result from multiple episodes of brecciations, melting and thermal metamorphism associated with impact events.

Numerous models for the source terrane of 12013 are possible. The model presented here postulates a terrane composed of crystalline basement rocks possibly capped by basaltic lava flows with a thin overlying regolith of "exotic" materials with histories of multiple impact events. The similar lithic components in the two breccias are not necessarily

genetically related. Mineralogic constraints allow that basalts and gabbros in both breccias may have been derived from a single thick flow or intrusion or from numerous similar but unrelated basaltic bodies. The quartzofeldspathic rocks in both breccias may be samples of a single "granitic" body, or from different bodies. Mineralogic and bulk chemical considerations, however, strongly suggest that the quartzofeldspathic rocks, basalt-gabbro rocks and norite constitute three genetically unrelated suites of intrusions and/or flows. The felsite may have formed by melting of a protolith similar to the quartzofeldspathic rocks. The breccia groundmass was the product of impact melting of a basaltic protolith that was highly enriched in incompatible elements.

A meteorite impact into such a complex terrane formed the 12013 breccia. The different clast populations, principal melt components and thermal histories of the gray and black breccias suggest that these two lithologies were derived from different parts of this parts of this terrane and were juxtaposed while in flight. Possibly, the impact event involved near simultaneous impact of several meteorites and the two breccias were thrown together by the mixing of ejecta splashes from adjacent craters.

SYNTHESIS

Characterization and Petrogenesis

Rock 12013 is best interpreted as a complex mixture of two polymict, impact generated breccias--one black, the other gray. These lithologies are made up of contrasting clastic and melt-derived components and apparently underwent somewhat different thermal histories. Nevertheless,

the high abundances of incompatible elements in both breccias, similarity of some clastic components, and limited shock histories suggest that these breccias were formed by the same impact or near simultaneous impacts into a single unusual terrane.

The black breccia is a fragment-laden melt-rock formed by mixing cold, impact-derived mineral and lithic clasts with superheated impact melt of basaltic composition. The clast population is dominated by plagioclase mineral clasts and lithic fragments of quartzofeldspathic and noritic rocks. The impact-melt crystallized to form a vesicular, extremely fine grained ($< 5\mu\text{m}$) intergrowth of plagioclase, pyroxene, ilmenite, and phosphate minerals.

The gray breccia was also formed as a mixture of melt and impact-derived mineral and lithic clasts. Mixing of these two components, however, was much less thorough than in the black breccia. The melt was "granitic" in composition and its patchy distribution suggests that it may have been incorporated as blobs of viscous melt or formed in situ by melting of fragments of glass or "granitic" protolith. The clast population is dominated by mineral and lithic fragments of basalt and gabbro rocks.

The temperatures reached in the two breccias were high. Thermal modeling on fragment-laden melt-rocks (Simonds et al., 1976) suggests that the black breccia formed by mixing superheated melt at an initial temperature of 1700-2000°C with cold clasts; the initial equilibration temperature for this mixture is estimated to have been ~ 1150-1180°C. Subsequent cooling must have been rapid because recrystallization of clasts is limited to the outer few microns. Most of the material in the

gray breccia must have been heated to temperatures of $> 1000^{\circ}\text{C}$ to account for the pervasive distribution of granitic melt. The basaltic and gabbro clasts did not melt indicating that the temperature did not exceed 1100°C . Recrystallization of clasts is more extensive than in the black breccia suggesting that the clasts in the gray breccia may have been hotter when incorporated into the gray breccia.

The breccias were juxtaposed while still partially molten and plastic. Smooth cusped contacts between them and between felsite and groundmass in the black breccia suggest that two melts--a felsic and a mafic melt--coexisted but did not mix. Therefore, it appears that both breccias were generated and brought together within a very short time. Rare components are absent from both breccias. The clastic and melt components alike are most similar to materials found in breccias from the Highlands. This fact, in addition to the old age (≥ 4.0 AE) of the components of 12013, suggest that the rock is exotic to the 12013 landing site.

Both breccias were derived from terranes that were extremely enriched in incompatible elements. Furthermore, although they differ in detail, the clast populations of both breccias contain norite, pathic rocks, and gabbro or basalt. These similarities suggest that the breccias were derived from materials in close proximity of the time of the breccia forming impact.

The source terrane for the clasts must have been composed of at least four unrelated components. The coarse grain size of the norite and quartzofeldspathic rocks suggests that they were derived from plutonic protoliths. The basalts and gabbros may have been derived from dikes

intruded into those plutonic rocks or from overlying basaltic flows. A limited number of clasts with complex polymetamorphic history (maskelynite, hornfels melt-rocks) may have been derived from an overlying regolith. Mineralogic petrographic and chemical constraints suggest that (1) the norites, (2) the quartzofeldspathic rocks, (3) the basalts and gabbros, and (4) the hornfels and melt-rocks were four genetically unrelated components in the terrane.

The origin of and relationship between components is problematic. Textures and major element compositions suggest that they could be immiscible melts. This high concentration of incompatible elements does suggest some genetic link, but details of their trace element chemistries suggest that they are unrelated. Details of their major element chemistries rule out conventional petrologic relationships such as fractional crystallization. Possibly the two melts were produced by impact melting of two genetically related protoliths and the chemical fingerprint of that relationship has been modified by the impact process. The mineralogy and mineral chemistry of the quartzofeldspathic rocks and the felsite suggest that those clasts may be fragments of the felsite protolith. No such candidate exists in the clast population for the protolith of the black breccia groundmass; fragments of the basalt-gabbro suite are too low in REE, P, U, Th, etc., to be representative of the groundmass protolith although their major element chemistries are appropriate.

It is suggested the 12013 formed during single impact, or perhaps two or more closely spaced impacts, into a terrane of norite and quartzofeldspathic plutonic rocks, basaltic and gabbro hypabyssal or extrusive rocks, and a regolith cover. This source terrane was extremely

unusual by lunar standards in that it contained lithologies with extremely high concentrations of incompatible elements. The clasts in gray breccia were derived from a part of the terrane dominated by basalt and gabbro while the black breccia was derived from a part of the terrane dominated by norite and quartzofeldspathic rocks. The two breccias were mixed together violently; a reasonable site for this mixing could be the ejecta cloud from the impact.

Most of the radiometric clocks were reset in both breccias at about 4.0 AE. This is interpreted as the age of the breccia forming event in light of the intense heating that occurred at that time.

The Lunatic Asylum (Albee et al., 1970) interpreted the Rb-Sr data to indicate that the felsite was an extremely ancient component and possibly as old as 4.5 AE. This hypothesis was reexamined using petrographic constraints that are now available. This date would be extremely significant because it would date the oldest known formation of lunar granitic rocks and thereby place important constraints on early lunar evolution. While 4.5 AE age remains a possible age for the felsite or its protolith and many of the components of 12013, it is not required to explain the Rb-Sr data. The salient features of these data can all be explained by a model in which the felsite (or its protolith) was no older than 4.15-4.2 AE.

Rock 12013 must have been affected by a mild recrystallization event at about ≤ 1.4 AE (Burnett et al., 1970) corresponding to the oldest fission track ages. 12013 is clearly exotic to the Apollo 12 landing site, and this age may date its transport to the mare surface. The Apollo 12 landing site is situated on a ray from the crater Copernicus and it has been suggested that 12013 may in fact have been ejected from

that crater (Eberhardt et al., 1973). Exposure ages suggest that 12013 was resident at or near the lunar surface for only about a total of 55 m.y..

REFERENCES

- Ahrens, T.J. and O'Keefe, J.D. (1972) Shock melting and vaporization of lunar rocks and minerals. *Moon*, 4, 214-219.
- Albee, A.L., Beaty, D.W., Chodos, A.A. and Quick, J.E. (in press) Quantitative analysis of petrographic properties and of mineral compositions with a computer-controlled energy dispersive system. Proc. 12th Nat'l Conf. Electron Probe Anal.
- Albee, A.L., Burnett, D.S., Chodos, A.A., Haines, E.L., Huneke, J.C., Papanastassiou, D.A., Podosek, F.A., Russ, G.P. and Wasserburg, G.J. (1970) Mineralogic and isotopic investigations on lunar rock 12013. *Earth Planet. Sci. Lett.*, 9, 137-163.
- Albee, A.L., Quick, J.E. and Chodos, A.A. (1977) Source and magnitude of errors in "broad-beam" analysis (DBA) with the electron probe (abstract). In Lunar Science VIII, 7-9. The Lunar Science Institute, Houston.
- Alexander, E.C. Jr. (1970) Rare gasses from stepwise heating of lunar rock 12013. *Earth Planet. Sci. Lett.*, 9, 201-208.
- Andersen, C.A. and Hinthorne, J.R. (1972) U, Th, Pb and REE abundances and Pb 207/206 ages of individual minerals in returned lunar materials by ion microprobe mass analysis (abstract). In Lunar Science III, 21-23. The Lunar Science Institute, Houston.
- Anderson, D.H. (1970) Introduction. The preliminary examination and preparation of lunar sample 12013. *Earth Planet. Sci. Lett.*, 9, 94-102.
- Baldrige, W.S., Beaty, D.W., Hill, S.M.R., and Albee, A.L. (1979) The petrology of the Apollo 12 pigeonite basalt suite. Proc. Lunar Planet. Sci. Conf. 10th, 141-180.
- Bansal, B.M., Gast, P.W., Hubbard, N.J., Nyquist, L.E., Rodes, J.M., Shih, C.-Y., and Wiesmann, H. (1973) Lunar rock types (abstract). In Lunar Science IV, 48-50. The Lunar Science Institute.
- Beaty, D.W. and Albee, A.L. (1978) Comparative petrology and possible genetic relations among the Apollo 11 basalts. Proc. Lunar Sci. Conf. 9th, 359-463.
- Beaty, D.W., Hill, S.M.R., Albee, A.L., Baldrige, W.S. (1979) Apollo 12 feldspathic basalts 12031, 12038 and 12072: Petrology, comparison and interpretations. Proc. Lunar Planet. Sci. Conf. 10th, 115-140.
- Blanchard, D.P., Jacobs, J.W., Branon, J.C., and Haskin, L.A. (1976) Major and trace element compositions of matrix and aphanitic clasts from consortium breccia 73215. Proc. Lunar Sci. Conf. 7th, 2179-2187.
- Blanchard, D.P., Branon, J.C., Jacobs, J.W., and Haskin, L.A. (1977) Major and trace element abundances in anorthositic gabbro clasts and

- a clast of K-rich felsite from consortium breccia 73215 (abstract). In Lunar Science VIII, 124-126. The Lunar Science Institute, Houston.
- Burnett, D., Monnin, M. Seitz, M., Walker, R., and Yuhas, D. (1971) Lunar astology--U-Th distributions and fission-track dating of lunar samples. Proc. Lunar Sci. Conf. 2nd, 1503-1519.
- Burnett, D.S., Monnin, M. Seitz, M., Walker, R., Woolum, D., and Yuhas, D. (1970) Charged particle track studies in lunar rock 12013. Earth Planet. Sci. Lett., 9, 127-137.
- Chodos, A.A., Albee, A.L., Gancarz, A.J., and Laird, J. (1973) Optimization of computer-controlled quantitative analysis of minerals. Proc. 8th Nat. Conf. on Electron Probe Analysis. New Orleans, Louisiana.
- Chodos, A.A., Albee, A.L., and Quick, J.E. (1977) The use of energy dispersive analysis for the study of phase aggregates (abstract). 12th Nat. Conf. on Electron Probe Analysis. Boston, Massachusetts.
- Compston, W., Foster, J.J., and Gray, C.M. (1977) Rb-Sr systematics in clasts and aphanites from consortium breccia 73215. Proc. Lunar Sci. Conf. 8th, 2525-2549.
- Crawford, M.L. and Hollister, L.S. (1974) KREEP basalt: a possible partial melt from the lunar interior. Proc. Lunar Sci. Conf. 5th, 399-419.
- Drake, M.J., McCallum, I.S., McKay, G.A., and Weill, D.F. (1970) Mineralogy and petrology of Apollo 12 sample no. 12013: A progress report. Earth Planet. Sci. Lett., 9, 103-123.
- Dymek, R.F., Quick, J.E., and Albee, A.L. (1977) The role of silicate liquid immiscibility: Constraints from a terrestrial example (abstract). In Lunar Science VIII, 272-274. The Lunar Science Institute, Houston.
- Dymek, R.F., Albee, A.L., and Chodos, A.A. (1976) Petrology and origin of Boulders #2 and #3 Apollo 17 Station 2. Proc. Lunar Sci. Conf. 7th, 2335-2374.
- Dymek, R.F., Albee, A.L., and Chodos, A.A. (1974) Glass-coated soil breccia 15205: selenologic history and petrologic constraints on the nature of its source region. Proc. Lunar Sci. Conf. 5th, 235-260.
- Eberhardt, P., Geiss, J. Grogler, N. and Stettler, A. (1973) How old is the crater Copernicus? Moon, 8, 104-114.
- Gay, P.; Brown, M.G.; Rickson, K.O. (1970) Mineralogic studies of lunar rock 12013,10. Earth Planet. Sci. Lett., 9, 103-123.
- Gibbons, R.V., Horz, F. Morris, R.V., and Thompson, T.D. (1975) Petrographic and ferromagnetic resonance studies of experimentally shocked regolith analogues. Proc. Lunar Sci. Conf. 6th, 3143-3171.

- Gibson, E.K., and Hubbard, N.J. (1972) Thermal volatilization studies on lunar samples. Proc. Lunar Sci. Conf. 3rd, 2003-2014.
- Grieve, R.A.F., Plant, A.G., and Dence, M.R. (1974) Lunar impact melts and terrestrial analogs: Their characteristics, formation and implications for crustal evolution. Proc. Lunar Sci. Conf. 5th, 261-273.
- Haines, E.L., Albee, A.L., Chodos, A.A., and Wasserburg, G.J. (1971) Uranium-bearing minerals of lunar rock 12013. Earth Planet. Sci. Lett. 12, 145-154.
- Hess, P.C., and Rutherford, M.J. (1974) Elemental fractionation between immiscible melts (abstract). In Lunar Science V, 328-330. The Lunar Science Institute, Houston.
- Hess, P.C., Rutherford, M.J., Guillemette, R.M., Ryerson, F.J., and Tuchfeld, H.A. (1975) Residual products of fractional crystallization of lunar magmas: An experimental study. Proc. Lunar Sci. Conf. 6th, 895-909.
- Hinthorne, J.R. and Andersen, C.A. (1974) Uranium-lead and lead-lead ratios in lunar samples 66095 and 12013 by ion microprobe mass analysis (abstract). In Lunar Science V, 337-339. The Lunar Science Institute, Houston.
- Hollister, L.S. (1975) Evolution of the moon between 4.6 and 3.3 AE. Proc. Lunar Sci. Conf. 6th, 1159-1178.
- Hubbard, N.J., Gast, P.W., and Wiesmann, H. (1970) Rare earth, alkaline and alkali metal and 87/86 Sr data for subsamples of lunar sample 12013. Earth Planet. Sci. Lett., 9, 181-184.
- James, O.B. (1970) Petrology of lunar microbreccia 12013,6. U.S. Geol. Survey Interagency Report: Astrogeology 23.
- James, O.B. (1975) Petrography of the matrix of light gray (consortium) breccia 73215 (abstract). In Lunar Science VI, 438-440. The Lunar Science Institute, Houston.
- James, O.B. (1976) Petrology of aphanitic lithologies in consortium breccia 73215. Proc. Lunar Sci. Conf. 7th, 2145-2178.
- James, O.B. and Hammarstrom, J.G. (1977) Petrology of four clasts from consortium breccia 73215. Proc. Lunar Sci. Conf. 8th, 2459-2494.
- James, O.B. and McGee, J.J. (1979) Consortium breccia 73255: Genesis and history of two coarse-grained "norite" clasts. Proc. Lunar Planet. Sci. Conf. 10th, 713-743.
- Laul, J.C., Keays, R.R., Ganapathy, R. and Anders, E. (1970) Abundance of 14 trace elements in lunar rock 12013,10. Earth Planet. Sci. Lett., 9, 211-215.

- Laul, J.C. and Schmitt, R.A. (1973) Chemical composition of Luna 20 rocks and soil and Apollo 16 soils. *Geochim. Cosmochim. Acta* 37, 927-942.
- LSPET (1970) Preliminary examination of lunar samples from Apollo 12. *Science* 167, 1325-1339.
- Ma M.-S., Murali, A.V., Schmitt, R.A., Quick, J.E., and Albee, A.L. (1977) Major, minor and trace element compositions of two petrologically significant lithologies in 12013 (abstract). In *Lunar Science VIII*, 602-604. The Lunar Science Institute, Houston.
- McKay, G.A., Wiesmann, H. Bansal, B.M. and Shih, C.-Y. (1979) Petrology, chemistry and chronology of Apollo 14 KREEP basalts. *Proc. Lunar Planet. Sci. Conf. 10th*, 181-205.
- Morgan, J.W., Ehmann, W.D. (1970) Lunar rock 12013: O, Si, Al and Fe abundances. *Earth Planet. Sci. Lett.*, 9, 164-169.
- Nagasawa, H. (1970) Rare earth concentrations in zircons and apatites and their host dacites and grainites. *Earth Planet. Sci. Lett.*, 9, 139-144.
- Nyquist, L.E., Wiesmann, H., Shih, C.-Y., and Bansal, B.M. (1977) REE and Rb-Sr analysis of 15405 quartz-monzodiorite (super KREEP) (abstract). In *Lunar Science VIII*, 738-740. The Lunar Science Institute, Houston.
- Papanastassiou, D.A. and Wasserburg, G.J. (1971) Lunar chronology and evolution from Rb-Sr studies of Apollo 11 and 12 samples. *Earth Planet. Sci. Lett.*, 11, 37-62.
- Powell, B.N., Dungan, M.A., and Weiblen, P.W. (1975) Apollo 16 feldspathic melt rocks: Clues to the magmatic history of the lunar crust. *Proc. Lunar Sci Conf. 6th*, 415-433.
- Quick, J.E. and Albee, A.L. (1976) 12013 revisited--Two clast-laden melts (abstract). In *Lunar Science VII*, 712-714. The Lunar Science Institute, Houston.
- Quick, J.E., Albee, A.L., Ma, M.-S., Murali, A.V. and Schmitt, R.A. (1977) Chemical compositions and possible immiscibility of two silicate melts in 12013. *Proc. Lunar Sci. Conf. 8th*, 2153-2189.
- Quick, J.E., Brock, B.S., and Albee, A.L. (1978) Petrology of Apollo 16 breccia 66075. *Proc. Lunar Planet. Sci. Conf. 9th*, 921-939.
- Reid, M.J., Gancarz, A.J., and Albee, A.L. (1973) Constrained least-squares analysis of petrologic problems with an application to lunar sample 12040. *Earth Planet. Sci. Lett.* 17, 433-445.
- Roedder, E., and Weiblen, P.W. (1970) Lunar petrology of silicate melt

- inclusions, Apollo 11 rocks. Proc. Apollo 11 Lunar Sci. Conf., 801-837.
- Roedder, E. and Weiblen, P.W. (1971) Petrology of silicate melt inclusions. Apollo 11 and 12 and terrestrial equivalents. Proc. Lunar Sci. Conf. 2nd, 507-528.
- Roedder, E. and Weiblen, P.W. (1972) Petrographic features and petrologic significance of melt inclusions in Apollo 14 and 15 rocks. Proc. Lunar Sci. Conf. 3rd, 251-279.
- Rutherford, M.J. and Hess, P.C. (1978) Immiscible silicate melts in 12013? (abstract). In Lunar and Planet. Sci. Conf. IX, 987-989. The Lunar and Planetary Institute, Houston.
- Rutherford, M.J., Hess, P.C., Ryerson, F.J., Campbell, H.W., and Dick, P.A. (1976) The chemistry, origin and petrogenetic implications of lunar granite and monzonite. Proc. Lunar Sci. Conf. 7th, 1723-1740. differentiated pluton. Earth Planet. Sci. Lett., 29, 255-268.
- Ryder, G. Stoesser, D.B., Marvin, U.B., and Bower, J.F. (1975) Lunar granites with unique ternary feldspar. Proc Lunar Sci. Conf. 6th, 435-449.
- Ryerson, F.J., and Hess, P.C. (1975) The partitioning of trace elements between immiscible silicate melts (abstract). EOS (Trans. Amer. Geophys. Union) 56, 470.
- Schairer, J.F. and Bowen, N.L. (1938) The system leucite-diopside-silica. Am. J. Sci., 35A, 289-309.
- Schnetzler, C.C., Philpotts, J.A., and Bottino, M.L. (1970) Li, K, Rb, Sr, Ba, and rare-earth concentrations, and Rb-Sr age of lunar rock 12013. Earth Planet. Sci. Lett., 9, 185-192.
- Shoemaker, E.M., Batson, R.M., Bean, A.L., Conrad, C. Jr., Dahlem, D.H., Goddard, E.N., Hait, M.H., Larson, K.B., Schaber, G.G., Schleicher, D.L., Sutton, R.L., Swann, G.A., and Waters, A.C. (1970) Geology of the Apollo 12 landing site. In Apollo 12: Preliminary Science Report. National Aeronautics and Space Administration.
- Simonds, C.H. (1975) Thermal regimes in impact melts and the petrology of the Apollo 17 Station 6 boulder. Proc. Lunar Sci. Conf. 6th, 641-672.
- Simonds, C.H., Phinney, W.C., McGee, P.E., and Cochran, A. (1978) West Clearwater, Quebec impact structure, part I: Field geology, structure and bulk chemistry. Proc. Lunar Planet. Sci. Conf. 9th, 2633-2658.
- Simonds, C.H., Warner, J.L., Phinney, W.C., and McGee, P.E. (1976) Thermal model for impact breccia lithification: Manicouagan and the moon. Proc. Lunar Sci. Conf. 7th, 2509-2528.
- Tatsumoto, M. (1970) U-Th-Pb age of Apollo 12 rock 12013. Earth Planet Sci. Lett., 9, 193-201.

- Tatsumoto, M. and Unruh, D.M. (1976) KREEP basalt age: Grain by grain U-Th-Pb systematics study of the quartz monzodiorite clast 15405,88. Proc. Lunar Sci. Conf. 7th, 2107-2129.
- Taylor, H.P. and Epstein, S.J. (1970) Oxygen and silicon isotope ratios of lunar rock 12013. Earth Planet. Lett., 9, 208-211.
- Taylor, S.R., Gorton, M.P., Muir, P., Nance, W., Rudowski, R, and Ware, N. (1973) Lunar highlands composition: Apennine Front. Proc. Lunar Sci. Conf. 4th, 1445-1459.
- Taylor, S.R. and Jakes, P. (1974) The geochemical evolution of the moon. Proc. Lunar Sci. Conf. 5th, 2387-1306.
- Taylor, S.R., Kaye, M., Muir, P., Nance, W., Rudowski, R., and Ware, N. (1973) Composition of the lunar uplands: Chemistry of Apollo 14 samples from Fra Mauro. Proc. Lunar Sci. Conf. 3rd, 1231-1249.
- Turner, G. (1970) ^{40}Ar - ^{39}Ar age determinations of lunar rock 12013. Earth Planet. Sci., 9, 177-181.
- Turner, G. (1971) ^{40}Ar - ^{39}Ar ages from the lunar maria. Earth Planet. Sci. Lett., 11, 169-191.
- Wakita, H. and Schmitt, R.A. (1970) Elemental abundances in seven fragments from lunar rock 12013. Earth Planet. Sci. Lett., 9, 169-176.
- Wakita, H., Schmitt, R.A., and Rey, P. (1970) Elemental abundances of major, minor and trace elements in Apollo 11 lunar rocks, soil and core samples. Proc. Apollo 11 Lunar Sci. Conf., 1685-1717.
- Watson, E.B. (1976) Two-liquid partition coefficients: Experimental data and geochemical implication. Contrib. Mineral. Petrol., 56, 119-134.
- Winzer, S.R., Nava, D.F., Meyerhoff, M., Lindstrom, D.J., Lum, R.K.L, Lindstrom, M.M., Schuhmann, P., Schuhmann, S., and Phipotts, J.A. (1977) The petrology and geochemistry of impact melts, granulites and hornfels from consortium breccia 61175. Proc. Lunar Sci. Conf. 8th, 1943-1966.
- Yoder, H.S. (1973) Contemporaneous basaltic and rhyolitic magmas. Amer. Mineral. 58, 153-171.